Oxford Brookes University

Department of Biological and Medical Sciences

The structure and dynamics of the plant endoplasmic reticulum

Author:

Charlotte Pain

Supervisors:

Dr. Verena Kriechbaumer

Prof. Chris Hawes

Dr. Mark Fricker

A thesis submitted for the degree of

Doctor of Philosophy

September 6, 2019

In memory of

Chris Hawes

Abstract

The structure and dynamics of the plant endoplasmic reticulum (ER) are highly variable, and are thought to be linked to the role of the ER in protein secretion. Neither the mechanisms behind the biogenesis and maintenance of the ER structural components, nor the mechanisms governing the specific functions of the ER structural subdomains have been fully elucidated. One of the primary challenges in the work of understanding these mechanisms is quantifying ER structure and dynamics in order to identify proteins and physiological conditions that affect the ER.

The contiguous nature of the ER, alongside the occurrence of ER dynamics over a range of scales and orientations, presents a unique challenge for quantification. This challenge is tackled by creating a software package, AnalyzER, designed to quantify the variations in the structure of the ER and dynamics in response to a variety of ER structural modifying techniques. This package is designed to be as widely applicable as possible, answering a wide variety of questions often posed regarding novel ER resident proteins, whilst also being capable of analysing images generated through a variety of image capture methods. This analysis was used to elucidate the function of novel ER shaping proteins.

At the start of this work, two protein families have previously been described as playing a key role in maintaining or modifying plant ER structure: root hair defective 3 (RHD3) a proposed ER fusogen, and the reticulon protein family which mediates ER membrane curvature. Here we introduce a new family of ER shaping proteins: the Lunapark protein family, comprised of AtLNP1 and 2. AtLNP1 localises specifically to ER cisternae whilst AtLNP2 localises throughout the ER structure. Reducing AtLNP1 and 2 transcription results in a reduced

proportion of cisternae within the ER whilst over-expression results in cisternae induction, with the cisternae induced by AtLNP1 and 2 possessing different structural characteristics.

Finally the first steps were made to investigate the dynamics of single particle movement within the ER membrane. In the future this will be used to inform on how the structure of the ER may affect its function in the context protein dynamics within the different ER structural subdomains.

Glossary

ANOVA Analysis of variance.

BFA Brefeldin A.

cDNA Complementary deoxyribonucleic acid.

CFP Cyan fluorescent protein.

co-IP Co-immunoprecipitation.

cv Cultivar.

DNA Deoxyribonucleic acid.

DTT Dithiothreitol.

EDM Euclidian distance map.

EDTA Ethylenediaminetetraacetic acid.

EPCS Endoplasmic reticulum plasma membrane contact site.

ER Endoplasmic reticulum.

ERAD Endoplasmic reticulum associated degradation.

ERES Endoplasmic reticulum exit site.

FRAP Fluorescence recovery after photobleaching.

FRET-FLIM Förster resonance energy transfer - fluorescence lifetime imaging.

FWHM Full width half maximum.

GaAsP Gallium arsenide phosphide.

GFP Green fluorescent protein.

GI-SIM Grazing incidence structural illumination microscopy.

GIMP GNU image manipulation.

GLCM Grey level co-occurrence matrix.

GUI Graphical user interface.

Lat B Latrunculin B.

LB Luria-Bertani.

LUT Lookup Table.

MANOVA Multivariate analysis of variance.

MES 2-(N-Morpholino)ethanesulfonic acid.

mRNA Messanger ribonucleic acid.

MS Murashige and Skoog medium.

OD Optical density.

paGFP Photo-activateable green fluorescent protein.

PCR Polymerase chain reaction.

PM Plasma membrane.

PMT Photomultiplier tube.

PSF Point spread function.

RFP Red fluorescent protein.

RHD Retciulon homology domain.

RNA Ribonucleic acid.

ROI Region of interest.

RT-PCR Reverse transcription polymerase chain reaction.

RTN Reticulon.

SBFSEM Serial block face scanning electron microscopy.

SPT Single particle tracking.

sptPALM single-particle-tracking photoactivation localization microscopy.

STED Stimulated emission depletion microscopy.

T-DNA Transfer DNA.

TAE Tris Acetate-EDTA buffer.

TIRF Total internal reflection.

TM Transmembrane domain.

TMD Transmembrane domain.

UB10 Ubiquitin-10 (promoter).

UPR Unfolded protein response.

VAEM Variable angle epifluorescence microscopy.

ZF Zinc finger.

ZIO Zinc iodide-osmium tetroxide (stain).


US OUT:



Acknowledgements

Throughout my PhD I have received a great deal of support, assistance and encouragement. I'd first like to thank my supervisors, Verena Kriechbaumer and Chris Hawes, for their unwavering support throughout this process, both of whom have been a fantastic source of knowledge and advice. I'd particularly like to thank Verena for keeping a straight face through my winding lab meetings, constant cake supply and not making me feel too bad about breaking a very expensive microscope. I will always be grateful for the opportunity to work as a member of the Chris Hawes lab, he is greatly missed by all of us.

I'd like to thank several collaborators, particularly Mark Fricker for his patience and guidance in all things software related. I am grateful to Emily Breeze for the use of her constructs which have been instrumental in this work. In addition Frances Tolmie, who provided continued assistance in the lab and was a much needed helping hand in cleaning up the majority of my messes. I would also like to thank Anna Frej, for helping provide the plant material that made this work possible, and her endless patience with my messy bench and off-key singing. Both Chris Tynan and Stan Botchway provided a great deal of support and expertise in the field of single particle microscopy and tracking.

For aiding and abetting I'd like to thank all the members of plant cell biology at Oxford Brookes, past and present, particularly Vanessa de Sousa Vieira, Bisa Andov, Tatiana Spatola Rossi, Stefan Wojik, Maike Kittelmann and Joe McKenna.

Finally I'd like to thank my parents for their numerous attempts at pronouncing 'endoplasmic reticulum' and their constant support throughout this PhD.

This work was supported by the BBSRC and the Oxford Interdisciplinary Bioscience Doctoral Training Partnership

Contents

Glossary **7**

1 Literature Review **31**

1.1 Overview 32

1.2 The function of the plant endoplasmic reticulum 33

1.2.1 The role of the ER in protein synthesis 33

1.2.2 The ER as a metabolite reservoir and a metabolon scaffold . 34

1.3 The structure of the plant ER 36

1.3.1 The ER is composed of morphologically and dynamically distinct subdomains 36

1.3.2 ER cisternae: Kístē or Kista? 37

1.3.3 Wild-type variation in ER structure 39

1.3.4 Maintaining ER structure 40

1.3.5 The geometry of the plant ER 42

1.4 The dynamics of the ER 44

1.4.1 Characterising the movement of the ER 44

1.4.1.1 ER particle dynamics 45

1.4.1.2 ER remodelling 46

1.4.1.3 Bulk flow 47

1.4.1.4 Inherent ER movement 48

1.4.2 The role of the actinomyosin cytoskeleton in ER dynamics . 50

1.5 Modifying ER structure and dynamics 51

1.5.1 Ectopic protein expression 51

1.5.1.1 Root hair defective 3 52

1.5.1.2 The reticulon protein family 53

1.5.1.3 The Lunapark protein family 54
1.5.2 Modified ER lipid content 56
1.5.3 Pharmacological treatments 57
1.5.3.1 Brefeldin A 57
1.5.3.2 Latrunculin B 57
1.5.4 Stress 58
1.6 Visualising cellular components using confocal microscopy 59
1.6.1 ER fluorescent protein markers 59
1.6.2 Lipid dyes to mark the ER 60
1.6.3 Actin markers 60
1.7 Quantifying the structure and dynamics of the ER 63
1.7.1 The importance of ER structure and dynamics quantification 63
1.7.2 Methods to quantify ER structure and dynamics 66
1.8 The relationship between the ER and other organelles 68
1.9 Aims 69

2 Materials and methods **70**

2.1 Plant material 71
2.1.1 Wild-type plant material and standard growth conditions . . 71
2.2 Microscopy 71
2.2.1 General 71
2.2.2 Confocal microscopy 72
2.2.3 VAEM microscopy 73
2.2.4 Light sheet microscopy 74
2.3 Plant transformation and transfection methods 75
2.3.1 Generation of arabidopsis stable lines 75
2.3.2 Transient flourescent protein expression in tobacco leaf epidermal cells 76

2.4 Rhodamine B staining for ER visualisation 76
2.5 Drug and stress treatments 77
2.6 RT-PCR analysis of wild-type and mutant lines 77
2.6.1 RT-PCR on wild-type seedlings 77
2.6.2 Confirmation of T-DNA insertion lines 79
2.7 Cloning and expression plasmids 80
2.7.1 Gateway cloning 80
2.7.2 Expression plasmids used 81
2.7.3 Transformation of competent agrobacterium 83
2.8 Truncation cloning 84
2.9 ImageJ analysis of Rhodamine B stained ER 85
2.10 AnalyzER analysis of ER structures 89
2.11 Single particle tracking 89
2.11.1 Single particle tracking diagram generation 90

3 AnalyzER **91**

3.1 Introduction: The challenges and goals of plant ER analysis 92
3.1.1 The plant ER is a complex, contiguous pleomorphic structure 92
3.1.2 ER parameters are influenced by each other 95
3.1.3 The aims of AnalyzER development 97
3.2 Methods and results 98
3.2.1 Image structure and quality requirements for optimal ER analysis 98
3.2.1.1 The importance of good quality images 98
3.2.1.2 Sufficient marker expression 98
3.2.1.3 Minimizing sample drift in z 99
3.2.1.4 Image acquisition enhancement - the airyscan . . . 100
3.2.2 Image structure considerations 100

3.2.2.1 Image saturation 100
3.2.2.2 Pixel density and Niquist sampling 101
3.2.2.3 Averaging 102
3.2.2.4 High quality images vs. sufficient rate of capture . 103
3.2.3 Developing a pipeline for plant ER segmentation - AnalyzER 103
3.2.4 Using AnalyzER 106
3.2.4.1 Segmenting the ER 106
3.2.5 Precision-recall analysis of the accuracy of ER structure . . 108
3.2.6 Estimation of ER tubule diameter 110
3.2.7 Preventing mis-classification of 'large' tubules 113
3.2.8 Calculating the structural parameters of the plant ER 114
3.2.9 Extending the range of AnalyzER: analysis of the time domain 114
3.2.9.1 Optical flow captures the rate of 'ER movement' . 114
3.2.9.2 Pharmacological interventions and stress modify ER dynamics 118
3.2.9.3 Persistency mapping of static elements 122
3.2.10 Quantifying fluorophore distributions throughout the ER . . 125
3.2.10.1 Quantifying fluorophore distributions: tubules . . . 125
3.2.10.2 Quantifying fluorophore distributions: cisternae perimeters 128
3.2.10.3 Quantifying fluorophore distributions: cisternae and texture analysis 130
3.2.11 Multivariate analysis of modified ER structure and dynamics 134
3.3 Discussion 138

4 Lunapark proteins and ER structure 141

4.1 Introduction 143
4.1.1 The Lunapark protein family 143

4.1.2 The arabidopsis Lunapark proteins 144
4.2 Results 146
4.2.1 The sub-cellular localisation of the arabidopsis Lunapark proteins 146
4.2.2 Transcription of Lunapark throughout development 147
4.2.3 Identification of T-DNA insertion lines with reduced AtLNP1 and AtLNP2 transcription 150
4.2.4 Reduced Lunapark expression results in modified ER structure 154
4.2.5 AnalyzER confirms modified ER structure in mutant plants 161
4.2.6 Native expression of AtLNP1-GFP in *lnp1* restores normal ER structure 166
4.2.7 Candidate domains for Lunapark function 168
4.2.7.1 N-terminal truncations 169
4.2.7.2 C-terminal truncations 173
4.2.8 AtLNP1 over-expression can induce densely tubulated regions of ER not seen on AtLNP2 over-expression 174
4.2.9 AtLNP1 and 2 induce cisternae with different lumenal characteristics 177
4.2.9.1 AtLNP1 aggregates perturb the ER lumen and can be identified by confocal imaging with Airyscan detector 177
4.2.9.2 AtLNP2 over-expression induces cisternae with an entirely contiguous lumen 179
4.2.10 AtLNP1 over-expression results in structurally aberrant cisternae formation, visible using VAEM 183
4.2.11 Reticulon proteins reveal regions of membrane curvature within ER cisternae 189
4.2.12 AtLNP1 does not co-localise with AtRTN1 or 3 191
4.2.13 AtLNP2 co-localises with AtRTN1 and 3 192

4.2.14 AtLNP1 and AtLNP2 truncations with altered ER localisation show modified co-localisation with AtRTN1 and AtRTN3 . . 193
4.2.15 AtLNP1 punctae can be recruited to form cisternae 197
4.3 Discussion 207
4.3.1 Arabidopsis has two Lunapark proteins that behave differently 207
4.3.2 Reduction of AtLNP1 and 2 transcription affects ER structure in arabidopsis 208
4.3.3 Candidate domains for AtLNP1 and 2 function 210
4.3.4 AtLNP1 and 2 over-expression produces different 'types' of cisternae 215
4.3.5 Several AtLNP1 and 2 truncations that show modified ER localisation also show modified AtRTN1 and 3 distributions 221
4.3.6 AtLNP1 forms cisternae through aggregate conglomeration as opposed to expansion 222

5 Protein movement in the plant ER 224

5.1 Introduction 224
5.2 Results 227
5.2.1 Achieving appropriate fluorophore density 227
5.2.2 The 3D nature of the plant ER 230
5.2.3 Modifying ER structure and movement for single particle movement analysis 232
5.2.3.1 Single particle movement in a modified ER structure background 232
5.2.3.2 Separating single particle movement from gross ER remodelling 234
5.2.4 Single particle movement in the plant ER 244
5.3 Discussion 251

6 General discussion **258**

6.1 On image quantification 258

6.2 On the role of the Lunapark proteins in ER structure 263

6.3 Lunapark structure in relation to protein function 269

6.4 Cisternae formation 273

6.5 SPT in the plant ER 274

7 Future Work **276**

7.1 Extending the applications of AnalyzER 276

7.2 Exploring the mechanism behind Lunapark function 278

7.2.1 Establishing Lunapark membrane topology 278

7.2.2 Creation of modified Lunapark proteins to investigate protein domain function 279

7.2.3 Generating an AtLNP2 knockout line 282

7.3 The biogenesis of cisternae 282

7.3.1 Proteomics analysis 283

7.4 Single particle movement in the ER 284

7.4.1 Exploring new methods 284

8 Publications resulting from this work **285**

8.1 Publications 285

8.2 Oral presentations 285

8.3 Poster presentations 286

9 Supplementary data **317**

S1 Chapter 3 - AnalyzER 317

S1.1 Graph parameters 317

S1.2 Tubule edge parameters 318

S1.3 Node parameters 320

S1.4 Tubule morphology parameters 321
S1.5 Cisternae morphology parameters 322
S1.6 Intensity-based cisternae metrics 323
S1.7 Texture metrics 325
S1.8 Morphological metrics of polygonal regions 325
Morphological metrics of polygonal regions 325
S2 Chapter 4 - The Lunapark proteins and ER structure 327
S3 Chapter 5 - Protein movement in the plant ER 338
S4 Supplementary movie list 342

List of Figures

1.1 The three proposed structures of mammalian ER cisternae 38

1.2 A comparison of the forces exerted by R- and S-proteins 42

1.3 A theoretical minimum spanning tree vs Steiner tree solution for the connection of 4 nodes 43

1.4 Proposed classification of plant ER 'movement' 49

1.5 Commonly employed plant actin marker strategies 62

2.1 Comparison of Epifluorescence, VAEM and TIRF microscopy 74

2.2 Endoplasmic reticulum (ER) network analysis workflow for Arabidopsis *lnp1* and *amilnp1lnp2* mutants. 88

3.1 Structural components of the plant ER 94

3.2 A schematic demonstration of the mutual sensitivity of ER structure and dynamics parameters to each other 96

3.3 Minimizing Z-drift 99

3.4 Pixel density and image structure 101

3.5 Averaging and image structure 102

3.6 The AnalyzER and AnalyzER statistical analysis graphical user interfaces 105

3.7 Using AnalyzER to segment the ER network 108

3.8 Mapping precision-recall analysis 109

3.9 Measuring ER widths using SBF-SEM 112

3.10 Identification and handling of ER punctae 113

3.11 Methods for calculating optical flow 115

3.12 Optical flow outputs 116

3.13 Diagrammatic representation of coherent flow 117

3.14 Latrunculin B and heat shock can be used to modify ER dynamics 119
3.15 Using optical flow analysis to assess global ER remodelling after treatment with Lat B and heat shock 120
3.16 Components of speed distributions after treatment with Lat B and heat shock 121
3.17 ER persistency mapping 123
3.18 Distributions of persistency 124
3.19 Co-expression of RFP-AtRTN1 and GFP-HDEL in tobacco leaf epidermal cells 126
3.20 Quantitative analysis of tubule morphology with RFP-AtRTN1 over-expression 127
3.21 The distribution of fluorophores normal to the cisternae perimeter . 129
3.22 Background image texture vs ER cisternae texture 132
3.23 GLCM analysis of modified ER cisternae 133
3.24 Multivariate analysis of modified ER structures 136
3.25 Results of multiple planned comparisons of ER metrics 137

4.1 The structure and localisation of AtLNP1 an 2 after transient expression in tobacco 145
4.2 Stable over-expression of P_{UBQ10}::AtLNP1-GFP and P_{UBQ10}::AtLNP2-GFP in arabidopsis 147
4.3 Identifying *AtLNP1* and *AtLNP2* transcription across different arabidopsis tissues and developmental stages 149
4.4 T-DNA insertion lines, and insertion positions, available for *AtLNP1* and *AtLNP2* 152
4.5 RT-PCR confirmation of reduced Lunapark transcription in Lunapark T-DNA insertion mutants 153
4.6 Reduced Lunapark expression modifies ER structure 156

4.7 *lnp1* and *lnp2* have modified ER structures 158
4.8 *amilnp1lnp2* shows a modified ER structure in cotyledonary cells . . 159
4.9 The effect of reduced Lunapark expression on ER tubule length . . 160
4.10 *amilnp1lnp2* shows modified polygonal region size 162
4.11 *amilnp1lnp2* shows modified tubule lengths 163
4.12 *amilnp1lnp2* shows modified cisternae persistency 164
4.13 *amilnp1lnp2* shows modified cisternae dynamics 165
4.14 The modified structure of *lnp1* can be reversed by expression of AtLNP1 under its native promoter 167
4.15 VAEM reveals native localizations of AtLNP1 168
4.16 N-terminal AtLNP1 truncations localisation 171
4.17 N-terminal AtLNP2 truncations localisation 172
4.18 Localisation of C-terminal zinc finger truncations 173
4.19 AtLNP1, but not AtLNP2 over-expression results in the formation of many short tubules, independent of expression levels 175
4.20 Densely reticulated regions of ER are produced on over-expression of AtLNP1 176
4.21 AtLNP1 over-expression affects the distribution of the ER lumenal marker RFP-HDEL but not the ER membrane marker CXN-mCherry 178
4.22 Negative correlation between AtLNP1 localisation and RFP-HDEL intensity 179
4.23 The distribution of GFP-HDEL within AtLNP2 induced cisternae . 182
4.24 Over-expression of AtLNP1 causes an altered cisternae morphology that can be captured using VAEM 185
4.25 Stable over-expression of P_{UB10}::AtLNP1-GFP in arabidopsis captured by VAEM 186
4.26 Stable over-expression of P_{UB10}::AtLNP2-GFP in arabidopsis captured by VAEM 187

4.27 Stable over-expression of P_{UB10}::AtLNP2-GFP induces cisternae that do not have an altered morphology 188
4.28 RFP-AtRTN1 and RFP-AtRTN3 localisation within GFP-CXN induced cisternae 190
4.29 RFP-AtRTN1 and RFP-AtRTN3 localisation within AtLNP1-GFP induced cisternae 191
4.30 RFP-AtRTN1 and RFP-AtRTN3 localisation within AtLNP2-GFP induced cisternae 192
4.31 Localisation of the AtLNP1 truncation AtL1T1-clover and RFP-AtRTN3 195
4.32 Localisation of the AtLNP2 truncation AtLNP2-ZF-clover and RFP-AtRTN3 196
4.33 Potential mechanisms for ER cisternae formation by AtLNP1 198
4.34 Light sheet imaging of stable P_{UBQ10}::AtLNP1-GFP expression in arabidopsis vs transient P_{UBQ10}::AtLNP1-GFP expression in tobacco 199
4.35 3 hour light sheet phototoxicity test 200
4.36 3 hour light sheet photobleaching test 201
4.37 Cisternae formation by aggregation of AtLNP1-GFP punctae (a) . . 203
4.38 Cisternae formation by aggregation of AtLNP1-GFP punctae (b) . . 204
4.39 Persistency of nascent AtLNP1-GFP generated cisternae 206
4.40 The localisation of selected N- and C- terminal truncations in relation to underlying sequence divergence between AtLNP1 and 2 211
4.41 A comparison of the forces exerted by R- and S-proteins 218
4.42 Schematic representation of the structure of cisternae induced by AtLNP1 and 2 over-expression 219
4.43 Cropped image taken from Nixon-Abell *et al.* (2016) showing variation in the reticulon content of cisternae in COS-7 cells 220

5.1 The different components of ER dynamics 226

5.2 Optimizing expression levels for single molecule visualization 228
5.3 Only a portion of particles are in the correct focal plane for single particle tracking in the ER 231
5.4 Spectral bleedthrough caused by dual colour infiltration 233
5.5 The effect of ER remodelling on detected particle movement 235
5.6 Representative images of the effect of Lat B treatment on ER structure 237
5.7 Representative images of the effect of actin marker expression on ER structure 241
5.8 Transient over-expression of GFP-FABD2 can cause ER fragmentation 243
5.9 Schematic representation of particle structure within the ER membrane 245
5.10 SPT using TrackMate 248
5.11 Automated SPT results 249
5.12 Comparison of single particle track speed and displacement 250

7.1 Pairwise alignment of the first 20 amino acids of AtLNP1 and 2 . . 280
7.2 The design of future modified AtLNP1 and 2 proteins 281

S1 Predicted expression of AtLNP1 and AtLNP2 327
S2 The geometry of cisternae in Col-0 expressing GFP-HDEL alone and alongside reduced *AtLNP1* and *AtLNP2* transcription 328
S3 Co-localisation of AtL1T3-Clover, AtL2T2-Clover and AtL2T3-Clover with RFP-ATG8 329
S4 Co-expression of AtL1T5-Clover, AtL2T4-Clover and AtL2T5-Clover with the Golgi body marker ST-RFP/CFP 330
S5 BLAST results of mammalian Rtn4 against the arabidopsis genome 331
S6 AtRTN1 and AtRTN3 localisation within AtLNP1 and AtLNP2 cisternae 332
S7 Adaxial side of a tobacco leaf three days after infiltration 334

S8 Variable expression levels of GFP-AtRTN1 and RFP-AtLNP2 across cells 335
S9 Full montage of cisternae formation by aggregation of AtLNP1-GFP punctae (a) 336
S10 Full montage of cisternae formation by aggregation of AtLNP1-GFP punctae (b) 337
S11 The effect of stable over-expression of actin marker constructs on the ER of arabidosis cotelydon cells (7 days post germination) . . . 338
S12 The effect of stable over-expression of actin marker constructs on the ER of arabidosis root cells (7 days post germination) 339
S13 Cullen an Frey graph of likely data distribution types 340
S14 Q-Q plot of maximum track speed and track displacement 341

List of Tables

1.1 Identification of ER structure modifiers over the last 10 years 64

2.1 Common fluorophore/dye excitation and detected emission wavelengths 72
2.2 Primers designed for RT-PCR analysis of AtLNP1, AtLNP2 and actin 78
2.3 Primers used for T-DNA insertion confirmation 80
2.4 Expression vectors used in this work 81
2.5 Gateway primers designed for Lunapark truncations 84

3.1 Calculating the properties of a GLCM 131

4.1 Results summary of tested T-DNA insertion lines 154
4.2 N-terminal AtLNP1 and 2 truncations and their localisations 170
4.3 AtLNP1 and AtLNP2 truncations that show a modified localisation within the ER 194
4.4 Summary of the salient features and localisation of all created truncations 213
4.5 Summary of the localisation of AtLNP1 and 2 truncations and whether they co-localise with AtRTN1 and 3 222

5.1 The effect of different concentrations of Lat B on ER structure and dynamics 238
5.2 The effect of different actin markers on ER structure and dynamics 240
5.3 A summary of the challenged of applying VAEM to SPT in the plant ER 255

6.1 Summary of the features of AtLNP1 and 2 induced cisternae 267

6.2 Summary of the localisation and key features of all AtLNP1 and 2 truncations 272

1 | Literature Review

Contents

1.1 Overview 31

1.2 The function of the plant endoplasmic reticulum . . . 32

1.2.1 The role of the ER in protein synthesis 32

1.2.2 The ER as a metabolite reservoir and a metabolon scaffold 33

1.3 The structure of the plant ER 35

1.3.1 The ER is composed of morphologically and dynamically distinct subdomains 35

1.3.2 ER cisternae: Kístē or Kista? 36

1.3.3 Wild-type variation in ER structure 38

1.3.4 Maintaining ER structure 39

1.3.5 The geometry of the plant ER 41

1.4 The dynamics of the ER 42

1.4.1 Characterising the movement of the ER 43

1.4.2 The role of the actinomyosin cytoskeleton in ER dynamics 48

1.5 Modifying ER structure and dynamics 49

1.5.1 Ectopic protein expression 49

1.5.2 Modified ER lipid content 54

1.5.3 Pharmacological treatments 54

1.5.4 Stress 55

1.6 Visualising cellular components using confocal microscopy 57

1.6.1 ER fluorescent protein markers 57

1.6.2 Lipid dyes to mark the ER 58

1.6.3 Actin markers 58

1.7 Quantifying the structure and dynamics of the ER . . 61

1.7.1 The importance of ER structure and dynamics quantification 61

1.7.2 Methods to quantify ER structure and dynamics 64

1.8 The relationship between the ER and other organelles 66

1.1 Overview

First identified in the 1960's by electron microscopy (Porter and Machado, 1960), the endoplasmic reticulum (ER) is a ubiquitous subcellular organelle found throughout the eukaryotic kingdom. Composed of a lipid bilayer, the ER forms a complex network of variable size and morphology (Harris and Chrispeels, 1980; Stephenson and Hawes, 1986) that extends throughout the areas of the cell that are occupied by cytoplasm (Porter and Machado, 1960). The total area of the cell occupied by the ER varies between species and cell type (Harris and Chrispeels, 1980; Stephenson and Hawes, 1986; Shibata *et al.*, 2006; Terasaki *et al.*, 2013) and plays an essential role in proteins synthesis (Jan *et al.*, 2014), metabolite storage (Chen *et al.*, 2002; Zhang *et al.*, 2013), metabolon scaffolding (Hawes *et al.*, 2015) and immunity (Eichmann and Schäfer, 2012). The structure and dynamics of the ER are complex and highly variable. Though little is known about the specific function of the different structural subdomains within the ER, the structure of the ER has been implicated in ER function in both plants and animals (Harris and Chrispeels, 1980; Stephenson and Hawes, 1986; Shibata *et al.*, 2006; Terasaki *et al.*, 2013). Three classes of ER shaping proteins have thus far been identified: the Lunapark (Kriechbaumer *et al.*, 2018) and reticulon protein families (Tolley *et al.*, 2008; Sparkes *et al.*, 2010) and root hair defective 3 (RHD3) a putative plant ER fusogen (Chen *et al.*, 2011; Lee *et al.*, 2013). ER dynamics, however, are largely controlled by the underlying actinomyosin cytoskeleton (Griffing *et al.*, 2014; Sparkes *et al.*, 2009a). Modifications to ER structure and dynamics can be induced by a range of pharmacological treatments (Sparkes *et al.*, 2009a; Runions *et al.*, 2006), ectopic protein expression (Griffing *et al.*, 2014), stresses such as mechanical stress and oomycete infection (Takemoto *et al.*, 2003) and plant development (Ridge *et al.*, 1999). Quantifying the modifications to the ER under these conditions is essential

to understand how the ER plays a key role in plant responses.

1.2 The function of the plant endoplasmic reticulum

1.2.1 The role of the ER in protein synthesis

The ER is the site of synthesis for integral membrane and secreted proteins (Jan *et al.*, 2014). Synthesis of these proteins requires localisation of ribosome complexes to the cytosolic face of the ER resulting in the docking of an mRNA:ribosome complex to the ER membrane. The translation of secretory and integral membrane proteins begins in the cytosol, ribosomes containing these mRNAs are recruited to the surface of the ER via a sequence within the nascent peptide, which is recognised and bound by the signal recognition particle (SRP) (Walter *et al.*, 1981). Translation continues on the ER surface and the nascent polypeptide co-translationally enters the ER lumen via the translocon (Rapoport, 2007), a channel composed of Sec proteins that spans the lipid bilayer (Deshaies *et al.*, 1991). During this time or just after translation (Braakman and Hebert, 2013), the short signal peptide of the nascent protein is cleaved via a signal peptidase, freeing the protein and enabling it to enter the ER lumen (Deshaies *et al.*, 1991). If the protein is meant to become an integral membrane protein, determined by the presence of a sequence of hydrophobic residues within the amino acid sequence of the protein itself, the process of translocation is paused to allow the protein to be shifted laterally, in order to become anchored within the lipid bilayer (Blobel, 1980; Fewell and Brodsky, 2009). Proteins that are not destined to become integral membrane proteins, but to enter the secretory pathway or the lumen of other

organelles, instead begin to be transported through the ER. Following protein synthesis and translocation into the ER lumen, proteins destined for secretion must be properly folded and modified via interactions with chaperones and folding enzymes. These modifications include N-linked glycosylation, disulphide bond formations and oligomerization (Braakman and Hebert, 2013). If the protein is designed for secretion, after modification the protein is released by chaperones and packaged for transfer (van der Zand *et al.*, 2012).

1.2.2 The ER as a metabolite reservoir and a metabolon scaffold

The plant ER is appressed to the periclinal plant cell wall and is distributed across the entire cell surface. It therefore acts as an ideal reservoir for critical cellular signalling components including hormone receptors, signalling complexes and calcium (Chen *et al.*, 2002; Friml and Jones, 2010; Zhang *et al.*, 2013). The large surface area of the ER also enables it to act as a scaffold for concentrating components of metabolic pathways, acting to regulate the organisation of metabolic pathways and enabling the mixing of metabolic products throughout the cytoplasm (Hawes *et al.*, 2015).

The entire family of known ethylene receptors (ETR1, ERS1, ETR2, ERS2, EIN4) localises to the ER (Chen *et al.*, 2002), which provides numerous advantages for signal transduction. Primarily the localisation of ethylene receptors to the ER is energetically efficient as the receptors are not required to go through the entire secretory pathway and the receptors are rapidly delivered to their site of action (Chen *et al.*, 2002). The presence of ethylene receptors on the ER may also allow for local regulation of other ER-dependent processes. For example, chitinase accumulation, triggered by ethylene signalling on pathogenesis is calcium

dependent (Raz and Fluhr, 1992) and the localisation of ethylene receptors to the ER may play a key role in rapid release of calcium from the ER in response to pathogens (Chen *et al.*, 2002).

In addition to hormone reservoirs, regulatory complexes such as the WAVE/SCAR (WASP family verprolin homologous/suppressor of cyclic AMP receptor) complex are also localised to the ER (Zhang *et al.*, 2013). This particular regulatory complex acts in partnership with the Actin-Related Protein (ARP)2/3 complex and controls actin-dependent morphogenesis throughout a variety of tissues at different developmental stages (reviewed Zhang *et al.* (2013)). The ER may be involved in the regulation of W/SCR complex as the upstream regulator of the WAVE/SCAR complex, SPK1, is localised to ER- exit sites (ERES) (Zhang *et al.*, 2010). In addition two of the key WAVE/SCAR inactive subunits, NAP1 (nucleosome assembly protein 1) and SCAR2 are located on the ER surface. Controlled release of calcium from the ER, which acts as a reservoir of Ca^{2+} (Bush, 1995) is essential for maintaining cellular homeostais, functioning in exocytosis, metabolism, transcription regulation and apoptosis (Bonza *et al.*, 2013). ER derived compartments can also play an essential functional role as a reservoir, most notably in developing seeds, acting as a store of key seed storage proteins such as globulins and prolamins (Galili, 2004).

The ER surface may act as a scaffold for concentrating the various components of metabolic pathways, forming metabolons (Hawes *et al.*, 2015). The ER surface offers a large surface over which blocks of enzymes can co-localise, firstly acting to regulate the organisation metabolic pathways in space and secondly enabling mixing of metabolic products throughout the cytoplasm (Hawes *et al.*, 2015). The locally controlled concentrations of the components of metabolic pathways on the ER surface results in process optimisation. The concept of regions of locally organised enzymes and metabolons was introduced by Srere (1987), and refers

to the enzymes of a specific biosynthetic pathway being transiently linked by non-covalent binding, stabilised by either a membrane or cytoskeletal anchoring (Hoppert and Mayer, 1999). One such ER localised metabolon is the dhurrin metabolon identified in *Sorghum bicolor*. Efficient production of this defence compound is achieved through the co-operation of two p450 cytochromes anchored to the ER membrane, co-operating with a soluble glucosyltransferase to rapidly process the dhurrin production intermediates (Laursen *et al.*, 2016).

1.3 The structure of the plant ER

1.3.1 The ER is composed of morphologically and dynamically distinct subdomains

The ER is composed of two structurally distinct domains: tubules and cisternae, which form a loose polygonal network, with tubules joining at three-way junctions. Additional suggested structural subdomains are punctae - points at which the plant ER connects to stable structures within the cell (presumably the plant cell plasma membrane, Sparkes *et al.* (2009a)). These ER subdomains can be identified by size, dynamics or a combination of the two. Cisternae are canonically defined as large flat regions of the ER forming a contiguous lumenal space between two large flat regions of ER membrane (Westrate *et al.*, 2015), though recent literature has begun to question this definition. Punctae are classified as being larger than a tubule and an upper bound on the size of a punctae was suggested by Sparkes *et al.* (2009a) at $0.3\,\mu m^2$ in order to separate them from cisternae. Aside from size, punctae are most easily identified by their dynamics, as they are fixed points within the network, typically persisting for approximately 5-10 seconds, though with many persisting for much longer than this (Sparkes *et al.*, 2009a; Griffing,

2018). Tubules are the thinnest components of the ER structure, composed of highly curved surfaces and connecting components of the plant ER (Westrate *et al.*, 2015).

The overall structure of the plant ER is largely determined by the relative proportions of these specific subdomains. Literature on mammalian ER suggests that there may be a functional reason for the relative proportions of the different structures, as mammalian cells with a high secretory demand, such as salivary gland cells, have a higher proportion of cisternae (Shibata *et al.*, 2006; Terasaki *et al.*, 2013) compared to cells with a lower secretory demand, such as cortex cells (Terasaki *et al.*, 2013). This has been supported in plant literature by analysis of the structure of the ER in the maize root cap, with secretory cells showing an increased ratio of cisternae:tubules (Stephenson and Hawes, 1986).

1.3.2 ER cisternae: Kístē or Kista?

Recent literature has challenged the canonical view of ER cisternae structure, suggesting that the view of ER cisternae as contiguous flat sheets may not be correct. Instead it has been suggested that cisternae may be composed of either densely reticulated networks of tubules, so tightly compressed that the individual tubules require super-resolution imaging in order to resolve them (Nixon-Abell *et al.*, 2016), or are in fact perforated with holes throughout the cisternae (Schroeder *et al.* (2019), fig. 1.1). Nixon-Abell *et al.* (2016) used Grazing Incidence Structured Illumination Microscopy (GI-SIM) to reveal dense reticulate matrices of tubules in both Cos-7 and U-2 OS cells expressing fluorescently tagged Sec61β (a commonly used ER membrane marker) that appeared as flat, intact cisternae when using diffraction-limited wide-field imaging. It is also suggested that cisternae can be generated from tubules by rapid assembly, but due to the speed of cisternae

formation and disassembly, homeotypic fusion of tubules is not required to generate cisternae (Nixon-Abell *et al.*, 2016). Schroeder *et al.* (2019) however used STED microscopy on Cos-7 cells expressing either Halo-KDEL or SNAP-KDEL (two ER lumenal markers) to reveall small, sub-diffraction holes throughout ER cisternae. These distinct holes, termed 'nanoholes' have variable motility and are described as having a similar size to the holes found within the nuclear envelope created by nuclear pore complexes (as measured using Nup160-Halo, a component of the nuclear pore complex). Reticulon 4 (RTN4), a protein required for ER tubulation (Jozsef *et al.*, 2014), was found to localise to a subset of nanoholes that are surrounded by unstructured cisternae containing no RTN4. Ironically the name cisternae itself is somewhat prophetic of the challenges of this work. The term cisterna can be traced back to ancient greek, kístē meaning "box", but most likely originated from a Proto-Indo-European term kista, meaning "woven container" (Pyysalo, 2017).

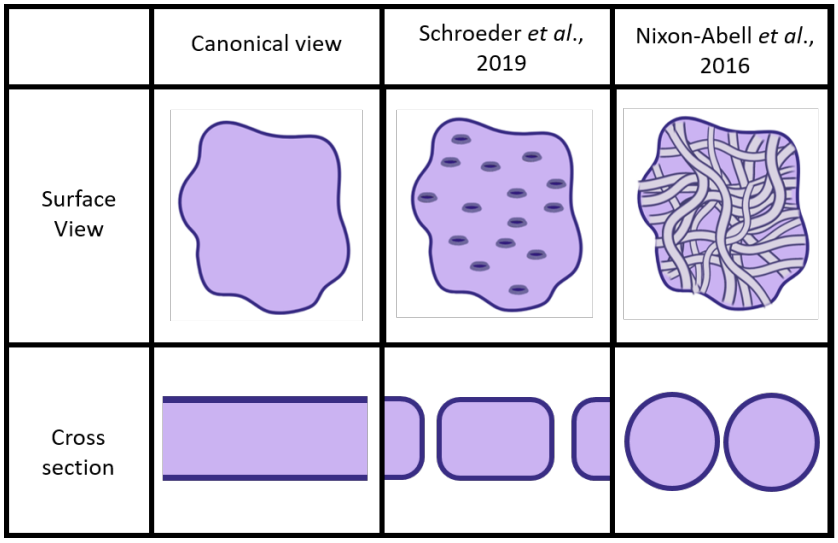


Figure 1.1: The three proposed structures of mammalian ER cisternae Schematic representation of the three main views of the structure of mammalian ER cisternae as viewed from above and a cross section. The canonical view is that of a single sheet of bilayer with an interrupted lumenal space, Schroeder *et al.*, 2019 present a view of cisternae puncatuated with nanoholes, induced by local concentrations of RTN4 and Nixon-Abell *et al.*, suggest cisternae are composed of densely reticulated networks.

1.3.3 Wild-type variation in ER structure

The structure of the plant ER varies throughout development and according to cell type. The function of this variation has not been definitively identified however it appears that the structure of the ER has some correlation with the predicted secretion of specific cell types. For example, electron microscopy analysis of ER structure through the root cap of maize identified a greater volume of cisternae in secretory cells, when compared to meristem and starch storage cells (Stephenson and Hawes, 1986). Furthermore, the total volume and surface area of the ER in a starch cells and secretory cells was measured to be 5 and 10 times greater than that of a meristem cell respectively (Stephenson and Hawes, 1986). After normalisation to cell size, the fraction of the cell occupied by ER was measured for meristem, starch and secretory cells to produce an ER occupancy fraction of each cell of 0.031, 0.030 and 0.069 respectively, revealing a more than double increase in the volume of the ER in secretory cells (Stephenson and Hawes, 1986). This pattern of increased cisternae in secretory cells has been further identified in mammalian secretory cells under a high secretory demand (Shibata *et al.*, 2006; Terasaki *et al.*, 2013). Subsequent live cell imaging of arabidopsis tissue revealed a general increase in the area of cisternae in the roots and a marker 'condensation' of the ER at the base of developing root hairs (Ridge *et al.*, 1999).

Treatment with the plant hormone abscisic acid (ABA) results in a 1.7-fold increase in in the total secreted protein in suspension-cultured cells of *Triticum aestivum* (winter wheat) (Chikako *et al.*, 1999). Though the effect of ABA on the structure of the ER was not investigated within the study by Chikako *et al.* (1999), ABA treatment in *Lepidium sativum* seeds results in the formation of large, stacked ER cisternae (Volkmann, 1976). Therefore it is reasonable to infer that externally induced secretory demand may be sufficient to induce changes in the structure of

the ER, in favour of increased cisternal area.

The majority of plant ER is functionally 2D, restricted to a region of cytoplasm just below the cell wall and appressed into this small space by the vacuole. Strands of the ER are able to cross the vacuole and connect with the nuclear envelope, however this represents a relatively small volume of the total ER. EM measurements of this region of cytoplasm estimates that the ER is constricted to a region of cytoplasm that is approximately 1.5-2.0 µm deep (measured in maize root cap cells, Stephenson and Hawes (1986)) whilst the ER has a width of between 40 and 55 nm (measured in arabidopsis leaf epidermal cells and maize root cap cells respectively, Pain *et al.* (2019); Stephenson and Hawes (1986)). This is opposed to mammalian and yeast ER which are not only predicted to have a slight different tubule diameter (60 nm and 30 nm respectively, Hu *et al.* (2011)) but also show a 3D distribution of the ER throughout the entirety of most cells (Friedman and Voeltz, 2011; West *et al.*, 2011).

1.3.4 Maintaining ER structure

The complex structure of the ER could theoretically be maintained by a balance of two types of ER-shaping proteins: R-proteins and S-proteins. Both S- and R-proteins would localise to curved ER surfaces and are able to induce this positive membrane curvature in one plane, typically thought of as the z-plane. In the y-plane, where y is the plane running along the edge of an ER tubule, R-proteins would promote straight edge formation (fig. 1.2, R-type protein), whilst a S-protein would induce negative membrane curvature in the y-plane (fig. 1.2, S-type protein). By modifying the local concentrations of these two classes of ER-shaping proteins, it is theoretically possible to generate all the structural subdomains seen in both plant and mammalian ER, including tubules, three-way junctions, cisternae and cisternal

fenestrations and helicodial stacks (not observed in plant cells) (Shemesh *et al.*, 2014). The model produced by Shemesh *et al.* (2014) is dependent on the logical assumption that the ER will form the most energetically favourable conformation based on both the total volume of the ER that is occupied by ER shaping proteins and the given size of the fraction of this total that are S-proteins. Modifying the total proportion of ER-shaping proteins within the ER will shift the structure of the ER from a predominately cisternal structure at low concentrations of ER-shaping proteins, to a structure composed predominantly of unbranched tubules at higher concentrations. Varying the fraction of S-proteins modifies the ratio of straight and curved ER edges, and increasing the fraction of S-proteins within the total population of ER-shaping proteins will favour structures that require junctions in the ER in order to form, such as three way junctions. The mammalian Lunapark protein (mLNP1), a protein that stabilised three-way junctions in the ER, has been suggested to be an example of an S-protein, whilst members of the reticulon protein family have been proposed as R-proteins (Chen *et al.*, 2012; Hu *et al.*, 2008; Shemesh *et al.*, 2014).

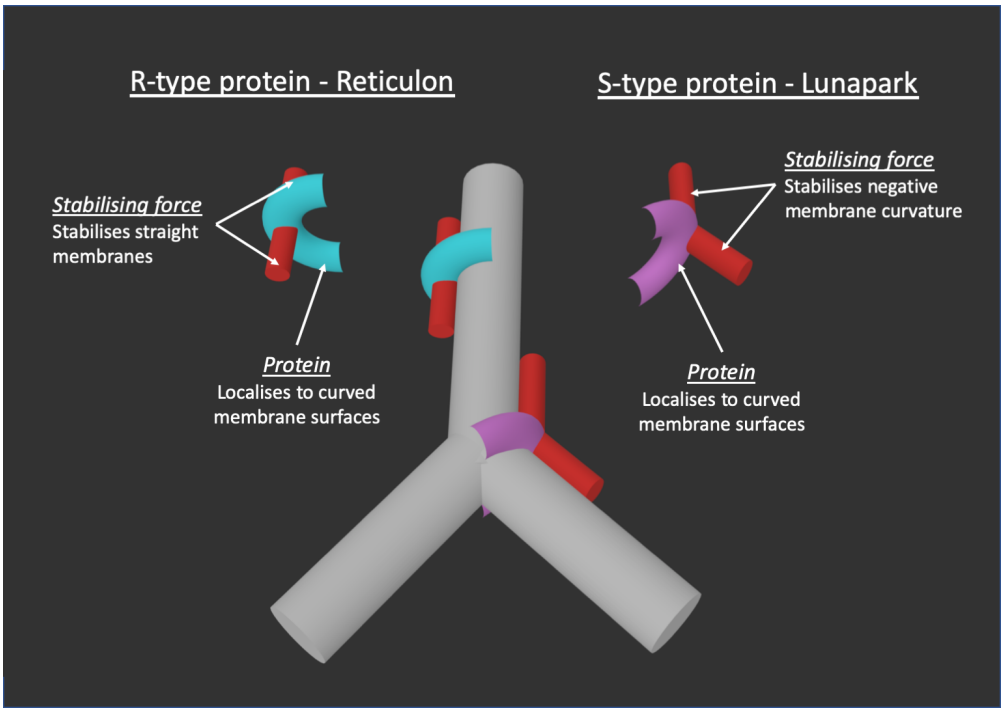


Figure 1.2: A comparison of the forces exerted by R- and S-proteins The theoretical localisation of R- and S-type proteins around an ER three-way junction (grey). Reticulon proteins such as RTN4 (blue) have been suggested to stabilise straight membranes along the length of ER tubules (direction of stabilising force in red). Lunapark proteins (magenta) have been suggested to stabilise or induce negative membrane curvature within the ER, such as at the center of three-way junctions.

1.3.5 The geometry of the plant ER

The ER contains numerous 'stable points' that are distributed throughout the network and are thought to be contact sites between the ER and the plasma membrane. These ER plasma membrane contact sites, or EPCSs, play a key role in several cellular functions, including endocytosis, local lipid homeostasis and potentially the formation of autophagosomes (Wang and Hussey, 2019). EPCSs can be thought of as a set of nodes between which the ER must assemble a series of connections, and this set of connections should theoretically use the minimum amount of ER surface to join these points in order to be an energetically

favourable state. The geometry of the ER tubular network is thought to form an Euclidean Steiner network (ESN) between these stable points in order to build a well-connected network (Lin *et al.*, 2014, 2015; Griffing *et al.*, 2017). An ESN is a generalised Steiner network, which in turn is a generalisation of a minimum spanning tree problem. A minimum spanning tree problem is as follows: given a set of nodes, each of which must be connected to each other node, a minimum spanning tree is an undirected set of vertices that will fully connect all the given nodes, whilst resulting in the shortest total length of vertices within the tree (fig. 1.3). A minimum spanning tree is not always the most efficient way to join a set of nodes. It can be more efficient to use an ESN to join this network as an ESN permits the addition of extra nodes, termed Steiner points, to the network in order to produce the most energetically efficient network (fig. 1.3, Hwang *et al.* (1992)). It appears that the ER does contain Steiner points in the form of three-way junctions and these may be crucial in the formation of polygonal regions, the area of cytoplasm, surround by the ER network (Lin *et al.*, 2017).

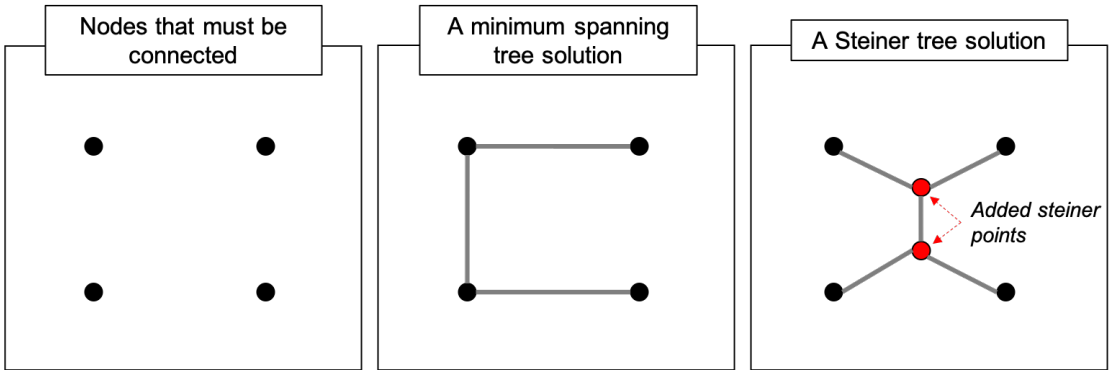


Figure 1.3: A theoretical minimum spanning tree vs Steiner tree solution for the connection of 4 nodes
A comparison of a minimum spanning tree and Steiner tree solution for connecting 4 nodes (shown in black), whilst minimising the total edge length required to form the connection between all the nodes. The key difference between the two solutions to connecting the nodes, is that the Steiner tree solution allows for the inclusion of additional nodes, termed 'Steiner points' (shown in red) to the network.

1.4 The dynamics of the ER

Since the development of fluorescent probes suitable for interrogating the structure of the ER in living cells, it has been known that the ER itself is highly dynamic (Ridge *et al.*, 1999). The functional importance of rapid ER remodelling is not yet understood, particularly in fully expanded, mature cell types such as leaf epidermal cells. When discussing the dynamics of the plant ER, the most considered aspect of dynamics are gross ER structural modifications, including the extension and contraction of tubules, cisternae translocation throughout the network, and ring closure of polygonal regions by tubule sliding. In addition tubules and cisternae are rapidly interconverted and bulk flow of ER membranes through the cell occur along actin bundles. The movement of the ER is ubiquitous throughout the majority of ER cell types and is driven by both myosins and the actin cytoskeleton (Sparkes *et al.*, 2009a; Ueda *et al.*, 2010; Griffing *et al.*, 2014).

1.4.1 Characterising the movement of the ER

Though the most commonly considered aspect of ER dynamics is the remodelling and translocation of the ER structure, the reality of ER dynamics is far more complex. ER movement occurs over a range of scales, starting from the movement of single particles through the structure of the ER, to the rapid bulk movement of the ER along thick actin cables. I propose a classification system of ER dynamics that not only covers the full scale of ER dynamics, but also that relates more accurately to the analysis methods that can be used to measure ER dynamics, as opposed to arbitrary classifications of movement types that cannot be measured. Four classifications of ER dynamics can be distinguished: 1) ER particle dynamics; 2) ER remodelling; 3) bulk flow; 4) inherent movement.

1.4.1.1 ER particle dynamics

ER particle dynamics refers to any 'particle' or group of particles capable of moving either through the lumen of the ER or within the membrane of the ER (fig. 1.4). Particle is a general term, referring to individual proteins, protein complexes, lipids, ions and whole structures such as arabidopsis fusiform bodies (Hawes *et al.*, 2001) etc. Lumenal particle dynamics considers, for example, the movement of ER lumen resident proteins such as calreticulin, responsible for binding Ca^{2+} within the plant ER (Opas *et al.*, 1991). This movement may be less bounded than the movement of, for example, the integral membrane protein calnexin (Bergeron *et al.*, 1994) which is restricted to the lipid membrane of the ER.It is also possible that the ER subdomain through which individual particles are moving may effect the rate of particle movement. Single particle tracking (SPT) in mammalian cells has indicated that single molecules move more rapidly through the lumen ER tubules than through three-way junctions (Holcman *et al.*, 2018). The potential effects of different ER structural domains on single particle movement will be investigated as part of this work.

The dynamics of single proteins or protein conglomerates on the ER membrane may be affected by binding to cellular components outside the ER. For example NET3C belongs to the NET protein superfamily that links endomembrane components (such as the ER) to the actin cytoskeleton (Deeks *et al.*, 2012) and appears to associate with the ER (Wang *et al.*, 2014). The rate of NET3C puncta recovery after photobleaching is enhanced after the depolymerisation of the actin cytoskeleton, suggesting that the actin cytoskeleton is affecting the dynamics of NET3C (Wang *et al.*, 2014). Methods available to assess particle dynamics in the plant ER are typically fluorophore bleaching/photoactivation experiments focusing on the recovery of a bleached fluorophore to a specific region of the ER, or tracking the

spread of a photo-activated fluorophore through the ER network (Griffing, 2018; Runions *et al.*, 2006; Sparkes *et al.*, 2009a). Lumenal and membrane particle movement can also be analysed using single particle tracking of fluorophores using variable-angle epifluorescence microscopy (VAEM), so far applied near the surface of the cell at the plasma membrane (Konopka and Bednarek, 2008) but can also be used to detect particles at a sufficient depth in the cell to capture ER particle dynamics (see chapter 5).

1.4.1.2 ER remodelling

The ER undergoes constant bulk remodelling, which is often characterised in terms of specific structural subdomains. For example, tubules show extension, retraction and sliding behaviors, whilst cisternae can translocate through the network and constantly re-shape showing variable perimeter dynamics (fig. 1.4, Griffing (2018)). Though descriptively useful, no software package is currently available to detect these specific classifications of ER remodelling. Instead analyses of ER remodelling can either be performed on the tubular network alone to such an extent the forces determining the dynamics of these tubules can be characterised and quantified (Lin *et al.*, 2014, 2015, 2017; Lemarchand *et al.*, 2014). Though essential for understanding the forces that dominate the dynamics of the ER network, this technique is limited in that it is computationally expensive and thus far can only be applied to the tubular network. Large-scale quantification of ER remodelling can be performed across the entire surface of the ER, but cannot be used to specifically identify the types of movement described previously, such as tubule extension and cisternae re-shaping. Instead cross-correlation techniques, such as optical flow analysis, are able to detect the rate and direction of ER translocation between frames, and can be extended to characterise the ER structural domain in which the movement is occurring (Ueda *et al.*, 2010; Pain *et al.*, 2019). For example the rate

of cisternae remodelling can be compared to the rate of tubule remodelling.

Whilst cross-correlation techniques are effective at detecting the rate of ER remodelling, some subregions of the ER remain highly persistent over extended periods of time, a feature of their dynamics which is not simply detected by cross-correlation techniques. These stable points or punctae are thought to play an essential role in the function of the ER, connecting the ER to the plasma membrane and determining the geometry of the ER (Lin *et al.*, 2014, 2015; Griffing *et al.*, 2017). As opposed to cross-correlation techniques, the relative stability of these points is most simply detected using persistency mapping. This technique identifies regions within the image that have been 'occupied' by ER over an extended period of time. This technique has been successfully employed to assess the role of the XI myosins in gross ER remodelling (Sparkes *et al.*, 2009a; Griffing *et al.*, 2014).

1.4.1.3 Bulk flow

Bulk flow refers to the rapid, mass translocation of regions of ER driven by the actin cytoskeleton in concert with myosin motors, in particular myosin XI-K (Ueda *et al.*, 2010). This form of ER movement is distinct from ER remodelling as it is significantly more rapid, occurring at speeds of up to $1.35\,\mu m\,s^{-1}$ compared to the remodelling of the rest of the ER network that is thought to occur at a rate of approximately $0.3\,\mu m\,s^{-1}$ (Ueda *et al.*, 2010). In addition ER streaming forms a distinct structure that can be identified from still images (fig. 1.4). Streaming ER forms long strands of densely grouped, highly reticulate sections of ER, as opposed to non-streaming ER which forms a significantly less dense structures.

1.4.1.4 Inherent ER movement

Inherent ER movement is the small, Brownian-like oscillatory movement of the ER that continues in the absence of known drivers of ER remodelling. For example, constant, small oscillations of relatively stable points of ER continue in the absence of the actin cytoskeleton after depolymerisation using the drug Latrunculin B (Lin *et al.*, 2014). This small oscillation can be observed at the edge of cisternae as well as along tubules and contributes to the overall movement of the ER, though is only observable when rapidly imaging the ER and in the absence of larger ER movement (fig. 1.4). The role of this Brownian-like motion in ER remodeling has not yet been fully elucidated, however it may play a role in determining the rate of the cross-connection processes during gross ER remodeling (Lin *et al.*, 2017).

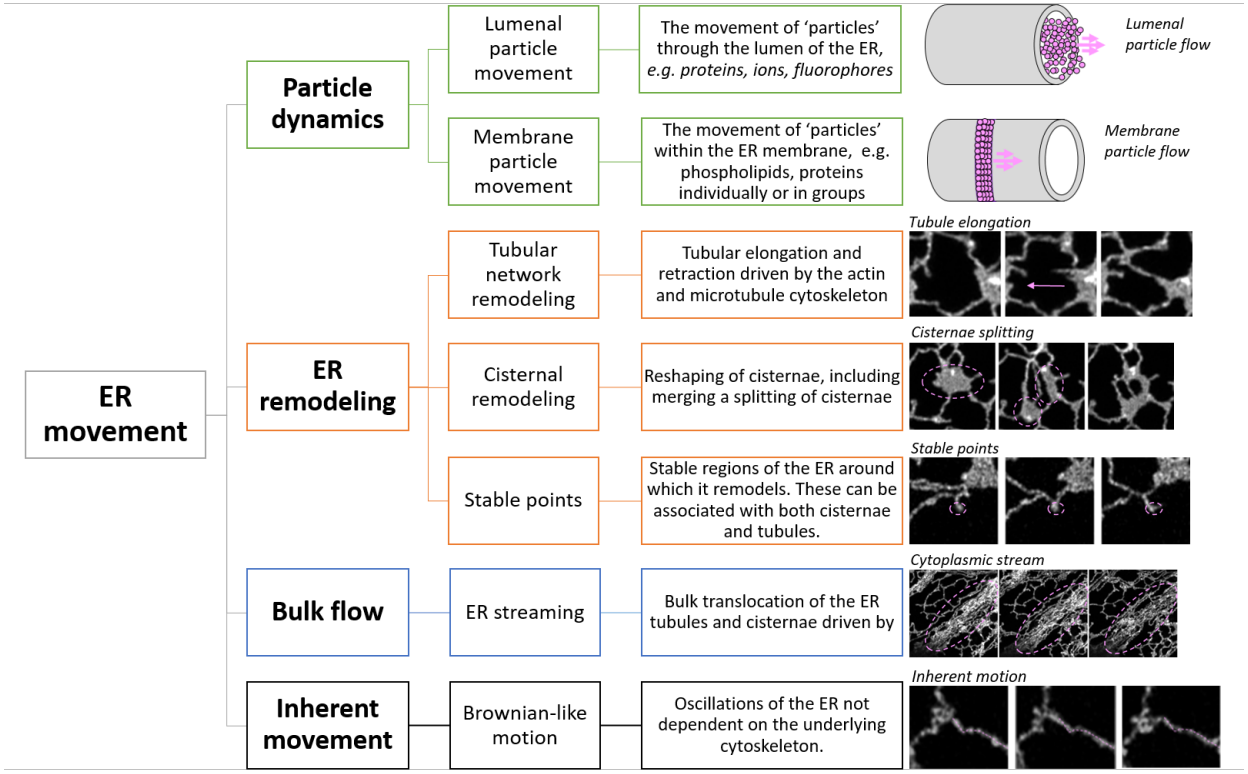


Figure 1.4: Proposed classification of plant ER 'movement'
The four key components of ER 'movement' including example diagrams of images of the types of ER movement. This includes lumenal and membrane particle flow diagrams; tubule extension, cisternae merging, stable points and cytoplasmic streaming examples from tobacco ER are also shown over variable timescales and the inherent movement of tubules after treatment with Latrunculin B, with the original center-line of the tubule shown in pink.

1.4.2 The role of the actinomyosin cytoskeleton in ER dynamics

The actin cytoskeleton is ubiquitous throughout eukaryotic organisms and has been implicated in plants in cellular signaling (Samaj *et al.*, 2006), proper cellular development (Deeks *et al.*, 2007) and plant responses to stress and infection (Hardham *et al.*, 2007; Opalski *et al.*, 2004). The filamentous (F-actin) cytoskeleton is assembled from a cytoplasmic pool of globular-actin (G-actin) to form helical 5-7 nm, polarised filaments that span the cytoplasm (Fujii *et al.*, 2010; Oda *et al.*, 2009). Myosin motor proteins make use of ATP hydrolysis to move along actin filaments (Krendel and Mooseker, 2005) and specific myosin sub-classes have been implicated in organelle movement within cells. The arabidopsis myosin protein family is divided into two classes: myosin XI (13 members) and myosin VIII (4 members) (Reddy and Day, 2001; Peremyslov *et al.*, 2011). Members of the former class have been implicated in organelle transport, including the ER. The over-expression of the tail domain of XI myosins have been used successfully as dominant-negative method to reduce myosin activity in plant cells, potentially by competing with native myosin for binding sites, though the specific mechanism is not understood (Sparkes *et al.*, 2008; Avisar *et al.*, 2009). A subset of the 13 XI myosins (XI-C, XI-E, XI-I, XI-K, XI-1, and XI-2) have been implicated in the control of Golgi, peroxisome, mitochonria and ER movement (Avisar *et al.*, 2008, 2009, 2012; Peremyslov *et al.*, 2008, 2010; Prokhnevsky *et al.*, 2008; Sparkes *et al.*, 2009a, 2008). XI-C, XI-E, XI-K, XI-l and XI-2 have all been shown to specifically reduce ER remodelling with some additional effects on ER structure (Griffing *et al.*, 2014; Sparkes *et al.*, 2008; Ueda *et al.*, 2010; Ojangu *et al.*, 2012). In addition myosin XI-K has been implicated as being particularly important for ER remodelling (Sparkes *et al.*, 2008; Ueda *et al.*, 2010). Inhibition of XI-1 and

XI-2 can also enhance the effect of XI-K inhibition, whilst exerting very little influence on ER remodelling alone (Ojangu *et al.*, 2012). Depolymerising the actin cytoskeleton has similar effects to inhibition the myosin motors (Sparkes *et al.*, 2008; Pain *et al.*, 2019).

1.5 Modifying ER structure and dynamics

The structure of the plant ER naturally varies during plant development and is dependent on the specific cell type (Ridge *et al.*, 1999; Stephenson and Hawes, 1986). The structure of the ER can also be modified through a variety of means including ectopic protein expression, pharmacological treatments and stress treatments. The direct effects of these treatments can be complex, and ER structure can be modified in response to both cellular physiological changes, modified secretion and modified lipid composition of the ER.

1.5.1 Ectopic protein expression

Ectopic, enhanced and reduced expression numerous proteins are known to affect ER structure, including proteins that directly shape the ER and those involved in lipid metabolism, including the double mutant *pah1pah2* (Eastmond *et al.*, 2010). Three classes of ER shaping protein have so far been identified: three root-hair defective isoforms (RHD3), the reticulon protein family and the Lunapark proteins.

1.5.1.1 Root hair defective 3

Homotypic membrane fusion of ER membranes, mediated by fusogens, is essential for normal functioning and connectivity of the ER in both animals and yeast. Fusogens identified so far include the animal protein atlastin and the yeast protein Sey1p (Synthetic Enhancement of Yop1), both of which are membrane-associated dynamin-like GTPases (Anwar *et al.*, 2012; Hu *et al.*, 2009; Orso *et al.*, 2009). Atlastin is proposed to function by transiently dimerizing when proteins on separate membranes are close to each other, leading to the two membranes becoming attached to each other (Bian *et al.*, 2011; Byrnes and Sondermann, 2011; Lin *et al.*, 2012; Moss *et al.*, 2011). The lipid bilayers of these attached membranes are then destabilized by an amphipathic helical domain at the C-terminus of the atlastin protein to mediate membrane fusion (Bian *et al.*, 2011; Faust *et al.*, 2015; Liu *et al.*, 2012). Knockdown of atlastin leads to ER fragmentation and unbranched ER tubules whilst over-expression enhances membrane fusion (Hu *et al.*, 2009; Orso *et al.*, 2009).

Root hair defective 3 (RHD3) was proposed as a potential plant fusogen as when its expression is disrupted the ER network forms large strands with few branches (Chen *et al.*, 2011; Stefano *et al.*, 2012; Zheng *et al.*, 2004). Over-expression of RHD3 proteins with mutations in the putative GTPase domain results in unbranched ER (Chen *et al.*, 2011), whereas *rhd3* plants exhibit a more cable-like ER structure in the roots (Zheng *et al.*, 2004), whilst the gom8 mutant (a misense mutation in RHD3 with a phenotype that is complemented by RHD3) shows enlarged, unbranched strands of ER (Stefano *et al.*, 2012).

RHD3 has been proposed as a functional ortholog of both atlastin and Sey1p due to a sequence similarity with Sey1p (Hu *et al.*, 2009), and RHD3's structural similarity with atlastin and Sey1p in the form a functional GTPase domain at the

N-terminal cytosolic domain (Stefano *et al.*, 2012). However, RHD3 is not required for tubule fusion in arabidopsis as both the *gom8* mutant and an *rhd3-7* mutant showed tubule fusion (Stefano *et al.*, 2012). Therefore, though RHD3 does modify the structure of the plant ER, it has not been shown definitively to act as a plant fusogen.

1.5.1.2 The reticulon protein family

Reticulon proteins are found throughout the eukaryotic kingdom (Yang and Strittmatter, 2007), with proteins of chordata taxa classified as reticulons (RTNs), the remaining homologues were divided into six RTN-like subfamilies. In the case of the plant subfamily reticulon homologues were designated as reticulon-like B (Oertle *et al.*, 2003), though they will be referred to simply as reticulons (AtRTNs) throughout this thesis. Common to the RTN family is the reticulon homology domain (RHD) conserved at the C-terminal end of the protein and containing two hydrophobic regions flanking a hydrophilic loop (Nziengui and Schoefs, 2009).

It has been proposed that the topology of RTNs, more specifically the amphipathic helix, is sufficient to induce membrane curvature through a combination of wedging and scaffolding (Shibata *et al.*, 2006; Zimmerberg and Kozlov, 2006). Protein scaffolding involves proteins acting as scaffolds for the ER using intrinsic protein curvature to induce curvature in the ER and in RTNs arises from low-mobility homo-oligomers forming between the RTN protein and the ER membrane (Breeze *et al.*, 2016). The wedging effect of the RTNs is most likely conferred by the specific transmembrane topology of the RHD.

Over-expression of the arabidopsis reticulon AtRTN13 revealed that it localises to cortical ER tubules where it induces constriction (Tolley *et al.*, 2010). Ectopic expression of AtRTN13 is sufficient to induce tubulation in the arabidopsis *pah1*

pah2 mutant (Tolley *et al.*, 2010), an arabidopsis double knock down mutant that shows a significant increase in the proportion of cisternae in cells (Eastmond *et al.*, 2011). It was shown in AtRTN13 that deletion of the putative amphipathic helix (APH) abolishes AtRTN13's ability to induce constrictions in ER tubules, though the AtRTN13 mutants retains the ability to form low-mobility oligomers with the ER membrane (Breeze *et al.*, 2016). The length of the transmembrane domains in the RHD has also been implicated in AtRTN function. Sequential shortening of the four transmembrane domains of AtRTN13 correlate with the ability of AtRTN13 to induce membrane tubulation (Tolley *et al.*, 2010). This same constriction phenotype has been observed on transient over-expression of several other arabidopsis reticulon protein family members, specifically AtRTN1-4 (Sparkes *et al.*, 2010).

1.5.1.3 The Lunapark protein family

The Lunapark protein family plays a key role in determining/maintaining ER structure, in particular three-way junctions and cisternae. The Lunapark protein family was first identified during a screen of a yeast deletion library for modified ER morphology, and is characterized by two conserved N-terminal transmembrane domains and a C-terminal zinc-finger motif that is conserved across eukaryotes (Chen *et al.*, 2012).

The sole member of the yeast Lunapark protein family (Lnp1p1) contains the amino acid motif LNPARK adjacent to the zinc-finger domain and is responsible for the protein family name, though this motif is poorly conserved (Chen *et al.*, 2012). Lnp1p1 localises to punctae on the tubular ER and junctions between the ER and the nuclear membrane, This distribution shifts in favour of three-way junctions at the yeast ER periphery (Chen *et al.*, 2012) in common with mammalian Lunapark

(Chen *et al.*, 2015). Loss of Lnp1p results in mutated ER phenotype, missing large sections of the cortical ER where the network appears to have collapsed (Chen *et al.*, 2012). This effect is mimicked by compromising the zinc finger motif, where sequential mutation of 4 conserved cysteine residues to alanine results in an increasingly perturbed ER structure. As the number of substitutions is increased, the ER becomes increasingly more collapsed and there is an overall reduction in the mean size of the polygonal regions of cytoplasm enclosed by the ER network (Chen *et al.*, 2012).

Disrupted expression of mLnp1 results in a modified ER structure, favouring an increase in cisternae and a reduction of the tubular elements of the ER (Chen *et al.*, 2015; Wang *et al.*, 2016b). In mammalian cells depletion of mLnp1 results in cisternae induction and a reduction in tubules the majority of mLnp1 is localised to three-way junctions (72.4%), whilst the remainder are localised to tubules (27.6%) (Chen *et al.*, 2015). Only approximately half (51.7%) of all three-way junctions are marked with mLnp1 (Chen *et al.*, 2015) and this distribution is lost when the N-terminal myristolation site is abolished using a G2A mutation and when a short unrelated linker sequence was inserted after the first coiled-coiled domain or before the second coiled-coil domain (Wang *et al.*, 2016b). Typically, in mammalian cells, three-way junctions are mobile regions of the ER, yet junctions associated with mLnp1 show reduced dynamics (Chen *et al.*, 2015). Approximately 39% of mLnp1 punctae remain mobile, capable of moving between junctions, merging junctions, splitting junctions and moving with a sliding junction (Chen *et al.*, 2015). Nascent three-way junctions are typically not persistent, and hence are not stable for more than 30 seconds. However, the majority of junctions that become stable acquired mLnp1, suggesting that mLnp1 plays a role in stabilising ER structure over time (Chen *et al.*, 2015). Loss of function mutations in human LNPK have also been linked to a severe neurodevelopmental syndrome, associated with modified ER

structure preventing proper establishment of the corpus callosum (Breuss *et al.*, 2018).

This protein family has recently been identified in plants by Kriechbaumer *et al.* (2018), and this work details the application of novel ER analysis tools to assess the role of the Lunapark protein family in ER plant structure. Furthermore, using molecular biology techniques this work aims to explore the mechanisms by which cisternae are formed/maintained within the plant ER by the Lunapark protein family.

1.5.2 Modified ER lipid content

It has been estimated that approximately 5-10% of the fresh weight of plant cells is made up of lipids, the majority of which are a part of the internal cellular membranes (Ohlrogge and Browse, 1995). Within the pool of lipids present within the cell, phospholipids (lipids that contain a phosphate group within their structure) are essential for the formation of lipid bilayers due to their amphipathic properties (Ohlrogge and Browse, 1995). Reduced activity of phosphatidic acid phosphohydrolase (PAH) in the *pah1pah2* mutant results in an increased absolute phospholipid content of the cell (Eastmond *et al.*, 2010). Specifically *pah1pah2* has an increased net phosphatidylcholine (PC) biosynthesis and this overproduction of PC results in what has been described as an 'over-proliferation' of the ER (Craddock *et al.*, 2015). Specifically the ER appears to become composed largely of cisternae, resulting in a total increase of ER lumen area (Eastmond *et al.*, 2010).

1.5.3 Pharmacological treatments

1.5.3.1 Brefeldin A

Brefeldin A (BFA) is a fungal toxin that in plants blocks secretion between the ER and Golgi/trans-Golgi network (Staehelin and Driouich, 1997). Firstly, the secretion of cell wall polysaccharides and proteins is blocked (Driouich *et al.*, 1993; Kunze *et al.*, 1995; Schindler *et al.*, 1994) and secondly transport of soluble protein transport to the vacuole is also blocked (Gomez and Chrispeels, 1993; Holwerda *et al.*, 1992). The responses of plant and animal cells to BFA are different, but in plant cells after BFA blocks secretion, there is a loss of cis-cisternae and an increase in trans-cisternae. In addition, in specific cell types such as leaf epidermal cells, the Golgi membranes form highly vesiculated clusters, termed BFA compartments, in some cases resulting in a fusion between the Golgi and the ER (Driouich and Staehelin, 1997; Rutten and Knuiman, 1993; Satiat-Jeunemaitre *et al.*, 1996).

1.5.3.2 Latrunculin B

Latrunculin B (Lat B) is a drug that inhibits polymerisation of the actin cytoskeleton, result in a shift from filamentous actin (F-actin) that is partially responsible for the remodeling of the ER to globular actin (G-actin) that has no known effect on ER structure (Gibbon *et al.*, 1999). Treatment with high concentration of Lat B severely reduces the rate of ER remodelling and affects the structure of the ER (Sparkes *et al.*, 2009a).

1.5.4 Stress

The effect of stress on the structure of the plant ER is poorly understood, though insights may be gained from the response of yeast ER to stress. Application of dithiothreitol (DTT), a strong reducing agent, to yeast cells activates the unfolded protein response (UPR) by inducing reductive stress (Eichmann and Schäfer, 2012). In yeast reductive stress results in the accumulation of misfolded proteins in the ER, through the prevention of disulphide bond formation (Simons *et al.*, 1995), which results in activation of the UPR through the signaling action of Ire1 transmembrane kinase/nuclease (Cox *et al.*, 1993; Kohno *et al.*, 1993). In yeast the UPR affects multiple cellular pathways known to promote the normal functioning of the ER by counteracting stress (Travers *et al.*, 2000), including the ER-associated degradation (ERAD) system that degrades misfolded ER proteins in the cytosol (reviewed by Bonifacino and Weissman (1998)). In this case, application of DTT in yeast results in an increase in the proportion of cisternae within the cell (Bernales *et al.*, 2006). The application of a mild acid (1M acetic acid) to onion bulb scales, however, results in the collapse of ER cisternae into a mass of short tubules (Quader and Fast, 1990).

Both hot and cold temperature treatments have been shown to affect the structure of the ER in *Nicotiana tobacum* BY-2 cells and onion bulb scale cells, respectively. Modification of ER structure in *N. tobacum* BY-2 cells is reported as occurring after a 5 minute treatment at 50°C, and results in an increase in cisternae (Malerba *et al.*, 2010), similar to the ER structural modifications observed in *N. tobacum* leaf epidermal cells after a 20 minutes heat shock at 42°C (Pain *et al.*, 2019). Cold treatment for 30-60 minutes at 0-4°C however results in a loss of long tubular strands in onion bulb cells, resulting in a structure composed of irregular short tubules that show modified dynamics (Quader *et al.*, 1989).

Infection by non-pathogenic, avirulent and virulent oomycete strains (*Phytophthora sojae* and *Peronospora parasitica* (Cala2 and Noks1), respectively) results in modifications to ER structure (Takemoto *et al.*, 2003). In each case the ER is shown to condense around the oomycete penetration site of infected arabidopsis plants and this condensation occurs alongside re-arrangement of the underlying cytoskeleton (Takemoto *et al.*, 2003). Mechanical pressure, that imitates the same penetration of cells by oomycete pathogens, induces the same response (Hardham *et al.*, 2008)

1.6 Visualising cellular components using confocal microscopy

1.6.1 ER fluorescent protein markers

The most commonly used method to visualise the ER for live cell imaging, with minimal predicted effects on ER structure, is to retain a fluorescent protein within the lumen of the ER. This is performed by designing a chimeric protein composed of a signal peptide, a fluorescent protein and an ER retention signal. The signal peptide is designed to ensure co-translational insertion of the nascent peptide into the ER lumen by interacting with the signal recognition particle (SRP) during the early stages of translation by a cytoplasmic ribosome. Interaction with the SRP slows the process of translation sufficiently for the ribosome to be recruited to the ER membrane. Once at the ER membrane the SRP interacts with its receptor, releasing the SRP and enabling resumption of translation into the ER through an ER pore (reviewed in Fewell and Brodsky (2009)). ER targeting of fluorescent proteins was originally performed in *N. tobacum* leaf epidermal cells

using a patatin signal peptide (Boevink *et al.*, 1996), however more recent methods, including those used in this study, apply a sporamin signal peptide which was shown to have increased efficiency on insertion into the ER (Boevink *et al.*, 1999). A C-terminal H/KDEL signal peptide has been shown to be sufficient for the retention of proteins within the ER (Denecke *et al.*, 1992; Napier *et al.*, 1992). One mechanism proposed for H/KDEL retention in the ER is that the retention signal is recognised by receptors such as ER RETENTION DEFECTIVE 2 (ERD2) that are localised to compartments involved in secretion, such as the Golgi bodies, and these function to recycle ER resident proteins back to the ER (Pelham, 1988; Lewis *et al.*, 1990; Silva-Alvim *et al.*, 2018). Another commonly used ER marker that is targeted to the ER membrane, as opposed to the ER lumen, is a truncated, fluorescently tagged arabidopsis calnexin protein (Irons *et al.*, 2003).

1.6.2 Lipid dyes to mark the ER

Where transfection designed to fluorescently mark the ER is not suitable, such as in arabidopsis stable lines where this process can be time consuming, the ER can be visualised using various lipophilic dyes. The most commonly used fluorescent dyes for ER staining are 3,3'-dihexyloxacarbocyanine $DiOC_6(3)$ and rhodamine B hexyl ester (Terasaki and Reese, 1992; Hawes *et al.*, 2018a). Of these dyes, rhodamine B hexyl ester is preferable to $DiOC_6$ as it shows a greater level of photostability (Grabski *et al.*, 1993).

1.6.3 Actin markers

Common cellular compartment labeling techniques, such as the use of direct antibody labelling and fluorescent tagging of protein of interest, are not easily

applicable to the actin cytoskeleton. One of the primary challenges of fluorescent marking of the actin cytoskeleton is that actin exists as two pools within cells - monomeric actin and polymerised actin that plays a role in cellular organisation and dynamics (Andersland and Parthasarathy, 1993). Labelling of actin directly results in a large pool of the monomeric actin becoming marked producing a high background interference when collecting images (Melak *et al.*, 2017). It has also been reported that chimeric actin with a large fluorescent tag, is not as efficiently incorporated into actin filaments as untagged actin (Melak *et al.*, 2017). Though much smaller chemical fluorophores exist, they are technically challenging to work with (Melak *et al.*, 2017). Instead the majority of actin imaging is performed by fluorescently tagging either entire, or active subdomains of actin binding proteins. Two commonly used actin binding protein subdomains are FABD2 and Lifeact, the C-terminal half of the arabidopsis fimbrin 1 protein and the first 17 amino acids of the actin binding protein Abp140 respectively (van der Honing *et al.* (2011); Voigt *et al.* (2005), fig. 1.5). A more recent development has been the actin chromobody (fig. 1.5), a 13kDA actin binding alpaca chromobody which has been used effectively for live cell actin imaging by confocal microscopy (Rocchetti *et al.*, 2014). Though over-expression of the actin chromobody affects the speed of Golgi body movement, it does not affect the meandering index and hence the type of the movement (Rocchetti *et al.*, 2014). In addition two fluorescent actin stains have been developed: phalloidin and SiR-actin (fig. 1.5). Phalloidin conjugates are the traditionally used actin stain but require cell fixation as phalloidin has a low permeability through the cell membrane and can stabilise actin filaments *in vivo* (Coluccio and Tilney, 1984; Visegrády *et al.*, 2004; Wehland *et al.*, 1977). SiR-actin is a relatively new actin probe that is derived from Jasplakinolide (D'Este *et al.*, 2015), another F-actin binding toxin that polymerises F-actin (Bubb *et al.*, 1994). SiR-actin has been proposed as a new actin probe suitable for live cell imaging, however its close structural similarity to Jasplakinolide could result in unwanted

effects such as actin polymerisation or stabilization (Melak *et al.*, 2017).

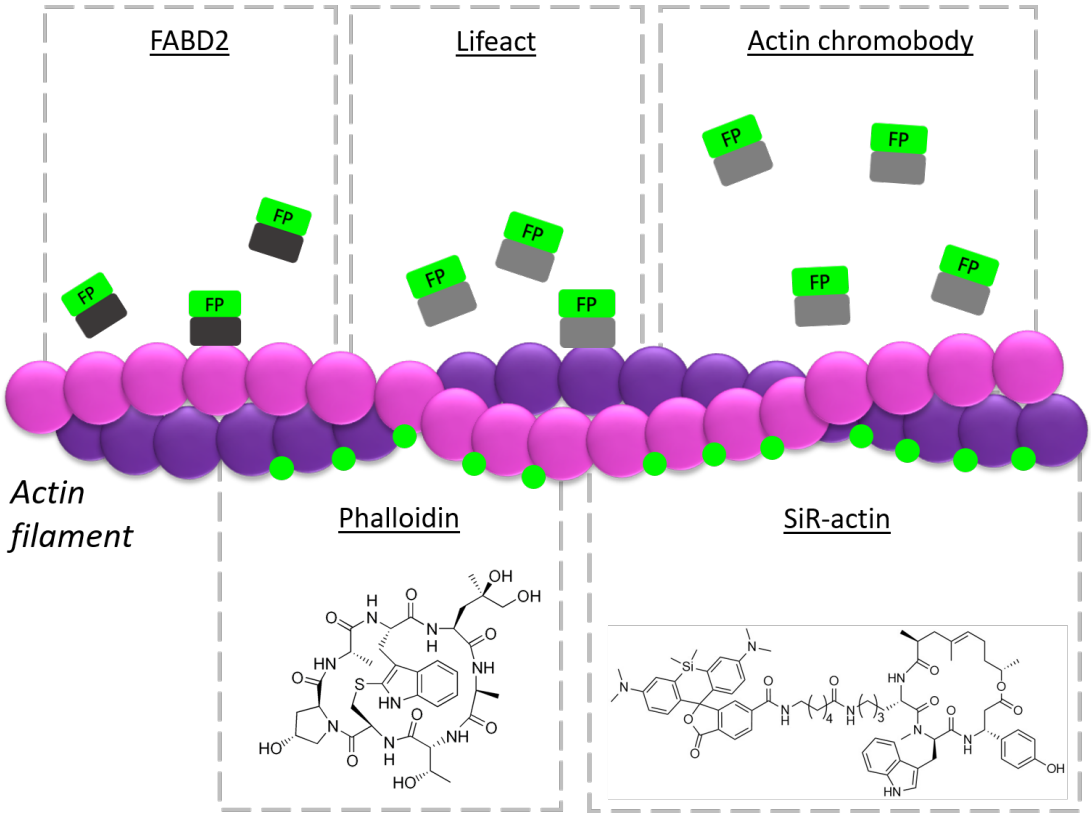


Figure 1.5: Commonly employed plant actin marker strategies
Schematic representation of commonly used actin markers, including markers derived from actin binding proteins (FABD2 and Lifeact), chromobody markers and two actin stains (phalloidin and SiR-actin).

1.7 Quantifying the structure and dynamics of the ER

1.7.1 The importance of ER structure and dynamics quantification

The lack of comprehensive analysis of ER structure and dynamics in plants is an emerging issue in plant cell biology. Within the last 10 years ER structure and dynamics modification have been reported in response to drug treatments, modified protein expression, phospholipid synthesis and viral infection (see table 1.1). Of these publications, the majority either provide only observational details of the modifications to the ER or have performed a manual quantification of the modification. Of the few that use image quantification methods, the techniques used tend to bespoke to the specific question, for example quantifying the proportion of cisternae (Griffing *et al.*, 2014) or the persistency of the network (Sparkes *et al.*, 2009a). The range of agents of modification signifies just how important the structure of the ER is in cellular responses stress and protein modifications. Therefore a broadly applicable method to analyse the structure of the ER is essential for developing our understanding of how the ER functions. This work aims to develop a software package that is capable of analysing ER structural and dynamic modifications induced through a variety of means, including ectopic expression of ER shaping proteins, pharmacological treatments and stress.

Table 1.1: Identification of plant ER structure modifiers over the last 10 years
Publications listing plant ER structure and dynamic modifications in response to protein expression modification, infection and drug treatments.

Method of modification	Agent of modification	Plant species assessed	ER structure and dynamics quantification	Author
Modified protein expression	Lunapark proteins (AtLNP1 and AtLNP2)	*Arabidopsis thaliana*	Quantification of structure and dynamics	Kriechbaumer *et al.* (2018)
	Reticulon-like proteins (RTNLB1-4 and RTNLB13)	*Arabidopsis thaliana*	Observational	Sparkes *et al.* (2010)
	Root hair defective 3	*Arabidopsis thaliana*	Observational	Zhang *et al.* (2013)
	Networked 3C and Vesicle-Associated Protein 27	*Arabidopsis thaliana*	Observational	Wang *et al.* (2014)
	Networked 3B	*Arabidopsis thaliana*	Observational	Wang and Hussey (2017)
	Synaptotagmin 1	*Arabidopsis thaliana*	Counting of three-way junctions	Siao *et al.* (2016)
	Phosphatidic acid phosphohydrolase 1 and 2	*Arabidopsis thaliana*	Observational	Eastmond *et al.* (2010)
	KSM1 and 2	*Arabidopsis thaliana*	Observational	Wang and Hussey (2017)
	GNOM-LIKE1 and Sec24a	*Arabidopsis thaliana*	Observational	Nakano *et al.* (2009)
	XI myosins (including those with tail domains XI-2 , XI-I, XI-C, XI-E, XI-K, and XI-1)	*Arabidopsis thaliana*	Dynamic analysis, some structural analysis	Ueda *et al.* (2010), Sparkes *et al.* (2009a), Griffing *et al.* (2014)
	SPK1	*Arabidopsis thaliana*	Observational	Zhang *et al.* (2010)

	Opaque1	*Zea mays* and transient expression in *Nicotiana benthamiana*	Observational	Wang *et al.* (2012)
Drug treatments	Oryzalin	*Arabidopsis thaliana*	Observational	Langhans *et al.* (2009)
	Latrunculin B	*Arabidopsis thaliana*	Persistency mapping (Sparkes), topology (Lin)	Sparkes *et al.* (2009a), Lin *et al.* (2014)
Infection	Beet black scorch virus	*Nicotiana tabacum*	Observational	Cao *et al.* (2015)
Stress	Heat shock	*Nicotiana tabacum* BY-2 cells	Observational	Malerba *et al.* (2010)
	Chilling	*Vigna radiata* roots	Observational	Szafrańska *et al.* (2013)
	Treatment with $CoCl_2$	*Vigna radiata* BY-2 cells	Observational	Malerba *et al.* (2010)

1.7.2 Methods to quantify ER structure and dynamics

The first attempt to quantify the structure of the plant endoplasmic was made in 1980 using electron microscopy images of ZIO (zinc iodide-osmium tetroxide) stained mung bean cells (Harris and Chrispeels, 1980). A Weibel grid was placed over the collected images and transects containing either tubules or cisternae were counted. Though limited and highly manual, this gave an early insight into the relative proportions of ER cisternae and tubules.

A comprehensive 3D quantification of the plant ER was performed by Bouchekhima *et al.* (2009). *N. tobacum* leaf epidermal cells transiently expressing the ER marker GFP-HDEL were first incubated in 1 µM Lat B for 30 minutes to reduce ER movement. Confocal microscopy was used to acquire z-stacks of the ER network (n=12) which in turn were reconstructed as 3D models of the plant ER. Key ER statistics, such as tubule length, diameter, surface area and volume were analysed in the context of the distance of the ER from the nucleus. No significant differences in these network statistics were observed in relation to distance from the nucleus. Though a significant step forward in the analysis of ER structure, the use of Lat B to slow ER remodelling is not tenable for future studies as it also affects the structure of the ER (Pain *et al.*, 2019). In addition this method, though comprehensive, is also a highly involved and relatively computationally expensive method for assessing ER structure. Quantification of plant ER structure in terms of the polygonal regions of cytoplasm enclosed by the network was performed by Lin *et al.* (2017). Results included the number, area and shape of polygonal regions, particularly the ratio of the major and minor axis of polygonal regions (Lin *et al.*, 2017).

Plant ER dynamics have been analysed independently of ER structure by Sparkes

et al. (2009a), using persistency mapping to characterize gross movement of the ER network. This work identified that approximately 5% of the ER network is highly persistent and these regions were termed punctae. This work was furthered by Lin *et al.* (2014), using Gaussian filtered images that were threshold and skeletonized using a thinning algorithm to produce an ER skeleton. Using graph theory and measured parameters it was shown that the network undergoes a level of tubule length optimization controlled by both random and deterministic forces. In *Caenorhabditis elegans* zygotes, the Farnebäck method has also been used to analyse the rate and direction of organelle movements during meiotic cytoplasmic streaming (Kimura *et al.*, 2017).

Several techniques to analyse particle movement in the using large scale microscopy techniques such as fluorescence recovery after photobleaching (FRAP) and photoactivation have been developed recently. One of these publicly available techniques is an ImageJ plugin developed by Griffing *et al.* (2017) that analyses the dispersal of fluorescence signal through the ER after photoactivation of fluorophores/FRAP. It also contains instructions linked to this plugin designed to assess some basic parameters of ER morphology and perform persistency mapping, however these techniques are not united under a single user interface.

Finally the morphology of ER tubules has also been quantified in the presence of membrane curvature inducing proteins (Breeze *et al.*, 2016). Transient over-expression of AtRTN13 induces constriction along ER tubules and the extend of this constriction was quantified in an earlier iteration of the AnalyzER, a software subsequently designed by Pain *et al.* (2019).

1.8 The relationship between the ER and other organelles

The ER is in physical contact with various subcellular compartments. Golgi bodies, for example, are physically linked to the ER surface, and optical tweezer experiments have demonstrated that when Golgi bodies are trapped and shifted by the laser, the ER remodels behind the moving Golgi (Sparkes *et al.*, 2009b). This connection can be considered to be the basis of the formation of a mobile secretory unit, composed of the physically interacting ER surface and Golgi bodies, the next stage in the secretory pathway (Hawes *et al.*, 2015). The ER is also physically linked to the plasma membrane (PM) at stable ER-plasma membrane contact sites (EPCSs) (Hepler *et al.*, 1990). EPCSs have also been defined as static persistent nodes around which the ER remodels (Sparkes *et al.*, 2009a). EPCSs in mammalian and fungal cells are implicated in essential cellular processes including lipid transport, calcium influx and morphological modifications of the ER as well as acting as an "organisational hub" for the actin cytoskeleton (reviewed by Stefan *et al.* (2013); Wang *et al.* (2016b)). The molecular structure of plant EPCSs has yet to be fully resolved, however two protein components of the arabidopsis EPCS have been identified as NET3C and VAP27. NET3C belongs to the Networked (NET) protein superfamily of actin-binding proteins, responsible for coupling various membranes, including the PM, the vacuole and nuclear membrane, to the actin cytoskeleton (Deeks *et al.*, 2012). VAP27 is a member of the vesicle-associated membrane protein (VAMP)-associated protein (VAP), a protein family common to all eukaryotic organisms (Lev *et al.*, 2008). NET3C acts to connect the PM to the actin cytoskeleton, whilst though the precise function of VAP27 has yet to be identified, over-expression of VAP27 results in enhanced association between the ER and PM (Wang *et al.*, 2016b).

1.9 Aims

The aims of this work are to:

- Develop new methods to analyse and quantify the structure and dynamics of the plant ER (chapter 3)
- Apply these methods to better understand the function of novel ER shaping proteins (chapter 4)
- Further investigate the role of the arabidopsis Lunapark protein family in cisternae formation and ER structure (chapter 4)
- Develop methodologies to explore the effect of ER structure on protein mobility within the ER (chapter 5)

2 | Materials and methods

Contents

2.1 Plant material 68

2.1.1 Wild-type plant material and standard growth conditions 68

2.2 Microscopy 68

2.2.1 General 68

2.2.2 Confocal microscopy 69

2.2.3 VAEM microscopy 70

2.2.4 Light sheet microscopy 71

2.3 Plant transformation and transfection methods 72

2.3.1 Generation of arabidopsis stable lines 72

2.3.2 Transient flourescent protein expression in tobacco leaf epidermal cells 73

2.4 Rhodamine B staining for ER visualisation 73

2.5 Drug and stress treatments 74

2.6 RT-PCR analysis of wild-type and mutant lines 74

2.6.1 RT-PCR on wild-type seedlings 74

2.6.2 Confirmation of T-DNA insertion lines 76

2.7 Cloning and expression plasmids 77

2.7.1 Gateway cloning 77

2.7.2 Expression plasmids used 78

2.7.3 Transformation of competent agrobacterium 80

2.8 Truncation cloning 81

2.9 ImageJ analysis of Rhodamine B stained ER 82

2.10 AnalyzER analysis of ER structures 86

2.11 Single particle tracking 86

2.11.1 Single particle tracking diagram generation 87

2.1 Plant material

2.1.1 Wild-type plant material and standard growth conditions

Unless otherwise stated, all experiments were performed on wild-type Colombia-o *A. thaliana* hereafter referred to as arabidopsis, or *Nicotiana tobacum* (SR1 cv Petit Havana) hereafter referred to as tobacco, grown under greenhouse conditions. To encourage synchronized and enhanced germination, all arabidopsis seeds are sterilised and subjected to a cold treatment before transfer to the appropriate growth chamber. Sterilisation is performed using a 70% ethanol mix with mild agitation for 3 minutes, before the seeds are dried on filter paper and transferred to sterile 1/2 MS plates (composed of 2.4g/L Murashige and Skoog medium, 0.8% phytoagar in deionised water, pH 5.6-5.8). All plates are sealed with micropore tape as opposed to parafilm in order to allow for gas exchange. Plates are then covered and chilled at 4°C for three days and then transferred to a growth cabinet. After an additional 7-10 days these seedlings are then transferred to soil or used immediately.

2.2 Microscopy

2.2.1 General

When imaging tobacco leaf epidermal cells, small leaf sections (typically a 25 mm^2) are cut from infiltrated tobacco leaves and the abaxial surface imaged. When imaging arabidopsis tissue, either the whole seedling is mounted or a single leaf

is removed and mounted. Leaf imaging is also performed on the abaxial surface except when using light sheet microscopy, where the adaxial side provides a more favorable surface curvature. Plants are mounted in water or an appropriately diluted drug for confocal microscopy and VAEM, whilst light sheet microscopy requires mounting in 1/2 MS media.

Standard excitation and detected emission wavelengths used for VAEM, confocal and lightsheet microscopy are as follows:

Table 2.1: Common fluorophore/dye excitation and detected emission wavelengths
Excitation and emission wavelengths used for flurophores/dyes used in this work.

Fluorophore/dye	**Excitation wavelength (nm)**	**Emission spectra (nm)**
Green fluorescent protein (GFP)	488	493-598
Clover (CLV)	488	493-598
Red fluorescent protein (RFP)	561	595-652
Rhodamine B	561	531-620
Cyan fluorescent protein (CFP)	405	454-507

Pixel scaling, averaging and exposure were varied as appropriate. All imaging was performed at room temperature unless explicitly stated otherwise.

2.2.2 Confocal microscopy

Confocal microscopy was performed at Oxford Brookes University using either a Zeiss LSM880 with an Airyscan detector or a Zeiss LSM800 with an Airyscan detector. Images were collected on Zeiss LSM880 with either a Zeiss PlanApo 100x/1.46 NA oil immersion objective or a Zeiss PlanApo 63x/1.46 NA oil immersion objective. Confocal laser-scanning microscopy focuses a small beam of light onto the sample, exciting the sample within this small area. Only the light emitted from the in-focus plane is collected, while out of focus light is excluded by the

pinhole, producing images with minimum out of focus light that is commonly collected by widefield microscopy. The beam is is scanned back and forth across the sample in order to generate the image (Jonkman and Brown, 2015). The Airyscan detector on the Zeiss 880 confocal employs a 32-channel GaAsP photomultiplier tube (PMT) array detector - 32 hexagonally packed detector arrays, with each array acting as its own pinhole and maintaining its own positional information (Huff, 2015). This greatly improves both the resolution of the images collected and their signal-to-noise ratio.

2.2.3 VAEM microscopy

VAEM (variable angle epifluorescence microscopy) is performed using a TIRF (total internal reflection fluorescence) microscopy system. TIRF microscopy generates an evanescent wave that is totally internally reflected at the coverslip-water interface. This provides illumination only at the surface of the sample nearest the coverslip and the evernescent wave cannot penetrate deeply into the sample. This technique requires the laser to hit the sample at a super-critical angle which is particularly challenging in plant cells due to the undulations of the plant leaf surface. VAEM however, still requires that the laser hits the sample at an angle, but the angle can itself be subcritical, which can result in a variable depth of illumination through the sample (Konopka and Bednarek, 2008). As we do not know the precise angle at which the laser hits the surface of the sample, due to variations in the angle of the sample surface, we term all imaging VAEM as opposed to TIRF microscopy.

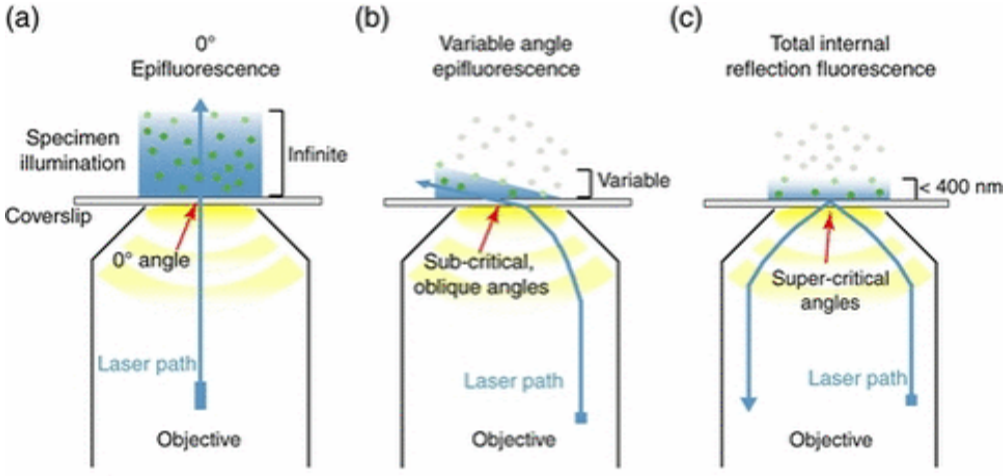


Figure 2.1: Comparison of Epifluorescence, VAEM and TIRF microscopy - image taken from (Konopka and Bednarek, 2008)
Comparison of the laser path (blue line) and the region of the sample illuminated (blue) for three types of microscopy (a) epifluorescence microscopy, (b) VAEM and (c) TIRF microscopy. Image taken from (Konopka and Bednarek, 2008) and adapted by cropping so only the relevant section of the image is included.

VAEM is performed using a Zeiss Axio-Observer z1 with a 100x/1.46 NA oil immersion objective. The attached optical system was the iLas^2 TIRF system which provides orbital excitation, providing even illumination across the field of view. Laser power was set to approximately 5nm (continuos wave) and an excitation wavelength of 488nm was used. Images were collected using an Andor iXon cooled EMCCD camera.

2.2.4 Light sheet microscopy

Light sheet microscopy was performed in the Leica TCS SP8 with DLS (Digital light sheet) with the HC Fluotar L 25x water dipping lens. Illumination was with the NKT white light laser (488nm excitation) and 5mm spaced DLS Twinflect mirrors were used to create a light sheet with a theoretical thickness of 3.7 µm^2. Images were captured using an ORCA flash 4 V2.

2.3 Plant transformation and transfection methods

Stable transfection of plants was performed in arabidopsis using the 'Floral dip' method, while transient transfection was performed using *Agrobacterium tumefaciens*-mediated transformation (hereafter referred to as agrobacteria).

2.3.1 Generation of arabidopsis stable lines

Floral dipping of arabidopsis was performed as recommended by Clough and Bent (1998). In short, pelleted transformed agrobacterium are re-suspended in a 5% sucrose, 500 µl L^{-1} Silwet 77 solution. Arabiopsis flowering stems are dipped into this culture and then agitated for approximately 1 minute, and the plants wrapped in cling film for 24 hours to ensure survival of the agrobacteria. This process is repeated 7 days later to increase the efficiency of transformation. After an additional week, watering is ceased and the plants are dried in preparation for seed collection. Once dried and collected, transformed seeds are identified by selection on 'Magic sand' as performed by Davis *et al.* (2009), whereby seeds are planted on silica dioxide soaked in 1/4 MS media and the relevant selection agent (hygromycin or BASTA at 5 µg mL^{-1}). Transformants can be identified by their significantly improved growth or ability to germinate, depending on the selection agent. Transformants are transferred to soil at approximately 10 days old and grown under greenhouse conditions.

2.3.2 Transient flourescent protein expression in tobacco leaf epidermal cells

Tobacco was grown for 4-6 weeks under greenhouse conditions in preparation for transient Agrobacteria-mediated expression according to Sparkes *et al.* (2005). Transient expression of fluorescent constructs was performed according to Sparkes *et al.* (2006). Transformed agrobacteria are pelleted by centrifugation at 2200 g at room temperature for 5 minutes. Infiltration buffer ($5\,\mathrm{mg\,ml^{-1}}$ glucose, 50mM MES, 2mM $Na_3PO_4 \cdot {}_{12}H_2O$ and 0.1 mM acetosyringone) is used to wash the pellet once and then to resuspend the agrobacteria. The bacterial suspension was diluted in the infiltration buffer to an OD_{600} of appropriate optical density (typically between OD_{600}0.1-0.01). The final dilution of the infiltration medium was injected through the small puncture, created using a pipette tip, on the underside of the tobacco leaf using a 1ml syringe. The extent to which the infiltration media spreads through the leaf is indicated by marking the tobacco leaf with a pen, in order to ensure infiltrated regions can be identified later. Infiltrated plants are kept at 23°C for 72 hours prior to imaging.

2.4 Rhodamine B staining for ER visualisation

Arabidopsis seedlings are transferred to 1 µM Rhodamine B hexyl ester and incubated for 15 minutes. After a wash in distilled water the seedlings were mounted on a glass slide in water as described by Hawes *et al.* (2018b).

2.5 Drug and stress treatments

In preparation for stress and drug treatments small leaf segments of approximately 25 mm^2 were cut from the transformed tobacco. Heat shock is induced by rapidly heating the leaf segment to 42°C for 20 minutes in water. Drug treatments are performed by incubating leaf segments in either latrunculin B (Lat B, 25 µM for 30 minutes) or Brefeldin A (BFA, 100 µg mL^{-1} for 1 hour) at room temperature. After heat shock leaf pieces are mounted in heated water, whilst after treatment with Lat B and BFA, samples are mounted in the drug solution used for incubation in order to avoid washout effects. Imaging of an individual leaf piece was completed within half an hour after heat shock in order to avoid changes in ER morphology in the subsequent absence of heat.

2.6 RT-PCR analysis of wild-type and mutant lines

2.6.1 RT-PCR on wild-type seedlings

Arabidopsis (Columbia-0) seeds are first sterilized using 70% ethanol for 3 minutes, then introduced to sterile 1/2 MS plates. Seeds were kept in the dark for 3 days at 4°C to ensure uniform germination, and then transferred to a growth cabinet with standard conditions. After 7 days growth, a clean razor blade was used to separate root from shoots and the tissue frozen in liquid nitrogen for storage at −80°C. At this stage, plants required for mature tissue extraction are placed on soil for further growth under greenhouse conditions. Tissue from mature plants was harvested after an additional 28 days, frozen in liquid nitrogen and then stored

at −80°C.

RNA is extracted from harvested tissue using the Monarch Total RNA Miniprep Kit (New England Biolabs) according to the manufacturer's instructions and RNA quality and quantity assessed using spectrophotometry. The AMV First Strand cDNA Synthesis Kit (New England Biolabs) was used according to the manufacturer's instructions to create cDNA, including negative controls for genomic DNA contamination. Primers for dissimilar regions of AtLNP1 (AtLNP1, AT2G24330), AtLNP2 (AtLNP2, AT4G31080) and actin (AtACT1, At2g37620) as a control were used to amplify the extracted cDNA and the resultant products analysed (table 2.2).

Table 2.2: Primers designed for RT-PCR analysis of AtLNP1, AtLNP2 and actin Forward and reverse primers designed to target dissimilar regions of AtLNP1, AtLNP2 and actin cDNA generated from extracted RNA.

Target	FWD primer	REV primer
AtLNP1	GCCTTTCTTCTCTATTCTTCACTTG	CCTCCCGAGTGTTTGG
AtLNP2	CTCTTGCTTATTCCTCAATCGTC	CGTGATTGGTTAACCTCCATG
Actin	TGGAACTGGAATGGTTAAGGCTGG	TCTCCAGAGTCGAGCACAATACCG

The intensity of cDNA bands were identified using gel electrophoresis (1% Agar and 1x TAE gel, with 2 µL SYBR Safe DNA Gel Stain (Invitrogen) per 100ml gel, samples run at approximately 80 volts for 20-30 minutes in 1x TAE buffer) and the resulting images were used to compare the intensity of detected bands under the assumption that there is a linear correlation between the intensity of the image obtained at the DNA concentration within the gel. The background intensity was identified from a randomly selected region of the image and subtracted from the measured intensity of each band. The band intensity was then normalised against the actin extraction as a control for the quality of the RNA extraction and cDNA synthesis to give a final relative measure of Lunapark transcription across different tissues.

2.6.2 Confirmation of T-DNA insertion lines

Arabidopsis T-DNA insertion lines are initially grown on half MS plates, after a 3 day vernalisation. They are then transferred to soil and grown under greenhouse conditions for an additional 10-20 days. Leaf tissue is extracted, frozen in liquid nitrogen and manually pulverized in preparation for genomic DNA extraction. A basic extraction buffer (200 mM Tris-HCl pH7.5, 250 mM NaCl, 25 mM EDTA and 0.5% SDS) is used to extract the DNA which, after centrifugation to separate the DNA from the crushed leaf tissue, is precipitated with isopropanol. The pellet is subsequently washed twice with cold 70% ethanol and re-suspended in nuclease-free water for downstream steps. Primers are designed using the online T-DNA Primer Design tool, provided by the Salk Institute Genomic Analysis Laboratory. Two primers are created that flank the predicted T-DNA insertion site (termed the right primer, RP and the left primer, LP) and an additional standard primer targeted to within the T-DNA insertion (the left border primer, LBb1.3, ATTTTGCCGATTTCGGAAC) (table 2.3). The absence of an insertion will result in an approximately 900 bp size band when tested with LP and RP, whilst lines homozygous for the T-DNA insertion will produce a band approximately 400 bp in size when tested with RP and LBb1.3. Heterozygous lines will produce both bands. PCR confirmation was performed using the One Taq Master Mix (New England Biolabs) according to the manufacturers instructions. Further confirmation of gene expression was performed on T-DNA insertions lines using RT-PCR as described previously.

Table 2.3: Primers used for T-DNA insertion confirmation
Table of the variable border primers used to confirm T-DNA insertion in arabidopsis, designed using the online T-DNA Primer Design tool, provided by the Salk Institute Genomic Analysis Laboratory.

Line	Target Gene	Primer name	Primer
SALK_034698	AtLNP1	Right primer	TTGGAAACCTGGATTGTTGAC
		Left primer	AGGAGCAATTTGAACTCCCTC
SALK_205001	AtLNP1	Right primer	ATCTGTGGAAACTGCCGTATG
		Left primer	AAACCTCATAATGTTGACGCG
SALK_031496	AtLNP2	Right primer	GATAGCAGCCCTTACCGATTC
		Left primer	GCCCCACTCCAGAAATAAAAG
SALK_072194	AtLNP2	Right primer	TGTAGCTCATGGTTCTCTGCC
		Left primer	ATGATGGCAGTTGGATCTCAC

2.7 Cloning and expression plasmids

2.7.1 Gateway cloning

A standard Gateway cloning protocol was followed for all stages of cloning into expression plasmids. Primers for initial amplification are obtained from Eurofins Genomics and used, alongside Q5 high-fidelity DNA polymerase (New England Biolabs) for cloning entire genes of interest or truncations of genes of interest. After initial amplification, genes of interest were cloned using Gateway technology (Invitrogen). Initially genes are cloned into a pDONR/221 Gateway Entry vector using BP Clonase II Enzyme Mix (ThermoFisher) according to the manufacturers instructions but using half volumes. The resulting product is then transformed into NEB 5-alpha Competent *Escherichia coli* (High efficiency) cells according to manufacturer's instructions, modified to use half the suggested volume of cells and a fifth of the recommended volume of SOC media for recovery. Selection media is initially composed of agar plates created to manufacturer's instructions, containing

an appropriate concentration of selection agent (50 µg mL^{-1} when using kanamycin or spectinomycin and 25 µg mL^{-1} when using rifampicin). Single cultures are selected and tested for the presence of the plasmid of interest by PCR. After plasmid confirmation by colony PCR, colonies are transferred to liquid culture and kept overnight at 37°C and shaking (approximately 200 rmp). Once colonies have grown sufficiently, DNA is extracted using the Monarch Plasmid Miniprep Kit (New England Biolabs) according to manufacturer's instructions. The DNA sequence of the gene of interest within the plasmid is confirmed by sequencing by Eurofins Genomics. Once the sequence is confirmed, an LR reaction, performed according to manufacturer's instructions supplied with the LR Clonase II Enzyme Mix (ThermoFisher) but with all suggested volumes halved, is used to generate the desired expression vector (see below). At this stage, constructs are again transformed into competent *E. coli*, transformation is confirmed by colony PCR and the plasmid extracted using the Monarch Plasmid Miniprep Kit (New England Biolabs).

2.7.2 Expression plasmids used

Below is a list of plasmids used in this work and the primary contributor to their creation:

Table 2.4: Expression vectors used in this work
A complete list of expression vectors used in the course of this work alongside the primary contributor to development/source, alongside the most relevant/first publication in which they were mentioned.

Construct	Plasmid	Source	Related
RFP-AtLNP1	pB7WG2	Verena Kriechbaumer	Pain *et al.* (2019)
RFP-AtLNP2	pB7WG2	Verena Kriechbaumer	Pain *et al.* (2019)
AtLNP1-GFP	pAHC17	Emily Breeze	Kriechbaumer *et al.* (2018)

AtLNP2-GFP	pAHC17	Emily Breeze	Kriechbaumer *et al.* (2018)
PLNP1::AtLNP1-GFP	pAHC17	Emily Breeze	Kriechbaumer *et al.* (2018)
L1T1-CLV	pV7FWG2	Charlotte Pain	Unpublished
L1T2-CLV	pV7FWG2	Charlotte Pain	Unpublished
L1T3-CLV	pV7FWG2	Charlotte Pain	Unpublished
L1T4-CLV	pV7FWG2	Charlotte Pain	Unpublished
L1T5-CLV	pV7FWG2	Charlotte Pain	Unpublished
L2T1-CLV	pV7FWG2	Charlotte Pain	Unpublished
L2T2-CLV	pV7FWG2	Charlotte Pain	Unpublished
L2T3-CLV	pV7FWG2	Charlotte Pain	Unpublished
L2T4-CLV	pV7FWG2	Charlotte Pain	Unpublished
L2T5-CLV	pV7FWG2	Charlotte Pain	Unpublished
AtLNP1-ZF-CLV	pV7FWG2	Charlotte Pain	Unpublished
AtLNP2-ZF-CLV	pV7FWG2	Charlotte Pain	Unpublished
RFP-RTN1	pB7WGR2	Imogen sparkes	Sparkes *et al.* (2010)
RFP-HDEL	pVKH18En6	Federica Brandizzi	Brandizzi *et al.* (2003)
GFP-HDEL	pVKH18En6	Federica Brandizzi	Brandizzi *et al.* (2003)
GFP-CXN	pVKH18En6	Sarah Irons	Irons *et al.* (2003)
CXN-mCherry	pVKH18En6	Norman Groves	Groves *et al.* (2019)
paGFP-CXN	pMDC32	John Runions	Runions *et al.* (2006)
ST-RFP	pVKH18En6	Federica Brandizzi	Renna *et al.* (2005)
ST-CFP	pVKH18En6	Federica Brandizzi	Renna *et al.* (2005)
GFP-TUA6	pBI121	Petra Boevink	Ueda *et al.* (1999)
YFP-actinCB	pB7WGY2	Verena Kriechbaumer	Rocchetti *et al.* (2014)
Lifeact-GFP	pMDC43	Alexandre Martinière	Riedl *et al.* (2008)
GFP-FABD2	pCB302	Boris Voigt	Voigt *et al.* (2005)
mEOS-TAR2	pB7FWG	Verena Kriechbaumer	Kriechbaumer *et al.* (2016)
RFP-ATG8	pB7WG2	Pengwei Wang	Wang *et al.* (2016a)

Lunapark constructs generated during this work came directly from AtLNP1 and AtLNP2 pDONR207 vectors supplied by Verena Kriechbaumer. These pDONR vectors where either used as a source of AtLNP1/AtLNP2 from which truncations could be cloned prior to insertion into separate pDONR vectors, or was used directly for transfer into appropriate expression vectors.

2.7.3 Transformation of competent agrobacterium

Competent agrobacteria (strain GV3101) are prepared by initially growing a large volume of agrobacteria, approximately 200ml, in LB media alongside the appropriate antibiotic (Lysogeny broth, LB, with 25 µg mL^{-1} rifampicin). This large volume of agrobacteria is pelleted using centrifugation at 3500rpm for 30 minutes at 4°C. This culture is re-suspended in cold 1M $CaCl_2$ for 15 minutes and then spun again at 5000rpm for 10 minutes at 4°C. The resulting pellet is re-suspended in 15 ml 1M $CaCl_2$, aliquots are created and the suspended, competent agrobacteria are frozen and stored at −80°C. Agrobacterium transformation requires that the competent agrobacterium are thawed on ice and mixed with the 400-600 ng of the expression plasmid of interest for approximately 5 minutes. This mixture is then plunged into liquid nitrogen, then rapidly thawed in a 37°C waterbath for rapid heat transfer. The agrobacteria are allowed to recover at 28°C with shaking in LB for 2-3 hours and are then transferred to an agar plate containing appropriate selection antibiotics (25 µg mL^{-1} of rifampicin and 50 µg mL^{-1} of either kanamycin or spectinomycin). Plates are incubated at 28°C for 2 days by which point colonies of agrobacteria can be observed. The transformed agrobacteria are then transferred to liquid culture from which point it can be used for agrobacterium-mediated transformation of plants or stored at −80°C in 50% sterile glycerol for long term storage.

2.8 Truncation cloning

6 truncations of both AtLNP1 and AtLNP2 were generated for analysis. The truncations were generated from AtLNP1 and AtLNP2 pDONR207 vectors and were created using modified Gateway primers. Cloning was performed using Q5 high-fidelity DNA polymerase (New England Biolabs) and primers obtained from Eurofins Genomics (Ebersberg). Each primer used is listed below:

Table 2.5: Gateway primers designed for Lunapark truncations
Full list of primers (designed for gateway cloning protocols) used to generate AtLNP1 and AtLNP2 truncations.

Truncation	Primer sequence
L1T1 FWD	GGGGACAAGTTTGTACAAAAAAGCAGGCTTCCCGCCA ATGGATTCCGCCG TTGTA
L1T2 FWD	GGGGACAAGTTTGTACAAAAAAGCAGGCTTCCCGCCA ATGAACTTCATTAGAAATCTCATCG
L1T3 FWD	GGGGACAAGTTTGTACAAAAAAGCAGGCTTCCCGCCA ATGACCACCAGAGATGAG
L1T4 FWD	GGGGACAAGTTTGTACAAAAAAGCAGGCTTCCCGCCA ATGAGGATCTTGCCAATGT
L1T5 FWD	GGGGACAAGTTTGTACAAAAAAGCAGGCTTCCCGCCA ATGAGGATGTGTGACCG
L1 REV	GGGGACCACTTTGTACAAGAAAGCTGGGTC GTTTGGTGTCTCATTCTC
L2T1 FWD	GGGGACAAGTTTGTACAAAAAAGCAGGCTTCCCGCCA ATGGCTGCCGTGGC
L2T2 FWD	GGGGACAAGTTTGTACAAAAAAGCAGGCTTCCCGCCA ATGCTCACCAGAAATCTCATC

L2T3 FWD	GGGGACAAGTTTGTACAAAAAAGCAGGCTTCCCGCCA ATGACGGAAGATTTGGATTG
L2T4 FWD	GGGGACAAGTTTGTACAAAAAAGCAGGCTTCCCGCCA ATGATCTTGCCAATGTTTATCTTAC
L2T5 FWD	GGGGACAAGTTTGTACAAAAAAGCAGGCTTCCCGCCA ATGTCAAAGATGTTTGACCG
L2 REV	GGGGACCACTTTGTACAAGAAAGCTGGGTC GCTCGGTGTCCC
AtLNP1-ZF FWD	GGGGACAAGTTTGTACAAAAAAGCAGGCTCT ATGGCGGTGGGAG
AtLNP1-ZF REV	GGGGACCACTTTGTACAAGAAAGCTGGGTCA ATGAGCGCATATGATTGTG
AtLNP2-ZF FWD	GGGGACAAGTTTGTACAAAAAAGCAGGCTCTA TGGCGCAGGAGC
AtLNP2-ZF REV	GGGGACCACTTTGTACAAGAAAGCTGGGTCA ATGAGCGCATATGATTGTG

2.9 ImageJ analysis of Rhodamine B stained ER

Images were collected using the Ziess 880 confocal microscope with Airyscan and were analysed using ImageJ and associated plugins (fig. 2.2a). After initial import into ImageJ, the contrast of the image was adjusted to improve the contrast between the ER network signal and the cell background, whilst over-saturating the mitochiondrial signal (fig. 2.2b). A smoothing function was also applied to reduce

image noise. ER signal segmentation was performed using the ImageJ plugin Trainable Weka Segmentation (fig. 2.2c). Using a digitizing tablet, unwanted signal was highlighted to train the segmentation software - this included mitochondrial signal, cell background signal and non-cell signal. Small regions of the desired ER network signal were also selected as a guide for the desired intensity. The result is a binary image composed only of the ER signal and background (fig. 2.2d). In order to remove small holes segmented ER signal, caused by image noise, a closing function is applied to the binary image. This prevents later detection of impossibly small polygonal regions caused by segmentation errors and ensures a high connectivity of the tubular network. Using a digitizing tablet, an outline of the cell was drawn and classed as a ROI and the area within that measured. This outline serves as the ROI required by the ImageJ command 'Analyse particles'. The image LUT is inverted at this stage, as is required by the 'Analyse particles' command and the polygonal regions are segmented from the binary image and analysed, with polygonal regions not fully enclosed by the ER network excluded from the analysis (fig. 2.2e). The 'Analyse particles' command produces an output of the outline of all analysed 'particles' (polygonal regions) and measures the particle area. The binary image of segmented ER structure is skeletonized using the ImageJ skeletonize command to produce a one pixel wide skeleton of the ER structure that runs along the center of the ER tubule (fig. 2.2f). Cisternae are also identified by applying an iterative opening function to the binarised, segmented ER image which removes tubules connecting cisternae. Cisternae are subtracted from the skeletonized network, using the ImageJ image calculator, resulting in a skeletonized version of the tubular ER network (fig. 2.2g). This removes skeletonisation errors that occur in thicker regions of ER, characterized as cisternae, enabling accurate characterization of tubular network three-way junctions (fig. 2.2h). The ImageJ 'Analyse skeleton (2D/3D)' command, which provides a count of the number of three-way branch points identified in the skeletonized tubular network alongside

tubule skeleton branch lengths.

Though this analysis method is most appropriate for analysis of ER images with high background intensity and unwanted high intensity regions, such as rhodamine B stained cells, it can also be applied to *amilnp1lnp2* lines which stably express GFP-HDEL.

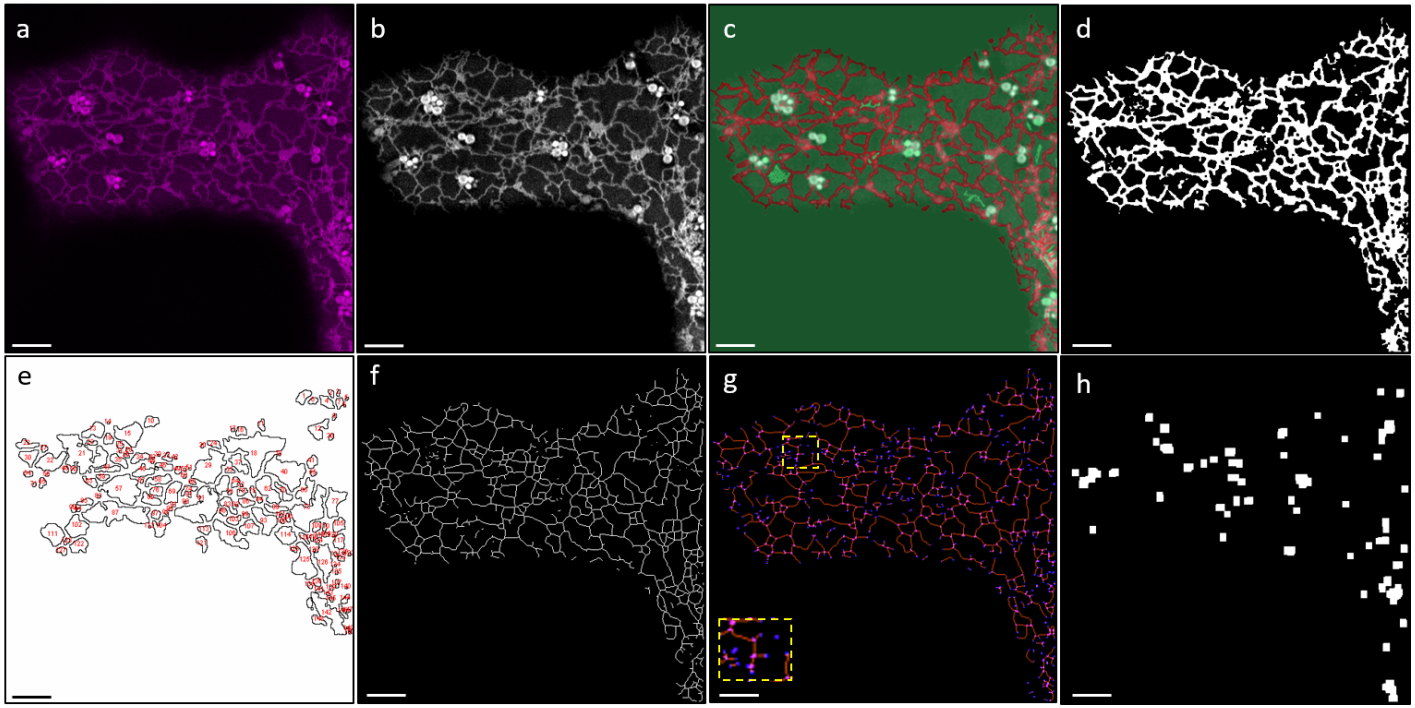


Figure 2.2: Endoplasmic reticulum (ER) network analysis workflow for arabidopsis *lnp1* and *amilnp1lnp2* mutants. The ER network was analysed and quantified using the following steps. Example images are shown for every step. (a) Initial image; (b) enhanced contrast; (c) Weka trainable segmentation: red regions correspond to detected ER structures, green highlights rejected ER regions (e.g. here for lnp1 mutant stained mitochondria); (d) binary image of segmented ER; (e) polygonal region analysis output with numbered outlines of each polygonal region that is fully enclosed by the ER; (f) skeletonized ER structure; (g) analysed ER skeleton with blue pixels indicating detected end points (single pixel wide) and magenta pixels showing detected junctions (2x enlarger region shown by dashed yellow lines); (h) cisternae detected by an iterative opening function. Scale bars 5 µm.

2.10 AnalyzER analysis of ER structures

Full details of the methods employed to analyze ER structures using AnalyzER are not included here due to their length. A full instruction manual, alongside the software and a tutorial is provided at www.markfricker.org and is available, open-access alongside 'Quantitative analysis of plant ER architecture and dynamics' (2019), Pain *et al. Nature Communications*, **10**(1):984.

2.11 Single particle tracking

Single particle tracking was performed using two free use software package: the TrackMate plugin (Tinevez *et al.*, 2017) run under FIJI (Schindelin *et al.*, 2012) and an automated single particle analysis software developed by Wilson *et al.* (2016). This work was performed on a small number of time series of single molecules collected by VAEM.

Single particle tracking using the automated particle tracking software developed by Wilson *et al.* (2016) requires little user input. After loading the time series into the GUI, the estimated image noise (categorized as very high, high, medium or low) is selected and an estimate of particle size (in pixels) and the number of particles is given, particle identification is performed Single particle tracking by TrackMate is performed as standard tracking. Single particles are identified using a LoG detector (Laplacian of Gaussian) to detect object edges after smoothing by a gaussian filter with the filters sigma (the area over which the filter is applied) suited to the estimated single particle size in pixels. Once particles have been identified and maxima that are too close together excluded, a simple LAP (Linear Assignment Problem) tracker, which is well suited for particles undergoing Brownian motion

(Tinevez *et al.*, 2017). Outputs are generated automatically and loaded into R for further analysis.

2.11.1 Single particle tracking diagram generation

Included below is the R code used to plot the distribution of particle speed by area:

```
source("LoadData.R")
require(ggplot2)

pdf("graphs/VelocityHexGraphs.pdf")
for(x in unique(LinksInTracks$Source)){
  dataSubset <- LinksInTracks[Source == x]

 gg <- ggplot(data = dataSubset,
              aes(x = EDGE_X_LOCATION,
                  y = EDGE_Y_LOCATION,
                  z = VELOCITY)) +
   stat_summary_hex(fun = function(x) mean(log10(x + 1)),bins = 50) +
   ggtitle(x) +
   coord_fixed() +
   theme_dark() +
   scale_fill_gradient2(midpoint=mean(log10(dataSubset$VELOCITY + 1)),
                        low="blue",
                        mid="white",
                        high="red")

 print(gg)
}
dev.off()
```

3 | AnalyzER

Contents

3.1 Introduction: The challenges and goals of plant ER analysis 89

3.1.1 The plant ER is a complex, contiguous pleomorphic structure 89

3.1.2 ER parameters are influenced by each other 92

3.1.3 The goals of AnalyzER development 94

3.2 Methods and results 95

3.2.1 Image structure and quality requirements for optimal ER analysis 95

3.2.2 Image structure considerations 97

3.2.3 Developing a pipeline for plant ER segmentation - AnalyzER 101

3.2.4 Using AnalyzER 103

3.2.5 Precision-recall analysis of the accuracy of ER structure 105

3.2.6 Estimation of ER tubule width 107

3.2.7 Preventing mis-classification of 'large' tubules 110

3.2.8 Calculating the structural parameters of the plant ER . 111

3.2.9 Extending the range of AnalyzER: analysis of the time domain 111

3.2.10 Quantifying fluorophore distributions throughout the ER 122

3.2.11 Multivariate analysis of modified ER structure and dynamics 131

3.3 Discussion 135

3.1 Introduction: The challenges and goals of plant ER analysis

3.1.1 The plant ER is a complex, contiguous pleomorphic structure

The plant ER is a highly complex, contiguous, dynamic structure that plays an essential role in maintaining cellular function. Structural and dynamic analysis of the plant ER is hindered in comparison to analysis of discrete organelles such as mitochondria (Watanabe *et al.*, 2007) and Golgi bodies (Runions *et al.*, 2006), as it presents unique challenges in terms of its structure. Primarily the plant ER is a continuous structure, and so must be segmented as a whole, requiring enhancement processes that preserve the continuity of the ER, despite variations in ER signal intensity when images are captured using confocal microscopy. Within this contiguous structure, distinct subdomains of the ER are separately characterized based on size and, in some cases, dynamics. Cisternae are relatively large regions of ER traditionally characterised by the presence of an extended flat region of membrane (Porter and Machado, 1960), and are typically classed as having a minimum area of 0.3 µm^2 (fig. 3.1a). This canonical view of cisternae structure has recently been questioned in mammalian systems (Nixon-Abell *et al.*, 2016; Schroeder *et al.*, 2019). For the purposes of confocal microscopy and image analysis, cisternae appear as dilated regions of ER with variation in intensity throughout the structure which may be indicative of sub-resolution structures within the cisternal regions. ER punctae are similar to cisternae in that they are dilated regions of ER but are typically 0.1-0.3 µm^2 in size and remain persistent over an extended period of time, previously defined as 5-10 seconds by Sparkes *et al.*

(2009a) (fig. 3.1b). These regions are thought to be contact sites between the plasma membrane and the ER and can form sub-regions of cisternae or can be associated with the center of a tubule as the ER surface moves across the contact point (fig. 3.1c, Sparkes *et al.* (2009a)). Tubules are long, thin regions of ER that join at either three-way junctions, to cisternae/punctae, or form free ends (fig. 3.1a). Though structurally distinct, these sub-regions can now also be identified by differential protein localisation with members of the reticulon protein family (AtRTN1-4 and AtRTN13) localising to curved edges of tubules and the edge of cisternae (Sparkes *et al.*, 2010), and Lunapark 1 (AtLNP1) localising to the center of cisternae (Kriechbaumer *et al.* (2018), chapter 4).

Plant ER dynamics, in terms of gross remodelling, present a unique challenge for analysis as remodelling occurs over a range of scales and orientation. That is to say, the movement of the ER membranes varies widely across cells, with bulk translocation occurring as 'streams' which move much more rapidly than the rest of the ER (Ueda *et al.*, 2010). Therefore any analysis of ER remodelling must be capable of tracking a large range of speeds and therefore consider ER remodelling at a range of scales. At the same time, within the confines of the cell, ER tubules and cisternae can theoretically move in any direction, requiring analysis of movement in a range of directions (orientations). While the rate at which ER remodels is of interest, a large proportion of the ER remains stable over extended periods of time. The length of time over which these punctae remain stable is not captured by standard cross-correlation measures, instead they require a different type of analysis, such as persistency mapping (Sparkes *et al.*, 2009a).

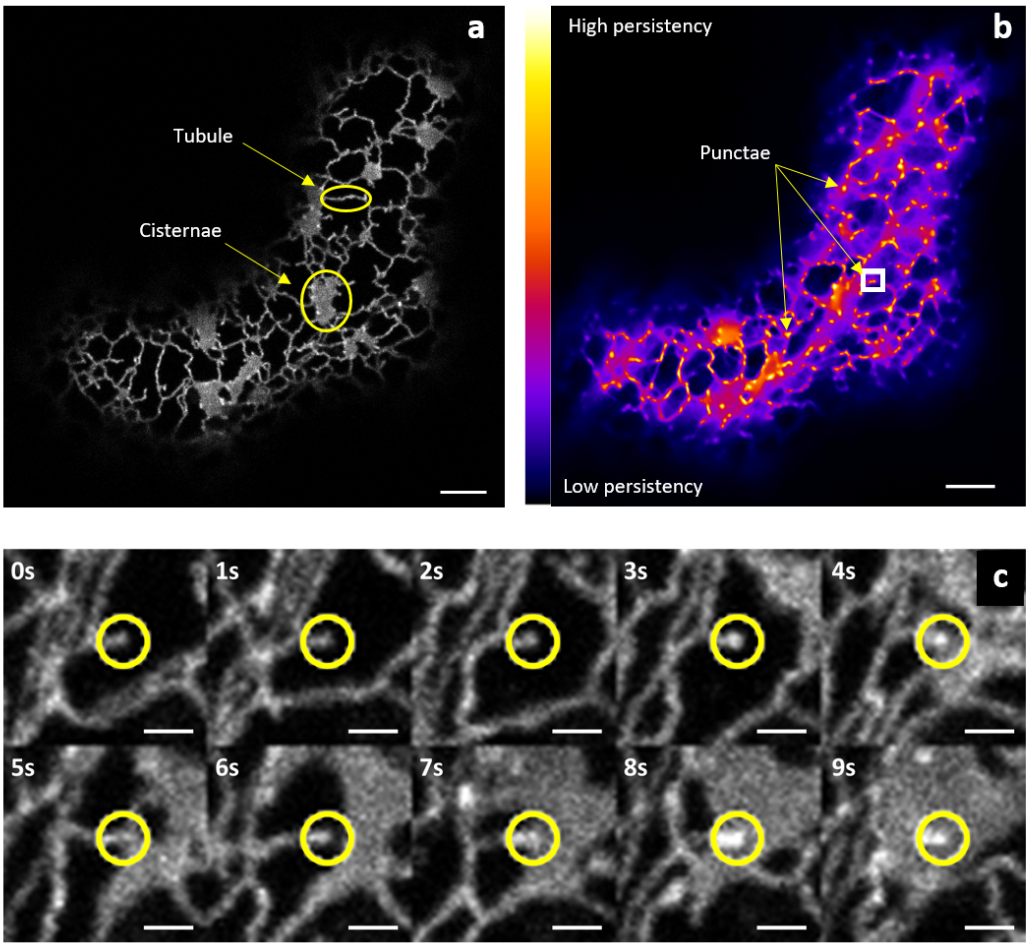


Figure 3.1: Structural components of the plant ER
Examples of the sub-regions of the plant ER identified in tobacco transiently expressing GFP-HDEL. (a) Tubules and cisternae are marked by yellow circles, scale bar scale bar 5 µm; (b) identification of putataive punctae through t-projection of a timeseries to identify regions that are highly persistent over time (250s). Highly persistent regions are shown in light yellow and localise to small punctae, example of which are marked by yellow arrows, scale bar 5 µm. (c) A single punctae originally identified on a tubule shown over time as a cisternae flows over the connection point. This point is highly persistent over 250 frames (b, white square), scale bar 1 µm.

3.1.2 ER parameters are influenced by each other

Parameters of ER structure and dynamics are at least partially mutually dependent, requiring the quantification of as many parameters as possible to ensure accurate description of modified ER. For example, reducing the mean area of polygonal regions could theoretically be achieved by either increasing the mean area of cisternae or increasing the density/number of ER tubules (fig. 3.2). Reducing the mean area of polygonal regions by increasing the mean cisternal area will have a knock on effect on other parameters, for example, mean persistency of the network will also be increased as larger regions do not show remodeling at the center which is detectable by persistency analysis. Increasing the number of ER tubules however, will result in a reduced mean tubule length, increased number of branch points and likely reduced persistency due to an increase in tubular structures, the remodlling of which is more easily detected using persistency analysis than that of cisternae. Therefore the same phenotype (reduced mean polygonal region area) can be achieved through the modification of multiple ER structure changes (increased cisternae area, or increased tubule number/density), which in turn effect additional ER network parameters (persistency/tubule branch number/mean tubule length).

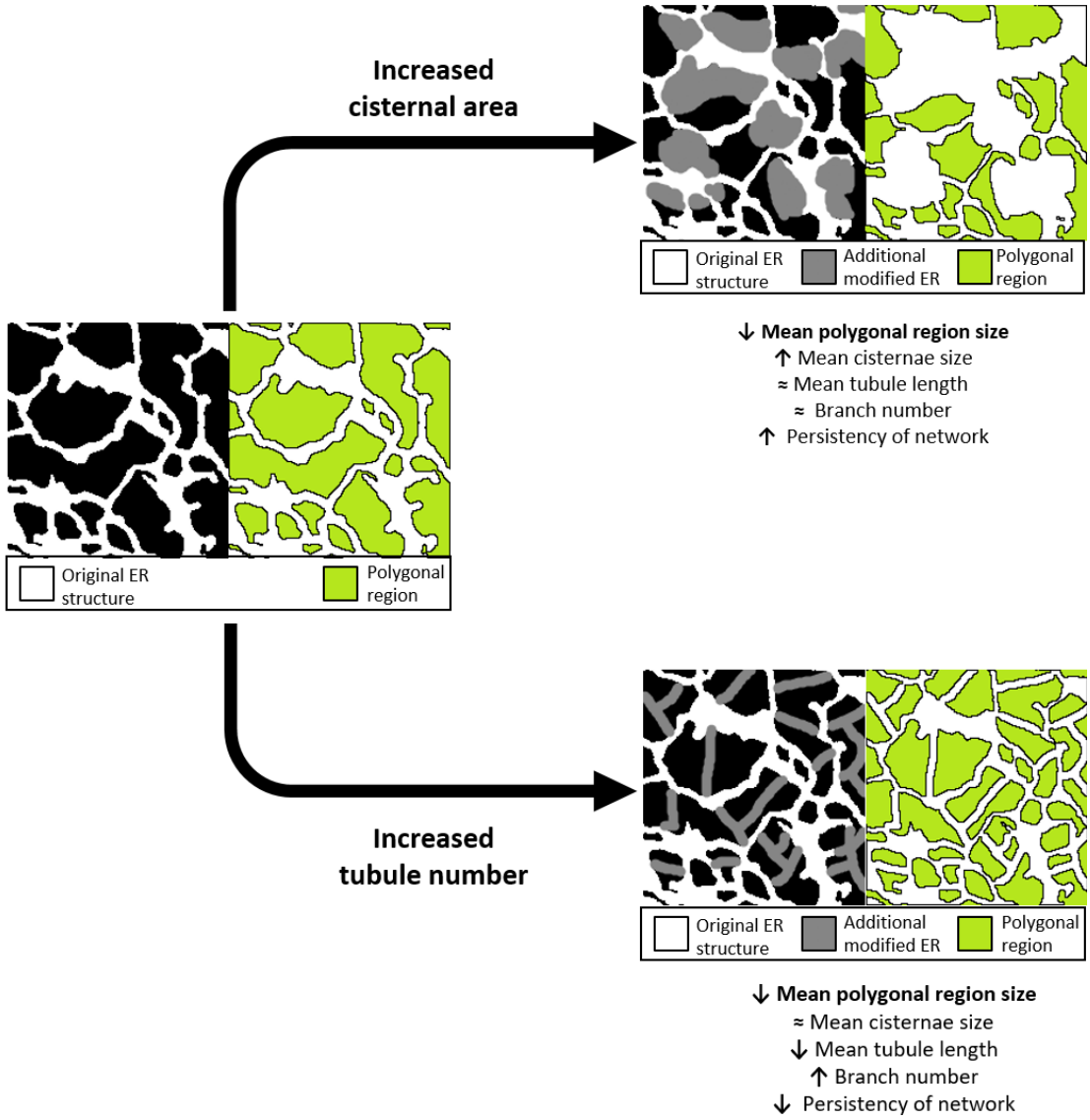


Figure 3.2: A schematic demonstration of the mutual sensitivity of ER structure and dynamics parameters to each other

A reduction in the mean size of polygonal regions enclosed by the network can be induced by either increasing the cisternal area of a network or by reducing mean tubule length, which in turn may effect the persistency of the network or the number of tubule branches. Both modifications have the same result but are only detectable by analysing more than a single ER structure parameter. Original ER structure is shown in white, with potential modifications to ER structure shown in grey. The resulting polygonal regions are shown in green and are, by definition, the inverse of the ER structure.

3.1.3 The aims of AnalyzER development

Tackling the quantification of plant ER structure and dynamics requires the development of a medium throughput, software package (AnalyzER), operating under a single graphical user interface (GUI). AnalyzER is designed to be capable of analysing images captured using multiple techniques and is able to calculate multiple parameters of ER structure/dynamics within a single analysis interface. We aim to quantify (i) the length, width, morphology and protein distribution along ER tubules; (ii) the size, shape, and protein distribution within and around the perimeter of the ER cisternae; (iii) the topological organisation of the tubular and cisternal network determined using graph-theoretic metrics; (iv) the local speed and direction of movement of tubules and cisternae; (v) the presence and distribution of immobile nodes, tubules and cisternae using persistency mapping; and (vi) the size and shape of the polygonal regions enclosed by the network using this novel software package. Throughout the development of the ER analysis software, both known and unknown ER structure modifications were used to test both the accuracy and sensitivity of AnalyzER. The code behind AnalyzER was written by Mark Fricker, the basis of which was adapted from Fricker *et al.* (2017). Experimental design, image collection, analysis and analysis accuracy testing was performed by Charlotte Pain. AnalyzER, the published manual and the tutorial that accompanies AnalyzER, is provided digitally alongside this thesis.

3.2 Methods and results

3.2.1 Image structure and quality requirements for optimal ER analysis

3.2.1.1 The importance of good quality images

All image analysis methods require a minimum 'quality' of image capture, ensuring sufficient resolution through space and time with minimum background noise and strong signals from the features of interest. Image capture also requires consideration of the functions applied in the software, for example persistency analysis requires all timeseries to be captured with the same frame rate as this is the basis for persistency calculations. All subsequent demonstration images in this section were captured using confocal microscopy of tobacco leaf epidermal cells transiently expressing the ER lumenal marker GFP-HDEL.

3.2.1.2 Sufficient marker expression

In order to ensure that accurate network segmentation is possible, the fluorescent construct chosen to mark the ER (typically GFP-HDEL, RFP-HDEL or GFP-CXN) must have sufficiently strong expression to enable accurate network segmentation. Poor expression results in a poorly defined ER network that cannot be properly segmented by the ER analysis software due to difficulties separating the ER network signal from the ambient background intensity of the image. Agrobacteria-mediated transient expression of ER marker constructs in tobacco leaf epidermal cells as described by Sparkes *et al.* (2006) is sufficient to enable suitable quality image acquisition for the chosen ER marker constructs. An OD_{600} 0.1 of transgenic

agrobacteria is required for infiltration to ensure correct segmentation of the network.

3.2.1.3 Minimizing sample drift in z

AnalyzER is capable of compensating for lateral sample drift in either X or Y, however it is not possible to compensate for vertical drift in Z. Sample drift in Z occurs when the sample itself shifts out of the focal plane of the microscope during scanning, resulting in a loss of focus between frame collections or during single frame capturing. This is a common issue with live tissue imaging and is resolved by ensuring that the cover slip is tightly affixed to the slide. An extreme example is shown in figure 3.3, where over an 11.16 second time series, the entire center of the cell drifts out of focus. Sample drift results in non-uniform ER network intensity through time, perturbing ER width calculations and preventing accurate ER dynamic assessments. Any acquired time series with evidence of sample drift are not analyzed.

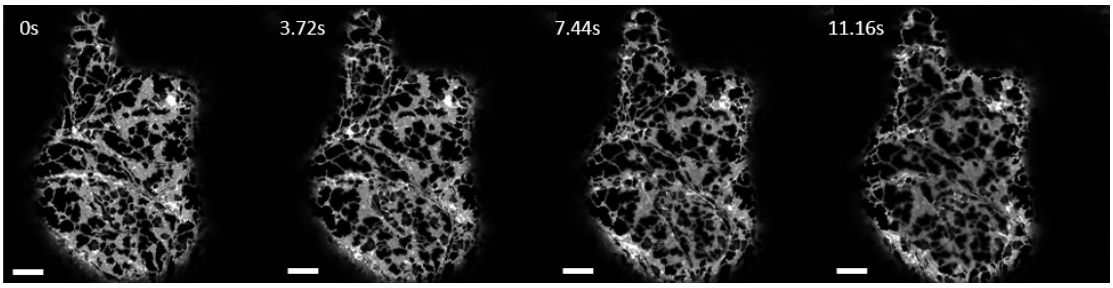


Figure 3.3: Minimizing z-drift
Sample drift at the center of a single cell over an 11.16 second time series, demonstrated by a loss of intensity and sharpness of the ER structure at the center of the cell. Scale bars 5 µm.

3.2.1.4 Image acquisition enhancement - the airyscan

All images collected for analysis were acquired using the Zeiss 880 confocal microscope with Airyscan detector. Standard confocal microscopes use the physical aperture of the pinhole and a unitary detector to produce high resolution images that are optically sectioned, using the pinhole aperture to block out of focus light collected by the objective, preventing it from reaching the detector. The Airyscan detector on the Zeiss 880 confocal employs a 32-channel GaAsP photomultiplier tube (PMT) array detector, 32 hexagonally packed detector arrays, with each array acting as its own pinhole and maintaining its own positional information. The use of the Airyscan detector is highly desirable as a method to improve image quality as it alone is sufficient to improve image signal-to-noise ratio by 4x-8x, whilst providing 1.7x higher resolution images when compared to conventional confocal microscopes, with a lateral resolution of 120 nm now achievable (Huff, 2015).

3.2.2 Image structure considerations

3.2.2.1 Image saturation

To ensure accurate ER width measurements image must be collected without any intensity saturation. Saturation of images, through inappropriately high laser power or image gain, causes all pixels with an intensity higher than the maximum intensity value to be assigned the maximum intensity value available. As a result, the full range of pixel intensity is not captured, making accurate assessments of ER structure impossible. The measured width of tubules depends on their relationship with pixel intensity. Saturation corrupts these measurements by altering the distribution of pixel intensity across tubules, leading to incorrect calculations of tubule and cisternae widths during later analysis. Saturation is reduced by reducing

laser power and image gain.

3.2.2.2 Pixel density and Niquist sampling

Images must be captured at a minimum pixel density of Nyquist sampling, that is the pixel size must be at least half the size of the smallest object that you wish to analyse. Practically, this requires each tubule to be at least three pixels wide, as these are the smallest structures in the ER. This will then be up-sampled within AnalyzER to prevent pixellation errors later in the analysis process. An example of the effect of reduced pixel density is shown in figure 3.4, where an area of plant leaf epidermis with the physical size of 85.02 µm^2 is shown with reduced pixel density. Lower pixel density gives the image a 'blurred' quality as a result of low resolution. This results in the loss of fine tubular structures hindering proper segmentation of the ER network. As pixel density is increased however, the scan speed of the confocal is reduced which can result in errors related to low scan speed.

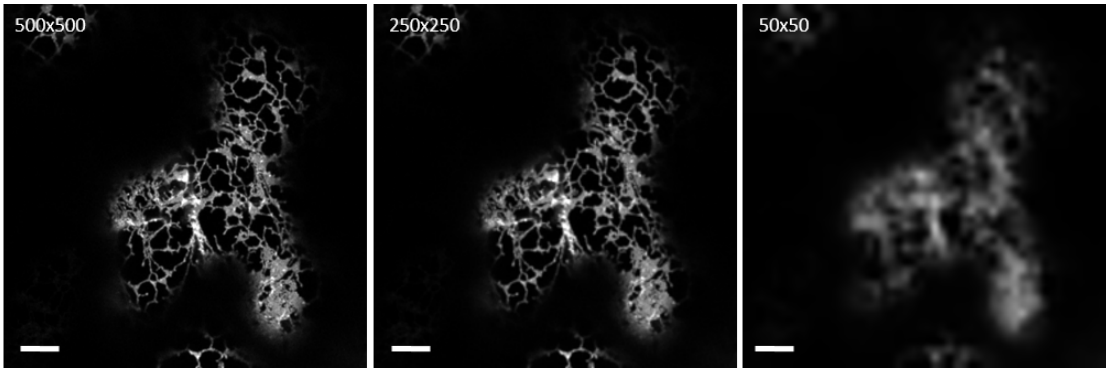


Figure 3.4: Pixel density and image structure
A single image of plant ER with varied pixel density, with highest pixel density set at 500x500 pixels and the lowest pixel density at 50x50. Actual image size calculated as 85.02 µm^2, scale bars 5 µm.

3.2.2.3 Averaging

Image averaging at the acquisition stage improves image quality by improving the signal-to-noise ratio. Averaging is available at between 1-16 times on the Zeiss 880 confocal (fig. 3.5). During the collection process a 4x averaged image requires each pixel to be collected 4 times. The mean intensity of each pixel will be displayed in the final image, reducing random image noise. There is a positive linear relationship between the rate of image capture and the number of averaging factors applied to an image which results in image capture errors at the highest levels of averaging (see section 3.2.2.4). Due to the reduced rate of acquisition speed, use of high levels of averaging is not appropriate for time-series of live cells as the extended exposure to confocal lasers increases the risk of inducing stress in the cell. A long timeframe between each image capture is also not desirable for dynamics analysis due to extensive, uncaptured ER remodelling occurring between frames.

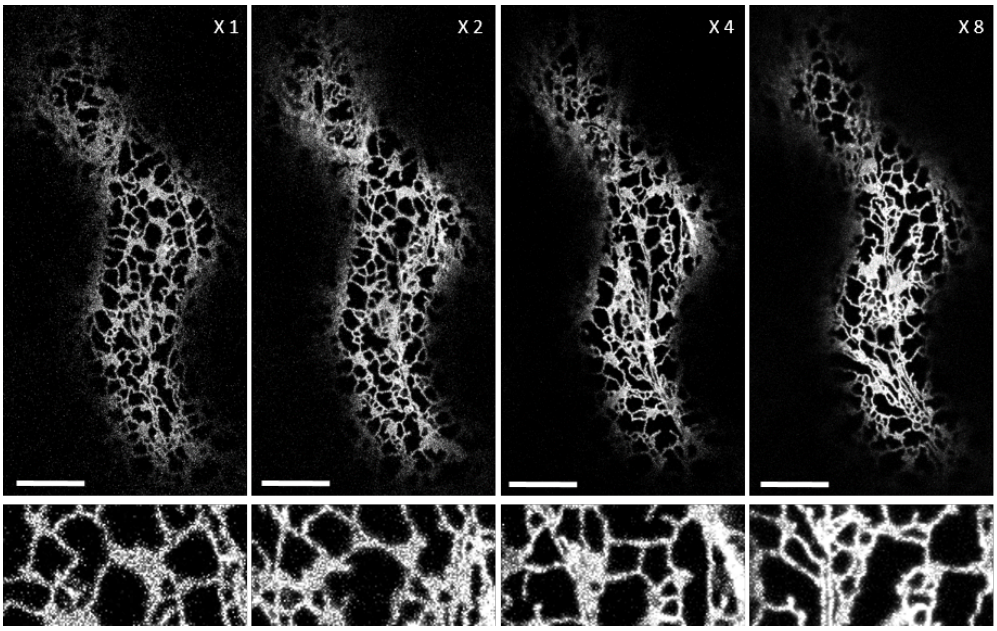


Figure 3.5: Averaging and image structure
Images acquired of a single cell using a confocal microscope with various levels of averaging: 1x, 2x, 4x and 8x averaging with enlarged region of ER displayed below each image. Signal to noise ratio improves as averaging increases. Scale bars 5 µm.

3.2.2.4 High quality images vs. sufficient rate of capture

The rate at which confocal images can be acquired greatly affects image fidelity to the underlying structure. Slow scan speeds, caused by increased pixel density, averaging and frame size cause image capture aberrations as a consequence of rapid ER remodelling through the duration of the scan. Previous estimates have suggested that the ER present in 7-day-old cotyledonary petioles of arabidopsis moves at an average rate of $0.33\,\mu m\,s^{-1}$ (Ueda *et al.*, 2010). As the ER shifts during the scan different aberrations are caused depending on how the image capture method. If each frame is collected there is a blurring effect around the tubules, whereas if a line scan is applied there tends to be a 'jagged' effect across the network as the ER moves between each line of the frame collected.

3.2.3 Developing a pipeline for plant ER segmentation - AnalyzER

AnalyzER is designed to enable rapid, medium-throughput quantification of the structure and dynamics of the plant ER using images acquired through various capture methods, ranging from serial block-face scanning electron microscopy (SBFSEM) reconstructions to confocal imaging. Whilst performing complex analysis on almost all ER structure and dynamics, AnalyzER is designed to act as a single 'all-in-one' ER analysis package, with all the necessary stages for analysis to be performed within a single graphical user interface (GUI) (fig. 3.6).

Version 1 of AnalyzER (originally named ER analysis software and published by Breeze *et al.* (2016)) was designed to analyse ER structure, geometry and tubule morphology and published by Breeze *et al.* (2016). Version 2 of AnalyzER, was

expanded to include ER remodelling and persistency, analysis of the distribution of fluorophores across ER cisternae, distribution of fluorophores along ER tubules and accurate calibration of ER tubule widths. All code relating to the software was developed by Mark Fricker, all software testing for version two, including image capture, analysis and troubleshooting was performed by Charlotte Pain.

Thus far AnalyzER has been applied to arabidopsis and tobacco leaf epidermal cells. Confocal microscopy of fluorescent dyes (such as rhodamine B), transient and stable expression of fluorescently tagged proteins are able to produce and capture sufficient quality images of the ER for analysis. Though AnalyzER has so far only been tested on a limited range of species and fluorophores, it has the potential to be applied to many more.

Rapid analyses of single images can be performed within the AnalyzER GUI. For multivariate analysis of large datasets, an additional statistical analysis package was developed alongside AnalyzER, designed specifically to handle the outputs of AnalyzER (fig. 3.6). The statistical analysis package is particularly important as a single timeseries analysis can produce up to 159 metrics per frame.

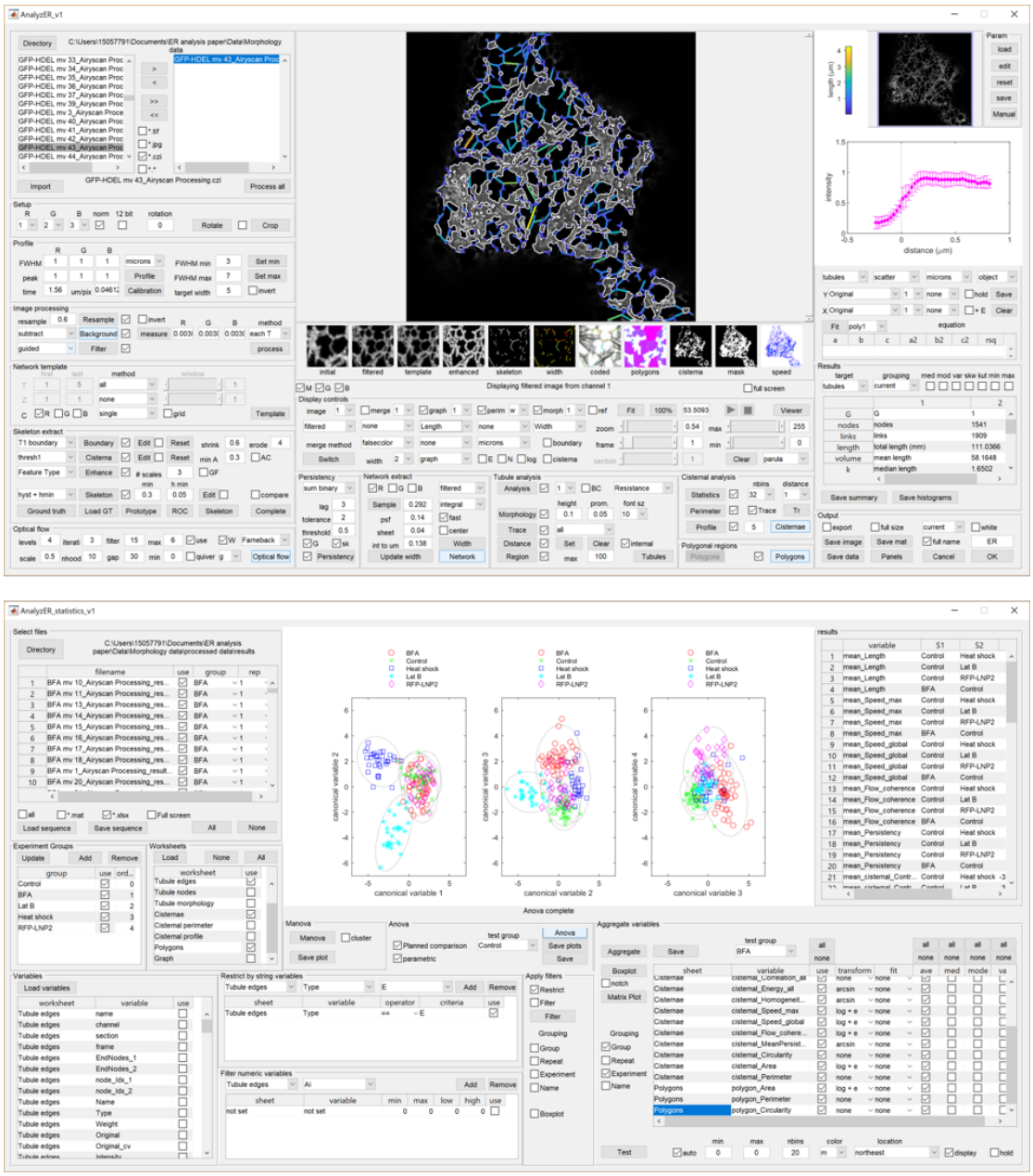


Figure 3.6: The AnalyzER and AnalyzER statistical analysis graphical user interfaces

The Graphical User Interface (GUI) of AnalyzER showing standard settings used to analyse a short timeseries (top) and the GUI of AnalyzER's accompanying statistical analysis package (bottom).

3.2.4 Using AnalyzER

3.2.4.1 Segmenting the ER

The analysis method adopted by AnalyzER is illustrated below using a sample timeseries of the ER lumenal marker GFP-HDEL transiently expressed in leaf epidermal cells of tobacco, captured over 7.8 seconds using a confocal microscope (fig. 3.7a).

Once loaded into the GUI, details of the image acquisition parameters must be input into the main interface. These include the scan speed per frame and the pixel scaling of the image. The minimum full width half maximum (FWHM) of a tubule width must be measured using a transect across a small tubule within the software to provide the minimum tubule width for the particular imported image (typically 3 pixels). This is repeated on a large tubule to measure the maximum FWHM of a tubule before it can be considered a cisterna (typically 7 pixels) and a target FWHM is set between the two as an estimate of mean tubule width (typically 5 pixels). To prevent pixellation errors later in analysis and standardise all subsequent processing and filtering operations, images are then up-sampled using linear interpolation to ensure that the minimum tubule width is approximately 5 pixels. The images are background subtracted using a manually defined region of interest (ROI) of the background to calculate the mean background intensity across the image, and then smoothed using a guided, edge-preserving anisotropic filter (He *et al.*, 2013), achieved by setting the kernel size to the $\mathrm{FWHM}_{\mathrm{min}}$. Regions of low signal intensity, caused by the curvature of the cell excluding the ER from the focal plane, are masked out of the image where the pixel intensity is below the threshold determined after partitioning the image histogram into between 2-4 sections using Otsu's method (Otsu, 1979). The choice

of which section of the partitioned image intensity is taken as the lower threshold is selected by the user. This multi-threshold partitioning of the image histogram is required when segmenting images with strongly labelled substructures, such as accumulation of GFP-HDEL after treatment with brefeldin A (BFA) and within arabidopsis fusiform bodies (Matsushima *et al.*, 2002). The outermost boundary (approximately corresponding with the edge of the infocus cell) is identified using a convex hull, shrunk by a factor of 0.5-0.8 and the final mask boundary is eroded by a user defined number of pixels, typically between 4-6. This erosion of the boundary is essential in removing the low intensity tubules at the edge of the image, which can segment poorly (fig. 3.7b).

The boundary of cisternal regions, defined as regions with a width greater than the $\mathrm{FWHM}_{\mathrm{max}}$ set at the start of an analysis, are identified using a morphological opening function (erosion then dilation), which removes tubules from the image (Sparkes *et al.*, 2009a). These cisternal objects are then refined using active contours back onto the underlying image intensity (fig. 3.7c). The identified cisternae are then filtered on their area to ensure all cisternae are larger than $0.3\,\mu\mathrm{m}^2$, as tubules that reach an area of approximately $0.3\,\mu\mathrm{m}^2$ are likely to be ER-organelle contact sites that form persistent nodes within the ER (Sparkes *et al.*, 2009a).

The image signal is enhanced against the background using a phase-congruency filter (Fricker *et al.*, 2017; Obara *et al.*, 2012) to enhance ridge-like elements, such as tubules, independently of their intensity (fig. 3.7d). Intensity independent enhancement is essential for accurate segmentation of confocal images of the ER network as many dim tubules are present (fig. 3.7e). The enhanced network is subsequently thinned with hysteresis thresholding followed by thinning to a single pixel wide skeleton, from which the segmented cisternae are removed. Polygonal regions that are fully enclosed by the ER network are segmented as a complement to the tubule skeleton and cisternal area.

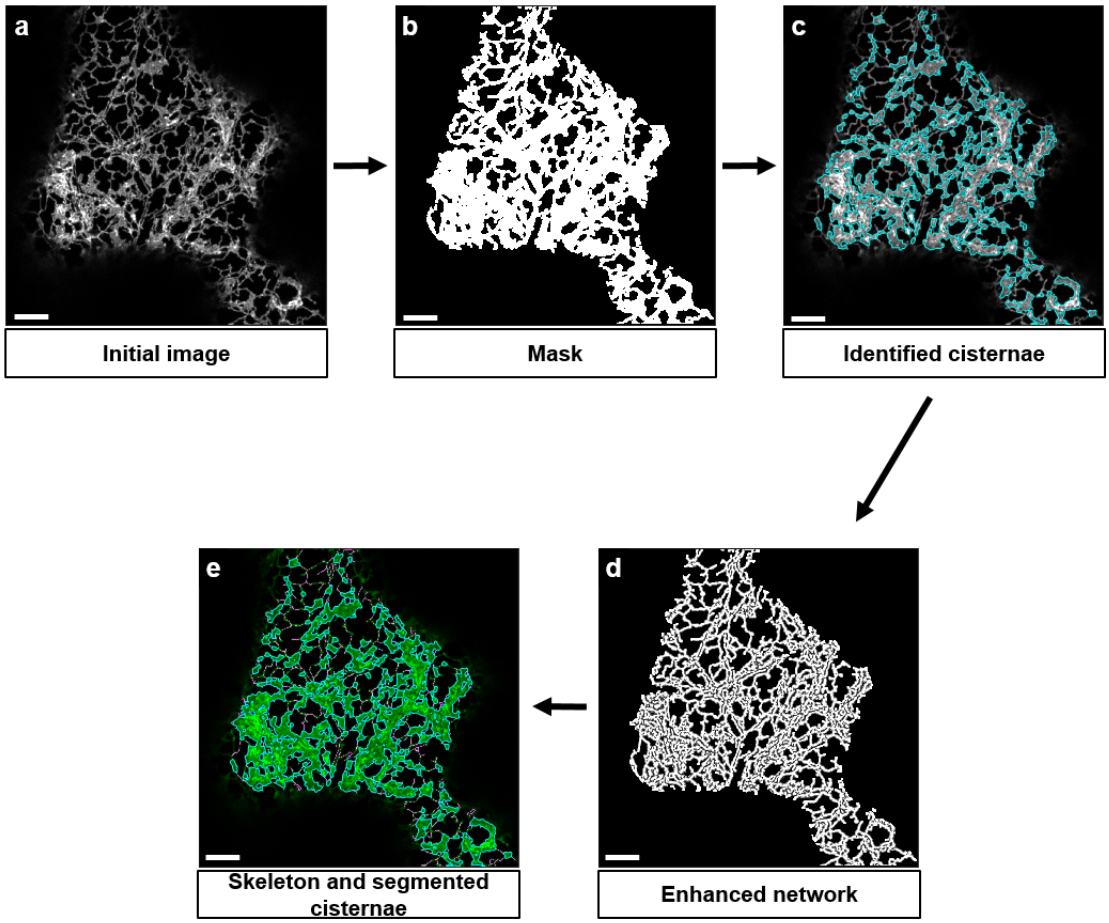


Figure 3.7: Using AnalyzER to segment the ER network
(a) An initial single frame of a time series of a tobacco leaf epidermal cell transiently expressing the ER lumenal marker GFP-HDEL (b) reduced to the masked region for analysis; (c) cisternae identified using an opening function (outlines, cyan); (d) Enhanced network using phase congruency prior to cisternae removal; (e) fully segmented cisternae (outlines cyan) and the single pixel wide skeleton (magenta) running along the center of tubules (green). Scale bar 5 µm.

3.2.5 Precision-recall analysis of the accuracy of ER structure

Accuracy of tubular skeleton segmentation (fig. 3.8a) can be assessed for representative images within a dataset using Precision-Recall analysis of a manually digitised ground truth. Ground truths are created using a digitising tablet and GIMP (GNU

Image Manipulation Program) software by tracing a single pixel wide skeleton over the original image, excluding/running through cisternae as appropriate (fig. 3.8b). The same mask applied to the segmented skeleton is applied to the manual skeleton and the cisternae removed. The segmented skeleton is subsequently mapped onto the manual skeleton and regions of concurrence and divergence are mapped onto a single image (fig. 3.8c).

The accuracy of the segmented tubular skeleton is calculated by measuring the number of true positives (T_P), true negatives (T_N), false positives (F_P) and false negatives (F_N), with the tolerance if half the $FWHM_{min}$. The accuracy of the segmentation is assessed using Precision-Recall analysis where precision (P) is calculated as $T_P/(T_P + F_P)T_P/(T_P + F_P)$ and recall is calculated as $T_P/(T_P + F_N)$. Performance is assessed with the F_1 score, the harmonic mean of precision and recall, $F_1 = 2(PR)/(P + R)$. An F_1 score of 1 is given for a perfect precision and recall, whilst the worst possible score is 0. In general network segmentation of the central region of the ER network works well ($F_1 = 0.94 \pm 0.019$, n=5), but inaccuracies are more common at the cell margins, where ER fluorescence signal dims due to the curvature of the cell.

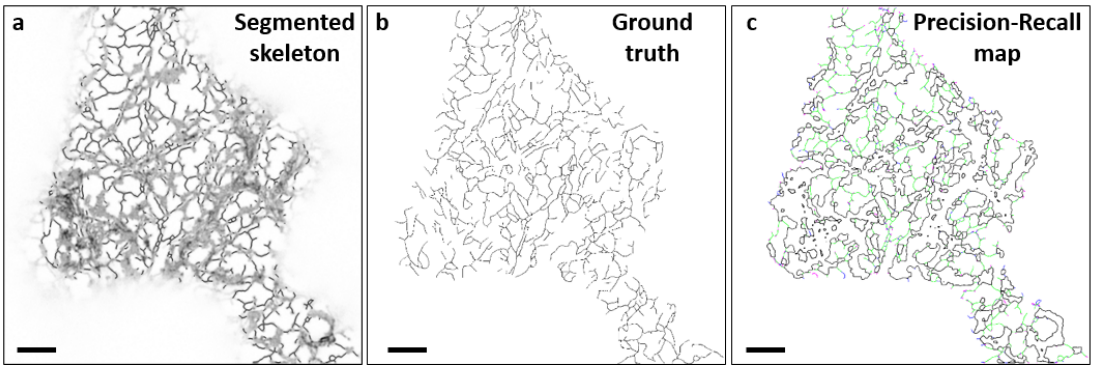


Figure 3.8: Mapping precision-recall analysis
(a) The tubular skeleton (black) segmented by AnalyzER overlaid on tobacco epidermal cell ER transiently expressing GFP-HDEL (grey); (b) the manually digitised ground truth of the ER of the same cell generated in GIMP; (c) the precision-recall analysis (cisternae, black; true positives, green; false positives, blue; false negatives, magenta). Scale bar 5 µm.

3.2.6 Estimation of ER tubule diameter

Tubule diameter is estimated using an integrated intensity granulometry developed by Fricker *et al.* (2017). The intensity image is subject to a series of morphological image opening functions that successively removes structures once the opening kernel exceeds the size of the underlying object. This creates an intermediate image (x,y,s) where s increases with the size of the disk-shaped kernel. Within the skeleton the intensity of each pixel decreases slowly with s as the kernel samples more of the object, but reduced rapidly once the boundary of the object is reached and the kernel only samples background. The integrated intensity under the granulometry curve is then calculated to give a measurement of the local image intensity which in turn provides the relative diameter of ER tubules. Physical diameter of ER tubules can be related to the image intensity using a series of assumptions about the relationship between fluorescence intensity and sample volume. Here we assume that the fluorescent probe in question (GFP-HDEL) is evenly distributed across the ER and that the ER diameter of the ER is within the sampling volume of the confocal defined by the idealised point spread function (psf) (Zhang *et al.*, 2007). The radius of ER tubules can be characterized under these assumptions as below:

$$r_t = \sqrt{(I_t/I_s)\,(psf_{xy}T_s/4)}$$

This calculation of tubule radius, developed by Mark Fricker, requires first a sample of the average intensity of a cisternae (I_s), an estimation of cisternae thickness (T_s) and the size of the lateral psf (psf_{xy}) to define the relationship between the measuring intensity of a known volume of ER with an entirely filled psf. The radius of a tubule (r_t) can therefore be estimated using the assumption that the volume

of tubules was sampled by the same idealized psf as the cisternae, and then scaling the intensity ratio of tubules to cisternae (I_t/I_s). The majority of these parameters can be calculated from confocal images, however an estimate of the diameter of the plant ER is required as a scaling factor to calculate the radius of tubules. This scaling factor can be modified by the user. The mean diameter of the ER was calculated using zinc iodide-osmium tetroxide (ZIO) staining of arabidopsis ER imaged using serial block face scanning electron microscopy (SBFSEM) by Maike Kittelmann (fig. 3.9). Measuring the stained ER revealed the vertical width of arabidopsis ER is 40.51 nm $\pm$ 0.82, (n=1, 25 technical repeats). This scaling factor is applied to all analysis performed as part of this work, but can be ignored or modified by subsequent users.

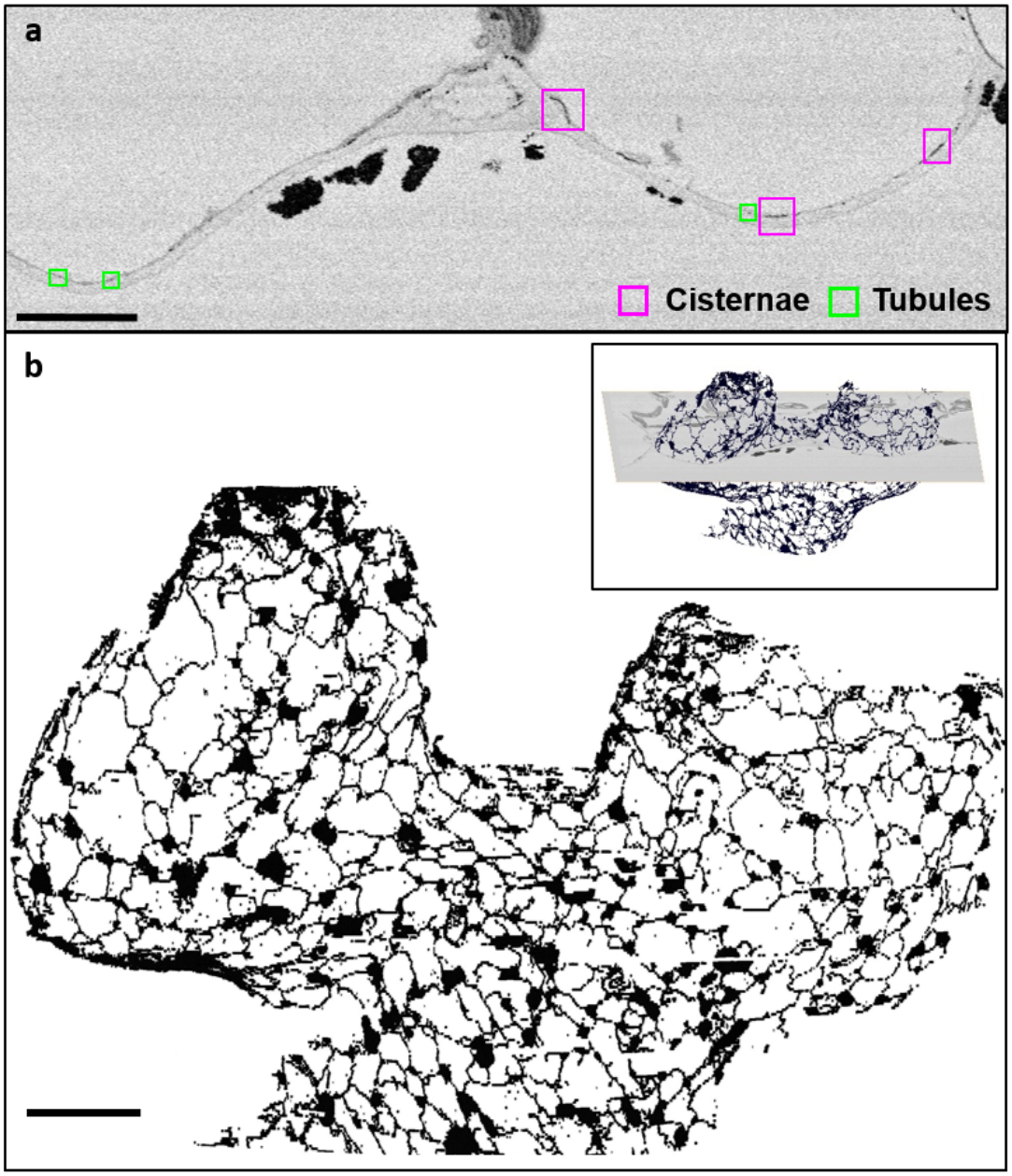


Figure 3.9: Measuring ER widths using SBF-SEM
(a) A cross-section of zinc-iodine-osmium (ZIO) stained Arabidopsis leaf tissue captured by SBFSEM, with stained regions of ER highlighted by pink and green squares. (b) A reconstruction of the all cross-sections collected by SBFSEM showing the ER structure of a single arabidopsis leaf epidermal cell. The inset localises the cross-section (a) onto the the 3D reconstruction (b). Scale bars 5 µm.

3.2.7 Preventing mis-classification of 'large' tubules

Tubule widths vary widely across the ER and discrimination between small cisternae and large tubules is based on a size classification developed by Sparkes *et al.* (2009a). Application of an opening function to identify cisternae results in many thicker than average regions of tubules being mis-identified as small cisternae. This occurs both at three-way junctions where the joining point of multiple tubules results in a thicker than average region, and at persistent tubule punctae which have a maximum area 0.3 µm^2 (Sparkes *et al.*, 2009a). An additional size filter is then applied to remove 'cisternae' identified with an area of below the definition of punctae, converting them to tubules instead (fig. 3.10). Re-classification of mis-identified stable punctae prevents these punctae dominating analysis of cisternal features and is essential for the correct characterisation of the structure of the ER.

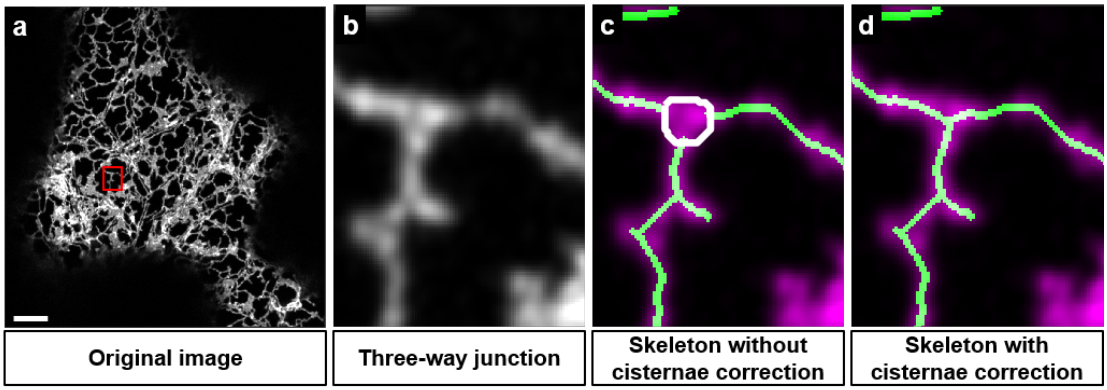


Figure 3.10: Identification and handling of ER punctae
(a) Original image of tobacco leaf epidermal cell transiently expressing GFP-HDEL, scale bar 5 µm, with the region of interest highlighted in red; (b) an enlarged example of a thickened region of ER caused by the joining of three tubules at a junction; (c) initial uncorrected segmentation identifies the centre of the junction (outlined in white) as a cisternae, instead of classifying the junction as a connection of tubules (skeleton overlay in green); (d) after cisternae identification correction and de-classinfcation of cisternae less than 0.3 µm^2 resulting in correct segmentation of the three-way junction.

3.2.8 Calculating the structural parameters of the plant ER

After appropriate segmentation of the plant ER, AnalyzER calculates a series of morphological measurements of the plant ER. These include tubule length, width, area and tortuosity and the area, elongation, roughness and circularity of both cisternae and polygonal regions. For full details of these calculations see appendix S1.

3.2.9 Extending the range of AnalyzER: analysis of the time domain

3.2.9.1 Optical flow captures the rate of 'ER movement'

Optical flow analysis captures the apparent movement of objects between frames, and so can be applied to analyse ER dynamics in terms of active network movement, including tubule extension and retraction, ER streaming and cisternal remodelling and translocation.

Three optical flow analysis methods were assessed for their potential capability to detect active ER remodeling: Horn-Schunck (Horn and Schunck, 1981), Lucas-Kanade (Lucas and Kanade, 1981) and Farnebäck (Farnebäck, 2003). Of these methods only the Farnebäck method was able to detect local ER remodeling, such as tubule extension (fig. 3.11). The Farnebäck method approximates neighborhoods in each frame to a set of quadratic polynomials. These neighborhoods are designated through the generation of an image pyramid, with each level of the pyramid increasing in resolution. Comparison of polynomials between neighborhoods across

frames is used to produce a signal of global displacement which can then be calculated and refined onto the underlying image, enabling capture of ER movement beyond the size of the local neighborhood scale (Farnebäck, 2003).

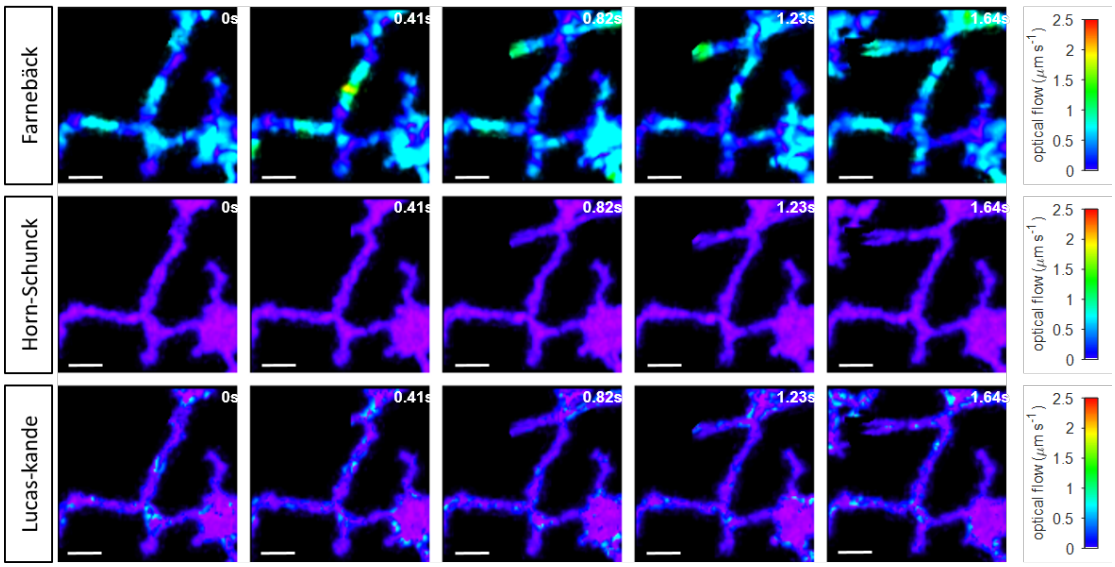


Figure 3.11: Methods for calculating optical flow
Application of three available methods of optical flow detection (Farnebäck, Horn-Schunck and Lucas-Kanade algorythmns) applied to a small region of ER, including an extending tubule, over a 1.64 second period. Dark blue pseudocolouring signals no movement detected whilst green and red pseudocolourings denote the detection of ER remodeling. Scale bars 1 µm.

Optical flow analysis provides a measurement of both the rate of ER remodelling (fig. 3.12a) and the direction of the detected ER movement (fig. 3.12b) which can be applied to rapidly identify modified ER dynamics. Further properties of the velocity vector field can also be calculated, such as measurements of flow curve (fig. 3.12c), the rotation of the flow normal to the velocity, and the flow divergence, which calculates whether the flow lines are converging or diverging (fig. 3.12d). The relative significance of both flow curve and divergence are as yet unclear, however flow coherence, the ratio of the scalar sum of speeds at each pixel in the tubule to the vector sum of all pixels can provide an indirect measure of the extent of directed movement (fig. 3.13). A value of 1 indicates that the entire region is

moving purely in one direction, whilst lower values indicate oscillations in moving structure.

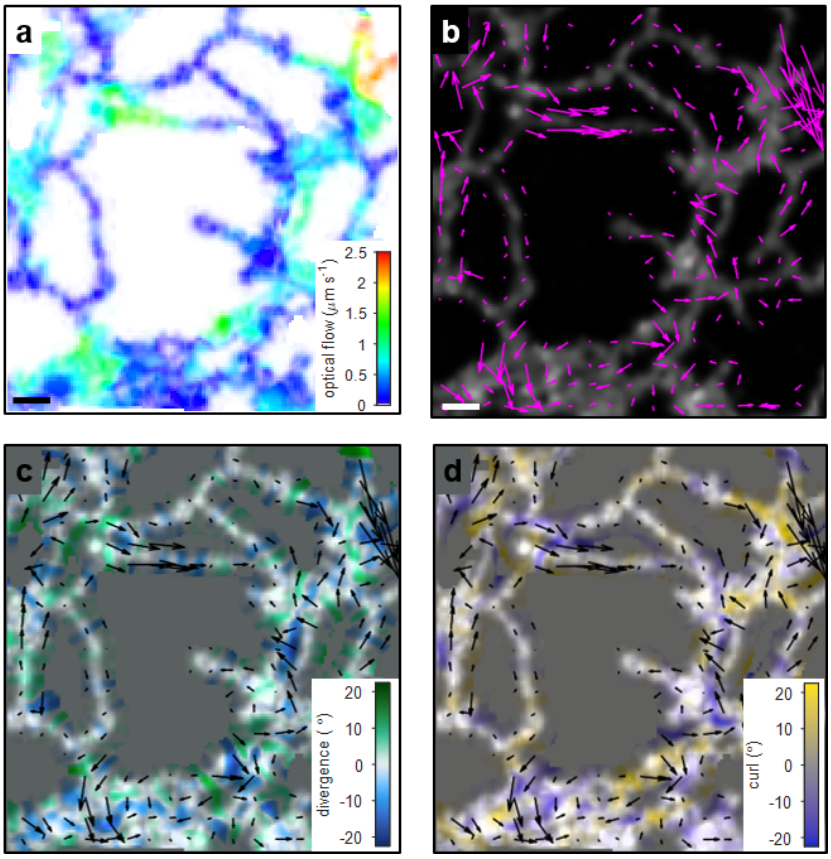


Figure 3.12: Optical flow outputs
Pseudocolour overlays of Farnebäck optical flow analysis in tobacco leaf epidermal cells transiently expressing GFP-HDEL, performed over 0.41s. (a) Optical flow pseudocolor overlay and (b) the direction of ER movement between two frames shown in magenta, with arrow size correlating to the extent of detected ER movement. The colour-coded representations of (d) local curl and (e) divergence. Scale bars 1 µm.

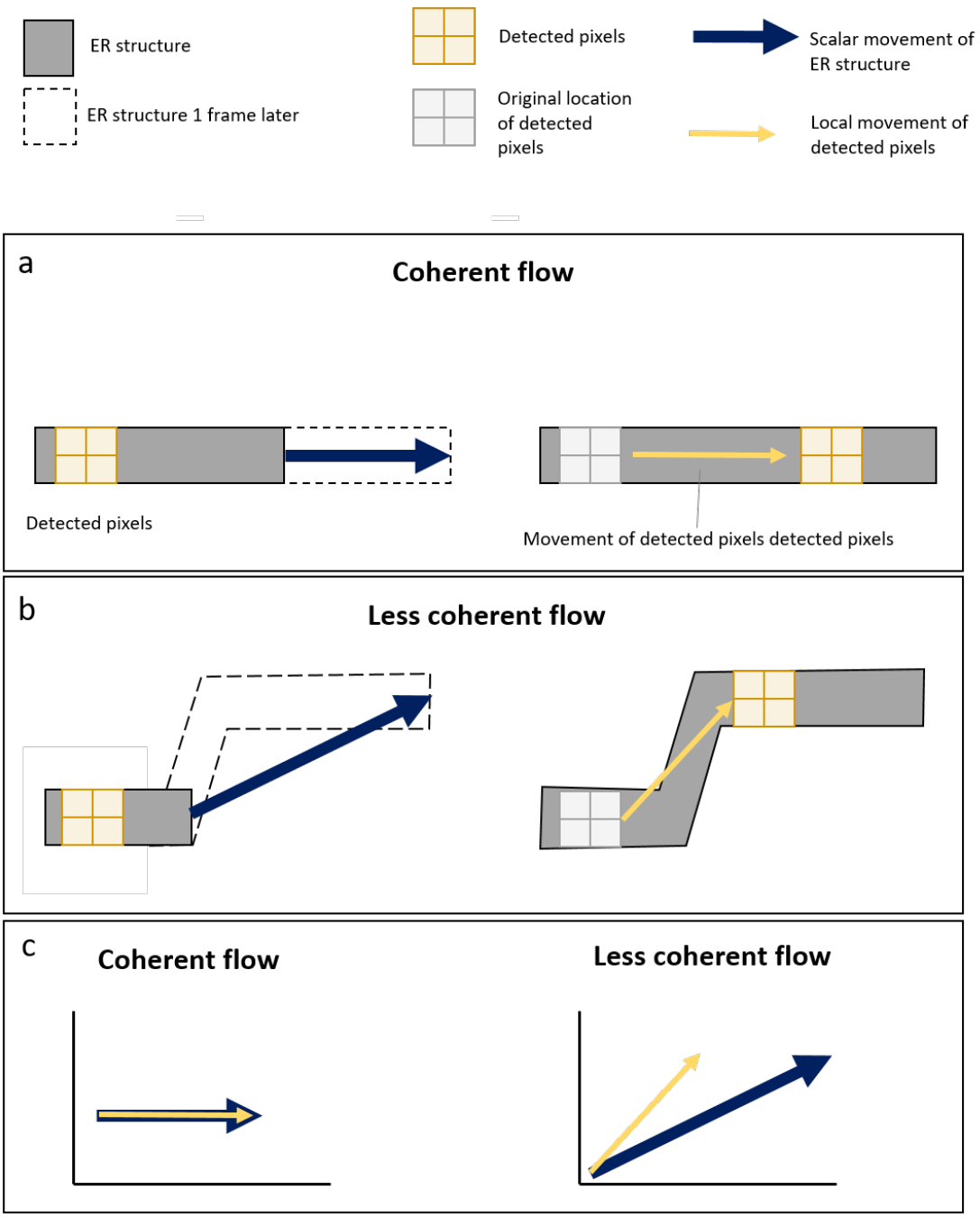


Figure 3.13: Diagrammatic representation of coherent flow
(a) Coherent flow is present when pixels detected along the length and ER structure, for example an extending tubule, move in the same direction of the structure. (b) Flow is less coherent when some pixels within the structure move at an angle to the overall direction of movement of the structure. (c) A comparison of the direction of movement of a cross-correlated pixel subset and the movement of the entire region of ER.

3.2.9.2 Pharmacological interventions and stress modify ER dynamics

Control ER, visualized in tobacco leaf epidermal cells transiently expressing GFP-HDEL, exhibits a range of dynamics including tubule extension, retraction and translocation, alongside cisternal remodelling (fig. 3.14a). The majority of this movement is abolished on treatment with latrunculin B (Lat B) which prevents polymerisation of the the actin cytoskeleton (Sparkes *et al.*, 2009a), except for continued oscillation of tubular elements (fig. 3.14b, supplementary movie 3.1). Heat shock to 42°C for 20 minutes is sufficient to modify both ER structure and dynamics, significantly reducing the rate of ER remodeling (fig. 3.14c).

As shown in figure 3.15 and supplementary movie 3.2 and 3.3, the most substantial translocation of the ER is identified to occur within cytoplasmic streaming events (Ueda *et al.*, 2010), often observed moving at speeds of greater than $2.5\,\mu m\,s^{-1}$. The distribution of all speeds (calculated for tubules, cisternae and nodes) was lognormal, and the control ER (n=6) showed speeds with a mean of $0.22\,\mu m\,s^{-1}$ for tubules and nodes, with maximum observed speeds being higher, with a mean of $0.53\,\mu m\,s^{-1}$ for tubules and $0.40\,\mu m\,s^{-1}$ for cisternae (fig. 3.16a). The maximum identified speeds were $0.53\,\mu m\,s^{-1}$ for tubules and $0.95\,\mu m\,s^{-1}$ for cisternae. Both Lat B treatment and heat shock reduced the distribution of speeds, most notably of higher identified speeds, with the effect more pronounced after heat shock. The mean speed of movement dropping to $0.19\,\mu m\,s^{-1}$ and $0.17\,\mu m\,s^{-1}$ after treatment with Lat B and heat shock respectively. The direction of the movement in the HDEL control is highly coherent, indicating directionality in the remodeling of the ER (fig. 3.15d-i). After treatment with Lat B and heat shock however, there is an increase in disordered movements throughout the ER, shown by the reduction in flow coherence (fig. 3.16a). Though the cause of this increased disorder is not yet

clear, it is likely that the oscillatory nature of tubule movement is contributing to the loss of flow coherence after both heat shock and Lat B treatment.

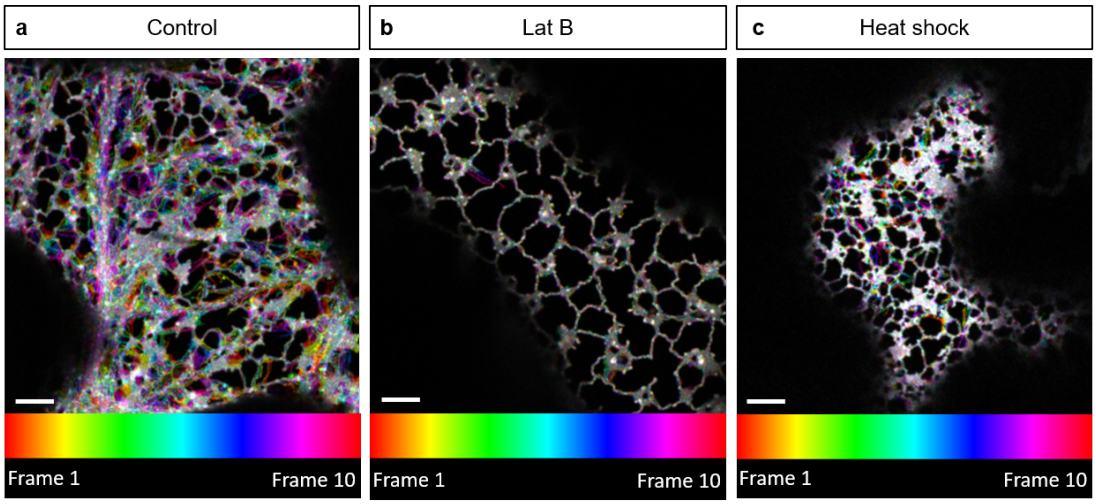


Figure 3.14: Latrunculin B and heat shock can be used to modify ER dynamics
Temporal colour-coded images of tobacco leaf epidermal cells transiently expressing (a) GFP-HDEL (b) after treatment with Lat B and (c) heat shock. 10 frames were collected over 20.5 seconds and white overlay regions indicate an overlay of ER structure across multiple frames. Scale bars 5 µm.

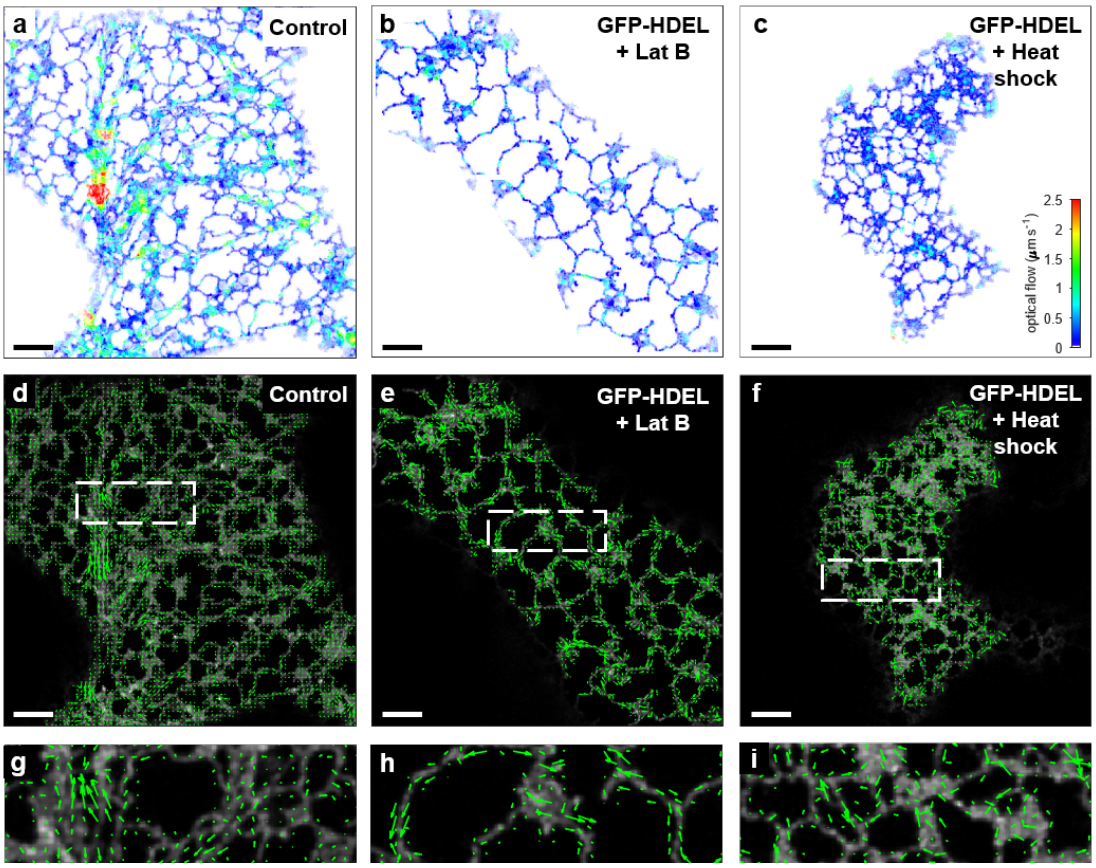


Figure 3.15: Using optical flow analysis to assess global ER remodelling after treatment with Lat B and heat shock

Optical flow analysis using the Färneback algorithm comparing movement over 2 frames of a 50 frame movie of a control cell transiently expressing GFP-HDEL (a) and after treatment with Lat B (b) and heat shock (c). The direction of overlay movement represented by a vector correlating to the magnitude of movement (green) in a control cell (d) and after treatment with Lat B (e) and heat shock (f). Three times magnified regions from the approximate centre of each cell (g-h). Scale bars 5 µm.

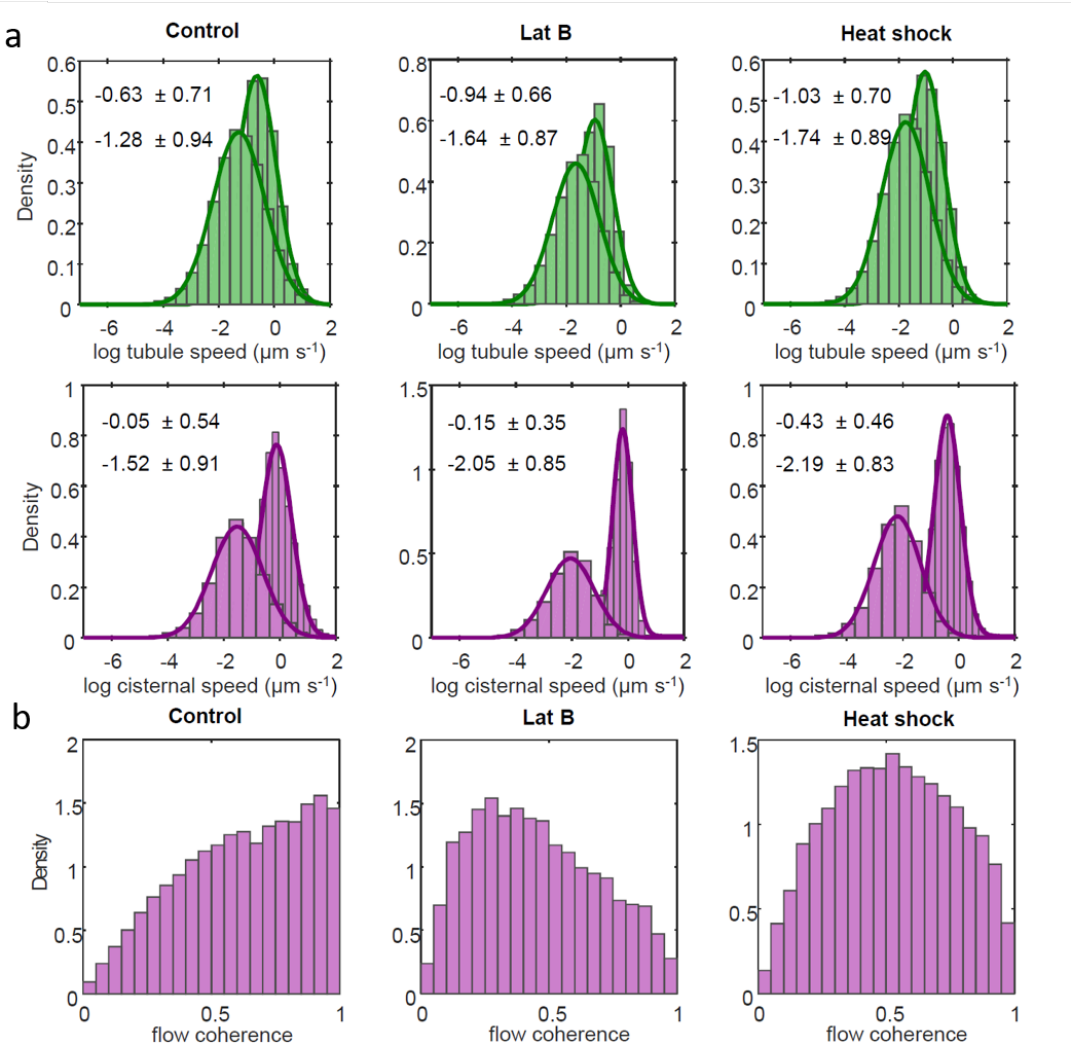


Figure 3.16: Components of speed distributions after treatment with Lat B and heat shock

(a) Probability density distributions of the log mean and log maximum speed of tubules (green) and cisternae (magenta), for the different treatments. The mean and SD for the Gaussian fits to the mean and max distributions are inset. (b) Flow coherence for cisternae for the different treatments (control, n=6 biological replicas, Lat B, n=8 biological replicas, heat shock, n=8 biological replicas, results obtained over three technical replicas).

3.2.9.3 Persistency mapping of static elements

Persistency mapping and analysis are implemented to consider an important aspect of ER dynamics that is over-looked by optical flow analysis - the persistency of ER structures over time. Though optical flow analysis is able to detect regions showing no movement, this detection is performed across two frames as opposed to identifying persistent regions over longer time spans. Currently, there is no universally accepted definition of a 'stable point' in the ER network, however if tubules and cisternae remain stable over a time period of approximately 5-10 seconds, this has previously been considered a long enough period to define the structure as 'persistent' (Griffing, 2018; Sparkes *et al.*, 2009a), whilst persistent nodes are characterized as existing for longer (Lin *et al.*, 2014, 2017).

Two methods for persistency analysis of ER time series were developed for AnalyzER. The first, following a similar methodology to that proposed by Sparkes *et al.* (2009a), assesses the differences in the image intensity over time (the period of which is defined by the user) masked by a thresholded binary image from both timepoints. The second option uses the skeleton where binary images of the cisternae are dilated by half the value of the set $FWHM_{min}$ and can be displayed a binary estimate of persistency, graded persisitency over time, a summed persistency between the start and end of the defined time period or by showing the difference between the start and end of the time window. Results are partitioned into either tubules, cisternae or nodes, highly persistent regions that exist over a longer time period. These nodes are considered to be stable points of the ER where it connects to other organelles, such as EPCSs, and therefore can be associated with both tubules and cisternae (Sparkes *et al.*, 2009a).

In untreated tobacco leaf epidermal cells transiently expressing GFP-HDEL with a lag period of 12 frames (~5s) a number of tubules remain persistent over time

(fig. 3.17, green, coded by intensity, with the tubule skeleton of the first timepoint shown in blue for comparison). Many cisternae also remain relatively stationary over this time period, though remodelling can be detected at the edges of cisternae (fig. 3.17, magenta, coded by intensity). Regions within both cisternae and tubules forming persistent nodes over a more substantial time period (~10s) can also be identified (fig. 3.17, white crosses). The persistency of the ER is increased by treatment with both Lat B (fig. 3.17b,e, supplementary movie 3.4) and heat shock (3.17c,f, supplementary movie 3.4).

Untreated control cells show low persistency of tubules and nodes (fig. 3.18, green and black histograms) but a greater persistency of cisternae (fig. 3.18, magenta histogram). Treatment of cells with both Lat B and heat shock results in a shift in the distribution towards increased persistency of all structures (fig. 3.18). However some structures remain minimally persistent under all treatments.

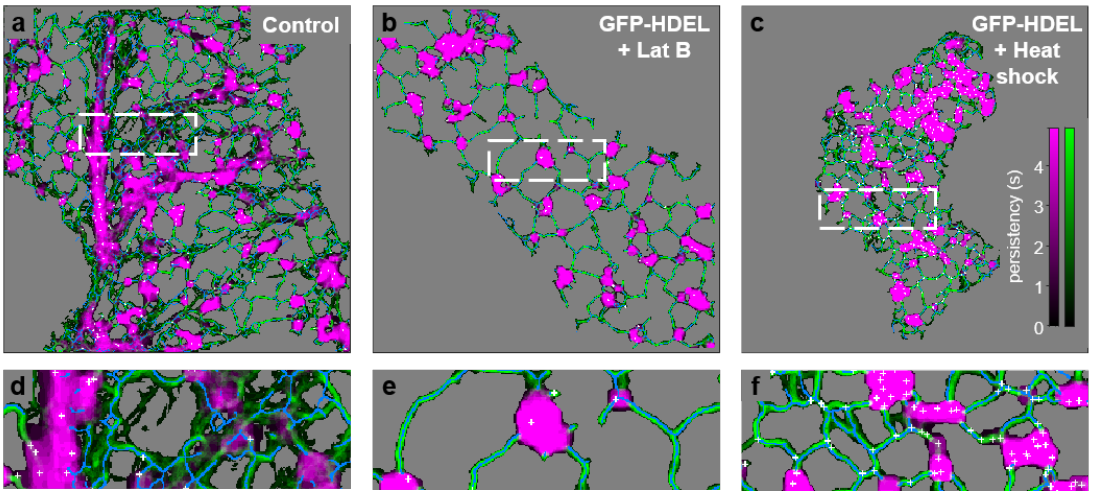


Figure 3.17: ER persistency mapping:
Whole cell persistency maps calculated with a 12 frame lag period (~5s) for tubules (green), cisternae (magenta) and nodes (white) with the tubular skeleton from the first time point shown in blue. The intensity correlated to the pixel occupation through the timeseries. Maps are generated from 50-frame timeseries collected at 0.41s intervals of tobacco leaf epidermal cells transiently expressing GFP-HDEL and after treatment with (b) Lat B and (c) heat shock. (d-f) 3x enlargements of the approximate center of the images (d-f). Scale bars 5 µm.

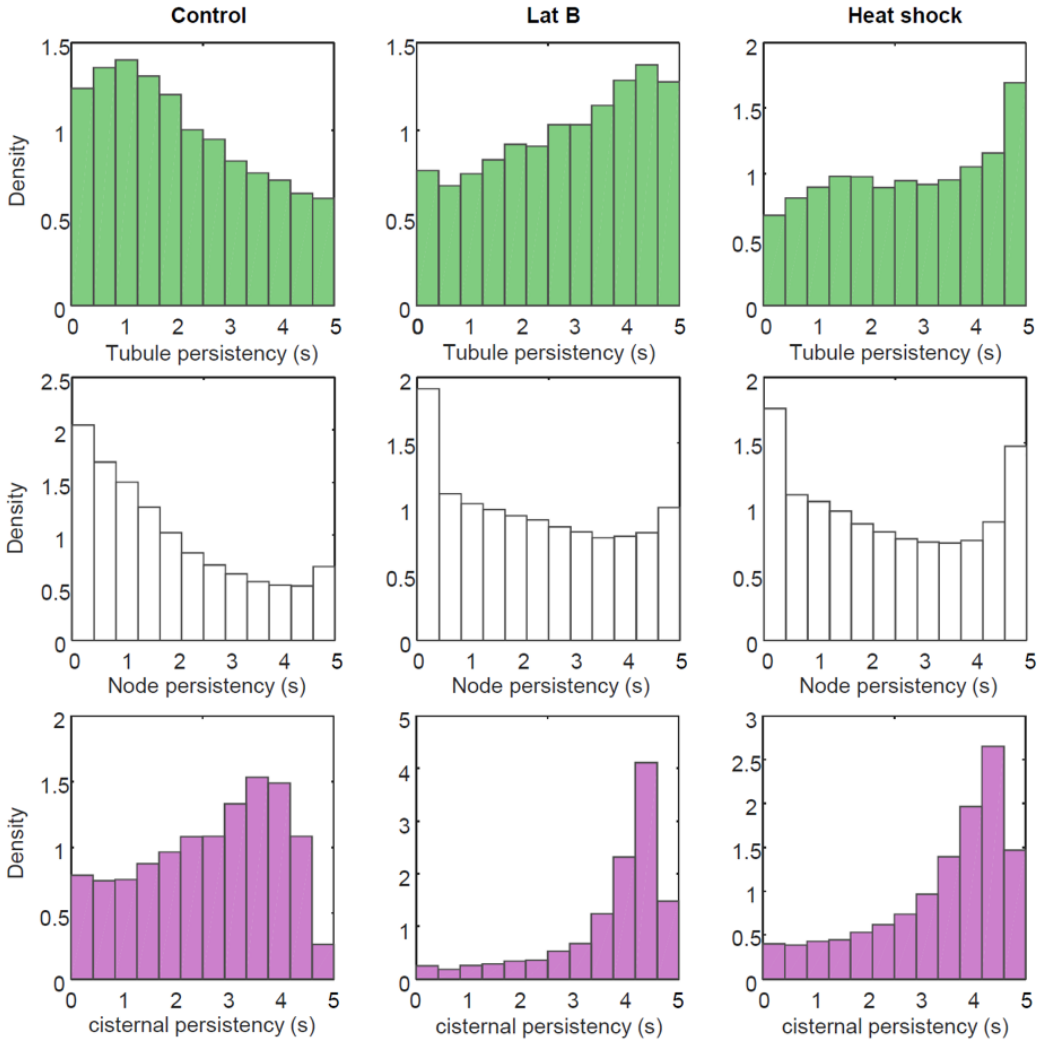


Figure 3.18: Distributions of persistency
Probability density distributions of the mean persistency for tubules (green), nodes (white) and cisternae (magenta) for tobacco leaf epidermal cells transiently expressing GFP-HDEL (control) after treatment with Lat B and heat shock. Control, n=6 biological replicas, Lat B, n=8 biological replicas, heat shock, n=8 biological replicas, results obtained over three technical replicas.

3.2.10 Quantifying fluorophore distributions throughout the ER

3.2.10.1 Quantifying fluorophore distributions: tubules

The intensity of lumenal and membrane markers fluctuate along the length of ER tubules, indicative of sub-resolution variation in ER width. In mammalian cells transient constriction of ER tubules has been assigned the putative function of driving lumenal flow through the ER by peristalsis (Holcman *et al.*, 2018), though this has yet to be shown for plants. The characteristics of ER width variation can be further modified by ER shaping proteins such as the membrane curvature inducing arabidopsis reticulon proteins 1-4 (hereafter referred to AtRTN1-4). Over-expression of these proteins induces constriction of ER tubules to such an extent that lumenal markers such as GFP-HDEL are restricted to small bulges spread along tubules (Sparkes *et al.* (2010), fig. 3.19). The effect of RFP-AtRTN1 over-expression can be quantified using a peak-finding algorithm to identify peaks and troughs in the intensity profile of tubules, which are significantly distinct from neighboring peaks, excluding nodes and cisternae. These results are also represented by a tubule intensity trace, integrated normal to the tubules axis in both channels. The tubule intensity variations were compared for GFP-HDEL alone and GFP-HDEL co-expressed with RFP-AtRTN1 to induce constriction of the ER tubules. Over-expression of AtRTN1 causes tubular constriction, restricting GFP-HDEL to discrete bulges along the length of the ER tubules, in which accumulation of AtRTN1 corresponds with a reduction in GFP-HDEL (fig. 3.20). Bulges in GFP-HDEL occur at approximately 1 per micron with similar peak intensity and tubule widths both alone and in the presence of RFP-AtRTN1 (fig. 3.20). However the troughs of GFP-HDEL were significantly dimmer (0.089 $\pm$

0.001 compared to 0.200 ± 0.020) and thinner (0.029 ± 0.004 µm compared to 0.046 ± 0.002 µm). In addition, when more than one GFP-HDEL trough occurs on a single tubule, the separation between the troughs is significantly, though slightly, increased (0.42 ± 0.018 µm compared to 0.490 ± 0.009 µm) when co-expressed with RFP-AtRTN1 reflected in a decrease in the mean trough density (1.400 ± 0.058 µm compared to 1.870 ± 0.148 µm).

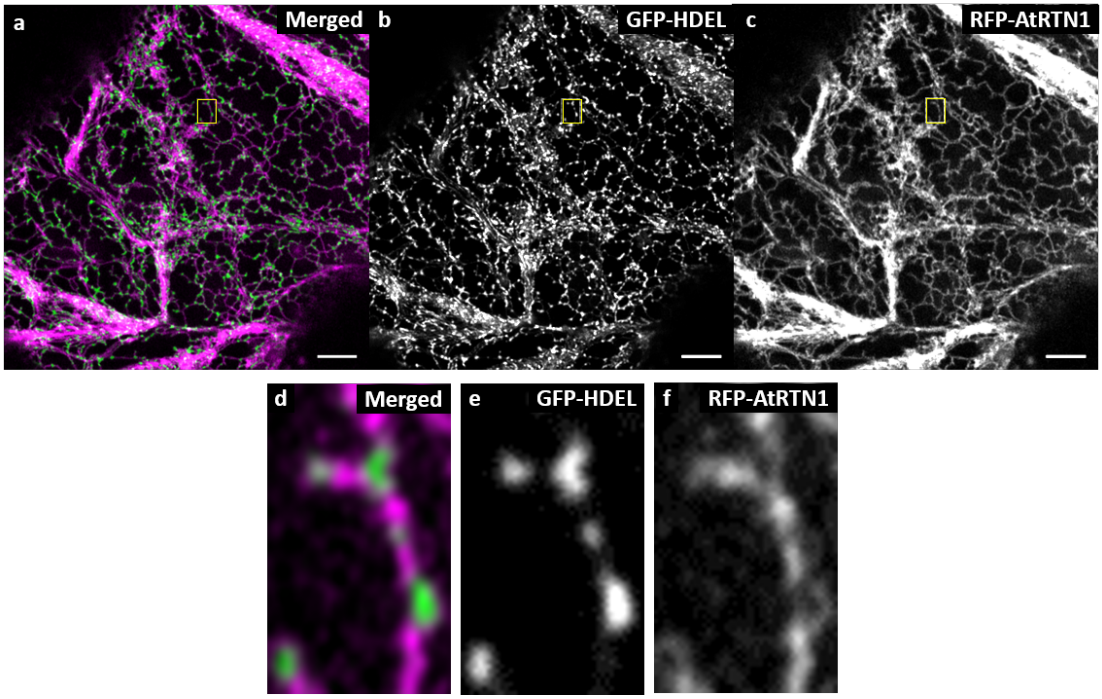
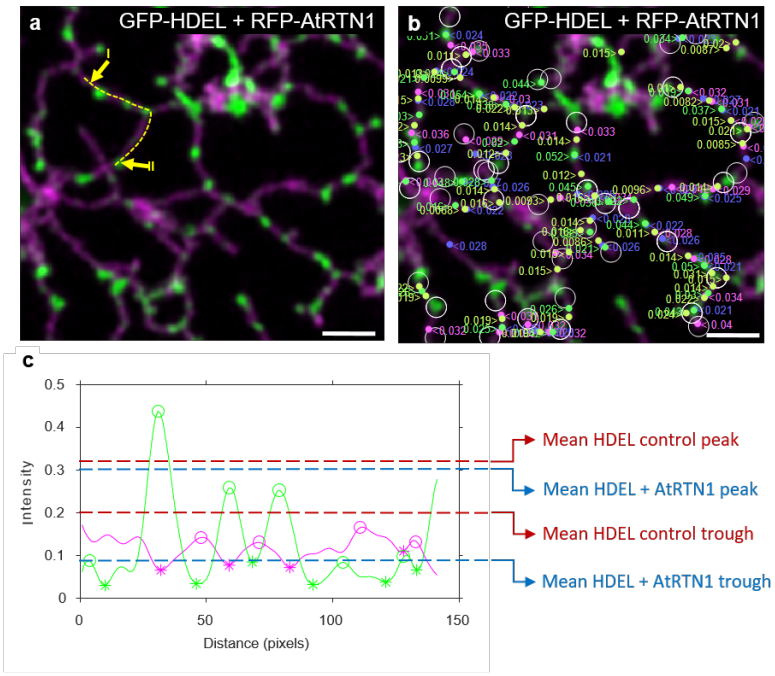


Figure 3.19: Co-expression of RFP-AtRTN1 and GFP-HDEL in tobacco leaf epidermal cells
(a) The merged 2 channel image of the ER lumenal marker GFP-HDEL (green) and RFP-AtRTN1 (magenta); (b) The distribution of GFP-HDEL to distinct punctae on co-expression with RFP-AtRTN1 (c). (d-f) An enlarged image of the region within the white square shown in a-c. Scale bars 5 µm.



d	GFP-HDEL (mean ± s.e.m., n=5)	RFP-AtRTN1 (mean ± s.e.m., n=6)	GFP-HDEL (mean ± s.e.m., n=6)	$t_{(9)}$	P value	Significance
bulge density (μm^{-1})	1.09 ±0.061	0.87 ±0.041	0.99 ±0.033	-1.35	0.222	
constriction density (μm^{-1})	1.87 ±0.148	0.94 ±0.068	1.40 ±0.058	-2.93	0.0309	*
bulge intensity	0.32 ±0.024	0.18 ±0.015	0.30 ±0.019	-0.55	0.600	
constriction intensity	0.200 ±0.020	0.097 ±0.0106	0.089 ±0.013	-4.50	0.0027	**
bulge width (μm)	0.058 ±0.0025	0.044 ±0.0036	0.054 ±0.0048	-1.45	0.188	
constriction width (μm)	0.046 ±0.0017	0.033 ±0.0031	0.029 ±0.0036	-4.68	0.0014	**
bulge separation (μm)	0.51 ±0.029	0.63 ±0.023	0.56 ±0.021	1.49	0.175	
constriction separation (μm)	0.42 ±0.018	0.62 ±0.034	0.49 ±0.0093	3.81	0.0084	**
intensity ratio at bulge		4.33 ±0.83	0.72 ±0.15			
intensity ratio at constriction		1.95 ±0.41	4.92 ±1.03			

Figure 3.20: Quantitative analysis of tubule morphology modification by RFP-AtRTN1 over-expression

(a) A merged two channel confocal optical section following transient over-expression of RFP-AtRTN1 (magenta) and GFP-HDEL (green) in tobacco leaf epidermal cells. (b) Automatic measurement of peaks and troughs for both RFP-AtRTN1 (left justified labels, peaks in magenta, troughs in blue) and GFP-HDEL (right justified labels, peaks in green, troughs in yellow). The underlying pixel skeleton is superimposed in white and the position of nodes indicated in cyan. Cisternae are also outlined in cyan. (c) Selected trace analysis between the yellow arrows in (a) showing the relative intensity for RFP-AtRTN1 (magenta) and GFP-HDEL (green), with the position of the peaks (open circles) and troughs (asterisks) indicated. The average values for peaks and troughs for the HDEL signal across all experiments are indicated in the presence and absence of RFP-AtRTN1. (d) Summary of tubule morphology metrics (mean ± s.e.m.) for GFP-HDEL alone (n=5 biological replicas) and co-expressed with RFP-AtRTN1 (n=6 biological replicas), results obtained over three technical replicas. Scale bars 5 μm.

3.2.10.2 Quantifying fluorophore distributions: cisternae perimeters

In addition to quantifying fluorophore distribution along tubules, similar methods can be applied to assess fluorophore distribution at the cisternal edges, both around the perimeter of cisternae or using transects normal to the cisternae. The ability of AnalyzER to identify differential localisation of two fluorophores normal to the cisternal edges was tested using over-expression of RFP-AtLNP1. Over-expression of RFP-AtLNP1 (leaves infiltrated at an OD_{600} 0.1) results in a higher concentration of the ER lumenal marker GFP-HDEL at the edges of the cisternae, whilst RFP-AtLNP1 remains approximately consistent across the cisternae edge (fig. 3.21a-c). An even distribution of fluorophores across is observed when two lumenal markers are co-expressed (GFP-HDEL and RFP-HDEL, fig. 3.21d-f).

The distribution of fluorophores is analysed in radial bins, the center of which is determined from the Euclidian distance map (EDM) of each cisternae and that are normal to the edge of the cisternal region. Results are presented as an average across multiple cisternae within a single image collected with a user defining minimum number of individual cisternae, in this case a minimum of 5 per image. While the intensity of GFP-HDEL peaks at approximately 0.2 µm into the edge of the cisternae and then reduces towards the center, whilst RFP-AtLNP1 intensity peaks in intensity further into the image (n=5), whilst the intensities of GFP-HDEL and RFP-HDEL are consistent through the cisternae (fig. 3.21g-h).

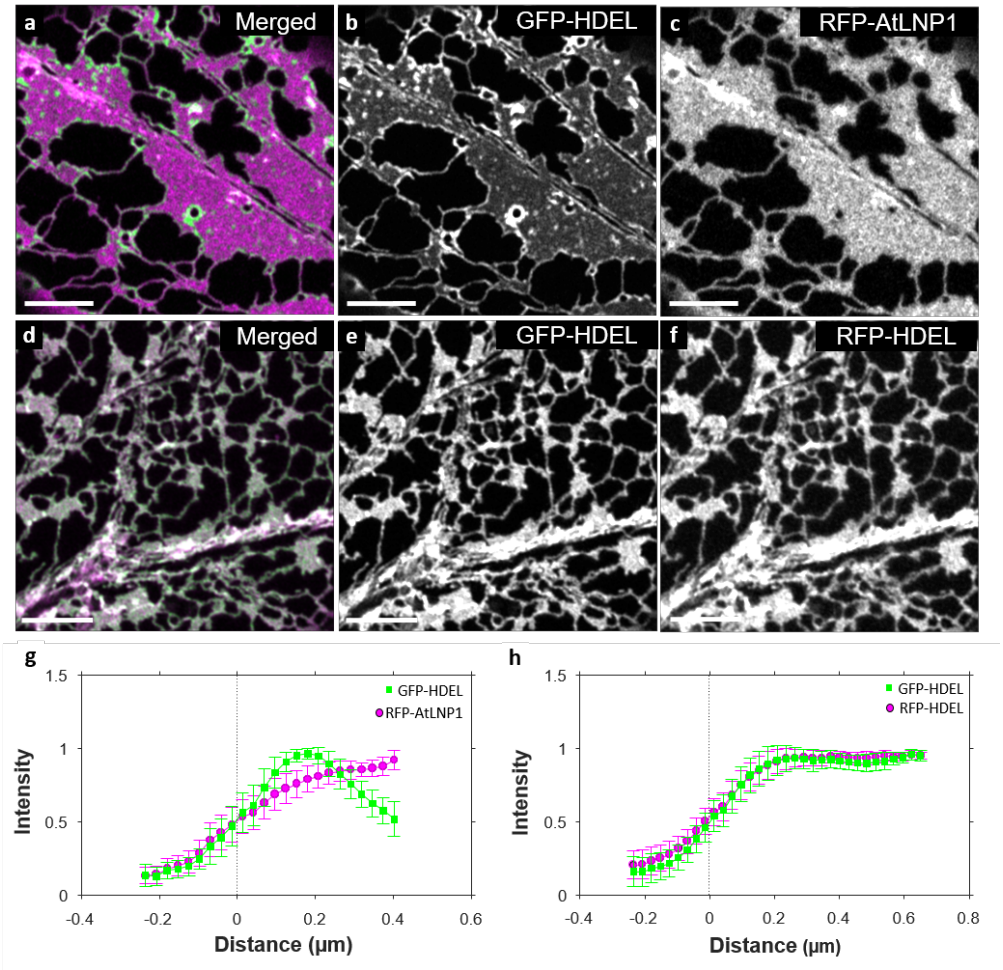


Figure 3.21: The distribution of fluorophores normal to the cisternae perimeter

A single optical section showing transient dual over-expression (a) of GFP-HDEL (green, b) and RFP-AtLNP1 (magenta, c). A single optical section showing transient dual over-expression (d) of GFP-HDEL (green, e) and RFP-HDEL (magenta, f). Scale bars 5 µm. When co-expressed with RFP-AtLNP1 (magenta), GFP-HDEL (green) shows a peak in intensity at the edge of cisternae (g), which is not seen when co-expressed with RFP-HDEL (h). The boundary of the cisternae is shown by a grey dashed line.

3.2.10.3 Quantifying fluorophore distributions: cisternae and texture analysis

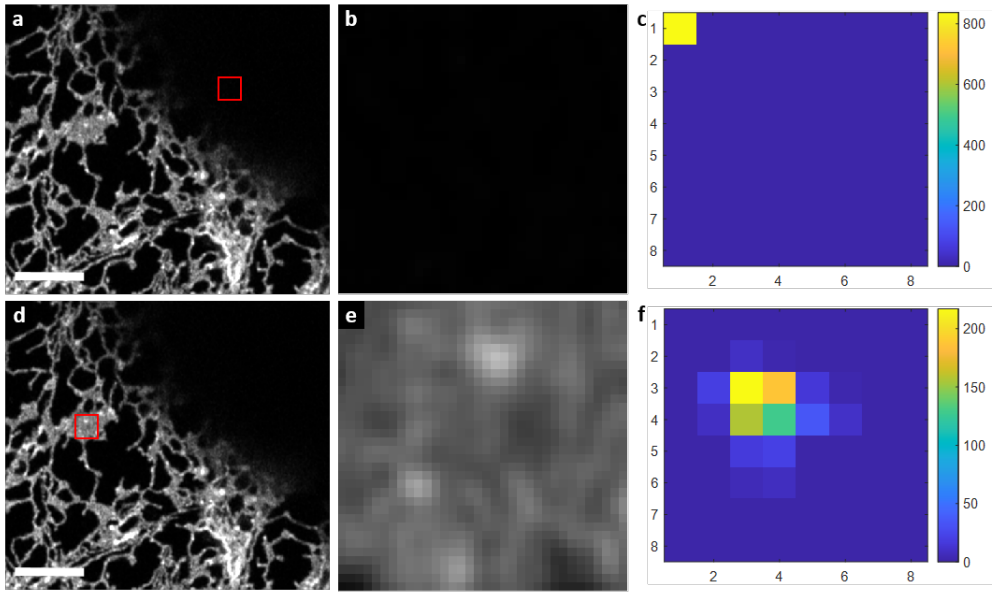
Within the plant ER fluorophores can be distributed approximately equally across the ER, form discrete punctae across the ER membrane surface or within the ER lumen or can be distributed in a complex pattern across ER cisternae. The complex distribution of fluorophores across cisternae can further be assessed using texture analysis, which identifies patterns in the variation of image intensity across cisternae. These variations may be indications of sub-resolution structure in ER cisternae.

Work by Schroeder *et al.* (2019) and Nixon-Abell *et al.* (2016) suggests that cisternae may have sub-resolution structure. In mammalian literature cisternae have been hypothesised to be composed of either a dense, reticulate network of tubules (Nixon-Abell *et al.*, 2016) or a large continuous region of ER that is punctuated with many sub-resolution holes (Schroeder *et al.*, 2019). In each case it is hypothesised that cisternae have small gaps within their structure. Analysis of a regions grey level co-occurrence matrix can indicate whether or not texture is present in an image (i.e. an image with a non-constant arrangement of intensities). For example, a constant image with no texture, and therefore a uniform image intensity will produce a GLCM with known values of texture property analysis (fig. 3.22). A grey level co-occurrence matrix is generated by comparing the intensity of an individual pixel with another pixel in the same neighborhood, with the neighborhood defined by user, and the difference in intensity stored in a matrix. For example a region of image background (fig. 3.22a,b) would be expected to have a constant texture, resulting in a simple GLCM (fig. 3.22c), whereas in the case of sub-resolution variability in fluorophore distribution, cisternae would be expected to have variable texture (fig. 3.22d,e) and therefore a more complex GLCM result

(fig. 3.22f). Properties of both GLCM (fig. 3.22g), specifically the contrast, correlation, energy and homogeneity of the given texture can be calculated (table 3.1) and demonstrate that, from this sample image, though the background region gives the expected properties of a constant image, using GLCM-based texture analysis, it is possible to detect a texture in cisternal regions.

Table 3.1: Calculating the properties of a GLCM
The calculation of the standard properties of a GLCM, as performed within MATLAB.

Property	Formula	Description
Contrast	The contrast in intensity of a pixel and it's neighbour considered over the whole image. A contrast of 0 would be output from a constant image.	$\sum_{i,j} \lvert i-j \rvert^2 p(i,j)$
Correlation	How correlated a pixel is to its neighbour across a whole image. A correlation of 1 or -1 could apply for a fully correlated image, whilst a result of NaN would be returned for a constant image.	$\sum_{i,j} \frac{(i-\mu i)(j-\mu i)p(i,j)}{\sigma_i \sigma_j}$
Energy	Also termed uniformity, energy is the sum of the squared elements in the GLCM. A constant image would give a result of 1.	$\sum_{i,j} p(i,j)^2$
Homogeneity	A measure of the closeness of the distribution of GLCM measurements to the diagonal of the GLCM. A homogeneity of 1 is returned for a constant image.	$\sum_{i,j} \frac{p(i,j)^2}{1+\lvert i-j \rvert}$



g

GLCM property	Background region	Cisternal region
Contrast	0	0.8662
Correlation	-1	0.1063
Energy	1	0.1793
Homogeneity	1	0.6923

Figure 3.22: Background image texture vs ER cisternae texture
A single image of tobacco leaf epidermal cells transiently expressing GFP-HDEL with a region of interest of the background marked in red (a) and a zoomed version of this region (b). The GLCM of this region, typical of a constant image, with a randomly selected offset of 3 by 7 pixels (c). A chosen region of interest overlying a cisternae outlined in red (d) and a zoomed version of this region (e). The GLCM of this region using the same randomly selected offsets (f). (g) The GLCM properties of both the background region selected in (a) and the cisternal region selected in (d).. Scale bars 1 µm.

Cisternae texture analysis was performed on a normalized grey-scale image within the identified cisternal regions, with the neighbourhood distance set to $FWHM_{min}/2$ and four 45 degree angles to ensure there is no directional effect on the measurements. The results calculated the properties of the cisternal texture individually for each cisternae, and also produced a final result weighted by cisternal size, to prevent overwhelming of the data from many small cisternal regions.

The texture of the cisternae is modified by some ER modification treatments, including BFA and transient over-expression of RFP-AtLNP2 (fig. 3.23). BFA treatment shows low contrast and high correlation which is expected of large homogeneous cisternae, the presence of high intensity accumulations of GFP-HDEL throughout the cisternae results in the increase in cisternal energy. Similar texture modifications to cisternal texture are also observed with over-expression of RFP-AtLNP2, though to a lesser extent.

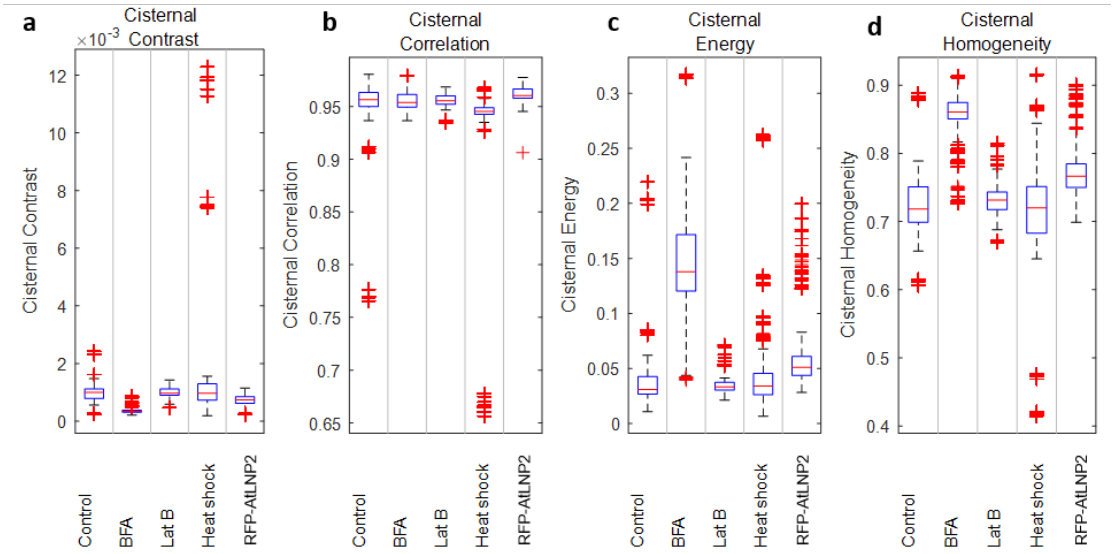


Figure 3.23: GLCM analysis of modified ER cisternae
The results of a GLCM property analysis of multiple samples treated either pharmacologically or modified through protein over-expression. Results are shown for (a) the contrast, (b) the correlation, (c) the energy and (d) the homogeneity of the GLCM analysis, weighted by the area of each contributing cisternae. Total n = 182 biological replicas: Control, n=46; BFA, n=46; Lat B, n=28; Heat shock, n=33 and RFP-AtLNP2, n=30, results obtained over 5 technical replicas.

3.2.11 Multivariate analysis of modified ER structure and dynamics

Within the last 10 years, modified ER structure and dynamics have been identified by observation in response to viral infection, modified protein expression, drug treatment and stress (see table 1.1). While comparison of specific metrics may be appropriate for specific studies, an unbiased comparison of the effect of any treatment compared to the control is a key starting step for identifying broad scale modification of the ER. A combination of multiple metrics can also provide a more accurate characterisation of the ER phenotype, which may not be detectable initially. Statistical analysis of multiple metrics requires: (i) normalisation of individual metrics through statistical transformation; (ii) a multivariate analysis (MANOVA) to test for an overall significant effect, while controlling for familywise errors; (iii) if the MANOVA identifies a significant overall effect, parametric ANOVAs comparing treatments with the control ER to identify significantly modified metrics. This provides a basis for further investigation of the likely function of ER modifying agents.

To test the ability of AnalyzER to distinguish modified ER structures, a dataset of 182 was analysed, 5-frame time series of control ER labelled with GFP-HDEL (n=46, fig. 3.24a); after treatment with BFA (n = 46, fig. 3.24b) a secretory pathway blocker; treatment with Lat B (n=28, fig. 3.24c) which disrupts the underlying actin cytoskeleton; after abiotic stress treatment using rapid heat shock (n=33, fig. 3.24d) and transient over-expression of the Er structure modifier RFP-AtLNP2 (n=29, fig. 3.24e). Initial MANOVA analysis identified significant difference between the structure and dynamics of the ER under these conditions (Pillai's trace, $F_{(72,648)} = 17.5$, $p = 2.7\text{x}10^{-110}$ or Roy's largest root, $F_{(18,162)} = 36.7$, $p = 7.9\text{x}10^{-48}$). The first two canonical variables provided complete separation

of Lat B and heat shock treatments from the other treatments and control (fig. 3.24f). The third canonical variable teased apart control from BFA and AtLNP2 (fig. 3.24g), whilst the fourth canonical variable separated BFA and AtLNP2 (fig. 3.24h). Subsequent ANOVAs can be used to identify the metrics that contribute to the detected differences in ER structure. For example treatment with Lat B and heat shock primarily affect the rate of ER remodeling, of both cisternae and tubules with little difference in cisternae texture metrics (fig. 3.25). BFA and AtLNP2 show modification of the cisternal texture metrics energy and homogeneity, and the size and geometry of both polygonal regions and cisternae.

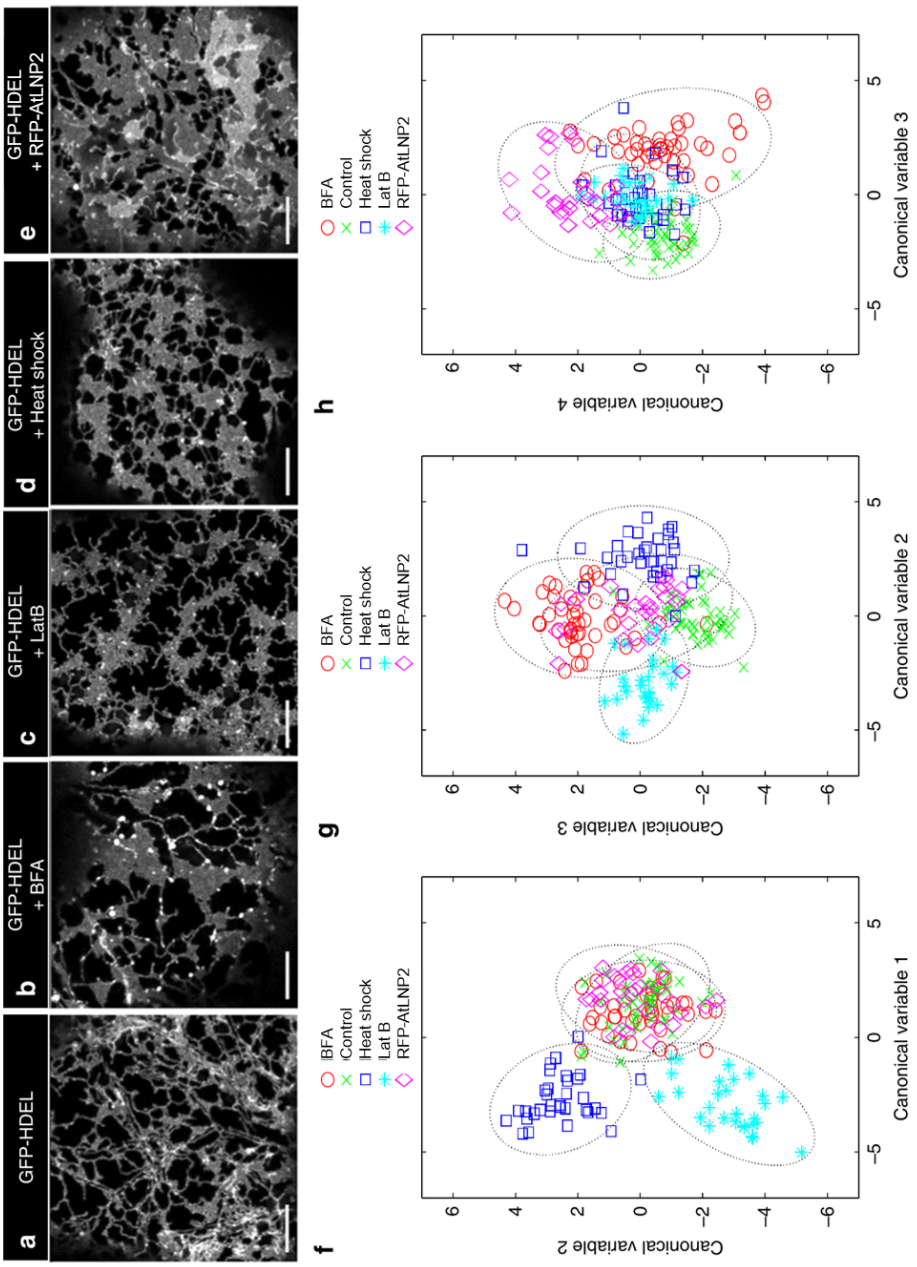


Figure 3.24: Multivariate analysis of modified ER structures
Outputs of a multivariate analysis of ER structure comparing control images (a) to ER structure after pharmacological modification (BFA (b), Lat B (c)), stress (heat shock (d)) and protein over-expression (RFP-AtLNP2 (e)); Grouped scatter plots of the first 3 significant canonical variables paired as: (f) canonical variables 1 and 2, (g) canonical variables 2 and 3 and (h) canonical variables 3 and 4. The dotted line around each group represents the 95% confidence limit. Total n = 182: Control, n=46; BFA, n=46; Lat B, n=28; Heat shock, n=33 and RFP-AtLNP2, n=30, results obtained over 5 technical replicas. Scale bars 5 µm.

ER structural subdomain	Variable	$F_{(4177)}$	p-Value	BFA	Lat B	Heat shock	RFP-AtLNP2
Tubules	Length	15.78	4.58×10^{-11}	***	***	***	***
Tubules	Maximum speed	50.52	2.59×10^{-28}	***	***	***	***
Tubules	Mean speed	46.16	1.60×10^{-26}	***	***	***	***
Tubules	Flow coherence	19.71	1.96×10^{-13}		*	***	
Tubules	Persistency	60.36	5.11×10^{-32}		***	***	
Cisternae	Contrast	5.894	1.78×10^{-04}	*			
Cisternae	Correlation	4.612	1.45×10^{-03}			*	
Cisternae	Energy	54.94	4.72×10^{-30}	***			***
Cisternae	Homogeneity	40.19	6.32×10^{-24}	***			***
Cisternae	Maximum speed	46.17	1.57×10^{-26}	***	***	***	***
Cisternae	Mean speed	74.1	8.72×10^{-37}	***	***	***	***
Cisternae	Flow coherence	77.42	7.61×10^{-38}	***	***	***	***
Cisternae	Persistency	53.46	2.00×10^{-29}	**	***	***	***
Cisternae	Circularity	8.325	3.56×10^{-06}	**	**	**	
Cisternae	Area	6.467	7.03×10^{-05}	**	***	**	*
Cisternae	Perimeter	15.56	6.29×10^{-11}	***			***
Polygonal regions	Area	40.14	6.61×10^{-24}	***	***		***
Polygonal regions	Perimeter	19.85	1.63×10^{-13}	***	***		***
Polygonal regions	Circularity	41.26	2.09×10^{-24}	***	***	*	***

Figure 3.25: Results of multiple planned comparisons of ER metrics
The ANOVA results of planned comparisons against wild-type across all ER metrics included in the MANOVA, identifying treatments that result in significantly different ($p<0.05$) ER structure and dynamics measurements. Total n = 182 biological replicas: Control, n=46; BFA, n=46; Lat B, n=28; Heat shock, n=33 and RFP-AtLNP2, n=30, results obtained over 5 technical replicas.

3.3 Discussion

AnalyzER is a novel, fully integrated software that can be routinely applied to quantify the structure and dynamics of the plant ER. AnalyzER's segmentation and subsequent generation of the tubular skeleton is robust and performs well as demonstrated by precision-recall analysis, with errors more common at the edges of cells where the fluorescence signal is reduced (section 3.2.5). We calibrate our measurements of ER structure by relating the fluorescence intensity of ER tubules to the estimated physical width of the plant ER. We measure this width as approximately 40 nm using electron microscopy, a result that is within the bounds of the ER widths measured in other species (45-50 nm in COS7 cells Shibata *et al.* (2010) and 28.5 nm in yeast West *et al.* (2011)). As there is a possibility of fixation artifacts when preparing samples for electron microscopy, this calibration value of 40 nm can be easily modified by the user within the GUI to reflect measurements provided by other methods.

Aspects of plant ER dynamics are captured using two methods: a modified version of the persistency mapping analysis developed by Sparkes *et al.* (2009a), and optical flow analysis, similar to the cross-correlation analyses applied by Ueda *et al.* (2010) to cotyledonary petioles of arabidopsis. The Farnebäck algorithm was chosen as the specific optical flow analysis method due to its ability to identify fine scale remodeling of the plant ER and its previous application to detect the speed of meiotic cytoplasmic streaming in *C. elegans* (Kimura *et al.*, 2017). Both methods ability to detect ER remodelling were tested by comparison of ER dynamics modified by Lat B and heat shock respectively. Lat B is a known to modify ER dynamics (Sparkes *et al.*, 2009a), whilst the heat shock treatment was developed specifically for this purpose. In both cases these analyses were able to detect the reduction of ER movement that is clearly visible post-modification (section 3.2.9.2).

In addition the coherence of optical flow can be assessed, revealing additional aspects of ER dynamics modification, which may have implications for future studies of protein movement through the ER.

The quantification of fluorophores throughout the ER were tested using AtRTN1, a protein known to cause constriction and restrict the GFP-HDEL to sub-regions of the ER (Sparkes *et al.*, 2010). Two channel analysis of fluorophore distribution along tubules revealed that GFP-HDEL was indeed restricted to bulges along tubules with relatively low RFP-AtRTN1 expression. The variation in GFP-HDEL along channels is modified by co-expression with RFP-AtRTN1 compared to when alone. It is now also possible to characterise the location of fluorescently tagged proteins at the edges of cisternae as well as assessing the distribution throughout the cisternae through the ER. This texture analysis may be applied in the future to identify sub-resolution modifications in the ER texture.

Finally all these metrics can be brought together into a large scale multivariate analysis comparing all identified ER metrics within a specific software developed for this purpose. These results have been tested on modifications of the ER induced through a range of different methods - physical stress, pharmacological intervention, modifying both secretion and the underlying actin cytoskeleton, and modifications induced by protein over-expression of two ER structure modifiers AtRTN1 (Sparkes *et al.*, 2010) and AtLNP1 and 2 (Kriechbaumer *et al.*, 2018). Results show that AnalyzER is capable of differentiating these treatments from each other and identifying the ways in which the structures have been modified.

AnalyzER has been published in an open access journal alongside extensive documentation to enable rapid uptake by the scientific community. It is hoped that AnalyzER will be used by the scientific community to investigate novel causes of ER structure and dynamics modification and will ultimately lead to a better

understanding of the different function roles of ER cisternae and tubules. As part of this work AnalzER was used to investigate the function of two novel ER shaping proteins: AtLNP1 and 2. This included analysis of ER structure and dynamic modifications in response to AtLNP1 and 2 depletion and sub-resolution analysis of the cisternal structures induced by transient AtLNP1 and 2 over-expression in tobacco (chapter 4). In addition AnalyzER has played a key role in determining appropriate controls for analysis single particle dynamics in the plant ER. Specifically the effect of proposed ER dynamics modifiers on the structure of the ER, including different concentration of Lat B and transient over-expression of actin markers that are known to reduce the movement of other sub-cellular organelles (chapter 5) (Holweg, 2007; van der Honing *et al.*, 2011; Rocchetti *et al.*, 2014).

4 | Lunapark proteins and ER structure

Contents

4.1 Introduction 138

4.1.1 The Lunapark protein family 138

4.1.2 The arabidopsis Lunapark proteins 139

4.2 Results 141

4.2.1 The sub-cellular localisation of the arabidopsis Lunapark proteins 141

4.2.2 Transcription of Lunapark throughout development . . . 142

4.2.3 Identification of T-DNA insertion lines with reduced AtLNP1 and AtLNP2 transcription 145

4.2.4 Reduced Lunapark expression results in modified ER structure 149

4.2.5 AnalyzER confirms modified ER structure in mutant plants 156

4.2.6 Native expression of AtLNP1 in *lnp1* restores normal ER structure 161

4.2.7 Candidate domains for Lunapark function 163

4.2.8 AtLNP1 over-expression can induce densely tubulated regions of ER not seen on AtLNP2 over-expression . . . 169

4.2.9 AtLNP1 and 2 induce cisternae with different lumenal characteristics 172

4.2.10 AtLNP1 over-expression results in structurally aberrant cisternae formation, visible using VAEM 178

4.2.11 Reticulon proteins reveal regions of membrane curvature within ER cisternae 184

4.2.12 AtLNP1 does not co-localise with AtRTN1 or 3 186

4.2.13 AtLNP2 co-localises with AtRTN1 and 3 187

4.2.14 AtLNP1 and AtLNP2 truncations with altered ER localisation show modified co-localisation with AtRTN1 and AtRTN3 188

4.2.15 AtLNP1 punctae can be recruited to form cisternae . . . 192

4.3 Discussion 202

4.3.1 Arabidopsis has two Lunapark proteins that behave differently 202

4.3.2 Reduction of AtLNP1 and 2 transcription affects ER structure in arabidopsis 203

4.3.3 Candidate domains for AtLNP1 and 2 function 205
4.3.4 AtLNP1 and 2 over-expression produces different 'types' of cisternae 208
4.3.5 Several AtLNP1 and 2 truncations that show modified ER localisation also show modified AtRTN1 and 3 distributions 214
4.3.6 AtLNP1 forms cisternae through aggregate conglomeration as opposed to expansion 215

4.1 Introduction

4.1.1 The Lunapark protein family

The Lunapark protein family is highly conserved, with orthologues identified across plants, yeast, fungi, vertebrate and fungi (Spitz *et al.*, 2003). The family name 'Lunapark' is derived from a conserved LNPARK peptide sequence located downstream of a C-terminal zinc finger domain (Spitz *et al.*, 2003). The characteristic structure of the Lunapark protein family members is as follows: two N-terminal transmembrane domains (TMDs) and a C-terminal zinc finger domain followed by the LNPARK peptide sequence (Spitz *et al.*, 2003). This structure is observed in both arabidopsis Lunapark proteins (AtLNP1, AT2G24330 and AtLNP2, AT4G31080) though the LNPARK peptide sequence is slightly modified to LNKPKH, a modification that is conserved throughout Embryophyta (Kriechbaumer *et al.*, 2018). The human Lunapark protein, in addition to the conserved structure of the Lunapark protein family, has an additional N-myristoylation site (Moriya *et al.*, 2013).

Lunapark proteins have been implicated in the maintenance of ER structure in both yeast (Lunapark: Lnp1p) and mammalian cells (Lunapark: mLnp1). Loss of Lnp1p in yeast results in a high proportion of cells exhibiting what has been described as a 'collapsed' and 'densely reticulated' ER network (Chen *et al.*, 2012). Whereas in mammalian COS-7 cells, loss of mLnp1 results in an increased proportion of cisternae within the ER network (Chen *et al.*, 2015). Both yeast and mammalian Lunapark proteins have been found to localize primarily to three-way junctions in the ER and have been implicated in having a role in stabilizing nascent three-way junctions (Chen *et al.*, 2012, 2015; Wang *et al.*, 2016b). Mammalian Lunapark (mLnp1) functionality is conferred by both the N-terminal myristoylation site and

the zinc finger domain (Moriya *et al.*, 2013). Conversion of four conserved cysteine residues in the zinc finger domain to alanine in both Lnp1p and mLnp1 results in an inability to induce ER structural morphology changes on over-expression (Moriya *et al.*, 2013; Chen *et al.*, 2012). The two TMDs of mLnp1 have also been assessed in terms of protein integration into the ER. The N-terminal TMD contains a type II signal anchor which orients the N-terminus to the cytoplasm and leaves the C-terminus exocytoplasmic, whilst the second TMD acts as a stop transfer sequence (Moriya *et al.*, 2013).

4.1.2 The arabidopsis Lunapark proteins

AtLNP1 and AtLNP2 share 67% amino acid identity and localize differently across the plant ER when over-expressed. AtLNP1 localises preferentially to cisternae and small punctae across the ER, whereas AtLNP2 localises throughout the entire ER (fig. 4.1). AtLNP2 is annotated as having two splice variants (AtLNP2.1 and AtLNP2.2), with an additional 34 residues in AtLNP2.2 downstream of the TMDs (Kriechbaumer *et al.*, 2018). However this region is poorly conserved in Lunapark proteins across different species, and no detectable sequence reads can be obtained from publicly obtained RNASeq data (Kriechbaumer *et al.*, 2018). Therefore, all further work has been performed on a single splice variant: AtLNP2.1, hereafter referred to as AtLNP2. Work by Kriechbaumer *et al.* (2018) has also shown that transient over-expression of AtLNP1 and AtLNP2 in tobacco leaf epidermal cells results in cisternae induction in a dose dependent manner. This work aims to explore the function of AtLNP1 and 2 as ER shaping proteins through a variety of novel ER analysis methods, the role of AtLNP1 in cisternae formation and will explore the role of various conserved protien domains in the function of AtLNP1 and 2.

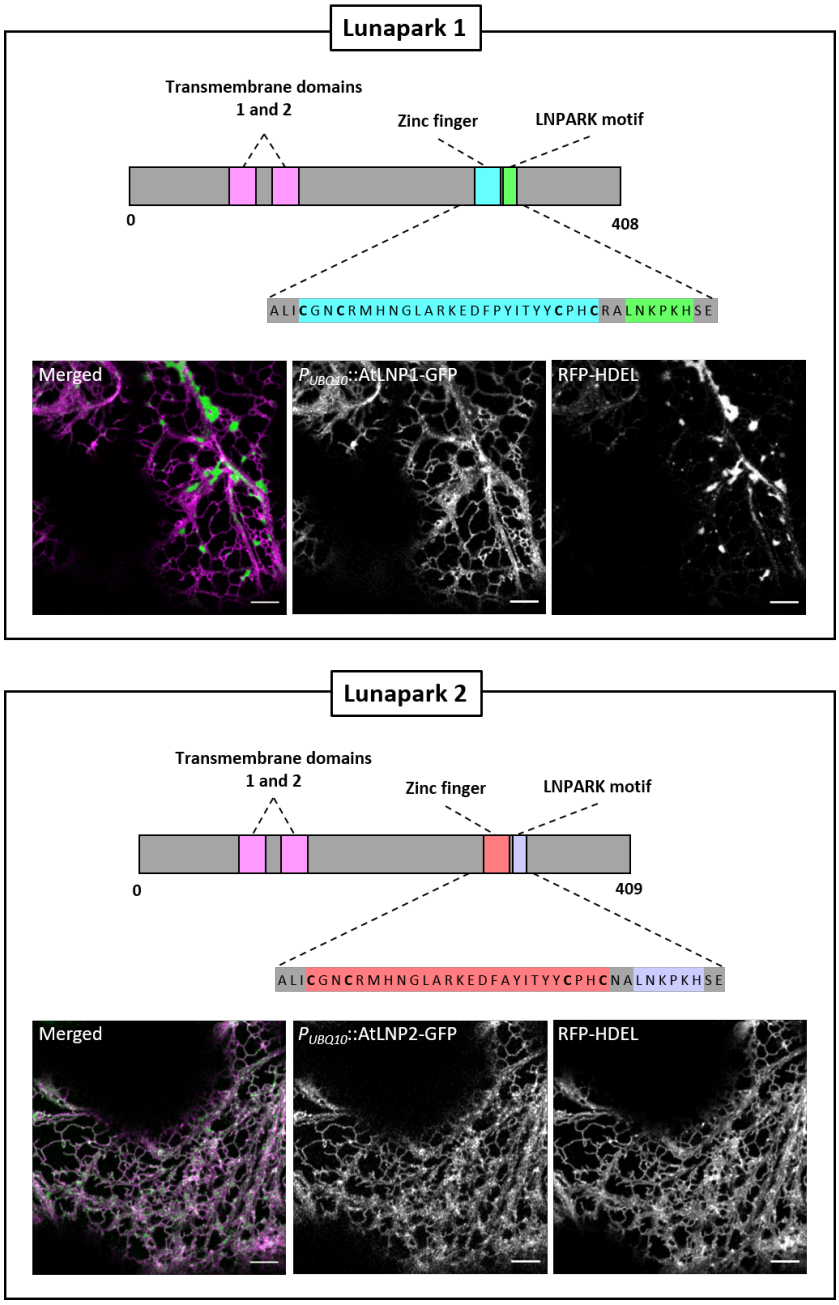


Figure 4.1: The structure and localisation of AtLNP1 an 2 after transient expression in tobacco

A graphical representation of the key features of the structure of AtLNP1 an 2, including two TMDs, a zinc finger domain and the LNPARK motif (modified to LNKPKH throughout the Embryophyta). Also shown is the localization of AtLNP1 and AtLNP2 expressed under the ubiquitin-10 promoter with a C-terminal green fluorescent protein (green) and the ER lumenal marker RFP-HDEL (magenta). Images shown are of transient over-expression in tobacco leaf epidermal cells. Scale bars 5 µm.

4.2 Results

4.2.1 The sub-cellular localisation of the arabidopsis Lunapark proteins

Transient over-expression of AtLNP1-GFP and AtLNP2-GFP in tobacco leaf epidermal cells via agrobacterium-mediated transformation shows localisation of AtLNP1 specifically to ER cisternae, whilst AtLNP2 is localised throughout the entire ER network (Kriechbaumer *et al.* (2018), fig. 4.1). The same localisation is seen on stable expression in arabidopsis leaf epidermal cells under the ubiquitin-10 promoter (plasmid provided by Grefen *et al.* (2010), construct generated, dipped and screened by Emily Breeze, further selection and confirmation by Charlotte Pain). P_{UBQ10}::AtLNP1-GFP localises to cisternae and small mobile punctae throughout the ER whereas P_{UBQ10}::AtLNP2-GFP localises throughout the entire ER (fig. 4.2). In the case of stable over-expression of AtLNP1 and AtLNP2, the plant ER remains highly dynamic (supplementary movie 4.1). Though transient over-expression of AtLNP1 and AtLNP2 in tobacco results in ER structure modifications, namely an increase in ER cisternae, the same modification is not easily discernible on stable over-expression in arabidopsis when images are collected using confocal microscopy.

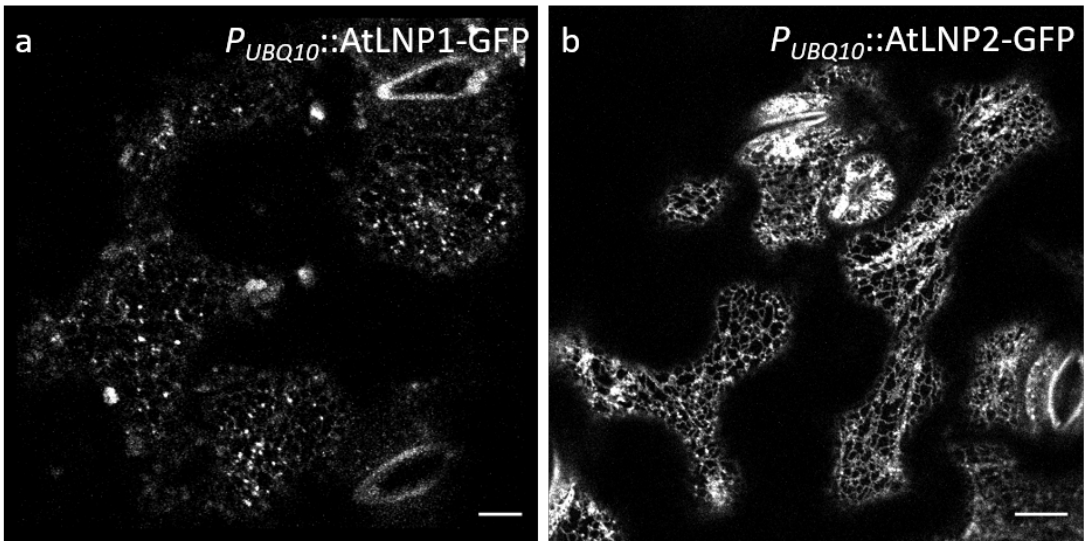


Figure 4.2: Stable over-expression of P_{UBQ10}::AtLNP1-GFP and P_{UBQ10}::AtLNP2-GFP in arabidopsis
Stable over-expression of (a) P_{UBQ10}::AtLNP1-GFP showing localization to specific punctae and (b) P_{UBQ10}::AtLNP2-GFP showing localization throughout the ER network in 7 day old arabidopsis leaf epidermal cells. Scale bar 5 µm.

4.2.2 Transcription of Lunapark throughout development

Large-scale microarray array data summarised in the Arabidopsis eFP Browser (Winter *et al.*, 2007), reveals that *AtLNP1* and *AtLNP2* are ubiquitously transcribed throughout arabidopsis tissues, though *AtLNP2* specifically has increased transcript abundance in mature pollen. In the arabidopsis tissues tested by Toufighi *et al.* (2005) and the AtGenExpress initiative, *AtLNP2* typically shows a higher transcript abundance than *AtLNP1* (supplementary fig. S1).

Semi-quantitative analysis of relative RNA abundance using reverse transcriptase PCR (RT-PCR) was performed on both 7 and 35 day old arabidopsis tissue. Primers were targeted to dissimilar regions of AtLNP1 and AtLNP2 and actin (ACT1, At2g37620) as a control. Tissue samples were collected from a minimum

of two plants per sample and multiple tissue samples were collected. Transcription of both *AtLNP1* and *AtLNP2* could be detected in the roots and shoots of 7-day old plants, though *AtLNP1* transcription was barely detectable in both tissues and couldn't be detected in 7-day old whole seedling. *AtLNP1* transcript could also not be detected in any mature tissues including 35 day old flowers and buds (n=3), nor mature siliques and mature rosette leaves (n=1), most likely due to poor sensitivity of the RT-PCR. *AtLNP2* transcript however could be detected in all mature tissues except the mature siliques, with a relative increase in detected RNA in the rosette leaves (fig. 4.3).

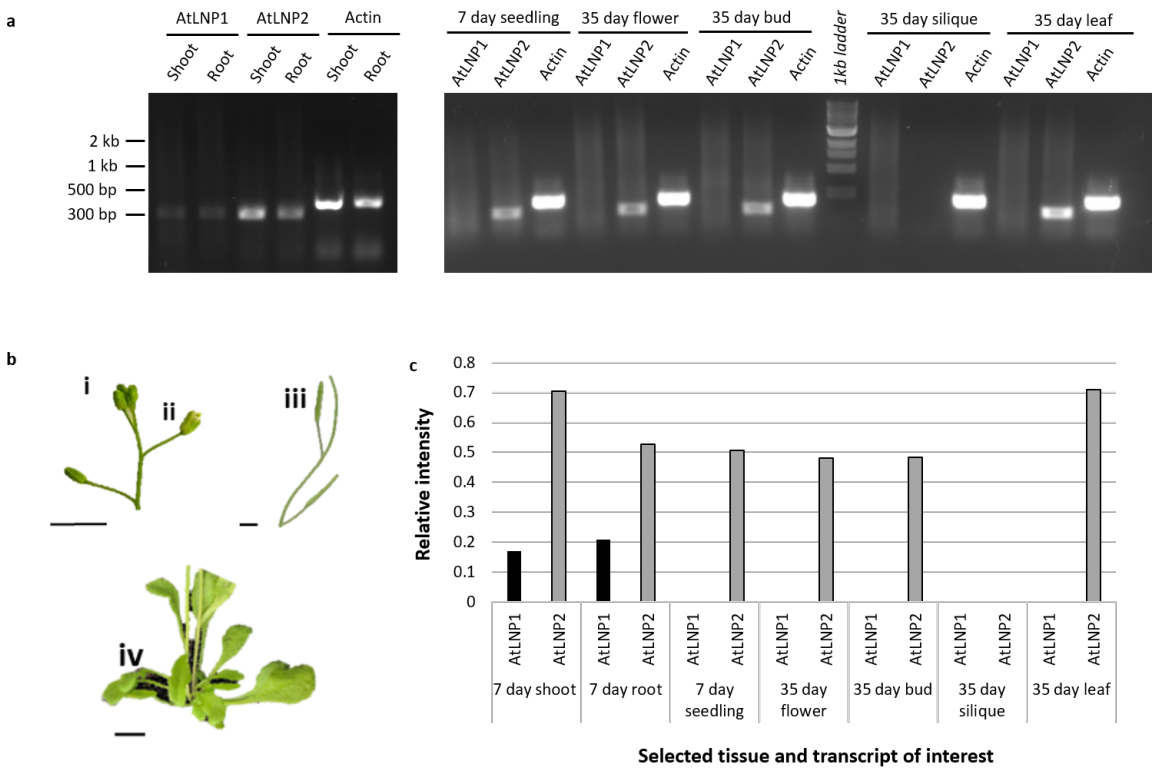


Figure 4.3: Identifying *AtLNP1* and *AtLNP2* transcription across different arabidopsis tissues and developmental stages

a) RT-PCR identifying *AtLNP1*, *AtLNP2* and actin transcription in 7-day old arabidopsis roots and shoots and 35 day old arabidopsis buds (n=3 biological replicas), flowers (n=3 biological replicas), siliques (n=1 biological replicas) and rosette leaves (n=1 biological replicas). (b) Images of the selected mature tissue harvested for RT-PCR analysis including (i) buds, (ii) flowers, (iii) siliques and (iv) rosette leaves, scale bar 5 cm. (c) Relative transcription of *AtLNP1* and *AtLNP2* across different tissues, normalized to the transcription of actin. Results obtained over 3 technical replicas.

4.2.3 Identification of T-DNA insertion lines with reduced AtLNP1 and AtLNP2 transcription

Several potential arabidopsis T-DNA insertion lines were identified from the TAIR database (for *AtLNP1*: SALK_034698 and SALK_205001, and for *AtLNP2*: SALK_031496 and SALK_072194). These lines were selected as they were reported as homozygous for the T-DNA insertion. Genomic DNA was extracted from mature T-DNA insertion lines and tested for the presence of a T-DNA insertion in the gene of interest using primers designed with the online T-DNA Primer Design tool, provided by the Salk Institute Genomic Analysis Laboratory. Two primers are created that flank the predicted T-DNA insertion site (termed the right primer, RP and the left primer, LP) and an additional standard primer targeted to within the T-DNA insertion (the left border primer, LBb1.3). The absence of an insertion will result in an approximately 900 bp size band when tested with LP and RP, whilst lines homozygous for the T-DNA insertion will produce a band approximately 400 bp in size when tested with RP and LBb1.3. Heterozygous lines will produce both bands. Of the lines tested, the T-DNA insertion could only be confirmed in SALK_034698 and SALK_031496 (hereafter referred to a *lnp1* and *lnp2* respectively). Testing SALK_205001 gave no clear results, whilst SALK_072194 gave results consistent with wild-type individuals.

For full confirmation of the efficacy of the T-DNA insertion, both *lnp1* and *lnp2* were tested for *AtLNP1* and *AtLNP2* transcript abundance respectively. The RT-PCR protocol used to quantify *AtLNP1* and *2* transcription in *lnp1* and *lnp2* is the same that was used to quantify *AtLNP1* and *2* transcription in wild-type arabidopsis. Actin transcript abundance was used as a control for RNA and cDNA production as well as transcript detection levels, and RNA was extracted from all plants at 7 days old. A RT-PCR negative control (RT-control) was performed for

all samples and is shown for wild type (fig. 4.5a), whereby the RNA extracted from this plant undergoes the same procedure for cDNA synthesis, but without the addition of the necessary enzymes. Therefore if any transcript can be identified within this construct, it is likely that the RNA is contaminated with genomic DNA. Transcription of *AtLNP1* could not be detected in *lnp1*, whilst transcript levels of LNP2 were severely reduced (by approximately 80%) in *lnp2* compared to wild-type (fig. 4.5). The presence of detectable AtLNP2 transcription in *lnp2* is most likely due to the location of the T-DNA insertion near the 3' end of the gene. This may result in partial transcription of a truncated portion of the gene, hence a reduced level of *AtLNP2* transcript can be identified.

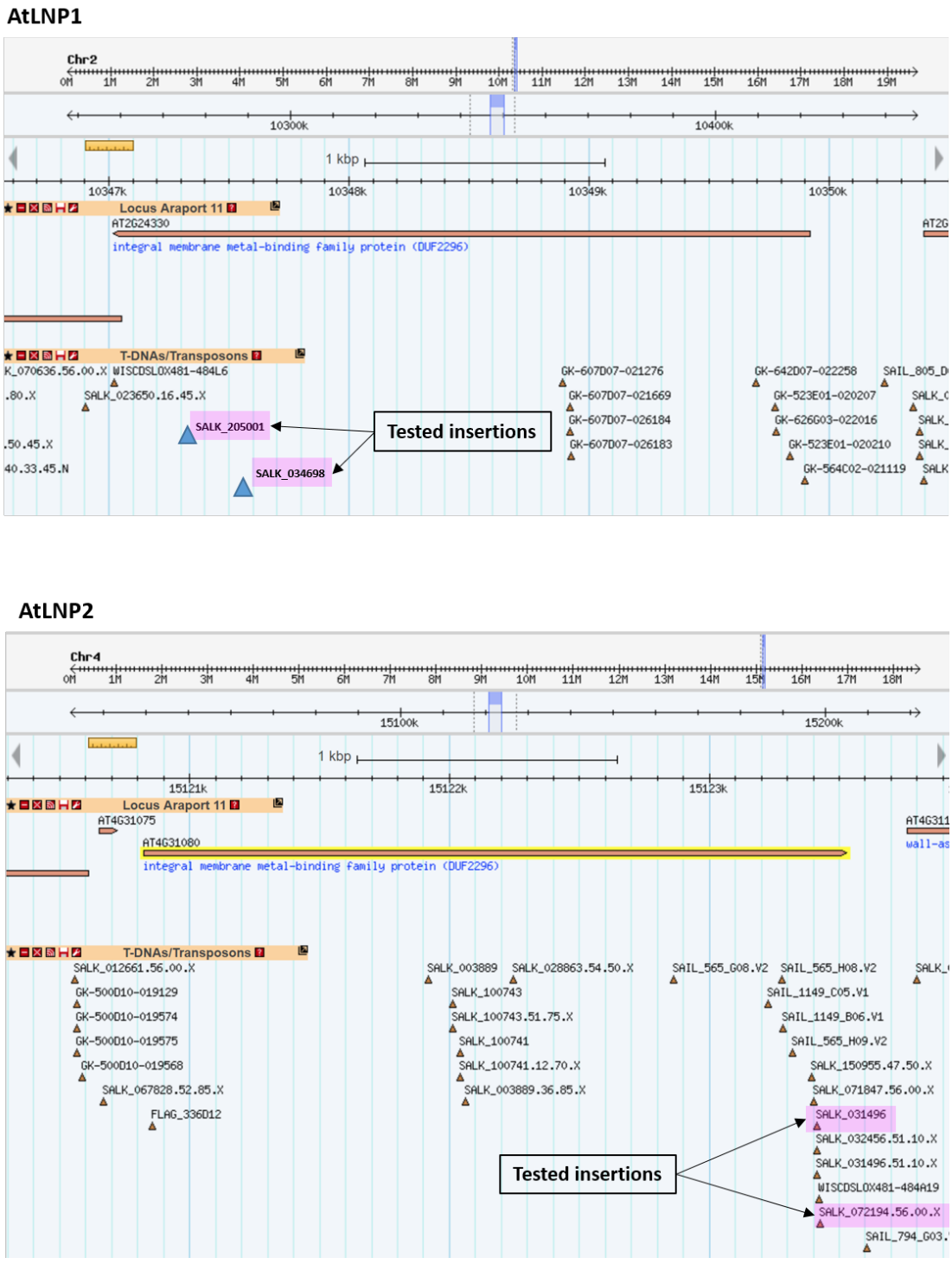


Figure 4.4: T-DNA insertion lines, and insertion positions, available for *AtLNP1* and *AtLNP2*

The location of the T-DNA insertions within *AtLNP1* and *AtLNP2* present within the available T-DNA insertion lines. Images generated using TAIR gbrowse but with SALK_034698 and SALK_205001 added manually as they are not currently included by gbrowse. Tested T-DNA lines highlighted in pink.

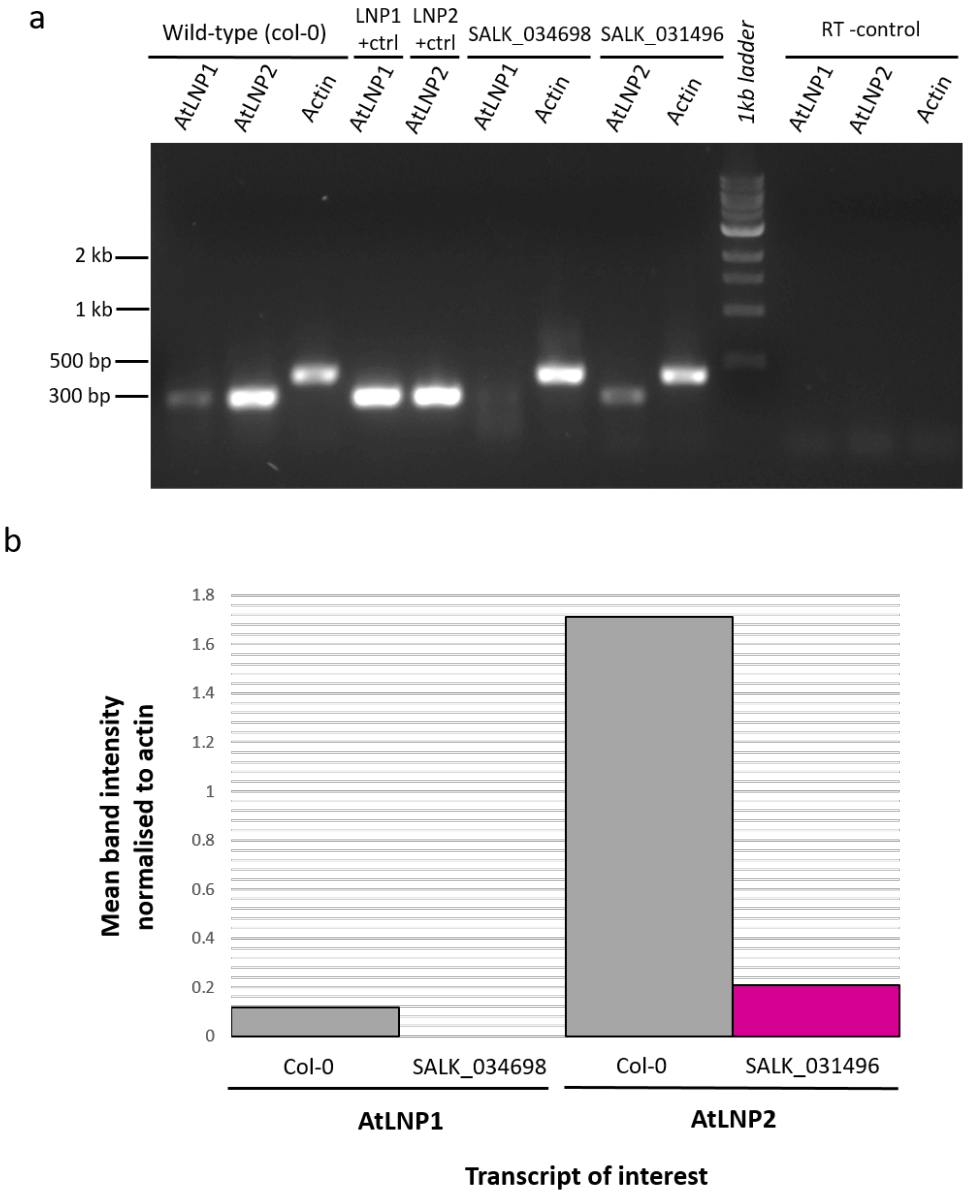


Figure 4.5: RT-PCR confirmation of reduced Lunapark transcription in Lunapark T-DNA insertion mutants
(a) RT-PCR results showing no detectable *AtLNP1* transcript in the *lnp1* mutant and reduction in the amount of *AtLNP2* transcript in the *lnp2* mutant. (b) Comparison of the amount of *AtLNP1* and *AtLNP2* transcript identified in 7 day old whole arabidopsis seedlings including Col-0, *lnp1* and *lnp2*. RNA extraction performed on 30-50 seedlings per sample, one cDNA synthesis and PCR performed per sample.

To summarise, four potential T-DNA insertion lines were tested for *AtLNP1* and *AtLNP2* for the presence of the T-DNA insertion and, where necessary, *AtLNP1* and *AtLNP2* transcription. A homozygous T-DNA insertion line (SALK_034698) with no detectable *AtLNP1* transcription, hereafter referred to as *lnp1*, and a homozygous T-DNA insertion line (SALK_031496) with greatly reduced *AtLNP2* transcription, hereafter referred to as *lnp2*, have been identified (table 4.1).

Table 4.1: Results summary of tested T-DNA insertion lines
The details for four T-DNA insertion lines tested for *AtLNP1* and *AtLNP2* transcription as appropriate. The location of the insertion, alongside the results of T-DNA insertion identification and transcription level testing are included.

Line name	Target Gene	Insertion location	T-DNA insertion status	Taranscription tested
SALK_034698	LNP1	Chr2:10347564	Homozygous	No transcription identified
SALK_205001	LNP1	Chr2:10347321	Unconfirmed	Not tested
SALK_031496	LNP2	Chr4:15123277	Homozygous	Reduced transcription
SALK_072194	LNP2	Chr4:15123425	Wild-type	Not tested

4.2.4 Reduced Lunapark expression results in modified ER structure

The ER structure of the 7 day old cotelydons of both *lnp1* and *lnp2* can be visualized using rapid staining by Rhodamine B (fig. 4.6). Meanwhile a double knockdown line of both *AtLNP1* and *AtLNP2* (*amilnp1lnp2*) was created by Emily Breeze (Kriechbaumer *et al.*, 2018). To generate this *amilnp1lnp2*, an amiRNA sequence targeted to the conserved zing finger domain of *AtLNP1* and *AtLNP2* was generated and floral dipped into plants stably expressing GFP-HDEL. Stable homozygous arabidopsis lines were created using the floral dip method, with the amiRNA construct dipped into an arabidopsis line that stably expresses the ER lumenal marker GFP-HDEL. Semi-quantitative RT-PCR performed by Emily

Breeze confirmed that this *amilnp1lnp2* line line showed reduced transcription of both *AtLNP1* and *AtLNP2*.

A novel ER analysis method was developed to assess modification of ER structure when staining with Rhodamine B is necessary (for full details see: chapter 2, section 2.9). This method requires greater user input compared to the methods employed by AnalyzER, as Rhodamine B strongly stains mitochondrial membranes and produces a relatively high background signal. As a result, manual trainable segmentation is required to ensure accurate segmentation of the network, this requires manual selection of the ER network as well as background regions of the strongly stained mitochondria. The ER structure of *lnp1* and *lnp2* was compared to Col-0 and and the structure of a Col-0 stably expressing GFP-HDEL alone was compared to the same line with reduced *AtLNP1* and *AtLNP2* expression (*amilnp1lnp2*).

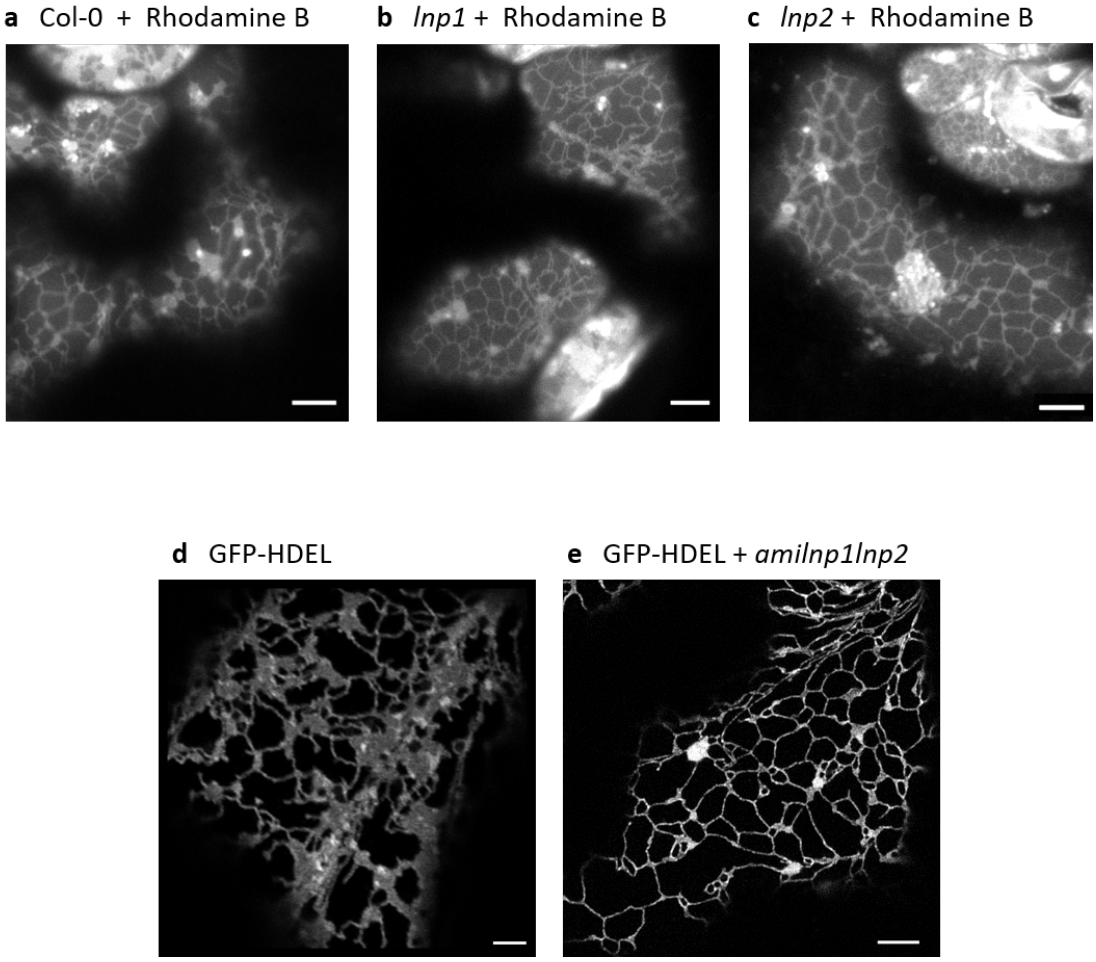


Figure 4.6: Reduced Lunapark expression modifies ER structure
7-day old cotelydonary cells of (a) Col-0, (b) *lnp1* and (c) *lnp2* after Rhodamine B staining which marks both the ER and the mitochondria. 7-day old cotelydonary cells of Col-0 stably expressing GFP-HDEL (d) alone and alongside (e) *amilnp1lnp2*. Scale bars 5 µm.

After identification of cisternae, the total area of the cisternae is normalized the area of the visible cell outline by calculating the percentage of this area that is characterized as cisternae. Reduction of both *AtLNP1* and *AtLNP2* transcription results in a reduced proportion of the ER network being composed of cisternae compared to the Col-0 control (Kruskal-Wallis rank sum test, p-value $= 3.88 \times 10^{-2}$). These results indicated an approximately 3 times reduction in proportion of ER cisternal area for both *lnp1* and *lnp2* (fig. 4.7 a,b). In addition, polygonal region size shows a significantly modified distribution (Independent 2-group Mann-Whitney

U test, Col-0/*lnp1*, p-value= 2.77×10^{-2}, Col-0/*lnp2*, p-value= 2.14×10^{-4}). The modified distribution of polygonal region sizes indicates that though wild-type ER has an approximately binomial distribution of size, *lnp1* and *lnp2* have a more even distribution of different sizes of polygonal regions (fig. 4.7 a,c). This indicates a greater variability in the mean size of polygonal region in either *lnp1* or *lnp2*. Neither *lnp1* or *lnp2* show a significant change in the length of ER tubules (fig. 4.9a,c). This analysis was performed on three biological repeats with 15 technical replicas.

The same analysis was performed on arabidopsis leaf epidermal cells stably expressing the ER marker GFP-HDEL as a control and arabidopsis leaf epidermal cells over-expressing both GFP-HDEL and *AtLNP1* and *2* targeted amiRNA that reduces the transcription of both *AtLNP1* and *AtLNP2* (fig. 4.8). Reduction of *AtLNP1* and *AtLNP2* transcription results in an approximately 4 times reduction of cisternal area as a percentage of total visible ER area (Wilcoxon rank-sum, p-value = 3.1×10^{-3}, fig. 4.8a,b). This is as opposed to a 3 times reduction in the *lnp1* and *lnp2* plants. *amilnp1lnp2* plants show increased polygonal region size (Wilcoxon rank-sum, p-value = 2.89×10^{-44}), but also an increased variation in the sizes of the polygonal regions (fig. 4.8a,c). This is consistent with an increasingly disordered network as well as a reduced proportion of cisternae. Tubules are significantly longer in the *amilnp1lnp2* line (t-test, p-value = 2.2×10^{-16}, fig. 4.9b,d) and show a greater range of tubule lengths (fig. 4.9). The comparison of the *amilnplnp2* lines was performed for three biological replicas with at least 12 technical repeats.

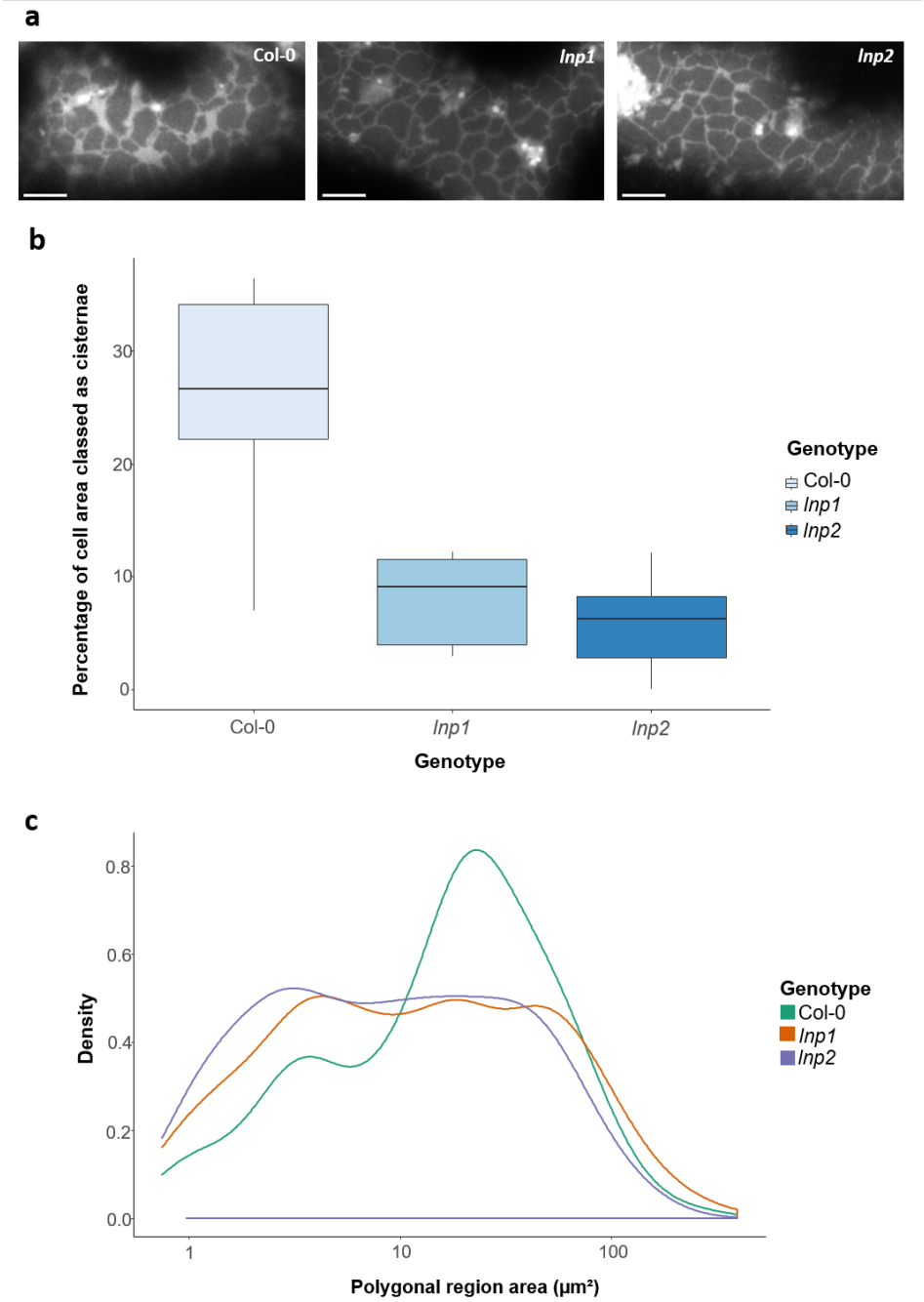


Figure 4.7: *lnp1* and *lnp2* have modified ER structures
(a) Comparison of ER structures in 7-day old cotyledonary cells of Col-0 (n=5 biological replicas), *lnp1* (n=5 biological replicas) and *lnp2* (n=5 biological replicas) after Rhodamine B staining. (b) Comparison of the percentage of the visible cell area that contains ER classed as cisternae. (c) Density plot of polygonal region sizes within the stained ER. Results obtained over three technical replicas, scale bars 5 µm.

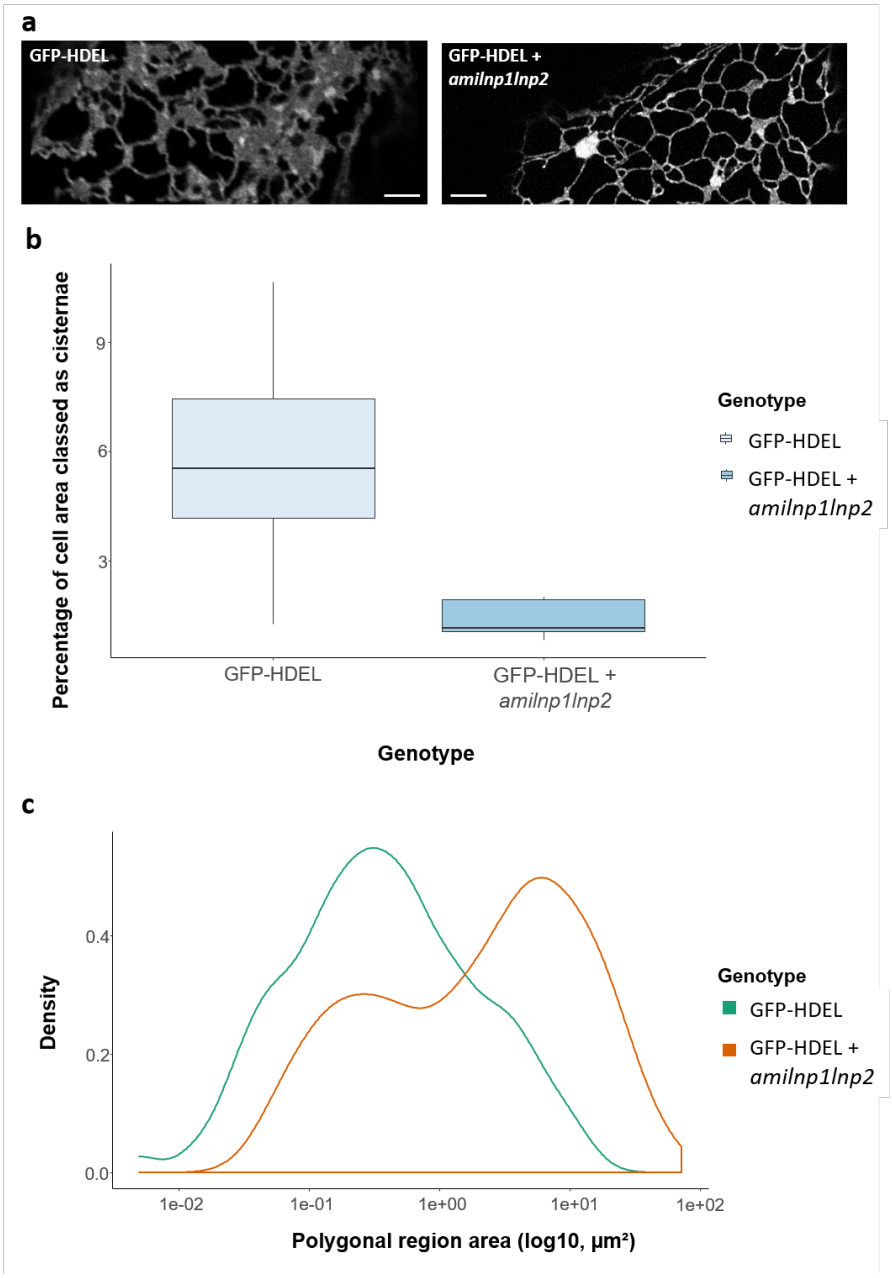


Figure 4.8: *amilnp1lnp2* shows a modified ER structure in cotyledonary cells

(a) 7-day old cotyledonary cells of Col-0 stably expressing GFP-HDEL alone (n=6 biological replicas) and alongside reduced *AtLNP1* and *AtLNP2* transcription in the *amilnp1lnp2* plants (n=6 biological replicas). (b) Comparison of the percentage of the visible cell area that contains ER classed as cisternae. (c) Density plot of polygonal region sizes within the stained ER. Results obtained over three technical replicas, scale bars 5 µm.

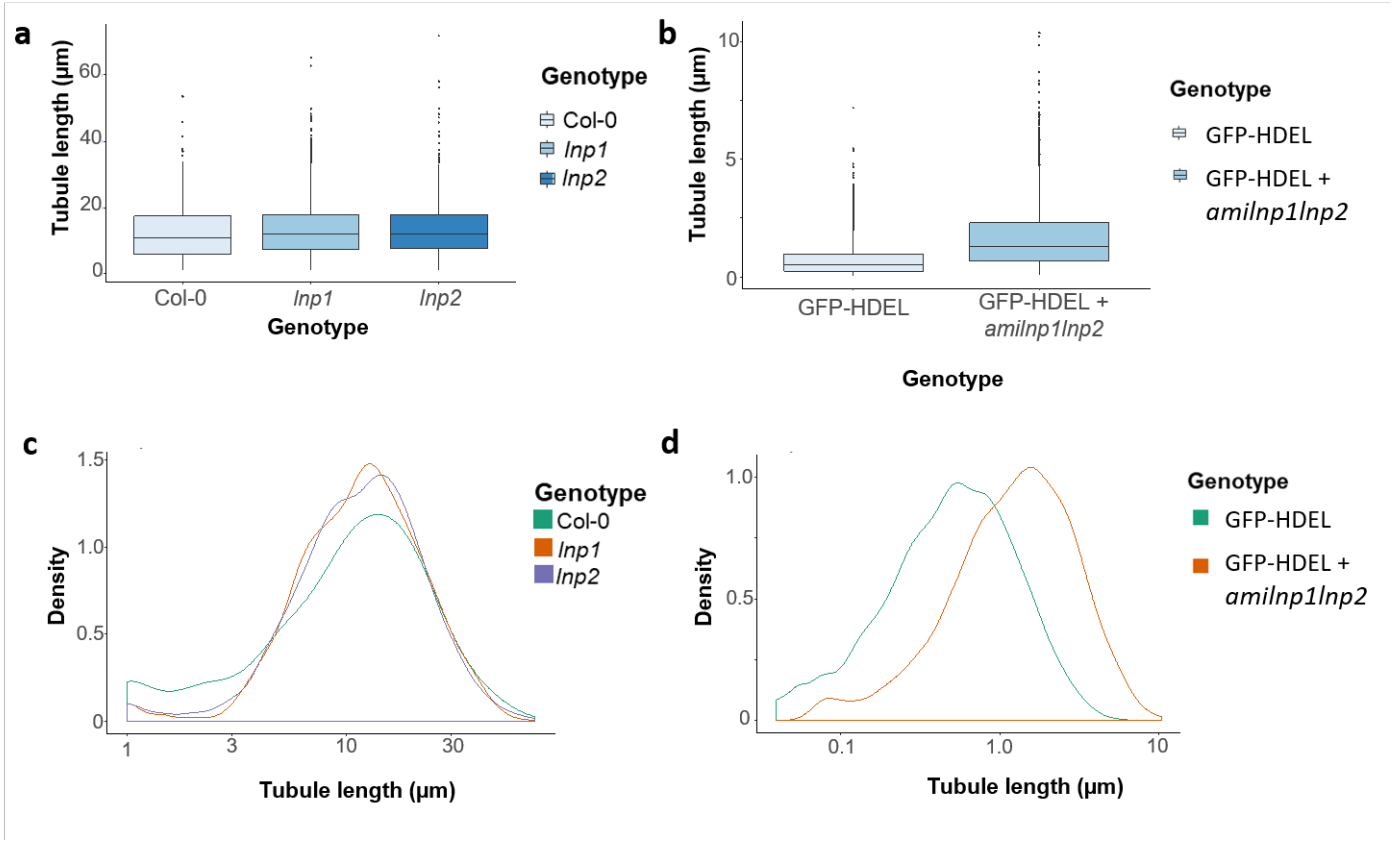


Figure 4.9: The effect of reduced Lunapark expression on ER tubule length
Boxplot comparison of tubule length in single Lunapark knockout/knockdown mutants *lnp1* (n=5 biological replicas), *lnp2* (n=5 biological replicas) and Col-0 (n=5 biological replicas) plants (a) and the double knockdown line *amilnp1lnp2* (n=6 biological replicas) compared to Col-0 plants stabily expressing GFP-HDEL (n=6 biological replicas) (b). Density plot comparison of ER tubules lengths in single Lunapark knockout/knockdown mutants *lnp1* and *lnp2* (c) and the double knockdown line *amilnp1lnp2* (d). Data for each comparison obtained over three technical replicas.

4.2.5 AnalyzER confirms modified ER structure in mutant plants

Where possible, the results obtained using the ImageJ ER analysis method developed by Kriechbaumer *et al.* (2018) were reconfirmed using AnalyzER. This was possible where comparing ER structure in plant stably expressing GFP-HDEL (n=5) alone and alongside amiRNA targeted to *AtLNP1* and *AtLNP2* (n=4). Analysis with AnalyzER confirmed modifications to ER structure with reduced transcription of *AtLNP1* and *AtLNP2*. The mean area of polygonal regions was again found to be significantly increased in the *amilnp1lnp2* line (ANOVA, p-value $= 1.59 \times 10^{-4}$, fig. 4.10) and shows the same approximately bimodal distribution of areas as observed previously. The mean tubule length was also found to be significantly increased (ANOVA, p-value $= 1.20 \times 10^{-4}$, fig. 4.11) on reduction of *AtLNP1* and *AtLNP2* transcription which may contribute to the aforementioned modification of polygonal region areas. Using AnalyzER it is possible to assess the dynamics of ER in the control cells and in the *amilnp1lnp2* line. Though there was no significant modification to the dynamics of ER tubules, the few cisternae identified in the *amilnp1lnp2* line show significantly increased persistency (ANOVA, p-value $= 1.98 \times 10^{-2}$, fig. 4.12, supplementary movie 4.2) and a reduced maximum speed of remodeling (ANOVA, p-value $= 1.67 \times 10^{-2}$, fig. 4.13, supplementary movie 4.2). In addition, these cisternae show a perturbed geometry compared to their wild-type counterparts, with an increased circularity (ANOVA, p-value $= 4.19 \times 10^{-3}$, supplementary fig. S2a,b) and decreased roughness (ANOVA, p-value $= 8.28 \times 10^{-3}$, supplementary fig. S2c,d).

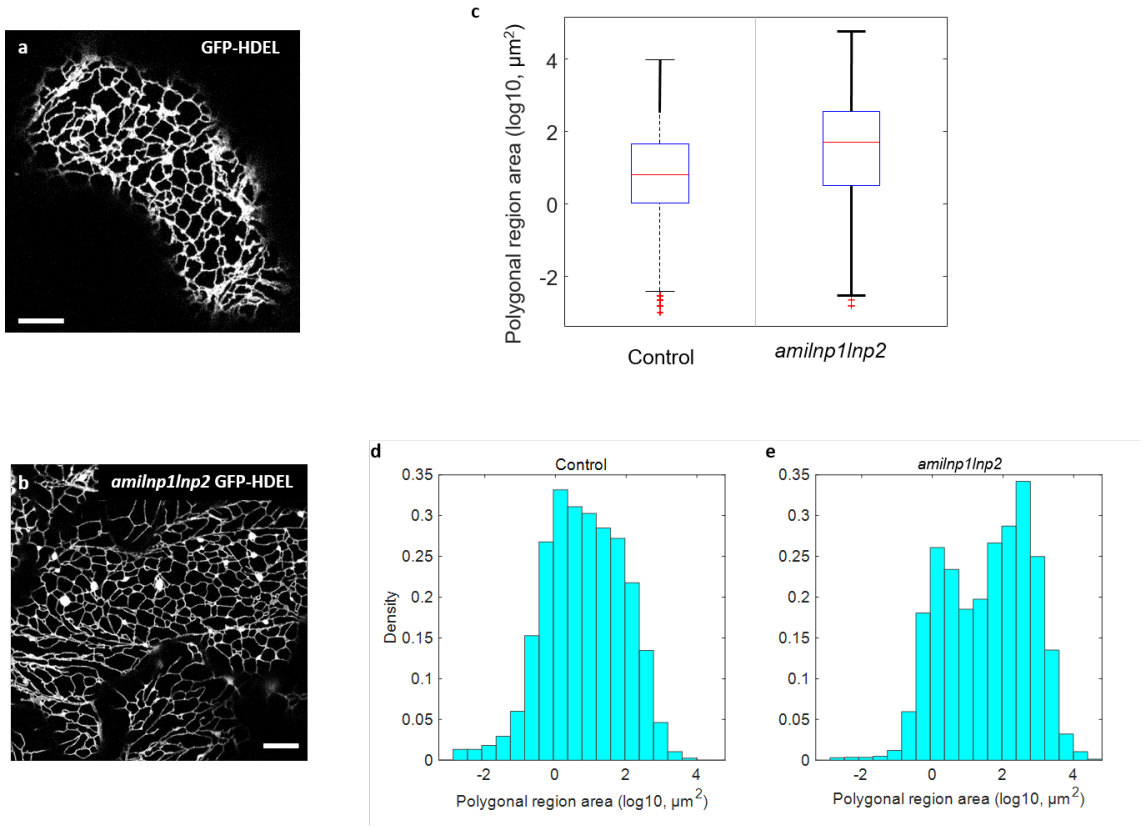


Figure 4.10: *amilnp1lnp2* shows modified polygonal region size
Representative images from a 64 second timeseries of 7 day old arabidopsis cotyledonary cells of plants stably expressing GFP-HDEL alone (n=5 biological replicas) (a) and in *amilnp1lnp2* (n=4 biological replicas) (b). Boxplot comparison of polygonal region area detected in all examined cells (c) and density plots of the same result (d,e). Results obtained over three technical replicas, scale bars 5 µm.

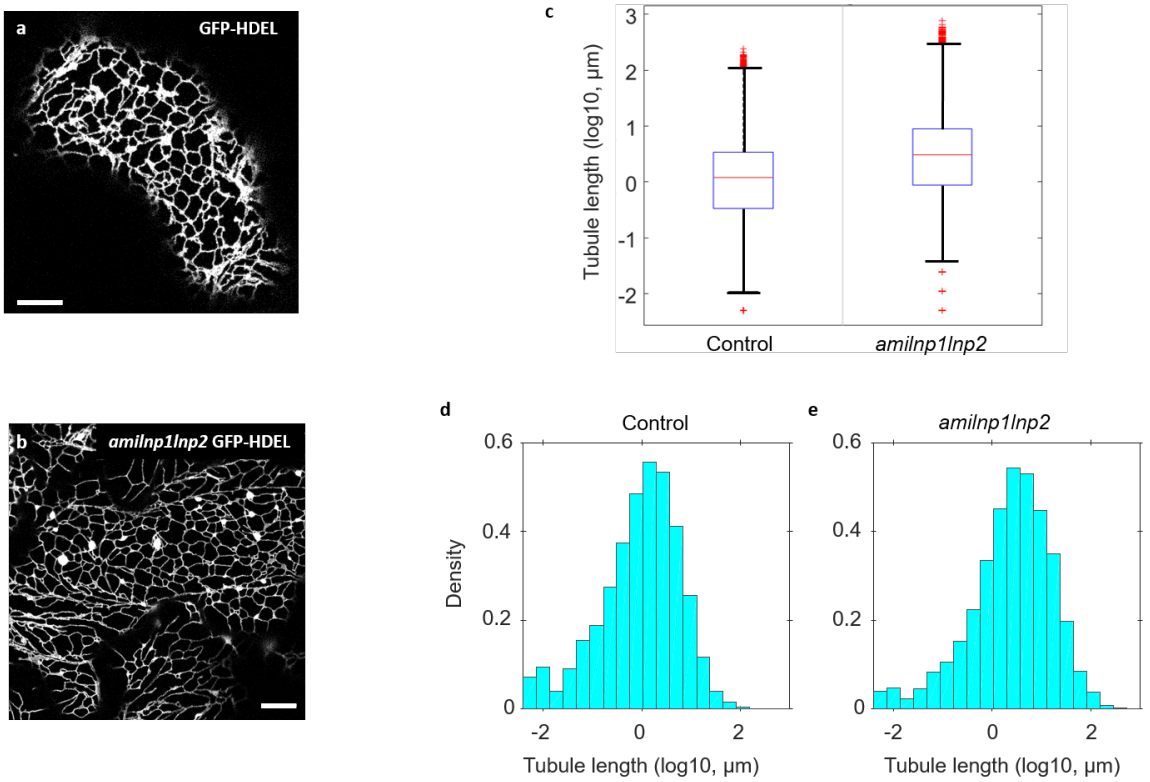


Figure 4.11: *amilnp1lnp2* shows modified tubule lengths
Representative images from a 64 second timeseries of 7 day old arabidopsis cotyledonary cells of plants stably expressing GFP-HDEL alone (n=5 biological replicas) (a) and in *amilnp1lnp2* (n=4 biological replicas) (b). Boxplot comparison of tubule length in all examined cells (c) and density plots of the same result (d,e). Results obtained over three technical replicas, scale bars 5 µm.

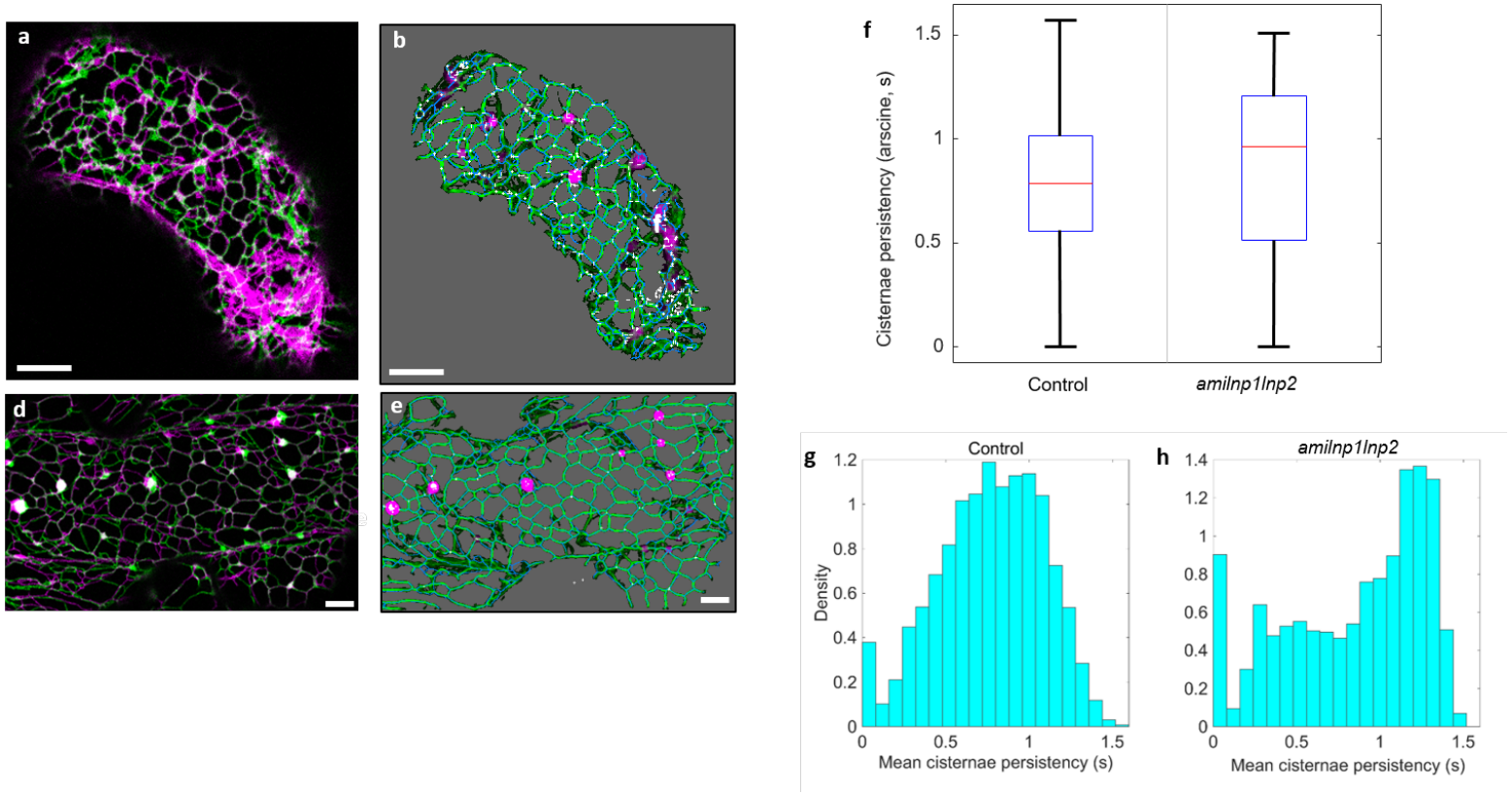


Figure 4.12: *amilnp1lnp2* shows modified cisternae persistency
Overlay of the first frame (green) and last frame (magenta) in a 64 second timeseries of arabidopsis cotyledonary cells of a plant stably expressing GFP-HDEL alone (n=5 biological replicas) (a) and in *amilnp1lnp2* (n=4 biological replicas) (d). Persistencey mapping of movement in the GFP-HDEL line (b) and the *amilnp1lnp2* line (e). Boxplot comparison of cisternae persistency through time detected in all examined cells (f) and density plots of the same result (g,h). Results obtained over three technical replicas, scale bars 5 µm.

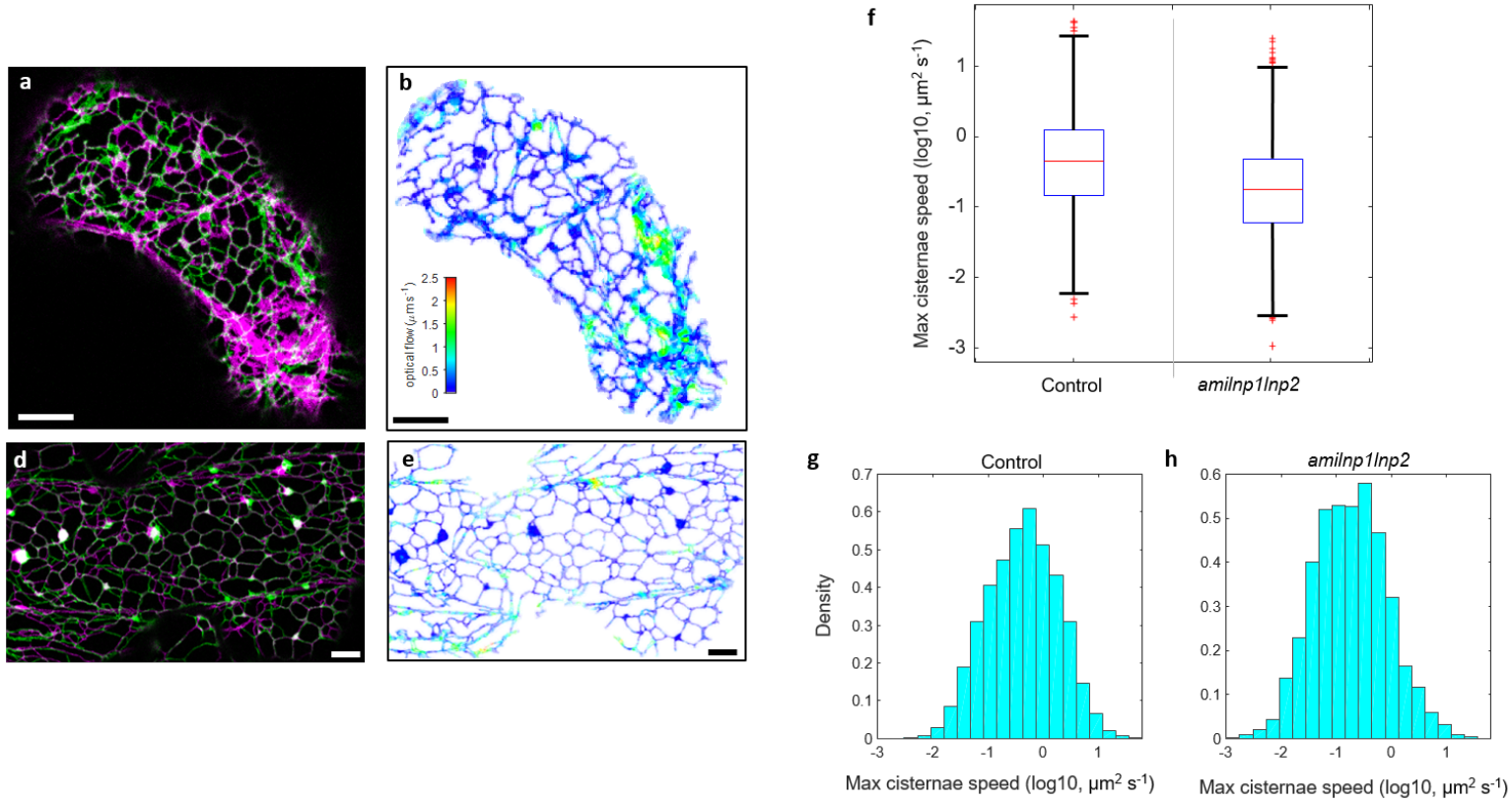


Figure 4.13: *amilnp1lnp2* shows modified cisternae dynamics
Overlay of the first frame (green) and last frame (magenta) in a 64 second timeseries of arabidopsis cotyledonary cells of a plant stably expressing GFP-HDEL alone (n=5 biological replicas) (a) and in *amilnp1lnp2* (n=4 biological replicas) (d). Optical flow mapping of movement in the GFP-HDEL line (b) and the *amilnp1lnp2* line (e). Boxplot comparison of maximum cisternae speed through time detected in all examined cells (f) and density plots of the same result (g,h). Results obtained over three technical replicas, scale bars 5 µm.

4.2.6 Native expression of AtLNP1-GFP in *lnp1* restores normal ER structure

In order to assess whether the changes in ER structure on *lnp1* are indeed related to the loss of *AtLNP1* transcription or due to off-target effects of T-DNA mutagenesis, fluorescently tagged AtLNP1 was stably expressed in *lnp1* under its native promoter (2 kb upstream from gene, construct generated by Emily Breeze, line floral dipped and screened by Charlotte Pain). After selection no fluorescence could be identified using confocal microscopy, however Rhodamine B staining indicated that a more 'normal' ER structure had been restored after expression of P_{AtLNP1}::AtLNP1-GFP (fig. 4.14). Specifically, cisternae could once again be identified within the 7-day old cotyledonary cells and there was a reduction in the size of the polygonal regions enclosed by the ER network. It is possible that no fluorescence could be detected in the ER due to cleaving of the GFP from AtLNP1. This could be tested using Western blotting to detect the presence of free GFP or AtLNP1-GFP within stable lines using existing GFP antibodies. However, this was not attempted as part of this work. Attempts were made to create a similar line for *lnp2*, however no floral dips thus far have created seedlings able to germinate on the appropriate selection media.

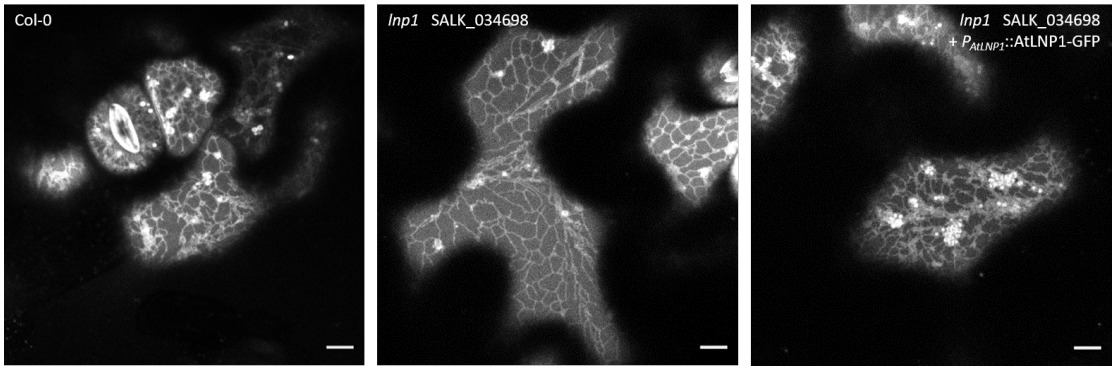


Figure 4.14: The modified structure of *lnp1* can be reversed by expression of AtLNP1 under it's native promoter
The ER of 7-day old cotyledon epidermal cells of Col-0, *lnp1* and *lnp1* stably expressing florescencently tagged AtLNP1 under its native promoter. The ER and mitochondria are visualized using Rhodamine B. Scale bars 5 µm.

Though GFP fluorescence could not be detected using conventional confocal microscopy, further testing using a more sensitive variable angle microscopy (VAEM) techniques revealed P_{AtLNP1}::AtLNP1-GFP fluorescence in all tissues analysed (fig. 4.15, supplementary movie 4.3). In each case there was a small amount of fluorescence throughout the entirety of the ER, however protein aggregates appeared common and were more often associated with putative cisternae. This observation held true for cells in cotyledon, hypocotyl and root tissue (fig. 4.15).

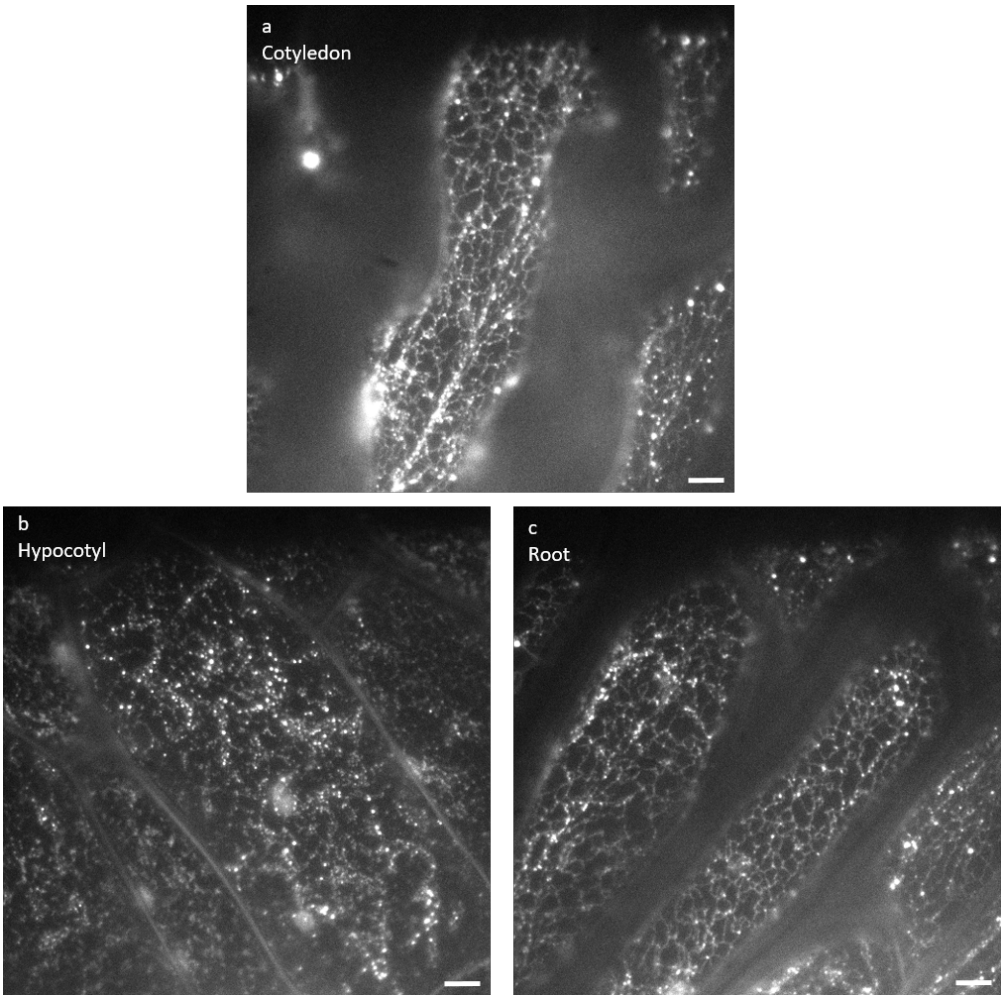


Figure 4.15: VAEM reveals native localizations of AtLNP1
8 day old tissues of *lnp1* stably expressing flourescently tagged AtLNP1 expressed under its own promoter. Localizations are shown for (a) cotyledon cells, (b) hypocotyl cells and (c) root cells. Scale bars 5 µm.

4.2.7 Candidate domains for Lunapark function

Several Lunapark protein domains have been identified as being responsible for Lunaparks function in modifying ER structure. These include an N-terminal myristoylation site in mammalian Lunapark (Moriya *et al.*, 2013) and a C-terminal zinc finger motif that is required for Lunapark function in yeast (Casey *et al.*, 2015; Wang *et al.*, 2016b). As such a series of N- and C-terminal truncations of both AtLNP1 and LNP2 were generated and their localisation and effect on ER

structure observed.

4.2.7.1 N-terminal truncations

Five truncations of both AtLNP1 and AtLNP2 were generated in order test the role of the Lunapark N-terminal protein domains (table 4.2). Each trunction involves a complete removal of the N-terminal of the protein up to a specific protein domain. Under standard transient over-expression conditions, AtLNP1 localises specifically to cisternae and small punctae throughout the ER network, whilst AtLNP2 localises throughout the ER network. Removal of the first 20 amino acids results in a reversal of the localization of AtLNP1 and AtLNP2, with the AtL1T1 truncation localizing throughout the ER and AtL2T1 becoming cisternae specific (fig.4.16 and 4.17). For both AtLNP1 and AtLNP2, removal of the N-terminal up to the first TMD, and beyond that to the connection between TMDs 1 and 2, results in re-localisation of punctae that are associated with the ER but not contiguous with the structure (fig.4.16 and 4.17). Variable levels of residual signal can be detected within the ER. Co-localisation of the punctae produced by AtLNP2 truncations 3 and 4 (AtL2T3, AtL2T4) revealed that these punctae do not co-localise with autophagosomes (marked using ATG8, supplementary figure S3) nor Golgi bodies (marked with ST-CFP or ST-RFP, supplementary figure S4). The final truncation of both AtLNP1 and AtLNP2 (AtL1T5 and AtL2T5 respectively), lacking both transmembrane domains entirely, localises to ring structures that form around Golgi bodies and have a large cytoplasmic component to their localisation (supplementary movie 4.4). From this it seems likely that AtL1T5-Clover, AtL2T4-Clover and AtL2T5-Clover localise to ER exit sites (fig.4.16 and 4.17).

Table 4.2: N-terminal AtLNP1 and 2 truncations and their localisations
Comparison of the localisation of full length AtLNP1 and AtLNP2 and various N-terminal truncations. The amino acids remaining after truncation are included, as is a list of the potential functional N-terminal protein domains remaining after truncation. Each of these truncations was expressed transiently in tobacco leaf epidermal cells with a C-terminal fluorescent tag (clover) for localisation.

Name	**Remaining amino acids**	**Remaining putative N-terminal functional domains**	**Localisation**
AtLNP1	1-408	Start domain (1-20aa), pre-TM domain, TM1, TM linker, TM2	Cisternae specific
AtL1T1	21-408	Pre-TM domain, TM1, TM linker, TM2	Throughout the ER
AtL1T2	83-408	TM1, TM linker, TM2	Throughout the ER
AtL1T3	106-408	TM linker, TM2	ER associated punctae
AtL1T4	120-408	TM2	Throughout the ER and ER associated punctae
AtL1T5	142-408	-	ER exit sites
AtLNP2	1-409	Start domain (1-20aa), pre-TM domain, TM1, TM linker, TM2	Throughout the ER
AtL2T1	21-409	Pre-TM domain, TM1, TM linker, TM2	Cisternae specific
AtL2T2	85-409	TM1, TM linker, TM2	Throughout ER and puncate associated with the ER
AtL2T3	108-409	TM linker, TM2	Throughout ER and puncate associated with the ER
AtL2T4	122-409	TM2	ER exit sites
AtL2T5	143-409	-	ER exit sites

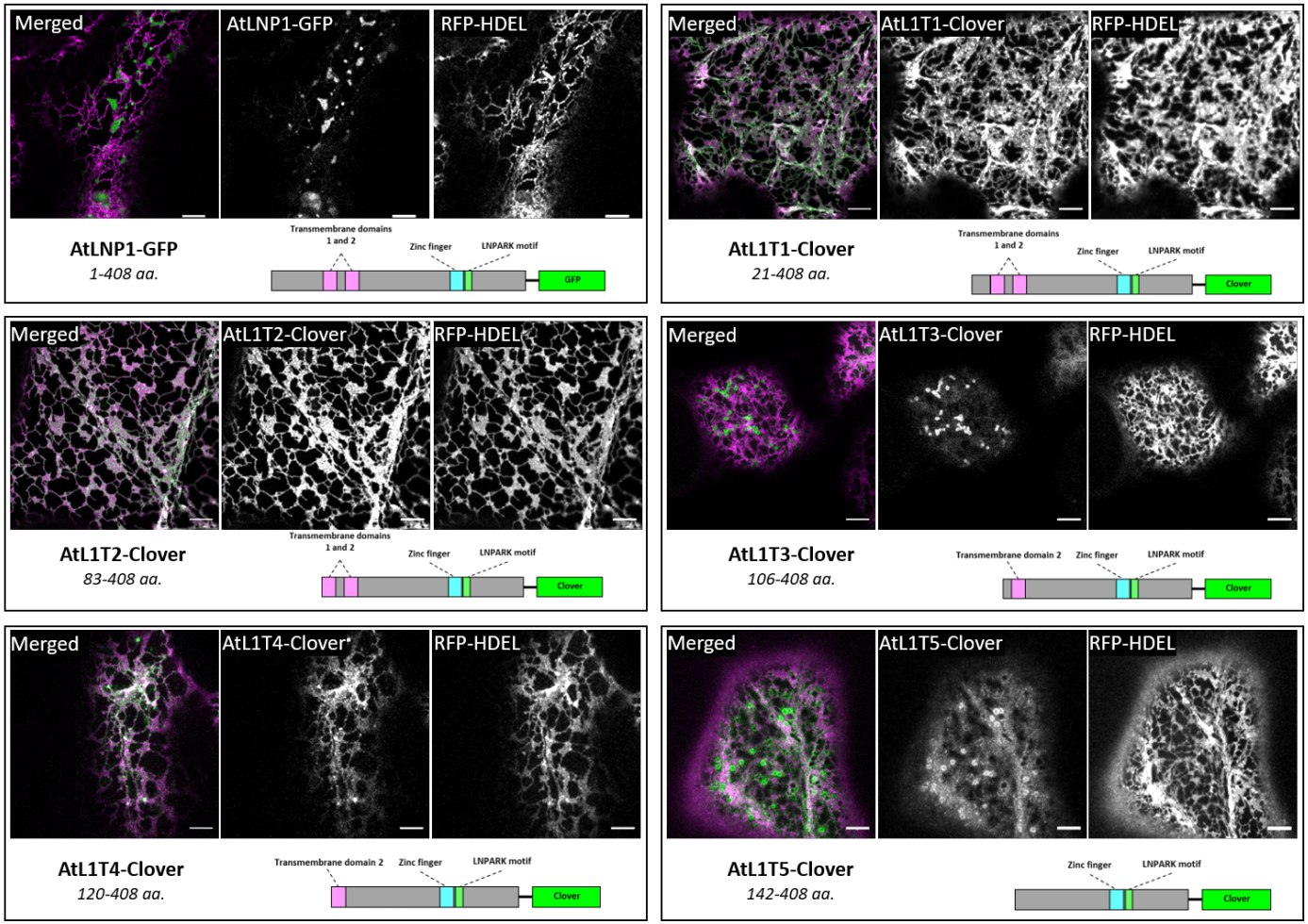


Figure 4.16: N-terminal AtLNP1 truncations localisation
Comparison of the localisation of AtLNP1-GFP and five N-terminal truncations to the ER lumenal marker RFP-HDEL on transient expression in tobacco leaf epidermal cells. In each case a schematic representation of the truncation is displayed below confocal images comparing localisation. Scale bars 5 µm.

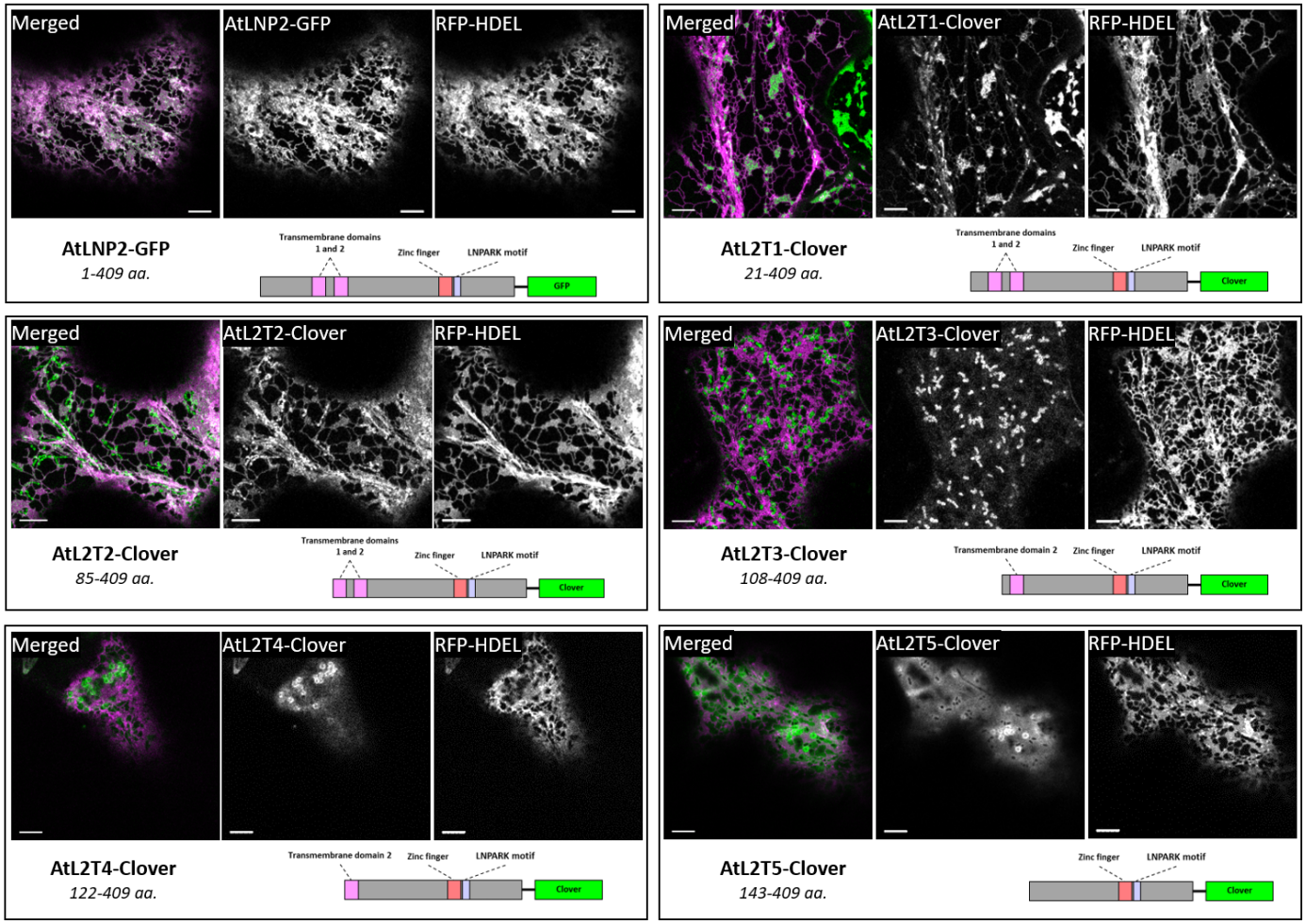


Figure 4.17: N-terminal AtLNP2 truncations localisation
Comparison of the localisation of AtLNP2-GFP and five N-terminal truncations to the ER lumenal marker RFP-HDEL on transient expression in tobacco leaf epidermal cells. In each case a schematic representation of the truncation is displayed below confocal images comparing localisation. Scale bars 5 µm.

4.2.7.2 C-terminal truncations

The C-terminal domain of both AtLNP1 and LNP2 was removed up to the start of the zinc finger motif, resulting in a truncation with the last 92 amino acids of both AtLNP1 and AtLNP2 removed. AtLNP1-ZF shows a typical AtLNP1 localisation to ER cisternae, whilst AtLNP2-ZF shows a modified localisation that is now cisternae specific (fig. 4.18, supplementary movie 4.5). Transient over-expression of both AtLNP1-ZF and AtLNP2-ZF in tobacco is sufficient to induce cisternae, indicating that the zinc finger motifs of AtLNP1 and AtLNP2 are not required for the function of Lunapark in cisternae formation.

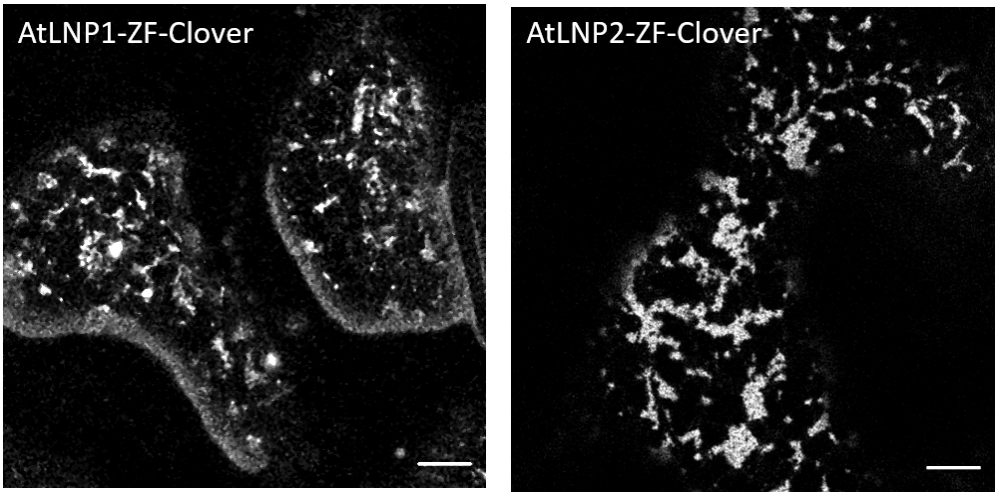


Figure 4.18: Localisation of C-terminal zinc finger truncations
Localisation of C-terminal zinc finger truncations of both AtLNP1 and AtLNP2 after transient expression in tobacco leaf epidermal cells. Scale bars 5 µm.

4.2.8 AtLNP1 over-expression can induce densely tubulated regions of ER not seen on AtLNP2 over-expression

The levels of protein over-expression can be modified using the agrobacteria-mediated transient over-expression system by increasing the concentration of agrobacteria infiltrated into the plant leaf epidermal cells. The concentration of agrobacteria within the infiltration media is estimated by measuring the final optical density of the infiltration media containing the agrobacteria. Higher optical density measurements indicate a greater concentration of agrobacteria within the infiltration media. Increasing the expression levels of AtLNP1 and 2 results in the mean cisternal area of the ER increasing in a dose dependent manner (Kriechbaumer *et al.* (2018), fig. 4.19). Transient over-expression of AtLNP1 has the additional effect of inducing the formation of aggregated regions of short tubules that are closely associated with the induced cisternae (fig. 4.19 and 4.20). The formation of dense regions of tubules in close proximity of ER cisternae does not occur on transient over-expression of AtLNP2 (fig. 4.19), suggesting different functional roles for AtLNP1 and 2 in the control of the structure of the ER.

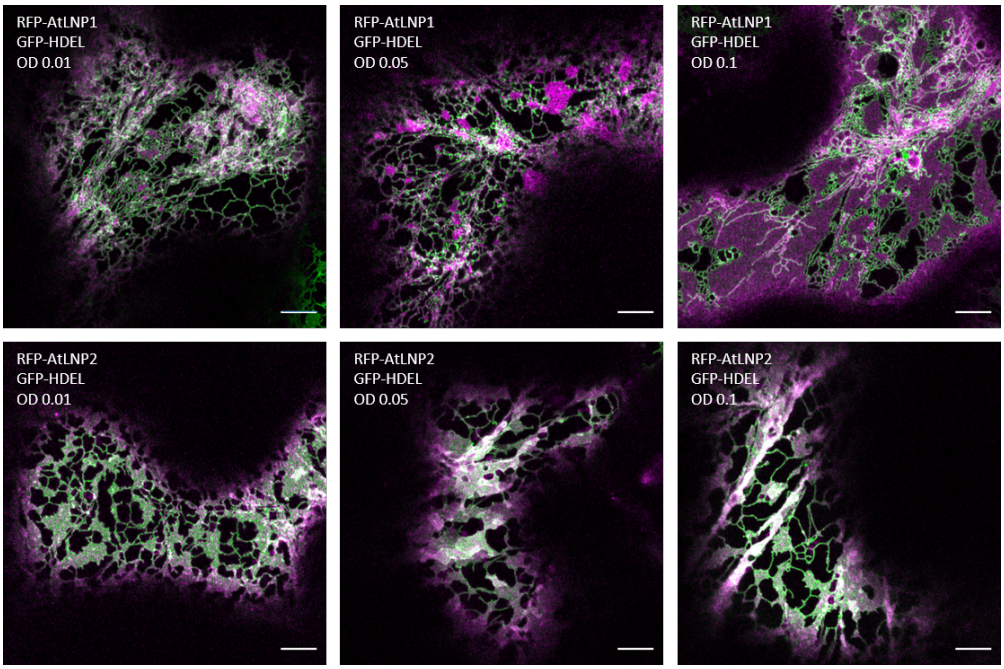


Figure 4.19: AtLNP1, but not AtLNP2 over-expression results in the formation of many short tubules, independent of expression levels
Comparison of RFP-AtLNP1 and RFP-AtLNP2 (magenta) transient over-expression in leaf epidermal cells alongside GFP-HDEL (green). Three optical densities of agrobacterium were infiltrated of both RFP-AtLNP1 and RFP-AtLNP2 (OD 0.01, 0.05 and 0.1). Scale bars 5 µm.

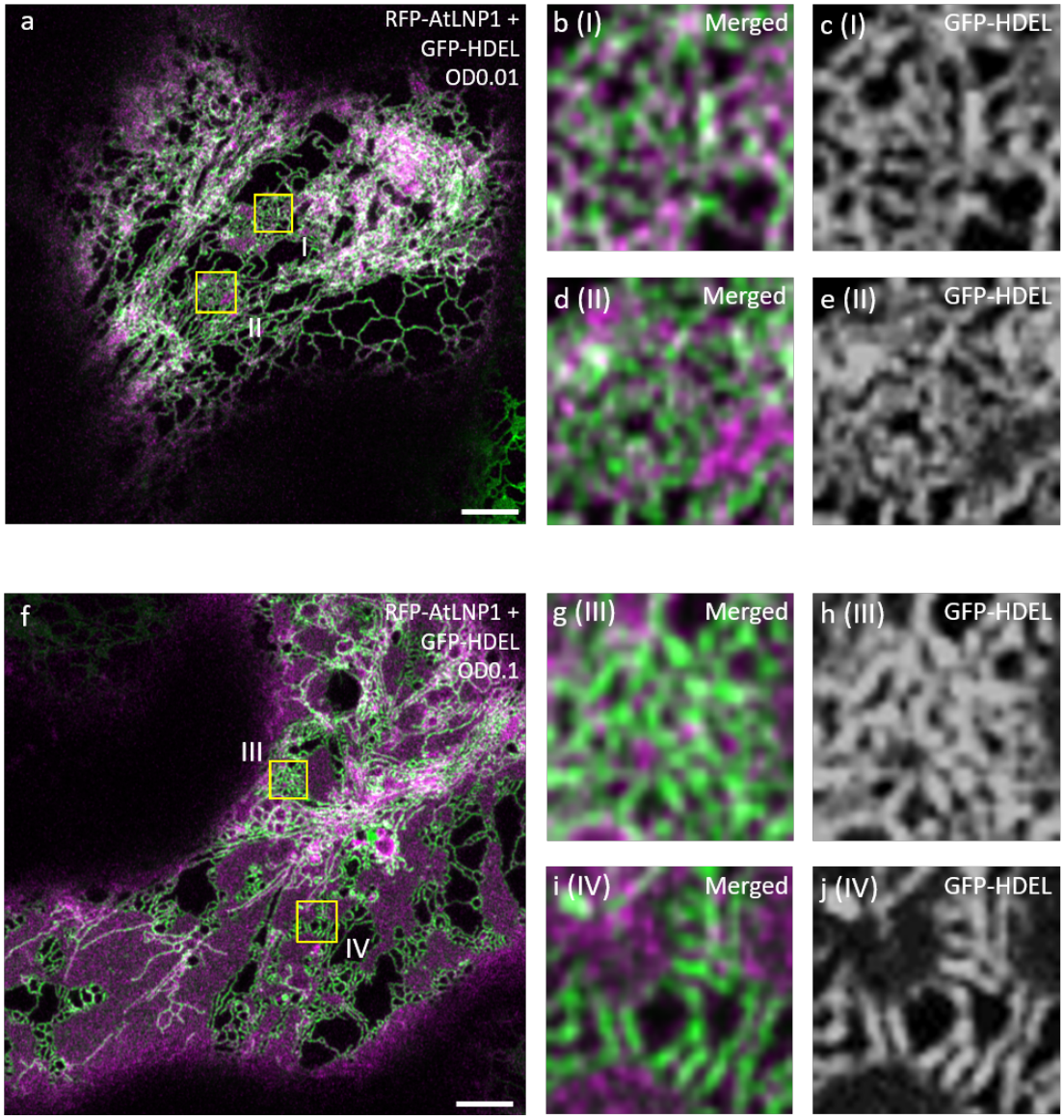


Figure 4.20: Densely reticulated regions of ER are produced on over-expression of AtLNP1

Two single tobacco leaf epidermal cells transiently expressing GFP-HDEL (green) and RFP-AtLNP1 (magenta) at OD 0.01 (a) and OD 0.1 (f). Each cell has two regions of dense tubules outlined in yellow (labelled I and II on image a and III and IV on image f). These regions have been enlarged and are shown as a merged image (b,d,g,i) and the single channel capturing the distribution of the ER lumenal marker GFP-HDEL (c,e,h,j). Scale bars 5 µm.

4.2.9 AtLNP1 and 2 induce cisternae with different lumenal characteristics

Transient over-expression of AtLNP1 and 2 induces cisternae that show different distributions of lumenal markers within the cisternae.

4.2.9.1 AtLNP1 aggregates perturb the ER lumen and can be identified by confocal imaging with Airyscan detector

Use of high resolution Airyscan imaging revealed that AtLNP1-GFP aggregates can be identified on transient over-expression of P_{UBQ10}::AtLNP1-GFP in tobacco leaf epidermal cells (fig. 4.21a,b). Transient over-expression results in AtLNP1-GFP forming aggregates within the centre of the cisternae. These aggregates are variable in size and are seen when AtLNP1-GFP is expressed alongside both a lumenal ER marker (RFP-HDEL) and an ER membrane marker (CXN-mCherry). The transient over-expression of AtLNP1-GFP also results in a modified distribution of the lumenal marker RFP-HDEL but does not apparently affect the distribution of the membrane marker CXN-mCherry, though CXN-mCherry shows a relatively patchy distribution throughout cisternae (fig. 4.21c,d). The presence of AtLNP1-GFP appears to exclude/reduce RFP-HDEL fluorescence in the center of the cisternae, though localised regions within the cisternae and at the cisternae edges remain detectable (fig. 4.22). This is also the case when RFP is used to tag the N-terminus of AtLNP1 as opposed to GFP being used to tag the C-terminus, as shown previously (fig. 3.21, chapter 3). Further analysis of the distribution of lumenal fluorescence and AtLNP1-GFP fluorescence reveals that within the center of cisternae, where AtLNP1-GFP may not be present, there is an increase in RFP-HDEL fluorescence (fig. 4.22.

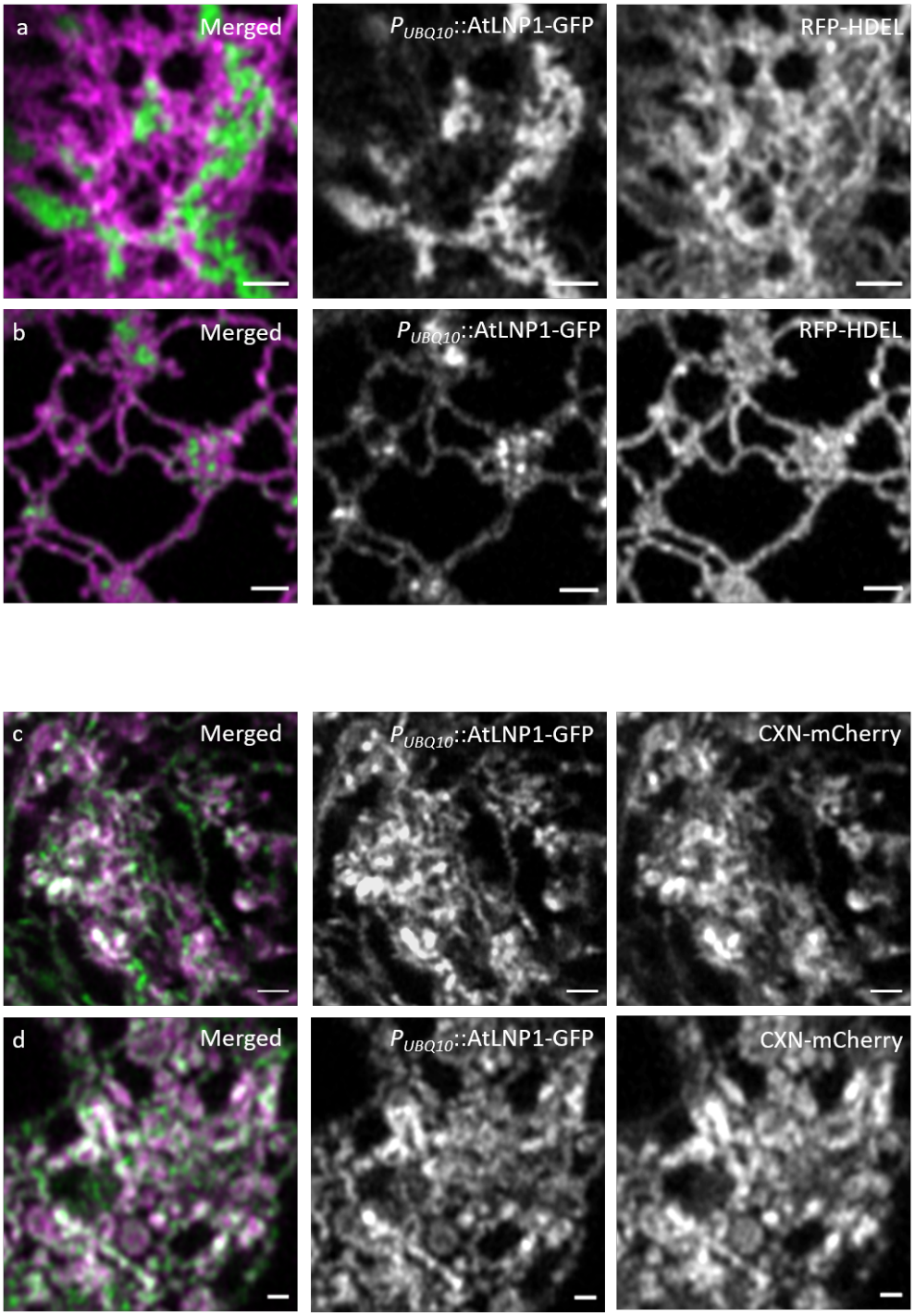


Figure 4.21: AtLNP1 over-expression affects the distribution of the ER lumenal marker RFP-HDEL but not the ER membrane marker CXN-mCherry

Transient over-expression of AtLNP1 (P_{UBQ10}::AtLNP1-GFP, green) in tobacco leaf epidermal cells alongside the ER lumenal marker RFP-HDEL (magenta, a, b) and the ER membrane marker CXN-mCherry (magenta, c, d). Scale bars 1 µm.

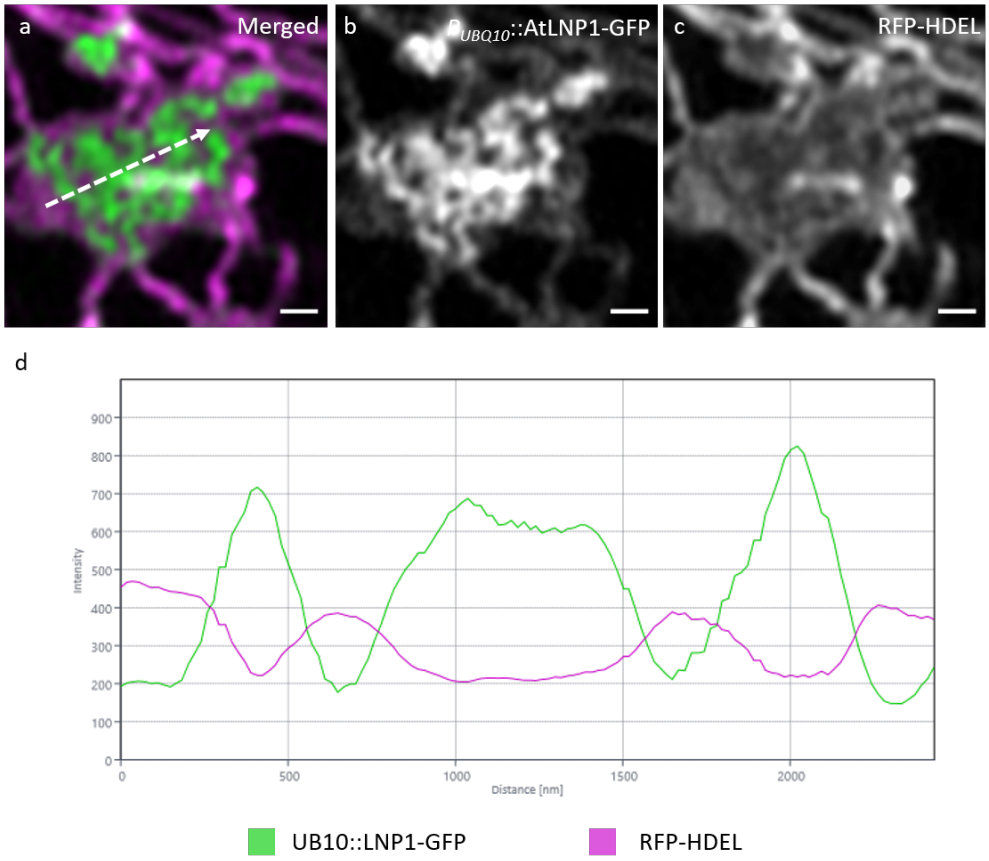


Figure 4.22: Negative correlation between AtLNP1 localisation and RFP-HDEL intensity
A single cisterna showing (a) P_{UBQ10}::AtLNP1-GFP (green) over-expression in tobacco leaf epidermal cells alongside RFP-HDEL (magenta), also shown alone (b, c). White dashed arrow represents the region selected for a line profile analysis, the results of which are shown in (d).

4.2.9.2 AtLNP2 over-expression induces cisternae with an entirely contiguous lumen

Cisternae are canonically expected to be composed of two flattened sheets of membrane that are closely appressed. However recent work in mammalian systems has suggested that cisternae may in fact be composed of many densely packed tubules (Nixon-Abell *et al.*, 2016) or may at least be punctuated by a series of nanoholes (Shemesh *et al.*, 2014) (Chapter 1, figure 1.1). Direct evidence for

these substructures can only obtained by super-resolution microscopy, however confocal microscopy with Airyscan detection may provide sufficient indirect evidence to inform as to the substructure of cisternae induced by AtLNP1 and AtLNP2 over-expression. Unlike transient over-expression of AtLNP1, transient over-expression of AtLNP2 does not result in exclusion of the ER lumenal marker GFP-HDEL from the lumen of the induced cisternae (4.23c). The distribution of this marker through induced cisternae could provide an indication as to the actual substructure of cisternae as the presence of either densely packed tubules or nanoholes within cisternae will result in an uneven distribution of GFP-HDEL through the cisternal lumen. This uneven distribution can be predicted to be characterised by small gaps forming within cisternae, caused by either the gaps in the tubular matrix making up the cisternae or due to the prescence of nanoholes. Texture analysis developed as part of AnalyzER, is designed to detected variations in the texture (i.e. the distribution of intensity through the image) throughout cisternae. Texture analysis of cisternae marked by GFP-HDEL alone reveals that the texture of these cisternae is not consistent with an entirely uniform distribution of fluorophores though the cisternae lumen. Instead the relatively high GLCM contrast and correlation and low energy and homogeneity would indicate variation in the distribution of GFP-HDEL throughout the cisternal lumen (4.23a). Closer examination of the images collected reveals the presence of what appear to be small gaps within the structure of the lumen (4.23b,1,2). The GLCM texture produced of GFP-HDEL, when co-expressed with RFP-AtLNP2, reveals a significant shift in the texture metrics towards a more uniform distribution of GFP-HDEL (4.23a). Specifically the results revealed significantly reduced contrast and increased energy and homogeneity of (ANOVA: cisternae contrast: $p>0.05$; cisternae correlation: $p = 1.27 \times 10^{-2}$; cisternae energy: $p = 9.3 \times 10^{-3}$ and cisternae homogeneity $p= 9.7 \times 10^{-3}$; n=10 GFP-HDEL and n=11 RFP-AtLNP2 + GFP-HDEL). Closer examination of the images collected with GFP-HDEL and RFP-AtLNP2 over-expression reveal less clear structural

abberations and none of the regions of lower intensity approach the same intensity as the background suggesting that they are either much smaller holes than observed in control cells or, more likely, are within the tolerance for noise based variation in GFP-HDEL intensity.

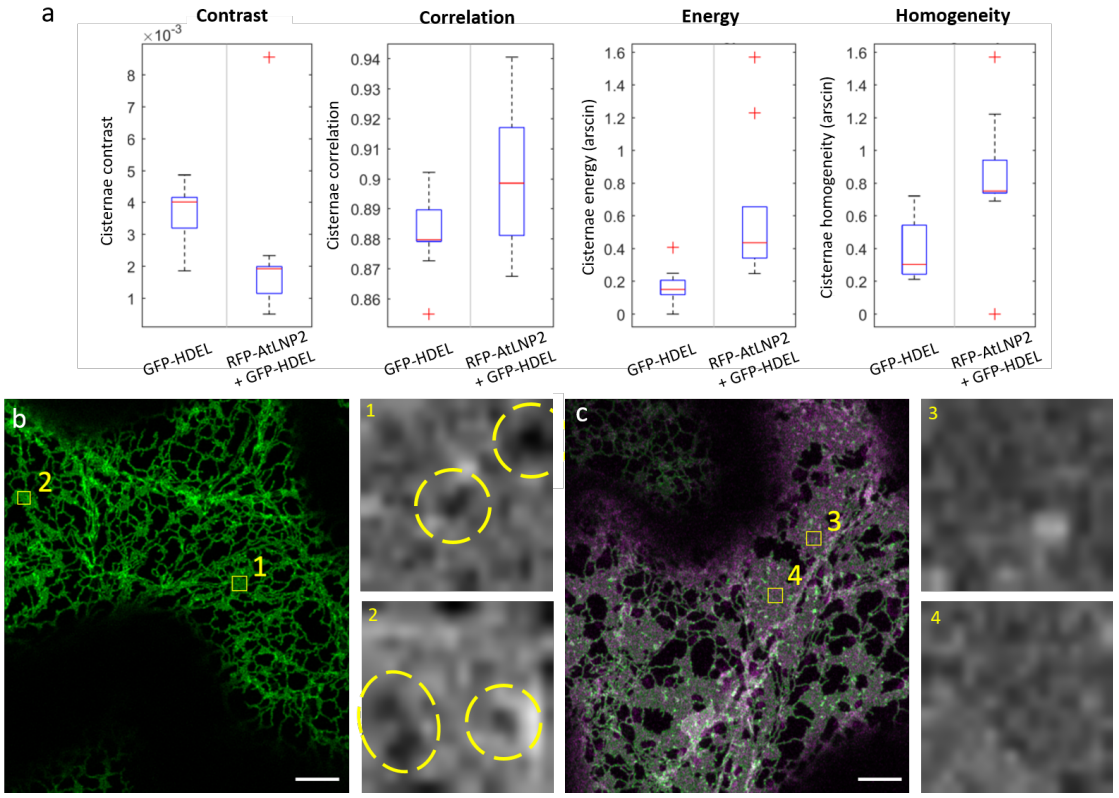


Figure 4.23: The distribution of GFP-HDEL within AtLNP2 induced cisternae
(a) Comparison of key texture metrics calculated using GLCM analysis of ER cisternae marked by GFP-HDEL (shown in green) as a control (n=10 biological replicas) and cisternae induced by RFP-AtLNP1 (shown in magenta, n=11 biological replicas). (b) representative control cisternae marked by GFP-HDEL and identified for analysis. Regions of interest are highlighted by yellow boxes and enlarged (1,2) with potential holes in the cisternae highlighted by yellow dashed circles. c) representative cisternae induced by RFP-AtLNP2 over-expression with regions of interest marked by yellow squares and enlarged (3,4). Results obtained over three technical replicas, scale bars 5 µm.

4.2.10 AtLNP1 over-expression results in structurally aberrant cisternae formation, visible using VAEM

Use of the more sensitive VAEM technique further revealed that stable over-expression of AtLNP1 (under the ubiquitin-10 promoter) induces ER cisternae with a modified structure. Images of stable over-expression of AtLNP1-GFP in arabidopsis (fig. 4.1), and transient over-expression of AtLNP1-GFP in tobacco show AtLNP1-GFP localised to relatively uniform distribution through induced ER cisternae when images are collected using confocal microscopy (fig. 4.2). This would follow the canonical view that cisternae are composed of two layers of relatively large, flat regions of ER membrane. However this view has been recently challenged using work on mammalian cells, which has suggested that cisternae may in fact be composed of either a dense aggregation of tubules (Nixon-Abell *et al.*, 2016) or may be densely fenestrated, with fenestrations identified by the presence of Rtn4 - a membrane curvature inducing protein (Schroeder *et al.*, 2019). Further assessment of the cisternae identified by stable over-expression of P_{UBQ10}::AtLNP1-GFP in arabidopsis using VAEM as opposed to confocal microscopy revealed that as opposed to the conventional view of cisternae as flat sheets of membrane, the cisternae marked by AtLNP1-GFP appear to be formed from densely aggregated tubules (fig. 4.24a). These highly tubulated regions of ER contain high numbers of AtLNP1-GFP aggregates, and these aggregates appear to preferentially localise to junctions within this highly tubulated subdomain (fig. 4.24a). These aggregates also appear to remain relatively stable within these tubulated region showing little movement within this region (supplementary movie 4.6). Expression of AtLNP1-GFP under a native promoter (P_{AtLNP1}::AtLNP1-GFP) however does not show these highly tubulated subdomains clearly (fig. 4.24b), yet P_{AtLNP1}::AtLNP1-GFP aggregates

also preferentially localise to cisternae and there are typically several P_{AtLNP1}::AtLNP1-GFP aggregates present within each cisternae (supplementary movie 4.6). These structurally aberrant cisternae were identified in all examined arabidopsis tissues, specifically cotelydon, hypercotyl and root tissues (fig. 4.25). The effect of stable over-expression of P_{UBQ10}::AtLNP2-GFP was also analysed in 8 day old arabidopsis plants (fig. 4.26). None of the tissues tested revealed cisternae with an aberrant, tubulated structure (fig. 4.27). Though aggreates of AtLNP2-GFP can be identified throughout the ER network, they appear to be much smaller than those induced by P_{UBQ10}::AtLNP1-GFP expression.

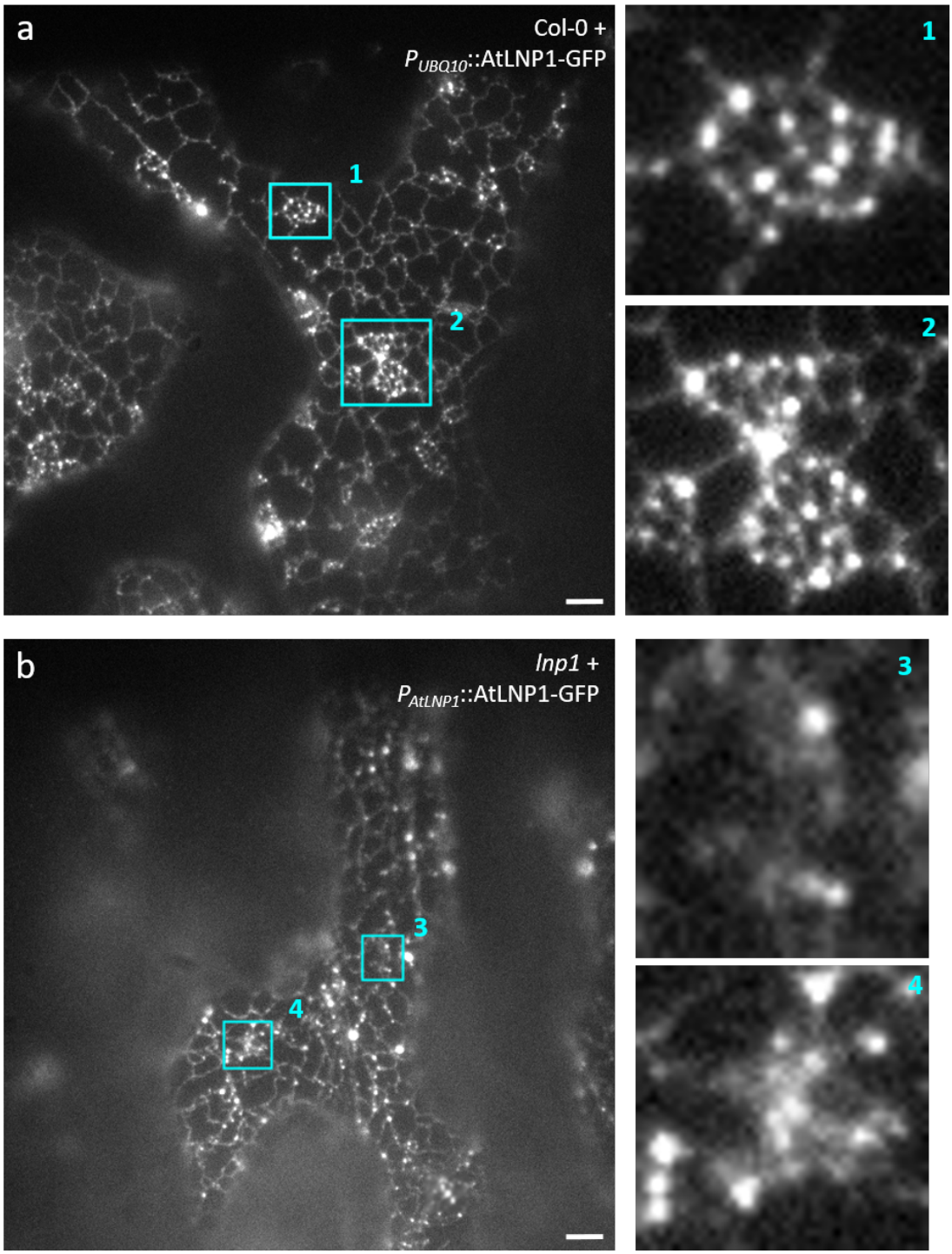


Figure 4.24: Over-expression of AtLNP1 causes an altered cisternae morphology that can be captured using VAEM
(a) Stable over-expression of fluorescently tagged AtLNP1 (P_{UBQ10}::AtLNP1-GFP in Col-0) visualised using VAEM with two enlarged sections showing cisternal structure (1,2) and (b) stable expression of fluorescently tagged AtLNP1 (P_{AtLNP1}::AtLNP1-GFP in *lnp1*) with two enlarged sections showing cisternal structure (3,4). Scale bars 5 µm.

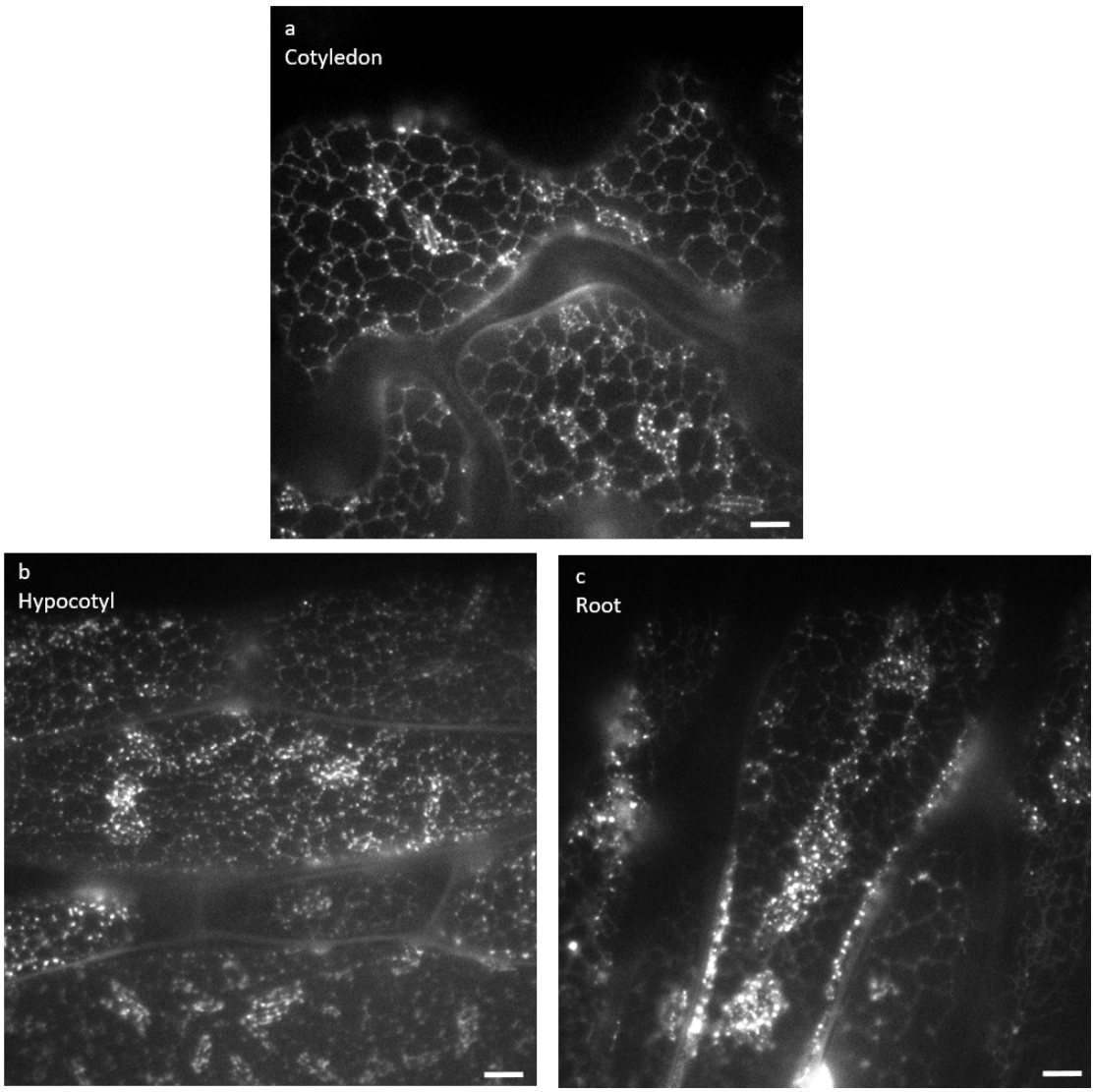


Figure 4.25: Stable over-expression of P_{UB10}::AtLNP1-GFP in arabidopsis captured by VAEM
The localisation of P_{UB10}::AtLNP1-GFP with 8-day old arabidopsis (a) cotelydon, (b) hypercotyl and (c) root tissue. P_{UB10}::AtLNP1-GFP is expressed stably in the plants, achieved by the floral dip method. Scale bars 5 µm.

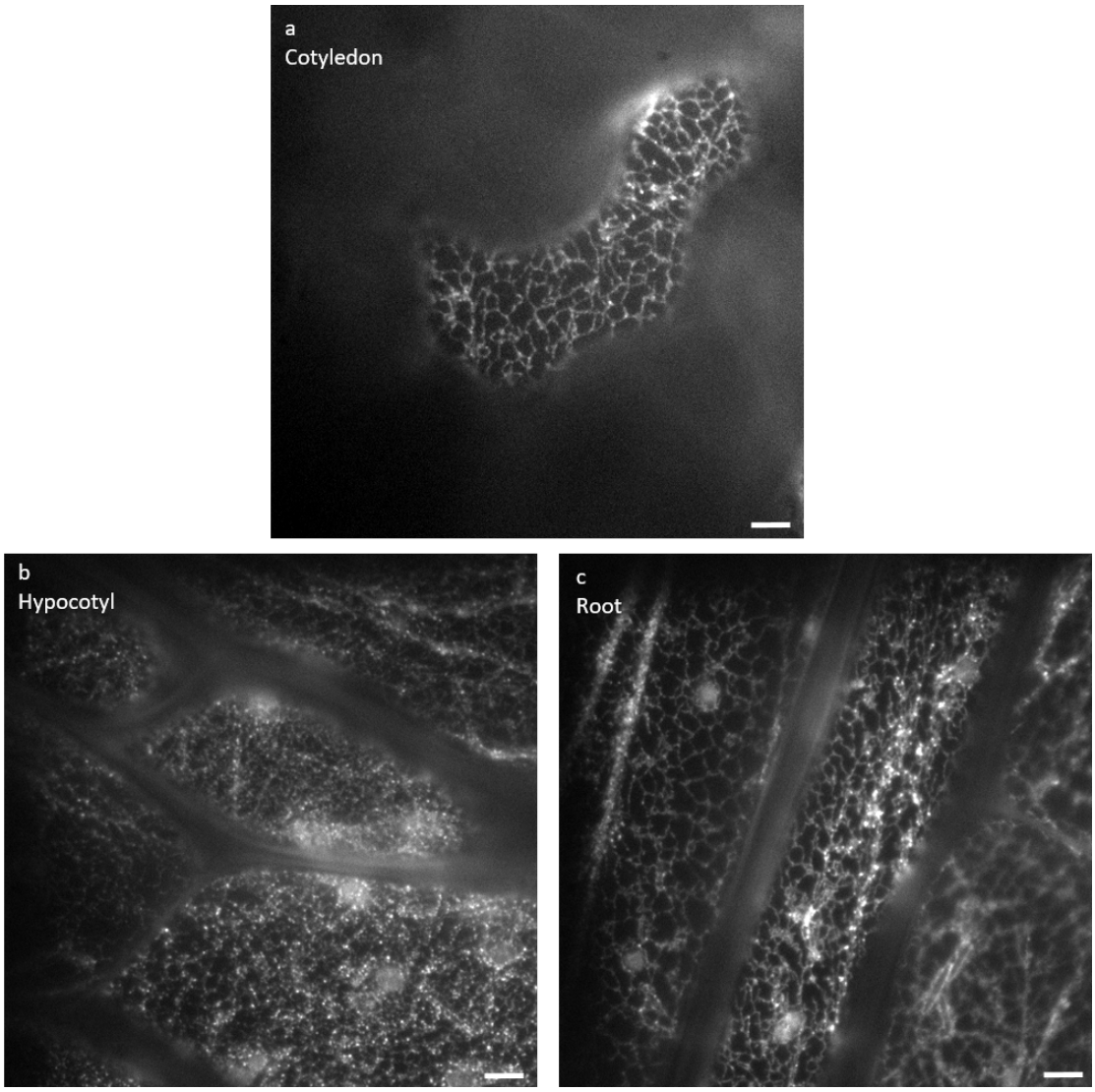


Figure 4.26: Stable over-expression of P_{UB10}::AtLNP2-GFP in arabidopsis captured by VAEM
The localisation of P_{UB10}::AtLNP2-GFP with 8-day old arabidopsis (a) cotelydon, (b) hypercotyl and (c) root tissue. P_{UB10}::AtLNP2-GFP is expressed stably in the plants, achieved by the floral dip method. Scale bars 5 µm.

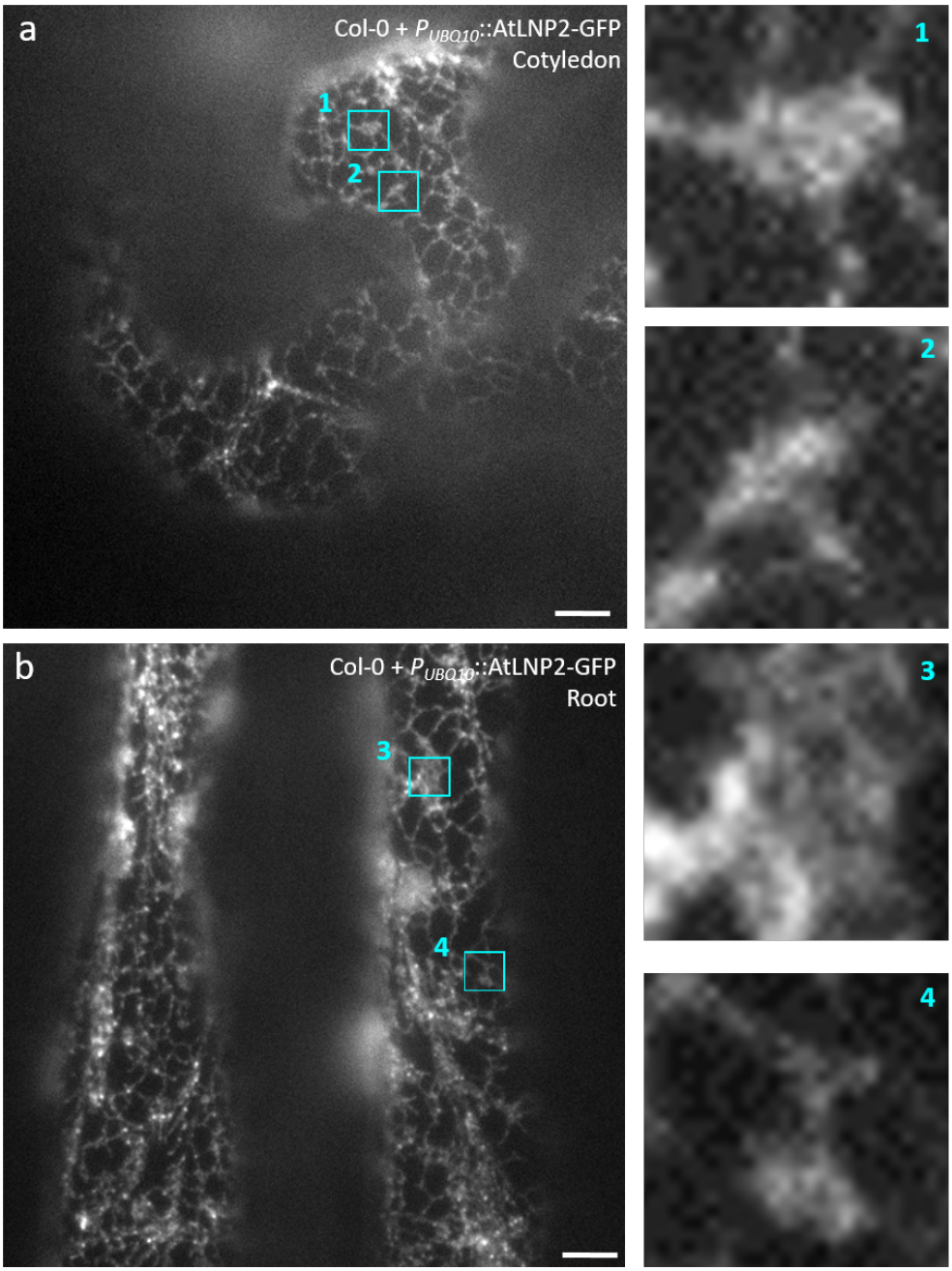


Figure 4.27: Stable over-expression of P_{UB10}::AtLNP2-GFP induces cisternae that do not have an altered morphology
(a) Stable over-expression of fluorescently tagged AtLNP2 (P_{UBQ10}::AtLNP2-GFP in Col-0) visualised using VAEM with two enlarged sections showing cisternal structure in cotelydonary tissue (1,2) and (b) root tissue (3,4). Scale bars 5 µm.

4.2.11 Reticulon proteins reveal regions of membrane curvature within ER cisternae

Arabidopsis reticulon proteins 1, 2, 3 and 4 (AtRTN1-4) have all been identified as localizing preferentially to highly curved surfaces within the plant ER and on over-expression are capable of inducing membrane curvature to such an extent that the internal lumen of the ER tubules is highly constricted (Sparkes *et al.*, 2010). This ability is conferred by the presence of a reticulon homology domain (RHD) and over-expression of AtRTN1-4 almost abolishes the presence of cisternae, except on co-expression with constructs that are capable of inducing cisternae, such as AtLNP1 and AtLNP2 and the TMD of calnexin (Sparkes *et al.*, 2010; Runions *et al.*, 2006). AtRTN1 and AtRTN3 were chosen to investigate the potential presence of curved membranes within ER cisternae as AtRTN1 is a known, strong membrane curvature inducing protein and AtRTN3 is the closest characterised arabidopsis ortholog to mammalian Rtn4 (supplementary fig. S5), which has been shown to localise to nanoholes within ER cisternae in mammalian cells (Schroeder *et al.*, 2019).

Co-expression of RFP-AtRTN1/RFP-AtRTN3 and GFP-CXN reveals the presence of tubules identified by AtRTN1 and AtRTN3 threading through the cisternae induced by GFP-CXN, or in some cases small AtRTN1 and AtRTN3 aggregates within the cisternae (fig. 4.28). Though marked tubular structures appear randomly distributed throughout the cisternae, AtRTN aggregates are typically localised towards the edges of cisternae or near small holes within the cisternae. The presence of tubules threading through ER cisternae is not always belied by modification to GFP-CXN distribution. That is, the distribution of ER membrane proteins does not always reveal the presence of curved membranes or tubules within ER cisternae (fig. 4.28b). It is possible for cisternae to appear to have a contiguous

structure when examined using ER membrane markers, but may actually possess complex internal sub-structures.

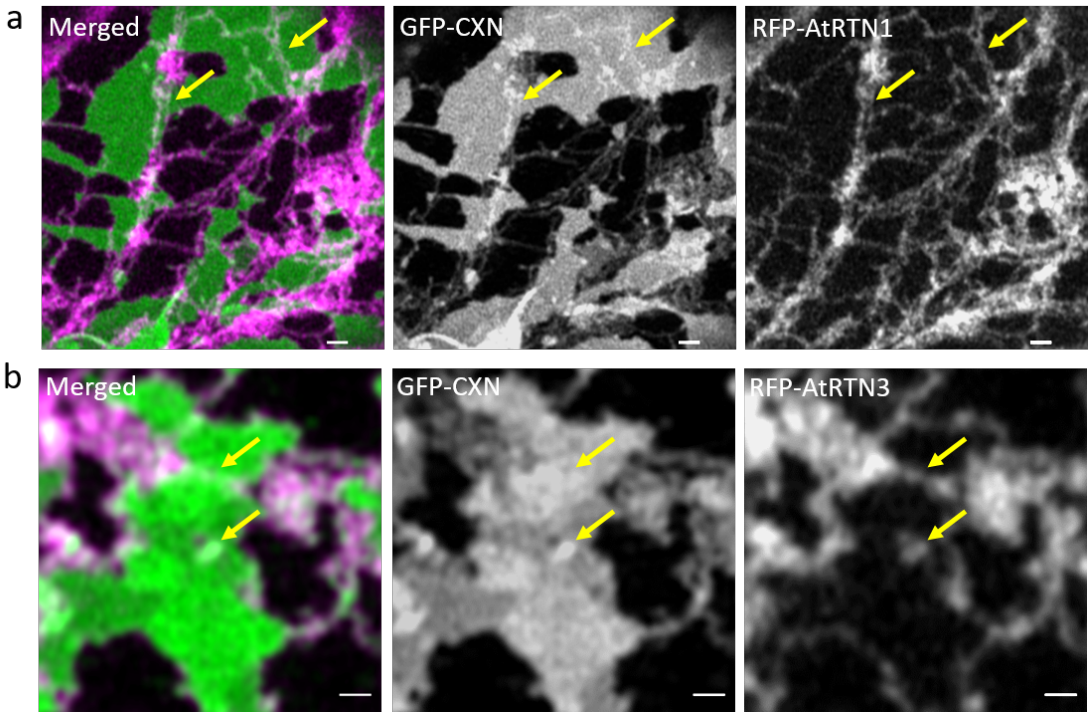


Figure 4.28: RFP-AtRTN1 and RFP-AtRTN3 localisation within GFP-CXN induced cisternae
Transient over-expression of GFP-CXN (green) and RFP-AtRTN1 (magenta, a) and RFP-AtRTN3 (magenta, b) in tobacco leaf epidermal cells. Yellow arrows are used to indicate reticulon aggregates/tubules within cisternae. Scale bar 1 µm.

4.2.12 AtLNP1 does not co-localise with AtRTN1 or 3

AtLNP1-GFP does not appear to commonly co-localise with either RFP-AtRTN1 or RFP-AtRTN3 on transient over-expression. There are some small regions of overlap between the localisation of AtLNP1 and AtRTN1 (4.29a, cyan arrows) however predominately it appears as though AtLNP1 and AtRTN1 do not co-localise within ER cisternae (4.29a, yellow arrows). A similar distribution of RFP-AtRTN3 within AtLNP1-GFP induced cisternae can also be observed (4.29b).

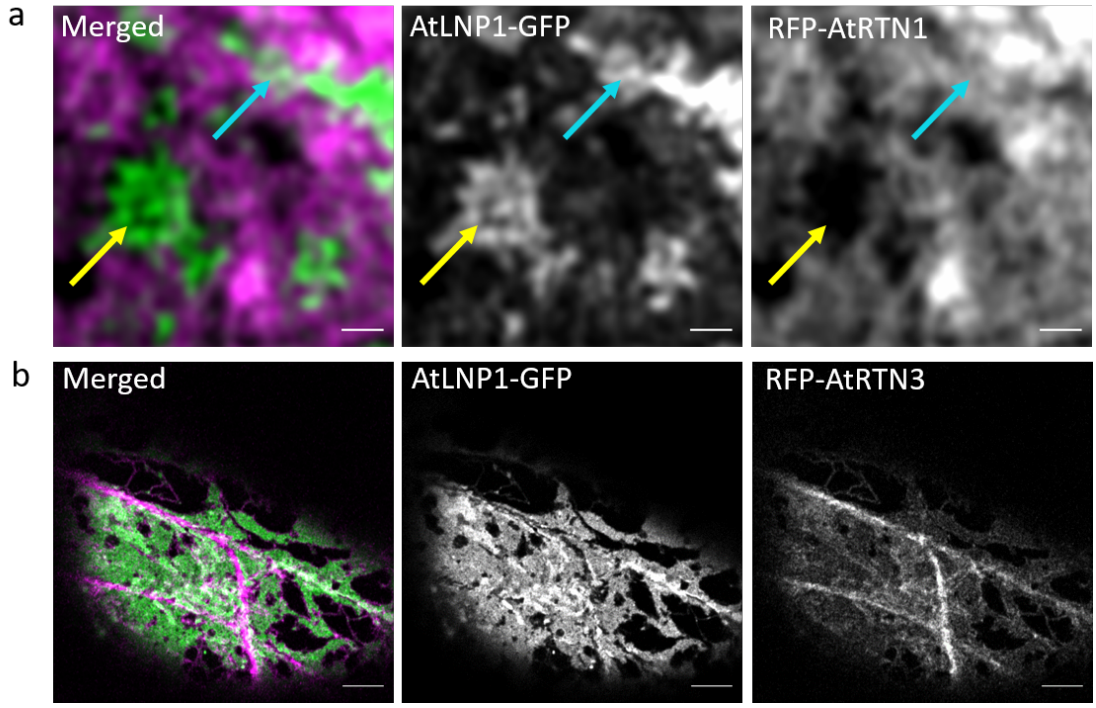


Figure 4.29: RFP-AtRTN1 and RFP-AtRTN3 localisation within AtLNP1-GFP induced cisternae
Transient over-expression of AtLNP1-GFP (green) and RFP-AtRTN1 (magenta, a) and RFP-AtRTN3 (magenta, b) in tobacco leaf epidermal cells. Yellow arrows are used to indicate regions where AtLNP1-GFP and RFP-AtRTN1 do not co-localise within cisternae, whilst cyan arrows indicate areas with some co-localisation. Scale bars 1 µm and 5 µm respectively.

4.2.13 AtLNP2 co-localises with AtRTN1 and 3

Both AtLNP2-GFP and RFP-AtRTN1/RFP-AtRTN3 localise throughout the ER network. Cisternae induced by LNP2-GFP reveal co-localisation of AtLNP2-GFP and RFP-AtRTN1/RFP-AtRTN3 (fig. 4.30).

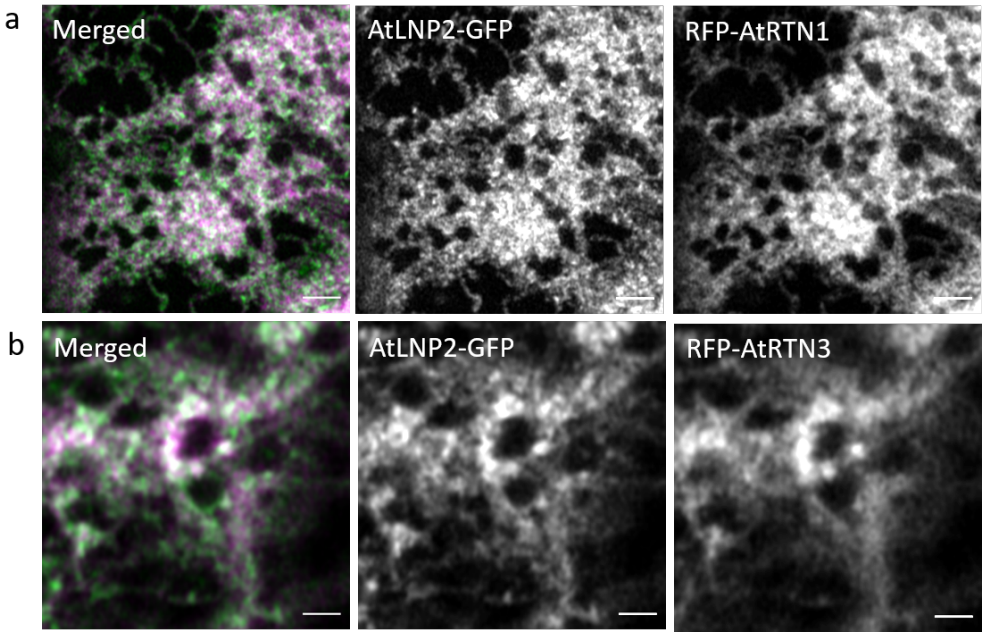


Figure 4.30: RFP-AtRTN1 and RFP-AtRTN3 localisation within AtLNP2-GFP induced cisternae
Transient over-expression of AtLNP2-GFP (green) and RFP-AtRTN1 (magenta, a) and RFP-AtRTN3 (magenta, b) in tobacco leaf epidermal cells. Scale bar 1 µm.

These results are repeated when swapping fluorophores (RFP to GFP and vice versa) and varying which terminal of AtLNP1 and AtLNP2 is tagged (supplementary fig. S6). Co-expression of reticulon proteins and Lunapark proteins is particularly challenging due to high levels of necrosis on dual expression (supplementary fig. S7) and due to different expression levels of each protein within each cell (supplementary fig. S8). As such, cells selected for analysis show a relatively equal level of Lunapark and reticulon expression, to the extent that the distribution of both constructs can be analysed in each cell.

4.2.14 AtLNP1 and AtLNP2 truncations with altered ER localisation show modified co-localisation with AtRTN1 and AtRTN3

AtLNP1 localises specifically to cisternae when over-expressed, whilst AtLNP2 localises throughout the ER. Several AtLNP1 and AtLNP2 truncations modify this localisation, resulting in AtLNP1 truncations that localise throughout the ER and AtLNP2 truncations that localise solely to cisternae. N-terminal truncations AtL1T1-clover and AtL1T2-clover are both localised throughout the ER, whilst N-terminal AtL2-T1-clover and AtLNP2-ZF-clover localises specifically to cisternae (table 4.3 and prior fig. 4.16, 4.17 and 4.18). Of these truncations, AtL1T1-clover and AtLNP2-ZF-clover were selected to test whether re-localisation of AtLNP1 and AtLNP2 by truncation, affects the spatial co-ordination of RFP-AtRTN3 within induced cisternae.

These results revealed that though AtLNP1-GFP does not co-localise with RFP-AtRTN3 (fig. 4.31a-f), L1T1-Clover does co-localise with RFP-AtRTN3 (fig. 4.31g-l). This co-localisation is reminiscent of the co-localisation between AtLNP2-GFP and RFP-AtRTN3 seen previously (fig. 4.30). Similarly whilst AtLNP2-GFP does co-localise with RFP-AtRTN3 (fig. 4.27a-f), AtLNP2-ZF-clover, which is cisternae specific, does not co-localise with RFP-AtRTN3 (fig. 4.32g-l). This co-localisation is reminiscent of the co-localisation between AtLNP1-GFP and RFP-AtRTN3 seen previously (fig. 4.29). Therefore in each case where the localisation is altered to match the localisation of the alternative Lunapark protein, the spatial relationship between the truncation and RFP-AtRTN3 is also altered to reflect the same relationship identified with the opposite full length Lunapark protein.

Table 4.3: AtLNP1 and AtLNP2 truncations that show a modified localisation within the ER
A list of all identified AtLNP1 and AtLNP2 truncations produced in this work that show a modified localisation with the ER and a description of the truncation that was created.

Protein	**Original localisation**	**Localisation after modification**	**Truncations showing modified ER localisation**	**Descirption**
AtLNP1	Cisternae specific	Throughout the ER	AtL1T1, AtL1T2	N-terminal truncations up to the first TMD
AtLNP2	Throughout the ER	Cisternae specific	AtL2T1 and AtLNP2-ZF	N-terminal truncation of the first 20 amino acids and C-terminal truncation up to the start of the zinc finger domain

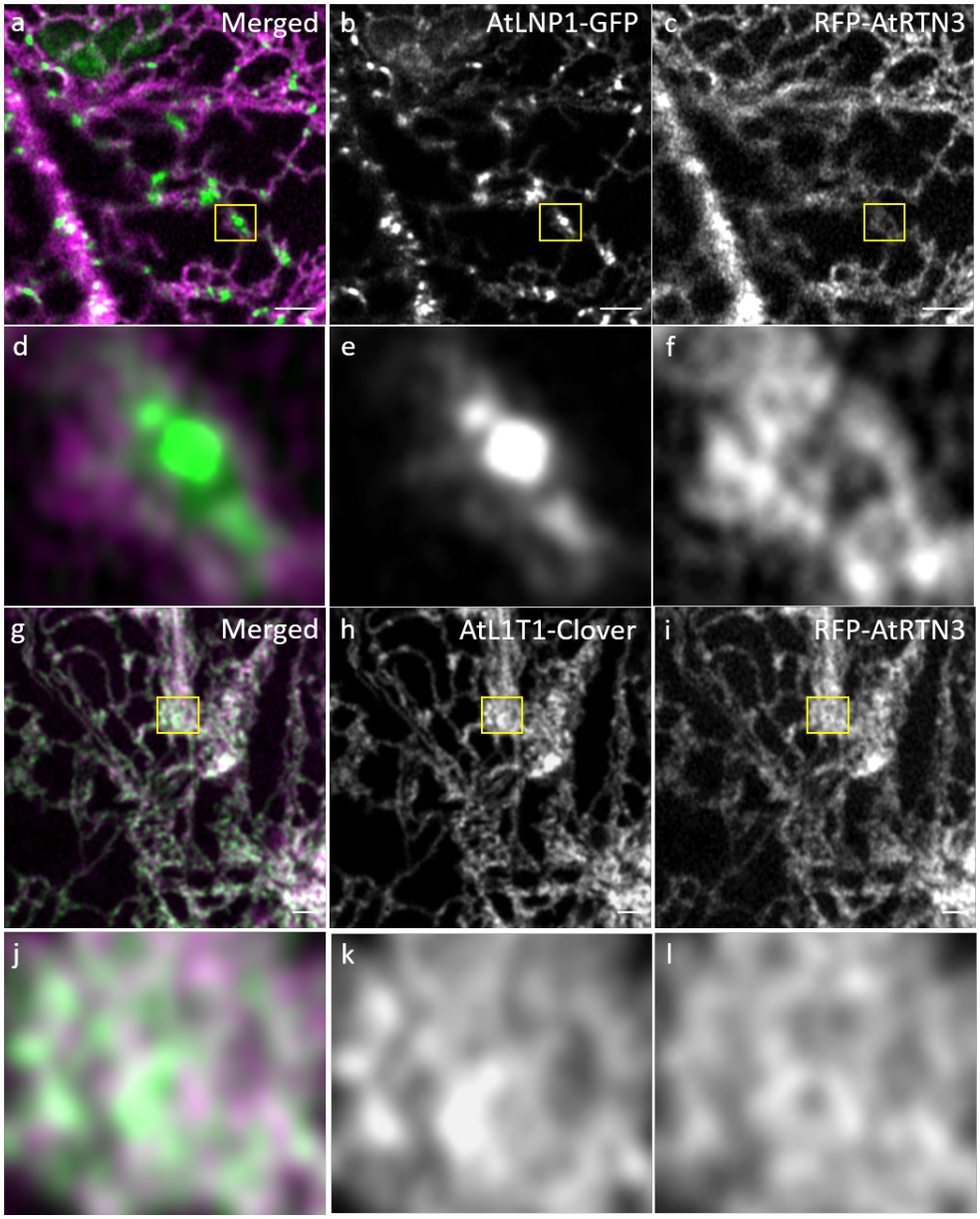


Figure 4.31: Localisation of the AtLNP1 truncation AtL1T1-clover and RFP-AtRTN3

Co-localisation (a) of AtLNP1-GFP (b) shown in green and RFP-AtRTN3 (c) shown on magenta. Regions of interest are highlighted by a yellow box and an enlarged version of this region is shown (d-f). Co-localisation (g) of AtL1T1-clover (h) shown in green and RFP-AtRTN3 (i) shown in magenta. Regions of interest are highlighted by a yellow box and an enlarged version of this region is shown (j-l). Scale bar 1 µm.

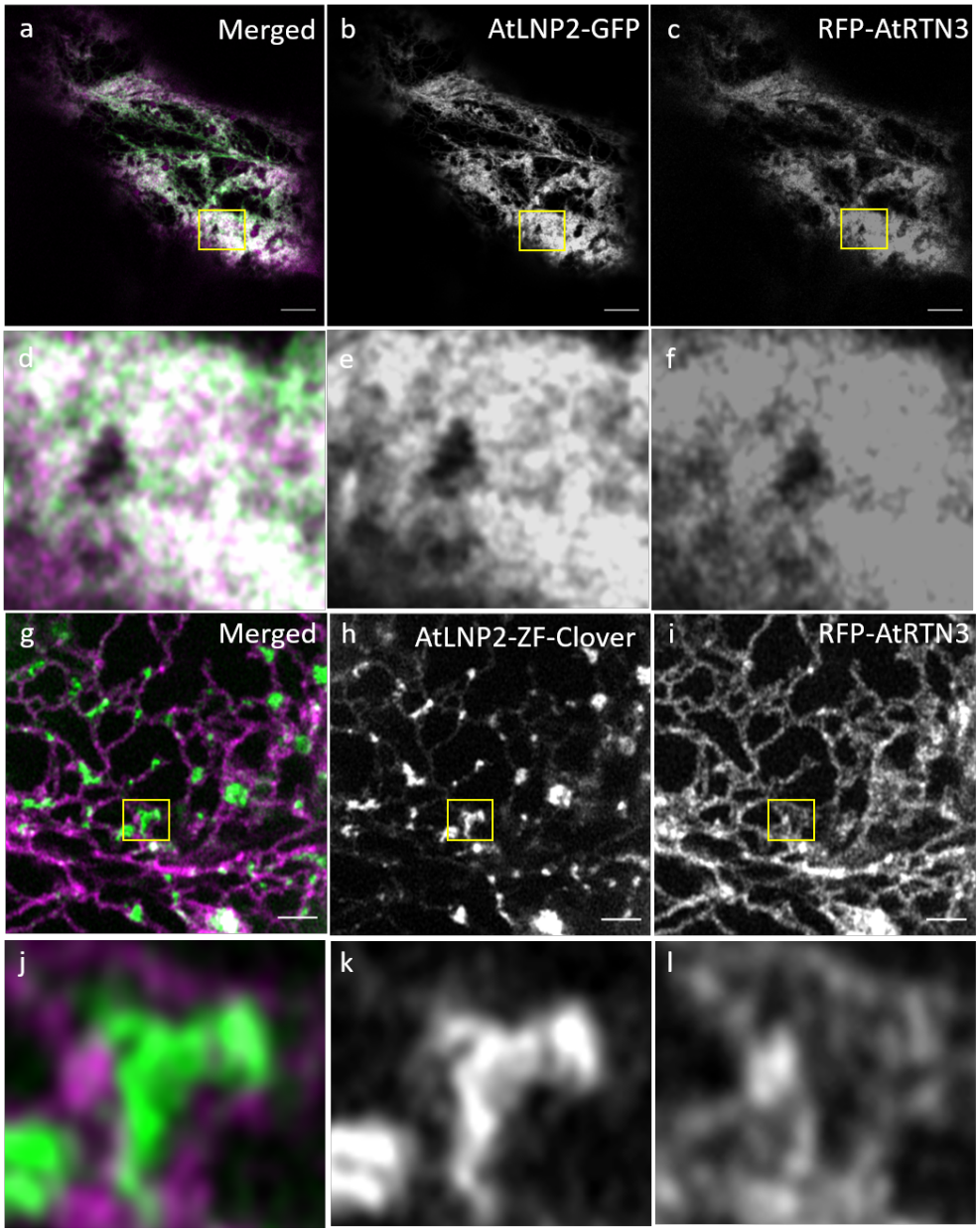


Figure 4.32: Localisation of the AtLNP2 truncation AtLNP2-ZF-clover and RFP-AtRTN3

Co-localisation (a) of AtLNP2-GFP (b) shown in green and RFP-AtRTN3 (c) shown on magenta, scale bar 5 µm. Regions of interest are highlighted by a yellow box and an enlarged version of this region is shown (d-f). Co-localisation (g) of AtLNP2-ZF-clover (h) shown in green and RFP-AtRTN3 (i) shown in magenta. Regions of interest are highlighted by a yellow box and an enlarged version of this region is shown (j-l). Scale bar 1 µm.

4.2.15 AtLNP1 punctae can be recruited to form cisternae

Due to the rapid bleaching of AtLNP1-GFP when using microscopy techniques such as VAEM and confocal microscopy and the rarity of cisternae formation within the ER, additional methods were sought for long term, low phototoxicity imaging of the plant ER. Light sheet fluorescence microscopy (LSFM) uses a thin plane of light, generated to optically section tissues and is highly suitable to long term fluorescence imaging due to low phototoxicity and photobleaching effects (Santi, 2011). These advantageous properties of the light sheet are achieved by only exposing a very thin section of the sample to light. Initially two theories of cisternae formation were considered: firstly, that cisternae may be formed by expansion of regions of membrane, marked by AtLNP1 or secondly, that AtLNP1-GFP aggregates may conglomerate to form cisternae (4.33).

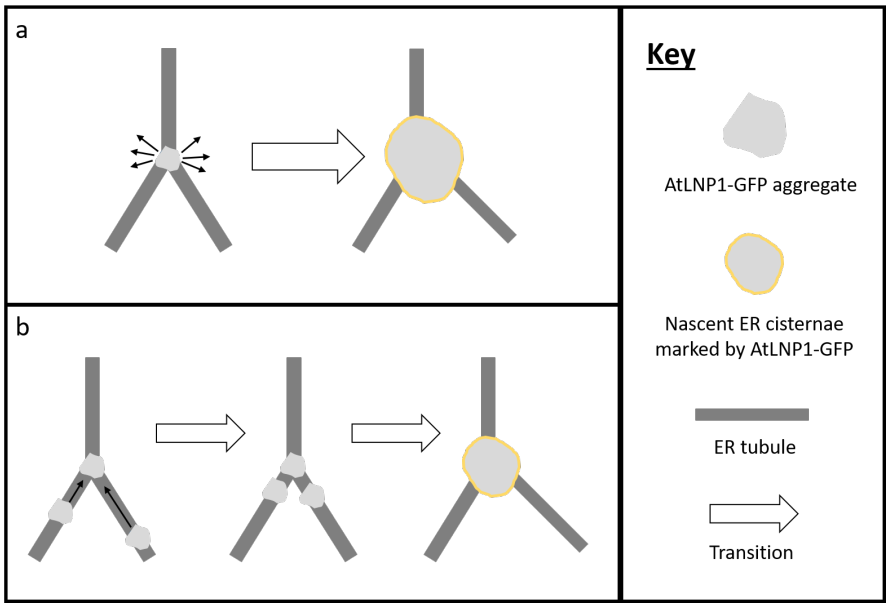


Figure 4.33: Potential mechanisms for ER cisternae formation by AtLNP1
Potential models for nascent cisternae formation by AtLNP1: (a) formation of nascent cisternae by expansion of AtLNP1 aggregates to form cisternae and (b) conglomeration of AtLNP1 aggregates to form a single nascent cisternae. Aggregates are shown in light grey, with formed nascent cisternae shown in grey with a yellow outline. Tubules are shown in dark grey and the transition between states shown by white arrows.

Light sheet microscopy was performed on arabidopsis stably expressing the lumenal marker GFP-HDEL and tobacco leaf sections transiently expression AtLNP1-GFP and AtLNP2-GFP (supplementary movie 4.7). Stable over-expression of AtLNP1-GFP in arabidopsis tissues was also tested but showing insufficient intensity for full analysis (fig. 4.34, supplementary movie 4.8). The potential for light sheet microscopy to have a phototoxic effect on the plant ER was tested using abaxial arabidopsis leaf epidermal cells stably expressing GFP-HDEL in a stable manner. Leaf pieces were mounted in 1/2 MS agar and submerged in PBS. They were then imaged continuously for 3 hours and assessed for phototoxicity. No signs of phototoxicity were detected within the first test and the ER structure remained unperturbed and dynamic (fig. 4.35).

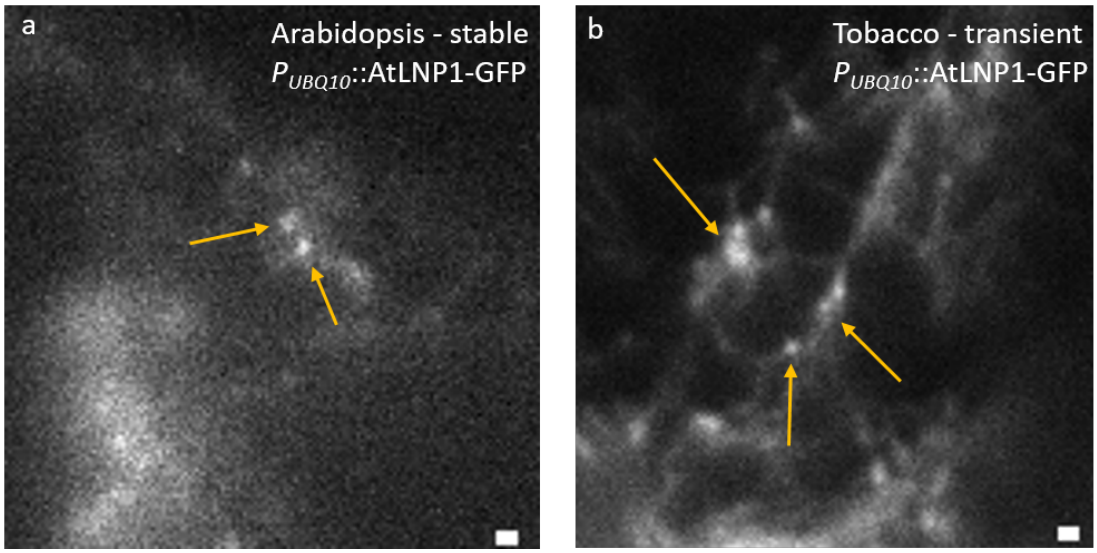


Figure 4.34: Light sheet imaging of stable P_{UBQ10}::AtLNP1-GFP expression in arabidopsis vs transient P_{UBQ10}::AtLNP1-GFP expression in tobacco

(a) Standard quality image of light sheet imaging of stable P_{UBQ10}::AtLNP1-GFP expression in arabidopsis compared to transient P_{UBQ10}::AtLNP1-GFP expression in tobacco. Yellow arrows denote selected AtLNP1-GFP aggregates that can be identified in these images. Scale bars 1 µm.

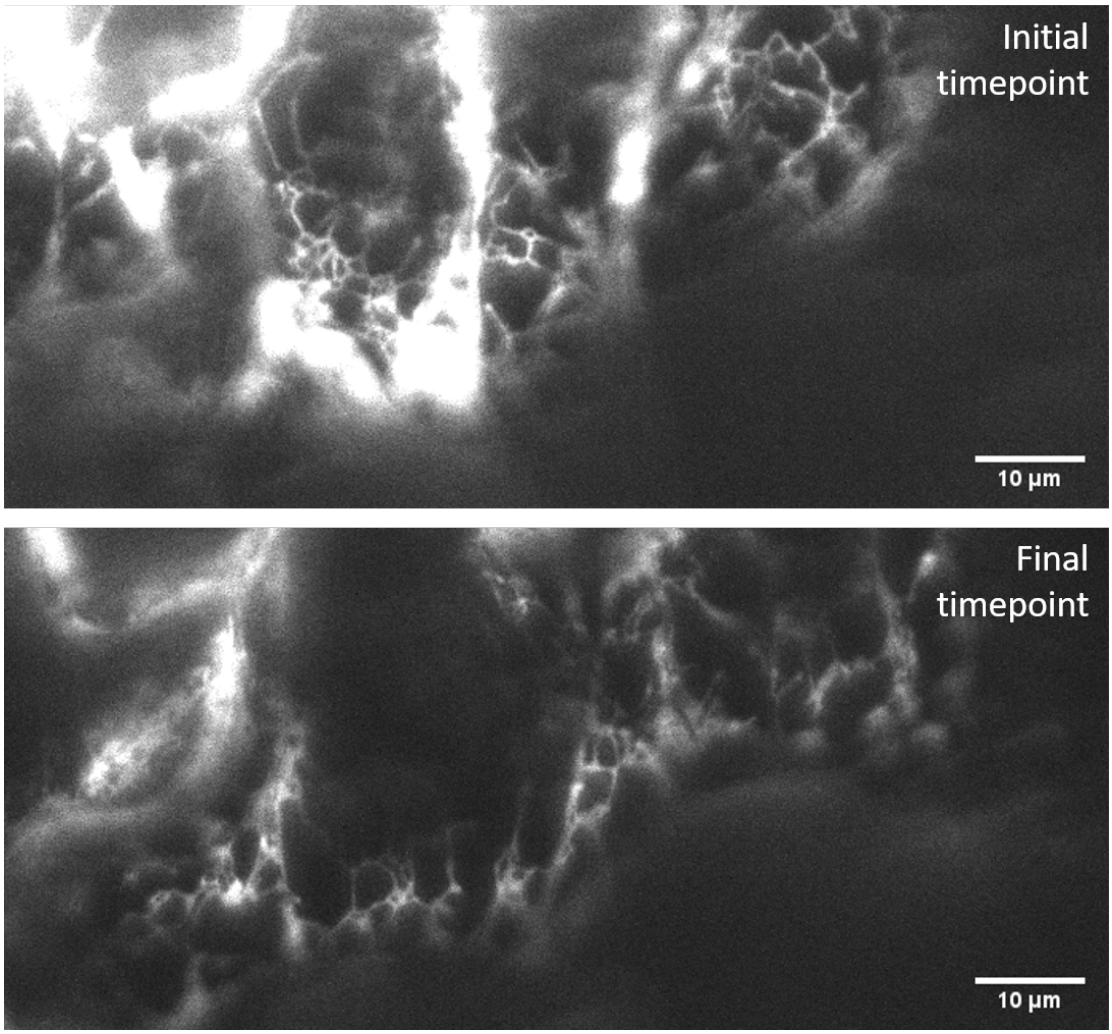


Figure 4.35: 3 hour light sheet phototoxicity test
Comparison of ER structure at the first time point in light sheet imaging (labelled initial time point) and the final frame of the time series collected 3 hours later (final timepoint). Images were collected on the abaxial side of arabidopsis leaves, with stable expression of GFP-HDEL. Scale bars 10 µm.

The same time series was also used to test for photobleaching. Three regions of interest containing the ER were selected, and the mean intensity of the ROI measured through time after conversion to an 8 bit image. The results reveal that region 1 shows a 18.35% decrease in intensity over approximately 3 hours, whilst regions 2 and 3 show a 1.98% and 10.32% increase in intensity over this time period (normalised comparison of mean intensity per region during the first and last 35 minutes, in order to account for the impact of ER dynamics on image intensity, fig. 4.36). This variability is most likely due to the dynamic nature of the ER, with streams and increased ER density in a region raising the mean intensity of an area, whilst drift, which did occur during the image collection period, contributing to a drop in the detected intensity. As a result, though it is likely that some photobleaching may have occurred and been obscured by ER dynamics, this bleaching is not so severe that it is likely to affect long term imaging.

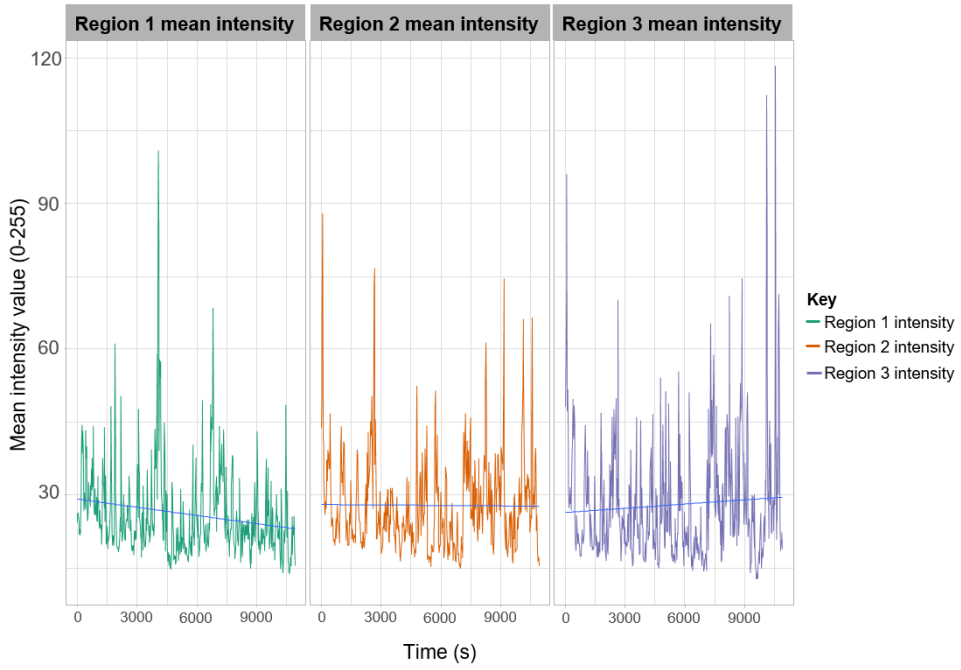


Figure 4.36: 3 hour light sheet photobleaching test
The mean intensity of 3 regions of interest of a time series collect of abaxial arabidopsis epidermal cells expressing GFP-HDEL. A smoothed mean of each intensity graph is shown in blue.

29 time series of 4 individual tobacco plants transiently expressing P_{UBQ10}::AtLNP1-GFP were collected, resulting in a dataset of approximately 5 hours and 42 minutes of captured ER movement. Cisternae formation by the P_{UBQ10}::AtLNP1-GFP aggregates was examined in these time series in order to identify how AtLNP1 may induce cisternae formation on over-expression. Initially two theories of cisternae formation were considered: firstly, that cisternae may be formed by expansion of regions of membrane, marked by AtLNP1 or secondly, that AtLNP1-GFP aggregates may conglomerate to form cisternae (4.33). The majority of novel, observable cisternae appear through apparent deposition/branching off from streams where they were already formed, having most likely just been re-distributed from an out of focus region of the cell. Through all the time series considered, no example of cisternae formation through expansion could be identified. However a total of 34 events of cisternae formation by aggregation of AtLNP1 punctae were identified (fig. 4.37a, 4.38a, raw montages with no collected frames omitted shown in supplementary fig. S9, S10 and time series shown in supplementary movie 4.9). The formation of a cisternae is considered to have occurred when AtLNP1-GFP punctae can no longer be distinguished from each other visually and this nascent structure persists as whole or as a larger structure, moving as a unit for an extended period of time (approximately 1 second, or 5 frames). Further events of fragmentation are acceptable as long as the total size of the cisternae is not reduced to pre-merger levels (fig. 4.37b, 4.38b).

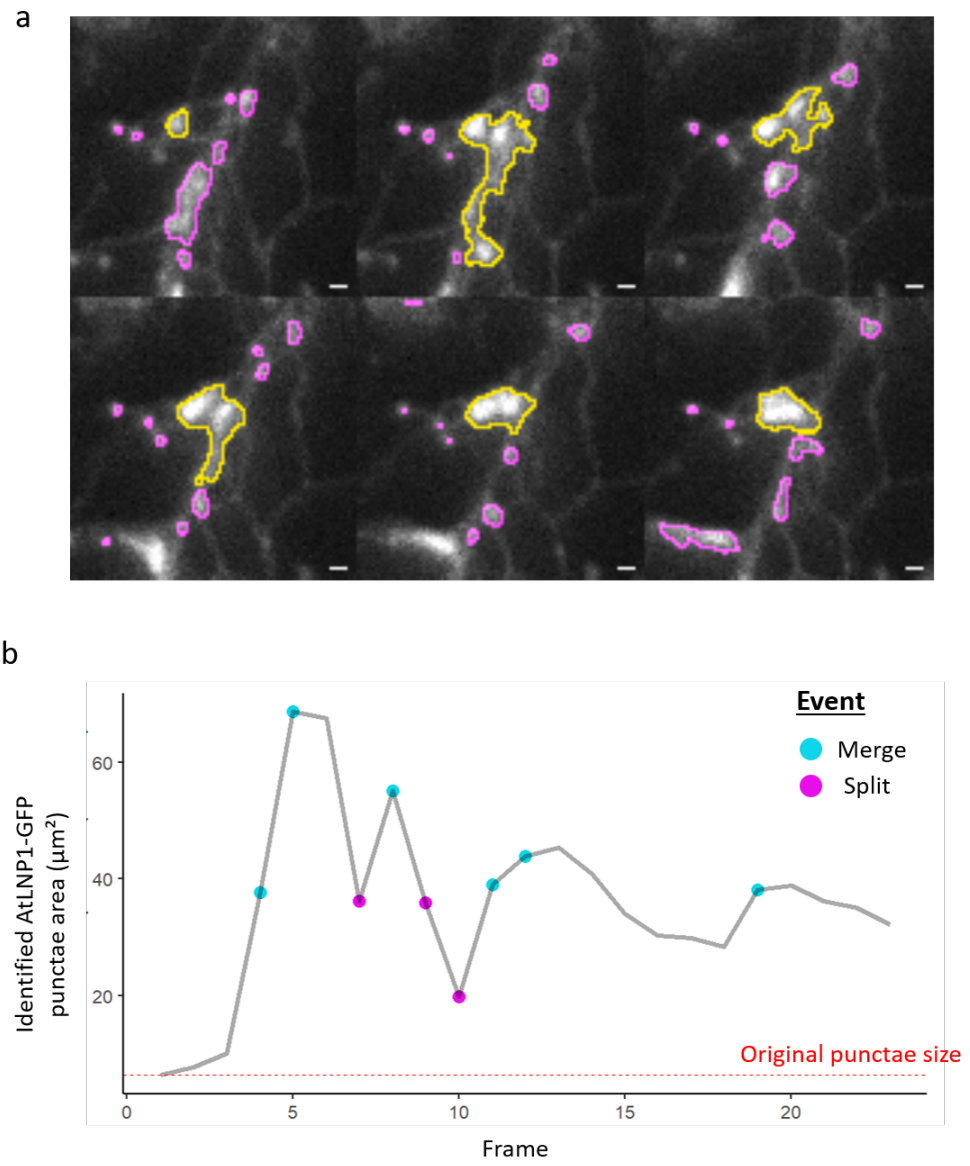


Figure 4.37: Cisternae formation by aggregation of AtLNP1-GFP punctae (a)
(a) Montage of the formation of a cisternae by aggregation of AtLNP1-GFP marked puncate. 1 in 4 frames are shown and the time between each of these frames is 0.84 seconds. (b) The area of the forming cisternae (highlighted in yellow in (a)) with aggregation events such as merging and splitting of aggregates shown in blue and magenta respectively. The horizontal dashed red line denotes the area of the selected original AtLNP1 punctae. Scale bars 1 µm, full montage shown supplementary fig. S9.

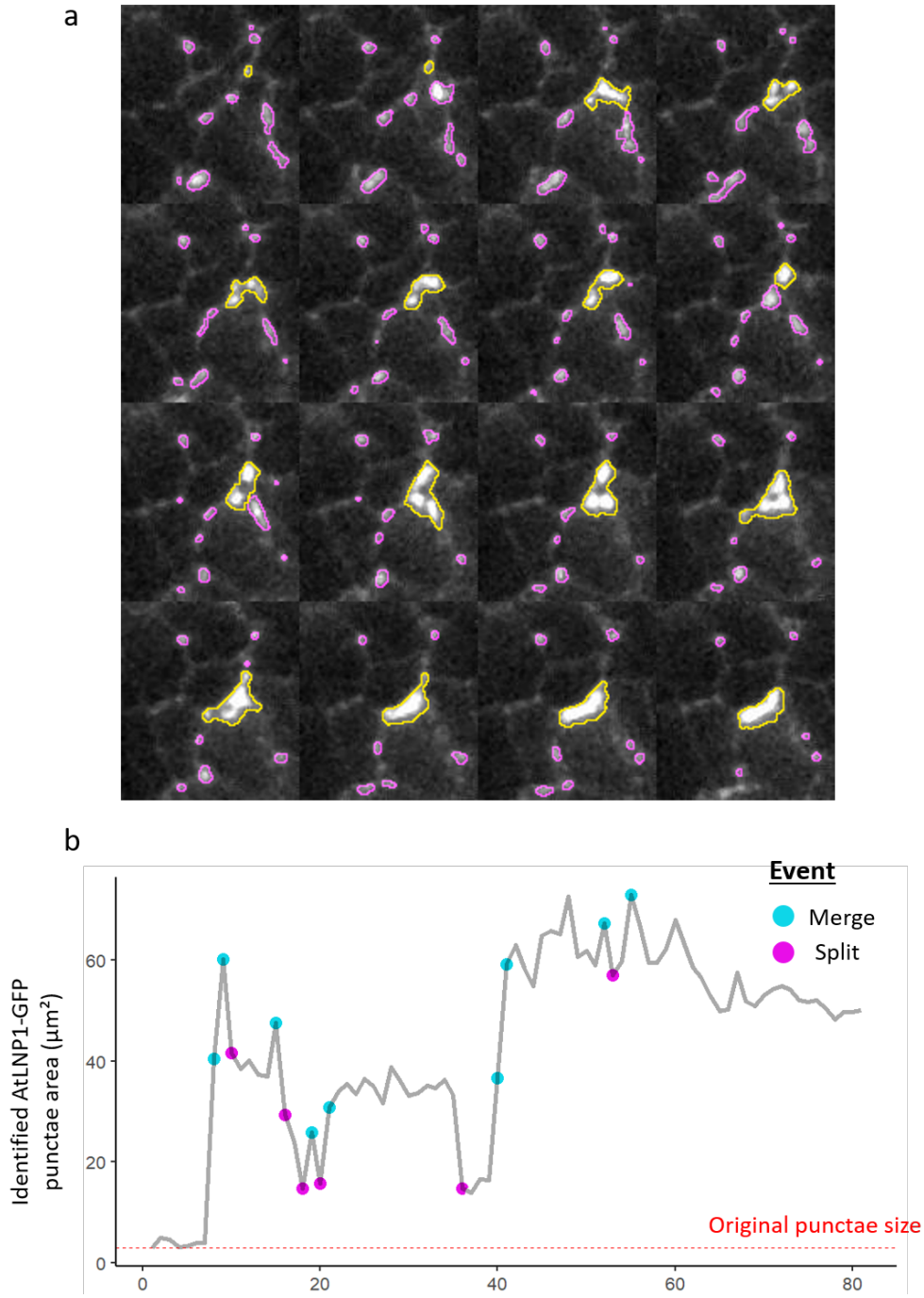


Figure 4.38: Cisternae formation by aggregation of AtLNP1-GFP punctae (b)

(a) Montage of the formation of a cisternae by aggregation of AtLNP1-GFP marked puncate. 1 in 5 frames are shown and the time between each of these frames is 0.84 seconds. (b) The area of the forming cisternae (highlighted in yellow in (a)) with aggregation events such as merging and splitting of aggregates shown in blue and magenta respectively. The horizontal dashed red line denotes the area of the selected original AtLNP1 punctae. Scale bars 1 µm, full montage shown supplementary fig. S9.

Of the 34 events identified, cisternae were observed for as long as possible, with cisternae often eventually captured by streams, or lost through drift or movement beyond the visible region of the cell. These nascent cisternae were classified in terms of how long they could be observed to persist, with an 'undetermined' classification applied to cisternae that were lost due to the end of the time series or as described previously. The majority of nascent cisternae persisted for more than 10 seconds (56%), with only 20% of these nascent showing rapid collapse within 5 seconds (fig. 4.39). These events however are both rare and rapid, as such only a few were captured despite using light sheet microscopy for long term image collection in order to capture these events of extended periods of times. The captured events happened within the space of only a few frames, up to 1 second, requiring good resolution through time.

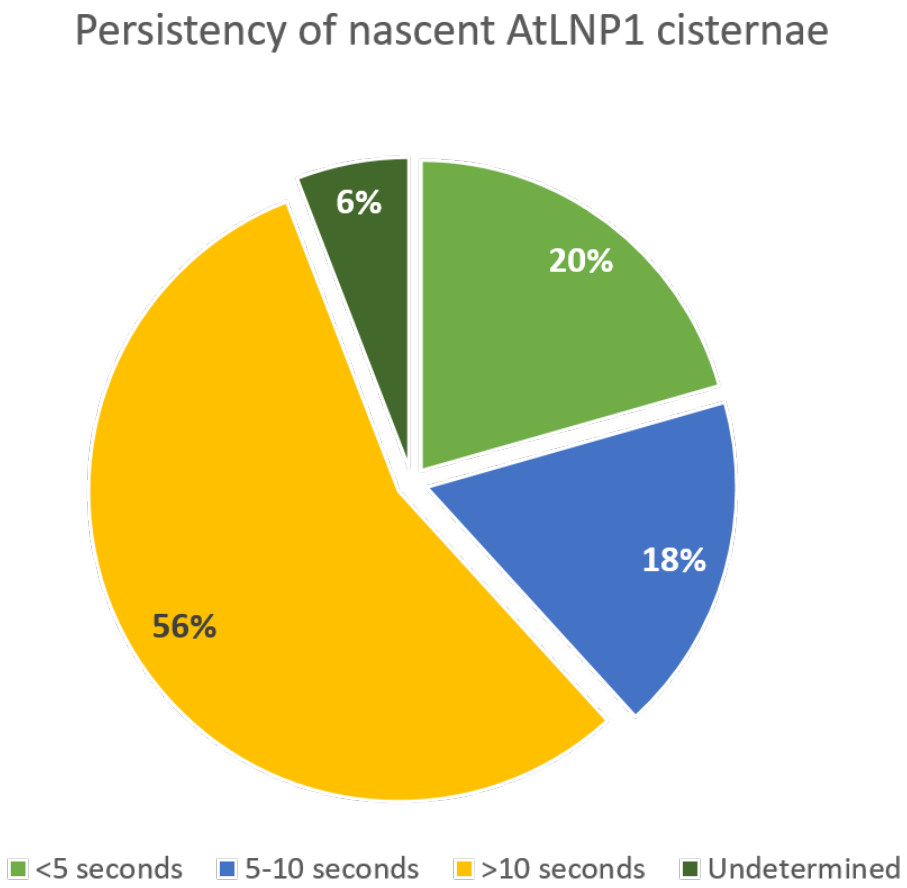


Figure 4.39: Persistency of nascent AtLNP1-GFP generated cisternae The recorded persistency of 34 identified nascent cisternae formed by the aggregation of ATLNP1-GFP marked punctae. The persistency of the nascent cisternae was classified into four groups defined by the length of time over which they could be observed yo persist: <5 seconds, 5-10 seconds, >10 seconds, and undetermined. The undetermined classification applies to cisternae that were lost shortly after formation, either through drift, movement to an out of focus region of the cell or after becoming captured by a stream. Data obtained from 29 individual timeseries, collected from a total of 4 individual tobacco plants.

4.3 Discussion

4.3.1 Arabidopsis has two Lunapark proteins that behave differently

Two orthologues of yeast Lnp1p and human Lnp have been identified in arabidopsis (Kriechbaumer *et al.*, 2018). Both share a strong structural similarity and are composed of two N-terminal TMDs, a C-terminal zinc finger domain and a LNKPKH amino acid motif. AtLNP1 and 2 share a 67% amino acid identity (Kriechbaumer *et al.*, 2018). Both localise to the ER but AtLNP1 shows a cisternae specific localisation, whereas AtLNP2 localises throughout the entirety of the ER (fig. 4.1). Transient over-expression of AtLNP1 and 2 induces cisternalisation of the ER, and this increase in cisternal area within each cell is related to the level of over-expression of AtLNP1 and 2, controlled by varying the number of agrobacteria infiltrated into each leaf. Stable over-expression of P_{UBQ10}::AtLNP1-GFP and P_{UBQ10}::AtLNP2-GFP in arabidopsis does not have the same effect of inducing cisternae, though AtLNP1 and 2 show similar localisations on transient over-expression in tobacco and stable expression in arabidopsis (fig. 4.2). Perhaps transient expression is successful at triggering an increase in cisternae within cells as the period of AtLNP1 and 2 up-regulation is relatively short, inhibiting the ability of plants to compensate for the effects of rapid over-expression. The effects of stable over-expression of AtLNP1 and 2 could be mitigated by plants over the longer timescale of stable expression, perhaps by up-regulation of proteins that induce tubulation of the ER, such as reticulon proteins (specifically AtRTN1-4 and AtRTN6, (Sparkes *et al.*, 2010)). AtLNP1 and 2 transcription can be identified in relatively young arabidopsis root and shoot tissue (7 days old), whilst only transcripts of AtLNP2 can be detected in matures tissues (25 day old rosette leaves,

flowers, buds and siliques, fig. 4.3). In young arabidopsis tissues, detection of AtLNP1 transcription is challenging and, as such, it is possible that AtLNP1 is transcribed in mature tissues but at a level lower than the sensitivity of RT-PCR.

4.3.2 Reduction of AtLNP1 and 2 transcription affects ER structure in arabidopsis

Identification of appropriate T-DNA knockout mutants for AtLNP1 and 2 was particularly challenging. Ideally multiple T-DNA lines would be identified for each gene of interest in order to ensure that differences observed in plants with reduced or eliminated gene transcription are not due to off-target insertions or effects of the T-DNA mutagenesis. However, of the T-DNA insertion lines requested from TAIR, one line was identified as being wild-type and the presence/absence of a T-DNA insertion could not be confirmed for the other line. The remaining two homozygous lines SALK_034698 (*lnp1*) and SALK_031496 (*lnp2*) were assessed for transcription of AtLNP1 and AtLNP2 respectively. The results revealed that *lnp1* has no detectable transcript of AtLNP1, whilst AtLNP2 transcription is only reduced in *lnp2* (fig. 4.5). The reduction of AtLNP2 transcription in *lnp2* is most likely due to the predicted location of the T-DNA insertion, near the 3'end of AtLNP2, which could potentially result in the transcription of a truncated version of AtLNP2. However, the majority of *lnp2* T-DNA insertion mutants are either recorded as heterozygous, requiring extended periods of selection in order to generate plants that are homozygous for the T-DNA insertion, or the insertion is localised at the 3' end of AtLNP2 (fig. 4.4). Therefore for the purposes of the work we proceeded with *lnp2* as it shows reduced AtLNP2 transcription. It is possible that the lack of availability of a homozygous *lnp2* knockout line is

indicative that AtLNP2 is required for arabidopsis survival. A potential AtLNP2 knockout line has been developed by Ueda *et al.* (2018), which has been reported as growing normally, however authors have thus far refused to respond to requests for access to material and so this line could not be included in this work. Both *lnp1* and *lnp2* show a modified ER structure (fig. 4.6) characterized by reduced proportion of ER classed as cisternae and a greater distribution of polygonal region area (figs. 4.7 and 4.9). These ER structural defects were also identified and enhanced in an amiRNA knockdown line created by Emily Breeze for this work. *amilnp1lnp2* showed a 4 times reduction of cisternal area and increased tubule length and polygonal region size (figs. 4.8, 4.9, 4.10 and 4.11). The remaining punctae identified within *amilnp1lnp2* ER that appeared larger than tubules do not show geometry or dynamics that are characteristic of cisternae (figs. 4.12 and 4.13). The structural defects observed on reduced AtLNP1 and 2 transcription indicate that AtLNP1 and 2 are required for normal ER structure. These modifications to arabidopsis ER structure are reminiscent to the modification seen in yeast and mammalian cells on reduction on of Lnp1p (Chen *et al.*, 2012) and mLnp1 (Shemesh *et al.*, 2014; Chen *et al.*, 2015). A normal ER structure can be recovered in *lnp1* by stable over-expression of P_{AtLNP1}::AtLNP1-GFP where the native promoter is presumed to be located within a 2kb region upstream of AtLNP1 (fig. 4.14). Though no fluorescence from the P_{AtLNP1}::AtLNP1-GFP could be detected on stable expression in *lnp1* using confocal microscopy, the more sensitive technique of VAEM reveals P_{AtLNP1}::AtLNP1-GFP expression across all tissues examined in the 8 day old arabidopsis lines (fig. 4.15). The recovery of ER structure on stable over-expression of P_{AtLNP1}::AtLNP1-GFP indicates that the modifications to *lnp1* ER structure that are observed are due to a cessation of AtLNP1 transcription as opposed to off-target effects of T-DNA mutagenesis.

4.3.3 Candidate domains for AtLNP1 and 2 function

Several truncations of AtLNP1 and 2 were generated in order to test whether particular conserved domains of AtLNP1 and 2 are likely to contribute to the function of the AtLNP1 and 2. Five N-terminal truncations were designed of AtLNP1 and 2, removing the first 20 amino acids (T1), up to the first TMD (T2), up to the end of the first TMD (T3), up to the start of the second TMD (T4) and up to the end of the second TMD (T5) (figs. 4.16 and 4.17). The T1 truncation is designed to mimic a modification of the N-terminal myristoylation site identified in mLnp1 whereby the myristoylation site was modified to be non-functional (Moriya *et al.*, 2013). This modified mLnp1 is not able to induce ER structural changes and immunoflourescent staining revealed a diffuse localisation of mLnp1. The T2 truncation, removing up the first TMD was generated to explore the function of the remaining N-terminal up to the TMDs. Subsequent truncations of TMDs were generated in order to investigate the role of TMDs in AtLNP1 and 2 function. The zinc finger domain has been implicated in the function of Lnp1p, as mutations within this domain result in a densely reticulated ER network (Casey *et al.*, 2015; Wang *et al.*, 2016b). Therefore, to test whether the zinc finger domain was likely to be required for AtLNP1 and 2 function, a truncation of the zinc finger domain onwards was generated. Though these truncations were targeted to conserved functional domains of AtLNP1 and 2, these conserved domains contained relatively denser regions of sequence divergence, in particular the AtL1T1 and AtL2T1 truncations (fig. 4.40) and the zinc finger truncations. Therefore, these regions are likely to represent the areas of the protein that contribute most to the differences between AtLNP1 and 2.

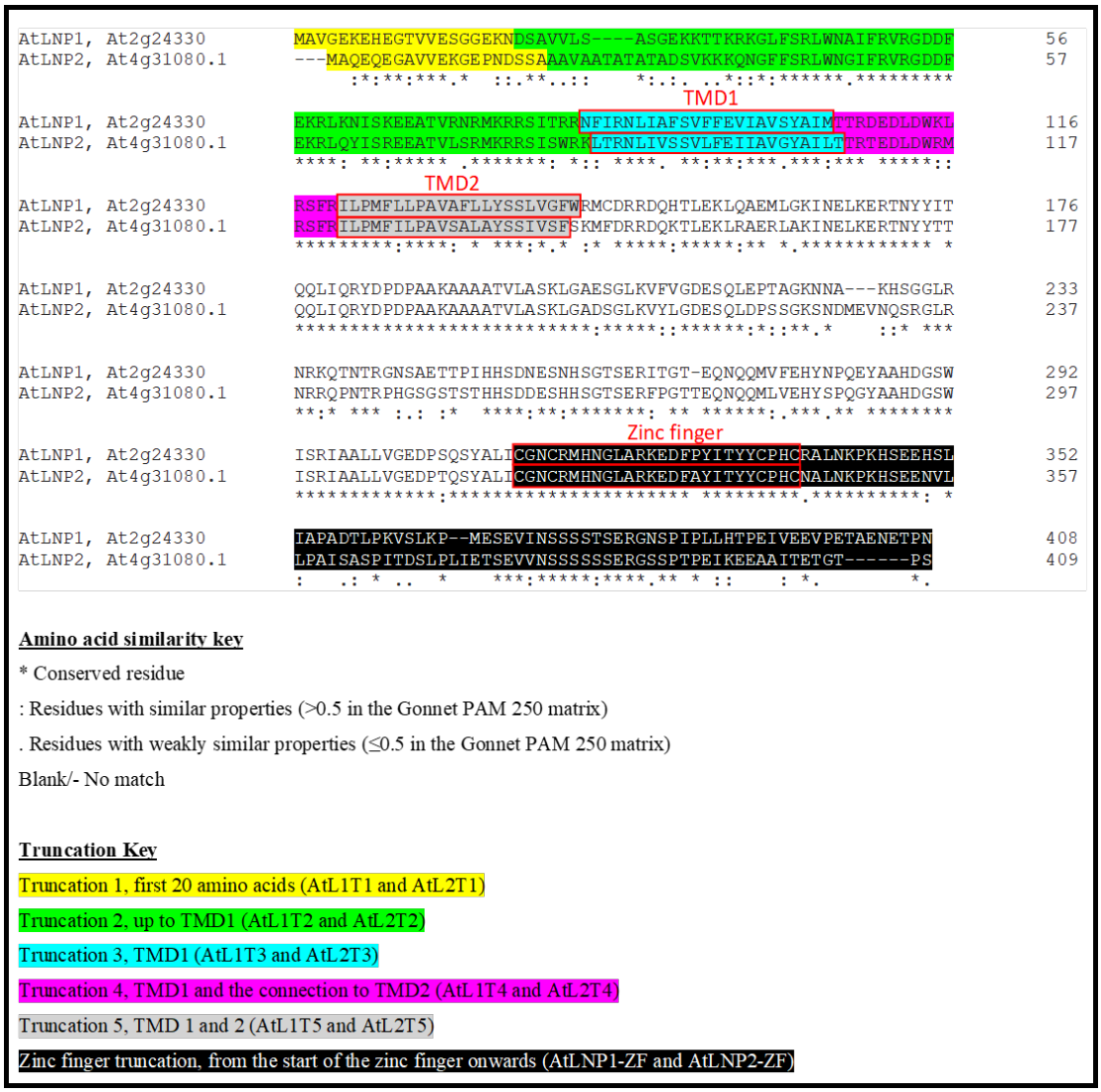


Figure 4.40: The localisation of selected N- and C- terminal truncations in relation to underlying sequence divergence between AtLNP1 and 2
Sequence alignment of AtLNP1 and 2 with residue similarity denoted by * for conserved residues, : for similar residues and . for weakly similar residues. Functional domains of particular interest (TMD1 and 2 and a zinc finger) are outlined in red. Truncations investigated as part of this work are highlighted in various colours. N-terminal truncations are from the N-terminus of AtLNP1 or 2, up to the end of the specified colour for each truncation.

Truncations from the N-terminus of AtLNP1 and 2 appeared to affect the localisation of AtLNP1 and 2, with AtLNP1 becoming localised throughout the entirety of the ER, and AtLNP2 becoming localised specifically to cisternae. Several N-terminal truncations (AtL1T3, AtL2T2, AtL2T3) either partially or fully localise

to unidentified, donut-shaped punctae that are closely associated with the ER. These punctae do not co-localise with either ATG8, a commonly used autphagosome marker (Contento *et al.*, 2005), or ST (53 N-terminal residues of the rat Golgi enzyme sialyltransferase, Batoko *et al.* (2000)), a commonly used medial/trans-Golgi marker. The most extensive truncations of both TMDs (AtL1T5 and AtL2T5) show a localisation characteristic of ER exit-sites in that they form small rings that surround Golgi bodies, but also have a cytoplasmic background component (Schoberer *et al.*, 2019). Extensive protein truncations can result in protein misfolding, which may be responsible for the modified localisation of the sever N-terminal truncations (in particular those that remove one or more TMD). Several AtLNP1 and 2 truncations show an altered localisation within the ER (table 4.4). N-terminal truncations, mostly prior to the first TMD, can show a modified distribution where they become distributed throughout the entire ER (AtLNP1 truncations: AtL1T1, AtL1T2 and AtL1T4), or can become restricted to cisternae specifically (AtLNP2 truncations: AtL2T1).

Additional C-terminal truncations of both AtLNP1 and AtLNP2, whereby all amino acids after the start of the zinc finger domain (the final 92 amino acids of both AtLNP1 and AtLNP2) have been removed, were also created. AtLNP1-ZF-Clover, has a relatively unmodified localisation and function, though it expresses poorly. AtLNP2-ZF-Clover shows a modified localisation that is cisternae specific (table 4.4, fig. 4.18).

Table 4.4: Summary of the salient features and localisation of all created truncations
A summary of all the AtLNP1 and 2 truncations created in this work including the remaining amino acids of the protein after the truncation and the localisation of the truncation.

Protien	Truncation name	Terminus	Remaining amino acids	ER localisation	Details
AtLNP1	AtL1T1	N	21-408	Yes	Throughout the ER
AtLNP1	AtL1T2	N	83-408	Yes	Throughout the ER
AtLNP1	AtL1T3	N	106-408	No	Unknown puncate
AtLNP1	AtL1T4	N	120-408	Yes	Throughout the ER
AtLNP1	AtL1T5	N	142-408	No	ER exit site
AtLNP1	AtLNP1-ZF	C	1-316	Yes	Cisternae specific
AtLNP2	AtL2T1	N	21-408	Yes	Cisternae specific
AtLNP2	AtL2T2	N	85-408	Yes	ER and unknown puncate
AtLNP2	AtL2T3	N	108-408	No	Unknown puncate
AtLNP2	AtL2T4	N	122-408	No	ER exit site
AtLNP2	AtL2T5	N	143-408	No	ER exit site
AtLNP2	AtLNP2-ZF	C	1-316	Yes	Cisternae specific

The T1 truncations reveal that the first 20 amino acids of AtLNP1 and 2 may play a key role in determining their relative localisations with the ER. The AtLNP1 truncation becomes localised throughout the entirety of the ER, whilst AtLNP2 specifically localises to cisternae. In addition, the loss of these 20 amino acids affects the co-localisation of AtLNP1 and 2 with additional ER shaping proteins âĂŞ the reticulons. Though it is possible that there may be some sort of localisation signal at the N-terminus of AtLNP1 and 2, it may be more likely that there is an interaction between the reticulon proteins and the Lunapark proteins that is mediated at the N-terminus, and this interaction may be the driver of AtLNP1 and 2 localisation. Further truncations of the N-terminus resulting in the removal of one or both transmembrane domains results in an inability of AtLNP1 and 2 to localise to the ER, and instead the protein localises to the ER exit sites. The reason for this is not entirely clear, nor is the identity of the unknown punctae formed after removal of the first transmembrane domain. Attempts to co-localise these truncations with possible candidates such as the Golgi and autophagosomes did not yield any clear results. A further truncation removing the C-terminal zinc finger domain of AtLNP1 did not appear to affect the localisation of AtLNP1, though the expression of AtLNP1-ZF was relatively poor when tested transiently in tobacco. The same truncation of AtLNP2 however resulted in a modified localisation to cisternae only, and also resulted in a loss of the co-localisation with reticulon proteins. This may suggest that though the zinc finger domain is not absolutely required for the function of AtLNP1, it is required for the normal functioning of AtLNP2.

4.3.4 AtLNP1 and 2 over-expression produces different 'types' of cisternae

Transient over-expression of RFP-AtLNP1 and 2 results in an increase in cisternal area that is dose-dependent (fig. 4.19). Transient over-expression of AtLNP1 appears to induce the formation of many small tubules connecting the enlarged cisternae, however these connecting tubules are not seen on over-expression of RFP-AtLNP2 despite the same increase in the area of cisternae (fig. 4.20).

The cisternae induced by AtLNP1 and 2 transient over-expression show different characteristics. AtLNP1 induced cisternae typically exclude the lumenal marker FP-HDEL (fluorescent protein fused to the ER retention signal HDEL, figs. 4.21 and 4.22). AtLNP2 induced cisternae however not only do not exclude lumenal markers, and lumenal markers are more evenly distributed through the lumen of the AtLNP2 induced cisternae than control cisternae marked only with GFP-HDEL (fig. 4.23).

VAEM is a highly sensitive technique that provides images with good spatial resolution of samples with low fluorescence. VAEM of arabidopsis plants stably expressing P_{UB10}::AtLNP1-GFP revealed densely reticulated regions in the place of cisternae. These regions appeared to be the same relative size as a typical cisternae, and AtLNP1 aggregates were present on the junctions between the tubules making up this densely reticulated network (figs. 4.24 and 4.25). Stable over-expression of P_{UB10}::AtLNP2-GFP in arabidopsis does not appear to increase the mean cisternal area and, though some small P_{UB10}::AtLNP2-GFP aggregates can be observed, the fluorescence is more evenly spread throughout the ER network (figs. 4.26 and 4.27). Over-expression of Lnp1p1 and mLnp1 (yeast and mammalian Lunapark proteins) is also described as inducing tubular structures, though this phenotype is

also observed on reduced Lunapark expression (Shemesh *et al.*, 2014; Chen *et al.*, 2012).

AtLNP1 induced cisternae exclude both RFP-AtRTN1 and RFP-AtRTN3, two proteins that typically localise to curved membrane edges (such as tubules and cisternal edges, fig. 4.29). Cisternae induced by AtLNP2 however have both RFP-AtRTN1 and RFP-AtRTN3 spread throughout the membrane surface when co-over-expressed (fig. 4.30). A model proposed by (Shemesh *et al.*, 2014) has suggested that all the structural components of the ER can be formed by varying the relative ratio of two classes of protein: R-proteins and S-proteins. Both proteins preferentially localise to curved membranes and, in the case of proteins such as AtRTN1-4, can further induce membrane curvature in a given plane. However perpendicular to this plane, they have been suggested to stabilize straight ER membranes (fig. 4.41), explaining the localisation of AtRTN1-4 to long, straight ER tubules. Meanwhile S-proteins, such as mLnp1, also locate to curved ER membranes in one plane, but in the other they promote negative membrane curvature (fig. 4.41). Negative membrane curvature is most easily seen at three-way junctions in the ER, where membranes are bent back on themselves in order to produce the necessary curvature between tubules at the junction (fig. 4.41). Hence AtLNP1 could act as a S-protein, inducing negative membrane curvature. Furthermore AtLNP1 induces cisternae with the structure described by Nixon-Abell *et al.* (2016): cisternae composed of a dense network of tubules rather than one flat structure with a contiguous lumen. AtLNP1 localises to the junctions within these dense reticulate networks (fig. 4.24), stabilising the internal structure of these regions in a similar way as described of the role of mLnp1 in stabilising three-way junctions in mammalian cells (Chen *et al.*, 2015). In order to maintain many junctions in such close proximity, R-proteins, such as AtRTN1 and 3 would have to be excluded from these cisternae, in order to prevent constant straightening of ER

tubules within cisternae and in order to maximize negative membrane curvature to ensure dense packing of the many ER tubules together (fig. 4.29). In addition, it wouldn't be entirely unreasonable to assume that the tight packing of ER tubules results in aggregation of tubules with a reduced lumenal space. Perhaps, as in the case of tubule constriction by AtRTN1 over-expression (Breeze *et al.*, 2016; Pain *et al.*, 2019), the reduced lumenal space prevents ER lumenal markers such FP-HDEL, from entering the lumen of these cisternae (figs. 4.22 and 4.42). Alternatively the extreme membrane curvature required for close packing of tubules in AtLNP1 induced cisternae may play a role in limiting FP-HDEL movement through the lumen of the cisternae. AtLNP2, however may induce cisternae with a canonically predicted structure, that is, cisternae composed of two appressed, flat membrane sheets. The lumenal marker GFP-HDEL is spread evenly through the AtLNP2 induced cisternae, more evenly than through control cisternae labelled by GFP-HDEL only (fig.4.23). The even distribution of the lumenal marker is indicative of a cisternae with an unstructured lumen, with no nanoholes present within the cisternae as predicted by Schroeder *et al.* (2019), nor being composed of many tubules as suggested by Nixon-Abell *et al.* (2016). Perhaps a cisternae of this type requires a balance of negative and flat membrane curvature enhancing proteins, explaining the relatively even distribution of AtLNP2 (a S-protein) and AtRTN1 and 3 (R-proteins) throughout the induced cisternae (fig. 4.42). The curvature induced by each may balance the effect of the other.

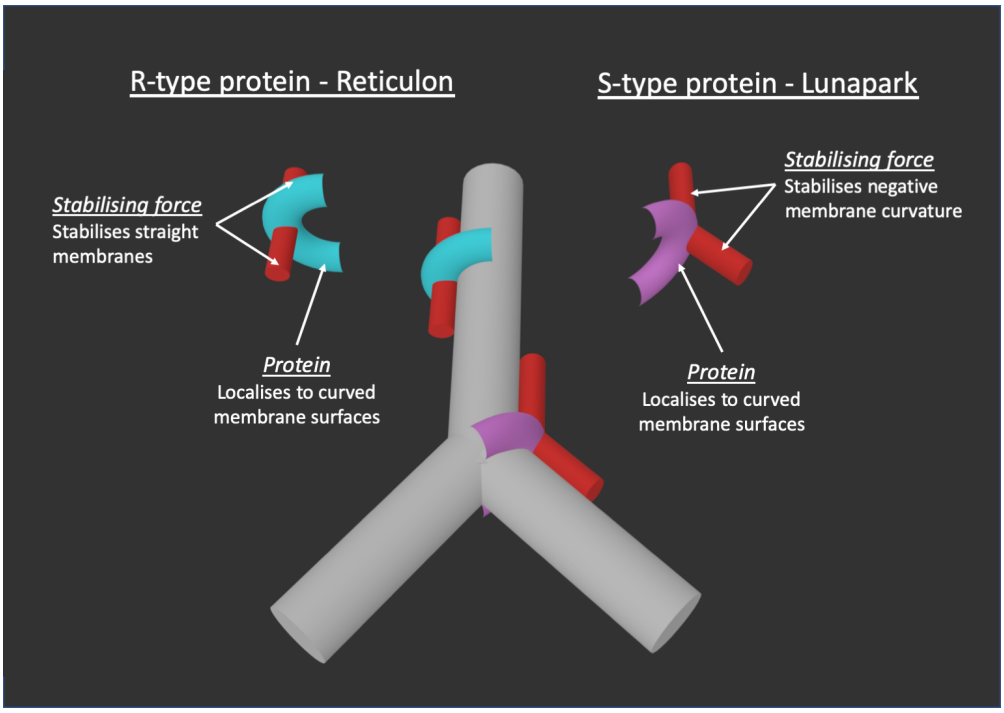


Figure 4.41: A comparison of the forces exerted by R- and S-proteins The theoretical localisation of R- and S-type proteins around an ER three-way junction (grey). Reticulon proteins such as RTN4 (blue) have been suggested to stabilise straight membranes along the length of ER tubules (direction of stabilising force in red). Lunapark proteins (magenta) have been suggested to stabilise or induce negative membrane curvature within the ER, such as at the center of three-way junctions.

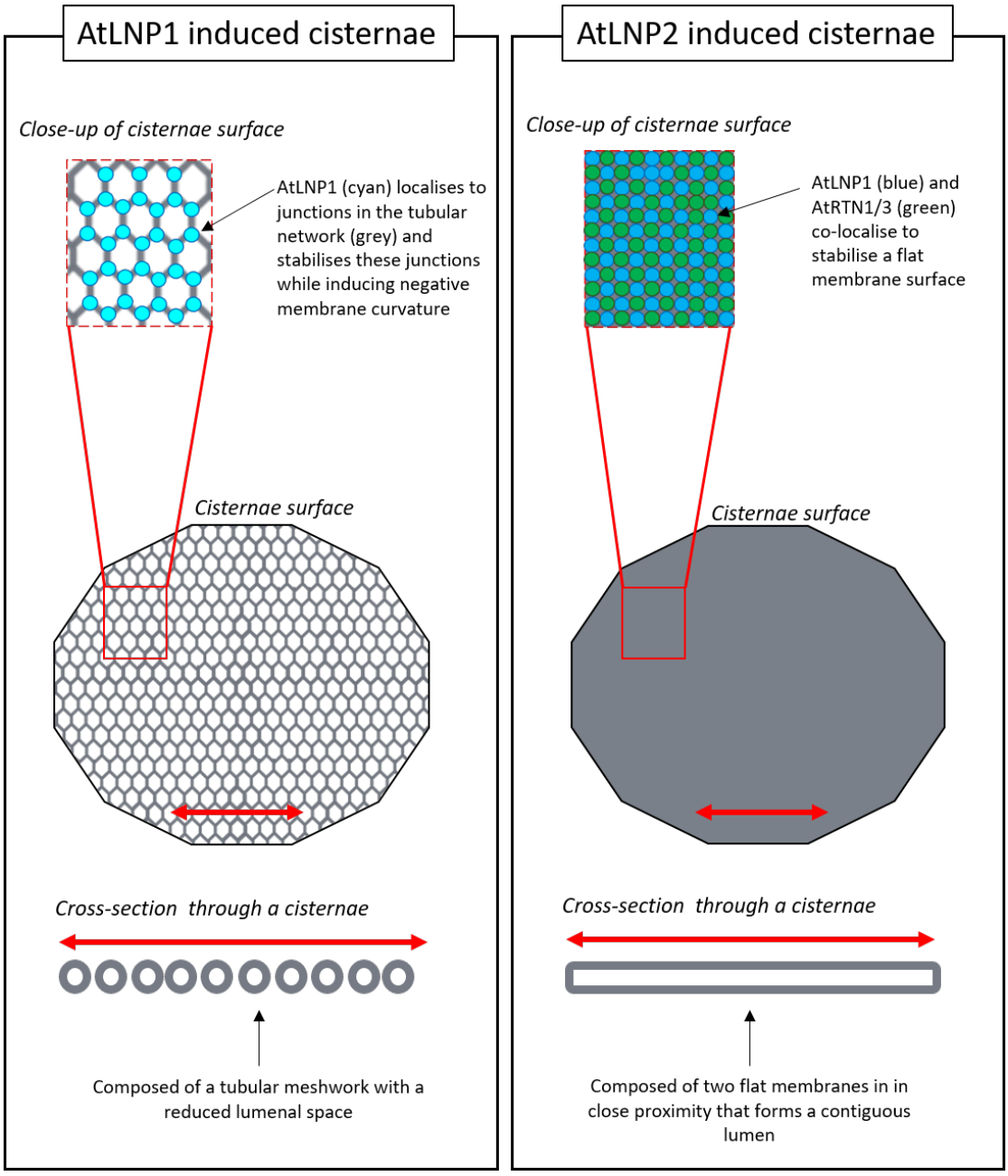


Figure 4.42: Schematic representation of the structure of cisternae induced by AtLNP1 and 2 over-expression
Schematic diagram of the proposed surface and cross-section of AtLNP1 and 2 induced cisternae. AtLNP1 may induce cisternae composed of a network of small, highly reticulated tubules with AtLNP1 acting to stabilise the junctions within this netwrok. AtLNP2 may induce cisternae with a flat, contiguous surface that is maintained by both AtLNP2 and reticulon proteins such as AtRTN1 and 3. The lumen of AtLNP1 induced cisternae could be spread between many small tubules while the lumen of AtLNP2 induced cisternae may be expected to be highly contiguous.

The presence of cisternae both excluding and including reticulon proteins across the ER membrane surface has been previously identified in mammalian cells (Nixon-Abell *et al.*, 2016). Within fixed Cos-7 cells stably expressing the ER marker mEmerald-Sec61β and immunostained for endogenous RTN4A/B localisation, cisternae with and without RTN4A/B can be identified (fig. 4.43). Cisternae with RTN4A/B show a similar distribution of RTN4A/B through cisternae as is seen with AtRTN1 and 3 through cisternae induced by AtLNP2. Whilst cisternae excluding RTN4A/B appear similar to the cisternae induced by AtLNP1.

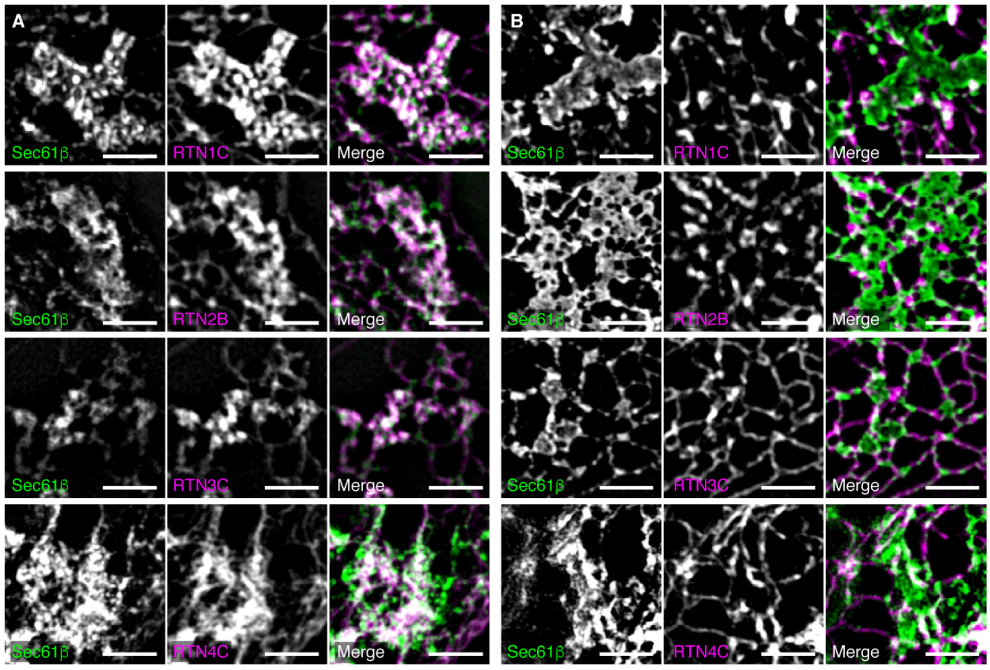


Figure 4.43: Cropped image taken from Nixon-Abell *et al.* (2016) showing variation in the reticulon content of cisternae in Cos7 cells
Image produced by Nixon-Abell *et al.* (2016) of fixed COS-7 expressing the ER marker mEmerald-Sec61β stained from the presence of endogenous RTN4A/B. (A) reveals cisternae that that contain endogenous RTN4A/B and (B) reveals cisternae from which RTN4A/B has been excluded. Images collected using 3D-SIM, scale bars 2 µm. An image colour correction has been applied using ImageJ, replacing all red colour in the image with magenta.

4.3.5 Several AtLNP1 and 2 truncations that show modified ER localisation also show modified AtRTN1 and 3 distributions

Both AtL1T1-Clover, an AtLNP1 trunction missing the first 20 amino acids, and AtLNP2-ZF-Clover, an AtLNP2 C-terminal truncation missing the zinc finger and remaining C-terminal, show altered localisation within the ER. AtL1T1-Clover localises throughout the entire ER, whilst AtLNP2-ZF-Clover is restricted to ER cisternae. As the localisations were swapped compared to the full length proteins, so too was the co-localisation between the given truncations and RFP-AtRTN3 within the induced cisternae. AtL1T1-Clover does not co-localise with RFP-AtRTN3 (fig.4.31), whereas AtLNP2-ZF-Clover does co-localise with RFP-AtRTN3 (fig. 4.32). Therefore modifying the localisation of AtLNP1 and 2 throughout the ER network seems to affect the localisation of tubulating proteins such as reticulons throughout the ER. Further work will need to be done to elucidate how the truncated components of AtLNP1 and 2 contribute to it's localisation, and perhaps how these truncations interact with the given reticulon proteins (further details in future work). It may be that an interaction between AtLNP1 and 2 and AtRTN1 and 3 determines the structure of the cisternae formed/maintained by AtLNP1 and 2. An interaction with reticulon proteins may be essential for the formation of a flat, contiguous cisternae, whilst reticlon proteins may have to be excluded from cisternae in order to form cisternae with complex, tubulated inner structures.

Table 4.5: Summary of the localisation of AtLNP1 and 2 truncations and whether they co-localise with AtRTN1 and 3 Comparison of the localisation of full length AtLNP1 and 2 and two selected truncations: AtL1T1-Clover and AtLNP2-ZF-Clover. The ability of these truncations and the full length protein to co-localise wit AtRTN1 and 3 is also shown.

Protein	Dsecription	Localisation	Co-localisation with AtRTN1 and 2
AtLNP1	Full length protein	Cisternae	No
AtL1T1-Clover	Missing first 20 amino acids	Throughout the ER	Yes
AtLNP2	Full length protein	Throughout the ER	Yes
AtLNP2-ZF-Clover	Missing last 96 amino acids	Cisternae	No

4.3.6 AtLNP1 forms cisternae through aggregate conglomeration as opposed to expansion

Long-term, low phototoxity imaging techniques are required to assess biogenesis of ER cisternae. Light sheet microscopy was found to be sufficient for capturing cisternae biogenesis in plant leaf epidermal cells over an extended time period (figs. 4.35 and 4.36). As well as localising to ER cisternae, AtLNP1 also localised to small punctae distributed throughout the ER. The dynamics and morphology of these puncate were investigated over an extended time period in order to identify whether they play a role in cisternae formation. Two theories for how these AtLNP1 punctae could form cisternae were proposed: either these punctae could expand through time to form a cisternae, or these punctae could aggregate to form a cisternae (fig. 4.33). Cisternae were only seen to be formed by the aggregation of AtLNP1 punctae as opposed to through punctae expansion (figs. 4.37 and 4.38). Though these nascent cisternae underwent many subsequent merging and splitting events, these cisternae do not return to the same size as at the start of the imaging, indicating that they have formed a new cohesive structure. In addition

the cisternae formed from AtLNP1 punctae aggregation appeared highly persistent, with over half of the nascent punctae persisting for more that 10 seconds (fig. 4.39).

It is possible that the different structures of cisternae identified by AtLNP1 and AtLNP2 over-expression could represent two stages of nascent cisternae formation. Under this model AtLNP1 could facilitate the aggregation of ER membranes, by densely packing a lot of ER membrane into a small space by inducing negative membrane curvature. These stabilised aggregates naturally merge with other aggregates to form larger cisternae. Perhaps then AtLNP2 is used to 'fill in' these aggregated tubules, forming a canonical ER cisternae out of two flattened membranes. That being said cisternae could also be formed by AtLNP2 in a different manner, which as yet to be identified.

5 | Protein movement in the plant ER

Contents

5.1 Introduction 218

5.2 Results 220

5.2.1 Achieving appropriate fluorophore density 220

5.2.2 The 3D nature of the plant ER 222

5.2.3 Modifying ER structure and movement for single particle movement analysis 224

5.2.4 Single particle movement in the plant ER 236

5.3 Discussion 243

5.1 Introduction

The movement of the ER is highly complex and occurs over a range of scales (fig. 5.1). At the smallest scale, single particles (individual proteins, protein aggregates, lipids and ions) move within the ER membrane and through the lumen of the ER. At the greatest scale, the entirety of the ER is remodelling through space, with tubules elongating a retracting, cisternae constantly re-shaping and translocating and bulk translocation of ER along thick actin bundles. A great deal of work has already been applied to analyse the highest level of ER dynamics (Pain *et al.*, 2019; Ueda *et al.*, 2010; Sparkes *et al.*, 2009a; Griffing *et al.*, 2014) but the movement of single particles through the ER is rarely considered, except using photoconversion techniques such as photoactivation (Runions *et al.*, 2006). Though these methods can give insight into the bulk movement of particles in the ER, they can only be

applied to large pools of molecules as these techniques lack the sensitivity to detect individual particles. Understanding how single particles move, and the effect of ER structure on the movement of these particles, could provide vital clues on the formation of metabolons on the surface of the ER, and the functional role of ER structure and dynamic changes through development. Single particle tracking has been performed in mammalian ER (Holcman *et al.*, 2018) and in the plasma membrane of both plant (Wan *et al.*, 2011; Martiniere *et al.*, 2012; Chen *et al.*, 2018; Hutten *et al.*, 2017; McKenna *et al.*, 2019) and mammalian cells (Burnecki *et al.*, 2019), however it has yet to be carried out in the plant ER. The movement of single particles within the ER can be captured using VAEM (variable-angle epifluorescence microscopy) and we have used this technique to visualise, and analyse, the movement of single particles through the plant ER. Using this highly sensitive technique we aim to visualise and track the movement of single particles through the plant ER under different conditions.

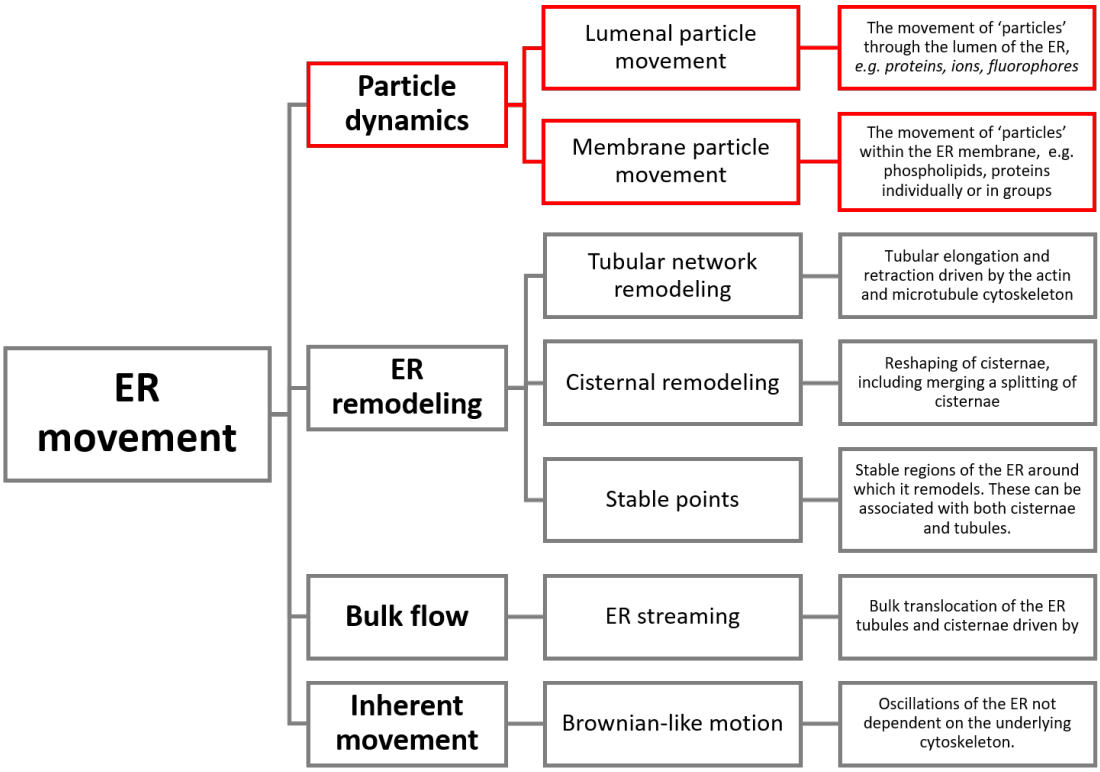


Figure 5.1: The different components of ER dynamics
Different types of ER movement that can be measured, with the movements considered within this chapter shown in red (the movement of particles through the ER membrane and lumen), and other aspects of ER movement that can effect analysis of particle movement in grey.

5.2 Results

5.2.1 Achieving appropriate fluorophore density

Single particle/molecule tracking requires a sufficiently low concentration of active fluorophores (fluorophores that are actively fluorescing at the desired wavelength) within the structure of interest in order to ensure that individual particles can be distinguished from one another. Too high concentration of active fluorophores in specific areas results in a a smearing effect where individual particles cannot be identified (fig. 5.2 and supplementary movie 5.1). Lowering the concentration of active fluorophores when using a transient expression system can be achieved in two ways:

- Lowering optical density of the agrobacteria in the infiltration buffer.
- The use of photoactivatable fluorophores.
- Stable expression systems with variable promoters.

Lowering the concentration of agrobacteria that are infiltrated into plant leaves, monitored by reducing the optical density of the infiltration buffer, is one potential method for reducing the levels of transient protein expression. By reducing the number of agrobacteria that are used to infect the plant it is therefore likely that each cell within the leaf has a lower number of infection events, resulting in fewer insertions of the sequence of interest into each cell, thus theoretically lowering the levels of transient expression. This method appears to be successful at reducing the expression of all proteins of interest (fig. 5.2). Though stable expression systems may also be attempted, identification of individuals with sufficiently low expression for single particle tracking using conventional confocal microscopy is not possible.

Screening would have to be completed on a highly sensitive TIRF microscope that is not freely available at the institute at which the majority of this work was performed. Therefore, a reduced optical density of infiltrated agrobacteria was selected as the best method for reducing the concentration of fluorescent particles in the ER.

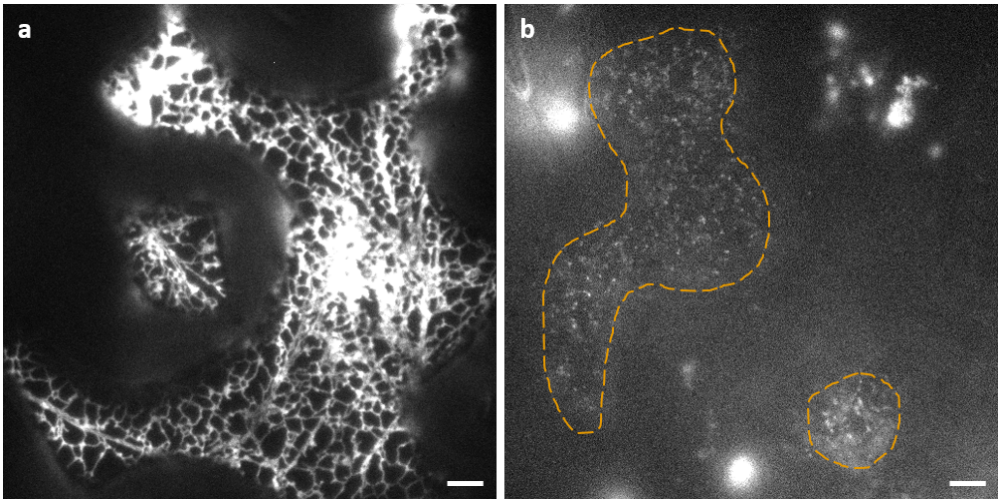


Figure 5.2: Optimizing expression levels for single molecule visualization
Transient over-expression of paGFP-CXN in tobacco leaf epidermal cells. (a) High expression of paGFP-CXN after infiltration of agrobacteria infiltration media at an OD_{600} of 0.1 and (b) lower expression of paGFP-CXN after infiltration of media with an OD_{600} of 0.001. Cell outlines shown where necessary by orange dashed overlay. Scale bars 5 µm.

The use of fluorophores that require activation or conversion are another potential method for reducing the number of actively fluorescing fluorophores within a single area. Two potential fluorophores were tested for this use: photoactivatable green fluorescent protein (paGFP) and mEOS (named for the Greek goddess of dawn). paGFP has a very low/no fluorescence in its native state, but its fluorescence under 488nm excitation is increased 100 times after intense irradiation under 413 nm light (Patterson and Lippincott-Schwartz, 2002). mEOS on the other hand, in its

native state, is a green fluorescent protein (emission wavelength: 516 nm) but can be converted to red fluorescence (emission wavelength: 581 nm) after conversion triggered by exposure to near-UV light (approximately 390 nm) (McKinney *et al.*, 2009; Wiedenmann *et al.*, 2004). Both paGFP and mEOS were selected to test single particle movement because theoretically a small pool of the fluorophores will fluoresce in the appropriate wavelength without appropriate activation (irradiation at 413 nm and 390 nm for paGFP and mEOS respectively). When using paGFP it is likely that 1% of the fluorophores may remain constitutively active, given the 100x increase in detected fluorescence intensity on activation (Patterson and Lippincott-Schwartz, 2002). Therefore we would be able to infiltrate agrobacteria at a sufficient optical density within the infiltration media to ensure that many cells are infected with agrobacteria but resulting a reduced proportion of detectable fluorophores per cell. mEOS could be used to actively reduce the proportion of fluorophores emitting green flourecsence (516 nm), which was detected by our VAEM system, by photoconverting the pool of fluorophores to red flourescence (581 nm), which was not detected by our VAEM system. This could theoretically allow a rapid reduction of fluorophores that can be detected in the ER, without requiring harsh bleaching techniques to remove a subset of fluorophores.

Ultimately photoactivation of paGFP is not required, as lowering the amount of agrobacteria infiltrated into the plant leaf is sufficient to reduce the density of fluorophores within the ER to a level at which individual molecules can be identified within the ER. Photoconversion of mEOS is also not required as again, lowering the number of agrobacteria infiltrated into the plant leaf was sufficient.

5.2.2 The 3D nature of the plant ER

An additional challenge of single particle imaging in the plant ER is that particles within the ER move in and out of focus due to the 3D nature of the ER throughout the period of data collection (fig. 5.3). Therefore, each frame has a small number of particles that are in focus and can be detected by standard particle detection methods, and a pool of out of focus particles with a very poor signal-to-noise ratio. Identification and tracking of out of focus particles is particularly challenging and no methods yet exist for accurate analysis. As a result of particles shifting in and out of frame, single particles on the ER can only be tracked over a relatively short distance - typically providing only instantaneous diffusion results and a very short tracking window.

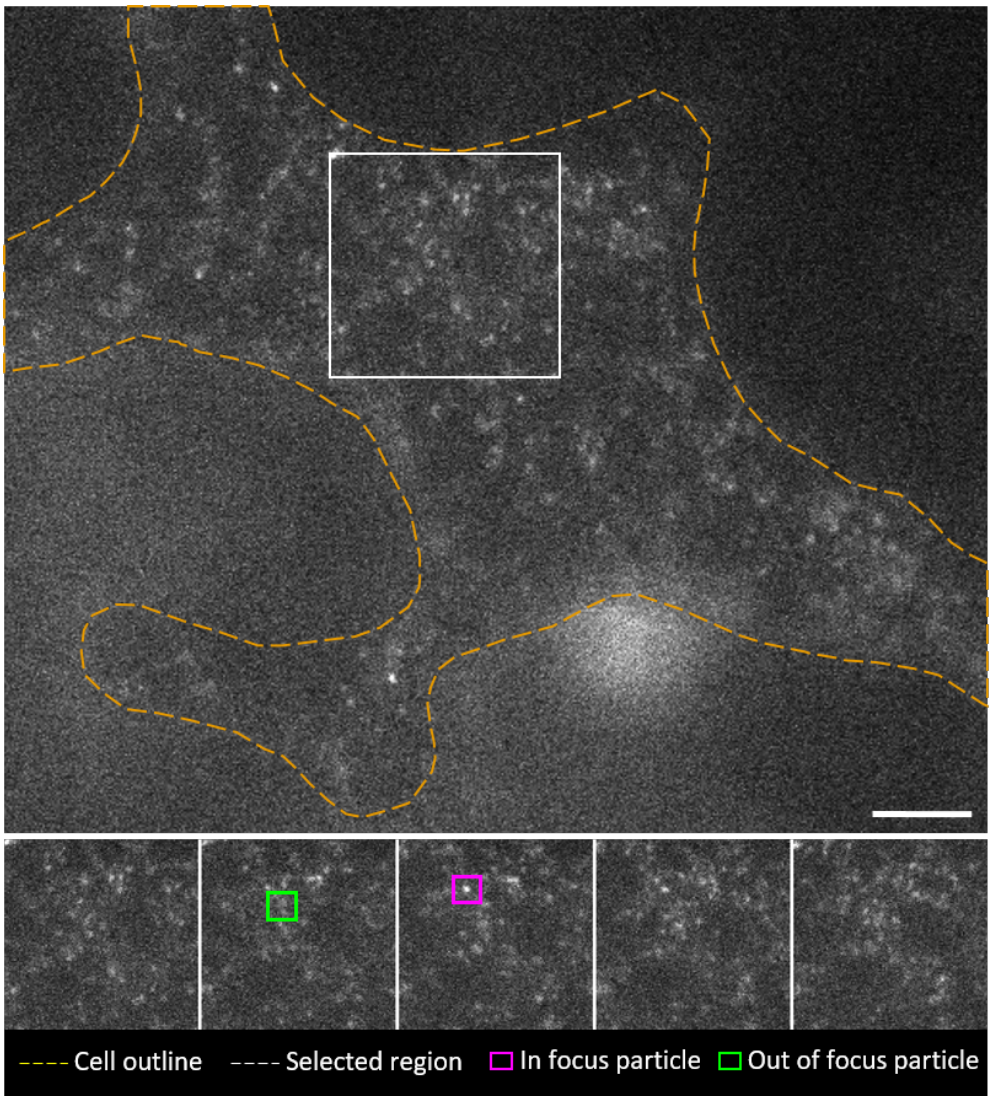


Figure 5.3: Only a portion of particles are in the correct focal plane for single particle tracking in the ER
Top panel: A single frame from a timeseries of single particle movement (mEOS-TAR2) in the ER of tobacco leaf epidermal cells. The outline of the cell is shown by a dotted yellow line and a specific region of the movie is outlined in white. Bottom panel: through this time series the signal of an out of focus particle is highlighted in a green box, whilst an infocus particle is highlighted in magenta. Scale bars 5 µm.

5.2.3 Modifying ER structure and movement for single particle movement analysis

5.2.3.1 Single particle movement in a modified ER structure background

Several different ER structure backgrounds were selected for potential analysis of particle movement through different ER structures. Transient over-expression of RFP-AtLNP1 was selected to induce an increased proportion of cisternae within the ER, whilst RFP-AtRTN1 was selected to increase the proportion of tubules present in the ER (thereby reducing the proportion of cisternae). Though the VAEM system used for this analysis was equipped with appropriate filters, theoretically capable of ensuring that red fluorescence given off by either RFP-AtLNP1 or RFP-AtRTN1 is not captured, the extreme sensitivity of the attached camera resulted in red fluorescence bleeding into the green channel (fig. 5.4, supplementary movie 5.2). This phenomenon, termed spectral bleedthrough, creates a blurring/noise effect on the green channel that is used to detect the single particles. As a result single particles within the ER could not be identified and separated from the increased background fluorescence.

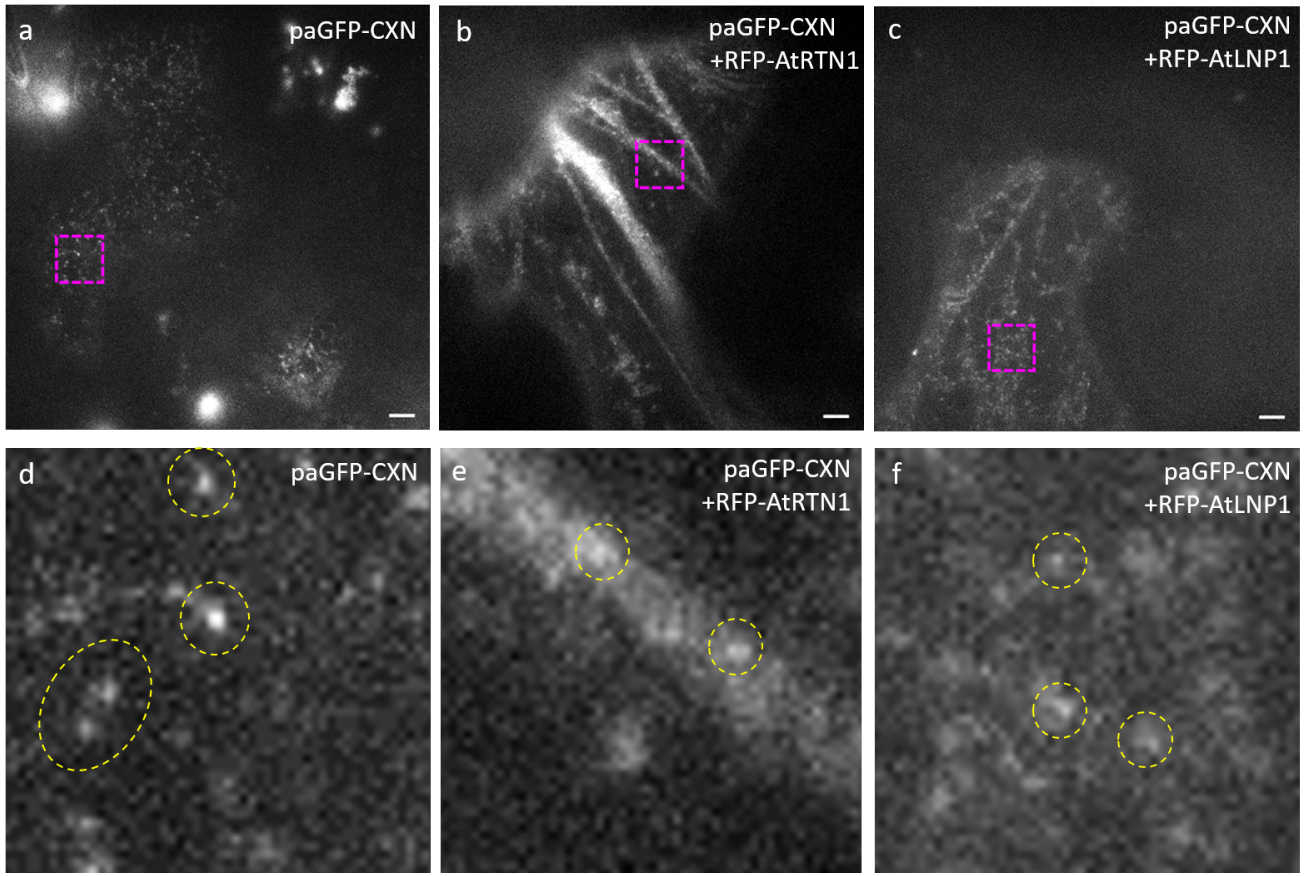


Figure 5.4: Spectral bleedthrough caused by dual colour infiltration
Single frame from a timeseries collected of tobacco leaf epidermal cells obtained using VAEM. (a) Signal from paGFP-CXN alone compared to paGFP-CXN signal on co-expression with (b) RFP-AtRTN1 and (c) RFP-AtLNP1, with the underlying ER structure visible due to spectral bleedthrough. (d-f) Zoomed view of each image, with yellow boxes used to show clear paGFP-CXN particles visible when not using co-infiltration (d). Scale bars 5 µm.

5.2.3.2 Separating single particle movement from gross ER remodelling

To investigate particle movement within the ER without conflating the results with gross ER remodelling, various methods of slowing ER remodeling were explored. Gross structural remodelling of the ER will have the tacit effect of modifying the movement of the particles within the ER. For example, detecting the movement of a single particle moving away from the tip of a tubule is possible when the tubule itself remains stationary (fig. 5.5). However if the tubule is extending at the same rate at which the particle moves in the opposite direction, the particle will not appear to move fig. 5.5). Moreover, if the tubule is extending rapidly, the rate of the overall tubule movement, may disguise the relatively slow movement of a particle in the opposite direction fig. 5.5). This would be the most troublesome scenario, as the movement of particles in the ER would be entirely disguised by the remodelling of the whole ER. Therefore several potential methods of preventing ER remodelling were explored, in order to avoid amalgamating many types of movement into one.

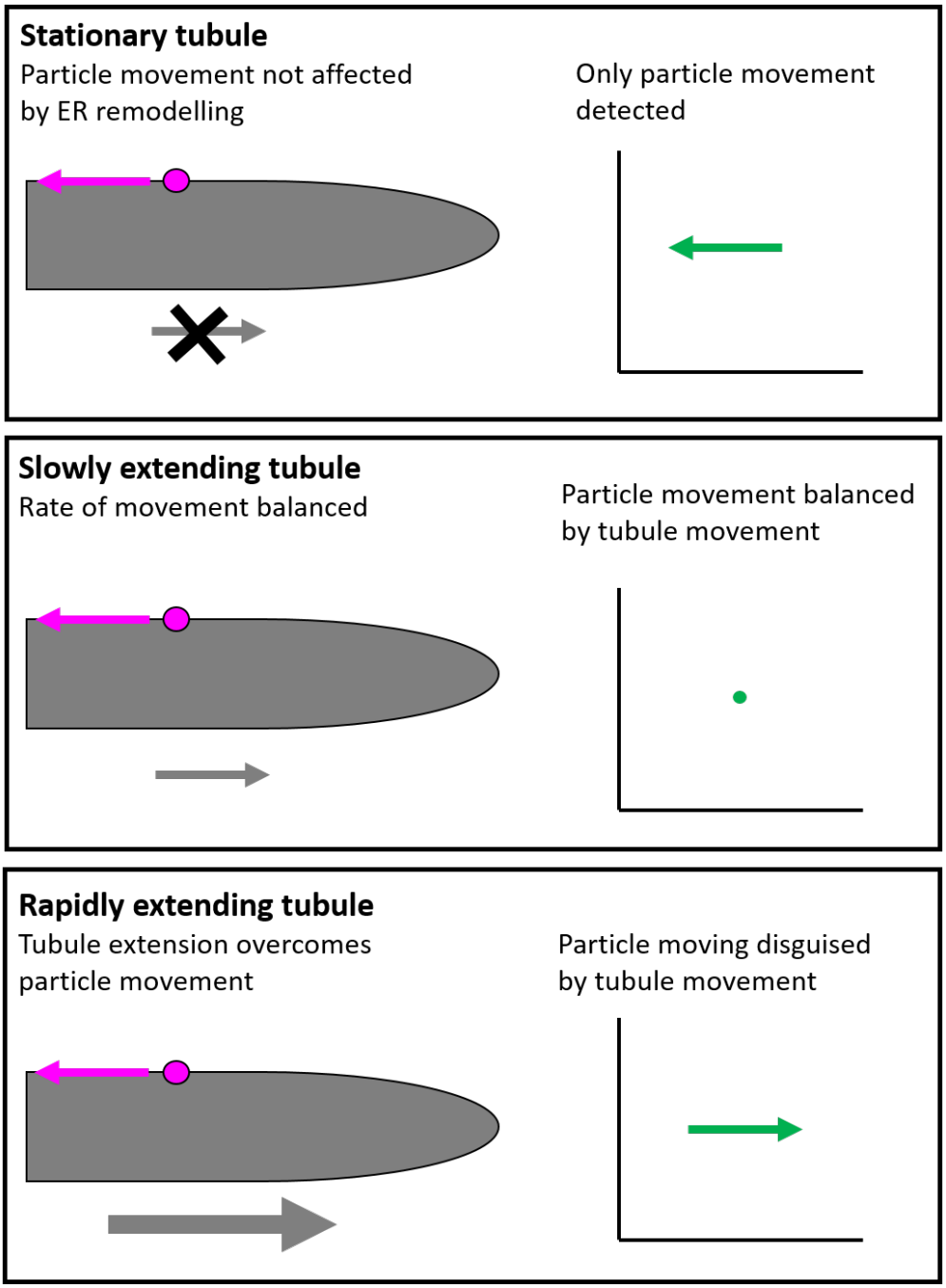


Figure 5.5: The effect of ER remodelling on detected particle movement Schematic representation of the movement of a single particle (magenta) within either a stationary tubule, a slowly extending tubule and a rapidly extending tubule (grey). The rate of movement is represented by the length of the arrow (magenta or grey). The direction of the detected movement of a single particle within a tubule undergoing different movements is shown in green.

Pharmacological treatment with Lat B, a drug that disrupts F-actin formation (Spector *et al.*, 1983), has previously been used to reduce ER remodelling to enable high quality image capture of ER (Bouchekhima *et al.*, 2009). This drug is capable of slowing down the plant ER (see chapter 1) however when effective, it does also affect the structure of the plant ER, in particular the structure and size of ER cisternae even at low concentrations (Pain *et al.* (2019), fig. 5.6 and table 5.1). At a concentration of 1 µM, Lat B does significantly affect ER cisternal area and circularity as well as ER dynamics (reducing both tubule and cisternae speed and persistency). However use of Lat B at this low concentration does not affect several other key measures of ER structure including tubule length, cisternae elongation and roughness, and the area of the polygonal regions (table 5.1). Therefore, though the structure of the ER is only slightly perturbed on treatment with 1 µM Lat B, several key characteristics of ER structure are unaffected and therefore Lat B may be used with care. In addition, higher concentrations of Lat B (20 µM) have a similar effect on ER structure, though interestingly higher concentrations do not appear to affect the dynamics of ER tubules (table 5.1).

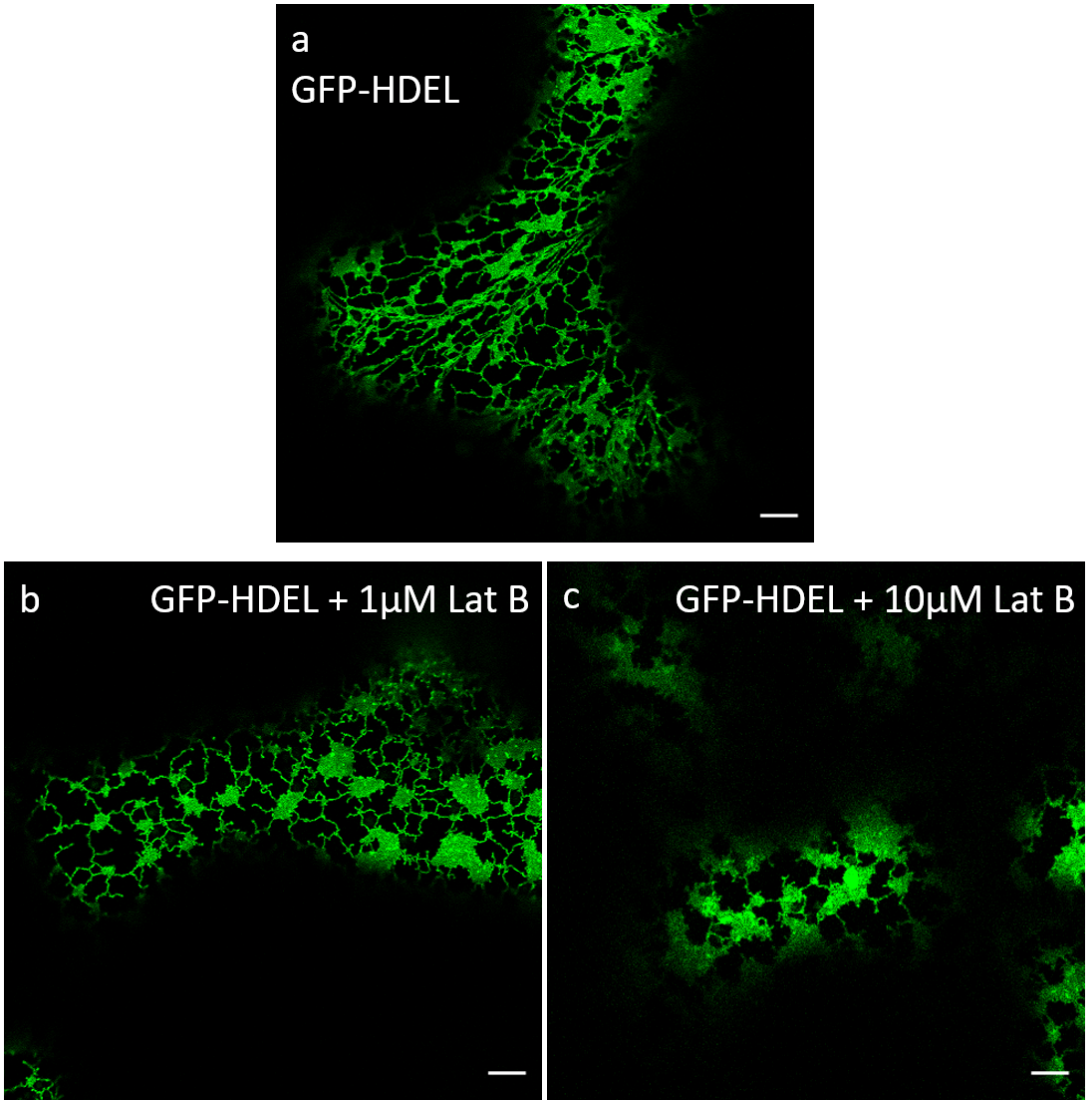


Figure 5.6: Representative images of the effect of Lat B treatment on ER structure
(a) Representative images of ER structure in tobacco leaf epidermal cells transiently expressing GFP-HDEL after treatment with (b) 1 µM Lat B and (c) 20 µM Lat B. Scale bars 5 µm.

Table 5.1: The effect of different concentrations of Lat B on ER structure and dynamics
The effect of 30 minutes treatments of Lat B at 2 concentrations (1 µM and 20 µM) on ER structure and dynamics. Treatments are compared to untreated cells, and all cells are tobacco leaf epidermal cells transiently expressing GFP-HDEL through a 15.18s timeseries. N/S indicates non-significant differences, whilst a p-vale $\leqslant 0.05$ is denoted by *, p-value $\leqslant 0.01$ by ** and p-value $\leqslant 0.001$ by ***. Results are shown for control cells (n=8 biological replicas) and Lat B treated cells (n=9 biological replicas for each Lat B treatment) and obtained over three technical repeats.

Variable classification	Variable	1 µM Lat B n=9	20 µM Lat B n=9
ER structure	Tubule length	N/S	N/S
	Cisternae circularity	*	*
	Cisternae elongation	N/S	N/S
	Cisternae roughness	N/S	N/S
	Cisternae area	*	**
	Polygonal region area	N/S	N/S
ER dynamics	Tuble speed	***	N/S
	Tubule persisteny	***	N/S
	Cisternae speed	**	*
	Cisternae persistency	***	***

Though the perturbation of ER structure can be considered minor, further investigation into alternative methods of slowing ER dynamics was also attempted. Actin markers, such as the actin chromobody (an actin targeted nanobody fused to a fluorescent protein, Rocchetti *et al.* (2014)), have previously been shown to affect the dynamics of Golgi bodies, a proxy for ER dynamics. The movement of Golgi bodies was reduced, whilst the meandering index (the ratio of the displacement to velocity) was not modified, indicating that the Golgi bodies were moving as usual, just more slowly (Rocchetti *et al.*, 2014). Lifeact-Venus (the first 17 amino acids of the actin binding protein Abp140 tagged with a fluorescent protein) has also been shown to modify actin bundle dynamics, slowing the movement of the bundles (tracked using cytoplasmic streaming) compared to wild-type and stable lines of GFP-FABD2 (the C-terminal half of the arabidopsis fimbrin 1 protein) (van der Honing *et al.*, 2011; Voigt *et al.*, 2005). However further work by Rocchetti *et al.* (2014) indicated that the movement of Golgi bodies was not affected by transient over-expression of Lifeact-GFP. FABD2-GFP, a marker that labels fine actin strands not seen on when using Lifeact and the actin chromobody, has also been reported to slow down organelle movement on stable expression in arabidopsis seedlings (Holweg, 2007). These markers could theoretically therefore be used to slow the movement of the plant ER, but without deploymerising the actin cytoskeleton, which may be required intact to maintain proper ER structure. Comparison of three well known actin markers - FABD2-GFP, GFP-Lifeact amd YFP-ActinCB revealed that only transient over-expression of FABD2-GFP slowed down ER remodelling. It also significantly affected ER structure, modifying cisternal geometry and size and polygonal region area (table 5.2).

Table 5.2: The effect of different actin markers on ER structure and dynamics
The effect of transient over-expression of three actin markers (YFP-actinCB, GFP-FABD2 and GFP-Lifeact) on ER structure and dynamics compared to ER structure with no co-expression with actin marker constructs. All cells analysed are tobacco leaf epidermal cells with transient over-expression of the ER lumenal marker GFP-HDEL (OD 0.1) with actin marker constructs (OD 0.1) through a 15.18s timeseries. N/S indicates non-significant differences, whilst a p-vale $\leqslant 0.05$ is denoted by *, p-value $\leqslant 0.01$ by ** and p-value $\leqslant 0.001$ by ***. Results are shown for control cells (n=5 biological replicas) and cells co-infiltrated with actin markers (YFP-actinCB, n=4, GFP-FABD2, n=4, GFP-Lifeact, n=6 biological replicas), obtained over three technical repeats.

Variable classification	Variable	YFP-actinCB n=4	GFP-FABD2 n = 4	GFP-Lifeact n=6
ER structure	Tubule length	N/S	N/S	N/S
	Cisternae circularity	N/S	**	N/S
	Cisternae elongation	N/S	N/S	N/S
	Cisternae roughness	N/S	*	N/S
	Cisternae area	N/S	**	N/S
	Polygonal region area	N/S	*	N/S
ER dynamics	Tubule speed	N/S	**	N/S
	Tubule persistency	N/S	**	N/S
	Cisternae speed	N/S	*	N/S
	Cisternae persistency	N/S	**	N/S

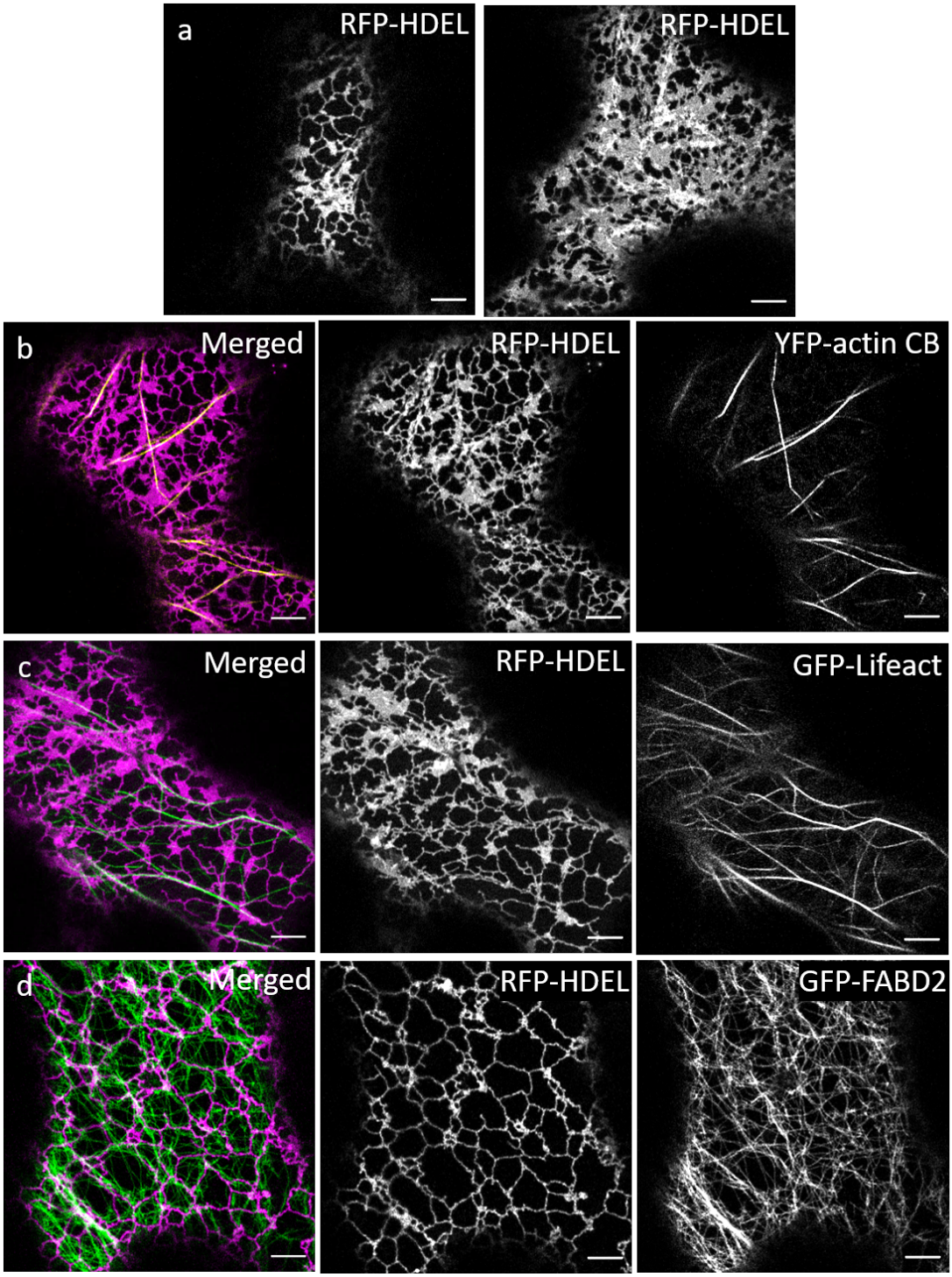


Figure 5.7: Representative images of the effect of actin marker expression on ER structure

Transient over-expression of RFP-HDEL alone (a) and alongside three commonly used actin marker constructs: YFP-actinCB (b), GFP-Lifeact (c) and GFP-FABD2 (d) in tobacco leaf epidermal cells. All images were collected using confocal microscopy, two images or RFP-HDEL alone are displayed in order to capture the variability in wild-type ER structure. Scale bars 5 µm.

Further to modifying ER structure and dynamics, on transient over-expression of GFP-FABD2 approximately 20% of cells demonstrate a fragmented ER network compared to 0% of cells over-expressing YFP-actinCB (n= 24 YFP-actinCB, 35 GFP-FABD2, fig 5.8). This presents a severe concern as ER fragmentation will severely effect the transmission of particles through the ER. This extreme phenotype was only visible on transient over-expression, though more subtle modifications of ER structure, in particular the size of cisternae and polygonal regions, can still be observed on stable expressing in 7 day old cotelydon and root cells (supplementary figs. S11 and S12 respectively). As such it was concluded that transient over-expression of actin markers was inappropriate to slow ER remodelling, either because they do not modify ER dynamics (YFP-actinCB and GFP-Lifeact), or because, whilst modifying ER dynamics, the structure of the ER is also severely affected (GFP-FABD2). Therefore Lat B, though still causing some minor modifications to ER structure, was considered the most suitable method for reducing ER movement for single particle movement analysis in the plant ER.

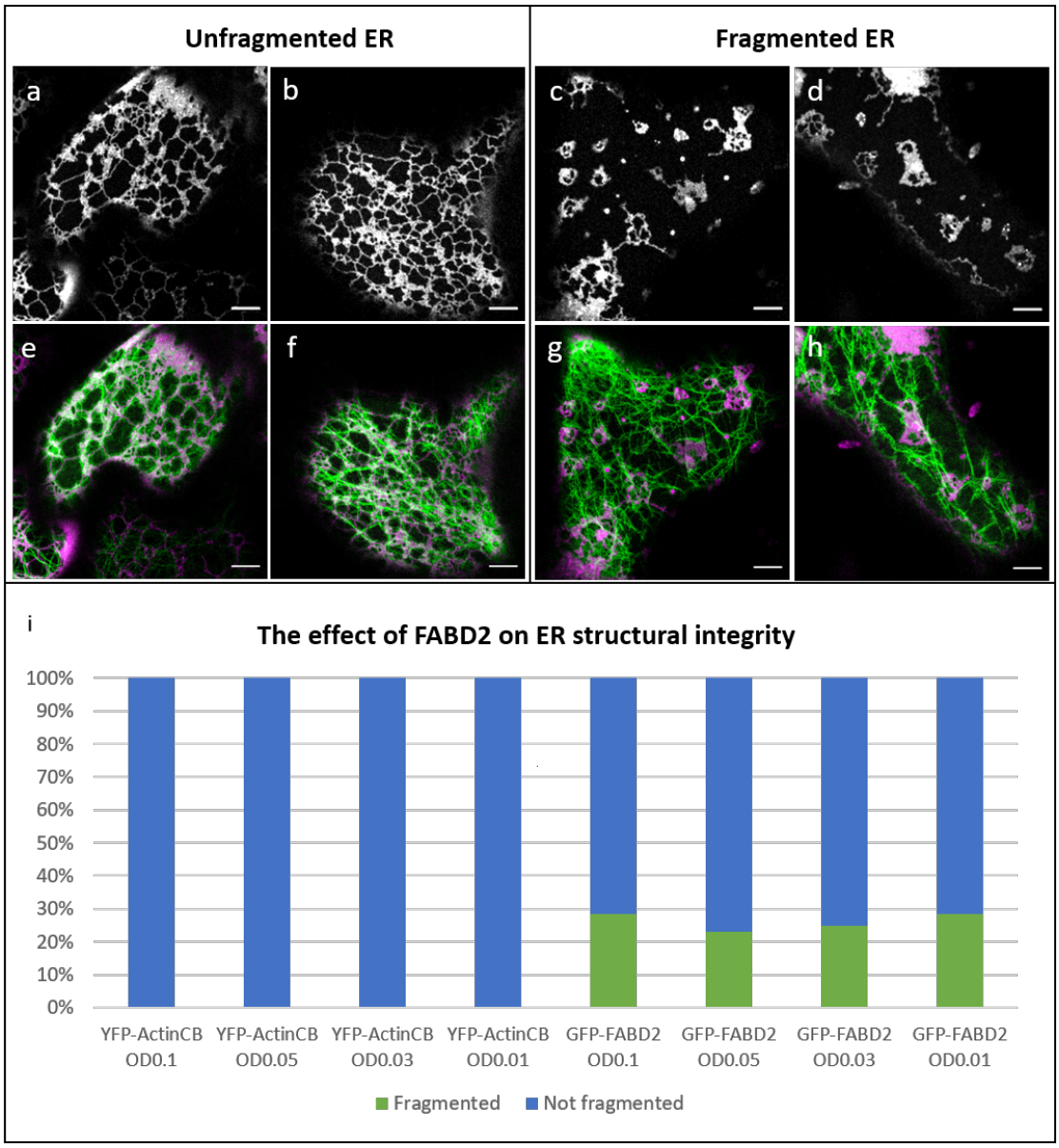


Figure 5.8: Transient over-expression of GFP-FABD2 can cause ER fragmentation

Transient over-expression of GFP-FABD2 with the ER marker RFP-HDEL can leave the ER unfragemented (each part of the ER network is contiguous with the whole) visualized as the ER alone (a,b) or as a composite image (e,f). In other cases the over-expression of GFP-FABD2 can cause frgamentation of the ER producing islands of ER, shown alone (c,d) and as a composite (g,h). The likelihood of ER fragmentation on different levels of transient over-expression of an alternative ER marker YFP-actinCB (n=24 biological replicas) compared to over-expression of GFP-FABD2 (n=35 biological replicas). Results obtained over four technical replicas, scale bars 5 µm.

5.2.4 Single particle movement in the plant ER

Due to the constraints of single particle imaging, including challenges in achieving an appropriate level of expression and bleaching single molecules, reliable data was obtained for only three single particle treatments. Data was obtained for the movement of a fluorescently tagged entire protein (mEOS-Tar2, an ER localised protein involved in auxin biosynthesis, Kriechbaumer *et al.* (2016)) and a truncated ER membrane protein (paGFP-CXN, Runions *et al.* (2006)) (fig. 5.9). Timeseries of single particle movement was also obtained of the truncated ER membrane protein paGFP-CXN after treatment with 2.5 µM Lat B for 1 hour. Though a concentration of 2.5 µM Lat B is slightly higher than the minimum concentration tested using confocal microscopy, there were no discernible effects on ER structure caused by increasing the concentration of Lat B (table 5.1). In addition treatment with Lat B at a concentration higher than 2 µM has been reported as being effective within 30 minutes (Hamada *et al.*, 2014), allowing for more rapid modification of ER structure if necessary.

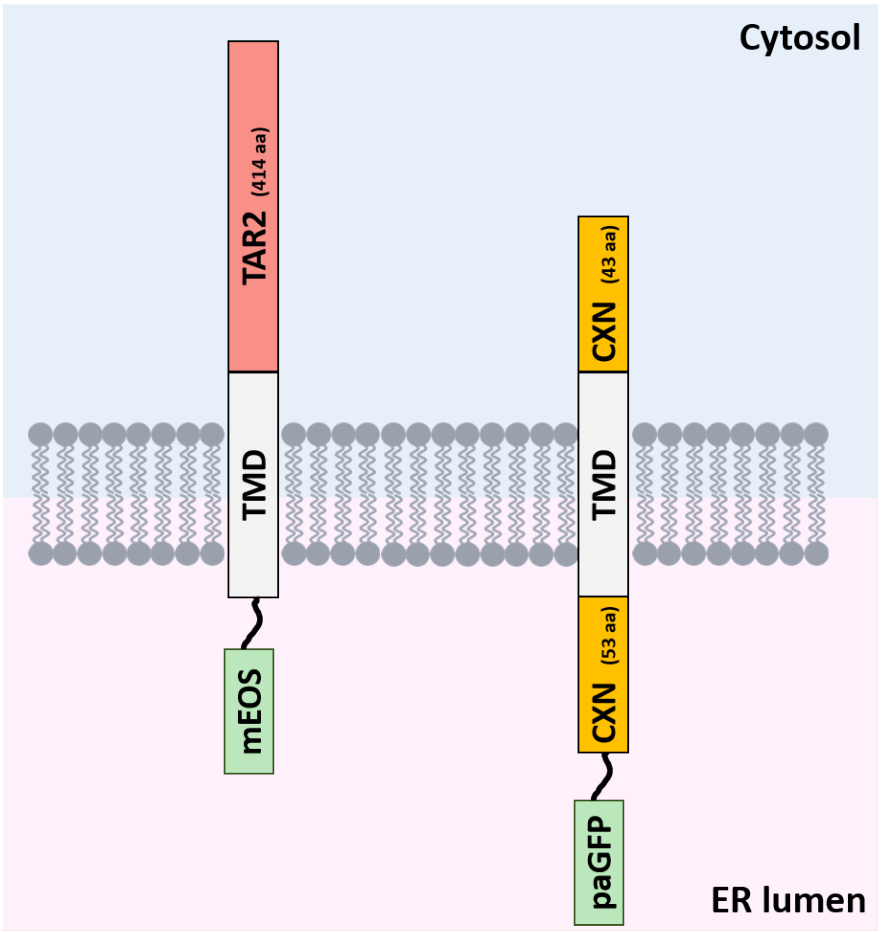


Figure 5.9: Schematic representation of particle structure within the ER membrane
Schematic of the structure of two protein constructs that were tracked moving through the membrane: mEOS-TAR2 (functional protein, 414 amino acids in length) and paGFP-CXN (truncated protein, 125 amino acids in length). The added fluorescent protein is predicted, in both cases, to localise within the ER lumen.

Two methods for single particle tracking (SPT) were tested in order to track single particle movement. Firstly single particles were tracked using TrackMate (Tinevez *et al.*, 2017), an ImageJ plugin designed to track the movement of bright particles (fig. 5.10a-c, supplementary movie 5.3). TrackMate requires an estimation of particle diameter and a relative threshold intensity for particle detection, followed by some basic constraints on particle linkage in tracks. A typical result from this

analysis, spatially mapping single particle speed to regions of the ER, revealed an approximately normal distribution of particle speed throughout the ER of both mEOS-TAR2 and paGFP-CXN. However on treatment with Lat B it appears that particles moved faster within the ER cisternae and more slowly through the ER tubules (fig. 5.10d-f).

These results were replicated using an automated single particle tracking method developed by Wilson *et al.* (2016), which requires an estimation of particle diameter, the relative noise of the image and the approximate number of particles present in each frame. Again some constraints on track linkage were also required. The results revealed a similar pattern that track speeds are uniformly distributed throughout the ER except after treatment with Lat B (fig. 5.11a-c). It also provides additional information on the density of particles identified and analysed. This revealed 'hotspots' of particle density, most likely due to more particles remaining in focus in a particular region (fig. 5.11d-f). There was no identifiable correlation between these points of increased intensity and noise.

The data produced by TrackMate was taken for further analysis of the single particle dynamics in the plant ER. The maximum speed of particle movement is not normal, nor is it from a similar distribution of all three treatments when considering all the available treatments (fig. 5.12), though all three distributions are likely to be classed as a subset of beta distributions (supplementary fig. S13) and so cannot be analysed easily using statistics. However, there is trend in the maximum speed of ER movement, suggesting that paGFP-CXN moves faster that mEOS-TAR2 and paGFP-CXN moves even faster after treatment with Lat B (n=7 mEOS-TAR2, n=4 paGFP-CXN and n=5 paGFP-CXN after Lat B treatment). Track displacement (measured in pixels) could be normalised (supplemental fig. S14) and therefore can be assessed for statistical significance. One-way ANOVA indicates that there is a significant difference between the groups (p-value =

$< 2 \times 10^{-16}$) whilst post-hoc mean comparison testing also indicates that each group is significantly different to the other (p-value $= < 2 \times 10^{-16}$ for each pairwise comparison, fig. 5.12).

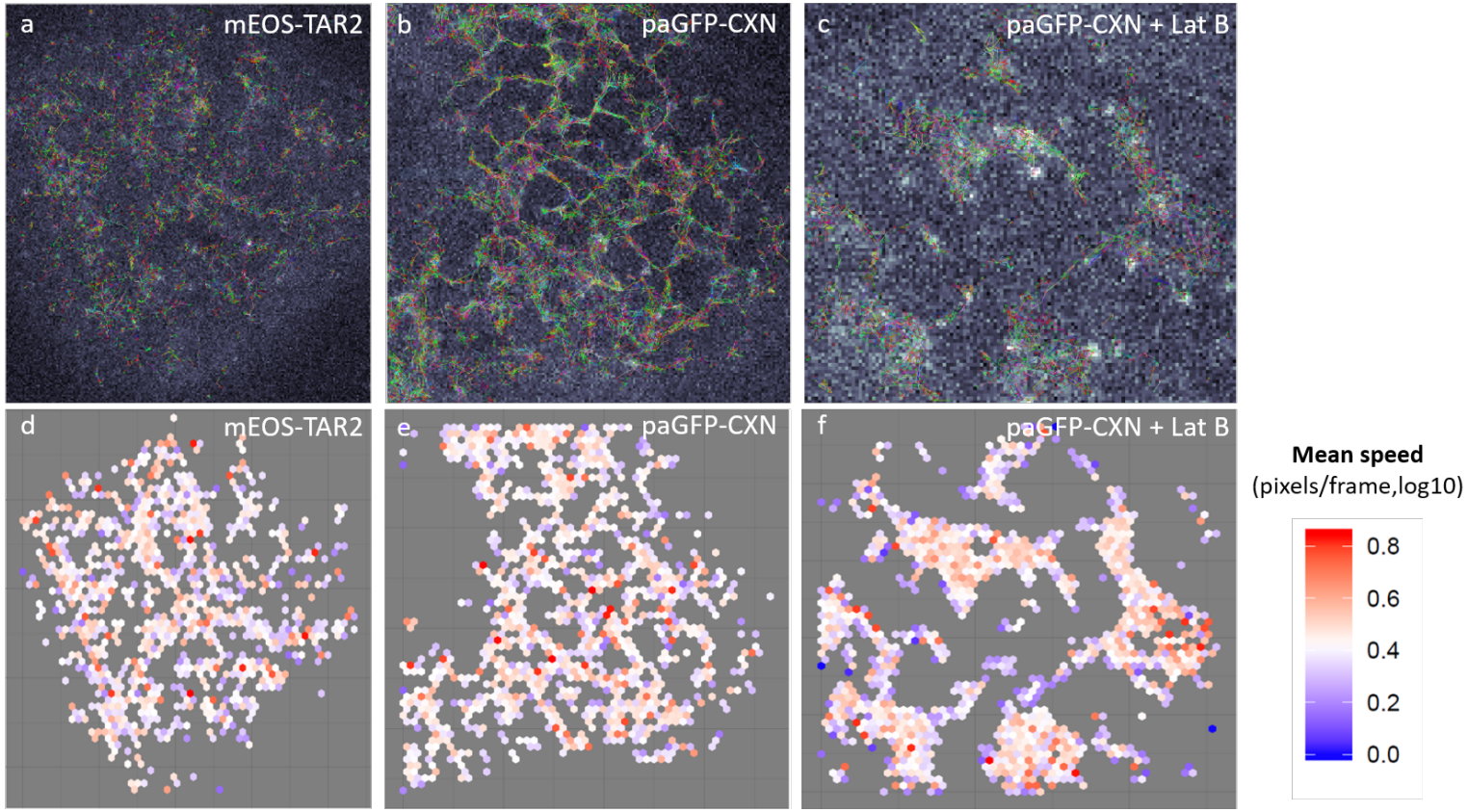


Figure 5.10: SPT using TrackMate

Particle tracking outputs for three sample representative VAEM microscopy timeseries of particle movement in tobacco leaf epidermal cells. Particles were identified and tracked using the ImageJ plugin TrackMate. Two different particles were tracked: mEOS-TAR2 (a) and paGFP-CXN (b), SPT of paGFP-CXN after treatment with Lat B is also included (c). A hexagonal heatmap of mean particle speed is displayed for the tracked particles (d-f).

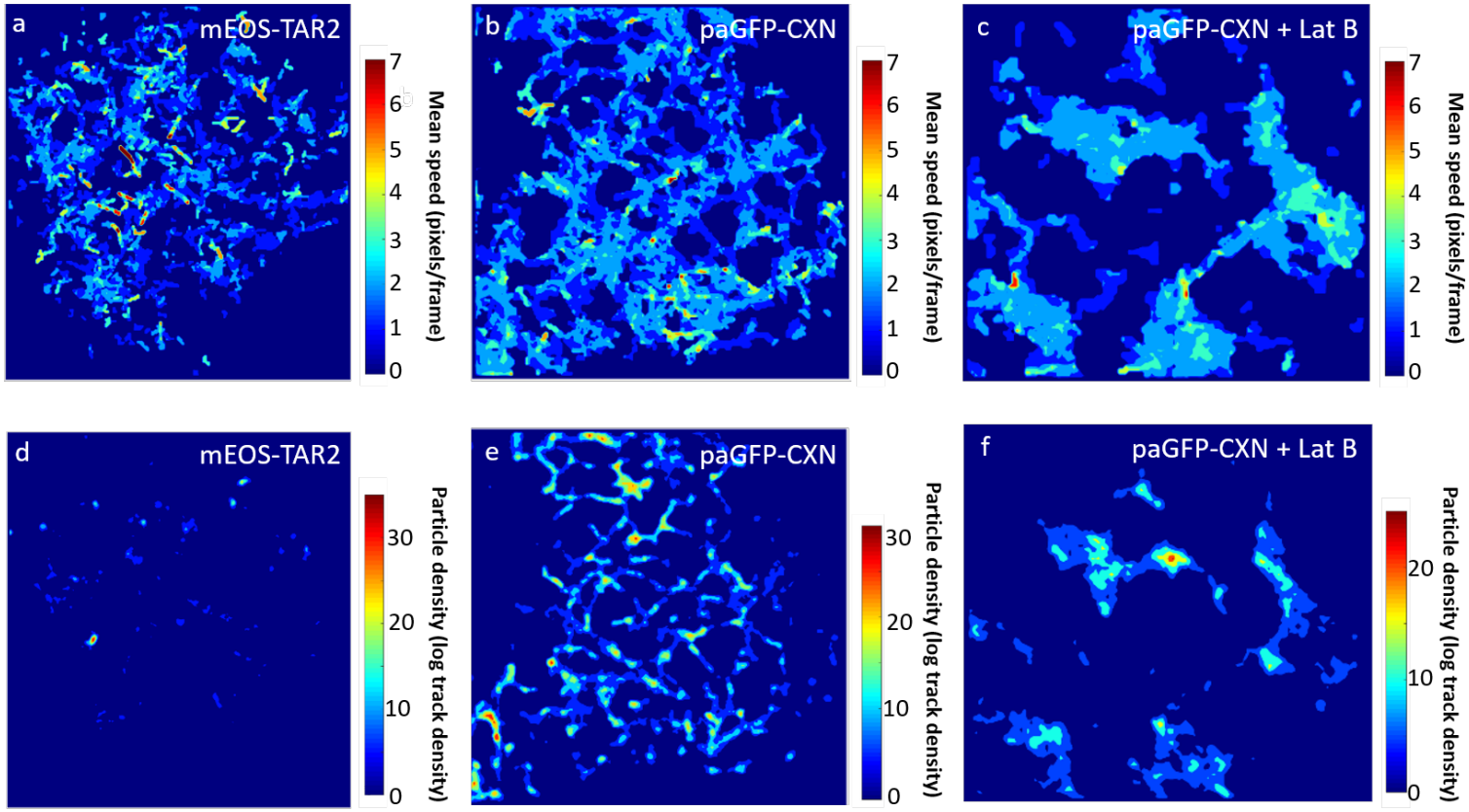


Figure 5.11: Automated SPT results
Particle tracking outputs for three sample representative VAEM microscopy timeseries of particle movement in tobacco leaf epidermal cells. Particles were identified and tracked using an automated SPT software devloped by Wilson *et al.* (2016). Two different particles were tracked: mEOS-TAR2 (a,d) and paGFP-CXN (b,e), SPT of paGFP-CXN after treatment with Lat B is also included (c,f). A heatmap of the mean detected speed is displayed (a-c) alongside a heatmap if detected particle density.

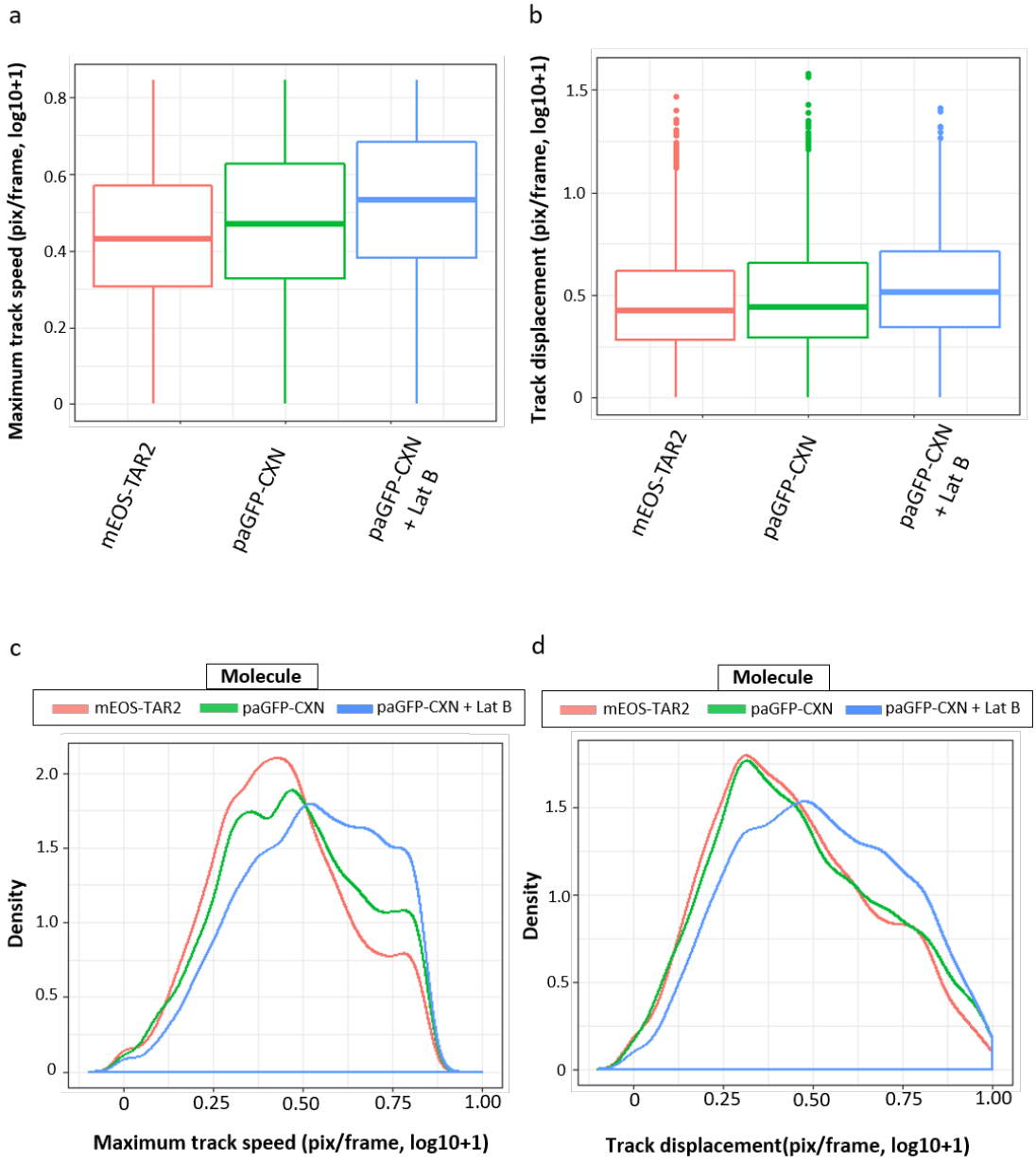


Figure 5.12: Comparison of single particle track speed and displacement Comparison of single particle track speed and displacement displayed as box plots (a,b) and showing the density distributions (c,d). Tracks were obtained for mEOS-TAR2 (n=7 biological replicas), paGFP-CXN (n=4 biological replicas) and paGFP-CXN (n=5 biological replicas) tracks after treatment with Lat B. Results obtained over four technical replicas.

5.3 Discussion

Single particle tracking has become a mainstream method to understand protein-protein interactions and membrane composition in plant cell membranes (Martiniere *et al.*, 2012; McKenna *et al.*, 2019; Wan *et al.*, 2011; Chen *et al.*, 2018; Hutten *et al.*, 2017). The application of VAEM SPT to plant and mammalian plasma membranes and the mammalian ER (Burnecki *et al.*, 2019) would indicate that it has potential for becoming a novel tool for understanding particles in the plant ER. However there are several barriers to universal uptake of this method for plant ER analysis including the physical location and structure of the ER and the additionally challenging photoproperties of plant leaf epidermal cells (table 5.3). The first challenge is that, in order to track single particles within a structure, these particle must not be so tightly packed together that they cannot be separated from one another, causing all single particles to blur into one. The majority of plant imaging is performed on whole plants or leaf segments as opposed to cells in suspension culture. Leaf epidermal cells are known to form an undulating surface (Ivakov and Persson, 2013) and as such, only relatively small areas of the cell that are tightly appressed to the coverslip, can be illuminated using VAEM. Plant imaging by light microscopy is inherently challenging due to the lager number of autofluorescent compounds and structures within plant cells. Chloroplasts in particular are a large source of autofluorescence (Agati, 1998; Vitha and Osteryoung, 2011) but also cellulose (cell wall, Pöhlker *et al.* (2012)) and phenols (vacuole, cells wall, chloroplasts, Roshchina and Karnaukhov (1999)). This autofluorescence, particularly that which originates from the chloroplasts, can be sufficient to drown out the weak signals produced by single particles within the plant ER. The plant ER is situated relatively deep in within plant cells compared to the plasma membrane, the typical target for SPT. The depth at which the ER exists within the cell requires a more adaptive

control of the VAEM incident angle of illumination. Microscopy systems with easily adaptable and controllable incident angles are only available on more modern optical systems such the one used in this study (specifically the iLas^2 TIRF system). Finally the structure and the dynamics of the ER cause particular challenges to SPT in plant ER. The ER is highly dynamic and so single molecule dynamics are conflated with gross ER remodelling - requiring specialist techniques to slow down the ER or separate the two types of movement. Due to the presence of the lumen between the two lipid bilayers, the plant ER is thicker than the plasma membrane and it is possible that both surfaces of the plant ER can be identified using VAEM.

Despite these challenges, this work demonstrates that many of these issues can be resolved (table 5.3). Ensuring an appropriate distribution of single molecules can be achieved by reducing the expression levels of fluorescently tagged proteins of interest. This is achieved simply, by reducing the measured optical density of agrobacteria in the infiltration media that is used to infect the plant (fig. 5.2). Use of the circular illumination field allows for maximum illumination and good penetration of the evanescent wave to the underlying ER structure. This ring illumination also ensures minimal interference patters and shadowing across the sample field of view. Autofluorescence is overcome by using appropriate filters to block as much autofluorescence as possible and is naturally limited by imaging at the abaxial leaf surface, whereas chloroplasts are naturally much more abundant at the internal face of the cell. The challenges posed by the 3D nature of the plant ER could not be overcome within this study. However SPT analysis revealed that the instantaneous diffusion of in focus single particles could still be analysed, and this in turn could inform on single particles movement through the ER (fig. 5.3). Resolving the issue of the highly dynamic nature of the ER proved more challenging as it appears that the dynamics of the ER may be intrinsically linked

to its structure. It is not unreasonable to assume that the structure of the ER may affect the overall dynamics of both lumenal and membrane single particles. Therefore teasing out the movement of particles in a manner that it is not conflated with ER remodelling is challenging. We tested several known methods to reduce ER remodelling while aiming to maintain ER structure. Latrunculin B is the most widely known pharmacological method applied to slow/halt actin based movements within the cell by depolymerising the actin cytoskeleton (Pain *et al.*, 2019; Sparkes *et al.*, 2008; Griffing *et al.*, 2017; Nakano *et al.*, 2009). Though the structure of the ER was perturbed at both the tested concentrations of Lat B treatment, only some aspects of ER structure were modified and ER remodelling was successfully reduced (fig. 5.6). Another potential method to reduce ER remodelling explored in this work is the application of three known actin cytoskeleton markers: FABD2, Lifeact and an actin chromobody (fig. 5.7). Several of these markers have been previously shown to modify the dynamics of other cell organelles, in particular Golgi bodies (Rocchetti *et al.*, 2014) and actin bundles (van der Honing *et al.*, 2011), which have been proposed as a suitable proxy for ER membrane surface movement. The actin chromobody was a particularly suitable candidate to slow ER remodelling without modifying ER structure as the meandering index of the Golgi bodies was unchanged (Rocchetti *et al.*, 2014), whilst suggesting that the ER structure was unaffected as Golgi and the ER are physically connected (Sparkes *et al.*, 2009b). Assessing the impact of several actin markers on ER structure revealed that only FABD2 is capable of modifying ER dynamics but over-expression severely affects the structure of the overlying ER, an effect that cannot be remedied by reducing the expression of the marker in a transient system (fig. 5.8). The fact that the actin chromobody does not slow ER remodelling, whilst slowing Golgi movement, could simply be that Golgi body movement is a poor proxy for ER movement, or it could be because the actin chromobody only affects the movement of particles within the ER membrane. There could be some precedent for a modified actin cytoskeleton

affecting the movement of the ER membrane as FRAP experiments performed on the ER membrane marker GFP-CXN revealed that, when co-expressed with the dominant-negative myosin tail domain YFP-XIK, there was a reduction in the mobile fraction of GFP-CXN (Sparkes *et al.*, 2009a). Expression of the XIK tail domain perturbs the movement of Golgi, peroxisomes, and mitochondria, while leaving the actin cytoskeleton intact therefore slowing the majority of actin-based movement within the cell, without depolymerising the underlying cytoskeleton (Sparkes *et al.*, 2008, 2009a). A reduction of the motility of proteins in the ER membrane may therefore be responsible for contributing to slowing Golgi body movement, without necessarily slowing ER remodelling.

Table 5.3: A summary of the challenged of applying VAEM to SPT in the plant ER
A summary of the challenges facing VAEM SPT in plant ER and the solutions developed throughout this work.

Challenge	Solution
Undulating leaf surface	The coverslip is pressed against the cell surface and relatively small in focus regions are used for image collection (as in confocal microscopy)
Autofluorescence	Imaging of abaxial leaf epidermal cells where chloroplasts are preferentially located on the surface furthest from the incident light
The depth of ER within the cell	Use a ellipical illumination field
The ER is dynamic	Lat B can be used to reduce ER remodelling, however a complete halt to ER remodelling most likely cannot be achieved without altering ER structure
The ER is 3D	SPT can be performed on particles that are in the correct plane for a brief period and still be informative of single particle movement

The structure of the ER in stable arabidopsis lines is also affected by stable FABD2 expression (supplementary figs. S11 and S12. This raises serious questions about the use of FABD2 as the sole marker of actin, particularly in transient expression systems where the ER can be reduced to a collection of discontinuous structures. Over-expression of both Lifeact and the actin chromobody fail to significantly slow down the remodelling of the ER, but also do not significantly modify the structure of the ER. This was somewhat unexpected as both Lifeact and actin chromobody over-expression show a thicker actin network as opposed to FABD2, previously thought to be due to the markers causing increased actin bundling or preferential marking of actin bundles, yet these markers are the most able to preserve the structure of the ER.

As a result of the aforementioned experiments, Lat B was selected as the best potential method to reduce ER remodelling. We were able to track various particles moving through the ER using two potential tracking methods, both of which gave similar results in terms of the localisation of fast moving particles and their displacement between frames (figs. 5.10 and 5.11). The 3D nature of the plant ER has thus far limited analysis to approximately instantaneous diffusion, with the majority of particles tracked only for a few frames. This limits analysis somewhat as the algorithms designed for more complex analysis of particle movement (including identifying indicators of passive vs active diffusion) require particles to remain in frame for significantly longer periods of time (McKenna *et al.*, 2019). However instantaneous diffusion can still be an informative measure of single particle movements and could already identify differences in the movement of proteins through the membrane potentially based on protein size (fig. 5.12). In addition the increase in the rate of protein movement (specifically paGFP-CXN) after Lat B treatment may be due to actin slowing CXN movement through the ER membrane when present. Though SPT in the plant ER has proven to be

challenging, the work here presents the first steps towards the use of VAEM in ER SPT, and has been used to measure particle dynamics and to compare between several different conditions.

6 | General discussion

Contents

6.1 On image quantification 250
6.2 On the role of the Lunapark proteins in ER structure 255
6.3 Lunapark structure in relation to protein function . . 261
6.4 Cisternae biogenesis 265
6.5 SPT in the plant ER 266

6.1 On image quantification

As microscopy imaging technologies continue to develop rapidly, methods to extract relevant data from the images produced must endeavor to keep pace with development. Sub-cellular imaging, particularly of structures like the ER which show high variability already in wild-type condition, require extensive analysis in order to identify significant changes in structure and dynamics. AnalyzER is designed to provide as many metrics and analysis methods as is feasible under a single GUI, so that it can be used to answer a range of common as well as novel questions about the ER and the distribution of proteins throughout it. The development of these tools requires a difficult balance - easy to use tools and interfaces typically allow a user to perform a rapid analysis, however by definition, their simplicity makes multiple applications challenging. Alternatively tools with more complex interfaces, with many different pathways for analysis, are more challenging for users to apply. Typically complex tools, for their advantages in analysis capability, require additional user input and experience, as well as a commitment to understand the many different analysis options provided. AnalyzER

is clearly designed as a latter analysis tool, requiring some understanding of the basics of image analysis. However, it is deliberately designed to allow many user options and it is published alongside extensive documentation and tutorials to try and aid user understanding. The complexity of AnalyzER is chosen deliberately to allow applications across a number of different imaging platforms and to ensure it can be applied to multiple image types. One of the clearest examples of the importance of providing a range of available user choices is the segmentation of the ER from the image background. The most common method of segmentation of signal from noise/background is to partition the image histogram into two groups, minimising the within group variation and separating light pixels from dark. This is suitable for most ER images but when segmenting arabidopsis ER marked with GFP-HDEL, which causes bright accumulations of fluorescence within fusiform bodies, the partition will typically only select the fusiform bodies and the dimmer ER structure will be partitioned into the background, making analysis impossible. AnalyzER however presents the user the choice to partition the image histogram at multiple points, allowing for the segmentation of both bright and dim structures from the background. Though the user is required to make a selection of which number of partitions to use, by enabling user choice AnalyzER can be applied to commonly used GFP-HDEL arabidopsis lines and tobacco epidermal cells, as opposed to being limited to one or the other. Though the AnalyzER interface is complex, recommended standard settings are automatically applied when using the software for the first time, and once a standard pipeline for the images collected on a particular system has been established, analysis can be very rapid.

A further challenge of image analysis in general is ensuring that the segmentation of the structure and the generated outputs are as accurate as possible. AnalyzER provides inbuilt analysis checks, comparing the segmented structure of the ER to a manually digitised ground truth. This allows the user to quantify, for a dataset, the

mean accuracy of the analyses performed. Ideally a measurement of accuracy could be provided for each image analysed, however manually digitised ground truth creation is incredibly time consuming, with a single image requiring a minimum of two hours for accurate ground truth creation. Instead we provide an image display for each stage of the analysis, allowing the user to visually inspect each stage of the analysis process to enable user identification of failure within the software. Ideally we would also be able to provide a direct comparison of the accuracy of AnalyzER compared to other available ER software, such as those developed by Bouchekhima *et al.* (2009), Sparkes *et al.* (2009a), Ueda *et al.* (2010), Lin *et al.* (2014), Lin *et al.* (2017) and Griffing *et al.* (2017). However many of these software packages cannot provide a direct comparison simply due to the imaging requirements they propose: Bouchekhima *et al.* (2009) requires 3D images of the ER, with the rate of ER remodelling reduced using low dose Lat B in order to collect sufficient quality images. The analysis provided by Lin *et al.* (2014) and Lin *et al.* (2017), while useful for assessing tubule segmentation accuracy, can only consider very small regions of ER and does not provide a measurement for ER cisternal structure. Sparkes *et al.* (2009a) does not specifically model tubule and cisternal area but an altered version of the persistency analysis which is already employed by AnalyzER. Other issues have included lack of accessibility to software due to an absence of a permanent dedicated online repository provided for storage by the scientific community (GitHub was founded in 2008 and so was not in common use when many versions of software were published). In addition, some software packages have had their information redacted or manuals limited in preparation of patent applications and so are not freely available to users. Finally comparison to other software can be problematic, as analysis accuracy can sometimes relate to the level of previous experience by the user and the amount of experience with a given software. As such basic comparisons between the accuracy of different software packages is inherently challenging and likely to produce biased or uninformative

results.

AnalyzER was designed to answer as many as of the common ER structure and dynamics questions as possible within the field, and was tested against as many types of known ER structure and dynamics modification agents as was feasible. This included known ER modifying agents including: pharmacological treatments affecting different aspects of cellular function (BFA and Lat B), abiotic stress (heat shock) and protein over-expression (RFP-AtLNP1, RFP-AtLNP2 and RFP-AtRTN1) (Pain *et al.*, 2019). It has also been used to test the effect of transient expression of actin markers on ER structure, in particular FABD2, Lifeact and an actin chromobody (van der Honing *et al.*, 2011; Riedl *et al.*, 2008; Rocchetti *et al.*, 2014). Up until now the effect of these markers on other cellular components has been limited to the movement of organelles such as Golgi bodies (Rocchetti *et al.*, 2014) and actin streaming itself (van der Honing *et al.*, 2011), with no specific focus on ER structure and dynamics. AnalyzER has helped to reveal the effect of these commonly used markers on the ER structure.

Another common question question that arises when investigating ER resident proteins, is the distribution of these proteins throughout the ER. Three methods were developed to analyse the distribution of proteins through the ER: tubules are assessed using a technique that identifies peaks and troughs in intensity along tubules, identifying whether the presence of one protein might exclude another from that region (Pain *et al.*, 2019). A technically similar approach is applied to analysing the distribution of markers through cisternae by assessing relative cisternae intensity in radial bins around the edge of the cisternae. This can be used to identify whether there is an even distribution of fluorophores through the cisternae. However, this does not provide information on the distribution of small puncate or minor structural aberrations within cisternae. Instead a GLCM approach is applied to identify variation in intensity through cisternae as a

measurement of image texture. This can provide metrics on fluorescent protein distribution through cisternae that is more complex than that which is detected using simple radial bin analysis for normalised intensity measurements.

The application of two methods to measure the remodeling of the ER - optical flow analysis and persistency mapping tackles the challenge of capturing ER movement from two angles. Firstly optical flow analysis captures the rate at which the ER remodels, whereas persistency mapping captures the proportion of the ER that remains in place over a defined period of time. This is particularly important as it provides two methods of analysis of ER movement within a single interface, and brings us away from the use of only qualitative representations of ER remodeling rates through temporal colour coding (Kriechbaumer *et al.*, 2018; Griffing *et al.*, 2017; Cao *et al.*, 2016) which though useful in displaying changes in movement, offers little/no quantitative information on the rate of this movement. Historically ER movement has been equated approximately to the movement of the Golgi bodies, due to their ability to form a single secretory unit with the surface of the ER (Langhans *et al.*, 2012), resulting in Golgi body movement often being used as a proxy for ER membrane surface movement.

We hope that by ensuring all code and datasets produced by during the development of AnalyzER are publicly available, and by providing both extensive documentation aimed at different levels of user (a tutorial designed for novel, surface users and an extensive manual for experienced users), this software will be of use to answer a variety of questions, not restricted solely to the plant ER.

6.2 On the role of the Lunapark proteins in ER structure

Arabidopsis possess two Lunapark protein orthologues AtLNP1 and AtLNP2, both of which localise to the ER. AtLNP1 demonstrates a cisternae specific localisation, whilst AtLNP2 localises throughout the entire ER network. Transcription of *AtLNP1* and *2* has been detected in young arabidopsis tissues (7 day old roots and shoots), and *AtLNP2* transcript has been detected in all tested mature tissues (35 day old rosette leaves, siliques, flowers and buds). Both *AtNP1* and *2* however have been predicted to be transcribed throughout all mature tissues, albeit at a relatively low level (BAR eFP Browser, Winter *et al.* (2007)) so it is possible that failure to detect *AtLNP1* transcription is due to sensitivity issues with RT-PCR analysis.

Both AtLNP1 and 2 are required for proper structure of the ER. Loss/reduction of either *AtLNP1* or *AtLNP2* transcription results in an aberrant ER network. When visualised in arabdiospsis leaf epidermal cells using Rhodamine B, there is a significant reduction in the proportion of the ER network that is classed as cisternae, and it is this alteration is most likely responsible for the significant modifications to the area of the polygonal regions surrounded by the ER network. Reduction of both *AtLNP1* and *2* transcription within the same plant results in an increasingly aberrant ER structure which also shows a reduction in the area and proportion of detectable cisternae, and increase in tubular length and significantly modified polygonal region areas (Kriechbaumer *et al.*, 2018). In addition, the ER of *amilnp1lnp2* knockdown mutants shows some residual bulges within its structure that have a significantly different geometry and structure to typical cisternae. This result has been subsequently confirmed by (Ueda *et al.*, 2018) and was implicated

in disruption of fuisform body structure.

Transient over-expression of AtLNP1 and 2 in tobacco results in an increase in the the area of cisternae within the ER (Kriechbaumer *et al.*, 2018; Pain *et al.*, 2019). The area of the induced cisternae appears to increase in a dose dependent manner with the concentration of agrobacteria within the infiltration media used to infect the tobacco plants (Kriechbaumer *et al.*, 2018). Transient over-expression of AtLNP2 affects many features of ER structure, including tubule length and cistenae and polygonal region area and geometry (Pain *et al.*, 2019). However these structural modifications appear to be a knock-on effect from the increased cisternal area. Transient over-expression of AtLNP1 however, not only modifies the area of cisternae, but also results in the formation of a large number of small, densely clustered tubules that span the small polygonal regions between cisternae. Therefore not only is AtLNP1 able to induce cisternae on transient over-expression but it is also able to induce the formation of clustered tubules between cisternae.

Stable over-expression of AtLNP2 in arabidopsis plants revealed that AtLNP2 is distributed throughout the ER network, as it is the case on transient over-expression. However unlike on transient over-expression, the structure of the ER appears relatively unperturbed. This is most likely due to the expression of AtLNP2 in arabidopsis lines being somewhat reduced compared to transient expression, potentially due to the likelihood of multiple insertion events by agrobacterium on transient over-expression vs fewer events on stable expression (Sheludko, 2008). Alternatively, stable over-expression of AtLNP2 could be limited in arabidopsis as high levels of AtLNP2 transcription may be lethal, allowing only individuals with relatively low expression to survive the growth process. Finally it is possible that the plant itself is downregulating the transcription of AtLNP2 on stable expression as opposed to transient expression, either through a silencing mechanism or by

up-regulating the expression of antagonistic ER shaping proteins (such as AtRTN1 and 3, Sparkes *et al.* (2010)). Using confocal microscopy for visualisation, stable over-expression of AtLNP1 is low and difficult to detect but AtLNP1-GFP appears to localise to cisternae with a few small punctae visible through the ER structure. Use of a more sensitive technique, VAEM, revealed that what appeared as cisternae were in fact aggregations of tubules that were tightly clustered with AtLNP1-GFP particularly localised to junctions between these closely packed tubules.

Loss of both Lnp1p and mLNP1 has been reported to result in the induction of cisternae as opposed to loss of cisternae seen on reduction of AtLNP1 and 2 transcription (Chen *et al.*, 2012, 2015; Kriechbaumer *et al.*, 2018). Increasing expression of mLNP1 reveals the formation of 'clusters of densly branched tubules', within which mLNP1 localised preferentially to junctions within these cells (Shemesh *et al.*, 2014). This phenotype is highly reminiscent of the phenotype observed on stable over-expression of AtLNP-GFP in arabidopsis. In addition, though these tubule clusters could only be imaged over a relatively short period of time (approximately 12 seconds) the tubule junctions marked by AtLNP1 appeared to be very stable throughout the period of observation. mLnp1 has been proposed to play an essential role in stabilising nascent three-way junctions, both in terms of reducing the movement of the nascent junctions and in increasing the persistency of nascent junctions (Chen *et al.*, 2015). It stands to reason that in order to generate clusters of tubules that are distinct from the entirety of the ER network, the junctions between the tubules must remain relatively stable in order to prevent rapid collapse/assimilation into the network. Perhaps in order to generate cisternae AtLNP1 functions in a similar manner as mLnp1, stabilising tubular junctions within the tubular clusters that make up cisternae, as opposed to stabilising junctions throughout the entire ER network like mLnp1 (Chen *et al.*, 2015). Perhaps as well as inducing cisternae formation, AtLNP1 functions as mLNP1

and is required to stabilise tubular junctions, except that AtLNP1 predominantly stabilises junctions within these tubular clusters, as opposed to mLNP1 which stabilises the majority of three-way junctions within cells (Chen *et al.*, 2015). However, when the expression of mLNP1 is sufficiently high, this ER structure undergoes a significant shift, forming a highly tubulated structure with very few identifiable junctions (Shemesh *et al.*, 2014). This phenotype was not observed on either stable or transient over-expression of AtLNP1 in arabidopsis and tobacco, respectively.

The cisternae induced by transient over-expression of AtLNP1 and 2 show different characteristics, revealed by co-expression with both lumenal markers and ER structural modifying proteins (table 6.1). AtLNP1 does not co-localise with either RFP-AtRTN1 and 3, and the lumenal markers GFP-HDEL and RFP-HDEL are excluded from the lumen of AtLNP1 induced cisternae (Pain *et al.*, 2019). AtLNP2, however, does co-localise with both RFP-AtRTN1 and 3 both within the induced cisternae and throughout the entire ER network. Not only is the lumenal marker RFP-HDEL present within AtLNP2 induced cisternae, it also shows a more even distribution throughout the cisternal lumen of AtLNP2 induced cisternae than the average control cisternae. It should be noted that though AtRTN1 and AtLNP1 are predicted to interact by FRET-FLIM analysis (Kriechbaumer *et al.*, 2018), these measurements were performed on the nuclear membrane where AtRTN1 and AtLNP1 co-localise on over-expression in tobacco, but they do not co-localise within the ER, suggesting that this interaction may not be taking place under native conditions. This leads to a model of two 'types' of cisternae that can be induced by AtLNP1 and/or AtLNP2, respectively. The evidence suggests that AtLNP1 induces cisternae that are composed of a dense tubular matrix. In order to form this matrix, AtLNP1, a S-type protein, must exclude R-type proteins (such as AtRTN1 and AtRTN3, Shemesh *et al.* (2014)) in order to induce the extreme

negative membrane curvature required for a tight clustering of tubules. The tubules within this cluster may exclude lumenal markers either because they possess a reduced lumen diameter in order to enable dense clustering, or perhaps because the presence of many sharp bends/kinks within ER tubules limits the flow of lumenal markers into the cluster. AtLNP2 however, does not form many small tubules between or within cisternae that can be identified on either stable or transient over-expression in arabidopsis and tobacco, respectively. Moreover, AtLNP2 does co-localise with both RFP-AtRTN1 and 3, both throughout the entirety of the ER network and within AtLNP2 induced cisternae. Furthermore, RFP-HDEL shows an even distribution throughout the lumen of the induced cisternae, even more so than in control cisternae. In this case AtLNP2 and reticulon proteins may be able to work together to generate a flat sheet, perhaps by balancing the relative local concentrations of S- and R-proteins. This could produce the canonically described cisternae, composed of two flat sheets of membrane appressed together, with an entirely contiguous lumen allowing for the even distribution of RFP-HDEL through the lumen of the cisternae.

Table 6.1: Summary of the features of AtLNP1 and 2 induced cisternae
A summary of the salient features of cisternae induced by either AtLNP1 or 2.

	AtLNP1	**AtLNP2**
Transient over-expression induces cisternae	Yes	No
Transient over-expression induces tubule aggregates	Yes	No
Co-localisation with RFP-AtRTN1	No	Yes
Co-localisation with RFP-AtRTN3	No	Yes
RFP-HDEL present within the cisternal lumen	No	Yes
Even distribution of RFP-HDEL within cisternal lumen		Yes

The presence of cisternae with an alternative structure has been suggested in mammalian cells by Nixon-Abell *et al.* (2016) and Schroeder *et al.* (2019). Schroeder *et al.* (2019) described the formation of nanoholes within cisternae, around the edges of which RTN4 was found to localise. Nixon-Abell *et al.* (2016) however, proposed that many detected cisternae were composed of dense, tubular matrices.

Though the presence of nanoholes within plant cisternae is entirely plausible, no such holes were identified during this work. However the presence of dense, tubular matrices are formed on stable over-expression of AtLNP1 in arabidopsis. Furthermore it seems likely that these densely tubulated regions are also formed on transient AtLNP1 expression in tobacco, however the density of these matrices is so extreme that they cannot be resolved using confocal microscopy, as is the case when analysing the structure of mammalian cisternae. Endogenous labelling of RTN4 in fixed Cos-7 cells reveals two types of cisternae, identified by the presence or lack of RTN4 within the cisternae (Nixon-Abell *et al.*, 2016). It is possible that the presence or absence of RTN4 within cisternae marks two stages of transition in cisternae formation or perhaps it is advantageous for plant cells to maintain two pools of structurally distinct cisternae. If we consider that AtLNP1 and 2 mediate two stages of cisternae formation AtLNP1 may be required for the first stage of cisternae formation, recruiting and tightly packing a large surface area of ER membrane into a small area in preparation of AtLNP2 to form cisternae with a contiguous lumen. Alternatively there may be advantages for a combination of cisternae composed of a dense tubular matrix versus cisternae composed of flattened sheets with a contiguous lumen. Mammalian cells often exhibit a stacked cisternae phenotype nearer to the core cells, a feature that has been suggested to maximise the number of polysomes that are able to aggregate on the surface of the ER for protein synthesis (Terasaki *et al.*, 2013). However cisternal stacking is not possible at the cell periphery due to a restriction of vertical space between the two cell membranes at the cell periphery. Interestingly both Xenopus and human LNP induce the formation of stacked bilyar disks when purified and mixed with liposomes composed of phosopholipids maintained in a similar ratio to that of the ER (Wang *et al.*, 2018). Mutations around two coiled-coild domains present in these proteins inhibit this function, though a complete truncation of the zinc finger domain does not inhibit this function (Wang *et al.*, 2018). Nixon-Abell *et al.* (2016) have suggested that in

the place of stacked cisternae at the peripheral edges of cisternae, dense tubular matrices could fulfil the function of stacked cisternae by creating a region of densely aggregated ER, providing a larger ER surface area within a relatively planar space. In the case of plant cells, the presence of a large vacuole appresses the ER to the cell surface, functionally limiting the ER to a two-dimensional space. Therefore cisternae stacking is unlikely to occur in plant cells (and indeed has never been identified in plant cells). Therefore it stands to reason that the formation of many cisternae composed of tubular matrices could be essential for high levels of protein production in plants, particularly at younger stages when the plant is growing rapidly (and when *AtLNP1* transcription is at its highest). However there may also be an advantage to maintaining a population of cisternae with the more canonical structure. Metabolons, aggregations of components of metabolic pathways such as the biosynthesis of the defence compound dhurrin in sorghum, are associated with the ER (Laursen *et al.*, 2016; Srere, 1987; Hawes *et al.*, 2015; Kriechbaumer *et al.*, 2016). The presence of a large, contiguous, flattened ER surfaces within cells could be crucial for the assembly and scaffolding of metabolons, by creating a large surface over which the components of the metabolon can assemble.

6.3 Lunapark structure in relation to protein function

Several trunctions of AtLNP1 and 2 were created in order to identify structural domains that may play a role in the function of AtLNP1 and 2 (table 6.2). Severe N-terminal trunctions result in the mislocalisation of AtLNP1 and 2 to either unknown punctae or to suspected ER exit sites. All other truncations, including shorter N- and C-terminal truncations e.g. to the start of the zinc finger domain

still localise to the ER, but can show a modified localisation of either throughout the entire ER (AtLNP1 truncations: L1T1, L1T2 and L1T4) or become restricted to cisternae (AtLNP2 truncations: L2T1 and LNP2-ZF). mLnp1 has an N-terminal myristoylation site that is required for mLnp1 function (Moriya *et al.*, 2013; Wang *et al.*, 2016c). A G2A mutation at this site not only abolishes the ability of mLNP1 to modify ER structure, but also results in re-localisation of mLnp1 to throughout the entire ER network (Moriya *et al.*, 2013; Wang *et al.*, 2016c). No such N-myristoylation site is predicted for AtLNP1 and AtLNP2, however a trunction of the first 20 amino acids is sufficient to swap the localisations of AtLNP1 and 2, with AtLNP1 becoming distributed throughout the ER. However it appears that both these truncations are still able to induce ER structural changes. The modified localisation of AtLNP1 is also accompanied by an ability to co-localise with RFP-AtRTN1, which does not occur on expression of full length AtLNP1. Therefore though AtL1T1 is still able to induce cisternae, it is likely that the cisternae induced by AtL1T1 have a different structure compared to those induced by full length AtLNP1, reminiscent of the cisternae induces by AtLNP2 over-expression. Work by Wang *et al.* (2016c) revealed that the insertion of a short linker sequence prior to the first TMD of mLnp1 also results in mLnp1 distribution throughout the whole network.

A truncation of the final 92 amino acids of AtLNP2 also results in a modified distribution through the ER, with AtLNP2-ZF becoming localised specifically to cisternae. The same truncation in AtLNP1 does not reveal any structural changes, though exhibits poor expression on transient over-expression in tobacco. Truncations of mLnp1 to just before the zinc finger domain results in a modified mLnp1 localisation to throughout the entire ER, whilst truncations to after the zinc finger domain at a more C-terminal site does not show the same modified structure (Wang *et al.*, 2016c). Mutation of four key cysteine residues within the

zinc finger domain has also been implicated in the function of mLnp1 and Lnp1p. Substitution of the four zinc finger cysteine residues to alanine in Lnp1p results in a non-function Lnp1p (Chen *et al.*, 2012), but has been reported as having no effect on AtLNP2 (Ueda *et al.*, 2018). However substitution of cysteine with proline residues which are designed to disrupt the secondary structure of the zinc finger, produces a construct that is unable to rescue the AtLNP2 knockout phenotype (Ueda *et al.*, 2018). This indicates that the zinc finger domain is important for the function of AtLNP2, however the cysteine residues themselves are not essential for the function of the zinc finger domain, but rather the structure of the zinc finger domain.

Table 6.2: Summary of the localisation and key features of all AtLNP1 and 2 truncations
A summary of all AtLNP1 and 2 truncations created as part of this work. The truncation name, the remaining amino acids and the truncation localisation are all included.

Protien	Truncation name	Terminus	Remaining amino acids	ER localisation	Details
AtLNP1	AtL1T1	N	21-408	Yes	Throughout the ER
AtLNP1	AtL1T2	N	83-408	Yes	Throughout the ER
AtLNP1	AtL1T3	N	106-408	No	Unknown punctae
AtLNP1	AtL1T4	N	120-408	Yes	Throughout the ER
AtLNP1	AtL1T5	N	142-408	No	ER exit site
AtLNP1	AtLNP1-ZF	C	1-316	Yes	Cisternae specific
AtLNP2	AtL2T1	N	21-408	Yes	Cisternae specific
AtLNP2	AtL2T2	N	85-408	Yes	ER and unknown punctae
AtLNP2	AtL2T3	N	108-408	No	Unknown punctae
AtLNP2	AtL2T4	N	122-408	No	ER exit site
AtLNP2	AtL2T5	N	143-408	No	ER exit site
AtLNP2	AtLNP2-ZF	C	1-316	Yes	Cisternae specific

6.4 Cisternae formation

The exact function of AtLNP1 and 2 in modifying the structure of the ER is as yet unknown. However it seems likely that they either play a role in the induction of cisternae or the maintenance of cisternae. Though both roles could be attributed to AtLNP1 and 2, it is most likely that AtLNP1 and 2 are required for the initial formation of cisternae, and then may play a subsequent role in cisternae maintenance. Dynamics analysis of *amilnp1lnp2* does not reveal the formation of any cisternae as might be expected if the role of AtLNP1 and 2 was limited to cisternae maintenance. Due to the dynamic nature of the ER, very little is known about the process of cisternae biogenesis. Identification of cisternae biogenesis by AtLNP2 is particularly challenging, as AtLNP2-GFP is localised throughout the ER network, making identification of nascent cisternae almost impossible. Instead we chose to focus on cisternae biogenesis by AtLNP1 as AtLNP1 punctae are trackable and are a likely starting point for the formation of cisternae. Two potential models for cisternae formation were explored: cisternae formation by the expansion of junctions already marked by AtLNP1, or aggregation of AtLNP1 puncate to form a cisternae. In order to capture cisternae biogenesis, light sheet microscopy was used. Of the 36 events of cisternae formation that could be observed, all followed a model of formation by aggregation of punctae. These cisternae are not necessarily entirely stable, with subsequent splitting and re-aggregation events, however the size of nascent cisternae formed by AtLNP1 aggregation was not observed to drop below the size of the original identified punctae. This suggests that cisternae formation requires aggregation of ER membranes, which can then be stabilised by AtLNP1 to form nascent cisternae. This type of cisternae formation may be advantageous as it allows for rapid cisternae formation (occurring in less that a second), and allows for rapid formation within a highly dynamic structure.

6.5 SPT in the plant ER

SPT across the plasma membrane is now ubiquitously applied to understand the interaction of particles and membrane nanodomains on a molecular scale. It has been used to identify the formation of complexes required for pathogen recognition and responses (McKenna *et al.*, 2019), to assess the variable dynamics of molecules such as inositol trisphosphate receptors which exist as stationary and mobile pools (Smith *et al.*, 2014) and to identify variable rates of lumenal flow through different ER structural domains (mammalian cells, Holcman *et al.* (2018)). SPT in the plant ER offers additional challenges to the methods applied to SPT in the plasma membrane, in particular the 3D nature of the plant ER, the depth of the ER within the cell and the gross dynamic remodeling of the plant ER that can conflate actin-mysoin driven movement of the whole structure with the movement of single particles in the membrane.

We have shown that it is likely that the the dynamics of the ER are intrinsically linked to its structure as all methods to slow or stop ER remodeling also affected the structure of the ER. Interestingly, a commonly used actin marker construct, GFP-FABD2, was shown to have detrimental effects on the structure of the ER when transiently over-expressed in tobacco and shows causes minor ER structural defects on stable expression in arabidopsis. In addition, though several studies have shown that all the actin markers tested (actin chromobody, lifeact and FABD2) affect the movement of subcellular organelles (Rocchetti *et al.*, 2014; van der Honing *et al.*, 2011; Holweg, 2007), neither the actin chromobody nor lifeact had any detectable effect on ER remodeling. It is possible that cytoplasmic streaming and Golgi body movements are poor proxies for ER movement. It may also be possible that the methods used to detect the movement of the ER, which by nature are more complex than those used to detect discrete organelle movement (Pain *et al.*,

2019), are not sufficiently sensitive to detect changes in the ER movement.

Our SPT analysis has revealed that larger proteins move more slowly through the ER membrane which was to be expected. Previous work has suggested that there is a weak positive correlation between artificial aggregate size and the rate of diffusion (Kucik *et al.*, 1999). In addition, treatment with Lat B was shown to increase the speed of particle movement throughout the entire ER surface. This result was particularly surprising as previous work has suggested that Lat B either slows down the rate of particle movement (when tested using photoactivation of particles, Runions *et al.* (2006)) or does not affect particle movement (when tested using FRAP, Sparkes *et al.* (2009a)). It is possible that these techniques provide different results due to the necessity of only testing movement in subregions of the ER. Photoactivation techniques require activation of a random area of the cell, which will often include tubules. Our results have shown that, though particles move through the ER more quickly in total, they appear to move more slowly through tubules than cisternae. Therefore, photoactivation of tubules, and measurements through tubular structures alone may result in falsely reduced rates of particle movement. FRAP, however, is only performed on cisternae and also is not as sensitive as single particle techniques, potential results in an inability to detect more raped particle movement within the cisternae in particular after treatment with Lat B.

7 | Future Work

Contents

7.1 Extending the applications of AnalyzER 268

7.2 Exploring the mechanism behind Lunapark function . 269

7.2.1 Establishing Lunapark membrane topology 269

7.2.2 Creation of modified Lunapark proteins to investigate protein domain function 271

7.2.3 Generating an AtLNP2 knockout line 274

7.3 The biogenesis of cisternae 274

7.3.1 Proteomics analysis 275

7.4 Single particle movement in the ER 276

7.4.1 Exploring new methods 276

7.1 Extending the applications of AnalyzER

Future work on the AnalyzER software will focus on the application of AnalyzER to eukaryotic organisms beyond plants, extending AnalyzER so that it can work through the Z-domain and incorporating other published analysis routines targeted to assessing the structure and dynamics of other organelles. Thus far AnalyzER has only been applied to plant leaf epidermal cells, where the ER structure is functionally 2D as the ER is appressed to the cell surface by the large internal vacuole (Pain *et al.*, 2019). Confocal microscopy is a commonly used, powerful tool for live cell imaging that improves image quality by only detecting light from a single plane. The combination of the naturally 2D structure of the ER and the use of confocal microscopy ensures that all images of the ER that have tested by AnalyzER are 2D. However there are many eukaryotic cells possessing ER with a

3D structure, this includes several plant cell types, including root hair cells (Zheng and Chen, 2011) and trichomes (Zhang *et al.*, 2013). Beyond the kingdom Plantae, the majority of cells currently under study by scientists have a 3D ER structure, such as the model mammalian cell line Cos-7 (Terasaki *et al.*, 2013), yeast cells (West *et al.*, 2011) and mouse neuronal cells (Wu *et al.*, 2017). Extending AnalyzER to work on 3D images will require a calculation on the angle of curvature of the ER structure, and the ability to identify and link the ER across multiple z-planes. Fortunately however, 3D images of the ER can be simply captured using confocal microscopy by applying a Z-stack routine to capture thin optical sections moving through Z.

AnalyzER can also be extended to include and analysis of other subcellular organelles, not just the ER. This could provide a single user interface that is capable of capturing the movement and structure of many cellular components such as the actin cytoskeleton, Golgi bodies, mitochondria and so on. This could be completed simply by integrating published packages such as TrackMate (Tinevez *et al.*, 2017), which is commonly used to track discrete organelles such as Golgi bodies (Sporsheim *et al.*, 2015) and mitochondria (Wilson *et al.*, 2019)); FibrilJ, that is used to quantify actin structure (Sokolov *et al.*, 2017)) and the 'analyze particles' routine from ImageJ that has been deployed alone or within other analysis routines to assess endocytosis (Bayle *et al.*, 2017) and Golgi body structure (Jarvela and Linstedt, 2012).

7.2 Exploring the mechanism behind Lunapark function

7.2.1 Establishing Lunapark membrane topology

The orientation of AtLNP1 and AtLNP2 in the ER membrane has been predicted, but not yet established. AtLNP1 and 2 are predicted to be oriented within the ER membrane so that both the N- and C-terminus of the protein are facing the cytosol, with only a small region of protein between the two TMDs facing the lumen of the ER. This orientation has been confirmed for mLNP1 (Moriya *et al.*, 2013). Confirmation of the orientation of AtLNP1 and AtLNP2 can be obtained by tagging both the N- and C-termini of AtLNP1 and 2, producing four constructs: AtLNP1-roGFP, roGFP-AtLNP1, AtLNP2-roGFP and roGFP-AtLNP2. roGFP2 is a green fluorescent protein that exhibits different peaks in excitation that are dependent on the local glutathione redox potential (E_{GSH}) of the subcellular compartment to which it is localised (Schwarzländer *et al.*, 2008). The plant ER has a different E_{GSH} to the cytosol, with exposure to the lumen of the ER resulting in oxidation of roGFP2 and exposure to the cytosol resulting in reduction of roGFP2. Depending on the oxidation state of roGFP2, roGFP2 will be excited more efficiently at either 405 nm (the oxidised form, typical of ER lumen localisation) or 488 nm (the reduced form, typical of a cytosolic localisation) (Brach *et al.*, 2009; Schwarzländer *et al.*, 2008). This topology analysis would be of particular interest as, should AtLNP1 and 2 orient within the membrane in such a way that the N- and C-terminal domains face the ER lumen, an alternative theory of the mechanism of ER function could be developed. Namely, this alternative orientation would results in a topological structure that is somewhat similar to

that of CLIMP63, a mammalian protein with no identified plant, bacteria or yeast orthologues, that induces cisternae (Sandoz and van der Goot, 2015). CLIMP63 maintains the structure of cisternae by forming intralumenal bridges between the two cisternal membranes, stabilising cisternae width (Klopfenstein *et al.*, 2001). The stabilisation of cisternae by CLIMP63 is mediated by a large C-terminal domain that localises to the ER lumen and undergoes oligomerization to form the intralumenal bridges (Klopfenstein *et al.*, 2001). Should it be revealed that the C-terminal domain of AtLNP1 and 2 localises to the ER lumen, the opposite of what is predicted, it could be theorized that AtLNP1 and 2 act as CLIMP63 proteins.

7.2.2 Creation of modified Lunapark proteins to investigate protein domain function

Several AtLNP1 and 2 truncations generated as part of this work showed altered localisations throughout the ER. Truncations of the first 20 amino acids of AtLNP1 and 2 results in a modified localisation whereby AtLNP1 relocalised from cisternae to throughout the entire ER, whilst AtLNP2 undergoes an opposite re-localisation (fig. 4.16 and 4.17). In order to investigate how the first 20 amino acids may affect AtLNP1 and AtLNP2, chimeric proteins with the first 20 amino acids of AtLNP1 and 2 are swapped, will be generated (fig. 7.2). The creation of chimeric proteins is required as the first 20 amino acids of AtLNP1 and 2 show 55.0% amino acid identity (fig. 7.1) and hence are poor candidates for site directed mutagenesis in order to modify this domain. The chimeric proteins will be used to assess whether the absence of the first 20 amino acids simply results in a misfolding of the protein, causing re-localisation, or whether the sequence of the first 20 amino acids is essential in determining the localisation of AtLNP1 and 2 within the ER.

AtLNP1 (1-20aa):	M	A	V	G	E	K	E	H	E	G	T	V	V	E	S	G	G	E	K	N
	|	|			:		|	.	|	|	.	|	|	|	.	|		|	.	|
AtLNP2 (1-20aa):	M	A	-	-	Q	-	E	Q	E	G	A	V	V	E	K	G	-	E	P	N

Key

| Single conserved residue

: Residues with similar properties (>0.5 in the Gonnet PAM 250 matrix)

. Residues with weakly similar properties (≤0.5 in the Gonnet PAM 250 matrix)

- No match

Figure 7.1: Pairwise alignment of the first 20 amino acids of AtLNP1 and 2

Pairwaise alignment of the first 20 amino acids of AtLNP1 and AtLNP2 performed using the ClustalW Matcher (EMBOSS). Residues are considered to have similar properties if they score >0.5 in the Gonnet PAM 250 matrix. Residues are considered to posses weakly similar properties if they score ⩽0.5. Conserved residues are highlighted in green.

In additional, initial C-terminal truncations of AtLNP1 and AtLNP2 revealed that removal of the final 92 C-terminal amino acids of AtLNP2 (from the start of a predicted zinc finger domain to the end of the protein) results in a modified localisation. AtLNP2 localises throughout the ER network, whilst AtLNP2-ZF-Clover shows a cisternae specific localisation (fig. 4.18). Firstly it needs to be confirmed that the re-localisation of AtLNP2 is due to the removal of the zinc finger alone by creating a C-terminal truncation of the final 62 amino acids - up to the end of the predicted zinc finger domain (fig. 7.2). If the zinc finger domain is implicated in modifying AtLNP2 localisation, site-directed mutagenesis will be used to replace the four key cysteine residues within the zinc finger domain with alanine and/or proline (fig. 7.2). This modification has been shown to affect the function of Lnp1p in yeast cells (Chen *et al.*, 2012) and so is a suitable target for modification in plants. Previous studies have reported that the secondary structure of the zinc finger of AtLNP2 is important for the function of AtLNP2, assessed by substituting the cysteine residues for proline (Ueda *et al.*, 2018). However the function at AtLNP2 is not dependent on the presence of cysteine residues specifically, as the

substitution of cysteine by alanine does not affect the function of AtLNP2 (Ueda *et al.*, 2018).

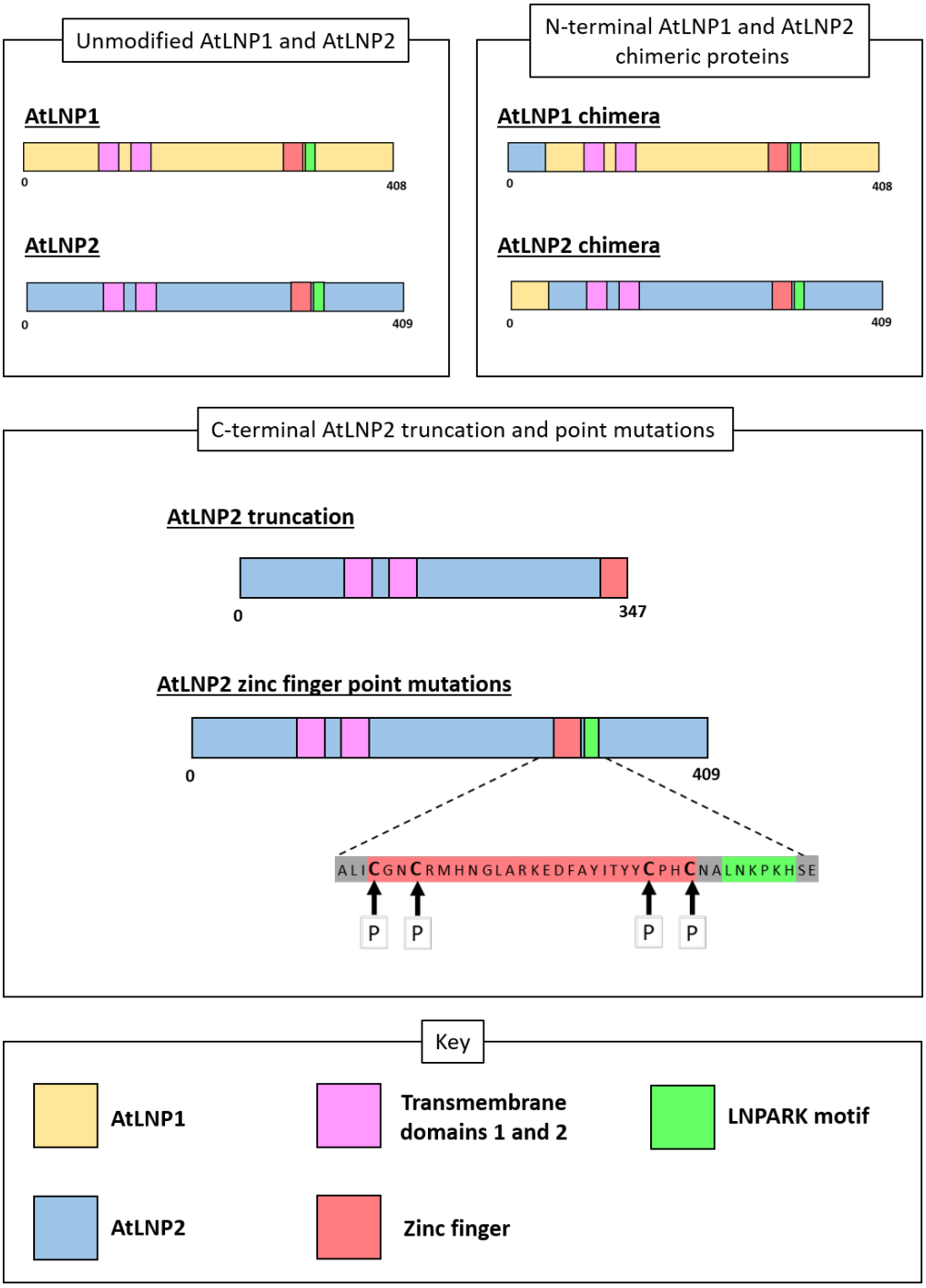


Figure 7.2: The design of future modified AtLNP1 and 2 proteins Truncations, point mutations and chimeric protein designs for future analysis of the mechanism behind AtLNP1 and 2 function.

7.2.3 Generating an AtLNP2 knockout line

A true *lnp2* knockout line could not be identified in the course of this work. Two options for the identification/generation of an AtLNP2 knockout will be explored: firstly further T-DNA insertion lines will be requested and tested for reduced transcription of *AtLNP2*. However the lack of many homozygous lines and the tendency of T-DNA insertions to occur near the 3' end of *AtLNP2* may indicate that no such line has been produced using T-DNA mutagenesis. Instead it may be more useful to use CRISPR-Cas9 technology to generate a *AtLNP2* knockout line. This line would then be tested for both viability and for the structure of the ER formed in the absence of AtLNP2. CRISPR-Cas9 technology could also theoretically be applied to endogenously tag both AtLNP1 and AtLNP2 through site specific insertion of the DNA sequence of a chosen fluorophore. This would provide a more reliable indication as to the native localisation of AtLNP1 and AtLNP2 within the ER of arabidopsis.

7.3 The biogenesis of cisternae

The role of AtLNP1 in cisternae biogenesis has been specifically explored during this work. Due to the localisation of AtLNP2 throughout the ER network, it is much more challenging to asses how AtLNP2 might induce cisternae on over-expression. However, further light sheet imaging will be applied in attempt to capture the induction of cisternae by AtLNP2. Alternatively inducible promoters could be used to test how AtLNP1 and AtLNP2 induce cisternae from an early stage. Unfortunately the majority of inducible promoters require treatment with a chemical, such as ethanol or dexamethasone (Borghi, 2010), which may have the potential to modify the structure of the ER alone. As such treatment with

available inducible promoter triggers would have to be thoroughly tested.

Applying the superresolution microscopy techniques described by Nixon-Abell *et al.* (2016), in particular GI-SIM, to plant cells could shed further light on the native, subresolution structure of ER cisternae in plants. Then the distribution of AtLNP1 and 2 through these cisternae, and the types of cisternae induced by AtLNP1 and 2 over-expression, could be more thoroughly explored.

7.3.1 Proteomics analysis

Finally mLnp1 and Lnp1p have been suggested to interact with other proteins involved in maintaining ER structure such as atlastin, Sey1p and YOP1 (Wang *et al.*, 2016c). A putative plant fusogen, root hair defective 3 (RHD3), has been suggested as a potential functional orthologue to atlastin (Chen *et al.*, 2011). RHD3 could therefore interact with AtLNP1 and 2 in order to control the structure of the ER. Establishing potential protein interactors by co-immunoprecipitation coupled with protein identification by mass spectrometry, would be desirable in order to develop a better understanding of the mechanism by which AtLNP1 and 2 may induce or maintain cisternae. This will be performed on arabidopsis plants stably expressing either P_{UB10}::AtLNP1-GFP or P_{UB10}::AtLNP2-GFP, with plants stably expressing either GFP-HDEL or GFP-CXN respectively to be used as negative controls. Chromotek GFP-Trap beads will be used to pull down AtLNP1 or 2 respectively, together with interacting proteins. The identity of these proteins will be established using mass spectrometry. Once interaction partners have been identified using proteomics, their interaction with AtLNP1 and 2 will be confirmed using FRET-FLIM (Förster resonance energy transfer - fluorescence lifetime imaging).

7.4 Single particle movement in the ER

7.4.1 Exploring new methods

Technologies centered around single particle imaging and tracking are rapidly advancing and in future can hopefully be applied to plant ER SPT. One promising technique that has been used to perform SPT is sptPALM (single-particle-tracking photoactivation localization microscopy). This technique produces images with greatly reduced noise compared to VAEM and has thus far been successfully applied to study single particle movement in the plant plasma membrane (Platre *et al.*, 2019) and mammalian ER (Smith *et al.*, 2014). The application of sptPALM to both plant and mammalian systems to the ER and the plasma membrane is a good indicator that it could be adapted for future work in the plant ER.

Two colour VAEM could not be achieved during this work due to spectral bleedthrough between channels. This work will be attempted again with improved filters to gain a better separation between wavelengths detected in each channel. With increased interest in the field of single particle tracking, 3D tracking of single particles may soon become a reality. Improvements are currently being made both in terms of hardware, such as improved microscopes able to produce rapid Z-stacks with a good resolution in Z, and software that can analyse the movement of particles in 3D (Ram *et al.*, 2012; Quirin *et al.*, 2012). Hopefully in the near future these techniques will be widely available on commercial microscope systems.

8 | Publications resulting from this work

8.1 Publications

The following publications were produced as part of this work:

1. **Arabidopsis Lunapark proteins are involved in ER cisternae formation.** Kriechbaumer, V., Breeze, E., Pain, C., Tolmie, F., Frigerio, L., and Hawes, C. (2018) *New Phytologist*, 219(3):990.

2. **Quantitative analysis of plant ER architecture and dynamics.** Pain, C., Kriechbaumer, V., Kittelmann, M., Hawes, C., and Fricker, M. (2019) *Nature Communications*, 10(1):984.

8.2 Oral presentations

The following oral presentations have been given on this work:

- **Analyzing the structure and function of the plant endoplasmic reticulum** - *SEMT 2017*

- **Analysing the architecture of the Endoplasmic reticulum** - *ENPER 2017*

- **Practical applications of plant endoplasmic reticulum structure**

and dynamics quantification - identifying arabidopsis proteins involved in cisternae formation - *University symposiums, The University of Oxford and Oxford Brookes University 2018*

- **Practical applications of plant endoplasmic reticulum structure and dynamics quantification - identifying arabidopsis proteins involved in cisternae formation** - *ENPER 2018*

- **Taking the perfect cell-fie: comparative image analysis on the effect of actin cytoskeleton modifications on ER structure** - *Botanical microscopy 2019*

8.3 Poster presentations

The following poster presentations have been given on this work:

- **Analysing the structure of the plant endoplasmic reticulum** - *elmi 2017*

- **Analysing the structure of the plant endoplasmic reticulum** - *MMC 2017*

- **Analysing the structure of the plant endoplasmic reticulum** - *University symposiums, The University of Oxford and Oxford Brookes University 2018*

- **AnalyzER: Quantitative analysis of plant ER architecture and dynamics** - *IWPMB 2019*

New Phytologist

Research

Arabidopsis Lunapark proteins are involved in ER cisternae formation

Verena Kriechbaumer[1], Emily Breeze[2], Charlotte Pain[1], Frances Tolmie[1], Lorenzo Frigerio[2] and Chris Hawes[1]

[1]Plant Cell Biology, Biological and Medical Sciences, Oxford Brookes University, Oxford, OX3 0BP, UK; [2]School of Life Sciences, University of Warwick, Gibbet Hill, Coventry, CV4 7AL, UK

Author for correspondence:
Verena Kriechbaumer
Tel: +44 (0)1865 48 8403
Email: vkriechbaumer@brookes.ac.uk

Received: *26 February 2018*
Accepted: *17 April 2018*

New Phytologist (2018)
doi: 10.1111/nph.15228

Key words: Arabidopsis, cisternae, endoplasmic reticulum, Lunapark (LNP), network, tubules.

Summary

- The plant endoplasmic reticulum (ER) is crucial to the maintenance of cellular homeostasis. The ER consists of a dynamic and continuously remodelling network of tubules and cisternae. Several conserved membrane proteins have been implicated in formation and maintenance of the ER network in plants, such as RHD3 and the reticulon proteins. Despite the recent work in mammalian and yeast cells, the detailed molecular mechanisms of ER network organization in plants remain largely unknown. Recently, novel ER network-shaping proteins called Lunapark (LNP) have been identified in yeast and mammalian cells.
- Here we identify two Arabidopsis LNP homologues and investigate their subcellular localization via confocal microscopy and potential function in shaping the ER network using protein–protein interaction assays and mutant analysis.
- We show that AtLNP1 overexpression in tobacco leaf epidermal cells mainly labels cisternae in the ER network, whereas AtLNP2 labels the whole ER. Overexpression of LNP proteins results in an increased abundance of ER cisternae and *lnp1* and *lnp1lnp2* amiRNA lines display a reduction in cisternae and larger polygonal areas.
- Thus, we hypothesize that AtLNP1 and AtLNP2 are involved in determining the network morphology of the plant ER, possibly by regulating the formation of ER cisternae.

Introduction

As the first biosynthetic organelle in the plant secretory pathway, the endoplasmic reticulum (ER) underpins the production, folding and quality control of proteins (Brandizzi *et al.*, 2003; Hawes *et al.*, 2015), as well as lipid biosynthesis (Wallis & Browse, 2010). In addition, it also has many other functions, such as calcium homeostasis (Hong *et al.*, 1999), oil and protein body formation (Huang, 1996; Herman, 2008), rubber particle formation (Brown *et al.*, 2017) and auxin regulation (Friml & Jones, 2010; Kriechbaumer *et al.*, 2015).

In plant cells, the ER consists of a dynamic network of cisternae (sheets) and, more predominantly, tubules which extend throughout the cytoplasm and across cellular boundaries, with intimate connections to other organelles such as the Golgi, the plasma membrane, the outer membrane of the nuclear envelope and the cytoskeleton (Goyal & Blackstone, 2013; Hawes *et al.*, 2015; Stefano & Brandizzi, 2017). Hence, the ER is crucial to the maintenance of cellular homeostasis. The ER network is continually remodelling, presumably in response to differing cellular demands, with the formation of new three-way junctions and polygons via tubule extension and fusion events, balanced with polygon loss from tubule sliding and ring closure (Griffing, 2010). Several conserved membrane proteins have been implicated in both the formation and maintenance of the ER network in plants, notably the GTPase ROOT HAIR DEFECTIVE3 (RHD3) and the reticulon (RTN) family of proteins. RHD3, orthologous to mammalian atlastins (ATL) and yeast Sey1p, may mediate membrane fusion and the formation of three-way junctions (Chen *et al.*, 2011; Zhang *et al.*, 2013). These three-way junctions of the ER consist of small triangular sheets with concave edges (Shemesh *et al.*, 2014). The fusogenic action of RHD3 is then complemented by the curvature-generating and/or stabilizing RTN proteins, which preferentially localize to ER tubules and the curved edges of cisternae. We recently demonstrated that an Arabidopsis reticulon (RTN13) relies on a conserved amphipathic helix to induce membrane curvature *in vivo* (Breeze *et al.*, 2016). Indeed, purified yeast and mammalian orthologues of these two groups of proteins (Sey1p or ATL with RTNs) are sufficient to reconstitute a dynamic tubular ER network in proteoliposomes in the presence of GTP (Powers *et al.*, 2017).

A third class of conserved ER network-shaping proteins called Lunapark (Lnp1p (yeast) and mLnp1 (mammals)) has additionally been identified in yeast and mammalian cells. Lunapark (LNP) proteins are characterized by the presence of two N-terminal transmembrane domains (TMDs) and an atypical Cys4 type C-terminal zinc finger motif which, in yeast, mediates homodimerization and is required for LNP function (Casey *et al.*, 2015; Wang *et al.*, 2016). Immediately adjacent to the zinc finger lies the amino acid sequence LNPARK or a variant thereof. Mammalian Lnp1 is dependent on *N*-myristoylation for its localization to ER junctions and morphogenic activity. The absence

© 2018 The Authors
New Phytologist © 2018 New Phytologist Trust
This is an open access article under the terms of the Creative Commons Attribution License, which permits use, distribution and reproduction in any medium, provided the original work is properly cited.

of this motif in yeast Lnp1p could indicate that LNP proteins in higher organisms have evolved an additional degree of functionality and/or regulation via post-translational lipid modifications (Moriya *et al.*, 2013; Wang *et al.*, 2016; Turnbull & Hemsley, 2017).

Yeast and mammalian LNP proteins preferentially localize to ER three-way junctions *in vivo* and, although they are not required for ER network formation, it has been suggested that LNP acts to stabilize these intersections, potentially acting as temporary scaffold in nascent junctions (Chen *et al.*, 2012, 2015; Wang *et al.*, 2016). Immunofluorescence staining of mammalian COS-7 cells with an anti-mLnp1 antibody showed that only around half of all three-way junctions contained mLnp1 but that mLnp1 acquisition was associated with enhanced junction survival probability and reduced junction mobility and ring closure (Chen *et al.*, 2015).

Lnp1p has been reported to work synergistically with RTNs and Yop1 (an additional curvature stabilizing protein found in yeast, orthologous to mammalian REEPs), but in antagonism to Sey1p to maintain the cortical ER network in yeast cells (Chen *et al.*, 2012). Indeed, in *sey1*Δ yeast mutants lacking functional Sey1p, Lnp1p is expressed in cisternae throughout the ER network, including the nuclear envelope, suggesting that in the wild-type, Sey1 acts upstream of Lnp1, restricting Lnp1 to ER tubule junctions (Chen *et al.*, 2012). Coimmunoprecipitation of epitope-tagged Lnp1p with RTN1p, Sey1p or Yop1p proteins showed that Lnp1p was capable of interacting with all three yeast ER morphogens *in vivo*, and that, moreover, the interaction of Lnp1p with Rtn1p is negatively regulated by Sey1p (Chen *et al.*, 2012). However, more recently Wang *et al.* (2016) reported that in mammalian cells stably expressing both Lnp-mCherry and GFP-ATL-3, ATL was in close proximity to Lnp-mCherry in the peripheral ER network but, crucially, the two proteins did not precisely colocalize and no interaction was found in reciprocal pull-down experiments.

Despite the recent work in mammalian and yeast cells, the detailed molecular mechanisms of ER network organization in plants remain largely unknown. Here we identify two Arabidopsis LNP homologues and show that their overexpression (as fluorescent protein fusions) in tobacco leaf epidermal cells results in the proteins labelling the ER and accumulating at cisternae and a small proportion of three-way junctions of the ER network. Furthermore, overexpression of LNP proteins results in an increased abundance of cisternae in the ER network. Thus, we hypothesize that AtLNP1 and AtLNP2 are involved in determining the dynamic morphology of the plant ER, possibly by regulating the formation of ER cisternae.

Materials and Methods

Comparative genomics

Genes orthologous to LNP1 and LNP2 in other species within the land plant lineage (Embryophyta) and containing the InterPro LNP domain (IPR019273) were identified using the Plaza 4.0 online platform (Proost *et al.*, 2009). This resulted in the identification of 87 LNP-like genes from 49 plant species. A phylogenetic tree of the homologous LNP gene family was assembled within Plaza, alongside a multiple sequence alignment of the amino acid sequences. A consensus sequence logo of the LNPRK amino acid motif from the multiple sequence alignment was generated using WebLogo3 (Crooks *et al.*, 2004).

Cloning of expression plasmids

Primers were obtained from Eurofins Genomics (Ebersberg, Germany). Q5 high-fidelity DNA polymerase (New England Biolabs, Ipswich, MA, USA) was used for all PCR reactions. Genes of interest were cloned with a C-terminal GFP fusion under a ubiquitin-10 promoter (P_{UBQ10}) (Grefen *et al.*, 2010) using Gateway technology (Invitrogen).

The *LNP1* and *LNP2* promoter and coding sequences were amplified from Col-0 genomic DNA using the gene-specific primers LP: TTCAAACAATTACAAACTTAACGGTAGC and RP: GTTTGGTGTCTCATTCTCAGCTGTTTCC for LNP1 and LP: CCAGCTTGTGTGAATATGGTTTGAGCTT and RP: GCTCGGTGTCCCGGTCTCAGTAATTGC for LNP2 and cloned into the pDONR/Zeo Gateway Entry vector. Thus, these *LNP1* and *LNP2* constructs contain 1910 and 2090 bp, respectively, upstream of the ATG start site, and terminate immediately before the TGA stop sites.

Preparation of *lnp1* and *lnp1lnp2* amiRNA lines

Candidate amiRNA sequences specific to both *LNP1* and *LNP2* coding regions were identified using the Web MicroRNA Designer (WMD) platform (http://wmd3.weigelworld.org) (Schwab *et al.*, 2006; Ossowski *et al.*, 2008). Two amiRNA sequences were selected (targeted against the region immediately downstream of TMD2 (amiRNA1) or the conserved zinc finger domain (amiRNA2); Supporting Information Fig. S1) and cloned into the naturally occurring Arabidopsis miR319a replacing the target-specific sequence using a series of overlapping PCRs (as described by Ossowski *et al.*, 2008) and with the addition of Gateway-compatible attB sites. The purified attB-amiRNA precursors were subsequently used to generate Entry (pDONR/Zeo) and 35S destination (pB7WG2) clones. The 35S constructs were transformed by heat shock into *Agrobacterium tumefaciens* strain GV3101 and stable homozygous Arabidopsis lines created via the floral dip procedure (Clough & Bent, 1998). RNA was extracted from dry seeds of two independent amiRNA1- and amiRNA2-containing lines and Col-0 as described by Meng & Feldman (2010) and first-strand cDNA synthesized using ReadyScript (Sigma Aldrich) according to the manufacturer's instructions. Semiquantitative reverse transcription polymerase chain reaction was performed using primers specific to LNP1 (LP: TGCCAAACACTCGGGAGG and RP: AGGGATTGGACTGTTACCGC) and LNP2 (LP: GAGCA ATGACATGGAGGTTAAC and RP: GTCTCAATCAGTGG CAGAGAG) (Fig. S1), together with At4g34270 (LP: GTGA AAACTGTTGGAGAGAAGCAA and RP: TCAACTGGATA CCCTTTCGCA) and At4g12590 (LP: GAGATGAAAATG

© 2018 The Authors
New Phytologist © 2018 New Phytologist Trust

CCATTGATGAC and RP: GCACCCAGACTCTTTGATG) (seed-specific housekeeping reference genes (Dekkers *et al.*, 2012)) as loading controls, and expression levels in the amiRNA mutants compared with that of wild-type, Col-0 (Fig. S1). The amiRNA1-containing lines were found to have reduced expression of *LNP1* but comparable expression of *LNP2* to that detected in the wild-type and was subsequently referred to as *lnp1*, whereas the amiRNA2-containing lines had markedly reduced expression levels of both *LNP1* and *LNP2* and were therefore denoted as *lnp1lnp2*. The differing specificity of the two amiRNAs for the *LNP* targets is likely to be the result of nucleotide mismatches between the two target sequences, notably in the crucial 5′ portion of the amiRNA (positions 2–12) (Schwab *et al.*, 2006). Design of amiRNAs to successfully silence a specific gene target is challenging given the absence of canonical miRNA sequence parameters.

Plant material and transient expression in tobacco leaves

For Agrobacterium-mediated transient expression, 5-wk-old tobacco (*Nicotiana tabacum* SR1 cv Petit Havana) plants grown in the glasshouse were used. Transient expression was carried out according to Sparkes *et al.* (2006). In brief, each construct was introduced into Agrobacterium strain GV3101 by heat shock. Transformants were inoculated into 3 ml of YEB medium (l^{-1}: 5 g of beef extract, 1 g of yeast extract, 5 g of sucrose and 0.5 g of $MgSO_4\,7H_2O$) with 50 μg ml^{-1} spectinomycin and 25 μg ml^{-1} rifampicin. After overnight shaking at 25°C, 1 ml of the bacterial culture was pelleted by centrifugation at 2200 ***g*** for 5 min at room temperature. The pellet was washed twice with 1 ml of infiltration buffer (50 mM MES, 2 mM $Na_3PO_4\,12H_2O$, 0.1 mM acetosyringone and 5 mg ml^{-1} glucose) and then resuspended in 1 ml of infiltration buffer. The bacterial suspension was diluted to a final OD_{600} of 0.05 (0.01–0.3 in the OD_{600} serial dilution series) and carefully pressed through the stomata on the lower epidermal surface using a 1 ml syringe. Infiltrated plants were then returned to glasshouse conditions for 48 h before imaging.

Confocal microscopy

Images were taken using a Zeiss 880 laser scanning confocal microscope with ×100/1.46 numerical aperture DIC M27 Elyra oil immersion objective. For imaging of the green/red fluorescent protein (GFP/RFP) combinations, samples were excited using 488 and 561 nm laser lines in multitrack mode with line switching. Signals were collected using the high-resolution Airyscan detector (Zeiss, Oberkochen, Germany) with emission wavelength of 523 nm for GFP and 579 nm for RFP. Images were edited using the ZEN image browser (Zeiss).

Lipid dye Rhodamine B hexyl ester

Staining the ER with Rhodamine B hexyl ester was carried out according to Hawes *et al.* (2018). Rhodamine B hexyl ester solution was prepared as a 1 mM stock solution in dimethyl sulphoxide and a 1 μM working solution in distilled water (DW). Whole Arabidopsis seedlings 7–10 d after germination were transferred to Eppendorf tubes containing 1 μM Rhodamine B hexyl ester. Seedlings were incubated for 15 min in the dye and washed in DW. Samples were imaged with a 514 nm argon ion laser emission detected using 470–500 and 560–615 nm bandpass filters.

FRET-FLIM data acquisition

Constructs were transiently expressed in tobacco leaf epidermal cells as described earlier. Leaf discs were excised and the GFP and mRFP expression levels in the plant within the region of interest were confirmed using a Nikon EC2 confocal microscope at 488 and 543 nm, respectively. Förster resonance energy transfer by fluorescence lifetime imaging microscopy (FRET-FLIM) data capture was performed according to Kriechbaumer *et al.* (2015) using a two-photon microscope at the Central Laser Facility of the Rutherford Appleton Laboratory. A two-photon microscope built around a Nikon TE2000-U inverted microscope was used with a modified Nikon EC2 confocal scanning microscope to allow for multiphoton FLIM (Schoberer & Botchway, 2014). At least three nuclei ($n_{(RTN1\text{-}RTN1)} = 3$; $n_{(RTN1\text{-}LNP1)} = 10$; $n_{(RTN1\text{-}LNP2)} = 12$) from at least two independent biological samples per protein–protein combination were analysed, and the average of the ranges was taken.

Quantification of ER structure parameters in WT and mutants

Images acquired with a Zeiss 880 confocal microscope with Airyscan (see methods confocal microscopy) were analysed using ImageJ (National Institutes of Health, Bethesda, MD, USA; Fig. 1). Confocal images were imported to ImageJ and smoothed in order to reduce noise. The ER signal was segmented from the background and mitochondrial signal using the ImageJ plugin Trainable Weka Segmentation. Once segmented, a closing function was applied to reduce segmentation errors and to ensure high connectivity of the network. To analyse the polygonal regions, a region of interest was drawn around the cell using a digitizing tablet, and the ImageJ 'Analyse particles' command was applied. Only polygonal regions completely enclosed by the network were considered for the analysis. As the data are not normal, the Wilcoxon rank sum test was applied. $P < 1.7282e^{-17}$ (*lnp1*) and $P < 2.8930e^{-44}$ (*lnp1lnp2*) were calculated for three biological replicas with at least 12 technical repeats each. To analyse ER network structure, an opening function with several iterations was applied to the segmented ER image to isolate cisternae. The total area of the cisternae was measured and the percentage of the cell surface classified as cisternae was calculated ($P < 6.0051e^{-4}$ in *lnp1* and $P < 0.0031$ for in *lnp1lnp2*). The segmented ER network was skeletononized and the cisternae identified in the previous step were subtracted to produce a skeleton of the tubular ER network. Using the 'Analyse skeleton' ImageJ command, all three-way junctions in the skeletonized tubular network were identified. The number of three-way junctions identified was normalized against the area of the cell surface ($P > 0.2643$ for *lnp1* and $P > 0.7427$).

© 2018 The Authors
New Phytologist © 2018 New Phytologist Trust

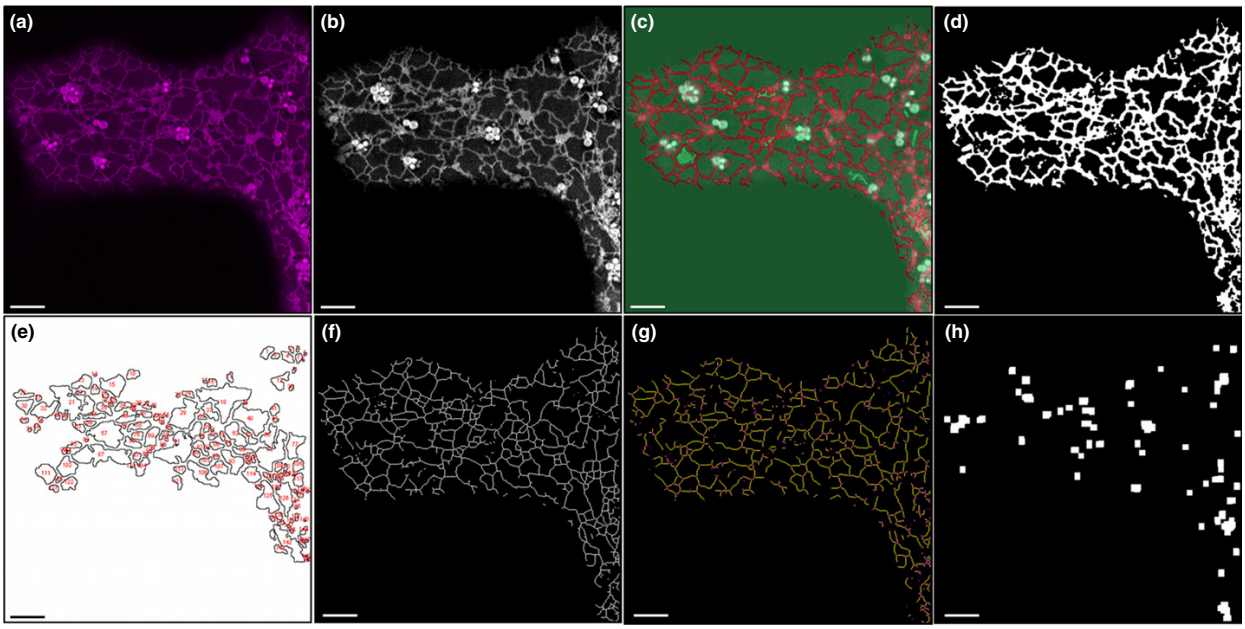


Fig. 1 Endoplasmic reticulum (ER) network analysis workflow for Arabidopsis *lnp1* and *lnp1lnp2* amiRNA mutants. The ER network was analysed and quantified using the following steps. Example images are shown for every step. Bars, 5 μm. (a) Initial image; (b) enhanced contrast; (c) Weka trainable segmentation: red regions correspond to detected ER structures, green highlights rejected ER regions (e.g. here for *lnp1* mutant stained mitochondria); (d) binary image of segmented ER; (e) polygonal region analysis output with numbered outlines of each polygonal region that is fully enclosed by the ER; (f) skeletonized ER structure; (g) analysed ER skeleton with blue pixels indicating detected end points (single pixel wide) and magenta pixels showing detected junctions; (h) cisternae detected by an iterative opening function.

Persistency analysis

To analyse persistency of LNP1-labelled punctae and cisternae, videos were taken using the Zeiss 880 confocal with Airyscan. RFP-HDEL was used as an ER luminal marker. The ImageJ plugin 'temporal color-code' was applied to colour-code movement over time; in this case, in three image frames at 0, 30 and 60 s. White areas indicate points of persistency throughout in the composite image, and red areas indicate highest mobility.

Accession numbers

AtLNP1, At2g24330.1; AtLNP2, At4g31080.1; AtLNP2.2, At4g31080.2.

Results

Identification of two LNP orthologues in Arabidopsis

The protein sequences of yeast Lnp1p and human Lnp were queried against the *Arabidopsis thaliana* proteome using Blastp (Altschul *et al.*, 1990). This analysis identified two LNP orthologues, At2g24330 and At4g31080 (subsequently named AtLNP1 and AtLNP2, respectively), both with *c.* 24% amino acid identity to the queried sequences across the entire length of the protein. AtLNP1 and 2 themselves share 67% amino acid identity. According to large-scale microarray data in the eFP browser (Winter *et al.*, 2007) both At*LNP1* and At*LNP2* are transcribed ubiquitously but At*LNP2* has increased transcription abundance in pollen (Fig. S2). Further comparison of the identified AtLNP protein sequences with their mammalian and yeast orthologues revealed the presence of several conserved features, notably two TMDs towards the N-termini and a zinc finger motif immediately adjacent to the LNPARK motif (Fig. 2). However, unlike the human (and mouse) Lnp proteins, AtLNP1 and 2 do not contain a Pro-rich domain upstream of the zinc finger motif (Fig. 2), although the functional significance of this domain in mammalian Lnp proteins is currently unknown.

The mammalian Lnp (mLnp1) protein features an N-terminal myristoylation site, and ER network changes induced by overexpression of LNP proteins were significantly inhibited by the mutation of protein *N*-myristoylation which rendered this motif nonfunctional (Moriya *et al.*, 2013). Yeast Lnp1p protein, by contrast, does not feature this motif (Moriya *et al.*, 2013). Arabidopsis LNP proteins similarly do not possess an N-terminal glycine and therefore are predicted to lack a myristoylation site as shown for mLnp1 (Moriya *et al.*, 2013).

The characteristic LNP amino acid motif (LNKPKH in AtLNP1 and 2) is conserved throughout the Embryophyta (land plants, i.e. flowering plants and mosses) group, although some variation in specific residues exists between species. The Plaza 4.0 online platform (Proost *et al.*, 2009) was used to identify 87 genes orthologous to LNP1 and LNP2 in 49 species within the land plant lineage (from a total of 53 Embryophyta genomes

© 2018 The Authors
New Phytologist © 2018 New Phytologist Trust

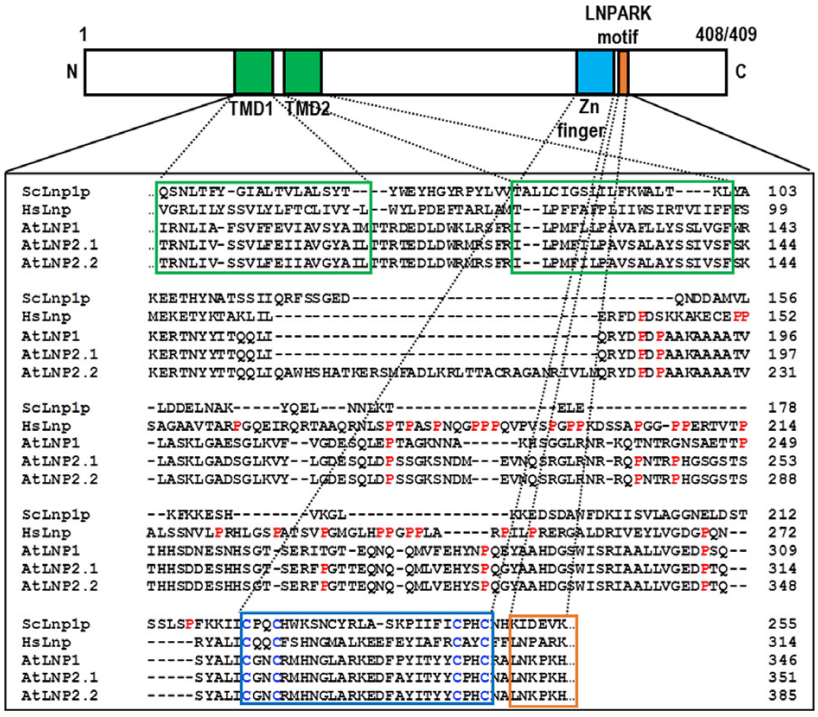


Fig. 2 AtLNP1 and AtLNP2 are orthologous to Lunapark proteins in other organisms. Two putative Lunapark (LNP) proteins were identified in *Arabidopsis thaliana*, with sequence homology and conserved motifs (two transmembrane domains, TMDs; zinc finger, and LNPARK motif (LNKPKH in Arabidopsis)) with previously annotated *Homo sapiens* Lnp (HsLnp) and *Saccharomyces cerevisiae* Lnp1p (ScLnp1p) proteins. Note that unlike yeast and Arabidopsis LNP proteins, HsLnp contains an additional Pro-rich region (Pro residues are shown in red). AtLNP1 and AtLNP2.1 are 408 and 409 amino acid residues in length, respectively.

present in the PLAZA database). Multiple sequence alignment of these LNP proteins produced a consensus sequence motif of ALNXPK[Q/H] (Fig. S3). The existence of multiple LNP homologues within a plant species is not unique to Arabidopsis, as 30 of the 49 plant species with an identified LNP gene had two or more copies in their genome with no obvious association between gene copy number and genome divergence time. However, the existence of two subfamilies of LNP proteins, which may have, for example, evolved unique functions (paralogues) is not supported by the phylogenetic analysis of the identified LNP homologues across the Embryophyta plant group (Fig. S3).

AtLNP2 is annotated as having two possible splice variants (AtLNP2.1 and AtLNP2.2) with AtLNP2.2 containing an additional 34 residues downstream of the TMDs. However, this region is not well conserved in LNP proteins from other organisms and, moreover, publicly available RNASeq data (Araport) obtained from a range of tissues show no detectable sequence reads for this region. Hence, all subsequent analysis was performed on splice variant AtLNP2.1 (subsequently referred to as AtLNP2).

AtLNP1 and AtLNP2 localize to different substructures within the ER network

To determine the subcellular location of AtLNP1 and AtLNP2, the full-length protein sequences were fused at the C-terminus to GFP under the control of the ubiquitin-10 promoter (P_{UBQ10}) (Grefen *et al.*, 2010). Transient expression of both constructs in *Nicotiana tabacum* leaf epidermal cells alongside the ER lumenal marker RFP-HDEL showed specific subcellular localization of AtLNP1 mainly to ER cisternae (Fig. 3a) as well as to a small proportion of three-way junction regions of the ER network (which could also be small cisternae). By contrast, AtLNP2 labels the whole ER network, including cisternae (Fig. 3b).

At higher resolution, At LNP1 appears to be evenly distributed over the cisternae when coexpressed with the lumenal marker GFP-HDEL (Fig. 3c); when coexpressed with the transmembrane region of the ER membrane marker calnexin (GFP-CXN) AtLNP1 levels appear elevated over the cisternae compared with the tubular structure surrounding the cisternal core (Fig. 3d).

At higher resolution it can be observed that AtLNP1 localizes to the centre of cisternae whereas the lumenal marker GFP-HDEL labels the edges of cisternae (Fig. 3c). By contrast, the transmembrane region of the ER membrane marker calnexin (GFP-CXN) labels the whole of the cisternae and is not restricted to the centre of the membrane as is AtLNP1 (Fig. 3d).

The two different LNP localization patterns observed, where AtLNP1 is cisternae-specific but AtLNP2 labels the whole ER network, were also found when using both native promoter constructs (2 kb upstream from gene; Fig. 3e,f) in transient expression assays and in Arabidopsis plants stably expressing AtLNP1 or AtLNP2, respectively (Fig. 3g).

Expression of Arabidopsis LNP proteins induces cisternae in a dose-dependent manner

The effect of protein expression dosage on the targeting of AtLNP1 and AtLNP2 to different ER structures was investigated by transient expression of P_{UBQ10}::AtLNP1-GFP and P_{UBQ10}::

© 2018 The Authors
New Phytologist © 2018 New Phytologist Trust

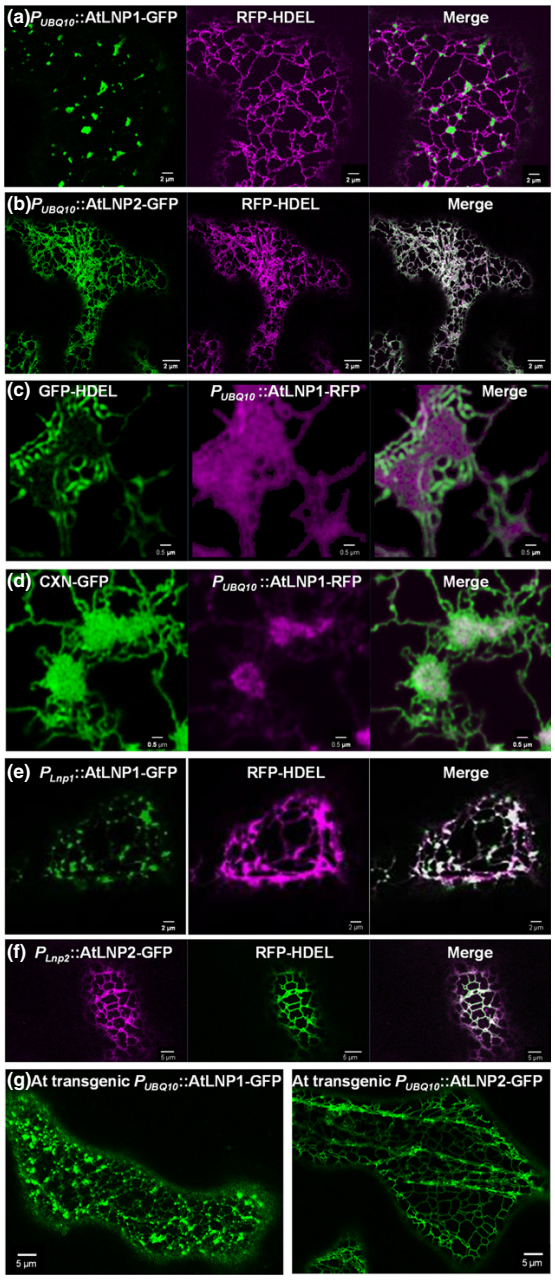


Fig. 3 Localization of AtLNP1 and AtLNP2 within the endoplasmic reticulum (ER) network. (a, b) Transient coexpression of the ER luminal marker RFP-HDEL with P_{UBQ10}::AtLNP1-GFP (a) or P_{UBQ10}::AtLNP2-GFP (b) in *Nicotiana tabacum* leaf epidermal cells. Both AtLNP1 and AtLNP2 are localized to ER cisternae and a proportion of three-way junctions, but AtLNP2 additionally localizes to ER tubules. (c, d) High-resolution imaging shows that AtLNP1 is more localized to the middle of the cisternae, with the lumenal marker HDEL getting pushed towards the edges (c), whereas the ER membrane marker calnexin (CXN) also labels the centre of the cisternae but expands more towards the edges than AtLNP1 (d). (e–g) Similar localization patterns are shown for P_{LNP1}::AtLNP1-GFP (e) or P_{LNP2}::AtLNP2-GFP (f) in *N. tabacum* and Arabidopsis lines stably expressing P_{UBQ10}::AtLNP1-GFP or P_{UBQ10}::AtLNP2-GFP, respectively (g).

AtLNP2-GFP constructs across a range of Agrobacterium optical densities (ODs), as a proxy for differing protein expression levels within the agroinfiltrated leaf (Figs 4, S4). At higher doses of P_{UBQ10}::AtLNP1-GFP, AtLNP1-labelled sheets became increasingly prominent with the prevalence of ER cisternae at the highest OD of the P_{UBQ10}::AtLNP1-GFP construct (Figs 4, S4a). Moreover, at higher levels of AtLNP1 expression, some AtLNP1-labelled ER tubules were additionally observed (Figs 4, S4a).

Protein dosage effects were also seen for AtLNP2, similarly achieved through agroinfiltration of P_{UBQ10}::AtLNP2-GFP at increasing ODs. At higher construct concentrations, AtLNP2-GFP labelling of ER three-way junctions became increasingly prevalent, together with a marked escalation of ER cisternae formation (Figs 4, S4b).

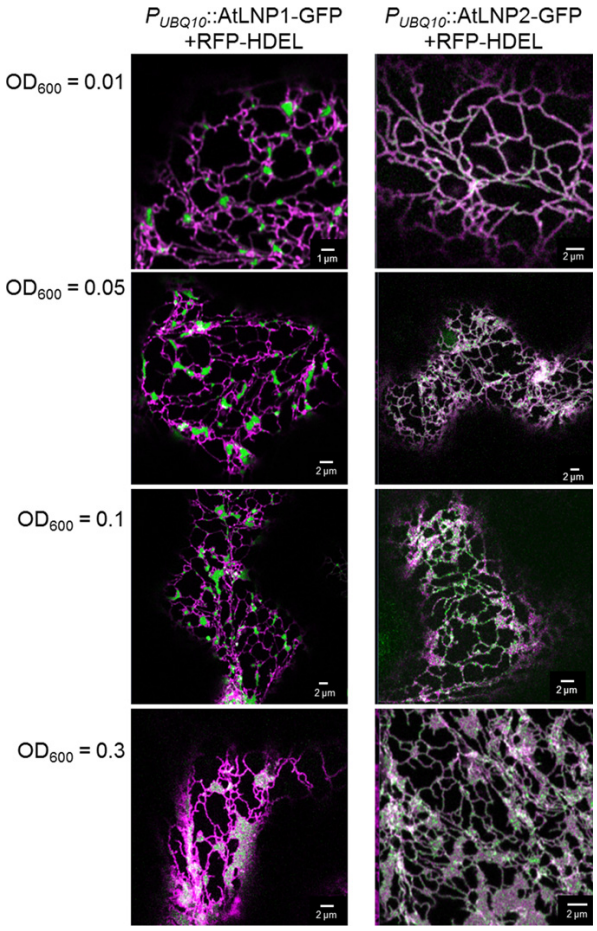


Fig. 4 Increasing levels of protein expression affect the localization of AtLNP1 and AtLNP2 within the endoplasmic reticulum (ER) network. Transient coexpression of *Agrobacterium tumefaciens* transformed with P_{UBQ10}::AtLNP1-GFP (left panels) and P_{UBQ10}::AtLNP2-GFP (right panels), respectively, at increasing ODs (alongside the ER luminal marker, RFP-HDEL at a constant OD of 0.1) in *Nicotiana tabacum* leaf epidermal cells. At higher ODs, an increasing formation of ER cisternae is observed for both constructs, and, for AtLNP1, additional labelling of ER tubules, which is absent at lower ODs.

© 2018 The Authors
New Phytologist © 2018 New Phytologist Trust

amiRNA *lnp1* and *lnp1lnp2* loss-of-function mutant shows altered ER network morphology

Given the abundance of LNP proteins at ER cisternae and their ability to induce cisternae formation when expressed at high levels *in vivo*, we hypothesize that down-regulation of LNP could affect cisternal areas and potentially the overall appearance of the ER network. The effect on the ER network morphology in the absence of LNP proteins was therefore examined. Stable Arabidopsis homozygous lines overexpressing GFP-HDEL and artificial microRNAs (amiRNA) designed to target either the conserved zinc finger region in both At*LNP1* and At*LNP2* (*lnp1lnp2*) or a region immediately downstream of TMD2 (*lnp1*) were generated (Fig. S1). Gene expression analysis showed expression levels of the relevant At*LNP* transcripts to be significantly reduced in these lines (Fig. S1). Loss of LNP had no noticeable effect on plant growth; unlike, for example, *rhd3* mutants which exhibit defects in plant development and are dwarfed (Zhang *et al.*, 2013).

The ER network in the stable homozygous *lnp1* amiRNA line was compared with Col-0 plants transformed with GFP-HDEL (Fig. 5). Cells from both lines were stained with the lipid dye Rhodamine B hexyl ester (Fig. 5a), which stains the ER but also mitochondria. Network analysis (Fig. 5b–d) revealed that *lnp1* mutants have a trend towards larger polygonal regions (mean size: GFP-HDEL 1.45 μm^2, *lnp1* 2.05 μm^2), reduced cisternae area per total cell area (mean percentage: GFP-HDEL 10.69%, *lnp1* 5.62%) and reduced numbers of three-way junctions per area (mean ratio: GFP-HDEL 0.53, *lnp1* 0.37). *t*-tests corrected for unequal variances were used to assess whether the ER features differed significantly between the knockdown lines and the wild-type. This analysis showed that polygonal region area is increased and cisternal areas are decreased in *lnp1* mutants in a statistically significant manner (Fig. 5b) compared with Col-0 plants but the number of three-way junctions in *lnp1* mutants are not statistically significantly different from wild-type cells at a 0.05 confidence level (Fig. 5c,d).

Comparison of the ER network structure in cotyledons from Col-0 and the *lnp1lnp2* knockdown line (Fig. 6), both stably transformed with GFP-HDEL, revealed visible ER morphological differences (Fig. 6a), whereby the polygons defined by the ER tubules appeared enlarged in *lnp1lnp2.* Subsequent quantitative *in silico* image analysis (Fig. 6b) using ImageJ's 'Analyse particles' showed that the average ER polygonal area in *lnp1lnp2* leaves was indeed significantly greater than in the corresponding GFP-HDEL controls (mean size: GFP-HDEL 1.23 μm^2, *lnp1lnp2* 6.47 μm^2) (Fig. 6c). In addition, this analysis revealed that the ER polygonal areas are less uniform and have a greater range of sizes than in the wild-type control (Fig. 6b,c). Analysis of the percentage of the overall cell volume classes as cisternae revealed a statistically significant reduction of cisternal areas (Fig. 6d) (mean percentage: GFP-HDEL 5.56%, *lnp1lnp2* 1.39%) in the *lnp1lnp2* mutant and a nonsignificant trend for a reduction of three-way junctions (Fig. 6e) in the double mutant (mean ratio: GFP-HDEL 0.1, *lnp1lnp2* 0.09%). We hypothesize that the observed alterations in ER structure and the more irregular polygonal areas in the Arabidopsis *lnp1* and *lnp1lnp2* lines here may instead be a result of the loss of cisternae, which might have an effect on network stability rather than the nonstatistically significant reduction in three-way junctions.

Interaction between LNP and reticulon proteins

The ER morphology phenotypes observed upon overexpression or down-regulation of AtLNP1 and/or AtLNP2 strongly suggest that LNP proteins are involved in the formation and/or stabilization of three-way junctions and cisternae in the ER network. Another class of proteins known to be required for the formation of a dynamic ER tubular network in plants are the reticulon (RTN) proteins, which induce and/or stabilize membrane curvature and are capable of constricting tubules whilst suppressing cisternae formation (Sparkes *et al.*, 2010). Hence, we explored the potential interplay between RTN and LNP proteins.

Initially, the formation of protein–protein interactions between RTN1 and both LNP proteins was tested using FRET-FLIM analysis *in vivo* (Figs 7, S5). RTN1 was selected as an exemplar of all RTN proteins as it has high sequence homology to other family members and is known to be expressed in all tissues throughout development (Arabidopsis eFP Browser; Winter *et al.*, 2007).

Time-resolved fluorescence spectroscopy in imaging biological systems allows for the implementation of FLIM. FRET-FLIM measures the reduction in the excited-state lifetime of GFP (donor) fluorescence in the presence of an acceptor fluorophore (e.g. mRFP) that is independent of the problems associated with steady-state intensity measurements. Reduction in GFP lifetime is an indication that the two proteins are within a distance of 1–10 nm, thus indicating a direct physical interaction between the two protein fusions (Sparkes *et al.*, 2010; Schoberer & Botchway, 2014). It was previously shown that a reduction of as little as 200 ps in the excited-state lifetime of the GFP-labelled protein represents quenching through a protein–protein interaction (Stubbs *et al.*, 2005).

Donor and acceptor constructs were coinfiltrated into *N. tabacum* leaf epidermal cells and FRET-FLIM analysis performed after 48 h to assess protein–protein interactions. For both AtLNP1 and AtLNP2, a significant reduction of 0.2 ns in the lifetime of the donor (GFP-RTN1) fluorescence in the presence of the acceptor fluorophore (RFP-RTN1 as a positive control and AtLNP1-RFP, AtLNP2-RFP) was observed, in comparison to expression of the donor alone (Figs 7, S5). These data suggest that AtLNP1 and AtLNP2 are both capable of physically interacting with RTN proteins *in vivo*.

As FRET-FLIM analysis demonstrated that LNP and RTN1 proteins interact *in vivo*, the existence of a possible relationship between the two proteins which influences ER morphogenesis was evaluated *in planta*. AtLNP1 and AtLNP2 constructs were expressed using an OD_{600} of 0.3 that usually results in the formation of enlarged cisternae (Fig. 4), RTN1 was infiltrated at a

© 2018 The Authors
New Phytologist © 2018 New Phytologist Trust

New Phytologist

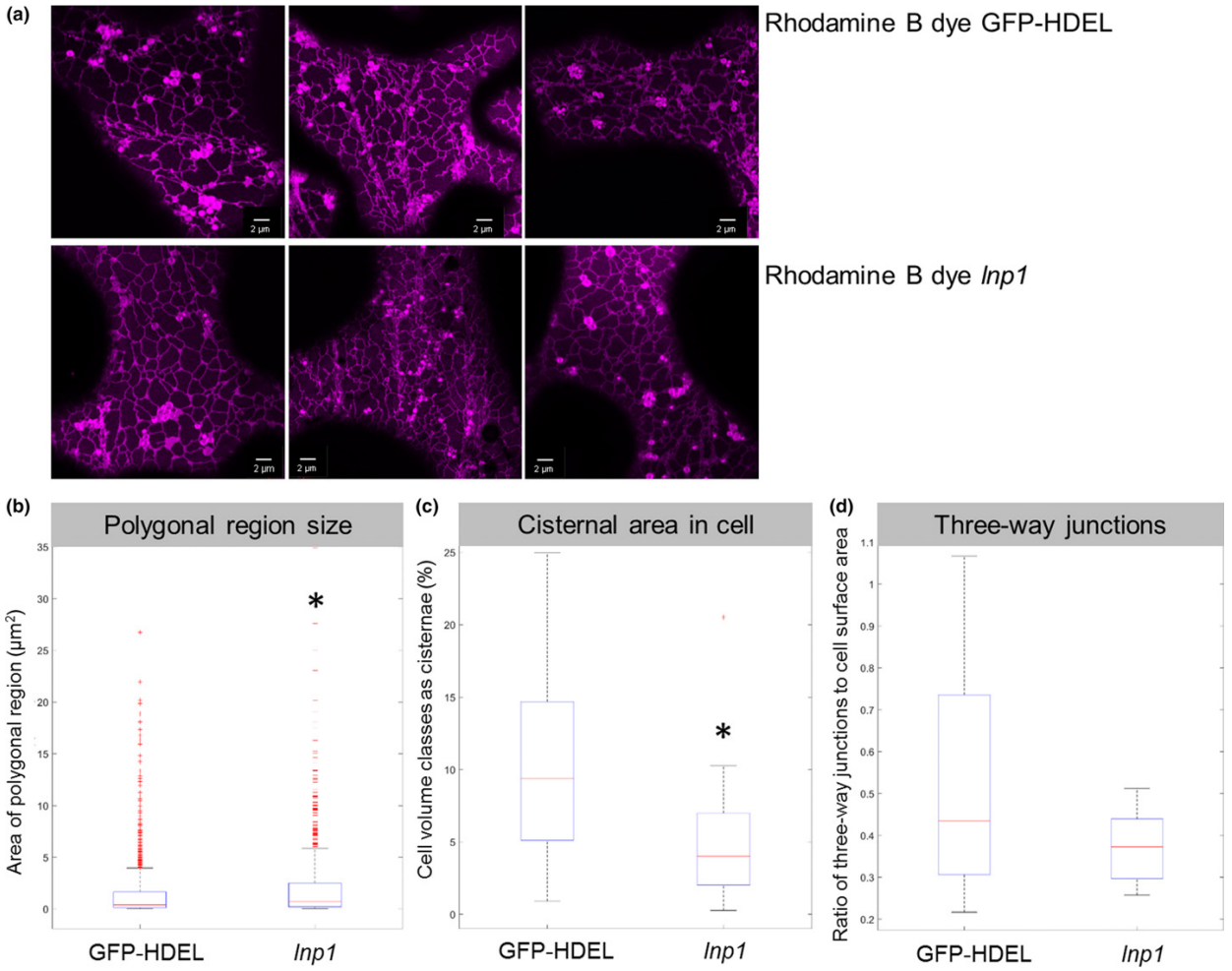


Fig. 5 Endoplasmic reticulum (ER) network structure in Arabidopsis *lnp1* amiRNA mutants. (a) The ER network in cotyledons of GFP-HDEL Arabidopsis plants and a stable homozygous *lnp1* amiRNA line was visualized with the lipid dye Rhodamine B hexyl ester. This dye labels the ER network but also mitochondria. Quantifications were carried out for: (b) the areas of the polygonal regions; (c) the percentage of cisternal areas in the cell volume; and (d) the ratio of three-way junctions to cell surface area. The red horizontal mark shows the data median, and bottom and top edges of the box mark the 25th and 75th percentiles, respectively. The whiskers on the dashed lines outline indicate the most distant data points that are not considered outliers. Outliers are plotted individually with '+' or '−' symbols, respectively. *, statistical significance.

standard OD_{600} of 0.1 known to result in ER tubule restriction (Sparkes *et al.*, 2010). Transient coexpression of AtLNP1-GFP with RFP-RTN1 (Fig. 8) appeared to suppress the proliferation of AtLNP1-labelled cisternae previously observed from infiltration of AtLNP1-GFP alone (Fig. 8, compare with Fig. 4). Instead AtLNP1-GFP labelling of smaller, partially fragmented cisternae was detected. As observed when AtLNP2-GFP was infiltrated on its own (Fig. 4), coexpression of AtLNP2-GFP with RFP-RTN1 resulted in the presence of both AtLNP2-containing sheets and tubules. In addition, overexpression of AtLNP2 together with RTN1 induced the formation of nodule-like structures in the ER tubular network (Fig. 8).

These data suggest that RTN1 is capable of counteracting the sheet-induction upon LNP overexpression, further strengthening the case for these proteins having linked roles *in vivo*, such as maintaining the balance between tubules and cisternae in the network.

Dynamics of LNP-labelled cisternae

Yeast and mammalian Lnp proteins preferentially localize to the three-way junctions of the ER network and it has been suggested that in these organisms Lnp proteins are involved in stabilizing these intersections (Chen *et al.*, 2012, 2015; Wang *et al.*, 2016). Although our results showed that AtLNP1 preferentially localizes to ER cisternae rather than junctions, we wanted to determine if AtLNP1 still has a comparable function in stabilizing the overall ER network.

The movement and remodelling dynamics of AtLNP1-labelled ER structures was investigated through time-lapse

© 2018 The Authors
New Phytologist © 2018 New Phytologist Trust

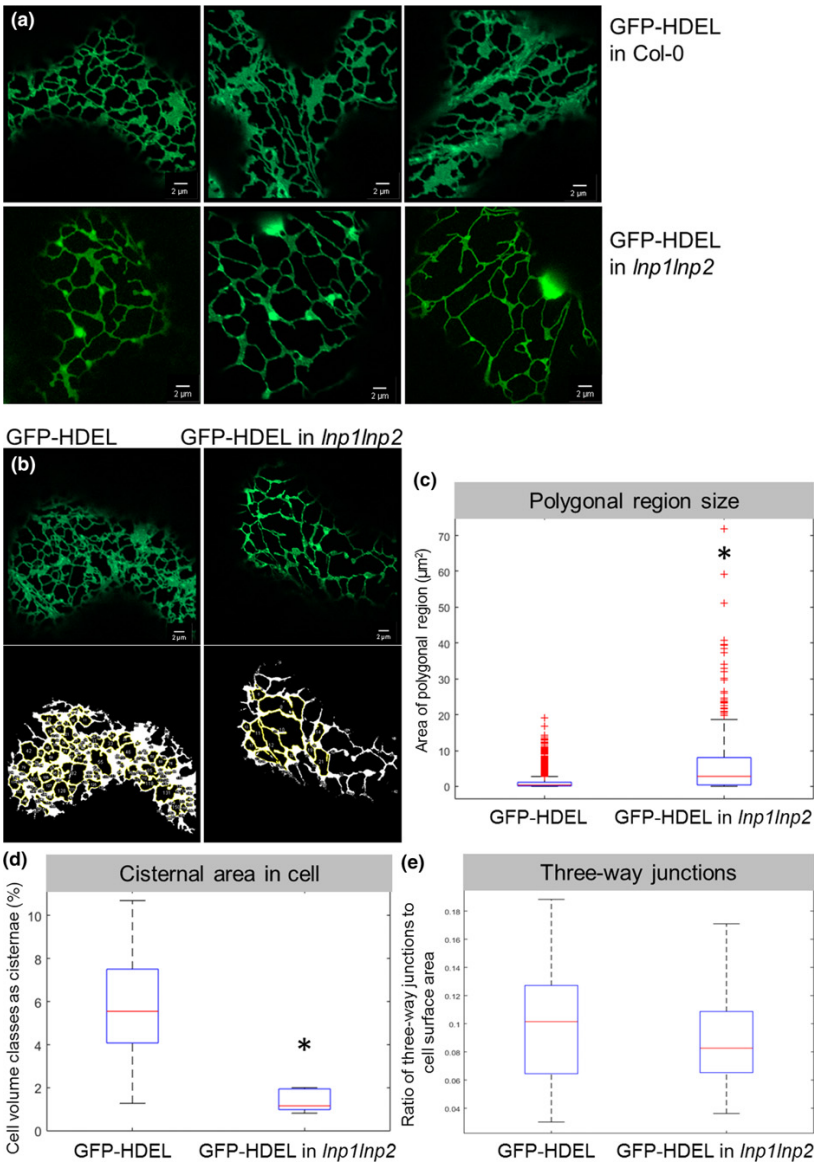


Fig. 6 Endoplasmic reticulum (ER) network structure in Arabidopsis *lnp1lnp2* amiRNA mutants. (a) The ER network in cotyledons of Col-0 and stable homozygous *lnp1lnp2* amiRNA lines were visualized by transformation with the ER luminal marker GFP-HDEL. Representative images for GFP-HDEL in the wild-type Col-0 and in the *lnp1lnp2* amiRNA plants are shown. (b) The areas of the polygonal regions in the ER network are outlined by GFP-HDEL in the wild-type Col-0 and in the *lnp1lnp2* amiRNA plants. Polygonal areas were quantified using ImageJ's 'Analyse particles'. The original confocal images are shown together with images post-processing. The yellow outlines show polygonal regions with their quantifications in the box plot below. (c) As the data are not normal, the Wilcoxon rank sum test was applied. Data are shown in a box plot with a *P*-value $< 2.8930e^{-44}$ for three biological replicates, each with at least 12 technical replicates. In addition, the percentage of cisternal areas in the cell volume (d) as well as the ratio of three-way junctions to cell surface area (e) were quantified. The red horizontal mark shows the data median, and bottom and top edges of the box mark the 25th and 75th percentiles, respectively. The whiskers on the dashed line outline indicate the most distant data points that are not considered outliers. Outliers are plotted individually with '+' symbols. *, statistical significance.

image processing. In general, several different types of motion were observed for Arabidopsis LNP proteins that can be classified in similar categories, as previously described for the mammalian Lnp1, despite the proteins most likely labelling different structures of the network (Chen *et al.*, 2015). These movements consist of stationary Brownian-like behaviour; directed movement of labelled regions along a tubule; merging of two adjacent puncta into a single punctum, and absorption and separation (mainly for cisternae) of discrete puncta into two independent puncta (Fig. S6).

© 2018 The Authors
New Phytologist © 2018 New Phytologist Trust

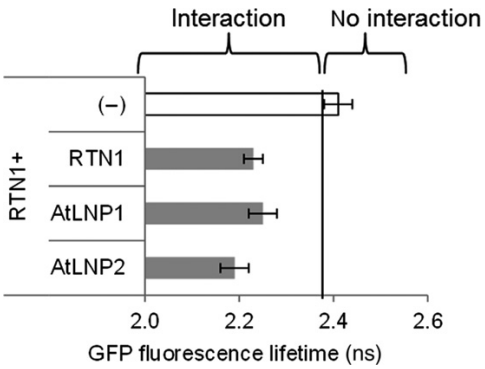


Fig. 7 AtLNP1 and AtLNP2 form protein–protein interactions with RTN1. Combinations of donor (GFP-RTN1) and acceptor constructs (RFP-RTN1, AtLNP1-RFP or AtLNP2-RFP) were coinfiltrated into *Nicotiana tabacum* leaf epidermal cells, and protein–protein interactions were assessed by Förster resonance energy transfer by fluorescence lifetime imaging microscopy analysis. For each measurement, a region of low-mobility endoplasmic reticulum continuous with the nuclear envelope was selected, and the fluorescence lifetime of the donor fluorophore was measured. Bar graphs depict the mean fluorescence lifetime (ns) ± SD. For each combination, at least two biological samples with a minimum of three technical replicates were used for the statistical analysis. The fluorescence lifetime of the donor construct (GFP-RTN1) in the absence of an acceptor was used as a negative control (white bar). As RTN1 is known to form homo-oligomers, the fluorescence lifetime of GFP-RTN1 in the presence of the RFP-RTN1 acceptor was used as a positive control. Lifetimes significantly lower than those of GFP-RTN1 alone (left side of the black line) indicate protein–protein interactions.

Further analysis of videos compiled from the time-lapse images (total of 30 images) revealed that out of the 90 AtLNP1-labelled puncta (junctions or smaller cisternae) analysed in 20 videos, 59 (66%) moved from their original position. The remaining 31 (34%) puncta stayed fixed in their location and did not move. Moreover, within the duration of the time-lapse experiment, 16 of these 90 AtLNP1-labelled puncta also fused together, whilst seven puncta were absorbed into ER sheets. This appears to differ from the mammalian system cells where a significant majority (74%) of stable junctions are labelled with mLnp1 and < 6% of unstable junctions actually acquire mLnp1 (Chen *et al.*, 2015).

To test if the presence of AtLNP1 actively stabilizes the ER network or if AtLNP1-labelled junctions and cisternae follow the overall movement of the network as a whole, the dynamics of AtLNP1-labelled junctions and cisternae were analysed in comparison to the surrounding network (Fig. 9). Persistency mapping was performed on videos capturing the movement of AtLNP1-GFP labelled junctions and cisternae (Fig. 9a,b). Persistency was assessed using spatiotemporal projections of AtLNP1-GFP labelled cells over 60 s with analysis performed on both relatively stable (Fig. 9c) and more dynamic (Fig. 9d) regions of the cortical ER network with cytoplasmic streaming. In the more stable areas of the ER where remodelling was minimal, AtLNP1-labelled ER elements similarly exhibited limited mobility and thus had high persistency (Fig. 9b,c). It should also be noted that stable three-way junctions and polygons were frequently observed not to have acquired AtLNP1. In areas of high motility, AtLNP1-labelled areas also show high motility and low persistency (Fig. 9b,d).

We also investigated if the expression of AtLNP1 has an influence on the overall ER network dynamics. For this, videos were acquired (Fig. S7) and the ER network persistency was analysed for RFP-HDEL with and without AtLNP1-GFP (Fig. 10). As a control, Latrunculin B, which disrupts F-actin formation and has

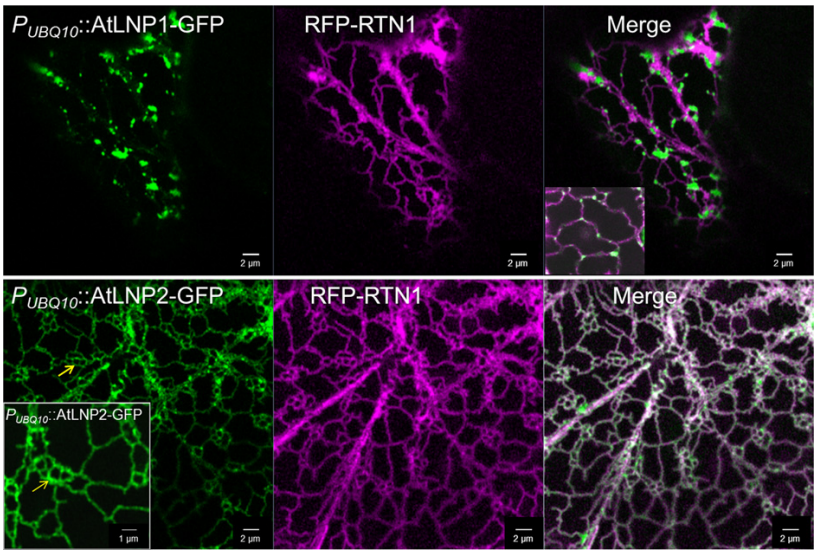


Fig. 8 Overexpression of RTN1 influences the localization of both AtLNP1 and AtLNP2. AtLNP1-GFP (P_{UBQ10}::AtLNP1-GFP, OD = 0.3) and AtLNP2-GFP (P_{UBQ10}::AtLNP2-GFP, OD = 0.3) were agroinfiltrated into *Nicotiana tabacum* leaf epidermal cells alongside RFP-RTN1 (35S::RFP-RTN1, OD = 0.1). Transient coexpression of AtLNP1 together with RTN1 results in the loss of large AtLNP1-labelled cisternae usually seen at this optical density. Coexpression of RTN1 and AtLNP2, which is less sheet-specific and also localizes to endoplasmic reticulum (ER) tubules, results in the formation of ER nodules (yellow arrow). Insets are magnifications of portions of the images.

© 2018 The Authors
New Phytologist © 2018 New Phytologist Trust

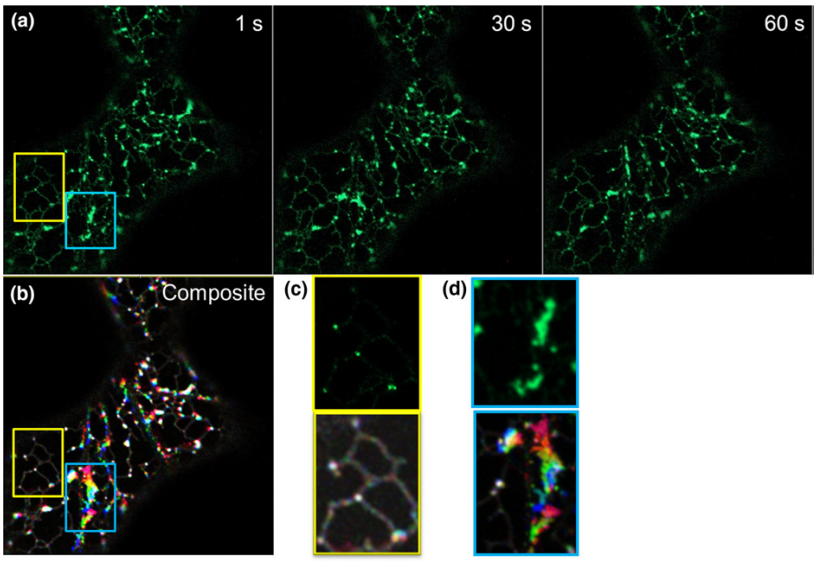


Fig. 9 Persistency mapping of AtLNP1-labelled endoplasmic reticulum (ER) cisternae and three-way junctions. (a) P_{UBQ10}::AtLNP1-GFP was transiently expressed in *Nicotiana tabacum* leaf epidermal cells. Videos of ER cisternae labelled with P_{UBQ10}::AtLNP1-GFP were taken over 60 s. Static images of the AtLNP1-GFP-labelled ER network are shown at 1, 30 and 60 s. (b) Composite image of the three time points shown in (a) following temporal colour coding of the video (performed in the ImageJ 'temporal color-code' plugin). White areas indicate points of persistency occurring for the duration of the time imaged, and coloured areas indicate movement, with areas in red showing the highest mobility. (c) Magnification of a stable region of the ER (framed in yellow in b). Confocal image of AtLNP1-GFP-labelled three-way junctions (top) and the corresponding persistency map (bottom). Within this relatively stable area of the ER network, both AtLNP1-labelled junctions and junctions with no detectable AtLNP1 expression remain persistent. (d) Magnification of a highly motile region of the ER undergoing rapid remodelling (framed in blue in b). Confocal image of AtLNP1-GFP-labelled three-way junctions and cisternae (top) and the corresponding persistency map (bottom).

been shown to stop/slow the ER network, was used together with RFP-HDEL. Cumulative fluorescence intensity (CFI) values of RFP-HDEL (with and without AtLNP1 or Latrunculin B) networks were calculated (Tolmie *et al.*, 2017); in this analysis a higher proportion of higher CFI values indicates a more static network, while a higher proportion of lower CFI values means a more dynamic network. Only Latrunculin B treatment, but not coexpression with AtLNP1, resulted in a significant increase of network persistency, indicating that AtLNP1 does not change network dynamics (Fig. 10).

Taken together, these data indicate that, unlike in mammalian systems, ER three-way junctions and network stability are not dependent on the presence of AtLNP1, but that the motility of AtLNP1-labelled junctions and cisternae follows the motility or persistency of the surrounding ER network architecture structure.

Discussion

Here we have reported the identification and characterization of two plant homologues (AtLNP1 and AtLNP2) of the mammalian and yeast LNP proteins.

Subcellular location of Arabidopsis LNP proteins

AtLNP1 localizes mainly to cisternae and a small proportion of three-way junctions in the ER network. This is in contrast to the subcellular localization described for yeast and mammalian Lnp proteins which is rather specific to three-way junctions; yeast and mammalian Lnp proteins label *c.* 50% of three-way junctions, resulting in their stabilization (Chen *et al.*, 2012; Shemesh *et al.*, 2014; Wang *et al.*, 2016). Both AtLNP1 and its animal counterpart can also label ER tubules at higher protein expression levels (Shemesh *et al.*, 2014; Wang *et al.*, 2016). By contrast, AtLNP2 expression was observed throughout the ER network, in both cisternae and tubules, suggesting that, despite sharing 67% protein sequence homology with AtLNP1, they are most likely not complete functional homologues. Single knockdown *lnp1* mutants display a less visible morphological phenotype than the double *lnp1lnp2* mutant (Figs 5, 6), but nonetheless the increase in polygonal area size and the decrease in the amount of cisternal areas are statistically significant (Fig. 5). Polygonal areas are increasing 1.4-fold in *lnp1* but over fivefold in *lnp1lnp2* compared with Col-0, and cisternal areas are reduced by 50% in *lnp1* but by 75% in *lnp1lnp2* compared with Col-0. As the additional knockdown in AtLNP2 seems to enhance the ER network phenotype, this could indicate some degree of functional redundancy. Furthermore, to date, no second LNP protein with an ER tubular localization has been described in yeast and mammalian systems that would correspond to AtLNP2, raising the question about function and redundancy of the second Arabidopsis LNP protein. Phylogenetic analysis of LNP orthologues in other land plant species also failed to reveal the existence of

© 2018 The Authors
New Phytologist © 2018 New Phytologist Trust

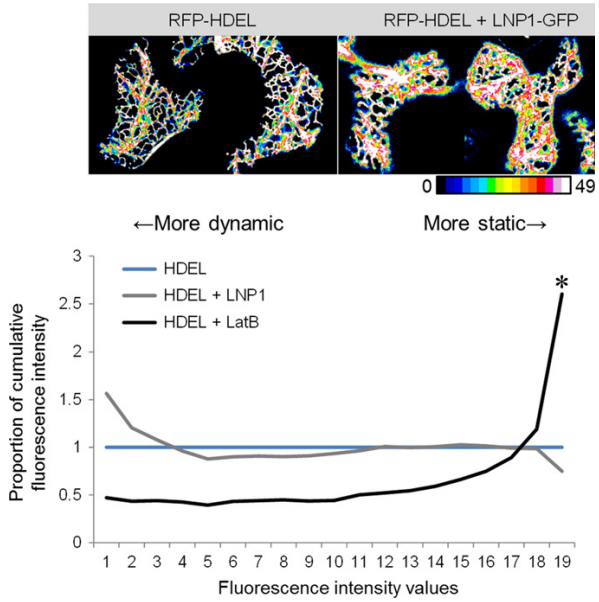


Fig. 10 Endoplasmic reticulum (ER) network dynamics with and without AtLNP1 protein. ER network persistency was analysed in *Nicotiana tabacum* leaf epidermal cells for RFP-HDEL alone (blue line), together with AtLNP1 (grey line), as well as after application of the drug Latrunculin B (black line) which disrupts F-actin formation and has been shown to stop/slow the ER network. Cumulative fluorescence intensity (CFI) values of RFP-HDEL networks are calculated using cumulative fluorescence intensity; a higher proportion of higher CFI values indicates a more static network, while a higher proportion of lower CFI values means a more dynamic network. Colour-coded example images are shown at the top as a heat map: white shows pixels that were occupied during the entire time-series (50 frames), and blue indicates pixels that were only occupied for a few time frames. The graph represents the CFI distribution. All conditions are expressed as a ratio compared with the RFP-HDEL control, hence the RFP-HDEL curve itself is always one. Data indicate that AtLNP1 expression does not affect ER network dynamics, but Latrunculin B significantly slows down ER network movement (indicated by asterisk *). $n = 10$.

two (or more) obvious subgroups of LNP proteins which may have, for example, developed distinct functionality. *Homo sapiens*, by contrast, code for at least five Lnp isoforms, which may potentially have different spatiotemporal expression patterns and/or functional specialization.

LNP function in the ER network

Overexpression of Arabidopsis LNP proteins results in increased cisternae formation in a dose-dependent manner (Fig. 4). By contrast, in mammalian cells it has previously been demonstrated that increasing amounts of mLnp1 protein result initially in ER cisternae induction, followed by the generation of thicker ER tubules at higher mLnp1 expression levels (Wang *et al.*, 2016). In COS cells (Shemesh *et al.*, 2014) mLnp1 localizes to three-way junctions at low expression levels as well as to some punctae on tubules. Higher mLnp1 expression levels result in clustered localization to densely branched tubules, also resulting in increased numbers of three-way junctions; at very high expression levels, Lnp localizes to longer, unbranched tubules concomitant with a decrease in three-way junctions. No such decrease in three-way junction abundance or thicker ER tubules were observed upon increased LNP expression in either tobacco or Arabidopsis (Figs 3, 4), although this may be a result of the limitations of achievable maximal protein expression levels in the transient expression system as very high doses of agrobacterium frequently result in leaf necrosis.

Analysis of both loss- and gain-of-function mutants in the two identified AtLNP proteins revealed further potential functional differences between plant and mammalian/yeast LNP proteins. Knockdown of AtLNP1 alone has a significant increase in polygonal region areas and a significant reduction in cisternae (Fig. 5). A *lnp1lnp2* × GFP-HDEL knockdown line exhibited a significant reduction in cisternal area (Fig. 6d) and a significantly increased mean ER polygonal area in comparison to the GFP-HDEL control (Fig. 6c). The polygonal areas of the mutant also spanned a greater size distribution than those of the wild-type control (Fig. 6c), ultimately resulting in a less structured, 'looser' ER network in the mutant. A trend towards fewer three-way junctions was observed in both the *lnp1* mutant (Fig. 5d) and the *lnp1lnp2* mutant (Fig. 6e) but this was not significant in both mutants. This observed ER morphology upon depletion of AtLNP again contrasts with that described in similar studies in yeast and mammalian systems. Mutations in the zinc finger motif of yeast Lnp1p led to a reduction in polygon size and thus resulted in a densely reticulated network (Chen *et al.*, 2012), and, similarly, the loss of mLnp1 gave rise to a more compact, sheet-like ER morphology (Chen *et al.*, 2015). Lnp mutant forms expressed in U2OS cells lacking Lnp show sheet generation with a reduction in tubules and junctions (Wang *et al.*, 2016). Moreover, addition of cytoplasmic fragments of *Xenopus* Lnp acting as a dominant-negative mutant to a *Xenopus* network formation resulted in the replacement of three-way junctions by small cisternae, as well as an overall reduction in three-way junctions (Wang *et al.*, 2016). These results recently led Wang *et al.* (2016) to conclude that mammalian mLnp1 is not essential for ER tubule and junction formation but instead affects three-way junction abundance. In the plant system we did not observe an increase in junctions (as described for yeast), or cisternae (as described in yeast and mammalian cells), but rather the opposite.

We hypothesize that the striking changes in polygonal structure and areas reported here for the Arabidopsis *lnp1* and *lnp1lnp2* knockdown lines are a result of the loss of cisternal areas rather than of the nonsignificant reduction in nascent three-way junctions. A possible explanation for the ER morphology observed in the mutants is that depletion of AtLNP1 (and AtLNP2) results in a decrease in cisternae and/or reduction in cisternal stability, which might result in a change in the biophysical properties of the ER, leading to a less stable and structured network. This is also in agreement with the formation of enlarged cisternal structures upon overexpression of Arabidopsis LNP proteins, as described earlier (Fig. 4).

Several functions for LNP proteins have been suggested in the various systems studied and these are rather diverse. In *Caenorhabditis elegans*, mutations in lnp-1 have been linked to

© 2018 The Authors
New Phytologist © 2018 New Phytologist Trust

neuronal defects similar to those in atlastin or the Yop1p homologue REEP1 mutants (Ghila & Gomez, 2008).

A function for mLnp1 in the stabilization of three-way junctions has been discussed (Chen *et al.*, 2015). Through immunolabelling of endogenous mLnp1, Chen *et al.* (2015) showed that the protein is only detectable in about half of the three-way junctions in the mammalian network. The group also reported that junctions with mLnp1 are less mobile than junctions without mLnp1 and are less likely to show junction loss through ring closure (Chen *et al.*, 2015). A fraction of newly formed junctions go on to acquire mLnp1 protein. Newly formed junctions that do not acquire mLnp1 have a high probability of loss through ring closure and are relatively mobile, whereas, conversely, those that do acquire mLnp1 have a greatly reduced probability of loss and are less mobile. This is especially prominent in newly formed junctions, indicating that mLnp1 stabilizes newly formed three-way junctions but is not required to be continually present on the junction thereafter (Chen *et al.*, 2015). In the absence of mLnp1, new junctions are still being formed but are less likely to persist, resulting in more sheet-like structures (Chen *et al.*, 2015). For the plant system we could not find any indication that AtLNP1 or 2 stabilizes three-way junctions. The network dynamics is instead dependent on the surrounding network rather than on the presence or absence of LNP proteins (Fig. 9).

For mammalian cells it was also suggested that mLnp1 is not necessary for the generation or maintenance of the ER network as, in the absence of mLnp1, there is still a reticular network, even if most three-way junctions are converted into larger cisternae (Wang *et al.*, 2016). Instead, mLnp1 proteins are proposed to move into three-way junctions with the overexpression of mLnp1 resulting in the expansion of cisternae, but atlastin proteins are suggested to be responsible for the initial formation of native junctions (Wang *et al.*, 2016).

Interestingly, a theoretical model predicts mLnp1 to be a so-called S-type protein capable of stabilizing curvature and favouring negative curvature, which plays an important role in generating and stabilizing three-way junctions (Shemesh *et al.*, 2014). This contradicts the hypothesis of Chen *et al.* (2012) that Lnp proteins are involved in abolishing three-way junctions in yeast. The latter was suggested following the observation that the ER in lnp1p mutants is highly reticulated resulting in an increased abundance of three-way junctions. However, Shemesh *et al.* (2014) suggest that this might well be a cisternal structure rather than a reticulated network as the two cannot be distinguished at the resolution of the images. The model of Shemesh *et al.* (2014) is also of interest to Arabidopsis LNP proteins as cisternae are often bordered by negatively curved edge lines. In Arabidopsis we find RTN proteins on the curved edges of cisternae (Sparkes *et al.*, 2010) whereas AtLNP1 labels more the flat part of the central membrane rather than the edges (Fig. 3c,d). This may hint at a mechanism for how AtLNP1 and 2 induce or stabilize cisternae and work in collaboration with RTN proteins to retain the cisternae–tubule ratio.

Interaction with reticulons

In yeast, it is suggested that Lnp1p acts in synergy with the reticulons and Yop1p. Indeed, Lnp1p has been shown to interact with Rtn1p, Yop1p and Sey1p, as a loss-of-function mutation in Lnp1p in a rtn1/rtn2/yop1 triple mutant results in growth and ER morphological defects (Chen *et al.*, 2012). Lnp1p physically interacts with Rtn1p, indicating that they may act on converging pathways, as mutants in these genes display different ER phenotypes: loss of Lnp1p leads to the formation of densely reticulated ER (Chen *et al.*, 2012), whereas the loss of Rtn1p results in non-fenestrated sheets (De Craene *et al.*, 2006).

In mammalian cells it has been proposed that Lnp proteins are not required for ER network formation but instead are involved in the formation of sheets at tubule junctions (Wang *et al.*, 2016). The presence of Lnp within the three-way junctions may then prevent the migration of reticulons into the junction, thereby preventing junction expansion; in the absence of LNP, three-way junctions could therefore expand into large sheets (Wang *et al.*, 2016).

We show here that the AtLNP1 and 2 proteins are capable of interacting with reticulons (Fig. 7) and, moreover, that the induction of large cisternal regions resulting from LNP overexpression is suppressed by coexpression of reticulon proteins (Fig. 8). We therefore hypothesize that, in Arabidopsis, LNP and reticulon proteins function in concert to maintain the ratio of ER cisternae to tubules and are capable of interconverting the two morphologies.

In conclusion, we propose that Arabidopsis LNP proteins are involved in the formation and/or stabilization of ER network cisternae. They are also highly likely to functionally cooperate with other ER morphogens such as the reticulon family of proteins, with which they interact *in planta*. One hypothetical scenario could be that LNP proteins which are labelling cisternae but not the edges (Fig. 3c,d) induce the flat membranes of cisternae, whereas reticulons that localize to the edge of cisternae (Sparkes *et al.*, 2010) induce curvature, thereby limiting cisternal expansion. In contrast to that described for their yeast and mammalian orthologues, Arabidopsis LNP proteins label only a small proportion of junctions which could also potentially be small cisternae, and we did not find any evidence that they stabilize ER three-way junctions. The presence of two LNP homologues within the Arabidopsis genome that show distinct subcellular localization but which might also have some degree of functional redundancy is of interest. We are currently investigating the impact of the different localizations of AtLNP1 and 2 on the ER and resulting functionality, as well as the interactions of the AtLNP proteins with other ER-shaping proteins.

Acknowledgements

The authors thank Dr Imogen Sparkes (University of Bristol, UK) for initial discussions on the LNP work and Samuel Williams for technical support. This work was supported by the British Biotechnology and Biological Sciences Research

© 2018 The Authors
New Phytologist © 2018 New Phytologist Trust

Council (grants BB/J017582/1 to L.F. and BB/M000168/1 to C.H.) via the ERA-CAPs programme 'Per Aspera' (grant no. BB/J004987/1), the Science and Technology Facilities Council Program (grant no. 14230008 to C.H.), and a Vice Chancellor's Research Fellowship from Oxford Brookes University (UK) to V.K.

Author contributions

V.K. and C.H. designed the research. E.B. and L.F. cloned constructs, generated the mutant lines and performed the LNPARK amino acid comparative motif analysis. C.P. and F.T. carried out the mutant and network movement analysis. V.K. cloned constructs and carried out confocal microscopy as well as the overexpression, persistency and FRET-FLIM analysis. All authors contributed to the writing of the article.

References

Altschul SF, Gish W, Miller W, Myer EW, Lipman DJ. 1990. Basic local alignment search tool. *Journal of Molecular Biology* **215**: 403–410.

Brandizzi F, Hanton S, Pinto DaSilva LL, Boevink P, Evans D, Oparka K, Denecke J, Hawes C. 2003. ER quality control can lead to retrograde transport from the ER lumen to the cytoplasm and the nucleoplasm in plants. *Plant Journal* **34**: 269–281.

Breeze E, Dzimitrowicz N, Kriechbaumer V, Brooks R, Botchway SW, Brady JP, Hawes C, Dixon AM, Schnell JR, Fricker MD *et al.* 2016. A C-terminal amphipathic helix is necessary for the *in vivo* tubule-shaping function of a plant reticulon. *Proceedings of the National Academy of Sciences, USA* **113**: 10902–10907.

Brown D, Feeney M, Ahmadi M, Lonoce C, Sajari R, Di Cola A, Frigerio L. 2017. Subcellular localization and interactions among rubber particle proteins from *Hevea brasiliensis*. *Journal of Experimental Botany* **68**: 5045–5055.

Casey AK, Chen S, Novick P, Ferro-Novick S, Wente SR. 2015. Nuclear pore complex integrity requires Lnp1, a regulator of cortical endoplasmic reticulum. *Molecular Biology of the Cell* **26**: 2833–2844.

Chen J, Stefano G, Brandizzi F, Zheng H. 2011. Arabidopsis RHD3 mediates the generation of the tubular ER network and is required for Golgi distribution and motility in plant cells. *Journal of Cell Science* **124**: 2241–2252.

Chen S, Desai T, McNew JA, Gerard P, Novick PJ, Ferro-Novick S. 2015. Lunapark stabilizes nascent three-way junctions in the endoplasmic reticulum. *Proceedings of the National Academy of Sciences, USA* **112**: 418–423.

Chen S, Novick P, Ferro-Novick S. 2012. ER network formation requires a balance of the dynamin-like GTPase Sey1p and the Lunapark family member Lnp1p. *Nature Cell Biology* **14**: 707–716.

Clough SJ, Bent AF. 1998. Floral dip: a simplified method for Agrobacterium-mediated transformation of *Arabidopsis thaliana*. *Plant Journal* **16**: 735–743.

Crooks GE, Hon G, Chandonia JM, Brenner SE. 2004. WebLogo: a sequence logo generator. *Genome Research* **14**: 1188–1190.

De Craene JO, Coleman J, Estrada de Martin P, Pypaert M, Anderson S, Yates JR, Ferro-Novick S, Novick P. 2006. Rtn1p is involved in structuring the cortical endoplasmic reticulum. *Molecular Biology of the Cell* **17**: 3009–3020.

Dekkers BJW, Willems L, Bassel GW, van Bolderen-Veldkamp RPM, Ligterink W, Hilhorst HWM, Bentsink L. 2012. Identification of reference genes for RT-qPCR expression analysis in Arabidopsis and tomato seeds. *Plant and Cell Physiology* **53**: 28–37.

Friml J, Jones AR. 2010. Endoplasmic reticulum: the rising compartment in auxin biology. *Plant Physiology* **154**: 458–462.

Ghila L, Gomez M. 2008. The evolutionarily conserved gene LNP-1 is required for synaptic vesicle trafficking and synaptic transmission. *European Journal of Neuroscience* **27**: 621–630.

Goyal U, Blackstone C. 2013. Untangling the web: mechanisms underlying ER network formation. *BBA – Molecular Cell Research* **1833**: 2492–2498.

Grefen C, Donald N, Hashimoto K, Kudla J, Schumacher K, Blatt MR. 2010. A ubiquitin-10 promoter-based vector set for fluorescent protein tagging facilitates temporal stability and native protein distribution in transient and stable expression studies. *Plant Journal* **64**: 355–365.

Griffing LR. 2010. Networking in the ER. *Biochemical Society Transactions* **38**: 747–753.

Hawes C, Kiviniemi P, Kriechbaumer V. 2015. The endoplasmic reticulum: a dynamic and well-connected organelle. *Journal of Integrative Plant Biology* **57**: 50–62.

Hawes C, Wang P, Kriechbaumer V. 2018. Labeling the ER for light and fluorescence microscopy. *Methods in Molecular Biology* **1691**: 1–14.

Herman EM. 2008. Endoplasmic reticulum bodies: solving the insoluble. *Current Opinion in Plant Biology* **11**: 672–679.

Hong B, Ichida A, Wang Y, Gens JS, Pickard BG, Harper JF. 1999. Identification of a calmodulin-regulated Ca^{++}-ATPase in the endoplasmic reticulum. *Plant Physiology* **119**: 1165–1175.

Huang AHC. 1996. Oleosins and oil bodies in seeds and other organs. *Plant Physiology* **110**: 1055–1061.

Kriechbaumer V, Botchway SW, Slade SE, Knox K, Frigerio L, Oparka K, Hawes C. 2015. Reticulomics: protein–protein interaction studies with two plasmodesmata-localized reticulon family proteins identify binding partners enriched at plasmodesmata, endoplasmic reticulum, and the plasma membrane. *Plant Physiology* **169**: 1933–1945.

Meng L, Feldman L. 2010. A rapid TRIzol-based two-step method for DNA-free RNA extraction from Arabidopsis siliques and dry seeds. *Biotechnology Journal* **5**: 183–186.

Moriya K, Nagatoshi K, Noriyasu Y, Okamura T, Takamitsu E, Suzuki T, Utsumi T. 2013. Protein *N*-myristoylation plays a critical role in the endoplasmic reticulum morphological change induced by overexpression of protein Lunapark, an integral membrane protein of the endoplasmic reticulum. *PLoS ONE* **8**: e78235-13.

Ossowski S, Schwab R, Weigel D. 2008. Gene silencing in plants using artificial microRNAs and other small RNAs. *Plant Journal* **53**: 674–690.

Powers RE, Wang S, Liu TY, Rapoport TA. 2017. Reconstitution of the tubular endoplasmic reticulum network with purified components. *Nature* **543**: 257–260.

Proost S, Van Bel M, Sterck L, Billiau K, Van Parys T, Van de Peer Y, Vandepoele K. 2009. PLAZA: a comparative genomics resource to study gene and genome evolution in plants. *Plant Cell* **21**: 3718–3731.

Schoberer J, Botchway SW. 2014. Investigating protein–protein interactions in the plant endomembrane system using multiphoton-induced FRET-FLIM. *Methods in Molecular Biology* **1209**: 81–95.

Schwab R, Ossowski S, Riester M, Warthmann N, Weigel D. 2006. Highly specific gene silencing by artificial microRNAs in Arabidopsis. *The Plant Cell Online* **18**: 1121–1133.

Shemesh T, Klemm RW, Romano FB, Wang S, Vaughan J, Zhuang X, Tukachinsky H, Kozlov MM, Rapoport TA. 2014. A model for the generation and interconversion of ER morphologies. *Proceedings of the National Academy of Sciences, USA* **111**: E5243–E5251.

Sparkes I, Tolley N, Aller I, Svozil J, Osterrieder A, Botchway S, Mueller C, Frigerio L, Hawes C. 2010. Five Arabidopsis reticulon isoforms share endoplasmic reticulum location, topology, and membrane-shaping properties. *Plant Cell* **22**: 1333–1343.

Sparkes IA, Runions J, Kearns A, Hawes C. 2006. Rapid, transient expression of fluorescent fusion proteins in tobacco plants and generation of stably transformed plants. *Nature Protocols* **1**: 2019–2025.

Stefano G, Brandizzi F. 2017. Advances in plant ER architecture and dynamics. *Plant Physiology* **6**: 01261.2017.

Stubbs CD, Botchway SW, Slater SJ, Parker AW. 2005. The use of time-resolved fluorescence imaging in the study of protein kinase C localisation in cells. *BMC Cell Biology* **6**: 22.

Tolmie F, Poulet A, McKenna J, Sassmann S, Graumann K, Deeks M, Runions J. 2017. The cell wall of *Arabidopsis thaliana* influences actin network dynamics. *Journal of Experimental Botany* **68**: 4517–4527.

© 2018 The Authors
New Phytologist © 2018 New Phytologist Trust

Turnbull D, Hemsley PA. 2017. ScienceDirect Fats and function: protein lipid modifications in plant cell signalling. *Current Opinion in Plant Biology* **40**: 63–70.

Wallis JG, Browse J. 2010. Lipid biochemists salute the genome. *Plant Journal* **61**: 1092–1106.

Wang S, Tukachinsky H, Romano FB, Rapoport TA. 2016. Cooperation of the ER-shaping proteins atlastin, lunapark, and reticulons to generate a tubular membrane network. *eLife* **5**: e18605.

Winter D, Vinegar B, Nahal H, Ammar R, Wilson GV, Provart NJ. 2007. An "Electronic Fluorescent Pictograph" browser for exploring and analyzing large-scale biological data sets. *PLoS ONE* **2**: e718.

Zhang M, Wu F, Shi J, Zhu Y, Zhu Z, Gong Q, Hu J. 2013. ROOT HAIR DEFECTIVE3 family of dynamin-like GTPases mediates homotypic endoplasmic reticulum fusion and is essential for Arabidopsis development. *Plant Physiology* **163**: 713–720.

Supporting Information

Additional Supporting Information may be found online in the Supporting Information section at the end of the article:

Fig. S1 Analysis of *LNP* transcript abundance in Arabidopsis amiRNA lines.

Fig. S2 Microarray data in the eFP browser for At*LNP1* and At*LNP2*.

Fig. S3 Lunapark motif analysis in Embryophyta species.

Fig. S4 OD expression series for AtLNP1 and AtLNP2 in tobacco epidermal leaf cells (addition to Fig. 4).

Fig. S5 Raw data for protein–protein interactions by FRET-FLIM (addition to Fig. 7).

Fig. S6 AtLNP1-labelled cisternae display different dynamic behaviours.

Fig. S7 Example movies for ER network persistency analysis in Fig. 10.

Please note: Wiley Blackwell are not responsible for the content or functionality of any Supporting Information supplied by the authors. Any queries (other than missing material) should be directed to the *New Phytologist* Central Office.



About *New Phytologist*

- *New Phytologist* is an electronic (online-only) journal owned by the New Phytologist Trust, a **not-for-profit organization** dedicated to the promotion of plant science, facilitating projects from symposia to free access for our Tansley reviews and Tansley insights.
- Regular papers, Letters, Research reviews, Rapid reports and both Modelling/Theory and Methods papers are encouraged. We are committed to rapid processing, from online submission through to publication 'as ready' via *Early View* – our average time to decision is <26 days. There are **no page or colour charges** and a PDF version will be provided for each article.
- The journal is available online at Wiley Online Library. Visit **www.newphytologist.com** to search the articles and register for table of contents email alerts.
- If you have any questions, do get in touch with Central Office (np-centraloffice@lancaster.ac.uk) or, if it is more convenient, our USA Office (np-usaoffice@lancaster.ac.uk)
- For submission instructions, subscription and all the latest information visit **www.newphytologist.com**

© 2018 The Authors
New Phytologist © 2018 New Phytologist Trust

nature COMMUNICATIONS

ARTICLE

https://doi.org/10.1038/s41467-019-08893-9 OPEN

Quantitative analysis of plant ER architecture and dynamics

Charlotte Pain [1], Verena Kriechbaumer [1], Maike Kittelmann [1], Chris Hawes [1] & Mark Fricker [2]

The endoplasmic reticulum (ER) is a highly dynamic polygonal membrane network composed of interconnected tubules and sheets (cisternae) that forms the first compartment in the secretory pathway involved in protein translocation, folding, glycosylation, quality control, lipid synthesis, calcium signalling, and metabolon formation. Despite its central role in this plethora of biosynthetic, metabolic and physiological processes, there is little quantitative information on ER structure, morphology or dynamics. Here we describe a software package (AnalyzER) to automatically extract ER tubules and cisternae from multi-dimensional fluorescence images of plant ER. The structure, topology, protein-localisation patterns, and dynamics are automatically quantified using spatial, intensity and graph-theoretic metrics. We validate the method against manually-traced ground-truth networks, and calibrate the sub-resolution width estimates against ER profiles identified in serial block-face SEM images. We apply the approach to quantify the effects on ER morphology of drug treatments, abiotic stress and over-expression of ER tubule-shaping and cisternal-modifying proteins.

[1] Department of Biological and Medical Sciences, Oxford Brookes University, Oxford OX3 0BP, UK. [2] Department of Plant Sciences, University of Oxford, South Parks Road, Oxford OX1 3RB, UK. Correspondence and requests for materials should be addressed to M.F. (email: mark.fricker@plants.ox.ac.uk)

Much of our understanding of the structure, function and dynamics of the endoplasmic reticulum (ER) in plants has come from live-cell imaging of the ER in epidermal cells using video-enhanced microscopy or after labelling with fluorescent dyes[1–3], or expression of transgenic reporters, such as GFP-HDEL[4–7]. Typically labelled ER is visualised in paradermal optical sections using confocal microscopy where the ER is constrained to an almost planar structure by the thin layer of cortical cytoplasm underlying the periclinal cell wall[5]. In general, the cortical ER forms a complex dynamic polygonal network of membrane-bounded tubules and flattened sheet-like cisternae that ramify throughout the cytoplasm[8–10]. However, the morphology of the tubules, the size and shape of the cisternae, and the proportion of tubules to cisternae varies during development[6,10–12], and under different experimental treatments[7,13]. For example, over-expression of members of the reticulon ER-shaping protein family[14–18], causes constrictions along the length of the tubules, and can convert cisternae to tubules[16]. Likewise, the morphology of the cisternae is affected by proteins, such as Lunapark 1 and 2, that can induce cisterna formation[19], and drug treatments, such as Brefeldin A (BFA)[13], which can vary the size and abundance of cisternae. The cisternae may not be simple uniform compartments. Thus, early in plant development the cisternae form large sheets punctuated by fenestrations[6,20], while in animal cells the distribution of ER lumen and tubule markers across cisternae fluctuates during live cell imaging, suggesting that cisternae may result from local appression of multiple tubules, resulting in a sub-resolution tubular matrix with internal spaces that can only be resolved with super-resolution techniques[21].

Quantitative measurements are further complicated in plants, as the ER network is highly dynamic, with rapid bulk streaming along actin cables, localised tubule extension, shrinkage, sliding and breakage, and expansion, contraction, reshaping and movement of cisternae[3,8,10,22]. While the velocity of discrete structures, such as the plant Golgi, can be readily quantified by tracking algorithms[22,23], alternative approaches based on optical flow[24], are required to estimate velocities for the ER. For example, local cross-correlation of small image patches was used to estimate ER movement between frames[25], and reported the maximum velocity around 1–2 μm s^{-1}. The maximum speeds in the thicker cytoplasmic strands running deeper into the cell range from 4 to 10 μm s^{-1} [3,26], similar to the maximum speeds for other organelles[22]. Motility of the ER is also dependent on cell type and developmental stage, and typically increases during cell expansion[20].

In addition to the highly dynamic movement, the plant ER network also has a subset of static elements, such as ER-plasma membrane contact sites (EPCS), that act as fixed anchors to stabilise the polygonal network[27]. These features are visible at the electron microscopy (EM) level[28] and have been characterised with nanometre resolution using TEM and electron tomography[12]. They have been identified in living cells using persistency analysis[5,29–34], and following manipulation using optical tweezers[22,29,35]. Increasing the expression of certain proteins, such as VAP27 and SYT1, modulate the number and size of EPCS, and also affect the stability of the ER network[27,33,34].

Overall it is clear that, a complete description of the ER should include metrics quantifying morphology, persistency and dynamics. However, previous quantitative morphological measurements of relative volumes of cisternae and tubules in plants have been made in fixed tissue using stereological analyses of EM images[36,37]. More recently, EM tomography and 3-D reconstruction have been used to analyse ER structure in yeast cells[38], and in cultured mammalian cells using fluorescence and serial block face SEM[39]. However, measurements of dynamics require living tissues, and live cell imaging techniques. This presents a further challenge as the width of the ER tubules is expected to be 30–50 nm[9], which is below the resolution of standard confocal microscopes. Super-resolution techniques, such as stimulated emission depletion microscopy (STED), have been used to resolve structures on this scale, but are not yet routinely available nor compatible with dynamic imaging of ER movement[40]. Nevertheless, the width of the ER can be estimated from the labelling intensity, assuming the relevant marker is evenly distributed within the lumen, there is a linear relationship between fluorescence intensity and volume, and the tubule is fully contained within the point-spread-function (psf) of the microscope[41,42].

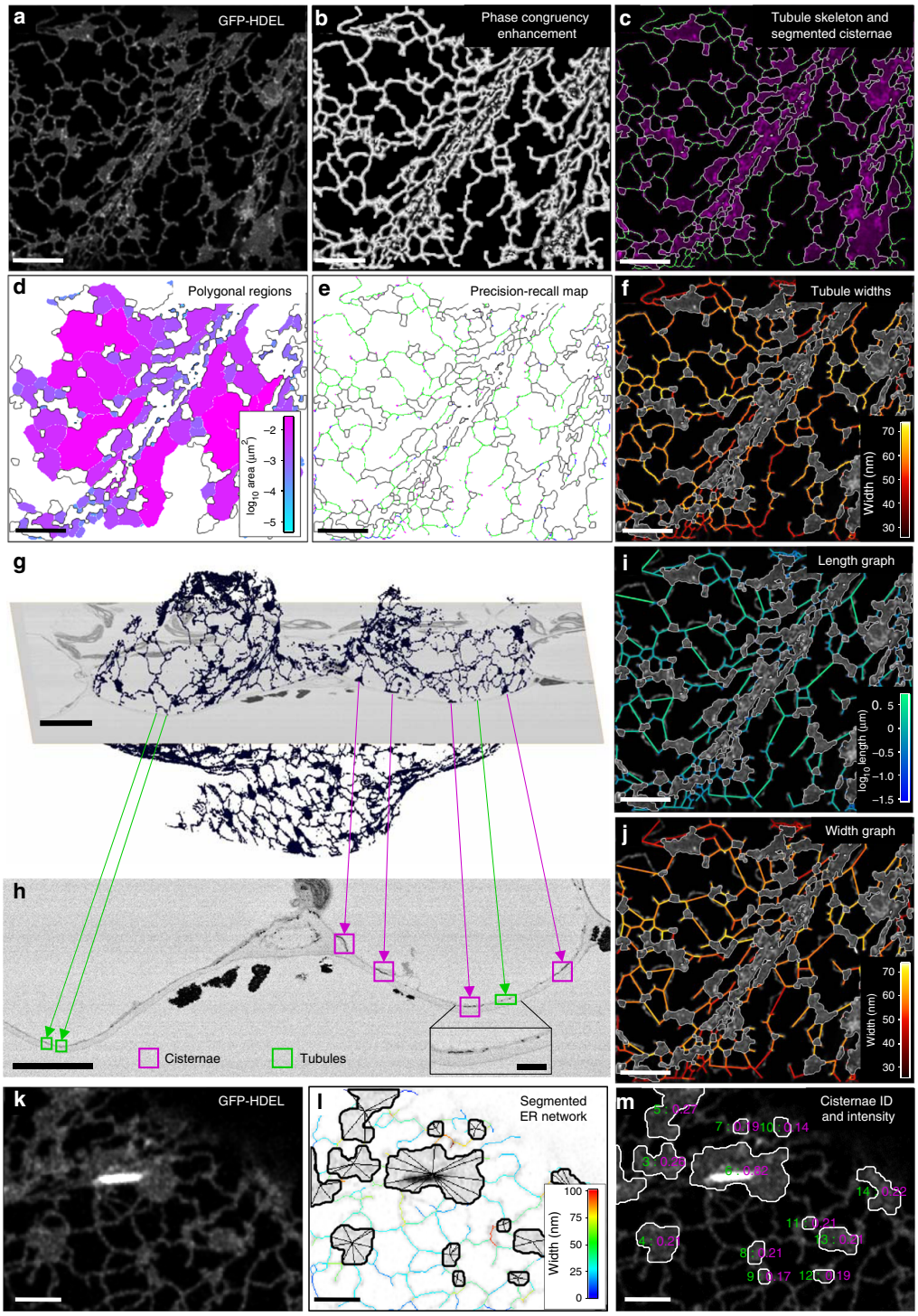
In addition to metric-based morphological measurements, topological measures of the ER network structure have been made from a graph representation of the network, where nodes represent junctions or free ends, and edges represent the interconnecting tubules[14,30,32,42,43]. Unlike morphological measurements, graph–theoretic measures reflect the connectivity of the ER, rather than the physical size of the components. They are therefore insensitive to errors in tubule width, but are critically dependent on extraction of a correctly connected network[43].

Given the wealth of information needed to characterise the structure and dynamics of the ER, and how these change with experimental treatments, we sought to develop an integrated analysis platform that combined existing measurement approaches into a coherent framework to provide complete quantitative information suitable for statistical evaluation. It is also important to enable rapid, medium throughput analysis to handle sufficient numbers of images to describe the variability present even within wild-type ER measurements. Here, we use a Zeiss 880 AiryScan confocal microscope to provide semi-high-resolution imaging of dynamic ER structures. The AnalyzER program then automatically quantifies (i) the length, width, morphology and protein distribution along ER tubules; (ii) the degree and branch angles at junctions (nodes) in the tubular network; (iii) the size, shape, and protein distribution in cisternae and around the perimeter of the cisternae; (iv) the topological organisation of the tubular and cisternal network determined using graph–theoretic metrics; (v) the distribution of immobile nodes, tubules and cisternae using persistency mapping; (vi) the local speed, direction, coherence, divergence and curl of movement of tubules and cisternae using optical flow; and (vii) the size and shape of the polygonal regions enclosed by the network.

The AnalyzER package is implemented in MatLab® (www.Mathworks.com) and available as a MatLab® app, or as a standalone package. It incorporates our previous tubule morphology analysis program[42], that was used to quantify tubule to analyse constrictions in the ER network caused by reticulon over-expression[14], but extends the analysis to quantitation of all aspects of ER structure and dynamics for multi-channel 4D time-series. The software package, manual, tutorial and test data sets are available from the Oxford Research Archive (ORA) (https://ora.ox.ac.uk/objects/uuid:cb0e2845-2a9c-495a-84f0-4dd2c5164463).

Results

Segmentation of tubules and cisternae. All aspects of the analyses are handled through a single graphical user interface (GUI) to provide an integrated platform (Supplementary Fig. 1). The analysis approach is illustrated for transient expression of the ER lumenal-marker GFP-HDEL in leaf epidermal cells of *Nicotiana tabacum* (Fig. 1a). The ER is typically segmented from confocal optical sections using an intensity-based threshold to give a binary image, often using Otsu's method[43–45]. However, a global



threshold excludes dimmer structures if it is set too high, or expands and fuses adjacent bright regions if it is set too low[43]. This is particularly problematic when the width, and hence intensity, of the tubules varies, for example, when analysing the effects of ER shaping proteins[14,42]. Segmentation of other biological network structures, including blood vessels[46], leaf veins[47], neurons[48], and fungal mycelia[49] use filters to highlight tubular structures based on local image gradients. However, these approaches tend to fail at junctions and also retain a significant component of the original image intensity, making subsequent thresholding challenging. Thus, we have used intensity-independent phase-congruency analysis over a range of scales and orientations to provide additional tubule enhancement and subsequent robust segmentation[50–52].

Fig. 1 Automated ER network analysis. **a** Analysis of a single tobacco leaf epidermal cell expressing the ER lumenal marker GFP-HDEL from a single paradermal optical section; **b** phase congruency enhancement of tubular elements using the local weighted mean phase angle; **c** hysteresis thresholding and thinning to produce a single pixel skeleton (green), and segmented cisternal structures (magenta with white boundary) following opening and active contour refinement; **d** polygonal regions pseudo-colour coded by $\log_{10}$ area; **e** comparison of the skeleton with a manually digitised ground truth (cisternae, black; true positives, green; false positives, blue; false negatives, magenta); **f** tubule width estimation using integrated granulometry; **g** A 3D reconstruction of the ER from an Arabidopsis leaf epidermal cell captured by SBF-SEM after zinc-iodine-osmium (ZIO) staining; **h** Enlargement of an SBF-SEM cross-section highlighting elements of tubular ER in green and cisternae in magenta, with a zoomed inset image (scale bar = 1 µm); **i**, **j** Graph representation of the ER network, with nodes at junctions linked by edges with a vector of properties including tubule length (**i**) and average width, excluding junctions (**j**). All scale bars = 5 µm, unless stated otherwise. **k** Arabidopsis plants stably expressing GFP-HDEL show high-intensity fluorescence concentrated in a single fusiform body within the ER; **l** segmentation of the cisterna containing the fusiform body using the lowest of multiple partitions of the image intensity histogram, with superimposed pixel skeleton colour-coded by width; **m** the maximum intensity value (magenta) is associated with a unique cisternal ID (green) which can be used to identify cisternae associated with fusiform bodies enabling separate quantification of their properties and behaviour. Scale bars = 2 µm

Tubule enhancement using the local weighted mean phase angle from phase-congruency analysis highlighted ridge-like elements, such as tubules, independent of their intensity (Fig. 1b), and ensured robust segmentation, even of tubules with low fluorescence, using subsequent hysteresis thresholding and thinning to give a single-pixel-wide skeleton (Fig. 1c). Sheet-like cisternae, regions of closely appressed tubules[21], or tubule/cisternal aggregates in moving streams were segmented independently using morphological opening (erosion followed by dilation) to remove the tubules[5]. The cisternal boundary was refined using active-contours to shrink the segmented region back onto the cisternal perimeter (Fig. 1c). The resulting objects were filtered to be above 0.3 µm^2, chosen to match the size of persistent puncta that are associated with immobile scaffold sites[5]. These puncta, although larger than the average junction in the network, were not considered as cisternae, but were included in the tubular network analysis as nodes. The other classes of non-tubular objects were not distinguished by morphology at this stage, but were classified using a combination of other features, such as speed and texture (see later). Completely enclosed polygonal regions within the ER network were also segmented from the complement of the combined tubule skeleton and cisternae (Fig. 1d).

We tested the accuracy of the automated segmentation against a set of manually-determined ground-truths using precision–recall analysis (Fig. 1e). Pixels matching the ground-truth were coded green, false positives coded blue and false negatives coded magenta, with a tolerance of half the minimum tubule diameter. In general, the automated extraction worked well for the central portion of any network (Dice Similarity Coefficient, $F_1 = 0.94 \pm 0.019$, mean ± s.e.m, $n = 5$), but there was more ambiguity at the margins where signals declined as the ER network moved out of focus following the curvature of the periclinal cell wall. To reduce these errors, we introduced additional masking around the boundary of the ER region using a contraction of the convex hull onto the irregular boundary, followed by erosion by 4–6 pixels to exclude low-level fluorescent structures on the periphery. The masked region was also used to define the area analysed for density-based measurements.

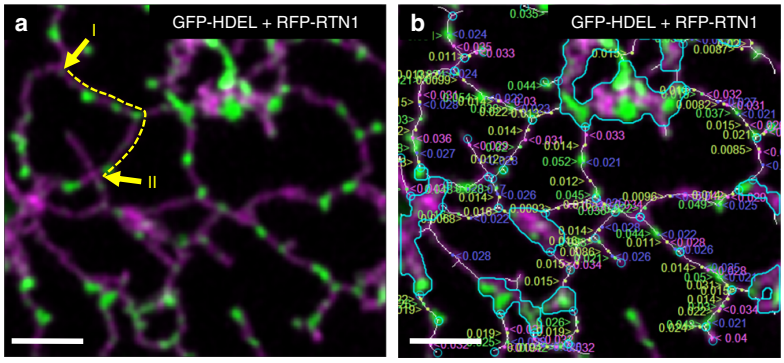
Estimation of tubule width. The initial estimate of the tubule width at each pixel in the skeleton was determined by granulometry techniques through a series of opening and closing operations with disk-shaped elements of increasing radii[51]. This builds up an intermediate (x,y,s) image, where s is the result of opening and closing at scale, s, which effectively maps the intensity of successive adjacent pixels back onto the skeleton in each layer in the (x,y,s) image. The result is an intensity profile normal to the tubule in s for each pixel in the skeleton. The width of each tubule was estimated from either the position of the maximum (negative) gradient of the granulometry curve, or the integrated intensity under the curve as a measure of the relative amount of probe present locally (Fig. 1f). The actual width of tubules and cisternae were determined independently from ER profiles in transverse sections using serial-section block-face SEM (SBF-SEM) of *Arabidopsis* leaf tissue stained with zinc-iodide-osmium tetroxide (ZIO), and subsequent reconstructions with 90° rotation to give a planar view of the cortical ER (Fig. 1g, h). The average ER width from these measurements (40.51 ± 0.82 nm, mean ± SD, $n = 1$, 25 technical repeats) was used to calibrate the integrated granulometry intensity values using an idealised microscope psf[53], and the average fluorescence intensity from a cisternal sheet as an internal reference to standardise the intensity of fluorescence from a unit volume of ER.

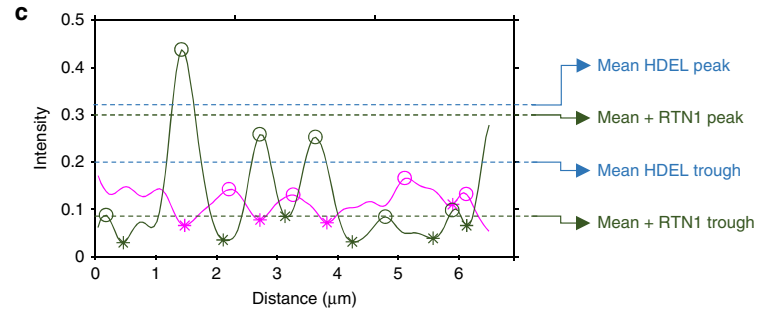
Conversion from a pixel-skeleton to a graph representation. The single-pixel skeleton was converted to a graph representation with nodes at junctions, including puncta, and free ends, connected by edges (Fig. 1i, j). Each edge was associated with a vector of properties, including the length (Fig. 1i), and average width for the segment excluding the node regions (Fig. 1j), speed and persistency (see below). Likewise, each node was associated with a vector of properties including the node degree, branch angles between the incident tubules, speed and persistency (see below).

The cisternae were represented in the network graph as a single central node connected to each of the tubules incident on the boundary (e.g. Fig. 1l). A vector of properties was also associated with each cisterna, with selected values overlaid on the image. In the case of *Arabidopsis* and other members of the order *Brassicales*, segmentation and analysis of cisternae are complicated by the presence of fusiform bodies within the ER[54–57] that are strongly labelled by GFP-HDEL[56,58]. While the fusiform body can be segmented and quantified using automated image analysis[59], their presence has previously hindered segmentation of the surrounding ER network itself (Fig. 1k). Here, by partitioning the intensity histogram into multiple categories, typically 3 or 4, an appropriate threshold was selected automatically to extract the cisternae around the fusiform bodies (Fig. 1l). Cisternae containing fusiform bodies were easily identified later as their properties were significantly different from other cisternae. For example, in this image the maximum intensity for all cisternae was 0.21 ± 0.01 (mean ± SD, $n = 16$), compared to 0.82 for the cisterna with the fusiform body (Fig. 1m).

Analysis of ER-shaping proteins and tubule morphology. The default measurement of tubule width in the network graph returned an average along each tubule, excluding the overlap at

junctions (e.g. Fig. 1j). However, the intensity of luminal or membrane markers fluctuated along the length, indicative of changes in the (sub-resolution) width. Furthermore, the number, size and distribution of these bulges and constrictions altered during over-expression of ER-shaping proteins, such as reticulons[14–17]. To quantify these effects, the change in morphology along each tubules was analysed using the network graph to extract an intensity trace, integrated normal to the tubule axis, for both a GFP-HDEL luminal marker and an *Arabidopsis* RFP-tagged reticulon1 (Fig. 2a). The method used a peak-finding algorithm to identify the peaks along the intensity profile, excluding the nodes, above a minimum height and sufficiently distinct from neighbouring peaks. The intervening troughs were defined similarly as peaks on an inverted intensity profile. These corresponded to bulges and constrictions, respectively, for the lumenal GFP-HDEL marker. Over-expression of RFP-RTN1 reduced the cisternal area and caused extensive constrictions along the ER tubules, with the lumenal GFP-HDEL marker restricted to discrete bulges. Analysis of the morphology for all tubules quantified the properties of the bulges and constrictions for GFP-HDEL and the degree of (negative) correlation with the distribution of the RFP-RTN1 (Fig. 2b). This can be seen clearly

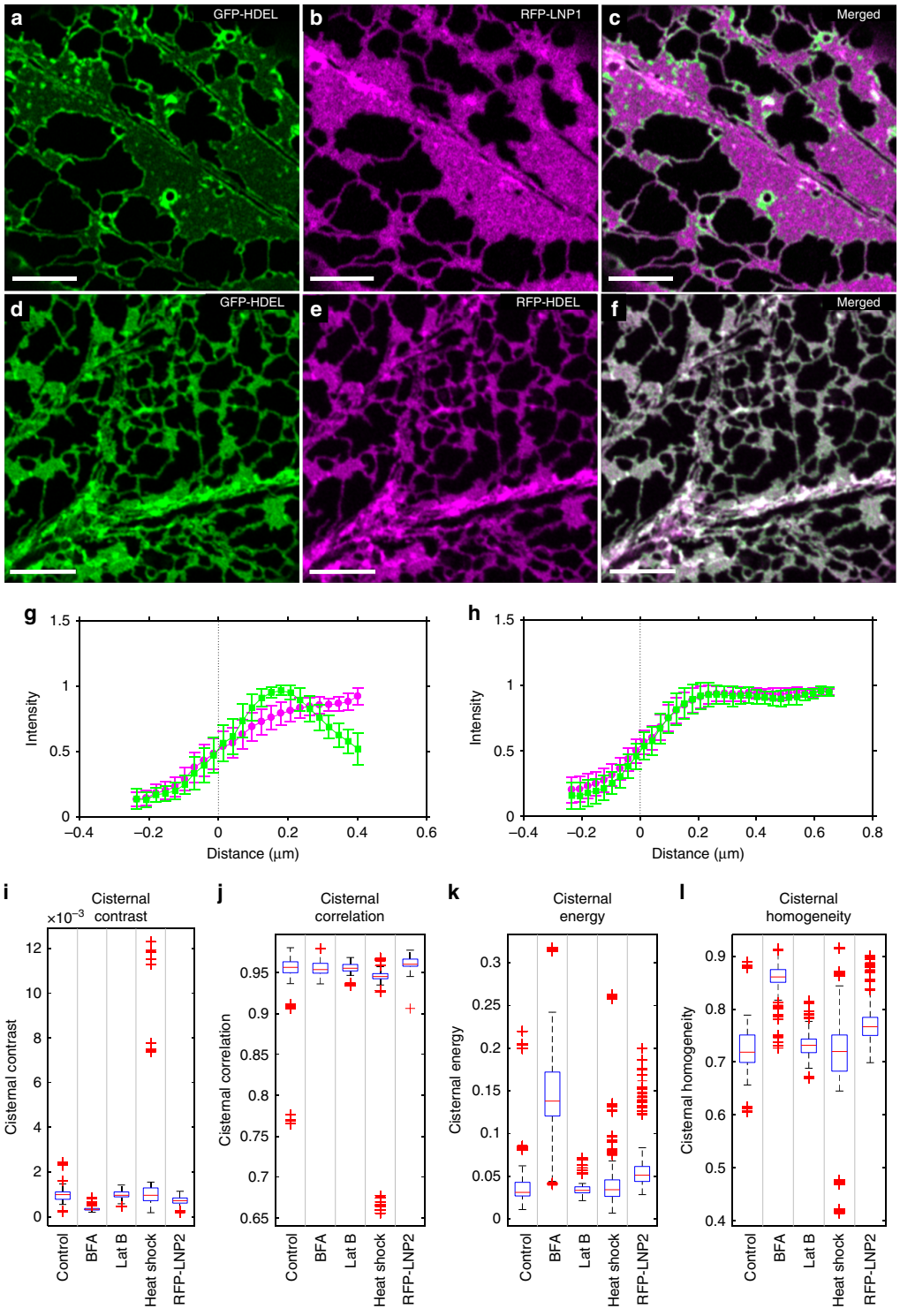




d

	GFP-HDEL mean ± s.e.m. $n = 5$	RFP-RTN1 mean ± s.e.m. $n = 6$	GFP-HDEL mean ± s.e.m. $n = 6$	$t_{(9)}$	*p* value	
Peak density (μm^{-1})	1.085 ± 0.061	0.865 ± 0.041	0.990 ± 0.033	–1.35	0.222	
Trough density (μm^{-1})	1.868 ± 0.148	0.939 ± 0.068	1.402 ± 0.058	–2.93	0.0309	*
Peak intensity	0.321 ± 0.024	0.184 ± 0.015	0.304 ± 0.019	–0.55	0.600	
Trough intensity	0.200 ± 0.020	0.097 ± 0.011	0.089 ± 0.013	–4.50	0.0027	**
Peak width (μm)	0.0621 ± 0.0051	0.044 ± 0.0036	0.0544 ± 0.0048	–1.45	0.188	
Trough width (μm)	0.0491 ± 0.0017	0.0334 ± 0.0031	0.0286 ± 0.0036	–4.68	0.0014	**
Peak separation (μm)	0.509 ± 0.029	0.628 ± 0.023	0.562 ± 0.021	1.49	0.175	
Trough separation (μm)	0.415 ± 0.018	0.624 ± 0.034	0.491 ± 0.0093	3.81	0.0084	**
Intensity ratio at peak	–	4.33 ± 0.83	0.72 ± 0.15			
Intensity ratio at trough	–	1.95 ± 0.41	4.92 ± 1.03			

Fig. 2 ER tubule morphology analysis. **a** A merged two-channel confocal optical section following transient over-expression of RFP-RTN1 (magenta) and GFP-HDEL (green) in tobacco leaf epidermal cells. **b** Automatic measurement of peaks and troughs for both RFP-RTN1 (left justified labels, peaks in magenta, troughs in blue) and GFP-HDEL (right justified labels, peaks in green, troughs in yellow). The underlying pixel skeleton is superimposed in white and the position of nodes indicated in cyan. Cisternae are also outlined in cyan. **c** Selected trace analysis between the yellow arrows in (**a**) showing the relative intensity for RFP-RTN1 (magenta) and GFP-HDEL (green), with the position of the peaks (open circles) and troughs (asterisks) indicated. The average values for peaks and troughs for the HDEL signal across all experiments are indicated in the presence and absence of RFP-RTN1. **d** Summary of tubule morphology metrics (mean ± s.e.m.) for GFP-HDEL alone ($n = 5$) and co-expressed with RFP-RTN1 ($n = 6$), with *T*-test statistic, associated *p*-value and significance, where $^*p < 0.05$ and $^{**}p < 0.01$. All scale bars = 5 μm. Source data are provided as a Source Data file



from the trace along a single tubule (Fig. 2c), between the yellow arrows shown in (Fig. 2a), where accumulation of RFP-RTN1 (magenta) caused a reduction in GFP-HDEL (green). In general, bulges in GFP-HDEL occurred every ~1 μm and peak intensity and width were not statistically different in the presence or absence of RFP-RTN1 (Fig. 2b, c). However, the troughs (constrictions) were significantly dimmer and thinner (Fig. 2d). Likewise, where two or more constrictions occurred on a single tubule, their separation was slightly, but significantly, increased in the presence of RFP-RTN1, leading to an overall reduction in

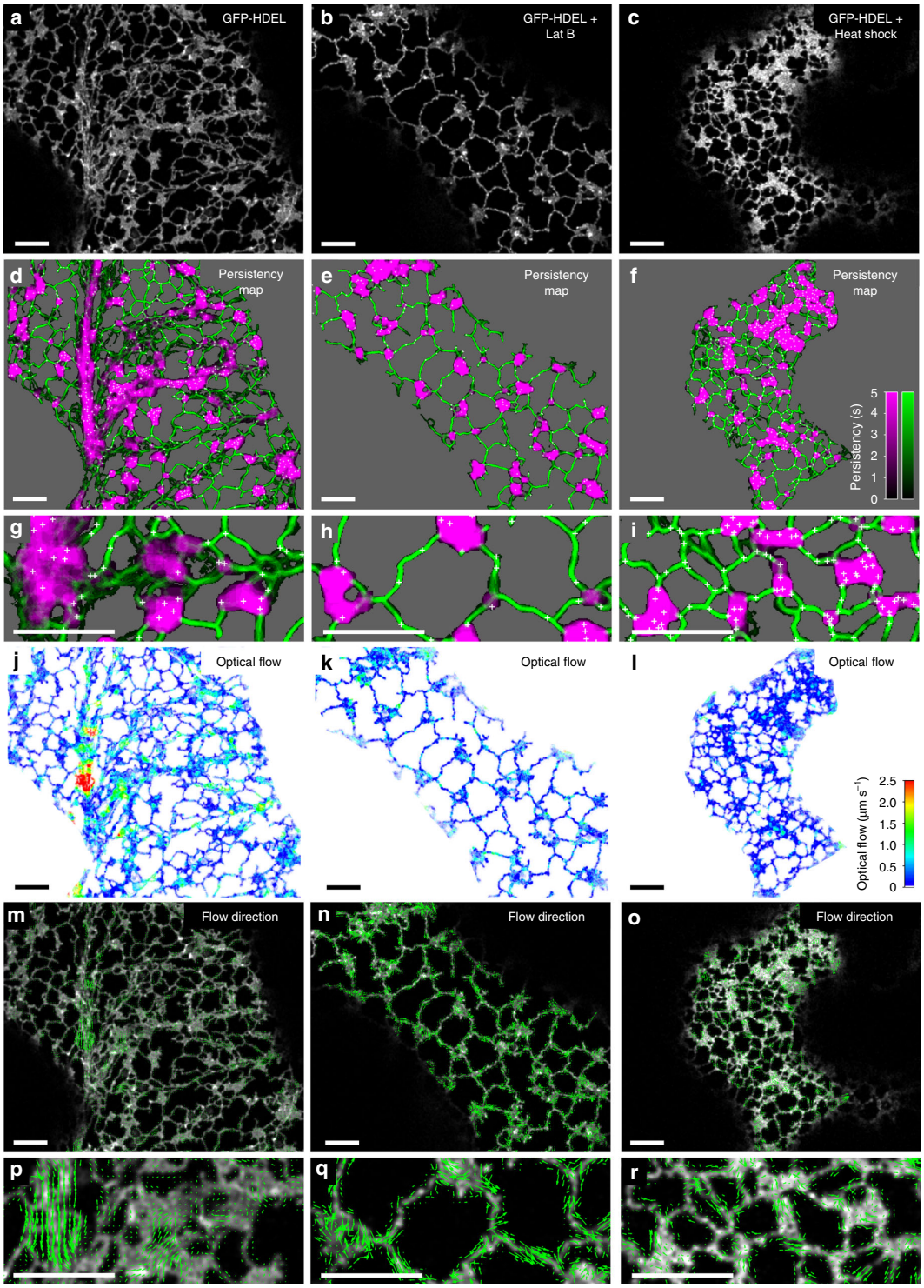
Fig. 3 Analysis of label protein distribution in cisternae. Single optical sections showing transient co-expression of GFP-HDEL (**a**) and RFP-LNP1 (**b**), along with the merged image (**c**). The GFP-HDEL shows a peak in the distribution normal to the cisternal boundaries in the presence of RFP-LNP1 (**g**, mean ± SD, $n = 15$ cisternae). In contrast, co-expression of two lumenal markers GFP-HDEL (**d**) and RFP-HDEL (**e**) show complete co-localisation (**f**), and identical distributions across the boundary (**h**, mean ± SD, $n = 83$ cisternae). All scale bars = 5 µm. Comparison of ER cisternae texture metrics calculated from GLCM analysis: **i** contrast, **j** correlation, **k** energy, **l** homogeneity for GFP-HDEL and different treatments including BFA, Lat B, heat shock and transient overexpression of RFP-LNP2 (wild-type, $n = 46$; BFA, $n = 46$; Lat B, $n = 28$; heat shock, $n = 33$; RFP-LNP2, $n = 29$, where n is the number of independent 5-frame time-series images). Box plot elements correspond to centre line, median; box limits, upper and lower quartiles; whiskers, 1.5× interquartile range; points, outliers. Source data are provided as a Source Data file

trough density. In the dual-labelled data, the ratio of intensities between the two channels at a bulge confirmed the anti-phase relationship between RFP-RTN1 localisation and GFP-HDEL distribution (Fig. 2c, d). Conversely, peaks in RFP-RTN1 localisation were associated with thinner tubules. The dual-labelling approach also confirms that the changes in GFP-HDEL intensity resulted from RFP-RTN1, not movement of the ER tubule out of the plane-of-focus.

Mapping the localisation of proteins in cisternae. Members of the reticulon family are also required along the periphery of the cisternae to induce curvature[9,38,60], while other proteins, such as *Arabidopsis* Lunapark 1 and 2, are suggested to maintain or induce the sheet-like structure[19]. Previous descriptions of protein localisation have been essentially qualitative, but these distributions can also be quantified. For example, following co-overexpression with RFP-LNP1, GFP-HDEL (Fig. 3a) was restricted to the perimeter of the cisternae (Fig. 3b, c), which resulted in a peak in the average intensity transect normal to the cisternal boundary (Fig. 3g). This was not due to non-specific crowding, as it was not observed with co-expression with RFP-HDEL as a second lumenal marker (Fig. 3d–f), where both markers showed identical profiles (Fig. 3h). Small flecks of GFP-HDEL were observed within the main sheet-like regions. These may arise from local bulges of the lumen within the sheet with a lower RFP-LNP1 density, or indicate accumulation along the cisternal perimeter around sub-resolution spaces[21], that may reflect the collapsed remnant of a previous polygonal region that has not yet undergone homotypic fusion[6,61].

Texture-based analysis of cisternal sub-structure. Quantifying sub-resolution spaces[21] or fenestrations[6] within cisternae or discriminating cisternae from a raft of appressed tubules, is challenging in living systems without recourse to super-resolution microscopy. Nevertheless, the different types of tubule and cisternal organisation predicted should leave a statistical imprint on the fluorescent intensities within the sheet-like regions, visible as a change in texture. Texture analysis has been widely used in medical imaging to identify features and patterns, often as inputs to machine-learning classifiers[62]. We therefore included a set of four standard orthogonal texture metrics (contrast, correlation, energy and homogeneity) calculated from a symmetric grey-level co-occurrence matrix (GLCM)[63,64], to describe the spatial distribution of intensities in each cisterna. The GLCM represents the pair-wise comparison of intensity values between each pixel and its neighbours at fixed geometric positions to give a joint probability distribution[63,64]. Thus, a completely homogeneous image would have a single entry on the diagonal of the GLCM. Noise causes non-zero entries to spread along and away from the diagonal, while texture increases the number of both on-axis and off-axis elements[63–65]. The structure of the GLCM can be summarised to give texture features that capture different aspects of the grey-level distribution. These features do not give a mechanistic understanding of sheet formation, but provide a set of comparative measures between experimental treatments to identify which candidate ER-shaping proteins impact tubule-sheet transitions and/or cisternal organisation. Typical distribution patterns are shown in (Fig. 3i–l) for GFP-HDEL alone, following perturbation of the secretory pathway with Brefeldin A (BFA), physical stress through rapid heat shock (42 °C, 20 min), pharmacological disruption of the actin cytoskeleton with Latrunculin B (Lat B), or through transient over-expression of the ER shaping protein RFP-LNP2, which induces excessive cisternae. The contrast (Fig. 3i) is a measure of the variance within the sheet that gives a high weight to pixel pairs with dissimilar intensities. Correlation (Fig. 3j) is a measure of linear dependency of intensities and is bounded in the range [−1 1]. Energy, or angular second moment, (Fig. 3k) summarises the evenness of the spatial distribution, and is bounded in the range [0 1]. Homogeneity (Fig. 3l) is related to the inverse difference moment[64], and measures the closeness of the distribution to the diagonal. It is also bounded in the range [0 1]. Thus, a completely homogeneous cisterna has values of zero for contrast and energy, and one for correlation and homogeneity. In contrast, cisternae following BFA treatment show low contrast and high correlation and homogeneity, as expected for large homogeneous sheets, but the development of brighter patches within the cisternae is also observed as an increase in cisternal energy (Fig. 3k). This is also seen with RFP-LNP2, which increases the size and intensity variation within the cisternae.

Persistency mapping of static elements. The metrics described above can be calculated for a single optical-section to provide a snapshot of ER morphology, but analysis of ER dynamics in time-series images provides much more information. Persistency mapping characterises features that remain static, such as EPCS, and allows quantification of immobile tubules compared to mobile elements[5,8,45]. At present, there is no agreed definition of the duration an object has to remain in position to be regarded as persistent, but current practice has adopted a period of ~5–10 s for tubules and cisternae[5,45], or longer periods for persistent nodes[30,32]. For example, in time-series images (50 frames lasting 20.5 s) of GFP-HDEL transiently expressed in tobacco epidermal cells (Fig. 4a), a number of tubules remained stationary over the lag period examined (12 frames, ~5 s), with their persistence coded by intensity (Fig. 4d, g, green). Likewise, many cisternae were relatively stationary, with only fluctuations at the margin over this time period, unless they were translocating in the streaming cytoplasm (Fig. 4d, g, magenta). Nevertheless, certain nodes remained in position over a substantial fraction of the complete time series (in this case 10 s) in both the tubular network, and where tubules or cisternae moved over a fixed node (Fig. 4d, g, white crosses). Both Lat B (Fig. 4b, e, h) and heat shock (42 °C, 20 min) (Fig. 4c, f, i) increased the proportion of persistent nodes, tubules and cisternae, and the period that they remained static (Supplementary Movie 1a). In untreated cells, the majority of tubules (Fig. 5a) and nodes (Fig. 5d) showed low persistency, that increased in the presence of Lat B (Fig. 5b, e) or heat shock (Fig. 5c, f). Nevertheless, even with these



treatments a small number of tubules and nodes had low or zero persistency, indicative of substantial movement between frames. The cisternae in untreated cells were more stable with a peak in the distribution around 3.5 s (Fig. 5g, magenta), while Lat B and heat shock shifted most of the distribution to increased persistency (Fig. 5h, i). Given the shapes of these distributions, the mean persistency alone does not fully capture the behaviour of the network, but division into categories of high and low persistence[5] are reasonable, and can now be made explicit using fits to the frequency distributions.

Fig. 4 Mapping ER persistency and movement over time. The middle frame from a 50-frame time-series image taken at 0.41 s intervals of GFP-HDEL transiently expressed in tobacco leaf epidermal cells (**a**); after treatment with Lat B (**b**); or heat shock (42 °C, 20 min) (**c**). **d**–**f** persistency maps calculated using a 12 frame lag period (~5 s) for cisternae (magenta), tubules (green) and nodes (white crosses), with the background set to grey. The intensity corresponds to the length of time each pixel is occupied in the time series according to the inset scales; **g**–**i** Enlarged (3×) regions from the approximate centre of each image. **j**–**l** Optical flow analysis between the middle two frames of the same time series images for comparison. Images are pseudo-colour coded on the inset scale between zero (blue) and 2.5 μm s^{-1} (red). **m**–**o** Predicted direction of ER network movement with arrows scaled to a maximum value of 2.5 μm s^{-1}. **p**–**r** Enlarged (3×) regions from the approximate centre of each image. All scale bars = 5 μm

Quantifying ER velocity in time-series using optical flow. The counterpoint to persistency measurements is characterisation of movement in the network. Previous work used optical flow measured by cross-correlation between local neighbourhoods[25], which provides an overall measure of movement, but does not distinguish between internal flows within the ER lumen or membrane, local ER remodelling, or bulk movement by cytoplasmic streaming[8,45]. Here we also characterise ER movement by optical flow, but using the Farnebäck algorithm, as this incorporates a scale-space analysis suited to quantify movement over different length scales, to give maps of speed (Fig. 4j–l) and direction (Fig. 4m–r), for untreated (Fig. 4j, m, p), Lat B (Fig. 4k, n, q), and heat shock (Fig. 4l, o, r) time-series (Supplementary Movie 1b, c). In untreated cells, there were small, localised movements from ER re-modelling and lateral wiggling of tubules through much of the network, with occasional substantial translocation of a bolus of ER along cytoplasmic strands (Fig. 4j). To quantify these speeds, the optical flow measurements were interrogated by the pixel skeleton and cisternal segmentation to extract the average local speed (scalar mean), average net speed (vector mean), and maximum speeds per tubule, node or cisterna. In all cases, the distribution of average speeds followed a log-normal distribution, with the back-transformed mean around 0.26 μm s^{-1} for tubules (Fig. 5j), and 0.21 μm s^{-1} for cisternae (Fig. 5l). The maximum speeds observed were higher, with means of 0.52 μm s^{-1} for tubules (Fig. 5m), and 0.95 μm s^{-1} for cisternae (Fig. 5l). Values greater than 2.5 μm s^{-1} were routinely observed for ER moving along cortical actin strands (Fig. 4j, m, p). Movements of cisternae were also identified, although, as with other studies, it is not clear whether movement relates to translocation of the entire structure, or just elements within the structure[8]. Lat B (Fig. 5k, n) and heat shock (Fig. 5l, o) caused a reduction in the distribution of speeds, with the mean dropping by 24% (tubules) and 45% (cisternae), following Lat B treatment (Fig. 5k, n), or 34% (tubules) and 49% (cisternae) following heat shock (Fig. 5l, o). The tail of the distribution at higher speeds (>1 μm s^{-1}) also disappeared in these treatments and the direction of movement was less correlated, reverting to just local fluctuations, rather than directed flows (Fig. 4n, o, q, r). The extent of random movement to directed flow was quantified using flow coherence, calculated as the vector sum of velocities divided by the scalar sum of speeds (Fig. 5p–r). A value of 1 indicates all flows moving in parallel, compared to zero for no net movement. This confirmed that flows were directed in the HDEL control with high coherence (Fig. 5p), a shift to predominantly disorganised fluctuations in Lat B treatments (Fig. 5q), with heat shock intermediate (Fig. 5r). Local variation of flow within cisternal sheets and tubules was also quantified by changes in the curl (Supplementary Fig. 4d-f) and divergence (Supplementary Fig. 4g-i) of the flow pattern. Quantitatively, both curl and divergence of the vector flows showed greater spread in the HDEL control (Supplementary Fig. 5a, d) than in Lat B (Supplementary Fig. 5b,e) or heat shock (Supplementary Fig. 5c, f) treatments, but inspection of the corresponding images did not yield clear signature patterns that could be easily related to microscopic behaviour. We also note that different classes of cisternae can be readily distinguished based on their morphology and dynamics that correspond to regions where the automated image analysis cannot distinguish sheets from aggregates or ribbons of tubules in the streaming cytoplasm (Supplementary Fig. 6a, b).

Quantitative comparisons using multiple network parameters. While examination of specific metrics such as tubule length, cisternal area, speed, coherence or persistency, can be used to test specific hypothesis about the role of a particular ER or cytoskeletal protein, calculation of a comprehensive set of metrics allows an un-biased comparison of any treatment with the GFP-HDEL control and provides potential input to automated classifiers to detect aberrant ER behaviour. This approach also captures subtle differences in behaviour that may not give a significant result for pairwise comparison of any single metric, but show a consistent phenotype as a combination of several metrics. The first stage of a parametric analysis explored here was based on multivariate analysis (MANOVA) to test the null hypothesis that the multivariate means were drawn from the same population, after transformation of individual metrics to achieve normality. As the null hypothesis was rejected, parametric ANOVA comparisons against the GFP-HDEL control were used to identify which metrics showed a significant difference. This helps to identify the potential site and mode of action of any given treatment as a guide to future investigation. The MANOVA also provided separation of the data by canonical discriminant variables to give a visual representation of the clustering relationships between the factors, and the potential for this approach for automated discriminant classifiers.

We illustrate this approach using a data set comprising 182, 5-frame movies of wild-type ER labelled with GFP-HDEL (Fig. 6a, $n = 46$), and with treatments including pharmacological perturbation with BFA (Fig. 6b, $n = 46$), and Lat B (Fig. 6c, $n = 28$), abiotic heat stress (Fig. 6d, $n = 33$), or transient over-expression of the ER shaping protein RFP-LNP2 (Fig. 6e, $n = 29$). Using a subset of 19 metrics, MANOVA analysis revealed the there was a highly significant difference in the structure and dynamics of the plant ER under these treatments (Pillai's trace, $F_{(72,648)} = 17.5$, $p = 2.7 \times 10^{-110}$; or Roy's largest root, $F_{(18,162)} = 36.7$, $p = 7.9 \times 10^{-48}$). The first two discriminant canonical variables from the MANOVA provided complete separation of Lat B and heat shock treatments from the other factors (Fig. 6f). The third canonical variable teased apart GFP-HDEL control from BFA (Fig. 6g), while the fourth canonical variable separated BFA, RFP-LNP2 and control (Fig. 6h). Subsequent ANOVAs revealed that BFA differed from control in almost every category of metric, apart from persistency and flow coherence. The main effects of Lat B and heat shock were on movement, as might be expected from disruption of the actin cytoskeleton, with some impact on the shape of cisternae and the intervening polygonal regions, but little difference in cisternal texture. Conversely, both BFA and RFP-LNP2 showed a significant difference from control in cisternal texture metrics of energy and homogeneity. Interestingly, while RFP-LNP2 predominantly affected shape and texture metrics, there was also a highly significant reduction in cisternal

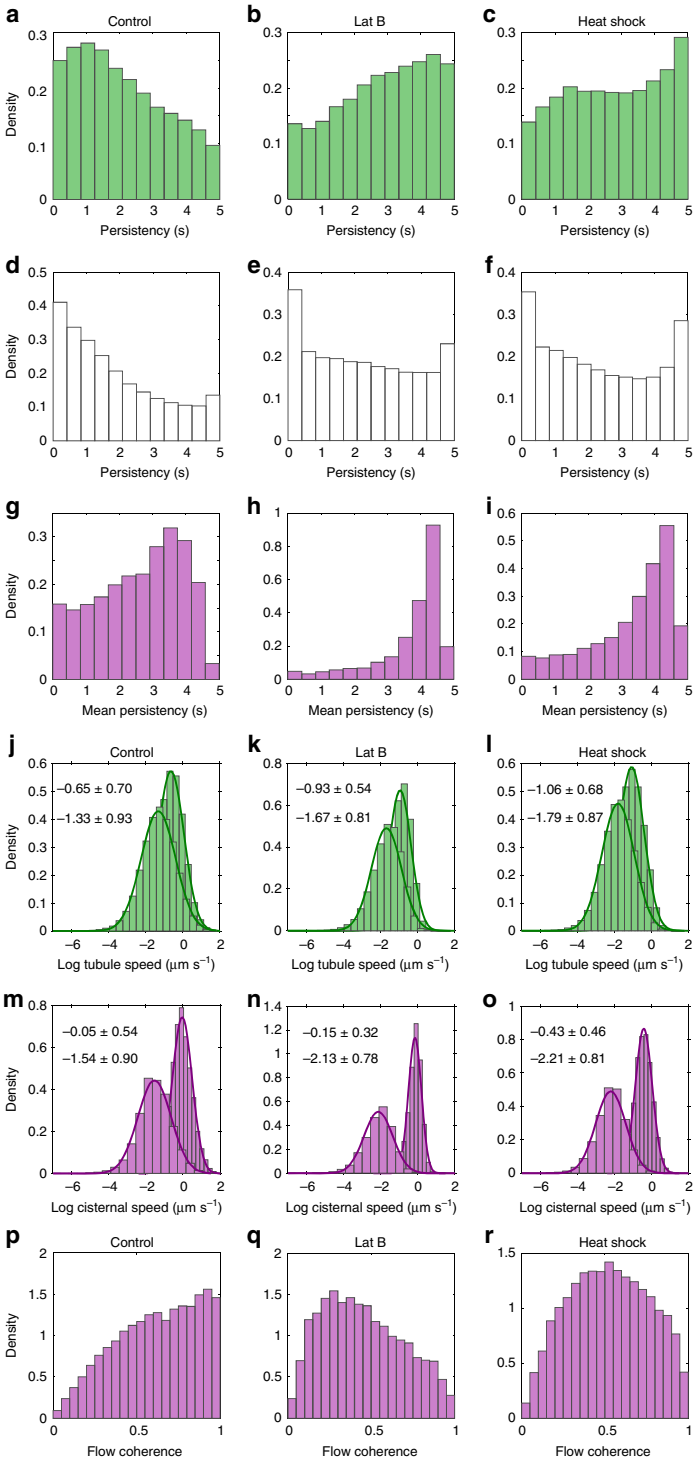


Fig. 5 Distributions of persistency and optical flow analysis of ER dynamics. Probability density distributions of the mean persistency for tubules (**a**–**c**, green), nodes (**d**–**f**, white), and cisternae (**g**–**i**, magenta) for GFP-HDEL (**a**, **d**, **g**), and following treatment with Lat B (**b**, **e**, **h**) or heat shock (**c**, **f**, **i**). Probability density distributions of the log mean vector magnitude and log maximum speed of tubules (**j**–**l**, green) and cisternae (**m**–**o**, magenta), for the different treatments. Numerical values for the mean ± SD for the Gaussian fits to the mean (lower text) and max (upper text) distributions are inset. **p**–**r** Flow coherence for cisternae for the different treatments. (GFP-HDEL, $n = 6$, Lat B, $n = 8$, Heat shock, $n = 8$, where n is the number independent 50-frame time-series images). Source data are provided as a Source Data file

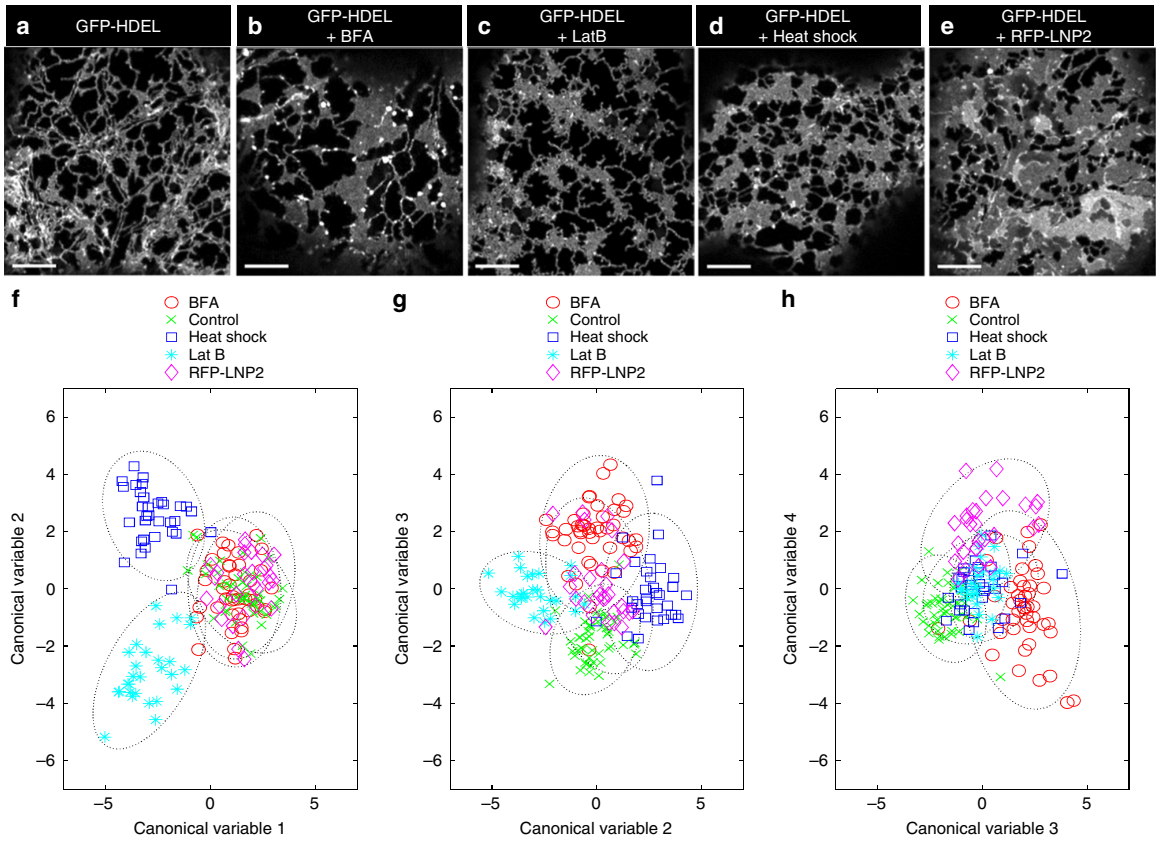


Fig. 6 Multivariate analysis of ER morphology and dynamics. Representative single optical sections of tobacco leaf epidermal cells transiently expressing GFP-HDEL (**a**, $n = 46$); after treatment with BFA (**b**, $n = 46$); Lat B (**c**, $n = 28$); heat shock (**d**, $n = 33$); or over-expression of RFP-LNP2 (**e**, $n = 29$), where n is the number of independent 5-frame time-series images. All scale bars = 5 µm. Pairwise scatter plots of the first 4 significant canonical variables from the MANOVA analysis grouped by treatment (**f**–**h**). The dotted line around each group represents the 95% confidence limit

speed, emphasising the importance of scoring across a wide range of both morphological and dynamic parameters when characterising ER-modifying protein function (Table 1).

Discussion

We have developed a set of integrated tools that can be routinely used to assess a wide range of parameters describing the structure and dynamics of the ER network in living plant cells. We have validated the approach against manual ground-truth images, and tested performance by artificially inducing changes to the ER network in leaf epidermis through physical perturbation (heat shock), drug treatments affecting ER-Golgi trafficking (BFA), the actin cytoskeleton (Lat B), ER shaping proteins (RFP-RTN1), or cisterna-modifying proteins (RFP-LNP1 and RFP-LNP2). Using these diverse treatments as test cases, we can readily quantify the effects on ER-morphology and dynamics using a wide range of metrics that can both readily discriminate between the different treatments and provide a rich source of information to understand the physiological impact of each intervention. Importantly, we quantify the consequential effects that modification of one aspect of ER morphology, such as cisternal reorganisation, can have on overall network behaviour, such as ER dynamics. The software can also handle multiple channels, which allows object-based co-localisation of different reporter constructs, or quantitation of ratiometric physiological reporters, such as roGFP[66]. The analysis requires minimal user interaction, mainly to set experiment-dependent parameters such as the background intensity, and can be run in batch mode to achieve a medium-throughput pipeline capable of handling hundreds of images required for statistical robustness or mutant screening. Taken together, this represents a major advance in un-biased, quantitative analysis of the plant ER, and should prove equally applicable to the analysis of mammalian or animal cortical ER.

Methods

Plant material and transient protein expression. *N. tabacum* (SR1 cv Petit Havana) were grown in preparation for transient Agrobacterium-mediated expression as previously reported[67]. Transient expression of fluorescent constructs was performed according to Sparkes et al.[4]. In brief, transformed agrobacteria were pelleted by centrifugation at 2200*g* at room temperature for 5 min. Infiltration buffer (5 mg ml^{-1} glucose, 50 mM MES, 2 mM $Na_3PO_4{\cdot}12H_2O$ and 0.1 mM acetosyringone) was used to wash the pellet once and then to resuspend the *agrobacteria*. The bacterial suspension was diluted in the infiltration buffer to an OD_{600} of 0.1 for GFP-HDEL, RFP-HDEL, RFP-LNP1 and RFP-LNP2 and an OD_{600} of 0.05 for RFP-RTN1. The final dilution of the infiltration medium was injected through the stomata on the underside of the tobacco leaf using a 1 ml syringe. Infiltrated plants were kept at 23 °C for 3 days prior to imaging. For imaging of fusiform bodies, *Arabidopsis* Col-0 seeds stably expressing GFP-HDEL were sterilised in 70% ethanol and placed on 1/2 strength MS plates. These were stratified for 3 days at 4 °C in the dark and then grown in an incubator at 22 °C for 2 weeks prior to imaging.

Cloning of expression plasmids. Primers were obtained from Eurofins Genomics. Q5 high-fidelity DNA polymerase (New England Biolabs, Ipswich, MA, USA) was used for all PCR reactions. Using Gateway technology (Invitrogen, Waltham,

Table 1 ANOVA for a subset of ER variables

ER structural subdomain	Variable	$F_{(4,177)}$	*p* Value	BFA	Lat B	Heat shock	RFP-LNP2
Tubule	Length	15.78	4.58×10^{-11}	***	***	***	***
Tubule	Maximum speed	50.52	2.59×10^{-28}	***	***	***	***
Tubule	Mean speed	46.16	1.60×10^{-26}	***	***	***	***
Tubule	Flow coherence	19.71	1.96×10^{-13}		*	***	
Tubule	Persistency	60.36	5.11×10^{-32}		***	***	
Cisternae	Contrast	5.894	1.78×10^{-04}	*			
Cisternae	Correlation	4.612	1.45×10^{-03}			*	
Cisternae	Energy	54.94	4.72×10^{-30}	***			***
Cisternae	Homogeneity	40.19	6.32×10^{-24}	***			***
Cisternae	Maximum speed	46.17	1.57×10^{-26}	***	***	***	***
Cisternae	Mean speed	74.1	8.72×10^{-37}	***	***	***	***
Cisternae	Flow coherence	77.42	7.61×10^{-38}	***	***	***	***
Cisternae	Persistency	53.46	2.00×10^{-29}	**	***	***	***
Cisternae	Circularity	8.325	3.56×10^{-06}	**	**	**	
Cisternae	Area	6.467	7.03×10^{-05}	**	***	**	*
Cisternae	Perimeter	15.56	6.29×10^{-11}	***			***
Polygonal regions	Area	40.14	6.61×10^{-24}	***	***		***
Polygonal regions	Perimeter	19.85	1.63×10^{-13}	***	***		***
Polygonal regions	Circularity	41.26	2.09×10^{-24}	***	***	*	***

ANOVA results of planned comparisons against the GFP-HDEL control for the sub-set of variables included in the MANOVA, with the associated *F*-statistic and *p*-value. Means that were significantly different from the control using Tukey HSD post-hoc test are coded as $*p < 0.05$; $**p < 0.01$; and $***p < 0.001$. (Wild-type, $n = 46$; BFA, $n = 46$; Lat B, $n = 28$; Heat shock, $n = 33$; RFP-LNP2, $n = 29$, where n is the number of independent 5-frame time-series images.) Source data are provided as a Source Data file

MA, USA), genes of interest were cloned into the modified binary vector pB7WGR2,0[68] using the cauliflower mosaic virus 35S promoter upstream of coding fusions to RFP.

Stress induction and drug treatments. In preparation for stress and drug treatments, small leaf segments of approximately 25 mm^2 were cut from the transformed *N. tabacum*. Heat shock was induced by rapidly heating the leaf segment to 42 °C for 20 min. Drug treatments were performed by incubating leaf segments in either Lat B (25 µM for 30 min) or BFA (100 µg ml^{-1} for 1 h) at room temperature.

Confocal microscopy. Leaf epidermal samples were imaged using a Zeiss PlanApo ×100/1.46 NA oil immersion objective on a Zeiss LSM880 confocal equipped with an Airyscan detector. Typically 512 × 512 images were collected in 8-bit with 2-line averaging at an (*x*,*y*) pixel spacing of 20–80 nm with excitation at 488 nm (GFP) and 561 nm (RFP), and emission at 495–550 nm and 570–615 nm, respectively.

Serial-section block-face SEM (SBFSEM). For EM, *Arabidopsis* Col-0 seeds expressing the Golgi marker ST-GFP were grown as described for 2 weeks. Seedlings were removed from the agar, cotyledon leaves cut off and submerged in fixative (1% paraformaldehyde, 1% glutaraldehyde, 2% sucrose and 2 mM $CaCl_2$ in 0.1 M sodium cacodylate buffer) under mild vacuum for 1 min and for a further hour without vacuum at room temperature. Leaves were then washed twice with 0.1 M sodium cacodylate buffer and once in deionized water for 10 min. Zinc-iodide was prepared by adding 3 g of zinc powder and 1 g of resublimed iodine to 20 ml distilled water with stirring for 10 min. The solution was filtered through filter paper and mixed 1:1 with 2% aqueous osmium tetroxide. Leaves were incubated in the ZIO mix overnight at room temperature with rocking, then washed with deionised water and dehydrated in an ethanol series from 10 to 100%. Infiltration with Spurr resin (hard) was carried out in a series from 10 to 100% for a minimum of 2 h for each step. Infiltration with 100% Spurr resin was exchanged 3 times over 2 days. Leaves were embedded in 100% Spurr resin in flat embedding dishes and polymerised at 70 °C for 11 h.

Leaves were mounted for cross-sectioning onto 3View stubs (Gatan, Abingdon, UK) with conductive epoxy (Chemtronics, Hoofddorp, Netherlands) and hardened for 4 h at 100 °C. The trimmed block was sputter coated with gold for 30 s to give a layer of around 20 nm to improve conductivity. Serial block face (SBF) images were collected with a Merlin Compact scanning electron microscope (Zeiss, Cambridge, UK) with the Gatan 3View system using a 30 µm aperture at 4 kV in variable pressure mode (50 Pa), a pixel dwell time 2 µs, and a pixel size of 6.9 nm. Serial sections were cut at 100 nm thickness.

SBF images were stacked, aligned, scaled to common mean and standard deviation and cropped to the area of interest using the IMOD software package[69]. Reconstruction of the ER was performed with Amira software (Thermo Fisher Scientific-FEI) using manual masking and thresholding tools. The rendering was visualised through surface generation and surface view in Amira.

Image processing. The GUI interface for ER image processing and analysis is shown in Supplementary Fig. 1. A complete description of all the processing steps and additional options available in the software is given in the accompanying manual available from the Oxford Research Archive (ORA) (https://ora.ox.ac.uk/objects/uuid:cb0e2845-2a9c-495a-84f0-4dd2c5164463). To standardise all subsequent processing and filtering operations, images were up-sampled using linear interpolation to ensure that the minimum tubule size, estimated from the full-width-half-maximum height ($FWHM_{min}$) of manual transects across the tubules, was around 5 pixels. Images were then background subtracted, using an average value determined from a manually-defined region-of-interest (ROI), and smoothed with a guided anisotropic filter[70], with the kernel size set to the $FWHM_{min}$ to avoid blurring across tubule edges. Regions where the signal decreased as the curvature of the cell took the ER out-of-focus, were masked where the pixel intensity fell below the lowest automatically determined threshold, after partitioning the image histogram into two, three or four sections using Otsu's method which minimises the intra-class variance within the pixel intensity histogram[44]. Multi-threshold partitioning was useful when the image included additional strongly labelled structures, such as Arabidopsis fusiform bodies[56,57,59]. Internal polygonal regions within the mask were initially filled to retain all internal structures, the outermost boundary identified by contraction of the convex hull using a shrink factor of 0.5–0.8, and the final boundary eroded by a fixed number of pixels, typically 4–6. The boundary was used to determine the area analysed for density-dependent metrics. The internal holes were then reintroduced to complete the mask for subsequent image processing operations

Tubule enhancement and segmentation. A number of options are included in the software to enhance the ER tubules including Vesselness[46], Neuriteness[48], second-order anisotropic Gaussian kernels (SOAGKs)[49], or intensity-independent phase-congruency filtering[50,71], typically applied over 3–5 spatial scales and 4–6 orientations. Although the phase-congruency filters characterise a number of relevant image properties, we have found the local weighted mean phase angle (Feature-Type) provided the most robust subsequent segmentation in a variety of contexts[51,52], including enhancement of ER-tubules[14,42]. Full details of the phase congruency analysis and alternative approaches to ridge enhancement are given in the accompanying manual available from ORA. The Feature-Type image was normalised to [0 1], and the tubular network segmented using hysteresis thresholding, with a lower threshold of 0.3 and upper threshold of 0.5. To ensure closely appressed regions were not merged during the hysteresis threshold, all local intensity minima were first identified using an h-minimum transform, with a threshold of 0.05, and set to zero. The binarised imaged was reduced to a single-pixel-wide skeleton by thinning using the Zhang and Suen algorithm[72].

Segmentation of cisternae and polygonal regions. ER cisternae were automatically segmented by image opening[5,8,45] to remove all features smaller than the maximum tubule diameter (estimated as the full-width half-maximum ($FWHM_{max}$) from manual transects across 3-way junctions). Segmentation was followed by an active-contour step[73] to shrink the segmented boundary back onto the intensity profile of the cisternae. The resulting objects were filtered on the basis of their area to be above a user-defined value of 0.3 μm^2, chosen as the area of

persistent puncta that are associated with immobile scaffold sites[5]. These puncta were included as nodes in the tubular network. A variety of morphological metrics (area, perimeter, major and minor axis length, solidity, elongation, circularity, and roughness) were determined for each sheet-like region (Supplementary Figure 2a). A similar set of morphological metrics was calculated for the polygonal regions enclosed by the ER network, following segmentation from the complement of the combined pixel skeleton and cisternae (Supplementary Figure 2b).

Precision–recall analysis of segmentation performance. Ground truth images were manually digitised from 5 single confocal images using a Wacom DTK-2241 digitising tablet (http://www.wacom.com/) and GIMP software (https://www.gimp.org/). The manual skeleton was thinned and masked in parallel to the automated skeleton, and the cisternae excluded. The number of true positives (T_P), true negatives (T_N), false positives (F_P) and false negatives (F_N) were calculated, allowing a tolerance of half $FWHM_{min}$[74]. Performance was assessed using precision–recall (P–R) analysis in preference to receiver operating characteristic (ROC) plots, as the former is better suited to imbalanced data sets, where the number of T_N from the background is expected to be much greater than T_P from the skeleton[75]. Precision (P) was calculated as $= \frac{T_P}{T_P+F_P}$, recall (R) as $R = \frac{T_P}{T_P+F_N}$ and overall performance assessed with the Dice Similarity Coefficient or F_1 score as the harmonic mean of precision and recall, $F_1 = 2\times\frac{P\times R}{P+R}$.

Estimation of tubule width. The width of the tubules was estimated by several different methods. To estimate the tubule FWHM, the peak height was determined from the intensity, sampled for each pixel in the skeleton; the distance from the skeleton was estimated from the Euclidean distance transform (EDT) of the pixel skeleton; and the 50% threshold estimated from where the pixel intensity fell below half the peak intensity of the background-subtracted image. This gave the FWHM of the tubule convolved with the psf. Alternatively, a granulometry approach[51,52] was used whereby the intensity image was processed through a set of image opening operations (erosion followed by dilation), with a circular kernel of radius 0 to $FWHM_{max}$. This resulted in an intermediate (x,y,s) image, where s increased with the size of the disk-shaped kernel, that effectively builds a stack of the intensity of each successive neighbouring pixel underneath each pixel in the skeleton. The gradient profile for a given skeleton pixel in s decreased slowly as the kernel sampled more of the object, but then reduced dramatically once the boundary of the object was reached, and the kernel sampled the background. The width was estimated as either the maximum (negative) gradient of this profile, or from the integrated intensity under the curve. However, in the former case, the radius was constrained to integer pixels values and results were limited by the discrete digital approximation of small kernels to a true disk-shaped kernel. Conversely, the latter provided an estimate of the local amount of fluorescence in the tubule which was related to the width, even if it was sub-resolution, provided it was assumed that the fluorescent probe was evenly distributed throughout the ER, there was a linear relationship between signal and the amount of probe, and the ER was fully within the sampling volume of the confocal defined by the psf[53]. The average intensity from the cisternal sheets (I_s), typically 0.35, the estimated sheet thickness (T_s) of 40 nm, and the size of the lateral psf (psf_{xy}) of 140 nm, were used to relate the measured intensity to the volume of ER that a fully-filled psf would yield when sampling sheets of defined thickness ($V_s = \pi psf_{xy}^2 T_s$) (Supplementary Figure 3). The radius of the tubules (r_t) was estimated by assuming the volume of the tubule sampled by the same stylised psf ($V_t = \pi r_t^2 psf_{xy}$) compared to the sheet, scaled as the ratio of the intensities from the tubule and sheet (I_t/I_s). Thus, the radius of the tubule (r_t) was estimated as $r_t = \sqrt{(I_t/I_s)\left(psf_{xy}T_s/4\right)}$ (Supplementary Figure 3).

Conversion to a graph representation. The pixel skeleton was converted to a graph representation with nodes at the junctions and free ends, connected by edges along each tubule[30,42,43,51,52] (Supplementary Figure 2d(i)), using the *edgelink* algorithm written by Kovesi[71], which exports a list of pixel co-ordinates for each edge. Duplicate edges connecting the same two nodes were resolved to two separate edges in the graph by introducing an additional node with degree 2 in one arm (Supplementary Figure 2d(ii)). The pixel co-ordinates for each edge were used to extract relevant information from different images, such as intensity, width, speed, direction, coherence, divergence, curl or persistency, and the mean (or other summary statistic) and SD for each metric stored in a vector of properties for each edge. The initial width was further refined by excluding pixels within a certain distance from each node, to give the centre-weighted width, which provides a better estimate of the tubule width that excludes the 3-way junctions or cisternae (Supplementary Figure 2d(iii)). The exclusion distance was determined as the maximum of the initial widths of tubules connected to the node. A vector of properties was also associated with each node, including the degree, widths of the incident tubules, branch angles between incident tubules (estimated from segments drawn between the node and the mid-point of each connected tubule), strength (measured as the sum of the centre-width of the incident edges), persistency and speed (Supplementary Figure 2c). Summary metrics for orientation and branching angles were calculated using circular statistics[76]. The cisternae were represented as a single-node placed at the intensity-weighted centroid of each cisterna, and connected to each edge incident on the boundary (Supplementary Figure 2d(i)). Edges within the cisternae were set to the average centre-width of all the tubules, along with their Euclidean length, for graph–theoretic calculations where the connectivity of the network is important, but were excluded from calculations of tubule statistics.

Variation in morphology along the length of tubules and cisternal edges. The position of bulges along the tubules (Supplementary Figure 2c) were estimated from peaks in the integrated intensity trace along each tubule, excluding the nodes, at each wavelength that were at least 5% of the maximum intensity (peak height) and also 3% of the maximum intensity greater than the signal on either side (peak prominence). Likewise, constrictions were determined using the same peak-finding process on the inverted intensity profile. The width of the tubule at these points was then extracted from the granulometry width image. The distribution of fluorescence around the perimeter of the cisternae was determined in the same manner.

Characterisation of cisternal sub-structure using texture metrics. The variation in intensities within the cisternal region was characterised using texture analysis from the normalised grey-level co-occurrence matrix (GLCM)[63–65]. In brief, for each pixel in the segmented cisternal region, the GLCM examined pixels at a distance that was set by the tubule radius to maximise the likelihood of revealing texture from appressed tubule regions. Results were aggregated in four directions (NW, N, NE, E) with symmetry to complete the angular sampling and ensure results were independent of orientation. Results were added to an accumulator array where the row (i) and column (j) indices correspond to the intensity value of the target pixel and the neighbour, grouped into a number of equal intensity bins to capture key differences in intensity without rendering the GLCM too sparse. The resultant GLCM was normalised to give a probability $p(i, j)$ of co-occurrence for each intensity pair. Choice of the number of intensity bins and spacing is known to affect texture features[65], thus to standardise results[65], images were collected under identical conditions, GLCM constructed using 32 fixed intensity bins over the full intensity range, at a distance equal to the minimum tubule radius, and with inclusion of all neighbouring pixels to give direction invariance. The contrast, $\sum_{i,j}|i-j|^2 p(i,j)$; correlation, $\sum_{i,j}\frac{(i-\mu i)(j-\mu j)p(i,j)}{\sigma_i\sigma_j}$, where μi and μj were the weighted mean intensities and σi and σj their standard deviation; energy, $\sum_{i,j}p(i,j)^2$; and homogeneity, $\sum_{i,j}\frac{p(i,j)}{1+|i-j|}$, of the GLCM were calculated individually for each cisterna and then averaged, and also as a single accumulated GLCM for all cisternae, which effectively weights the contribution of each cisterna to the overall statistic by the number of pixels. Contrast measures the local variation in the GLCM, correlation measures the joint-probability distribution, energy measures the sum of the squares, while homogeneity measures how close elements in the GLCM are to the diagonal. Conveniently, correlation is scaled from [−1 1], while energy and homogeneity are scaled between [0 1]. An idealised cisternal sheet would have a value of 1 for correlation and homogeneity, and zero for energy. The contrast scales from 0 to $(nbins-1)^2$, but was normalised here by $(nbins-1)^2$ as all images were processed with the same number of bins, to constrain the range to [0 1], where an idealised sheet would have a value of zero.

The distribution of fluorescence intensities across the cisternal boundary was determined by averaging intensities in incrementing (external) and decrementing (internal) integer radial bins, determined from the EDT, normal to the edge of each cisternal region.

Measurement of movement using optical flow. A number of different methods are available in the software that draw from the MATLAB® Computer Vision Toolbox including Horn–Schunck[24], Lucas–Kanade[77] and Farnebäck[78]. Here, we have used the Farnebäck algorithm[78] which uses local quadratic polynomial expansions to approximate image intensities over a given neighbourhood, with weightings based on the strength of the signal and the distance from the central pixel. The algorithm also includes a coarse-to-fine pyramidal scale-space iteration to improve the a priori estimate of the initial displacement field, which allows the method to handle larger displacements. Typically a neighbourhood of 5 pixels was used, with a three-level image pyramid. The resultant vectors were then averaged over a 15-pixel region to estimate the local velocity. The average velocity for tubules and cisternae was calculated as the scalar mean to give an estimate of the total amount of movement irrespective of direction, while the net directed movement was estimated from the vector mean. The maximum speed was also recorded. Flow coherence was calculated as the vector mean divided by scalar mean, and gives a ratio of one for fully directed flow and zero for random movement. Divergence and curl were calculated from the velocity field. Summary metrics for optical flow direction were calculated using circular statistics[76].

Persistency mapping of static elements. In the original approach to persistency mapping[5], tubule and cisternal persistency were estimated from the difference between two images with a lag of 5–8 frames (8–14 s), following by a Boolean AND operation between time-points to only include features present in both. Results

were normalised to the total segmented area present in all frames (Boolean OR operation on the image stack). Here we implement two approaches. The first method followed Sparkes et al.[5] using the difference in the intensity image over a user-defined time-period, masked by a thresholded binary image from both time-points. The second used the segmented skeleton and cisternal regions directly. Binary images of the skeleton and cisterna were dilated by $FWHM_{min}/2$ and analysed separately or in combination, by either summing over a defined time window, giving a graded estimate of persistency, or by differencing between the start and end of the time window, giving a binary estimate of persistency. Results were displayed as a persistency map, summed over the entire time course, and were also aggregated for each edge and cisterna and included in their vector of properties. Nodes that were persistent over longer periods that might transiently be associated with tubules or cisternae moving across the anchor points[30,32], were identified following a 1D median filter in time across the entire time course followed by Gaussian smoothing in xy with $\sigma = FWHM_{min}/2$, normalisation to [0 1], and extraction of the position of local maxima above an intensity threshold of 0.3–0.5.

Statistical methods. Results for different transgene expression and drug treatments were compared against a GFP-HDEL control using a parametric MANOVA with Pillai's trace and Roy's largest root as test statistics. Metrics that were bounded in the range [0 1] were arcsin transformed to improve normality, while those spanning a wide range, such as length, area or speed, were typically normalised using a log, logit or square root transform. Logit data was adjusted to the interval 0.025–0.975 before transformation. We note that some metrics, such as persistency, may be problematic as they deviate strongly from normality and cannot be reduced easily to a single summary statistic (mean, mode or median) that is well behaved. We also note that collectively, the co-variances may fail Mauchly's test for sphericity, which then requires additional correction factors to apply to the degrees of freedom before calculation of p-values. Nevertheless, the F-ratio and p-values we have encountered so far are all so low and highly significant (typically $< 10^{-30}$), that the conclusions are insensitive to these corrections. Parametric ANOVA comparison between individual means and the control used Tukey–Kramer HSD with results reported at least at the 95% significance level. Other statistics are given as mean ± SD when results are illustrative for a single experiment, or mean ± s.e.m. when averaged across experiments for a given n.

Software implementation and code availability. All of the analysis routines were implemented in MATLAB (The Mathworks) and are available in a standalone package for 64-bit Windows 10, or a MATLAB 2017a app from the Oxford Research Archive (https://ora.ox.ac.uk/objects/uuid:cb0e2845-2a9c-495a-84f0-4dd2c5164463). The app also provides access to the source code when installed in the ../MATLAB/Add-Ons/Apps/AnalyzER_v1_app/code folder.

Reporting summary. Further information on experimental design is available in the Nature Research Reporting Summary linked to this article.

Data availability

All images, parameter files used in the software to analyse them, and the results are available from the Oxford Research Archive (ORA) (https://ora.ox.ac.uk/objects/uuid:cb0e2845-2a9c-495a-84f0-4dd2c5164463).

Received: 31 July 2018 Accepted: 5 February 2019
Published online: 28 February 2019

References

1. Terasaki, M., Song, J., Wong, J. R., Weiss, M. J. & Chen, L. B. Localization of endoplasmic-reticulum in living and glutaraldehyde-fixed cells with fluorescent dyes. *Cell* **38**, 101–108 (1984).
2. Quader, H. & Schnepf, E. Endoplasmic-reticulum and cytoplasmic streaming—fluorescence microscopic observations in adaxial epidermis cells of onion bulb scales. *Protoplasma* **131**, 250–252 (1986).
3. Lichtscheidl, I. K. & Url, W. G. Organization and dynamics of cortical endoplasmic reticulum in inner epidermal cells of onion bulb scales. *Protoplasma* **157**, 203–215 (1990).
4. Sparkes, I. A., Runions, J., Kearns, A. & Hawes, C. Rapid, transient expression of fluorescent fusion proteins in tobacco plants and generation of stably transformed plants. *Nat. Protoc.* **1**, 2019–2025 (2006).
5. Sparkes, I., Runions, J., Hawes, C. & Griffing, L. Movement and remodeling of the endoplasmic reticulum in nondividing cells of tobacco leaves. *Plant Cell* **21**, 3937–3949 (2009).
6. Ridge, R. W., Uozumi, Y., Plazinski, J., Hurley, U. A. & Williamson, R. E. Developmental transitions and dynamics of the cortical ER of Arabidopsis cells seen with green fluorescent protein. *Plant Cell Physiol.* **40**, 1253–1261 (1999).
7. Jaipargas, E.-A., Barton, K., Mathur, N. & Mathur, J. Mitochondrial pleomorphy in plant cells is driven by contiguous ER dynamics. *Front. Plant Sci.* **6**, 783 (2015).
8. Griffing, L. R., Lin, C., Perico, C., White, R. R. & Sparkes, I. Plant ER geometry and dynamics: biophysical and cytoskeletal control during growth and biotic response. *Protoplasma* **254**, 43–56 (2017).
9. Westrate, L. M., Lee, J. E., Prinz, W. A. & Voeltz, G. K. Form follows function: the importance of endoplasmic reticulum shape. *Annu. Rev. Biochem.* **84**, 791–811 (2015).
10. Hepler, P. K., Palevitz, B. A., Lancelle, S. A., McCauley, M. M. & Lichtscheidl, I. K. Cortical endoplasmic reticulum in plants. *J. Cell Sci.* **96**, 355–373 (1990).
11. Stefano, G. & Brandizzi, F. Advances in plant ER architecture and dynamics. *Plant Physiol.* **176**, 178–186 (2018).
12. McFarlane, H. E. et al. Multiscale structural analysis of plant ER–PM contact sites. *Plant Cell Physiol.* **58**, 478–484 (2017).
13. Saint-Jore, C. M. et al. Redistribution of membrane proteins between the Golgi apparatus and endoplasmic reticulum in plants is reversible and not dependent on cytoskeletal networks. *Plant J.* **29**, 661–678 (2002).
14. Breeze, E. et al. A C-terminal amphipathic helix is necessary for the in vivo tubule-shaping function of a plant reticulon. *Proc. Natl. Acad. Sci. USA* **113**, 10902–10907 (2016).
15. Sparkes, I. et al. Five Arabidopsis reticulon isoforms share endoplasmic reticulum location, topology, and membrane-shaping properties. *Plant Cell* **22**, 1333–1343 (2010).
16. Tolley, N. et al. Transmembrane domain length is responsible for the ability of a plant reticulon to shape endoplasmic reticulum tubules in vivo. *Plant J.* **64**, 411–418 (2010).
17. Tolley, N. et al. Overexpression of a plant reticulon remodels the lumen of the cortical endoplasmic reticulum but does not perturb protein transport. *Traffic* **9**, 94–102 (2008).
18. Kriechbaumer, V. et al. Reticulomics: protein–protein interaction studies with two plasmodesmata-localized reticulon family proteins identify binding partners enriched at plasmodesmata, endoplasmic reticulum, and the plasma membrane. *Plant Physiol.* **169**, 1933–1945 (2015).
19. Kriechbaumer, V. et al. Arabidopsis Lunapark proteins are involved in ER cisternae formation. *New Phytol.* **219**, 990–1004 (2018).
20. Stefano, G., Renna, L. & Brandizzi, F. The endoplasmic reticulum exerts control over organelle streaming during cell expansion. *J. Cell Sci.* **127**, 947–953 (2014).
21. Nixon-Abell, J. et al. Increased spatiotemporal resolution reveals highly dynamic dense tubular matrices in the peripheral ER. *Science* **354**, aaf3928 (2016).
22. Perico, C. & Sparkes, I. Plant organelle dynamics: cytoskeletal control and membrane contact sites. *New Phytol.* **220**, 381–394 (2018).
23. Sparkes, I., Teanby, N. & Hawes, C. In vivo imaging of Arabidopsis myosins: class XI myosins perturb organelle movement. *Comp. Biochem. Physiol. Part A Mol. Integr. Physiol.* **150**, S201 (2008).
24. Horn, B. K. P. & Schunck, B. G. Determining optical flow. *Artif. Intell.* **17**, 185–203 (1981).
25. Ueda, H. et al. Myosin-dependent endoplasmic reticulum motility and F-actin organization in plant cells. *Proc. Natl. Acad. Sci. USA* **107**, 6894–6899 (2010).
26. Ueda, H., Tamura, K. & Hara-Nishimura, I. Functions of plant-specific myosin XI: from intracellular motility to plant postures. *Curr. Opin. Plant Biol.* **28**, 30–38 (2015).
27. Wang, P., Hawes, C. & Hussey, P. J. Plant endoplasmic reticulum–plasma membrane contact sites. *Trends Plant Sci.* **22**, 289–297 (2017).
28. Staehelin, L. A. The plant ER: a dynamic organelle composed of a large number of discrete functional domains. *Plant J.* **11**, 1151–1165 (1997).
29. Sparkes, I. A., Ketelaar, T., de Ruijter, N. C. A. & Hawes, C. Grab a Golgi: laser trapping of Golgi bodies reveals in vivo interactions with the endoplasmic reticulum. *Traffic* **10**, 567–571 (2009).
30. Lin, C. P., Zhang, Y. W., Sparkes, I. & Ashwin, P. Structure and dynamics of ER: minimal networks and biophysical constraints. *Biophys. J.* **107**, 763–772 (2014).
31. Wang, P. W. et al. The plant cytoskeleton, NET3C, and VAP27 mediate the link between the plasma membrane and endoplasmic reticulum. *Curr. Biol.* **24**, 1397–1405 (2014).
32. Lin, C., White, R. R., Sparkes, I. & Ashwin, P. Modeling endoplasmic reticulum network maintenance in a plant cell. *Biophys. J.* **113**, 214–222 (2017).
33. Siao, W., Wang, P., Voigt, B., Hussey, P. J. & Baluska, F. Arabidopsis SYT1 maintains stability of cortical endoplasmic reticulum networks and VAP27-1-enriched endoplasmic reticulum–plasma membrane contact sites. *J. Exp. Bot.* **67**, 6161–6171 (2016).
34. Wang, P. et al. Plant VAP27 proteins: domain characterization, intracellular localization and role in plant development. *New Phytol.* **210**, 1311–1326 (2016).

35. Sparkes, I. Lessons from optical tweezers: quantifying organelle interactions, dynamics and modelling subcellular events. *Curr. Opin. Plant Biol.* **46**, 55–61 (2018).
36. Harris, N. & Chrispeels, M. J. The endoplasmic reticulum of mung-bean cotyledons: quantitative morphology of cisternal and tubular ER during seedling growth. *Planta* **148**, 293–303 (1980).
37. Stephenson, J. L. M. & Hawes, C. R. Stereology and stereometry of endoplasmic reticulum during differentiation in the maize root cap. *Protoplasma* **131**, 32–46 (1986).
38. West, M., Zurek, N., Hoenger, A. & Voeltz, G. K. A 3D analysis of yeast ER structure reveals how ER domains are organized by membrane curvature. *J. Cell Biol.* **193**, 333–346 (2011).
39. Joensuu, M. et al. ER sheet persistence is coupled to myosin 1c-regulated dynamic actin filament arrays. *Mol. Biol. Cell* **25**, 1111–1126 (2014).
40. Lambert, T. J. & Waters, J. C. Navigating challenges in the application of superresolution microscopy. *J. Cell Biol.* **216**, 53–63 (2016).
41. Streekstra, G. J. & van Pelt, J. Analysis of tubular structures in three-dimensional confocal images. *Network* **13**, 381–395 (2002).
42. Fricker, M. et al. in *The Plant Endoplasmic Reticulum: Methods and Protocols* (eds Hawes, C. & Kriechbaumer, V.) 43–66 (Springer, New York, 2018).
43. Bouchekhima, A. N., Frigerio, L. & Kirkilionis, M. Geometric quantification of the plant endoplasmic reticulum. *J. Microsc.* **234**, 158–172 (2009).
44. Otsu, N. Threshold selection method from gray-level histograms. *IEEE Trans. Syst. Man Cybern.* **9**, 62–66 (1979).
45. Griffing, L. R. in *The Plant Endoplasmic Reticulum: Methods and Protocols* (eds Hawes, C. & Kriechbaumer, V.) 75–102 (Springer, New York, 2018).
46. Frangi, A., Niessen, W., Vincken, K. & Viergever, M. in *Medical Image Computing and Computer-Assisted Intervention, Vol. 1496 Lecture Notes in Computer Science* (eds Wells, W. et al.) 130–137 (Springer, Berlin/Heidelberg, 1998).
47. Bühler, J. et al. phenoVein—a tool for leaf vein segmentation and analysis. *Plant Physiol.* **169**, 2359–2370 (2015).
48. Meijering, E. et al. Design and validation of a tool for neurite tracing and analysis in fluorescence microscopy images. *Cytometry A* **58**, 167–176 (2004).
49. Lopez-Molina, C., de Ulzurrun, G. V. D., Baetens, J. M., Van den Bulcke, J. & De Baets, B. Unsupervised ridge detection using second order anisotropic Gaussian kernels. *Signal Process.* **116**, 55–67 (2015).
50. Kovesi, P. D. Image features from phase congruency. *Videre* **1**, 1–26 (1999).
51. Obara, B., Grau, V. & Fricker, M. D. A bioimage informatics approach to automatically extract complex fungal networks. *Bioinformatics* **28**, 2374–2381 (2012).
52. Fricker, M. D. et al. Automated analysis of *Physarum* network structure and dynamics. *J. Phys. D* **50**, 254005 (2017).
53. Zhang, B., Zerubia, J. & Olivo-Marin, J.-C. Gaussian approximations of fluorescence microscope point-spread function models. *Appl. Opt.* **46**, 1819–1829 (2007).
54. Behnke, H.-D. & Eschlbeck, G. Dilated cisternae in Capparales—an attempt towards the characterization of a specific endoplasmic reticulum. *Protoplasma* **97**, 351–363 (1978).
55. Iversen, T.-H. & Flood, P. R. Rod-shaped accumulations in cisternae of the endoplasmic reticulum in root cells of *Lepidium sativum* seedlings. *Planta* **86**, 295–298 (1969).
56. Hawes, C., Saint-Jore, C., Martin, B. & Zheng, H. Q. ER confirmed as the location of mystery organelles in Arabidopsis plants expressing GFP! *Trends Plant Sci.* **6**, 245–246 (2001).
57. Nakano, R. T., Yamada, K., Bednarek, P., Nishimura, M. & Hara-Nishimura, I. ER bodies in plants of the Brassicales order: biogenesis and association with innate immunity. *Front. Plant Sci.* **5**, 73 (2014).
58. Gunning, B. E. The identity of mystery organelles in Arabidopsis plants expressing GFP. *Trends Plant Sci.* **3**, 417 (1998).
59. Nagano, A. J. et al. Quantitative analysis of ER body morphology in an Arabidopsis mutant. *Plant Cell Physiol.* **50**, 2015–2022 (2009).
60. Shemesh, T. et al. A model for the generation and interconversion of ER morphologies. *Proc. Natl. Acad. Sci. USA* **111**, E5243–E5251 (2014).
61. Hu, J. & Zhang, M. Homotypic fusion of endoplasmic reticulum membranes in plant cells. *Front. Plant Sci.* **4**, 514 (2013).
62. Boland, M. V. & Murphy, R. F. A neural network classifier capable of recognizing the patterns of all major subcellular structures in fluorescence microscope images of HeLa cells. *Bioinformatics* **17**, 1213–1223 (2001).
63. Haralick, R. M. Statistical and structural approaches to texture. *Proc. IEEE* **67**, 786–804 (1979).
64. Haralick, R. M., Shanmugam, K. & Dinstein, I. H. Textural features for image classification. *IEEE Trans. Syst. Man Cybern.* **3**, 610–621 (1973).
65. Brynolfsson, P. et al. Haralick texture features from apparent diffusion coefficient (ADC) MRI images depend on imaging and pre-processing parameters. *Sci. Rep.* **7**, 4041 (2017).
66. Fricker, M. D. Quantitative redox imaging software. *Antioxid. Redox Signal.* **24**, 752–762 (2015).
67. Sparkes, I. A., Hawes, C. & Baker, A. AtPEX2 and AtPEX10 are targeted to peroxisomes independently of known endoplasmic reticulum trafficking routes. *Plant Physiol.* **139**, 690–700 (2005).
68. Karimi, M., De Meyer, B. & Hilson, P. Modular cloning in plant cells. *Trends Plant Sci.* **10**, 103–105 (2005).
69. Kremer, J. R., Mastronarde, D. N. & McIntosh, J. R. Computer visualization of three-dimensional image data using IMOD. *J. Struct. Biol.* **116**, 71–76 (1996).
70. He, K. M., Sun, J. & Tang, X. O. Guided image filtering. *IEEE Trans. Pattern Anal. Mach. Intell.* **35**, 1397–1409 (2013).
71. Kovesi, P. D. *MATLAB and Octave Functions for Computer Vision and Image Processing*. http://www.csse.uwa.edu.au/~pk/research/matlabfns/ (2000).
72. Zhang, T. Y. & Suen, C. Y. A fast parallel algorithm for thinning digital patterns. *Commun. ACM* **27**, 236–239 (1984).
73. Chan, T. F. & Vese, L. A. Active contours without edges. *IEEE Trans. Image Process* **10**, 266–277 (2001).
74. Lopez-Molina, C., De Baets, B. & Bustince, H. Quantitative error measures for edge detection. *Pattern Recognit.* **46**, 1125–1139 (2013).
75. Saito, T. & Rehmsmeier, M. The precision–recall plot is more informative than the ROC plot when evaluating binary classifiers on imbalanced datasets. *PLoS ONE* **10**, e0118432 (2015).
76. Berens, P. CircStat: a MATLAB toolbox for circular statistics. *J. Stat. Softw.* **31**, 1–21 (2009).
77. Lucas, B. D. & Kanade, T. in *Proceedings of the 7th International Joint Conference on Artificial Intelligence (IJCAI)* 674–679 (1981).
78. Farnebäck, G. in *Image Analysis: Proceedings of the 13th Scandinavian Conference, SCIA 2003, Halmstad, Sweden, June 29–July 2, 2003* (eds Bigun, J. & Gustavsson, T.) 363–370 (Springer, Berlin/Heidelberg, 2003).

Acknowledgements

This work was supported by the Human Frontier Science Program (RGP0053/2012, M.F.); the Leverhulme Trust (RPG-2015-437, M.F.); the Institute of Advanced Studies, Durham (M.F.); BBSRC (BB/M000168/1, C.H.) via the ERA-CAPs programme Per Aspera; BBSRC 17ALERT (BB/R014086/1, M.F.); The John Fell Oxford University Press (OUP) Fund (M.F.); a Vice Chancellor's Research Fellowship from Oxford Brookes University (UK) to V.K. and a BBSRC DTP studentship to C.P. (BB/M011224/1).

Author contributions

V.K., C.H. and M.F. conceived the work, C.P. performed the confocal experiments and analyses, M.K. performed the SBFSEM, V.K. and C.H. supervised the experiments, M.F. wrote the software and performed the analyses, C.P. wrote the tutorial, C.P., V.K., C.H. and M.F. wrote the paper.

Additional information

Supplementary Information accompanies this paper at https://doi.org/10.1038/s41467-019-08893-9.

Competing interests: The authors declare no competing interests.

Reprints and permission information is available online at http://npg.nature.com/reprintsandpermissions/

Journal peer review information: *Nature Communications* thanks Lawrence Griffing and the other anonymous reviewer(s) for their contribution to the peer review of this work. Peer reviewer reports are available.

Publisher's note: Springer Nature remains neutral with regard to jurisdictional claims in published maps and institutional affiliations.

Open Access This article is licensed under a Creative Commons Attribution 4.0 International License, which permits use, sharing, adaptation, distribution and reproduction in any medium or format, as long as you give appropriate credit to the original author(s) and the source, provide a link to the Creative Commons license, and indicate if changes were made. The images or other third party material in this article are included in the article's Creative Commons license, unless indicated otherwise in a credit line to the material. If material is not included in the article's Creative Commons license and your intended use is not permitted by statutory regulation or exceeds the permitted use, you will need to obtain permission directly from the copyright holder. To view a copy of this license, visit http://creativecommons.org/licenses/by/4.0/.

© The Author(s) 2019

9 | Supplementary data

S1 Chapter 3 - AnalyzER

Appendix 1 contains a list of the ER structural and dynamic parameters calculated by AnalyzER and an explanation of their calculation.

S1.1 Graph parameters

G The number of sub-graphs in the network. This is typically one as only the largest connected component is selected

nodes The number of nodes (excluding cisternal nodes)

links The number of edges (excluding cisternal edges)

total length The total length of the network tubules (mm)

mean length The average length of the tubules (µm)

median length The median length of the tubules (µm)

mean width The average width of the tubules (µm)

median width The median width of the tubules (µm)

volume The total volume of the network (mm^3)

k The average node degree

G efficiency The global efficiency of the network

R efficiency The root efficiency of the network calculated to the first cisternal node

cyclomatic no. The cyclomatic number

alpha The alpha coefficient or meshedness

beta The beta coefficient

gamma The gamma coefficient

diameter The longest shortest path through the network

S1.2 Tubule edge parameters

Original, cv The mean intensity of pixels in the edge from the original image, along with the coefficient of variation (cv)

Intensity, cv The mean intensity and cv after background subtraction

Width, Width cv The estimated width (2r) and cv (µm)

Width center The estimated width excluding overlap regions at the node

Length, length center The total length and length excluding the overlap at nodes (l, µm)

Area, Volume The cross-sectional area ($a = \pi r^2$, µm^2) and volume ($v = a \times l$, µm^3)

Resistance The predicted resistance to flow assuming Poiseuille flow (l/r^4, µm^{-3})

Number The number of pixels in the edge

Tortuosity The Euclidean distance between the nodes divided by the total length of the edge

Speed - local The scalar sum of the speeds calculated for each pixel ($\mu m\,s^{-1}$)

Speed - max The maximum speed for any pixel ($\mu m\,s^{-1}$)

Speed - global The vector sum of speeds for each pixel ($\mu m\,s^{-1}$)

Dir - local, std The angular mean and standard deviation of the flow direction at each pixel (°)

Dir - global The direction of the vector sum (°)

Flow coherence The ratio of the local speed (scalar sum) to the global speed (vector sum)

Flow curl, std The local angular rotation of the vector field (°)

Flow AV, std The local angular velocity of the vector field ($^\circ\,s^{-1}$)

Flow divergence, std The divergence of the vector flow field (°)

Persistency, cv The mean period of time that each pixel forms part of a tubule (s)

Distance The geodesic distance of each pixel from a manually defined reference point (µm)

Region The integrated sum of intensities in the region closest to each edge

BC The edge betweenness centrality

S1.3 Node parameters

node degree The number of tubules connected to each node, excluding cisternal nodes

total width The sum of the tubule widths incident at each node

mean width The average of the tubule widths incident at each node

intensity The original intensity at the node

persistency Node persistency

speed Node speed

direction Node direction

distance The distance from the reference point

Maj, Mid and Min The widths of the three main tubules incident at the node. Only one value is given for a terminal node, whilst few node have a degree greater than three

Min-Maj, Mid-Maj and Min-Mid The ratio of the tubule widths for the three main incident tubules

Omaj, Omid and Omin The orientation of the three main incident tubules, determined as a linear segment between the node and the midpoint of the tubule

Omin-Omaj, Omid-Omaj and Omin-Omid Branch angles between the three main incident tubules, determined from a linear segment from the node to the midpoint of each tubule

S1.4 Tubule morphology parameters

peak number The total number of peaks measured excluding nodes. Values are given for each channel analysed

peak density The number of peaks per unit length (μm^{-1})

length The total length of tubules analysed (µm)

peak value The mean intensity at the peak (I_P)

peak width The estimated width of the peak (µm)

peak separation The mean separation of peaks, which is only calculated if there is more than one peak per tubule (µm)

peak covar The mean covariance of intensities from two channels measured at the peak ($(I_{P1} - \overline{I_{P1}}) \times (I_{P2} - \overline{I_{P2}})$). Positive values indicate both channels show similar behaviour, whilst negative values indicate they move in opposite directions

peak ratio The mean ratio of intensities at the peak from two channels (I_{P1}/I_{P2}) trough number The number of troughs (measured as peaks in the inverted intensity profile)

trough density The number of troughs per unit length of tubule (µm)

trough value The mean intensity in the trough (I_T)

trough width The mean width of the trough (µm)

trough separation The mean separation of troughs if there is more than one trough per tubule (µm)

trough covar The mean covariance of intensities from two channels measured in the trough $((I_{T1} - \overline{I_{T1}}) \times (I_{T2} - \overline{I_{T2}}))$

trough ratio The mean ratio of intensities from two channels measured in the trough (I_{T1}/I_{T2})

S1.5 Cisternae morphology parameters

ID The node identity displayed on the image overlay

area The area of each cisterna

major axis and minor axis length (in pixels) of the major and minor axis of the ellipse that has the same normalized second central moments as the cisterna

orientation The angle between the x-axis and the major axis

solidity The proportion of the pixels in the convex hull that are also in the cisterna

perimeter The perimeter of the cisterna

elongation The ratio of the major axis to the the minor axis

roughness The ratio of the perimeter2 to the area

circularity The ratio of the radius determined from the area to the radius determined from the perimeter

S1.6 Intensity-based cisternae metrics

mean Intensity, max Intensity and min Intensity metrics calculated for each cisterna from the background-subtracted image

node degree The number of connecting tubules incident on the cisterna

node strength The sum of the widths of the tubules connecting to the cisterna (µm)

average node strength The node strength divided by the node degree, (µm)

max and mean persistency The maximum and average persistency of pixels in each cisterna (s)

speed - local, speed - max and speed - global The scalar sum of local speeds at every pixel, the maximum speed across all pixels, and the global (vector sum) speed ($\mu m\, s^{-1}$)

Dir - local, Dir - std, and Dir - global The mean angular direction of movement for all pixels in the cisterna along with the angular standard deviation, and the mean global direction from the vector sum (°)

Flow coherence The ratio of the local speed (scalar sum) to the global speed (vector sum)

Flow curl, std The local angular rotation of the vector field within the cisternae (°)

Flow AV, std The local angular velocity of the vector field ($^\circ\, s^{-1}$)

Flow divergence, std The divergence of the vector flow field (°)

Persistency, cv The mean period of time that each pixel forms part of a tubule (s)

max distance and mean distance The maximum and average distance of any pixel to the edge of the cisterna (µm)

variance The square of the difference in intensity of each pixel from the mean within the cisterna

S1.7 Texture metrics

Contrast A measure of the intensity contrast between a pixel and its neighbour. Values range from 0 to $(nbins - 1)^2$. An idealised cisternal sheet would have a contrast of zero.

Correlation A measure of how correlated a pixel is to its neighbour. Values range from -1 (un-correlated) to 1 (fully correlated). An idealised cisternal sheet would have a value of 1.

Energy Gives the sum of squared elements in the GLCM. Values range from 0 to 1. An idealised cisternal sheet would have an energy of 1.

Homogeneity Measures the closeness of the distribution of elements in the GLCM to the diagonal. Values range from 0 to 1. An idealised cisternal sheet would have a value of 1.

S1.8 Morphological metrics of polygonal regions

ID The identity of the polygonal region

area The area of each polygonal region with the ER tubules thinned to a single-pixel wide skeleton

major axis and minor axis length (in pixels) of the major and minor axis of the ellipse that has the same normalized second central moments as the region

orientation The angle between the x-axis and the major axis

solidity The proportion of the pixels in the convex hull that are also in the region

perimeter The perimeter of the region

elongation The ratio of the major axis to the the minor axis

roughness The ratio of the perimeter^2 to the area

circularity The ratio of the radius determined from the area to the radius determined from the perimeter

max distance The furthest distance within the region to the ER network

mean distance The average distance within the region to the ER network

exclusive area The area excluding the width of the ER tubules

S2 Chapter 4 - The Lunapark proteins and ER structure

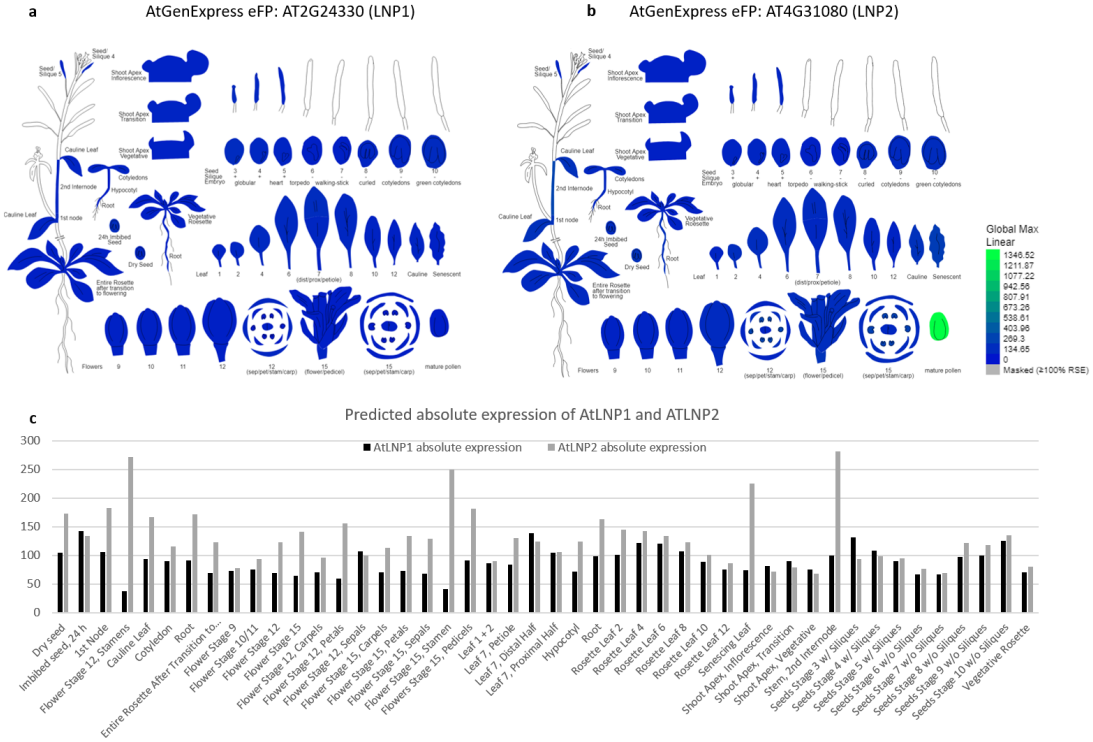


Figure S1: Predicted expression of AtLNP1 and AtLNP2
(a,b) The predicted absolute expression levels of AtLNP1 and AtLNP2 displayed using a global linear scale (image by BAR eFP browser). (c) Predicted tissue specific absolute expression of AtLNP1 and AtLNP2 (with mature pollen values omitted) showing the range of expression levels predicted through development.

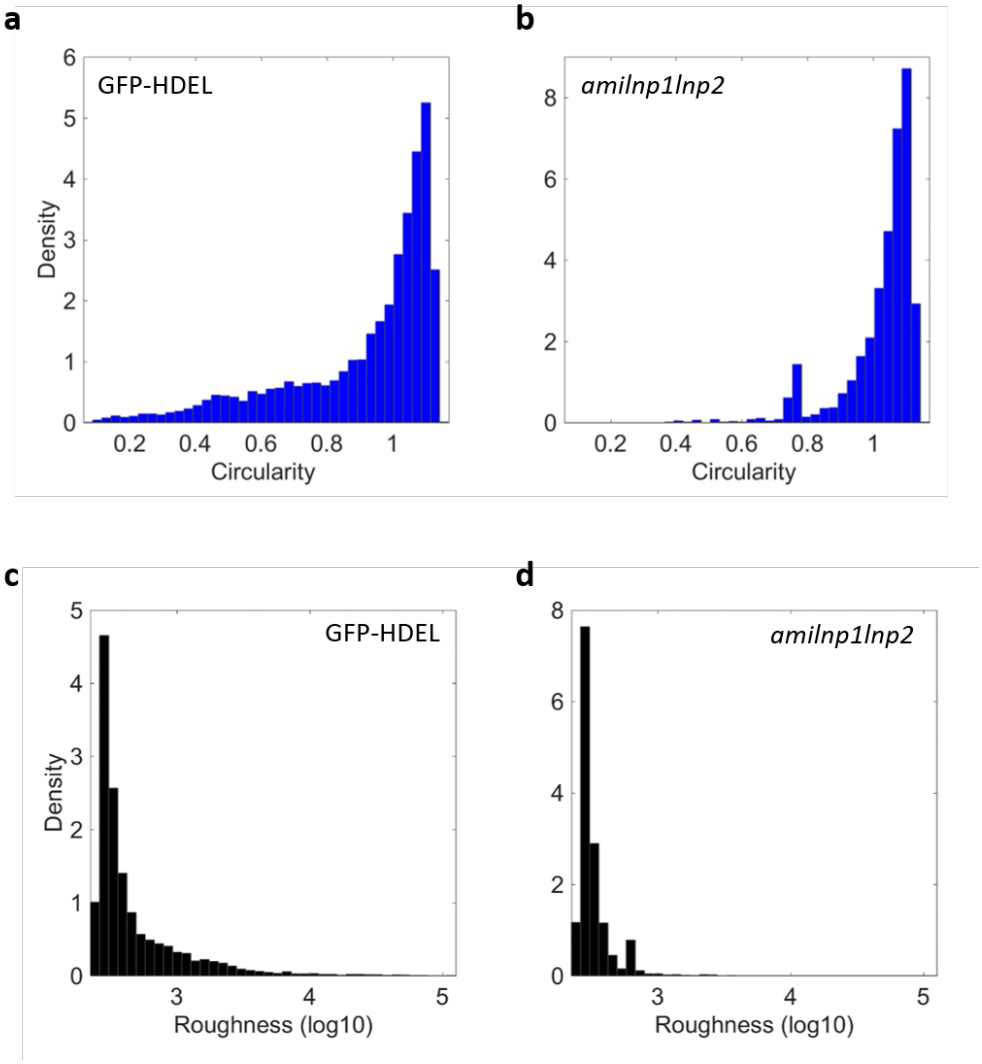


Figure S2: The geometry of cisternae in Col-0 expressing GFP-HDEL alone and alongside reduced *AtLNP1* and *AtLNP2* transcription
Density plots of cisternae circularity measured in plants expressing GFP-HDEL alone (a) and alongside reduced AtLNP1 and AtLNP2 transcription in the *amilnp1lnp2* line (b). Density plots of cisternae roughness in GFP-HDEL and the *amilnp1lnp2* line. Images collected of 7 day old cotyledon cells using confocal microscopy.

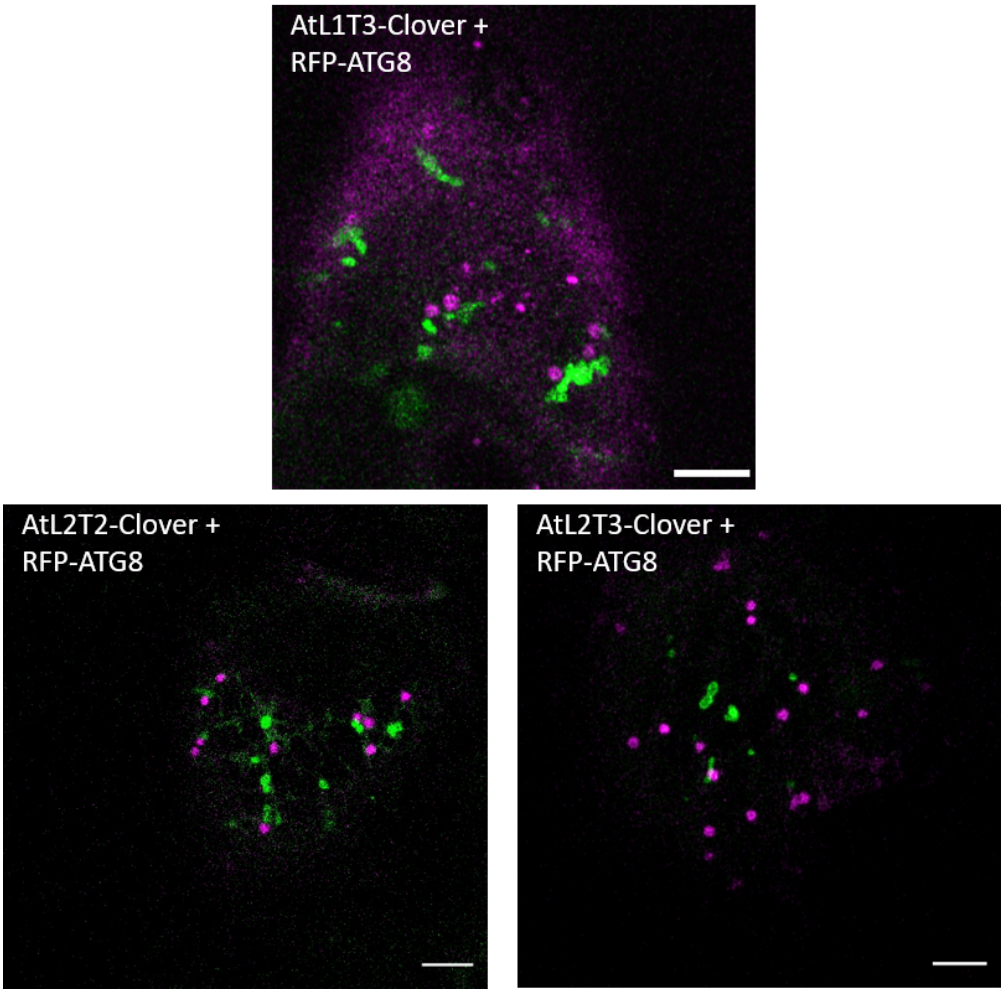


Figure S3: Co-localisation of AtL1T3-Clover, AtL2T2-Clover and AtL2T3-Clover with RFP-ATG8

Co-expression of the autophagosome marker RFP-ATG8 (magenta) with three AtLNP1 and 2 truncations: AtL1T3-Clover, AtL2T2-Clover and AtL2T3-Clover (green) in tobacco leaf epidermal cells. Scale bars 5 µm.

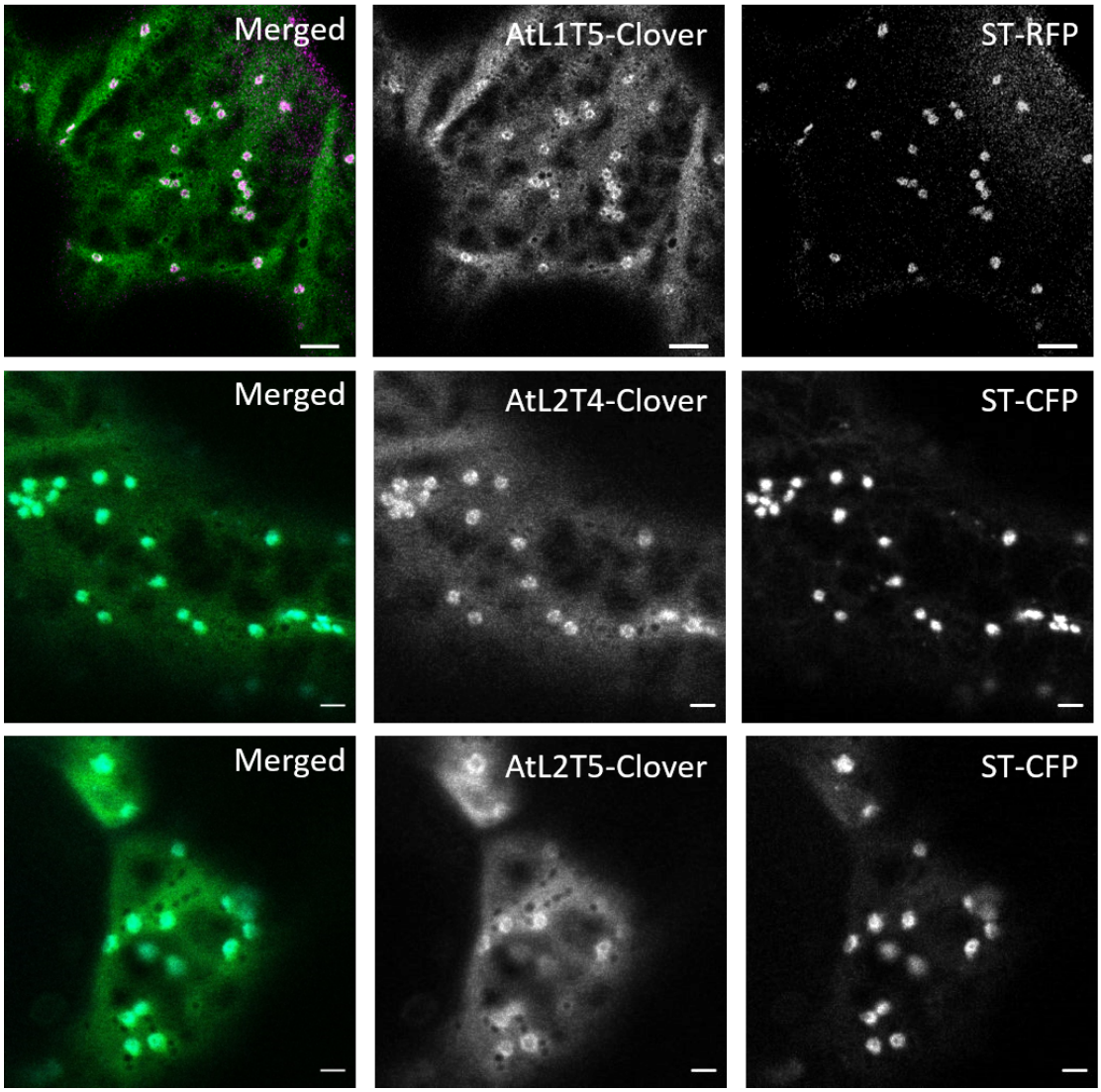
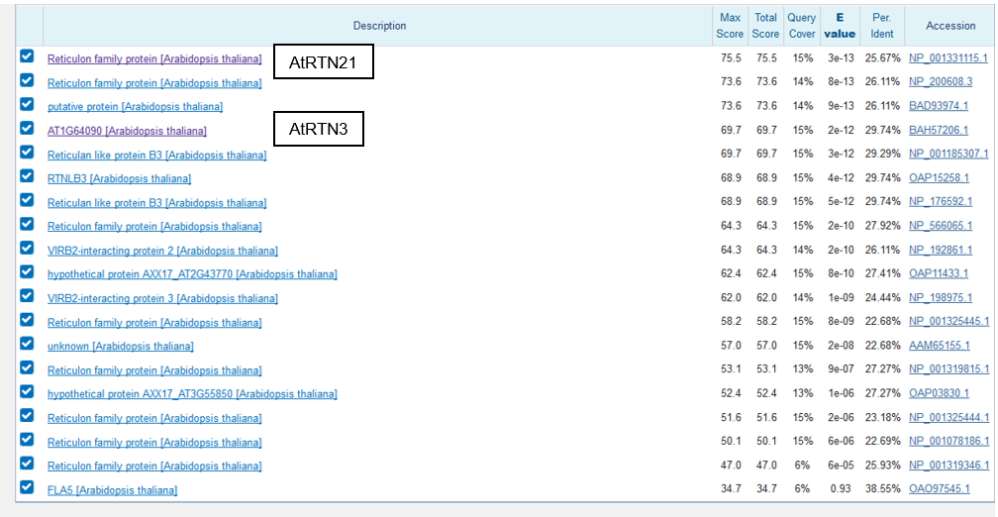


Figure S4: Co-expression of AtL1T5-Clover, AtL2T4-Clover and AtL2T5-Clover with the Golgi body marker ST-RFP/CFP
Transient co-expression one AtLNP1 truncation (AtL1T5-Clover, green) and two AtLNP2 truncations (AtL2T4-Clover and AtL2T5-Clover, green) with the Golgi marker ST-RFP (magenta) or ST-CFP (cyan). Images collected of tobacco leaf epidermal cells using confocal microscopy. Scale bars 5 µm.



Description	Max Score	Total Score	Query Cover	E value	Per. Ident	Accession
Reticulon family protein [Arabidopsis thaliana] AtRTN21	75.5	75.5	15%	3e-13	25.67%	NP_001331115.1
Reticulon family protein [Arabidopsis thaliana]	73.6	73.6	14%	8e-13	26.11%	NP_200608.3
putative protein [Arabidopsis thaliana]	73.6	73.6	14%	9e-13	26.11%	BAD93974.1
AT1G64090 [Arabidopsis thaliana] AtRTN3	69.7	69.7	15%	2e-12	29.74%	BAH57206.1
Reticulan like protein B3 [Arabidopsis thaliana]	69.7	69.7	15%	3e-12	29.29%	NP_001185307.1
RTNLB3 [Arabidopsis thaliana]	68.9	68.9	15%	4e-12	29.74%	OAP15258.1
Reticulan like protein B3 [Arabidopsis thaliana]	68.9	68.9	15%	5e-12	29.74%	NP_176592.1
Reticulon family protein [Arabidopsis thaliana]	64.3	64.3	15%	2e-10	27.92%	NP_566065.1
VIRB2-interacting protein 2 [Arabidopsis thaliana]	64.3	64.3	14%	2e-10	26.11%	NP_192861.1
hypothetical protein AXX17_AT2G43770 [Arabidopsis thaliana]	62.4	62.4	15%	8e-10	27.41%	OAP11433.1
VIRB2-interacting protein 3 [Arabidopsis thaliana]	62.0	62.0	14%	1e-09	24.44%	NP_198975.1
Reticulon family protein [Arabidopsis thaliana]	58.2	58.2	15%	8e-09	22.68%	NP_001325445.1
unknown [Arabidopsis thaliana]	57.0	57.0	15%	2e-08	22.68%	AAM65155.1
Reticulon family protein [Arabidopsis thaliana]	53.1	53.1	13%	9e-07	27.27%	NP_001319815.1
hypothetical protein AXX17_AT3G55850 [Arabidopsis thaliana]	52.4	52.4	13%	1e-06	27.27%	OAP03830.1
Reticulon family protein [Arabidopsis thaliana]	51.6	51.6	15%	2e-06	23.18%	NP_001325444.1
Reticulon family protein [Arabidopsis thaliana]	50.1	50.1	15%	6e-06	22.69%	NP_001078186.1
Reticulon family protein [Arabidopsis thaliana]	47.0	47.0	6%	6e-05	25.93%	NP_001319346.1
FLA5 [Arabidopsis thaliana]	34.7	34.7	6%	0.93	38.55%	OAO97545.1

Figure S5: BLAST results of mammalian Rtn4 against the arabidopsis genome

BLAST is used to identify the closest Rtn4 ortholog in arabidopsis out of 21 known reticulons. AtRTN3 and 21 were both found to be the closest available orthologues.

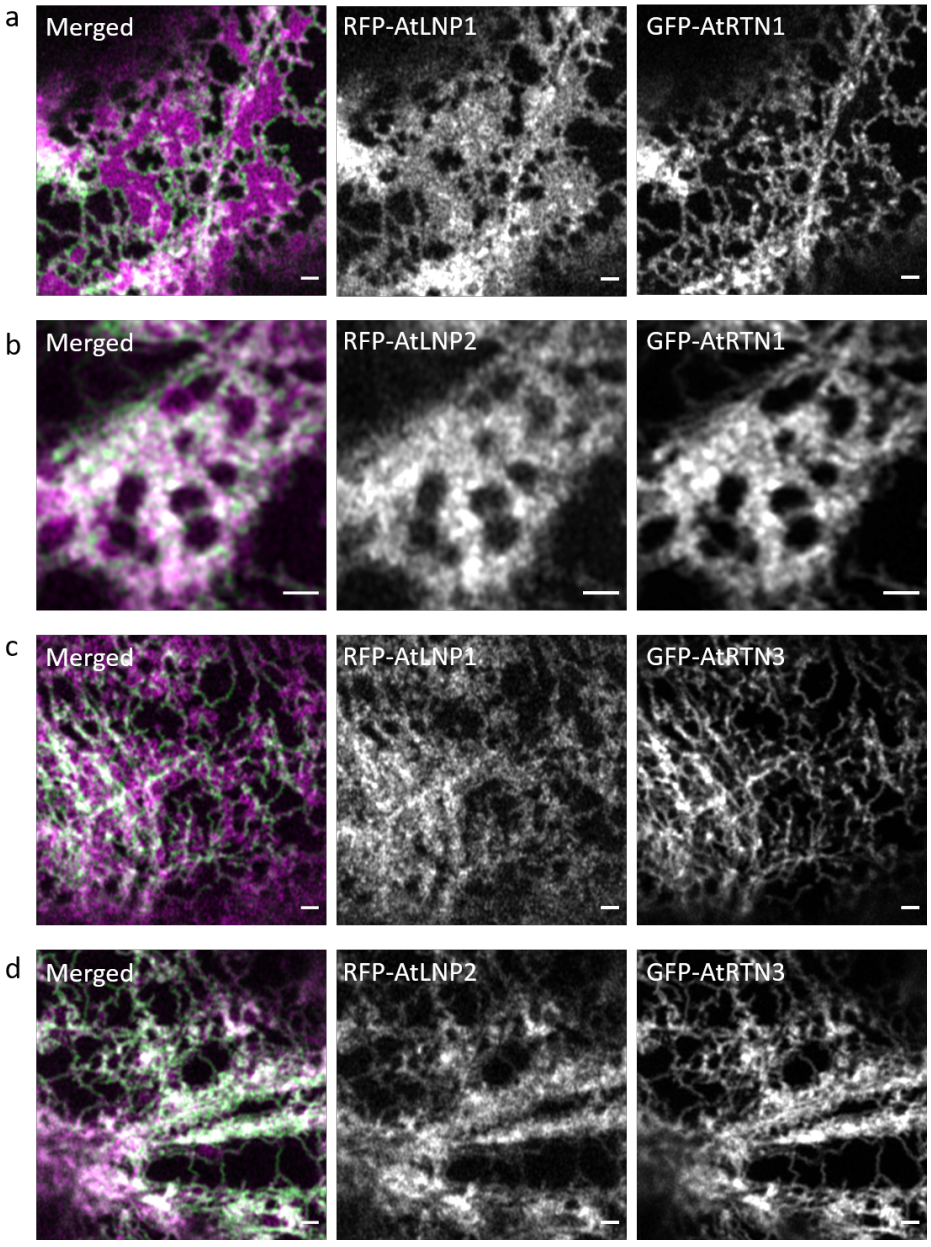


Figure S6: AtRTN1 and AtRTN3 localisation within AtLNP1 and AtLNP2 cisternae

Transient co-expression of GFP-AtRTN1 (green) with (a) RFP-AtLNP1 (magenta) reveals the presence of apparent tubules spanning a RFP-AtLNP1 induced cisternae and (b) RFP-AtLNP2 (magenta) shows co-localisation with GFP-AtRTN1 (green). Transient co-expression of GFP-AtRTN3 (green) with (c) RFP-AtLNP1 (magenta) reveals the presence of apparent tubules spanning a RFP-AtLNP1 (magenta) aggregate and (d) RFP-AtLNP2 (magenta) shows co-localisation with GFP-AtRTN3 (green). Scale bar 1 µm.

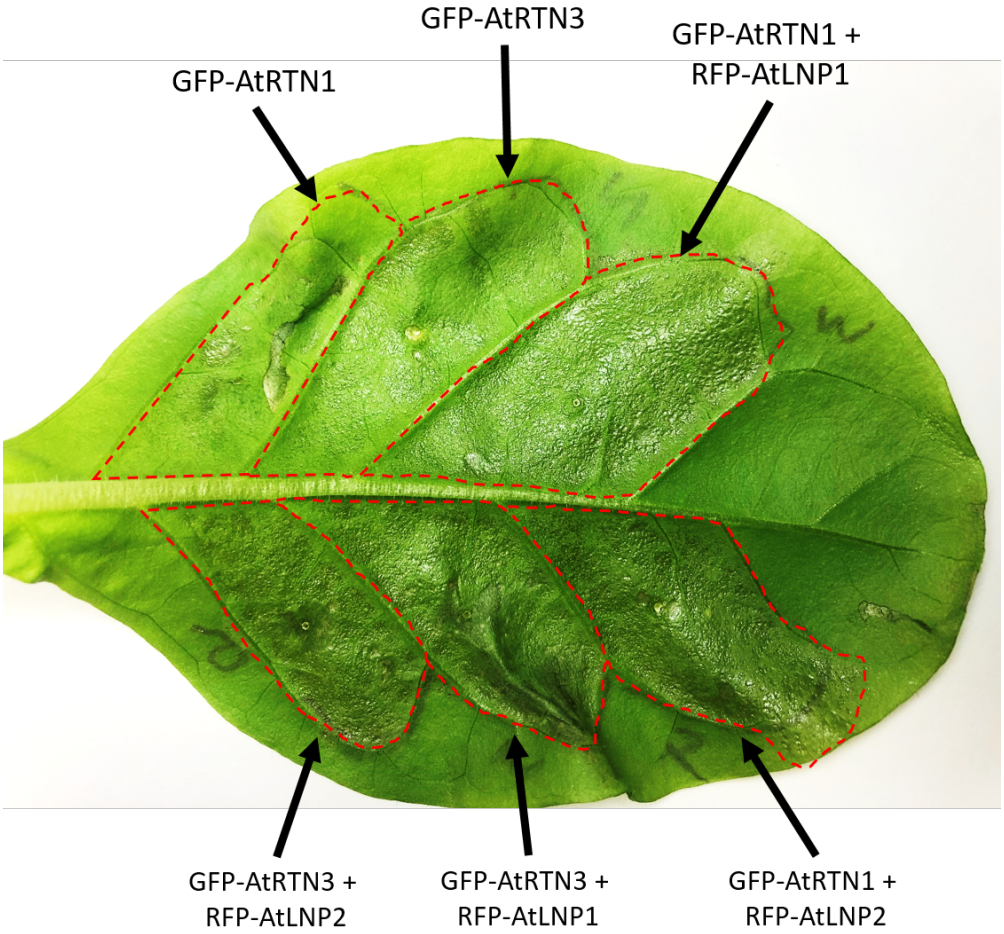


Figure S7: Adaxial side of a tobacco leaf three days after infiltration The adaxial side of a mature tobacco leaf three days after infiltration with GFP-AtRTN1 and GFP-AtRTN3 alone and alongside RFP-AtLNP1 and RFP-AtLNP2. Increased necrosis is visible on leaf segments that have dual expression of Lunapark and reticulon.

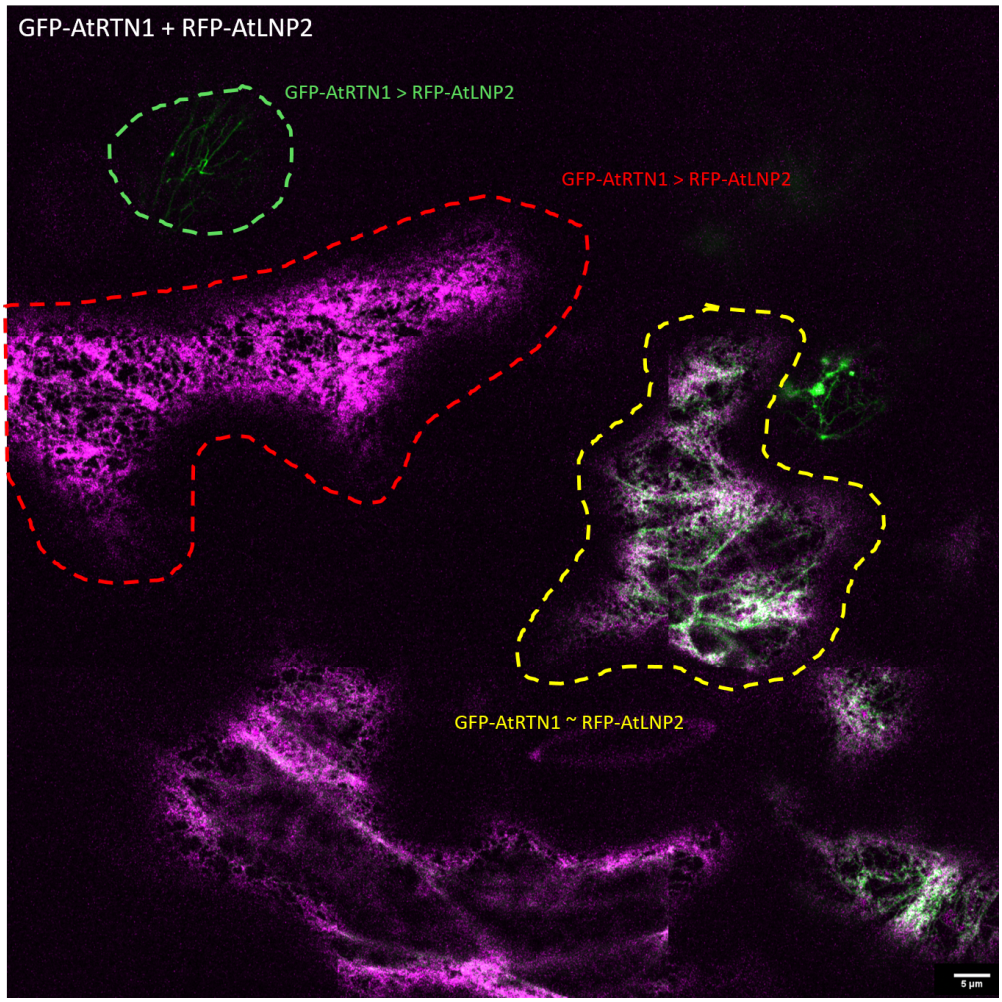


Figure S8: Variable expression levels of GFP-AtRTN1 and RFP-AtLNP2 across cells

Tiled image of multiple cells in the same tobacco leaf epidermal cell plane, revealing the variable expression levels of GFP-AtRTN1 and RFP-AtLNP1 within different cells. Cells with a tubulated (and more green) ER structure are indicative of GFP-AtRTN1 expression being higher than RFP-AtLNP2, whereas the reverse is true of cells with magenta ER and more cisternae. Where the ER is both green and magenta, the expression of GFP-AtRTN1 and RFP-AtLNP2 are considered to be sufficiently balances for analysis of ER cisternae structure. Scale bar 5 µm.

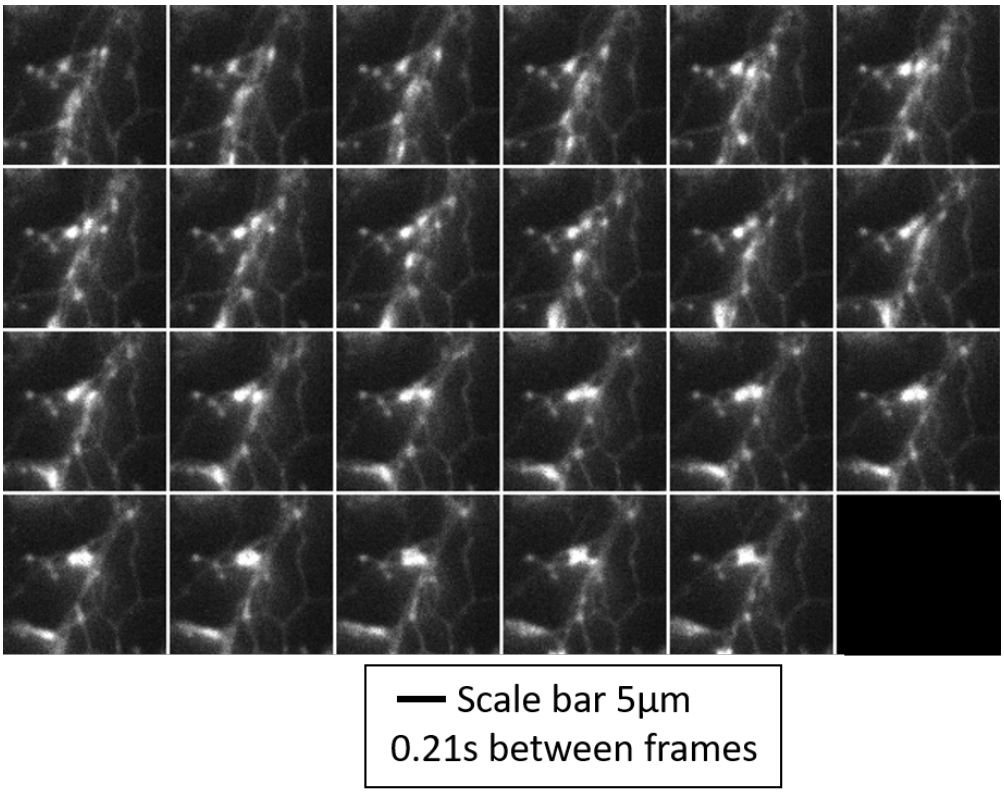


Figure S9: Full montage of cisternae formation by aggregation of AtLNP1-GFP punctae (a)
A time series montage of tobacco leaf epidermal cells transiently expressing AtLNP1-GFP. Individual AtLNP-GFP punctae are shown forming a nascent cisternae (also marked with AtLNP1-GFP) over a total period of 4.83 seconds. Scale bar 5 µm.

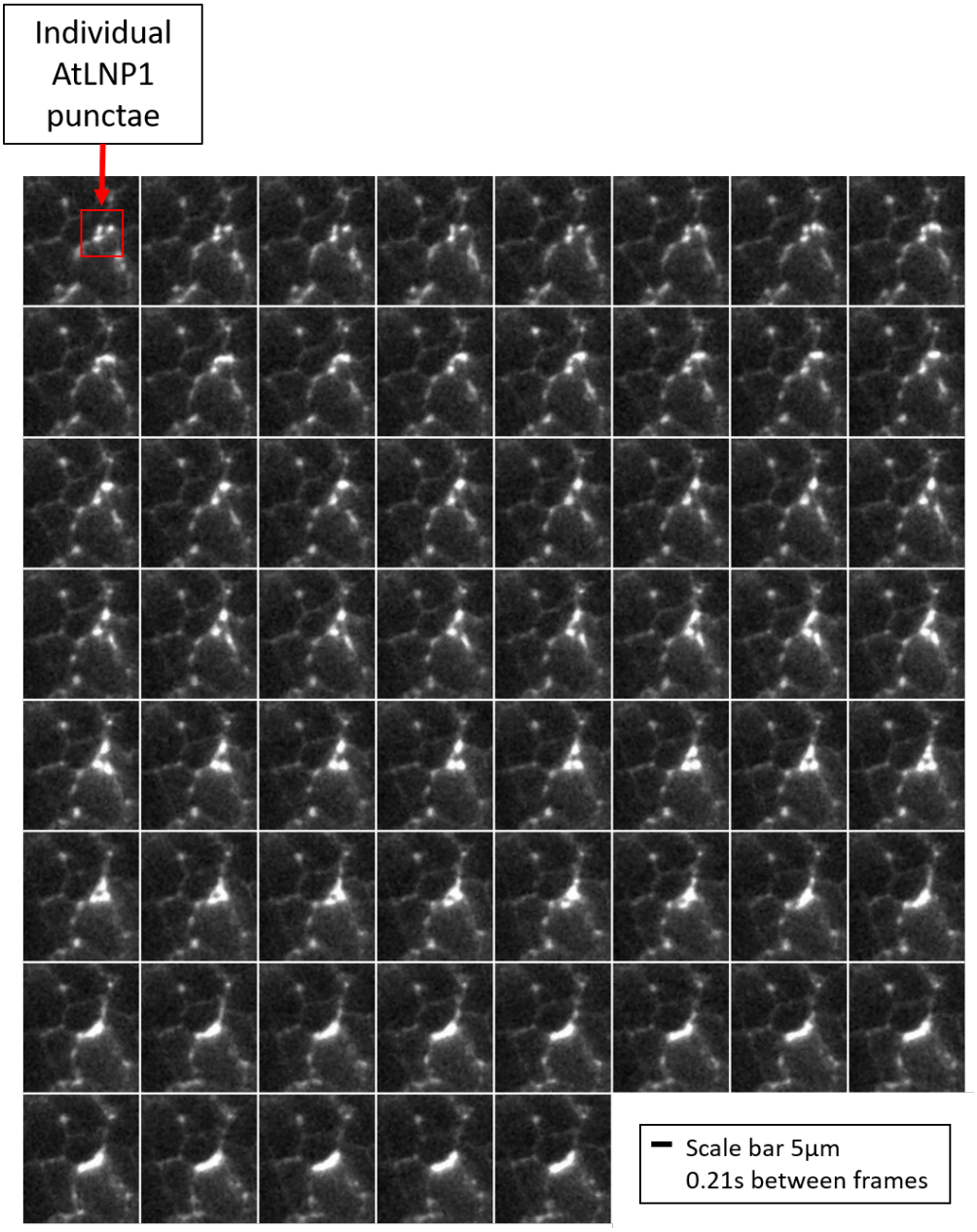


Figure S10: Full montage of cisternae formation by aggregation of AtLNP1-GFP punctae (b)
A time series montage of tobacco leaf epidermal cells transiently expressing AtLNP1-GFP. Individual AtLNP-GFP punctae are shown forming a nascent cisternae (also marked with AtLNP1-GFP) over a total period of 57.05 seconds. Scale bar 5 µm.

S3 Chapter 5 - Protein movement in the plant ER

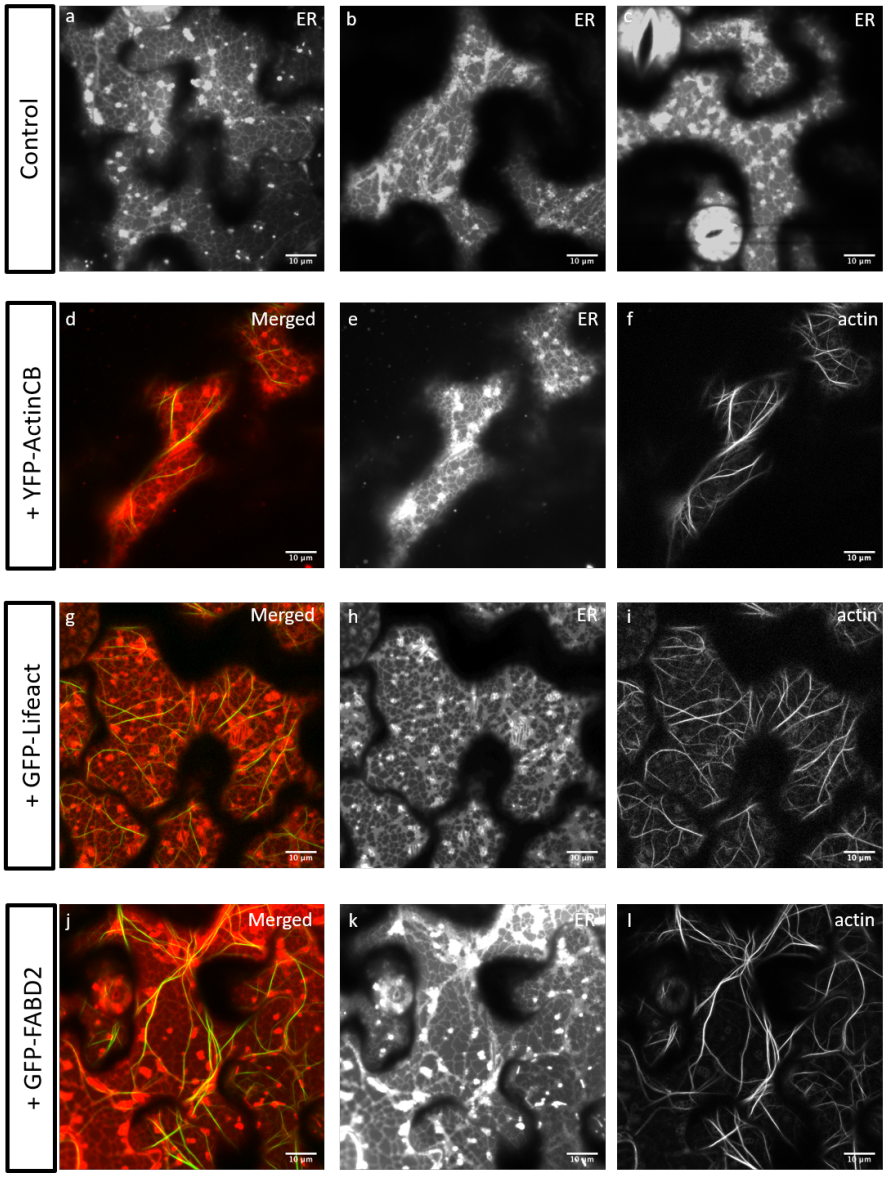


Figure S11: The effect of stable over-expression of actin marker constructs on the ER of arabidosis cotelydon cells (7 days post germination)
Rhoadmine B staining of ER in 7 day old arabidopsis cotelydon cells (a-c) alongside stable over-expression of three actin marker constructs: YFP-actinCB (d-f), GFP-Lifeact (g-i) and GFP-FABD2 (j-l). Scale bars 10 µm.

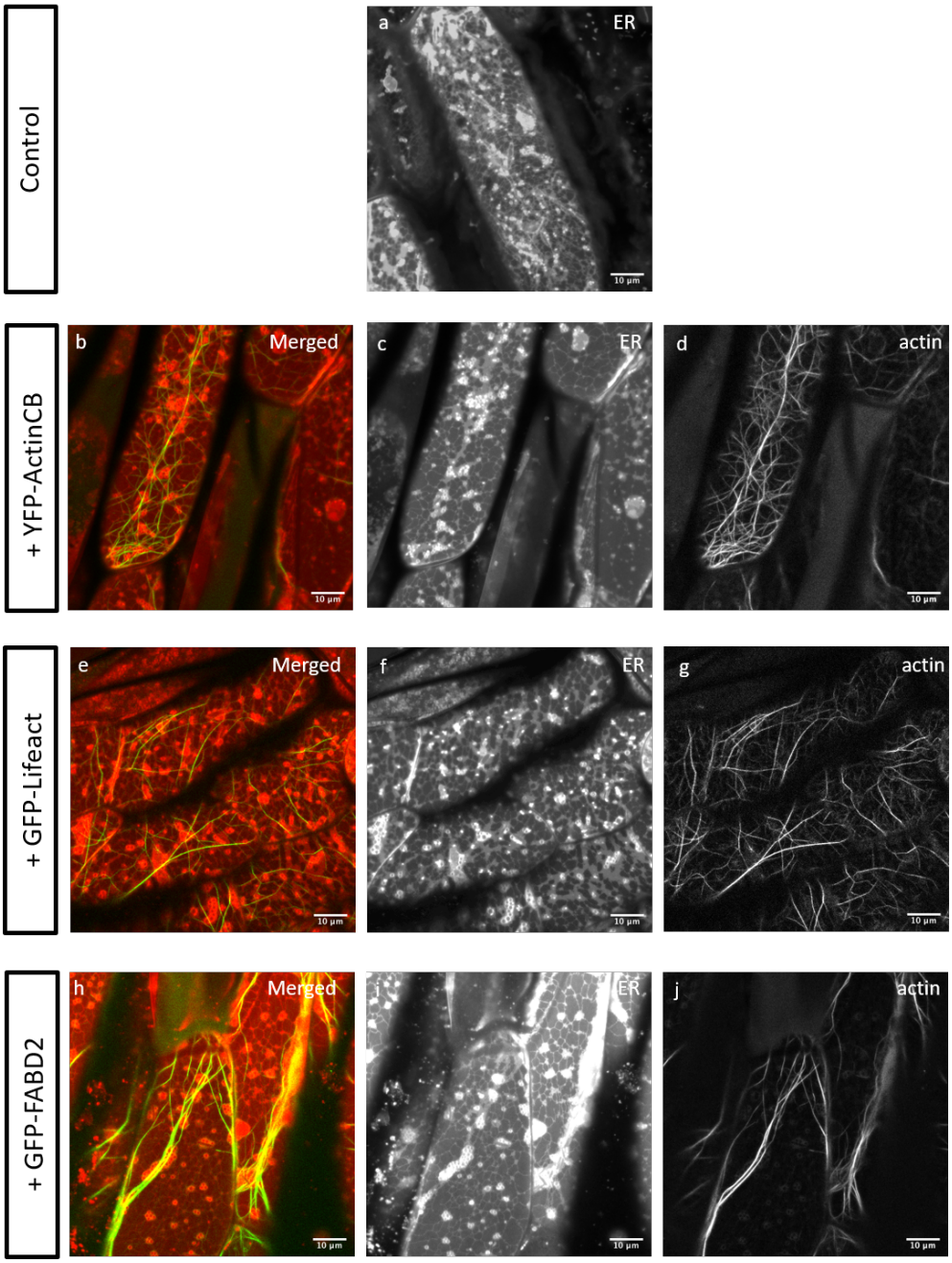


Figure S12: The effect of stable over-expression of actin marker constructs on the ER of arabidosis root cells (7 days post germination) Rhodamine B staining of ER in 7 day old arabidopsis root cells (a) alongside stable over-expression of three actin marker constructs: YFP-actinCB (b-d), GFP-Lifeact (e-g) and GFP-FABD2 (h-j). Scale bars 10 µm.

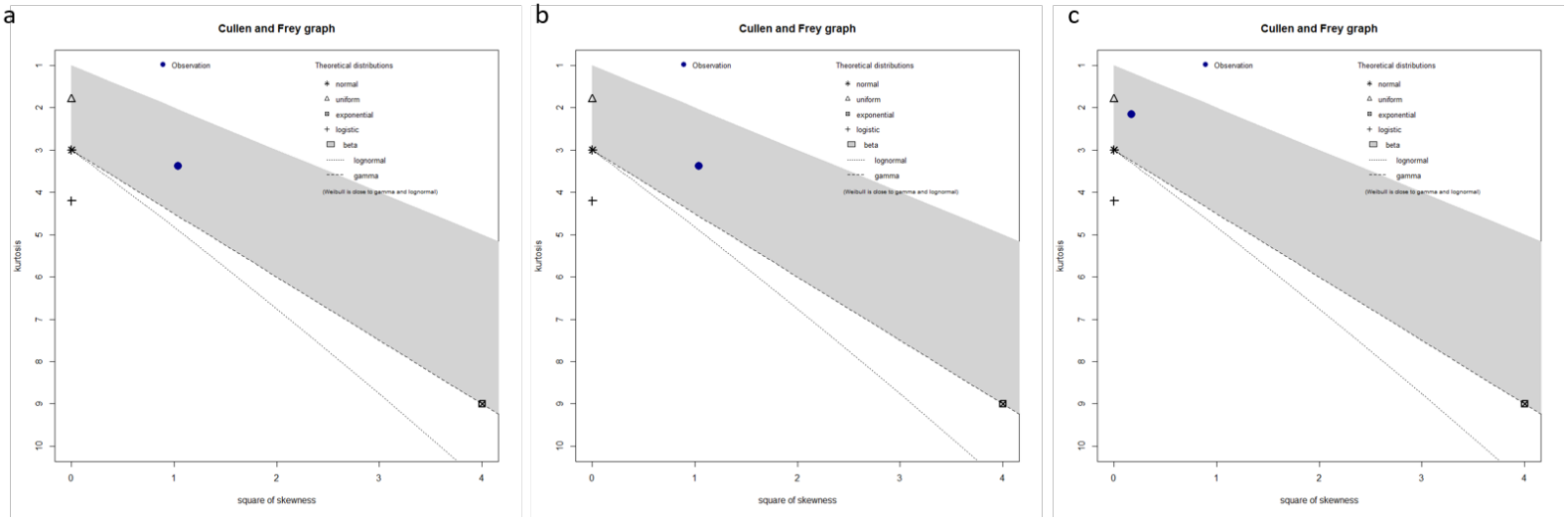


Figure S13: Cullen an Frey graph of likely data distribution types
Three Cullen and Frey graphs used to estimate the distribution type of the track speed data produced by TrackMate of (a) mEOS-TAR2 (b) paGFP-CXN (c) paGFP-CXN and Lat B.

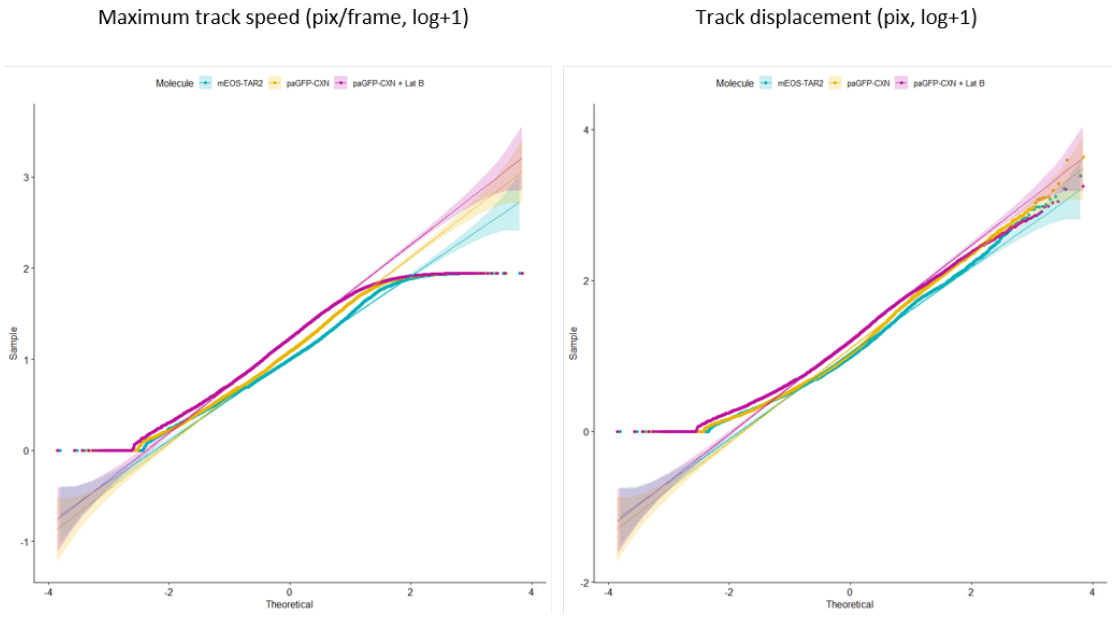


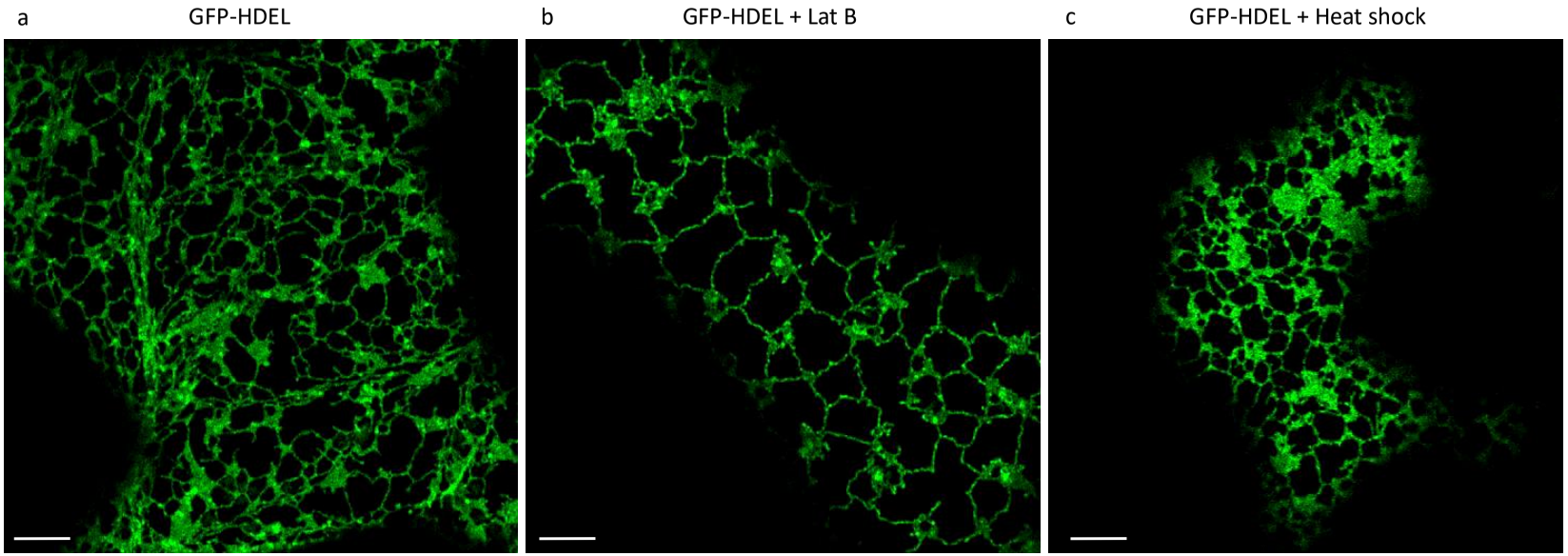
Figure S14: Q-Q plot of maximum track speed and track displacement Q-Q plot (Quantile-Quantile plot) of maximum track speed and track displacement measured using TrackMate. Different line colours represent the three treatment groups (mEOS-TAR2 and paGFP-CXN with/without treatment with Lat B. The shaded area shows the normal confidence limits.

S4 Supplementary movie list

Supplementary Movies

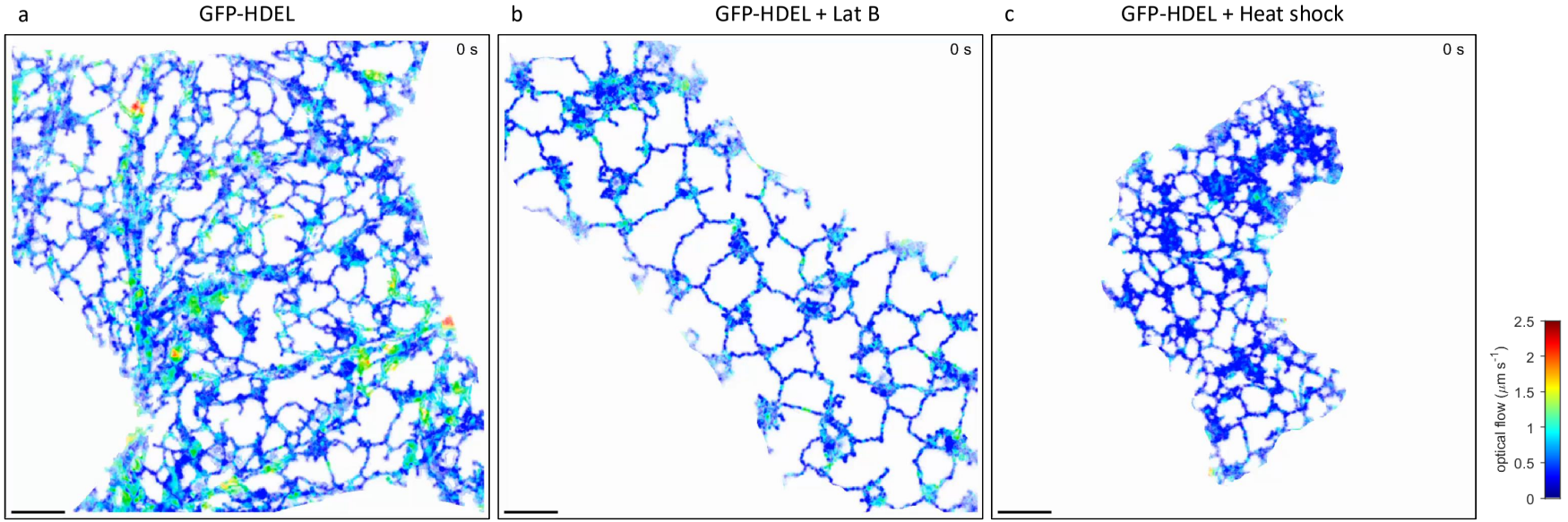
Supplementary movie 3.1:	*The effect of heat shock and Lat B treatment on ER dynamics*
Supplementary movie 3.2:	*Optical flow mapping of ER remodelling after treatment with Lat B and heat shock*
Supplementary movie 3.3:	*Optical flow detection of the direction of ER remodelling after treatment with Lat B and heat shock*
Supplementary movie 3.4:	*Persistency mapping of ER remodelling after treatment with Lat B and heat shock*
Supplementary movie 4.1:	*ER dynamics in 7 day old cotelydons with stable over-expression of P_{UB10}::AtLNP1-GFP or P_{UB10}::AtLNP2-GFP*
Supplementary movie 4.2:	*ER dynamics in 7 day old Arabidopsis stably expressing GFP-HDEL alone and in amiLNP1LNP2*
Supplementary movie 4.3:	*P_{AtLNP1}::AtLNP1-GFP expression in 7 day old lnp1 Arabidopsis cotyledon tissue visualised using VAEM*
Supplementary movie 4.4:	*Dynamics of L1T5-GFP and the Golgi body marker ST-RFP*
Supplementary movie 4.5:	*ER dynamics in tobacco leaf epidermal cells transiently expressing AtLNP1-ZF-GFP and AtLNP2-ZF-GFP*
Supplementary movie 4.6:	*P_{UB10}::AtLNP1-GFP over-expression in 7 day old Arabidopsis tissues, imaged collected using VAEM*
Supplementary movie 4.7:	*Light sheet imaging of the abaxial surface of tobacco leaf epidermal cells transiently expressing P_{UB10}::AtLNP1-GFP and P_{UB10}::AtLNP2-GFP*
Supplementary movie 4.8:	*Light sheet imaging P_{UB10}::AtLNP1-GFP stable expression in Arabidopsis vs transient expression in tobacco*
Supplementary movie 4.9:	*Cisternae formation from multiple P_{UB10}::AtLNP1-GFP aggregates.*
Supplementary movie 5.1:	*VAEM of tobacco leaf epidermal cells transiently expressing paGFP-CXN*
Supplementary movie 5.2:	*Extensive 'bleed through' between channels prohibits single particle tracking with fluorescently tagged ER structure modifying proteins in the background*
Supplementary movie 5.3:	*SPT using TrackMate*

Chapter 3 – Supplementary movie 1



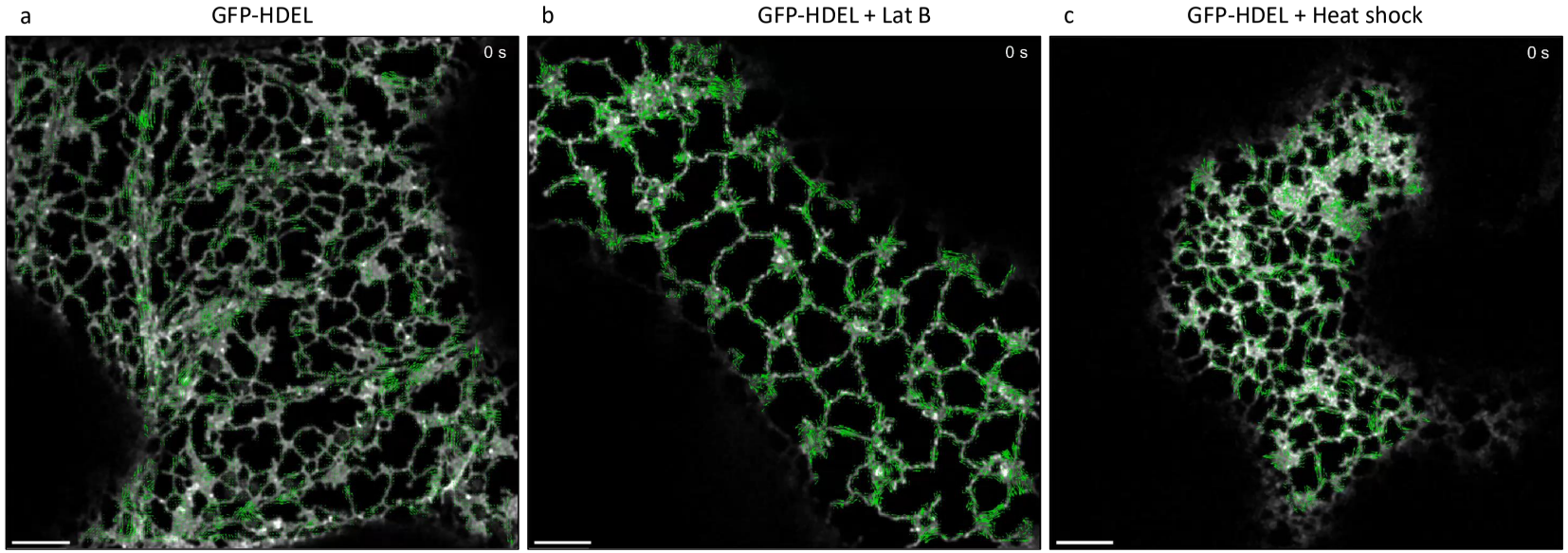
Supplementary movie 3.1: The effect of heat shock and Lat B treatment on ER dynamics
The dynamics of the ER in tobacco leaf epidermal cells transiently expressing GFP-HDEL (a) after treatment with Lat B (b) or heat shock (c). Images collected with confocal microscopy, scale bars 5µm, time series length 20.15 seconds.

Chapter 3 – Supplementary movie 2



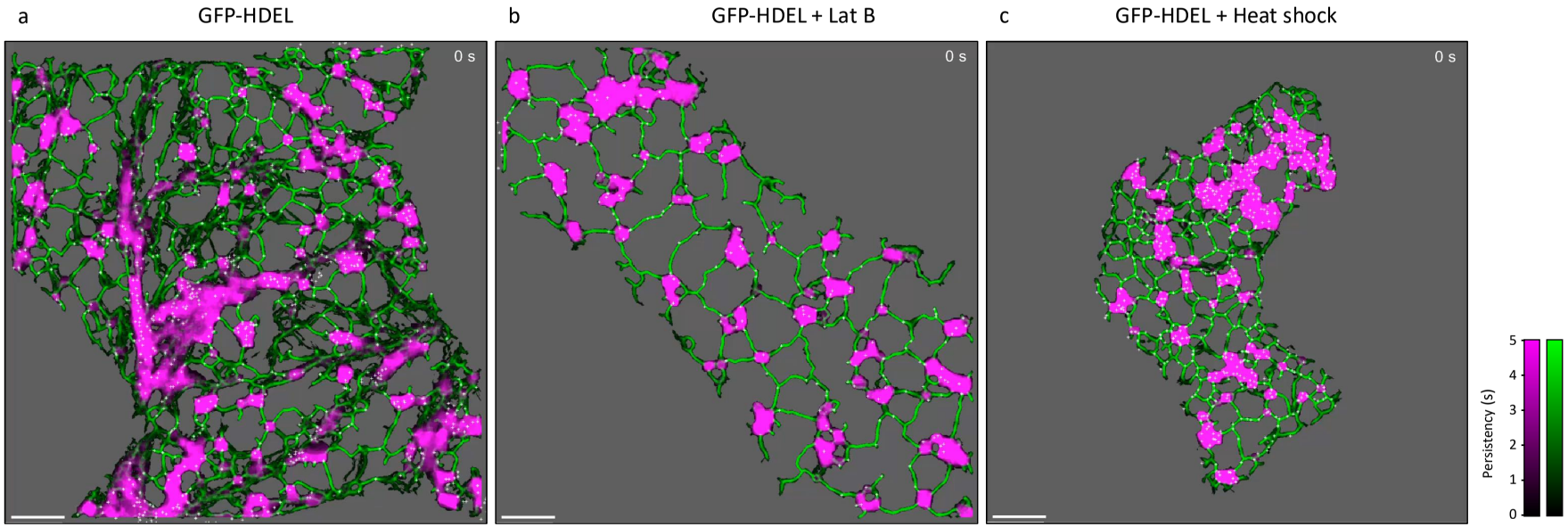
Supplementary movie 3.2: Optical flow mapping of ER remodelling after treatment with Lat B and heat shock
Optical flow mapping of ER remodelling using the Farnebäck method, performed on a 50 frame timeseries of tobacco leaf epidermal cells transiently expressing GFP-HDEL (a) and after treatment with Lat B (b) or heat shock (c). Psuedocoloured overlay of detected ER movement is scaled between 0-2.5 μm s^{-1}, images collected using confocal microscopy, scale bars 5μm, time series length 20.15 seconds.

Chapter 3 – Supplementary movie 3



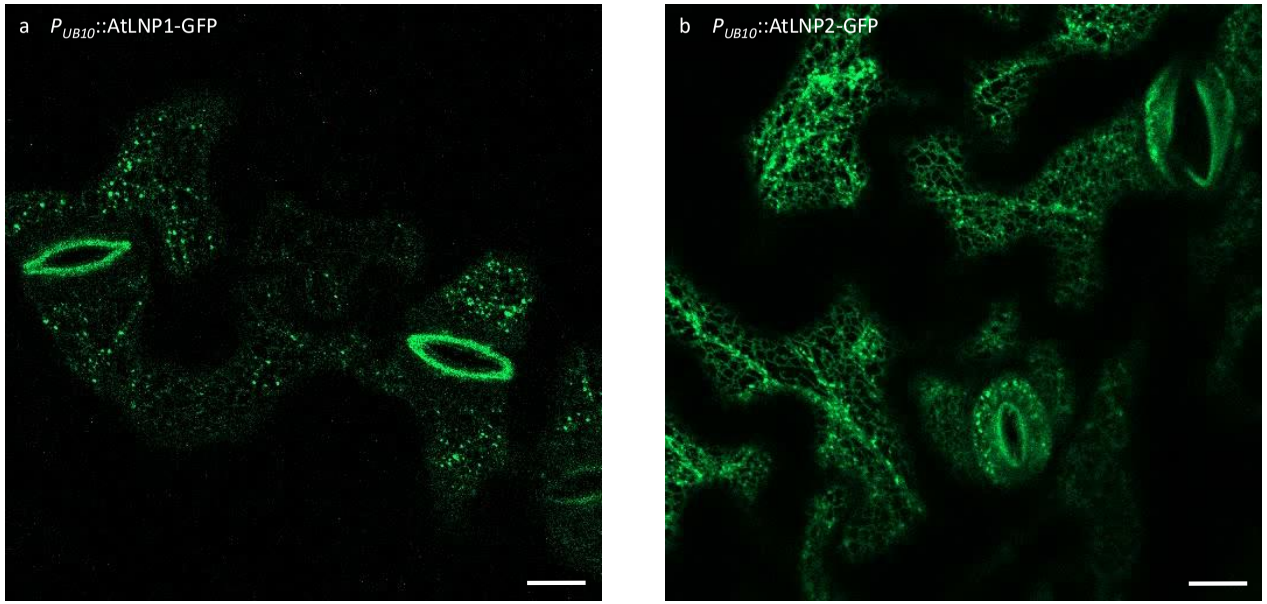
Supplementary movie 3.3: Optical flow detection of the direction of ER remodelling after treatment with Lat B and heat shock
Vector overlay of the speed and direction of ER remodelling performed on 50 frame timeseries of tobacco leaf epidermal cells transiently expressing GFP-HDEL (a) and after treatment with Lat B (b) or heat shock (c). Arrow overlay of detected ER movement is scaled between 0-2.5 µm s^{-1}, images collected using confocal microscopy, scale bars 5µm, time series length 20.15 seconds.

Chapter 3 – Supplementary movie 4



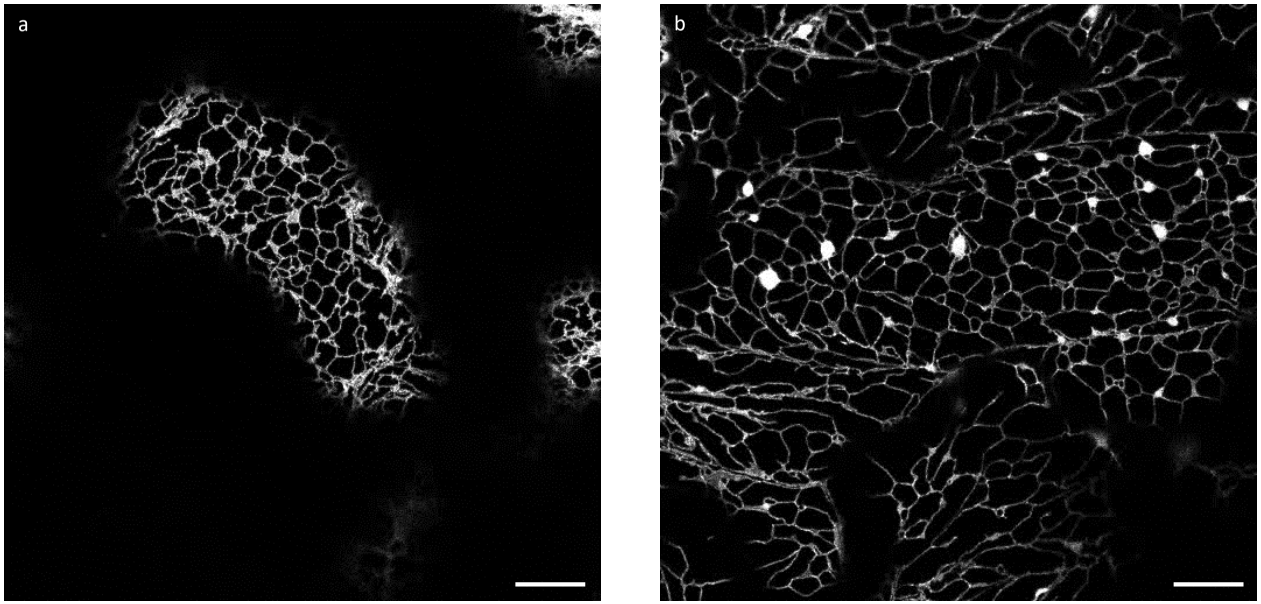
Supplementary movie 3.4: Persistency mapping of ER remodelling after treatment with Lat B and heat shock
Persistency mapping calculated for a 12 frame lag period (approximately 5 seconds) performed on 50 frame timeseries of tobacco leaf epidermal cells transiently expressing GFP-HDEL (a) and after treatment with Lat B (b) or heat shock (c). Cisternae persistency is shown in magenta and tubule persistency in green. Images collected using confocal microscopy, scale bars 5µm, time series length 20.15 seconds.

Chapter 4 – Supplementary movie 1



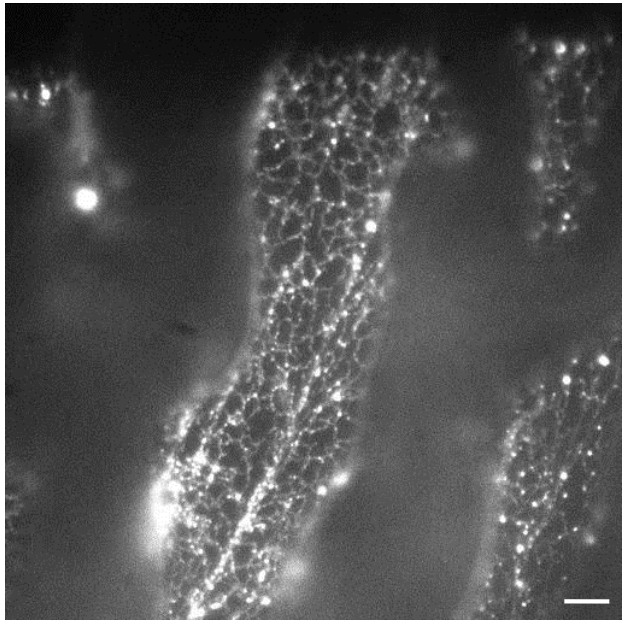
Supplementary movie 4.1: ER dynamics in 7 day old cotelydons with stable over-expression of P_{UB10}::AtLNP1-GFP or P_{UB10}::AtLNP2-GFP
A timeseries of 7 day old Arabidopsis cotelydons stably over-expressing of P_{UB10}::AtLNP1-GFP (a) and P_{UB10}::AtLNP2-GFP (b). Images collected with confocal microscopy, scale bars 10µm, time series length 12.07 seconds.

Chapter 4 – Supplementary movie 2



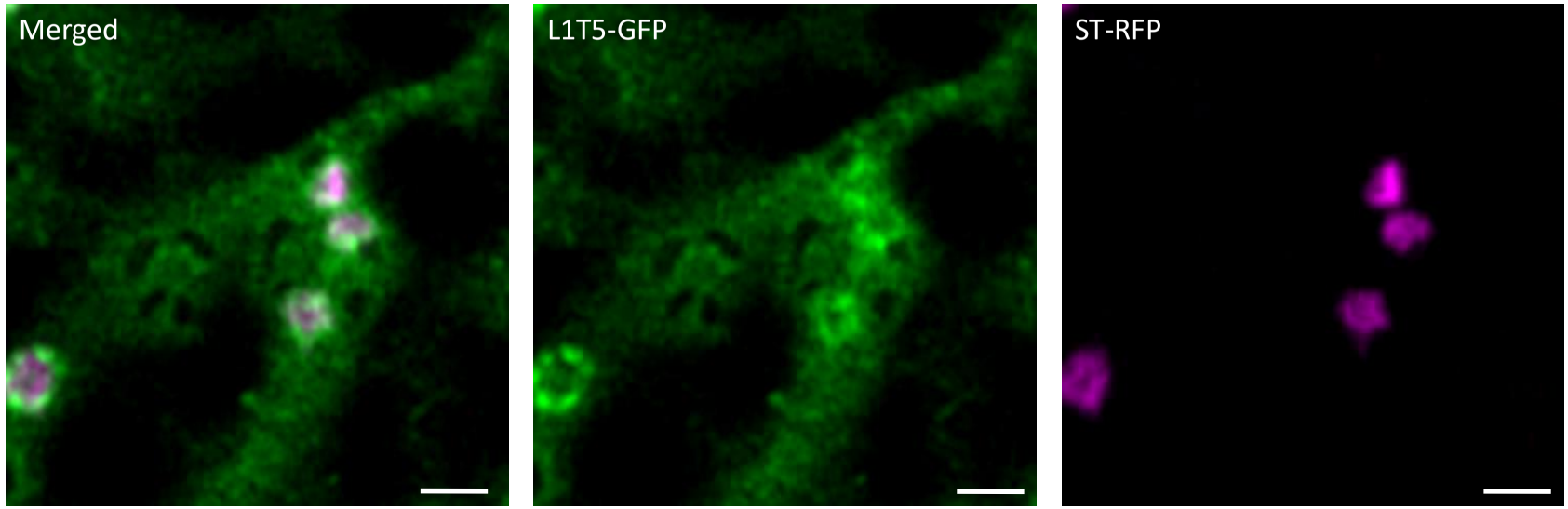
Supplementary movie 4.2: ER dynamics in 7 day old Arabidopsis stably expressing GFP-HDEL alone and in amiLNP1LNP2
Stable expression of GFP-HDEL alone (a) or in the amiLNP1LNP2 background. Time series was collected with confocal microscopy, scale bars 10µm, time series length 64 seconds.

Chapter 4 – Supplementary movie 3



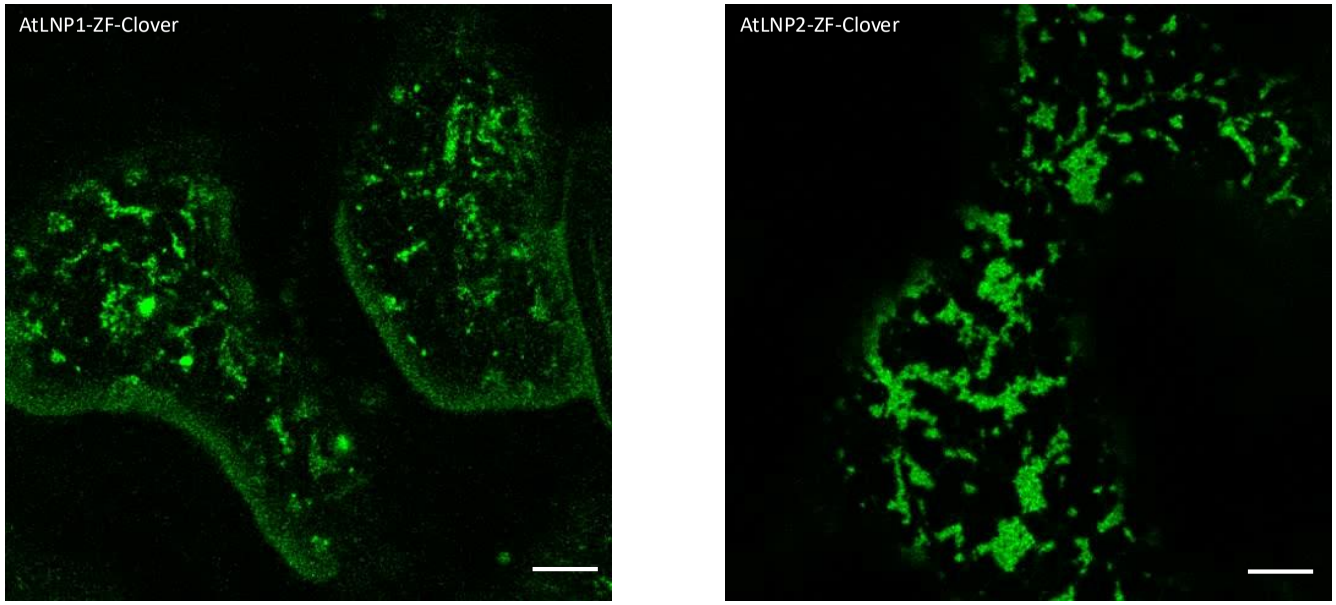
Supplementary movie 4.3: P_{AtLNP1}::AtLNP1-GFP expression in 7 day old lnp1 Arabidopsis cotyledon tissue visualised using VAEM
P_{AtLNP1}::AtLNP1-GFP expression in 7 day old lnp1 arabidopsis cotyledon tissue visualised using VAEM. Scale bars 5 µm, time series length 7.5 seconds.

Chapter 4 – Supplementary movie 4



Supplementary movie 4.4: Dynamics of L1T5-GFP and the Golgi body marker ST-RFP
Time series showing the dynamics of L1T5-GFP and the Golgi body marker ST-RFP. Time series are shown as a merged movie and subsequently the two channels are shown separately. Scale bars 1µm, time series length 32.38 seconds.

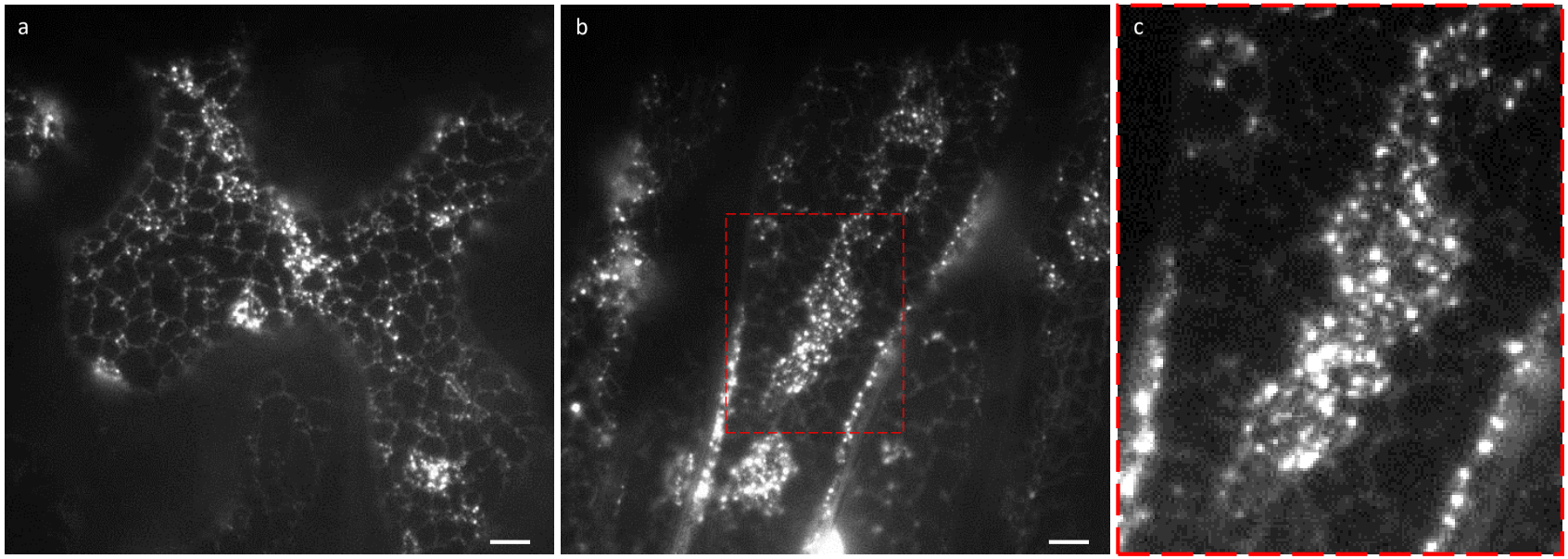
Chapter 4 – Supplementary movie 5



Supplementary movie 4.5: ER dynamics in tobacco leaf epidermal cells transiently expressing AtLNP1-ZF-GFP and AtLNP2-ZF-GFP
The movement of cisternae marked by AtLNP1-ZF-Clover and AtLNP1-ZF-Clover transiently expressed in tobacco leaf epidermal cells. Scale bars 5µm, time series length 15.18 seconds.

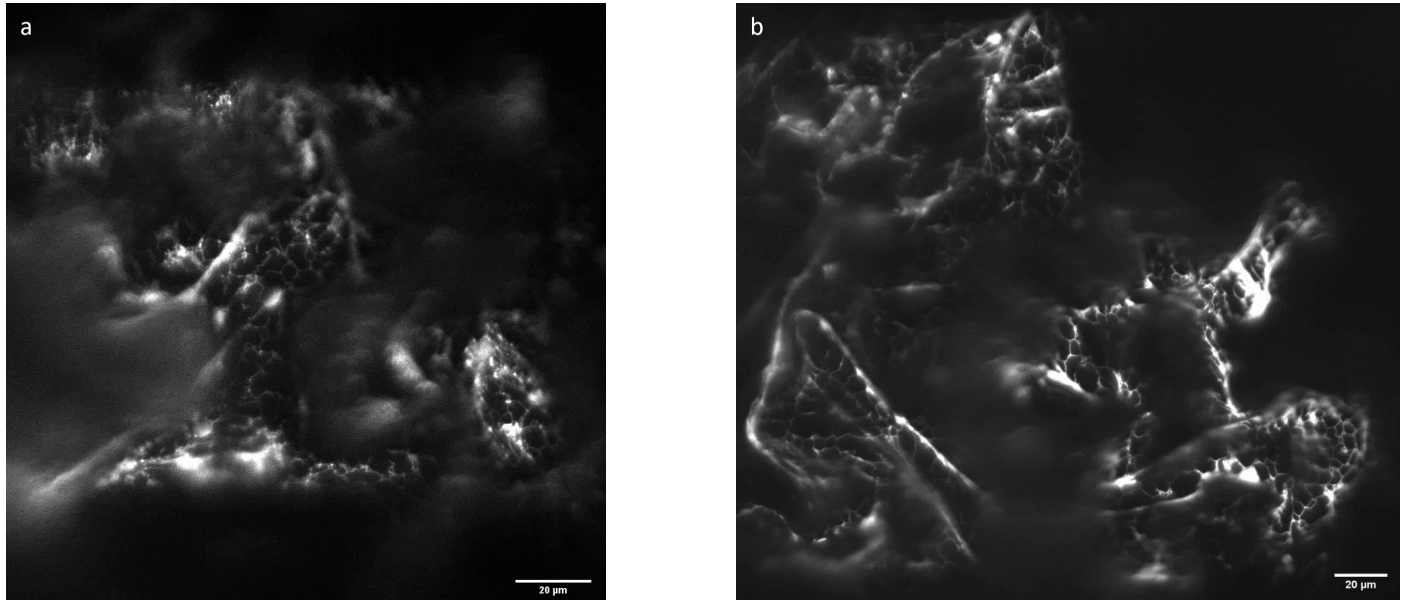
15.18s

Chapter 4 – Supplementary movie 6



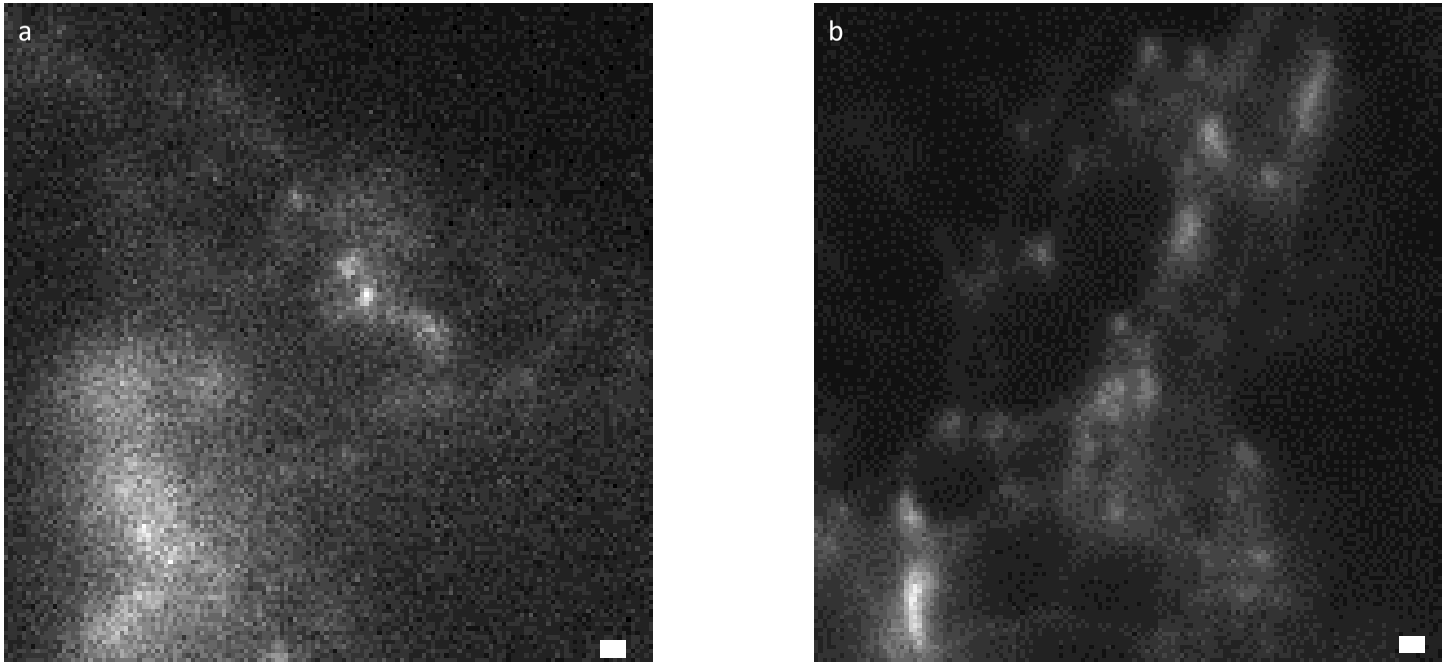
Supplementary movie 4.6: P_{UB10}::AtLNP1-GFP over-expression in 7 day old Arabidopsis tissues, imaged collected using VAEM
P_{UB10}::AtLNP1-GFP over-expression in 7 day old Arabidopsis cotelydons (a) and roots (b) images collected using VAEM. (c) An enlarged image of a single, representative cisternae in imaged arabdiposis root tissue (selected region highlighted by the red dotted line on movie b). Scale bars 5 µm, time series length 15 seconds.

Chapter 4 – Supplementary movie 7



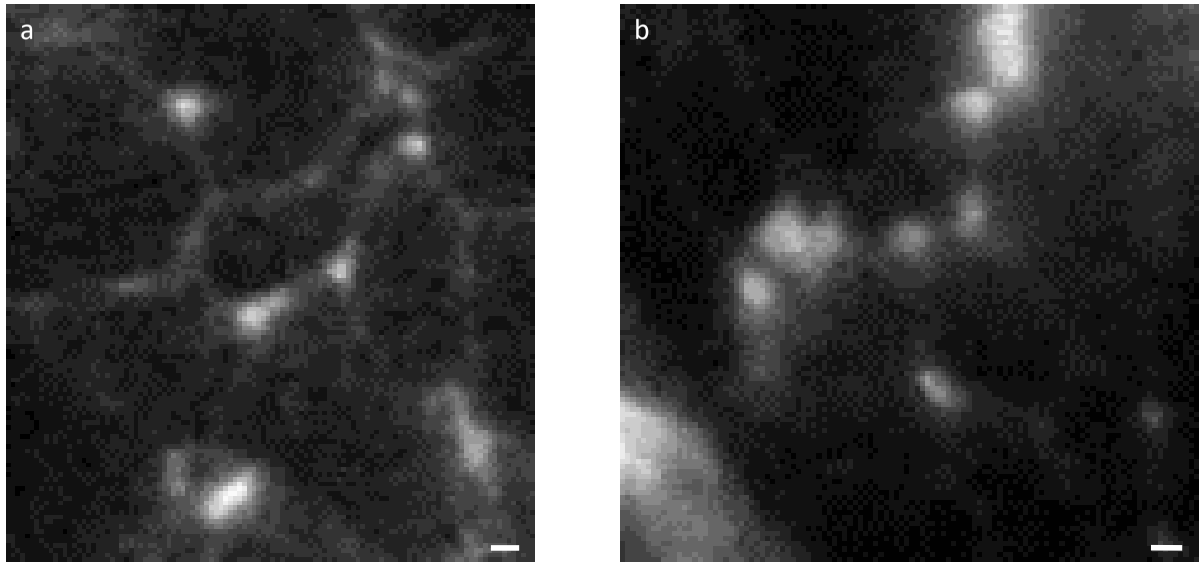
Supplementary movie 4.7: Light sheet imaging of the abaxial surface of tobacco leaf epidermal cells transiently expressing P_{UB10}::AtLNP1-GFP and P_{UB10}::AtLNP2-GFP
Light sheet imaging of the abaxial surface of tobacco leaf epidermal cells transiently expressing P_{UB10}::AtLNP1-GFP (a) and P_{UB10}::AtLNP2-GFP (b). Scale bars 20 µm, time series length 105 seconds.

Chapter 4 – Supplementary movie 8



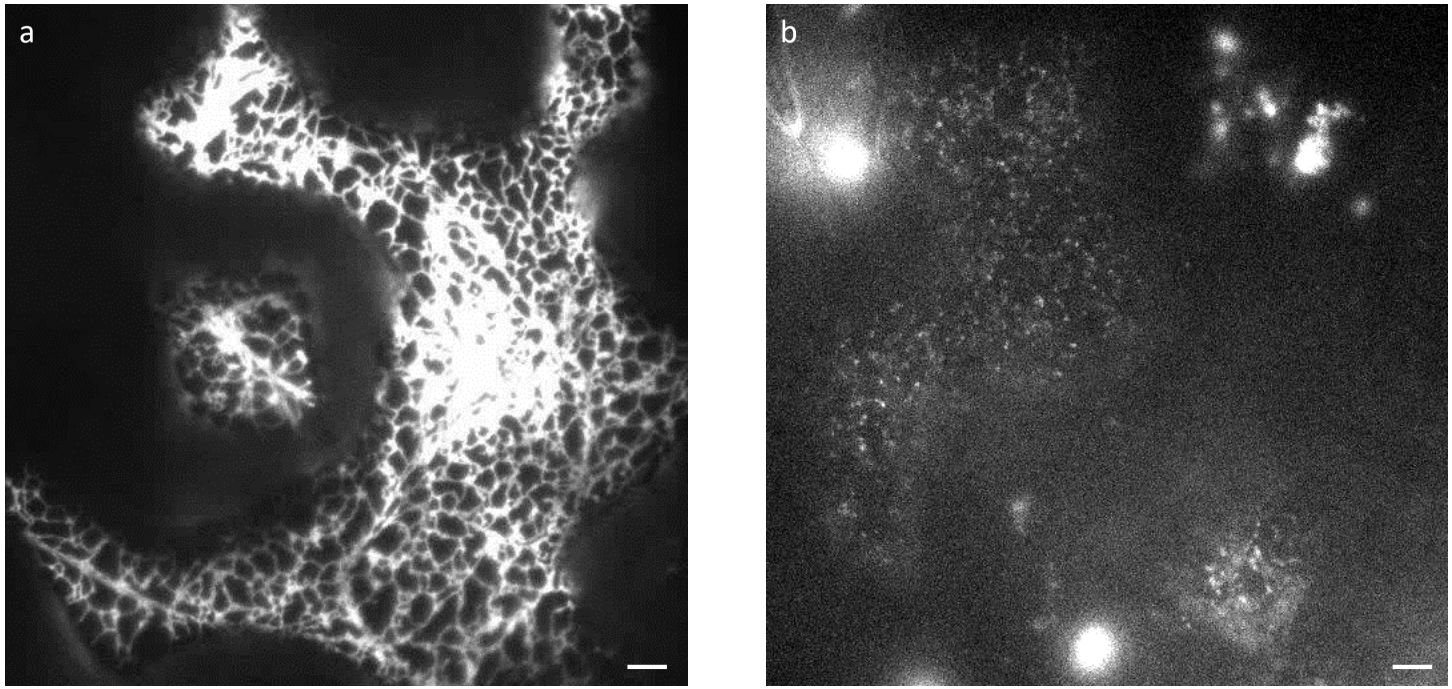
Supplementary movie 4.8: Light sheet imaging P_{UB10}::AtLNP1-GFP stable expression in Arabidopsis vs transient expression in tobacco
Light sheet imaging of the abaxial surface of 7 day old Arabidopsis cotelydon cells stably expressing P_{UB10}::AtLNP1-GFP (a) and transient expression of P_{UB10}::AtLNP1-GFP in mature tobacco leaf epidermal cells (b). Scale bars 1 µm, time series length 29.4 seconds.

Chapter 4 – Supplementary movie 9



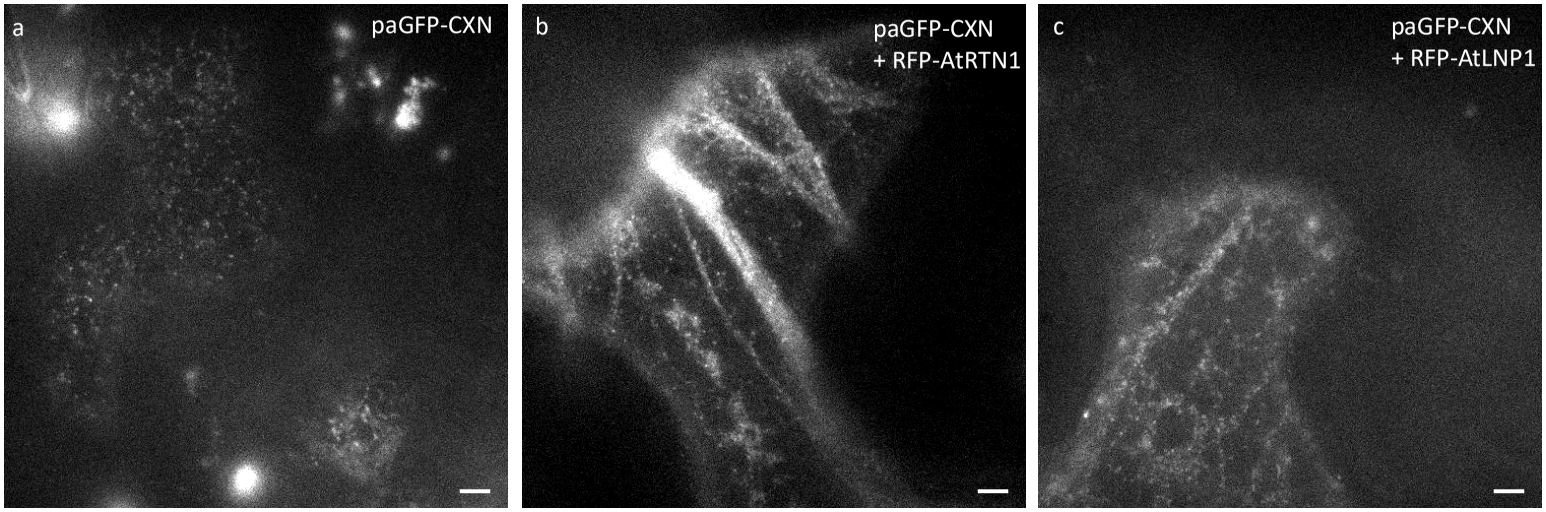
Supplementary movie 4.9: Cisternae formation from multiple P_{UB10}::AtLNP1-GFP aggregates
Light sheet imaging of the abaxial surface of tobacco leaf epidermal cells transiently expressing P_{UB10}::AtLNP1-GFP , revealing cisternae formation by aggregation of P_{UB10}::AtLNP1-GFP (a,b). Time series have been despeckled for clarity, scale bars 1 µm, time series length (a) 86.73 seconds and (b) 35.07 seconds.

Chapter 5 – Supplementary movie 1



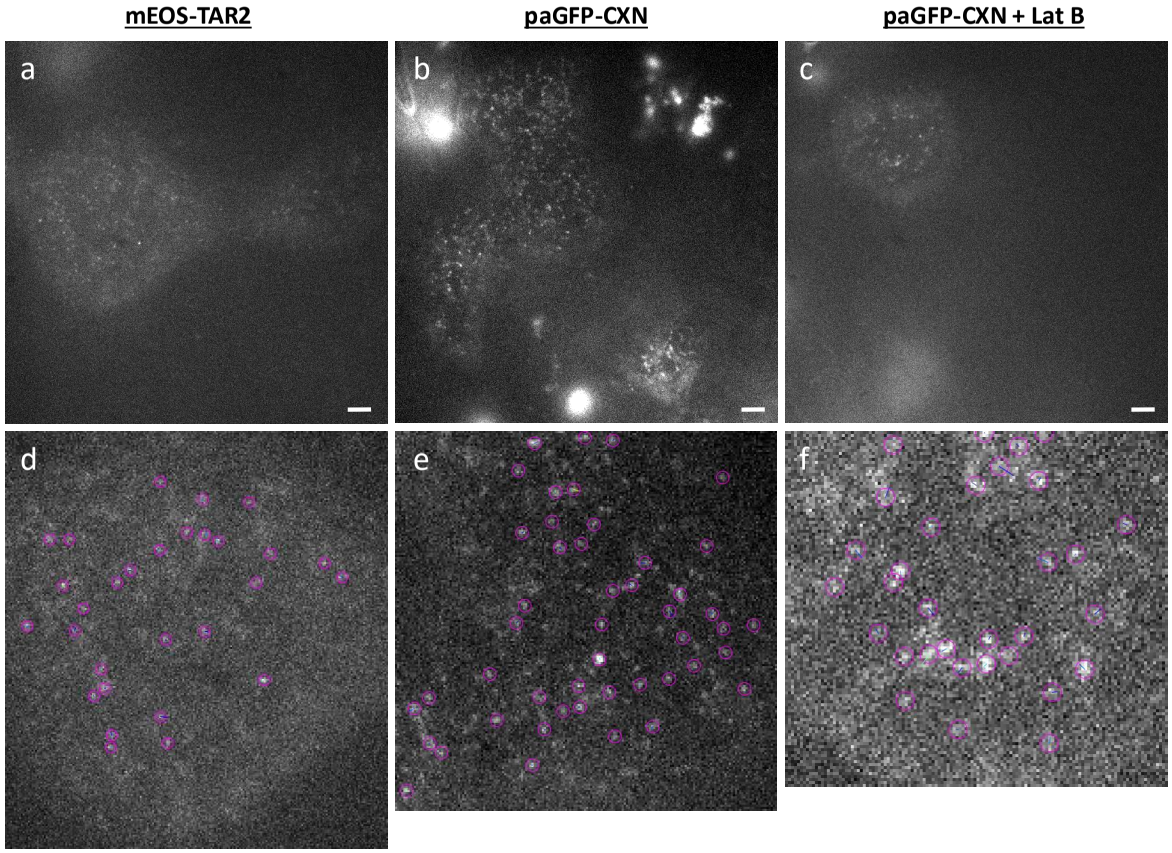
Supplementary movie 5.1: VAEM of tobacco leaf epidermal cells transiently expressing paGFP-CXN
Transient over-expression of the ER membrane maker paGFP-CXN in tobacco leaf epidermal cells visualised using VAEM. (a) Demonstrates a cell where expression of paGFP-CXN is too high, obscuring details at the single particle level, whilst (b) shows an level of expression whereby single particles can be visualised. Scale bars 5µm, time series length 12 seconds.

Chapter 5 – Supplementary movie 2



Supplementary movie 5.2: Extensive 'bleed through' between channels prohibits single particle tracking with fluorescently tagged ER structure modifying proteins in the background
Representative timseries of transient over-expression of paGFP-CXN alone (a) and alongside RFP-AtRTN1 (b) and RFP-AtLNP1 (c) in tobacco leaf epidermal cells. Only the green channel is shown, but specteral bleedthrough can be seen on co-over-expression with RFP-AtRTN1 and RFP-AtLNP1. Scale bars 5µm, time series length 12 seconds.

Chapter 5 – Supplementary movie 3



Supplementary movie 5.3: SPT using TrackMate Representative timseries of transient over-expression of mEOS-TAR2 (a) and paGFP-CXN alone (b) and after treatment with Lat B (c) in tobacco leaf epidermal cells. The output of SPT produced by TrackMate are shown below the original timeseries (d-f). Identified particles are circled in magenta, whilst tracks are coloured by start time. Scale bars 5µm, time series length 12 seconds.

References

Agati, G. (1998) Response of the in vivo chlorophyll fluorescence spectrum to environmental factors and laser excitation wavelength. *Pure and Applied Optics: Journal of the European Optical Society Part A*, **7**(4):797–807.

Andersland, J.M. and Parthasarathy, M.V. (1993) Conditions affecting depolymerization of actin in plant homogenates. *Journal of Cell Science*, **104**:1273–1279.

Anwar, K., Klemm, R.W., Condon, A., Severin, K.N., Zhang, M., Ghirlando, R., Hu, J., Rapoport, T.A., and Prinz, W.A. (2012) The dynamin-like GTPase Sey1p mediates homotypic ER fusion in S. cerevisiae. *The Journal of Cell Biology*, **197**(2):209–217.

Avisar, D., Abu-Abied, M., Belausov, E., and Sadot, E. (2012) Myosin XIK is a major player in cytoplasm dynamics and is regulated by two amino acids in its tail. *Journal of Experimental Botany*, **63**(1):241–249.

Avisar, D., Abu-Abied, M., Belausov, E., Sadot, E., Hawes, C., and Sparkes, I.A. (2009) A comparative study of the involvement of 17 Arabidopsis myosin family members on the motility of Golgi and other organelles. *Plant Physiology*, **150**(2):700–709.

Avisar, D., Prokhnevsky, A.I., Makarova, K.S., Koonin, E.V., and Dolja, V.V. (2008) Myosin XI-K Is required for rapid trafficking of Golgi stacks, peroxisomes, and mitochondria in leaf cells of Nicotiana benthamiana. *Plant Physiology*, **146**(3):1098–1108.

Batoko, H., Zheng, H.Q., Hawes, C., and Moore, I. (2000) A rab1 GTPase is

required for transport between the endoplasmic reticulum and golgi apparatus and for normal golgi movement in plants. *The Plant Cell*, **12**(11):2201–18.

Bayle, V., Platre, M.P., and Jaillais, Y. (2017) Automatic quantification of the number of intracellular compartments in Arabidopsis thaliana root cells. *Bio-protocol*, **7**(4):1–12.

Bergeron, J.J., Brenner, M.B., Thomas, D.Y., and Williams, D.B. (1994) Calnexin: a membrane-bound chaperone of the endoplasmic reticulum. *Trends in Biochemical Sciences*, **19**(3):124–128.

Bernales, S., McDonald, K.L., and Walter, P. (2006) Autophagy counterbalances endoplasmic reticulum expansion during the unfolded protein response. *PLoS Biology*, **4**(12):2311–2324.

Bian, X., Klemm, R.W., Liu, T.Y., Zhang, M., Sun, S., Sui, X., Liu, X., Rapoport, T.A., and Hu, J. (2011) Structures of the atlastin GTPase provide insight into homotypic fusion of endoplasmic reticulum membranes. *Proceedings of the National Academy of Sciences of the United States of America*, **108**(10):3976–3981.

Blobel, G. (1980) Intracellular protein topogenesis. *Proceedings of the National Academy of Sciences of the United States of America*, **77**(3):1496–1500.

Boevink, P., Cruz, S., Hawes, C., Harris, N., and Oparka, K. (1996) Virus-mediated delivery of the green fluorescent protein to the endoplasmic reticulum of plant cells. *The Plant Journal*, **10**(5):935–941.

Boevink, P., Martin, B., Oparka, K., Santa Cruz, S., and Hawes, C. (1999) Transport of virally expressed green fluorescent protein through the secretory pathway in tobacco leaves is inhibited by cold shock and brefeldin A. *Planta*, **208**(3):392–400.

Bonifacino, J.S. and Weissman, A.M. (1998) Ubiquitin and the control of protein fate in the secretory and endocytic pathways. *Annual Review of Cell and Developmental Biology*, **14**(1):19–57.

Bonza, M.C., Loro, G., Behera, S., Wong, A., Kudla, J., and Costa, A. (2013) Analyses of Ca2+ accumulation and dynamics in the endoplasmic reticulum of arabidopsis root cells using a genetically encoded cameleon sensor. *Plant Physiology*, **163**(3):1230–1241.

Borghi, L. (2010) Inducible gene expression systems for plants. In L. Köhler and C. Hennig, editors, *Plant Developmental Biology*, pages 65–75.

Bouchekhima, A.N., Frigerio, L., and Kirkilionis, M. (2009) Geometric quantification of the plant endoplasmic reticulum. *Journal of Microscopy*, **234**(2):158–172.

Braakman, I. and Hebert, D.N. (2013) Protein folding in the endoplasmic reticulum. *Cold Spring Harbor Perspectives in Biology*, **5**(5):1–17.

Brach, T., Soyk, S., Müller, C., Hinz, G., Hell, R., Brandizzi, F., and Meyer, A.J. (2009) Non-invasive topology analysis of membrane proteins in the secretory pathway. *The Plant Journal*, **57**(3):534–541.

Brandizzi, F., Hanton, S., DaSilva, L.L.P., Boevink, P., Evans, D., Oparka, K., Denecke, J., and Hawes, C. (2003) ER quality control can lead to retrograde transport from the ER lumen to the cytosol and the nucleoplasm in plants. *The Plant Journal*, **34**(3):269–281.

Breeze, E., Dzimitrowicz, N., Kriechbaumer, V., Brooks, R., Botchway, S.W., Brady, J.P., Hawes, C., Dixon, A.M., Schnell, J.R., Fricker, M.D., and Frigerio, L. (2016) A C-terminal amphipathic helix is necessary for the in vivo tubule-shaping

function of a plant reticulon. *Proceedings of the National Academy of Sciences*, **113**(39):10,902–10,907.

Breuss, M.W., Nguyen, A., Song, Q., Nguyen, T., Stanley, V., James, K.N., Musaev, D., Chai, G., Wirth, S.A., Anzenberg, P., George, R.D., Johansen, A., Ali, S., Zia-Ur-Rehman, M., Sultan, T., Zaki, M.S., and Gleeson, J.G. (2018) Mutations in LNPK, encoding the endoplasmic reticulum junction stabilizer lunapark, cause a recessive neurodevelopmental syndrome. *American Journal of Human Genetics*, **103**(2):296–304.

Bubb, M.R., Senderowicz, A.M., Sausville, E., Duncan, K.L., and Korn, E.D. (1994) Jasplakinolide, a cytotoxic natural product, induces actin polymerization and competitively inhibits the binding of phalloidin to F-actin. *The Journal of Biological Chemistry*, **269**(21):14,869–14,871.

Burnecki, K., Sikora, G., Weron, A., Tamkun, M.M., and Krapf, D. (2019) Identifying diffusive motions in single-particle trajectories on the plasma membrane via fractional time-series models. *Physical Review E*, **99**(1):1–10.

Bush, D.S. (1995) Calcium regulation in plant cells and its role in signalling. *Annual Review of Plant Physiology and Plant Molecular Biology*, **46**:95–122.

Byrnes, L.J. and Sondermann, H. (2011) Structural basis for the nucleotide-dependent dimerization of the large G protein atlastin-1/SPG3A. *Proceedings of the National Academy of Sciences of the United States of America*, **108**(6):2216–2221.

Cao, P., Renna, L., Stefano, G., and Brandizzi, F. (2016) SYP73 anchors the ER to the actin cytoskeleton for maintenance of ER integrity and streaming in Arabidopsis. *Current Biology*, **26**(23):3245–3254.

Cao, X., Jin, X., Zhang, X., Li, Y., Wang, C., Wang, X., Hong, J., Wang,

X., Li, D., and Zhang, Y. (2015) Morphogenesis of endoplasmic reticulum membrane-invaginated vesicles during beet black scorch virus infection: role of auxiliary replication protein and new implications of three-dimensional architecture. *Journal of Virology*, **89**(12):6184–6195.

Casey, A.K., Chen, S., Novick, P., Ferro-Novick, S., and Wente, S.R. (2015) Nuclear pore complex integrity requires Lnp1, a regulator of cortical endoplasmic reticulum. *Molecular Biology of the Cell*, **26**(15):2833–2844.

Chen, J., Stefano, G., Brandizzi, F., and Zheng, H. (2011) Arabidopsis RHD3 mediates the generation of the tubular ER network and is required for Golgi distribution and motility in plant cells. *Journal of Cell Science*, **124**(13):2241–2252.

Chen, S., Desai, T., McNew, J.A., Gerard, P., Novick, P.J., and Ferro-Novick, S. (2015) Lunapark stabilizes nascent three-way junctions in the endoplasmic reticulum. *Proceedings of the National Academy of Sciences of the United States of America*, **112**(2):418–23.

Chen, S., Novick, P., and Ferro-Novick, S. (2012) ER network formation requires a balance of the dynamin-like GTPase Sey1p and the Lunapark family member Lnp1p. *Nature Cell Biology*, **14**(7):707–716.

Chen, T., Ji, D., and Tian, S. (2018) Variable-angle epifluorescence microscopy characterizes protein dynamics in the vicinity of plasma membrane in plant cells. *BMC Plant Biology*, **18**(43):1–17.

Chen, Y.F., Randlett, M.D., Findell, J.L., and Schaller, G.E. (2002) Localization of the ethylene receptor ETR1 to the endoplasmic reticulum of arabidopsis. *Journal of Biological Chemistry*, **277**(22):19,861–19,866.

Chikako, K., Arakawa, K., and Yoshida, S. (1999) Abscisic acid-induced secretory

proteins in suspension-cultured cells of winter wheat. *Plant Cell Physiology*, **40**(2):184–191.

Clough, S.J. and Bent, A.F. (1998) Floral dip: a simplified method for Agrobacterium-mediated transformation of Arabidopsis thaliana. *The Plant Journal*, **16**(6):735–743.

Coluccio, L.M. and Tilney, L.G. (1984) Phalloidin enhances actin assembly by preventing monomer dissociation. *The Journal of Cell Biology*, **99**(2):529–535.

Contento, A.L., Xiong, Y., and Bassham, D.C. (2005) Visualization of autophagy in Arabidopsis using the fluorescent dye monodansylcadaverine and a GFP-AtATG8e fusion protein. *The Plant Journal*, **42**(4):598–608.

Cox, J.S., Shamu, C.E., and Walter, P. (1993) Transcriptional induction of genes encoding endoplasmic reticulum resident proteins requires a transmembrane protein kinase. *Cell*, **73**(6):1197–1206.

Craddock, C.P., Adams, N., Bryant, F.M., Kurup, S., and Eastmond, P.J. (2015) Regulation of endomembrane biogenesis in arabidopsis by phospatidic acid hydrolase. *Plant Signaling & Behavior*, **10**(10):1–4.

Davis, A.M., Hall, A., Millar, A.J., Darrah, C., and Davis, S.J. (2009) Protocol: Streamlined sub-protocols for floral-dip transformation and selection of transformants in Arabidopsis thaliana. *Plant Methods*, **5**(1):1–7.

Deeks, M.J., Calcutt, J.R., Ingle, E.K.S., Hawkins, T.J., Chapman, S., Richardson, A.C., Mentlak, D.A., Dixon, M.R., Cartwright, F., Smertenko, A.P., Oparka, K., and Hussey, P.J. (2012) A superfamily of actin-binding proteins at the actin-membrane nexus of higher plants. *Current Biology*, **22**(17):1595–1600.

Deeks, M.J., Rodrigues, C., Dimmock, S., Ketelaar, T., Maciver, S.K., Malhó,

R., and Hussey, P.J. (2007) Arabidopsis CAP1 âĂŞ a key regulator of actin organisation and development. *Journal of Cell Science*, **107**(6):1671–1678.

Denecke, J., De Rycke, R., and Botterman, J. (1992) Plant and mammalian sorting signals for protein retention in the endoplasmic reticulum contain a conserved epitope. *The EMBO Journal*, **11**(6):2345–2355.

Deshaies, R.J., Sanders, S.L., Feldheim, D.A., and Schekman, R. (1991) Assembly of yeast Sec proteins involved in translocation into the endoplasmic reticulum into a membrane-bound multisubunit complex. *Nature*, **349**(6312):806–808.

D'Este, E., Kamin, D., Göttfert, F., El-Hady, A., and Hell, S.W. (2015) STED nanoscopy reveals the ubiquity of subcortical cytoskeleton periodicity in living neurons. *Cell Reports*, **10**(8):1246–1251.

Driouich, A., Faye, L., and Staehelin, L.A. (1993) The plant Golgi apparatus: a factory for complex polysaccharides and glycoproteins. *Trends in Biochemical Sciences*, **18**(6):210–214.

Driouich, A. and Staehelin, L.A. (1997) The plant Golgi apparatus: Structural organization and functional properties. In *The Golgi Apparatus*, pages 275–301. Birkhäuser Basel, Basel.

Eastmond, P.J., Quettier, A.L., Kroon, J.T., Craddock, C., Adams, N., and Slabas, A.R. (2011) A phosphatidate phosphatase double mutant provides a new insight into plant membrane lipid homeostasis. *Plant Signaling & Behavior*, **6**(4):526–527.

Eastmond, P.J., Quettier, A.L., Kroon, J.T.M., Craddock, C., Adams, N., and Slabas, A.R. (2010) PHOSPHATIDIC ACID PHOSPHOHYDROLASE1 and 2 regulate phospholipid synthesis at the endoplasmic reticulum in arabidopsis. *The Plant Cell*, **22**(8):2796–2811.

Eichmann, R. and Schäfer, P. (2012) The endoplasmic reticulum in plant immunity and cell death. *Frontiers in Plant Science*, **3**(200):1–6.

Farnebäck, G. (2003) Two-frame motion estimation based on polynomial expansion. In *Proceedings of the 13th Scandinavian Conference on Image Analysis.*, pages 363–370. Springer, Berlin, Heidelberg.

Faust, J.E., Desai, T., Verma, A., Ulengin, I., Sun, T.L., Moss, T.J., Betancourt-Solis, M.A., Huang, H.W., Lee, T., and McNew, J.A. (2015) The Atlastin C-terminal tail is an amphipathic helix that perturbs the bilayer structure during endoplasmic reticulum homotypic fusion. *The Journal of Biological Chemistry*, **290**(8):4772–4783.

Fewell, S.W. and Brodsky, J.L. (2009) Entry into the endoplasmic reticulum: protein translocation, folding and quality control. In *Trafficking Inside Cells*, pages 119–142. Springer New York, New York, NY.

Fricker, M.D., Akita, D., Heaton, L.L., Jones, N., Obara, B., and Nakagaki, T. (2017) Automated analysis of Physarum network structure and dynamics. *Journal of Physics D: Applied Physics*, **50**(254005):1–14.

Friedman, J.R. and Voeltz, G.K. (2011) The ER in 3D: a multifunctional dynamic membrane network. *Trends in Cell Biology*, **21**(12):709–717.

Friml, J.J. and Jones, A.R. (2010) Endoplasmic reticulum: the rising compartment in auxin biology. *Plant Physiology*, **154**(2):458–462.

Fujii, T., Iwane, A.H., Yanagida, T., and Namba, K. (2010) Direct visualization of secondary structures of F-actin by electron cryomicroscopy. *Nature*, **467**(7316):724–728.

Galili, G. (2004) ER-derived compartments are formed by highly regulated processes and have special functions in plants. *Plant Physiology*, **136**:3411–3413.

Gibbon, B.C., Kovar, D.R., and Staiger, C.J. (1999) Latrunculin B has different effects on pollen germination and tube growth. *The Plant Cell*, **11**(12):2349–2363.

Gomez, L. and Chrispeels, M.J. (1993) Tonoplast and soluble vacuolar proteins are targeted by different mechanisms. *The Plant Cell Online*, **5**(9):1113–1124.

Grabski, S., De Feijter, A.W., and Schindler, M. (1993) Endoplasmic reticulum forms a dynamic continuum for lipid diffusion between contiguous soybean root cells. Technical report.

Grefen, C., Donald, N., Hashimoto, K., Kudla, J., Schumacher, K., and Blatt, M.R. (2010) A ubiquitin-10 promoter-based vector set for fluorescent protein tagging facilitates temporal stability and native protein distribution in transient and stable expression studies. *The Plant Journal*, **64**(2):355–365.

Griffing, L.R. (2018) Dancing with the stars: using image analysis to study the choreography of the endoplasmic reticulum and its partners and of movement within its tubules. In C. Hawes and V. Kriechbaumer, editors, *The Plant Endoplasmic Reticulum*, volume 1691, pages 75–102.

Griffing, L.R., Gao, H.T., and Sparkes, I. (2014) ER network dynamics are differentially controlled by myosins XI-K, XI-C, XI-E, XI-I, XI-1, and XI-2. *Frontiers in Plant Science*, **5**(218):1–12.

Griffing, L.R., Lin, C., Perico, C., White, R.R., and Sparkes, I. (2017) Plant ER geometry and dynamics: biophysical and cytoskeletal control during growth and biotic response. *Protoplasma*, **254**(1):43–56.

Groves, N.R., McKenna, J.F., Evans, D.E., Graumann, K., and Meier, I. (2019) A nuclear localization signal targets tail-anchored membrane proteins to the inner nuclear envelope in plants. *Journal of Cell Science*, **132**(7):1–14.

Hamada, T., Ueda, H., Kawase, T., and Hara-Nishimura, I. (2014) Microtubules contribute to tubule elongation and anchoring of endoplasmic reticulum, resulting in high network complexity in Arabidopsis. *Plant Physiology*, **166**(4):1869–1876.

Hardham, A.R., Jones, D.A., and Takemoto, D. (2007) Cytoskeleton and cell wall function in penetration resistance. *Current Opinion in Plant Biology*, **10**(4):342–348.

Hardham, A.R., Takemoto, D., and White, R.G. (2008) Rapid and dynamic subcellular reorganization following mechanical stimulation of Arabidopsis epidermal cells mimics responses to fungal and oomycete attack. *BMC Plant Biology*, **8**(63):1–14.

Harris, N. and Chrispeels, M.J. (1980) The endoplasmic reticulum of mung-bean cotyledons: Quantitative morphology of cisternal and tubular ER during seedling growth. *Planta*, **148**(3):293–303.

Hawes, C., Kiviniemi, P., and Kriechbaumer, V. (2015) The endoplasmic reticulum: A dynamic and well-connected organelle. *Journal of Integrative Plant Biology*, **57**(1):50–62.

Hawes, C., Saint-Jore, C., Martin, B., and Zheng, H.Q. (2001) ER confirmed as the location of mystery organelles in Arabidopsis plants expressing GFP!

Hawes, C., Wang, P., and Kriechbaumer, V. (2018a) Labeling the ER for light and fluorescence microscopy. In *The Plant Endoplasmic Reticulum*, pages 1–14.

Hawes, C., Wang, P., and Kriechbaumer, V. (2018b) Labeling the ER for light and fluorescence microscopy. In C. Hawes and V. Kriechbaumer, editors, *The Plant Endoplasmic Reticulum: Methods and Protocols*, pages 1–14.

He, K., Sun, J., and Tang, X. (2013) Guided Image Filtering. *IEEE Transactions on Pattern Analysis and Machine Intelligence*, **35**(6):1397–1409.

Hepler, P.K., Palevitz, B.A., Lancelle, S.A., McCauley, M.M., and Lichtschidl, L. (1990) Cortical endoplasmic reticulum in plants. *Journal of Cell Science*, **96**:355–373.

Holcman, D., Parutto, P., Chambers, J.E., Fantham, M., Young, L.J., Marciniak, S.J., Kaminski, C.F., Ron, D., and Avezov, E. (2018) Single particle trajectories reveal active endoplasmic reticulum luminal flow. *Nature Cell Biology*, **20**(10):1118–1125.

Holweg, C.L. (2007) Living markers for actin block myosin-dependent motility of plant organelles and auxin. *Cell Motility and the Cytoskeleton*, **64**(2):69–81.

Holwerda, B.C., Padgett, H.S., and Rogers, J.C. (1992) Proaleurain vacuolar targeting is mediated by short contiguous peptide interactions. *The Plant Cell Online*, **4**(3):307–318.

Hoppert, M. and Mayer, F. (1999) Principles of macromolecular organization and cell function in bacteria and archaea. *Cell Biochemistry and Biophysics*, **31**(3):247–284.

Horn, B.K. and Schunck, B.G. (1981) Determining optical flow. *Artificial Intelligence*, **17**(1-3):185–203.

Hu, J., Prinz, W.A., and Rapoport, T.A. (2011) Weaving the web of ER tubules. *Cell*, **147**(6):1226–1231.

Hu, J., Shibata, Y., Voss, C., Shemesh, T., Li, Z., Coughlin, M., Kozlov, M.M., Rapoport, T.A., and Prinz, W.A. (2008) Membrane proteins of the endoplasmic reticulum induce high-curvature tubules. *Science*, **319**(5867):1247–1250.

Hu, J., Shibata, Y., Zhu, P.P., Voss, C., Rismanchi, N., Prinz, W.A., Rapoport, T.A., and Blackstone, C. (2009) A class of dynamin-like GTPases involved in the generation of the tubular ER network. *Cell*, **138**(3):549–561.

Huff, J. (2015) The Airyscan detector from ZEISS: confocal imaging with improved signal-to-noise ratio and super-resolution. *Nature Methods*, **12**(12):1–2.

Hutten, S.J., Hamers, D.S., Aan den Toorn, M., van Esse, W., Nolles, A., Bücherl, C.A., de Vries, S.C., Hohlbein, J., and Borst, J.W. (2017) Visualization of BRI1 and SERK3/BAK1 Nanoclusters in Arabidopsis Roots. *PLoS ONE*, **12**(1):1–19.

Hwang, F.K., Richards, D.S., and Winter, P. (1992) *The Steiner tree problem*, volume 53.

Irons, S.L., Evans, D.E., and Brandizzi, F. (2003) The first 238 amino acids of the human lamin B receptor are targeted to the nuclear envelope in plants. *Journal of Experimental Botany*, **54**(384):943–950.

Ivakov, A. and Persson, S. (2013) Plant cell shape: modulators and measurements. *Frontiers in Plant Science*, **4**(439):1–13.

Jan, C.H., Williams, C.C., and Weissman, J.S. (2014) Principles of ER cotranslational translocation revealed by proximity-specific ribosome profiling. *Science*, **346**(6210):1–8.

Jarvela, T. and Linstedt, A.D. (2012) Irradiation-induced protein inactivation reveals Golgi enzyme cycling to cell periphery. *Journal of Cell Science*, **125**(4):973–980.

Jonkman, J. and Brown, C.M. (2015) Any way you slice it - a comparison of confocal microscopy techniques. *Journal of Biomolecular Techniques : JBT*, **26**(2):54–65.

Jozsef, L., Tashiro, K., Kuo, A., Park, E.J., Skoura, A., Albinsson, S., Rivera-Molina, F., Harrison, K.D., Iwakiri, Y., Toomre, D., and Sessa, W.C. (2014) Reticulon 4 is necessary for endoplasmic reticulum tubulation,

STIM1-Orai1 coupling, and store-operated calcium entry. *The Journal of Biological Chemistry*, **289**(13):9380–9395.

Kimura, K., Mamane, A., Sasaki, T., Sato, K., Takagi, J., Niwayama, R., Hufnagel, L., Shimamoto, Y., Joanny, J.F., Uchida, S., and Kimura, A. (2017) Endoplasmic-reticulum-mediated microtubule alignment governs cytoplasmic streaming. *Nature Cell Biology*, **19**(4):399–406.

Klopfenstein, D.R., Klumperman, J., Lustig, A., Kammerer, R.A., Oorschot, V., and Hauri, H.P. (2001) Subdomain-specific localization of CLIMP-63 (p63) in the endoplasmic reticulum is mediated by its luminal alpha-helical segment. *The Journal of Cell Biology*, **153**(6):1287–1300.

Kohno, K., Normington, K., Sambrook, J., Gething, M.J., and Mori, K. (1993) The promoter region of the yeast KAR2 (BiP) gene contains a regulatory domain that responds to the presence of unfolded proteins in the endoplasmic reticulum. *Molecular and Cellular Biology*, **13**(2):877–890.

Konopka, C.A. and Bednarek, S.Y. (2008) Variable-angle epifluorescence microscopy: a new way to look at protein dynamics in the plant cell cortex. *The Plant Journal*, **53**(1):186–196.

Krendel, M. and Mooseker, M.S. (2005) Myosins: tails (and heads) of functional diversity. *Physiology*, **20**(4):239–251.

Kriechbaumer, V., Botchway, S.W., and Hawes, C. (2016) Localization and interactions between Arabidopsis auxin biosynthetic enzymes in the TAA/YUC-dependent pathway. *Journal of Experimental Botany*, **67**(14):4195–4207.

Kriechbaumer, V., Breeze, E., Pain, C., Tolmie, F., Frigerio, L., and Hawes, C.

(2018) Arabidopsis Lunapark proteins are involved in ER cisternae formation. *New Phytologist*, **219**(3):990–1004.

Kucik, D.F., Elson, E.L., and Sheetz, M.P. (1999) Weak dependence of mobility of membrane protein aggregates on aggregate size supports a viscous model of retardation of diffusion. *Biophysical Journal*, **76**(1):314–322.

Kunze, I., Hillmer, S., Kunze, G., and Klaus, M. (1995) Brefeldin A differentially affects protein secretion from suspension-cultured tobacco cells (Nicotiana tabacum L.). *Journal of Plant Physiology*, **146**(1-2):71–80.

Langhans, M., Meckel, T., Kress, A., Lerich, A., and Robinson, D.G. (2012) ERES (ER exit sites) and the âĂIJSecretory Unit ConceptâĂİ. *Journal of Microscopy*, **247**(1):48–59.

Langhans, M., Niemes, S., Pimpl, P., and Robinson, D.G. (2009) Oryzalin bodies: in addition to its anti-microtubule properties, the dinitroaniline herbicide oryzalin causes nodulation of the endoplasmic reticulum. *Protoplasma*, **236**:73–84.

Laursen, T., Borch, J., Knudsen, C., Bavishi, K., Torta, F., Martens, H.J., Silvestro, D., Hatzakis, N.S., Wenk, M.R., Dafforn, T.R., Olsen, C.E., Motawia, M.S., Hamberger, B., Møller, B.L., and Bassard, J.E. (2016) Characterization of a dynamic metabolon producing the defense compound dhurrin in sorghum. *Science*, **354**(6314):890–893.

Lee, H., Sparkes, I., Gattolin, S., Dzimitrowicz, N., Roberts, L.M., Hawes, C., and Frigerio, L. (2013) An Arabidopsis reticulon and the atlastin homologue RHD3-like2 act together in shaping the tubular endoplasmic reticulum. *New Phytologist*, **197**(2):481–489.

Lemarchand, L., Euler, R., Lin, C., and Sparkes, I. (2014) Modeling the geometry

of the endoplasmic reticulum network. In *Algorithms for Computational Biology*, pages 131–145. Springer, Cham.

Lev, S., Halevy, D.B., Peretti, D., and Dahan, N. (2008) The VAP protein family: from cellular functions to motor neuron disease. *Trends in Cell Biology*, **18**(6):282–290.

Lewis, M.J., Sweet, D.J., and Pelham, H.R. (1990) The ERD2 gene determines the specificity of the luminal ER protein retention system. *Cell*, **61**(7):1359–1363.

Lin, C., Lemarchand, L., Euler, R., and Sparkes, I.A. (2015) Modeling the geometry and dynamics of the Endoplasmic Reticulum network. *IEEE/ACM Transactions on Computational Biology and Bioinformatics*, **15**(2):1545–5963.

Lin, C., White, R.R., Sparkes, I.A., and Ashwin, P. (2017) Modeling endoplasmic reticulum network maintenance in a plant cells. *Biophysical Journal*, **113**(1):214–222.

Lin, C., Zhang, Y., Sparkes, I., and Ashwin, P. (2014) Structure and dynamics of ER: minimal networks and biophysical constraints. *Biophysical Journal*, **107**(3):763–772.

Lin, S., Sun, S., and Hu, J. (2012) Molecular basis for sculpting the endoplasmic reticulum membrane. *The International Journal of Biochemistry and Cell Biology*, **44**(9):1436–1443.

Liu, T.Y., Bian, X., Sun, S., Hu, X., Klemm, R.W., Prinz, W.A., Rapoport, T.A., and Hu, J. (2012) Lipid interaction of the C terminus and association of the transmembrane segments facilitate atlastin-mediated homotypic endoplasmic reticulum fusion. *Proceedings of the National Academy of Sciences*, **109**(32):2146–2154.

Lucas, B.D. and Kanade, T. (1981) An iterative image registration technique with an application to stereo vision.

Malerba, M., Crosti, P., and Cerana, R. (2010) Effect of heat stress on actin cytoskeleton and endoplasmic reticulum of tobacco BY-2 cultured cells and its inhibition by Co2+. *Protoplasma*, **239**:23–30.

Martiniere, A., Lavagi, I., Nageswaran, G., Rolfe, D.J., Maneta-Peyret, L., Luu, D.T., Botchway, S.W., Webb, S.E.D., Mongrand, S., Maurel, C., Martin-Fernandez, M.L., Kleine-Vehn, J., Friml, J., Moreau, P., and Runions, J. (2012) Cell wall constrains lateral diffusion of plant plasma-membrane proteins. *Proceedings of the National Academy of Sciences*, **109**(31):12,805–12,810.

Matsushima, R., Hayashi, Y., Kondo, M., Shimada, T., Nishimura, M., and Hara-Nishimura, I. (2002) An endoplasmic reticulum-derived structure that is induced under stress conditions in Arabidopsis. *Plant Physiology*, **130**(4):1807–1814.

McKenna, J.F., Rolfe, D.J., Webb, S.E.D., Tolmie, A.F., Botchway, S.W., Martin-Fernandez, M.L., Hawes, C., and Runions, J. (2019) The cell wall regulates dynamics and size of plasma-membrane nanodomains in Arabidopsis. *Proceedings of the National Academy of Sciences of the United States of America*, **116**(26):12,857–12,862.

McKinney, S.A., Murphy, C.S., Hazelwood, K.L., Davidson, M.W., and Looger, L.L. (2009) A bright and photostable photoconvertible fluorescent protein. *Nature Methods*, **6**(2):131–133.

Melak, M., Plessner, M., and Grosse, R. (2017) Actin visualization at a glance. *Journal of Cell Science*, **130**(3):525–530.

Moriya, K., Nagatoshi, K., Noriyasu, Y., Okamura, T., Takamitsu, E., Suzuki,

T., and Utsumi, T. (2013) Protein N-myristoylation plays a critical role in the endoplasmic reticulum morphological change induced by overexpression of protein lunapark, an integral membrane protein of the endoplasmic reticulum. *PLoS ONE*, **8**(11):1–13.

Moss, T.J., Andreazza, C., Verma, A., Daga, A., and McNew, J.A. (2011) Membrane fusion by the GTPase atlastin requires a conserved C-terminal cytoplasmic tail and dimerization through the middle domain. *Proceedings of the National Academy of Sciences of the United States of America*, **108**(27):11,133–11,138.

Nakano, R.T., Matsushima, R., Ueda, H., Tamura, K., Shimada, T., Li, L., Hayashi, Y., Kondo, M., Nishimura, M., and Hara-Nishimura, I. (2009) GNOM-LIKE1/ERMO1 and SEC24a/ERMO2 are required for maintenance of endoplasmic reticulum morphology in Arabidopsis thaliana. *The Plant Cell*, **21**(11):3672–3685.

Napier, R., Fowke, L., Hawes, C., Lewis, M., and Pelham, H. (1992) Immunological evidence that plants use both HDEL and KDEL for targeting proteins to the endoplasmic reticulum. *Journal of Cell Science*, **102**(2):261–271.

Nixon-Abell, J., Obara, C.J., Weigel, A.V., Li, D., Legant, W.R., Xu, C.S., Pasolli, H.A., Harvey, K., Hess, H.F., Betzig, E., Blackstone, C., and Lippincott-Schwartz, J. (2016) Increased spatiotemporal resolution reveals highly dynamic dense tubular matrices in the peripheral ER. *Science*, **354**(6311):433–445.

Nziengui, H. and Schoefs, B. (2009) Functions of reticulons in plants: What we can learn from animals and yeasts. *Cellular and Molecular Life Sciences*, **66**(4):584–595.

Obara, B., Grau, V., and Fricker, M.D. (2012) A bioimage informatics

approach to automatically extract complex fungal networks. *Bioinformatics*, **28**(18):2374–2381.

Oda, T., Iwasa, M., Aihara, T., Maéda, Y., and Narita, A. (2009) The nature of the globular- to fibrous-actin transition. *Nature*, **457**(7228):441–445.

Oertle, T., Klinger, M., Stuermer, C.A.O., and Schwab, M.E. (2003) A reticular rhapsody: phylogenic evolution and nomenclature of the RTN/Nogo gene family. *FASEB journal : official publication of the Federation of American Societies for Experimental Biology*, **17**(10):1238–47.

Ohlrogge, J. and Browse, J. (1995) Lipid biosynthesis. *The Plant Cell*, **7**(7):957–70.

Ojangu, E.L., Tanner, K., Pata, P., Järve, K., Holweg, C.L., Truve, E., and Paves, H. (2012) Myosins XI-K, XI-1, and XI-2 are required for development of pavement cells, trichomes, and stigmatic papillae in Arabidopsis. *BMC Plant Biology*, **12**(81):1–16.

Opalski, K.S., Schultheiss, H., Kogel, K.H., and Hückelhoven, R. (2004) The receptor-like MLO protein and the RAC/ROP family G-protein RACB modulate actin reorganization in barley attacked by the biotrophic powdery mildew fungus Blumeria graminis f.sp. hordei. *The Plant Journal*, **41**(2):291–303.

Opas, M., Dziak, E., Fliegel, L., and Michalak, M. (1991) Regulation of expression and intracellular distribution of calreticulin, a major calcium binding protein of nonmuscle cells. *Journal of Cellular Physiology*, **149**(1):160–171.

Orso, G., Pendin, D., Liu, S., Tosetto, J., Moss, T.J., Faust, J.E., Micaroni, M., Egorova, A., Martinuzzi, A., McNew, J.A., and Daga, A. (2009) Homotypic fusion of ER membranes requires the dynamin-like GTPase Atlastin. *Nature*, **460**(7258):978–983.

Otsu, N. (1979) A threshold selection method from gray-level histograms. *IEEE Transactions on Systems, Man and Cybernetics*, **9**(1):62–66.

Pain, C., Kriechbaumer, V., Kittelmann, M., Hawes, C., and Fricker, M. (2019) Quantitative analysis of plant ER architecture and dynamics. *Nature Communications*, **10**(984):1–15.

Patterson, G.H. and Lippincott-Schwartz, J. (2002) A photoactivatable GFP for selective photolabeling of proteins and cells. *Science*, **297**(5588):1873–7.

Pelham, H.R. (1988) Evidence that luminal ER proteins are sorted from secreted proteins in a post-ER compartment. *The EMBO Journal*, **7**(4):913–8.

Peremyslov, V.V., Mockler, T.C., Filichkin, S.A., Fox, S.E., Jaiswal, P., Makarova, K.S., Koonin, E.V., and Dolja, V.V. (2011) Expression, splicing, and evolution of the myosin gene family in plants. *Plant Physiology*, **155**(3):1191–1204.

Peremyslov, V.V., Prokhnevsky, A.I., Avisar, D., and Dolja, V.V. (2008) Two class XI myosins function in organelle trafficking and root hair development in Arabidopsis. *Plant Physiology*, **146**(3):1109–1116.

Peremyslov, V.V., Prokhnevsky, A.I., and Dolja, V.V. (2010) Class XI myosins are required for development, cell expansion, and F-actin organization in arabidopsis. *The Plant Cell*, **22**(6):1883–1897.

Platre, M.P., Bayle, V., Armengot, L., Bareille, J., Marquès-Bueno, M.D.M., Creff, A., Maneta-Peyret, L., Fiche, J.B., Nollmann, M., Miège, C., Moreau, P., Martinière, A., and Jaillais, Y. (2019) Developmental control of plant Rho GTPase nano-organization by the lipid phosphatidylserine. *Science*, **364**(6435):57–62.

Pöhlker, C., Huffman, J.A., and Pöschl, U. (2012) Autofluorescence of atmospheric

bioaerosols âĂŞ fluorescent biomolecules and potential interferences. *Atmospheric Measurement Techniques*, **5**(1):37–71.

Porter, K.R. and Machado, R.D. (1960) Studies on the endoplasmic reticulum. *The Journal of Cell Biology*, **7**(1):167–210.

Prokhnevsky, A.I., Peremyslov, V.V., and Dolja, V.V. (2008) Overlapping functions of the four class XI myosins in Arabidopsis growth, root hair elongation, and organelle motility. *Proceedings of the National Academy of Sciences of the United States of America*, **105**(50):19,744–19,749.

Pyysalo, J. (2017) Proto-Indo-European lexicon: the generative etymological dictionary of Indo-European languages. In *Proceedings of the 21st Nordic Conference of Computational Linguistics*, pages 259–262. Gothenburg.

Quader, H. and Fast, H. (1990) Influence of cytosolic pH changes on the organisation of the endoplasmic reticulum in epidermal cells of onion bulb scales: Acidification by loading with weak organic acids. *Protoplasma*, **157**(1-3):216–224.

Quader, H., Hofmann, A., and Schnepf, E. (1989) Reorganization of the endoplasmic reticulum in epidermal cells of onion bulb scales after cold stress: Involvement of cytoskeletal elements. *Planta*, **177**(2):273–280.

Quirin, S., Pavani, S.R.P., and Piestun, R. (2012) Optimal 3D single-molecule localization for superresolution microscopy with aberrations and engineered point spread functions. *Proceedings of the National Academy of Sciences of the United States of America*, **109**(3):675–679.

Ram, S., Kim, D., Ober, R.J., and Ward, E.S. (2012) 3D single molecule tracking with multifocal plane microscopy reveals rapid intercellular transferrin transport at epithelial cell barriers. *Biophysical Journal*, **103**(7):1594–1603.

Rapoport, T.A. (2007) Protein translocation across the eukaryotic endoplasmic reticulum and bacterial plasma membranes. *Nature*, **450**(7170):663–669.

Raz, V. and Fluhr, R. (1992) Calcium requirement for ethylene-dependent responses. *The Plant Cell*, **4**(9):1123–1130.

Reddy, A.S. and Day, I.S. (2001) Analysis of the myosins encoded in the recently completed Arabidopsis thaliana genome sequence. *Genome Biology*, **2**(7):1–17.

Renna, L., Hanton, S.L., Stefano, G., Bortolotti, L., Misra, V., and Brandizzi, F. (2005) Identification and characterization of AtCASP, a plant transmembrane Golgi matrix protein. *Plant Molecular Biology*, **58**:109–122.

Ridge, R.W., Uozumi, Y., Plazinski, J., Hurley, U.A., and Williamson, R.E. (1999) Developmental transitions and dynamics of the coritical ER of arabidopsis cells seen with green fluorescent protein. *Plant and Cell Physiology*, **40**(12):1253–1261.

Riedl, J., Crevenna, A.H., Kessenbrock, K., Yu, J.H., Neukirchen, D., Bista, M., Bradke, F., Jenne, D., Holak, T.A., Werb, Z., Sixt, M., and Wedlich-Soldner, R. (2008) Lifeact: a versatile marker to visualize F-actin. *Nature Methods*, **5**(7):605–607.

Rocchetti, A., Hawes, C., and Kriechbaumer, V. (2014) Fluorescent labelling of the actin cytoskeleton in plants using a cameloid antibody. *Plant Methods*, **10**(12):1–8.

Roshchina, V. and Karnaukhov, V. (1999) Changes in pollen autofluorescence induced by ozone. *Biologia Plantarum*, **42**(2):273–278.

Runions, J., Brach, T., Kühner, S., and Hawes, C. (2006) Photoactivation of GFP reveals protein dynamics within the endoplasmic reticulum membrane. *Journal of experimental botany*, **57**(1):43–50.

Rutten, T.L. and Knuiman, B. (1993) Brefeldin A effects on tobacco pollen tubes. *European Journal of Cell Biology*, **61**(2):247–55.

Samaj, J., Müller, J., Beck, M., Böhm, N., and Menzel, D. (2006) Vesicular trafficking, cytoskeleton and signalling in root hairs and pollen tubes. *Trends in Plant Science*, **11**(12):594–600.

Sandoz, P. and van der Goot, F. (2015) How many lives does CLIMP-63 have? *Biochemical Society Transactions*, **43**(2):222–228.

Santi, P.A. (2011) Light sheet fluorescence microscopy: a review. *The journal of Histochemistry and Cytochemistry : Official Journal of the Histochemistry Society*, **59**(2):129–138.

Satiat-Jeunemaitre, B., Cole, L., Bourett, T., Howard, R., and Hawes, C. (1996) Brefeldin A effects in plant and fungal cells: something new about vesicle trafficking? *Journal of Microscopy*, **181**(2):162–177.

Schindelin, J., Arganda-Carreras, I., Frise, E., Kaynig, V., Longair, M., Pietzsch, T., Preibisch, S., Rueden, C., Saalfeld, S., Schmid, B., Tinevez, J.Y., White, D.J., Hartenstein, V., Eliceiri, K., Tomancak, P., and Cardona, A. (2012) Fiji: an open-source platform for biological-image analysis. *Nature Methods*, **9**(7):676–682.

Schindler, T., Bergfeld, R., Hohl, M., and Schopfer, P. (1994) Inhibition of Golgi-apparatus function by brefeldin A in maize coleoptiles and its consequences on auxin-mediated growth, cell-wall extensibility and secretion of cell-wall proteins. *Planta*, **192**(3):404–413.

Schoberer, J., König, J., Veit, C., Vavra, U., Liebminger, E., Botchway, S.W., Altmann, F., Kriechbaumer, V., Hawes, C., and Strasser, R. (2019) A signal

motif retains Arabidopsis ER-α-mannosidase I in the cis-Golgi and prevents enhanced glycoprotein ERAD. *Nature Communications*, **10**(3701):1–15.

Schroeder, L.K., Barentine, A.E., Merta, H., Schweighofer, S., Zhang, Y., Baddeley, D., Bewersdorf, J., and Bahmanyar, S. (2019) Dynamic nanoscale morphology of the ER surveyed by STED microscopy. *The Journal of Cell Biology*, **218**(1):83–96.

Schwarzländer, M., Fricker, M., Müller, C., Marty MARTY, L., Brach, T., Novak, J., Sweetlove, L., Hell, R., and Meyer, A. (2008) Confocal imaging of glutathione redox potential in living plant cells. *Journal of Microscopy*, **231**(2):299–316.

Sheludko, Y.V. (2008) Agrobacterium-mediated transient expression as an approach to production of recombinant Proteins in Plants. *Recent Patents on Biotechnology*, **2**:198–208.

Shemesh, T., Klemm, R.W., Romano, F.B., Wang, S., Vaughan, J., Zhuang, X., Tukachinsky, H., Kozlov, M.M., and Rapoport, T.A. (2014) A model for the generation and interconversion of ER morphologies. *Proceedings of the National Academy of Sciences of the United States of America*, **111**(49):5243–5251.

Shibata, Y., Shemesh, T., Prinz, W.A., Palazzo, A.F., Kozlov, M.M., and Rapoport, T.A. (2010) Mechanisms determining the morphology of the peripheral ER. *Cell*, **143**(5):774–88.

Shibata, Y., Voeltz, G.K., and Rapoport, T.A. (2006) Rough sheets and smooth tubules. *Cell*, **126**(3):435–439.

Siao, W., Wang, P., Voigt, B., Hussey, P.J., and Baluska, F. (2016) Arabidopsis SYT1 maintains stability of cortical endoplasmic reticulum networks and VAP27-1-enriched endoplasmic reticulum-plasma membrane contact sites. *Journal of Experimental Botany*, **67**(21):6161–6171.

Silva-Alvim, F.A., An, J., Alvim, J.C., Foresti, O., Grippa, A., Pelgrom, A., Adams, T.L., Hawes, C., and Denecke, J. (2018) Predominant Golgi residency of the plant K/HDEL receptor is essential for its function in mediating ER retention. *The Plant Cell*, **30**:2174–2196.

Simons, J.F., Ferro-Novick, S., Rose, M.D., and Helenius, A. (1995) BiP/Kar2p serves as a molecular chaperone during carboxypeptidase Y folding in yeast. *The Journal of Cell Biology*, **130**(1):41–49.

Smith, I.F., Swaminathan, D., Dickinson, G.D., and Parker, I. (2014) Single-molecule tracking of inositol trisphosphate receptors reveals different motilities and distributions. *Biophysical Journal*, **107**(4):834–845.

Sokolov, P., Belousov, M., Bondarev, S., Zhouravleva, G., and Kasyanenko, N. (2017) FibrilJ: ImageJ plugin for fibrils' diameter and persistence length determination. *Computer Physics Communications*, **214**:199–206.

Sparkes, I., Runions, J., Hawes, C., and Griffing, L. (2009a) Movement and remodeling of the endoplasmic reticulum in nondividing cells of tobacco leaves. *The Plant Cell*, **21**(12):3937–3949.

Sparkes, I.A., Hawes, C., and Baker, A. (2005) AtPEX2 and AtPEX10 are targeted to peroxisomes independently of known endoplasmic reticulum trafficking routes. *Plant Physiology*, **139**(2):690–700.

Sparkes, I.A., Ketelaar, T., De Ruijter, N.C.A., and Hawes, C. (2009b) Grab a golgi: Laser trapping of golgi bodies reveals in vivo interactions with the endoplasmic reticulum. *Traffic*, **10**(5):567–571.

Sparkes, I.A., Runions, J., Kearns, A., and Hawes, C. (2006) Rapid, transient expression of fluorescent fusion proteins in tobacco plants and generation of stably transformed plants. *Nature Protocols*, **1**(4):2019–2025.

Sparkes, I.A., Teanby, N.A., and Hawes, C. (2008) Truncated myosin XI tail fusions inhibit peroxisome, Golgi, and mitochondrial movement in tobacco leaf epidermal cells: A genetic tool for the next generation. *Journal of Experimental Botany*, **59**(9):2499–2512.

Sparkes, I.A., Tolley, N., Aller, I., Svozil, J., Osterrieder, A., Botchway, S., Mueller, C., Frigerio, L., and Hawes, C. (2010) Five Arabidopsis reticulon isoforms share endoplasmic reticulum location, topology, and membrane-shaping properties. *The Plant Cell*, **22**(4):1333–1343.

Spector, I., Shochet, N.R., Kashman, Y., and Groweiss, A. (1983) Latrunculins: novel marine toxins that disrupt microfilament organization in cultured cells. *Science*, **219**(4584):493–495.

Spitz, F., Gonzalez, F., and Duboule, D. (2003) A global control region defines a chromosomal regulatory landscape containing the HoxD cluster. *Cell*, **113**(3):405–417.

Sporsheim, B., Øverby, A., Bones, A., Sporsheim, B., Øverby, A., and Bones, A.M. (2015) Allyl isothiocyanate inhibits actin-dependent intracellular transport in Arabidopsis thaliana. *International Journal of Molecular Sciences*, **16**(12):29,134–29,147.

Srere, P.A. (1987) Complexes of sequential metabolic enzymes. *Annual Review of Biochemistry*, **56**(1):89–124.

Staehelin, L.A. and Driouich, A. (1997) Brefeldin A effects in plants' are different Golgi responses caused by different sites of action? *Plant Physiology*, **114**:401–403.

Stefan, C.J., Manford, A.G., and Emr, S.D. (2013) ERâĂŞPM connections: sites

of information transfer and inter-organelle communication. *Current Opinion in Cell Biology*, **25**(4):434–442.

Stefano, G., Renna, L., Moss, T., McNew, J.A., and Brandizzi, F. (2012) In Arabidopsis, the spatial and dynamic organization of the endoplasmic reticulum and Golgi apparatus is influenced by the integrity of the C-terminal domain of RHD3, a non-essential GTPase. *The Plant Journal*, **69**(6):957–966.

Stephenson, J.L.M. and Hawes, C.R. (1986) Stereology and stereometry of endoplasmic reticulum during differentiation in the maize root cap. *Protoplasma*, **131**(1):32–46.

Szafrańska, K., Glińska, S., and Janas, K.M. (2013) Ameliorative effect of melatonin on meristematic cells of chilled and re-warmed Vigna radiata roots. *Biologia Plantarum*, **57**(1):91–96.

Takemoto, D., Jones, D.A., and Hardham, A.R. (2003) GFP-tagging of cell components reveals the dynamics of subcellular re-organization in response to infection of Arabidopsis by oomycete pathogens. *The Plant Journal*, **33**(4):775–792.

Terasaki, M. and Reese, T.S. (1992) Characterization of endoplasmic reticulum by co-localization of BiP and dicarbocyanine dyes. Technical report.

Terasaki, M., Shemesh, T., Kasthuri, N., Klemm, R.W., Schalek, R., Hayworth, K.J., Hand, A.R., Yankova, M., Huber, G., Lichtman, J.W., Rapoport, T.A., and Kozlov, M.M. (2013) Stacked endoplasmic reticulum sheets are connected by helicoidal membrane motifs. *Cell*, **154**(2):285–296.

Tinevez, J.Y., Perry, N., Schindelin, J., Hoopes, G.M., Reynolds, G.D., Laplantine, E., Bednarek, S.Y., Shorte, S.L., and Eliceiri, K.W. (2017) TrackMate: An open and extensible platform for single-particle tracking. *Methods*, **115**:80–90.

Tolley, N., Sparkes, I.A., Craddock, C.P., Eastmond, P.J., Runions, J., Hawes, C., and Frigerio, L. (2010) Transmembrane domain length is responsible for the ability of a plant reticulon to shape endoplasmic reticulum tubules in vivo. *The Plant Journal*, **64**(3):411–418.

Tolley, N., Sparkes, I.A., Hunter, P.R., Craddock, C.P., Nuttall, J., Roberts, L.M., Hawes, C., Pedrazzini, E., and Frigerio, L. (2008) Overexpression of a plant reticulon remodels the lumen of the cortical endoplasmic reticulum but does not perturb protein transport. *Traffic*, **9**(1):94–102.

Toufighi, K., Brady, S.M., Austin, R., Ly, E., and Provart, N.J. (2005) The botany array resource: e-northerns, expression angling, and promoter analyses. *The Plant Journal*, **43**(1):153–163.

Travers, K.J., Patil, C.K., Wodicka, L., Lockhart, D.J., Weissman, J.S., and Walter, P. (2000) Functional and genomic analyses reveal an essential coordination between the unfolded protein response and ER-associated degradation. *Cell*, **101**(3):249–258.

Ueda, H., Ohta, N., Kimori, Y., Uchida, T., Shimada, T., Tamura, K., and Hara-Nishimura, I. (2018) Endoplasmic reticulum (ER) membrane proteins (LUNAPARKs) are required for proper configuration of the cortical ER network in plant cells. *Plant and Cell Physiology*, **59**(10):1931–1941.

Ueda, H., Yokota, E., Kutsuna, N., Shimada, T., Tamura, K., Shimmen, T., Hasezawa, S., Dolja, V.V., and Hara-Nishimura, I. (2010) Myosin-dependent endoplasmic reticulum motility and F-actin organization in plant cells. *Proceedings of the National Academy of Sciences of the United States of America*, **107**(15):6894–6899.

Ueda, K., Matsuyama, T., and Hashimoto, T. (1999) Visualization of microtubules in living cells of transgenic Arabidopsis thaliana. *Protoplasma*, **206**(1-3):201–206.

van der Honing, H.S., van Bezouwen, L.S., Emons, A.M.C., and Ketelaar, T. (2011) High expression of Lifeact in Arabidopsis thaliana reduces dynamic reorganization of actin filaments but does not affect plant development. *Cytoskeleton*, **68**(10):578–587.

van der Zand, A., Gent, J., Braakman, I., Tabak, H.F., Rakwalska, M., Schmitt, H., Schwappach, B., Weissman, J., and Kunau, W. (2012) Biochemically distinct vesicles from the endoplasmic reticulum fuse to form peroxisomes. *Cell*, **149**(2):397–409.

Visegrády, B., LÅŚrinczy, D., Hild, G., Somogyi, B., and Nyitrai, M. (2004) The effect of phalloidin and jasplakinolide on the flexibility and thermal stability of actin filaments. *FEBS Letters*, **565**(1-3):163–166.

Vitha, S. and Osteryoung, K.W. (2011) *Immunofluorescence microscopy for localization of arabidopsis chloroplast proteins*, volume 774.

Voigt, B., Timmers, A.C., Šamaj, J., Müller, J., Baluška, F., and Menzel, D. (2005) GFP-FABD2 fusion construct allows in vivo visualization of the dynamic actin cytoskeleton in all cells of Arabidopsis seedlings. *European Journal of Cell Biology*, **84**(6):595–608.

Volkmann, D. (1976) In cress roots (Lepidium sativum L.), abscisic acid prevents the development of the central cap cells into statocytes. *Planta*, **130**(1):89–91.

Walter, P., Ibrahimi, I., and Blobel, G. (1981) Translocation of proteins across the endoplasmic reticulum. I. Signal recognition protein (SRP) binds to in-vitro-assembled polysomes synthesizing secretory protein. *The Journal of Cell Biology*, **91**(2):545–50.

Wan, Y., Ash, W.M., Fan, L., Hao, H., Kim, M.K., and Lin, J. (2011) Variable-angle

total internal reflection fluorescence microscopy of intact cells of Arabidopsis thaliana. *Plant Methods*, **7**(27):1–7.

Wang, G., Wang, F., Wang, G., Wang, F., Zhang, X., Zhong, M., Zhang, J., Lin, D., Tang, Y., Xu, Z., and Song, R. (2012) Opaque1 encodes a myosin XI motor protein that is required for endoplasmic reticulum motility and protein body formation in maize endosperm. *The Plant Cell*, **24**(8):3447–3462.

Wang, P., Hawkins, T.J., Richardson, C., Cummins, I., Deeks, M.J., Sparkes, I., Hawes, C., and Hussey, P.J. (2014) The plant cytoskeleton, NET3C, and VAP27 mediate the link between the plasma membrane and endoplasmic reticulum. *Current Biology*, **24**(12):1397–1405.

Wang, P. and Hussey, P.J. (2017) NETWORKED 3B: a novel protein in the actin cytoskeleton-endoplasmic reticulum interaction. *Journal of Experimental Botany*, **68**(7):1441–1450.

Wang, P. and Hussey, P.J. (2019) Plant ER-PM contact sites in endocytosis and autophagy: does the local composition of membrane phospholipid play a role? *Frontiers in Plant Science*, **10**(23):1–5.

Wang, P., Richardson, C., Hawes, C., and Hussey, P.J. (2016a) Arabidopsis NAP1 regulates the formation of autophagosomes. *Current Biology*, **26**:2060–2069.

Wang, P., Richardson, C., Hawkins, T., Sparkes, I., Hawes, C., and Hussey, P. (2016b) Plant VAP27 proteins: domain characterization, intracellular localization and role in plant development. *New Phytologist*, **210**(4):1311–1326.

Wang, S., Powers, R.E., Gold, V.A., and Rapoport, T.A. (2018) The ER morphology-regulating lunapark protein induces the formation of stacked bilayer discs. *Life Science Alliance*, **1**(1):1–11.

Wang, S., Tukachinsky, H., Romano, F.B., and Rapoport, T.A. (2016c) Cooperation of the ER-shaping proteins atlastin, lunapark, and reticulons to generate a tubular membrane network. *eLife*, **5**:209–217.

Watanabe, W., Shimada, T., Matsunaga, S., Kurihara, D., Fukui, K., Arimura, S.i., Tsutsumi, N., Isobe, K., and Itoh, K. (2007) Single-organelle tracking by two-photon conversion. *Optics Express*, **15**(5):2490–2498.

Wehland, J., Osborn, M., and Weber, K. (1977) Phalloidin-induced actin polymerization in the cytoplasm of cultured cells interferes with cell locomotion and growth. *Proceedings of the National Academy of Sciences of the United States of America*, **74**(12):5613–5617.

West, M., Zurek, N., Hoenger, A., and Voeltz, G.K. (2011) A 3D analysis of yeast ER structure reveals how ER domains are organized by membrane curvature. *The Journal of Cell Biology*, **193**(2):333–346.

Westrate, L., Lee, J., Prinz, W., and Voeltz, G. (2015) Form follows function: the importance of endoplasmic reticulum shape. *Annual Review of Biochemistry*, **84**(1):791–811.

Wiedenmann, J., Ivanchenko, S., Oswald, F., Schmitt, F., Röcker, C., Salih, A., Spindler, K.D., and Nienhaus, G.U. (2004) EosFP, a fluorescent marker protein with UV-inducible green-to-red fluorescence conversion. *Proceedings of the National Academy of Sciences of the United States of America*, **101**(45):15,905–15,910.

Wilson, C., Lee, M.D., Heathcote, H.R., Zhang, X., Buckley, C., Girkin, J.M., Saunter, C.D., and McCarron, J.G. (2019) Mitochondrial ATP production provides long-range control of endothelial inositol trisphosphate-evoked calcium signaling. *The Journal of Biological Chemistry*, **294**(3):737–758.

Wilson, R.S., Yang, L., Dun, A., Smyth, A.M., Duncan, R.R., Rickman, C., and Lu, W. (2016) Automated single particle detection and tracking for large microscopy datasets. *Royal Society Open Science*, **3**(160225):1–13.

Winter, D., Vinegar, B., Nahal, H., Ammar, R., Wilson, G.V., and Provart, N.J. (2007) An 'Electronic Fluorescent Pictograph' browser for exploring and analyzing large-scale biological data sets. *PLoS ONE*, **2**(8):1–12.

Wu, Y., Whiteus, C., Xu, C.S., Hayworth, K.J., Weinberg, R.J., Hess, H.F., and De Camilli, P. (2017) Contacts between the endoplasmic reticulum and other membranes in neurons. *Proceedings of the National Academy of Sciences of the United States of America*, **114**(24):4859–4867.

Yang, Y.S. and Strittmatter, S.M. (2007) The reticulons: a family of proteins with diverse functions. *Genome Biology*, **8**(12):234–244.

Zhang, B., Zerubia, J., and Olivo-Marin, J.C. (2007) Gaussian approximations of fluorescence microscope point-spread function models. *Applied Optics*, **46**(10):1819–1829.

Zhang, C., Kotchoni, S.O., Samuels, A.L., and Szymanski, D.B. (2010) SPIKE1 signals originate from and assemble specialized domains of the endoplasmic reticulum. *Current Biology*, **20**(23):2144–2149.

Zhang, C., Mallery, E., Reagan, S., Boyko, V.P., Kotchoni, S.O., and Szymanski, D.B. (2013) The endoplasmic reticulum is a reservoir for WAVE/SCAR regulatory complex signaling in the Arabidopsis leaf. *Plant Physiology*, **162**(2):689–706.

Zheng, H. and Chen, J. (2011) Emerging aspects of ER organization in root hair tip growth: lessons from RHD3 and Atlastin. *Plant Signaling & Behavior*, **6**(11):1710–1713.

Zheng, H., Kunst, L., Hawes, C., and Moore, I. (2004) A GFP-based assay reveals a role for RHD3 in transport between the endoplasmic reticulum and Golgi apparatus. *The Plant Journal*, **37**(3):398–414.

Zimmerberg, J. and Kozlov, M.M. (2006) How proteins produce cellular membrane curvature. *Nature reviews. Molecular cell biology*, **7**(1):9–19.